Edited by
Philippe Grelu

Nonlinear Optical Cavity Dynamics

Related Titles

Ferreira, M.F.

Nonlinear Effects in Optical Fibers

2011
Print ISBN: 978-0-470-46466-3

Agrawal, G.P.

Fiber-Optic Communication Systems 4e w/CD

4th Edition
2010
Print ISBN: 978-0-470-50511-3

Buck, J.A.

Fundamentals of Optical Fibers, Second Edition

2nd Edition
2004
Print ISBN: 978-0-471-22191-3

Saleh, B.E., Teich, M.C.

Fundamentals of Photonics

2nd Edition
2007
Print ISBN: 978-0-471-83965-1

Stegeman, G.I., Stegeman, R.F.

Nonlinear Optics

Phenomena, Materials, and Devices

2012
Print ISBN: 978-1-118-07272-1

Handbook of Chaos Control

2nd Edition
2008
Print ISBN: 978-3-527-40605-0

Paschotta, R.

Encyclopedia of Laser Physics and Technology

2008
Print ISBN: 978-3-527-40828-3

Uchida, A.

Optical Communication with Chaotic Lasers

Applications of Nonlinear Dynamics and Synchronization

2012
Print ISBN: 978-3-527-40869-6

Mandel, P.

Nonlinear Optics

An Analytical Approach

2010
Print ISBN: 978-3-527-40923-5

Diels, J., Arissian, L.

Lasers

The Power and Precision of Light

2011
Print ISBN: 978-3-527-41039-2

Okhotnikov, O.G. (ed.)

Fiber Lasers

2012
Print ISBN: 978-3-527-41114-6

Edited by Philippe Grelu

Nonlinear Optical Cavity Dynamics

From Microresonators to Fiber Lasers

WILEY-VCH
Verlag GmbH & Co. KGaA

Editor

Professor Philippe Grelu
Univ. Bourgogne Franche-Comté
Laboratoire ICB
U.M.R. 6303 C.N.R.S.
9, avenue A. Savary
F-21078 Dijon
France

All books published by **Wiley-VCH** are carefully produced. Nevertheless, authors, editors, and publisher do not warrant the information contained in these books, including this book, to be free of errors. Readers are advised to keep in mind that statements, data, illustrations, procedural details or other items may inadvertently be inaccurate.

Library of Congress Card No.: applied for

British Library Cataloguing-in-Publication Data
A catalogue record for this book is available from the British Library.

Bibliographic information published by the Deutsche Nationalbibliothek
The Deutsche Nationalbibliothek lists this publication in the Deutsche Nationalbibliografie; detailed bibliographic data are available on the Internet at <http://dnb.d-nb.de>.

© 2016 Wiley-VCH Verlag GmbH & Co. KGaA, Boschstr. 12, 69469 Weinheim, Germany

All rights reserved (including those of translation into other languages). No part of this book may be reproduced in any form – by photoprinting, microfilm, or any other means – nor transmitted or translated into a machine language without written permission from the publishers. Registered names, trademarks, etc. used in this book, even when not specifically marked as such, are not to be considered unprotected by law.

Print ISBN: 978-3-527-41332-4
ePDF ISBN: 978-3-527-68581-3
ePub ISBN: 978-3-527-68585-1
Mobi ISBN: 978-3-527-68583-7
oBook ISBN: 978-3-527-68647-6

Cover Design Formgeber, Mannheim, Germany
Typesetting SPi Global, Chennai, India
Printing and Binding

Printed on acid-free paper

Contents

List of Contributors *XIII*
Foreword *XXIII*

1 Introduction *1*
Philippe Grelu
References *8*

2 Temporal Cavity Solitons in Kerr Media *11*
Stéphane Coen and Miro Erkintalo
2.1 Introduction *11*
2.2 Mean-Field Equation of Coherently Driven Passive Kerr Resonators *13*
2.3 Steady-State Solutions of the Mean-Field Equation *15*
2.4 Existence and Characteristics of One-Dimensional Kerr Cavity Solitons *18*
2.5 Original Experimental Observation of Temporal Kerr Cavity Solitons *21*
2.6 Interactions of Temporal CSs *25*
2.7 Breathing Temporal CSs *29*
2.8 Emission of Dispersive Waves by Temporal CSs *31*
2.9 Conclusion *34*
References *34*

3 Dynamics and Interaction of Laser Cavity Solitons in Broad-Area Semiconductor Lasers *41*
Thorsten Ackemann, Jesus Jimenez, Yoann Noblet, Neal Radwell, Guangyu Ren, Pavel V. Paulau, Craig McIntyre, Gian-Luca Oppo, Joshua P. Toomey, and Deborah M. Kane
3.1 Introduction *41*
3.2 Devices and Setup *43*
3.2.1 Devices *43*
3.2.2 Experimental Setup *44*
3.3 Basic Observations and Dispersive Optical Bistability *45*

3.3.1 Basic Observation of Spatial Solitons 45
3.3.2 Interpretation as Dispersive Optical Bistability 47
3.3.3 Comparison to Absorptive Case 49
3.4 Modelling of LS and Theoretical Expectations in Homogenous System 50
3.4.1 Model Equations 50
3.4.2 Interaction of Laser Solitons in a Homogenous System 52
3.5 Phase and Frequency Locking of Trapped Laser Cavity Solitons 54
3.5.1 Basic Observation 54
3.5.2 Experiments on Locking Phase 55
3.5.3 Adler Locking: Theory 59
3.6 Dynamics of Single Solitons 60
3.6.1 Transient Dynamics 62
3.6.2 Outlook on Asymptotic Dynamics 65
3.7 Summary and Outlook 68
Acknowledgments 70
References 70

4 Localized States in Semiconductor Microcavities, from Transverse to Longitudinal Structures and Delayed Systems 77
Stéphane Barland, Massimo Guidici, Julien Javaloyes, and Giovanna Tissoni
4.1 Introduction 77
4.2 Lasing Localized States 80
4.2.1 Transverse Localized States in Coupled Microcavities 80
4.2.2 Time-Localized Structures in Passive Mode-Locked Semiconductor Laser 82
4.3 Localized States in Nonlinear Element with Delayed Retroaction 87
4.3.1 Front Pinning in Bistable System with Delay 88
4.3.2 Topological Dissipative Solitons in Excitable System with Delay 92
4.4 Conclusion and Outlook 98
Acknowledgements 99
References 99

5 Dynamics of Dissipative Solitons in Presence of Inhomogeneities and Drift 107
Pedro Parra-Rivas, Damià Gomila, Lendert Gelens, Manuel A. Matías, and Pere Colet
5.1 Introduction 107
5.2 General Theory: Swift – Hohenberg Equation with Inhomogeneities and Drift 108
5.3 Excitability Regimes 113
5.4 Fiber Cavities and Microresonators: The Lugiato – Lefever model 116

5.5 Periodically Pumped Ring Cavities *119*
5.6 Effects of Drift in a Periodically Pumped Ring Cavity *120*
5.7 Summary *125*
Acknowledgments *125*
References *125*

6 Dissipative Kerr Solitons in Optical Microresonators *129*
Tobias Herr, Michael L. Gorodetsky, and Tobias J. Kippenberg
6.1 Introduction to Optical Microresonator Kerr-Frequency Combs *129*
6.2 Resonator Platforms *131*
6.2.1 Ultra High-Q (MgF_2) Crystalline Microresonators *131*
6.2.2 Integrated Photonic Chip Microring Resonators *132*
6.3 Physics of the Kerr-comb Formation Process *132*
6.3.1 Nonlinear Coupled Mode Equations *135*
6.3.2 Degenerate Hyperparametric Oscillations *138*
6.3.3 Primary Sidebands *140*
6.4 Dissipative Kerr Solitons in Optical Microresonators *141*
6.4.1 Analytical Theory of Dissipative Kerr Solitons *141*
6.5 Signatures of Dissipative Kerr Soliton Formation in Crystalline Resonators *145*
6.6 Laser Tuning into the Dissipative Kerr Soliton States *147*
6.7 Simulating Soliton Formation in Microresonators *148*
6.8 Characterization of Temporal Dissipative Solitons in Crystalline Microresonators *149*
6.9 Resonator Mode Structure and Soliton Formation *151*
6.10 Using Dissipative Kerr solitons to Count the Cycles of Light *152*
6.11 Temporal Solitons and Soliton-Induced Cherenkov Radiation in an Si_3N_4 Photonic Chip *155*
6.12 Summary *157*
References *158*

7 Dynamical Regimes in Kerr Optical Frequency Combs: Theory and Experiments *163*
Aurélien Coillet, Nan Yu, Curtis R. Menyuk, and Yanne K. Chembo
7.1 Introduction *163*
7.2 The System *164*
7.3 The Models *166*
7.3.1 Modal Expansion Model *166*
7.3.2 Spatiotemporal Model *167*
7.3.3 Stability Analysis *168*
7.4 Dynamical States *171*
7.4.1 Primary Combs *171*
7.4.2 Solitons *176*
7.4.3 Chaos *179*

7.5 Conclusion *183*
7.6 Acknowledgments *184*
References *184*

8 Nonlinear Effects in Microfibers and Microcoil Resonators *189*
Muhammad I. M. Abdul Khudus, Rand Ismaeel, Gilberto Brambilla, Neil G. R. Broderick, and Timothy Lee
8.1 Introduction *189*
8.2 Linear Optical Properties of Optical Microfibers *191*
8.3 Linear Properties of Optical Microcoil Resonators *193*
8.4 Bistability in Nonlinear Optical Microcoil Resonators *195*
8.4.1 Broken Microcoil Resonators *197*
8.4.2 Polarization Effects in Nonlinear Optical Microcoil Resonators *198*
8.4.3 Possible Experimental Verification *199*
8.5 Harmonic Generation in Optical Microfibers and Microloop Resonators *200*
8.5.1 Mathematical Modeling and Efficiency of Third Harmonic Generation *201*
8.5.2 Third Harmonic Generation in Microloop Resonators *204*
8.5.3 Second-Harmonic Generation *208*
8.6 Conclusions and Outlook *209*
References *209*

9 Harmonic Laser Mode-Locking Based on Nonlinear Microresonators *213*
Alessia Pasquazi, Marco Peccianti, David J. Moss, Sai Tac Chu, Brent E. Little, and Roberto Morandotti
9.1 Introduction *213*
9.2 Modeling *215*
9.3 Experiments *219*
9.3.1 Short Cavity, Unstable Laser Oscillation *223*
9.3.2 Short Cavity, Stable Laser Oscillation *224*
9.3.3 Short Cavity, Dual-Line Laser Oscillation *226*
9.4 Conclusions *228*
References *229*

10 Collective Dissipative Soliton Dynamics in Passively Mode-Locked Fiber Lasers *231*
François Sanchez, Andrey Komarov, Philippe Grelu, Mohamed Salhi, Konstantin Komarov, and Hervé Leblond
10.1 Introduction *231*
10.1.1 Dissipative Solitons and Mode-Locked Lasers *231*
10.1.2 Multiple Pulses and Their Interactions *232*
10.2 Multistability and Hysteresis Phenomena *234*
10.2.1 Multiple Pulsing *234*

10.2.2 Multistability Observations *235*
10.2.3 Modeling Multiple Pulsing and Hysteresis *236*
10.3 Soliton Crystals *238*
10.3.1 From Soliton Molecules to Soliton Crystals *238*
10.3.2 Soliton Crystal Experiments *239*
10.3.3 Modeling Soliton Crystal Formations *240*
10.3.4 Soliton Crystal Instability *243*
10.4 Toward the Control of Harmonic Mode-Locking by Optical Injection *244*
10.5 Complex Soliton Dynamics *247*
10.5.1 Unfolding Complexity *247*
10.5.2 Analogy Between Soliton Patterns and the States of Matter *247*
10.5.3 Soliton Rain Dynamics *250*
10.5.4 Chaotic Pulse Bunches *252*
10.6 Summary *256*
Acknowledgments *257*
References *257*

11 Exploding Solitons and Rogue Waves in Optical Cavities *263*
Wonkeun Chang and Nail Akhmediev
11.1 Introduction *263*
11.2 Passively Mode-Locked Laser Model *266*
11.3 The Results of Numerical Simulations *268*
11.4 Probability Density Function *270*
11.5 Conclusions *272*
11.6 Acknowledgements *272*
References *273*

12 SRS-Driven Evolution of Dissipative Solitons in Fiber Lasers *277*
Sergey A. Babin, Evgeniy V. Podivilov, Denis S. Kharenko, Anastasia E. Bednyakova, Mikhail P. Fedoruk, Olga V. Shtyrina, Vladimir L. Kalashnikov, and Alexander A. Apolonski
12.1 Introduction *277*
12.2 Generation of Highly Chirped Dissipative Solitons in Fiber Laser Cavity *279*
12.2.1 Modeling *279*
12.2.1.1 Analytical Solution of CQGLE in the High Chirp Limit *281*
12.2.1.2 Comparison of Analytics with Numerics *284*
12.2.2 Experiment and its Comparison with Simulation *286*
12.2.3 NPE Overdriving and its Influence on Dissipative Solitons *288*
12.3 Scaling of Dissipative Solitons in All-Fiber Configuration *290*
12.3.1 Different Ways to Increase Pulse Energy, Limiting Factors *290*
12.3.2 SRS Threshold for Dissipative Solitons at Cavity Lengthening *292*
12.4 SRS-Driven Evolution of Dissipative Solitons in Fiber Laser Cavity *297*

12.4.1 NSE-Based Model in Presence of SRS 297
12.4.1.1 Model Details 298
12.4.1.2 Simulation, Comparison with Experiment 299
12.4.2 Generation of Stokes-Shifted Raman Dissipative Solitons 302
12.4.2.1 Proof-of-Principle Experiment 304
12.4.3 Characteristics of Raman dissipative Solitons 306
12.4.3.1 Variation of the Soliton Spectra with Filter Parameters 306
12.4.3.2 Variation of the Soliton Spectra with the Raman Feedback Parameters 307
12.4.4 Generation of Multicolor Soliton Complexes and Their Characteristics 307
12.5 Conclusions and Future Developments 310
References 312

13 Synchronization in Vectorial Solid-State Lasers 317
Marc Brunel, Marco Romanelli, and Marc Vallet
13.1 Introduction 317
13.2 Self-Locking in Dual-Polarization Lasers 318
13.2.1 Vectorial Description of the Cavity 318
13.2.2 Self-Pulsing in Lasers with Crossed Loss and Phase Anisotropies 319
13.2.3 Polarization Self-Modulated Lasers 321
13.2.4 Mode-Locked Dual-Polarization Lasers 323
13.2.4.1 Phase Locking at $c/4L$ 325
13.3 Dynamics of Solid-State Lasers Submitted to a Frequency-Shifted Feedback 327
13.3.1 Description of the System 327
13.3.1.1 Experimental Setup 328
13.3.2 Lang–Kobayashi Rate Equations 330
13.3.2.1 Phase Dynamics 331
13.3.2.2 Time-Scaled Rate Equations 331
13.3.3 Phase Locking 332
13.3.3.1 Continuous-Wave Case 332
13.3.3.2 Passive Q-Switching Case 333
13.3.4 Bounded Phase Dynamics 334
13.3.4.1 Intensity Bifurcation Diagram 334
13.3.4.2 Phase Bifurcation Diagram 336
13.3.4.3 Phasors 337
13.3.4.4 Role of the Coupling in the Active Medium 338
13.3.5 Measure of the Synchronization in the Bounded Phase Regime 339
13.4 Conclusion 341
Acknowledgments 341
References 341

14 Vector Patterns and Dynamics in Fiber Laser Cavities *347*
Stefan Wabnitz, Caroline Lecaplain, and Philippe Grelu
14.1 Introduction *347*
14.1.1 Pulsed Vector Dynamics with a Saturable Absorber *347*
14.1.2 Vector Dynamics Without a Saturable Absorber *348*
14.2 Fiber Laser Models *349*
14.2.1 The Scalar Cubic Ginzburg–Landau Equation *350*
14.2.2 Vector Ginzburg–Landau Equations *352*
14.2.3 Vector Nonlinear Schrödinger Equation *355*
14.2.4 Numerical Simulations *357*
14.3 Experiments of Vector Dynamics *357*
14.3.1 The Anomalous GVD: From Chaos to Antiphase Dissipative Dynamics *359*
14.3.2 The Normal GVD: Polarization-Domain Walls *362*
14.4 Summary *364*
Acknowledgments *364*
References *364*

15 Cavity Polariton Solitons *369*
Oleg A. Egorov and Falk Lederer
15.1 Introduction *369*
15.2 Mathematical Model *371*
15.3 One-Dimensional Bright Cavity Polariton Solitons *373*
15.3.1 Amplitude Equation in the Polaritonic Basis *374*
15.3.2 CPSs Beyond the “Magic Angle” and Their Stability *376*
15.3.3 Multi-Hump Cavity Polariton Solitons *378*
15.4 Two-Dimensional Parametric Polariton Solitons *380*
15.4.1 Amplitude Equations for the Participating Waves *380*
15.4.2 Families of Parametric Polariton Solitons *382*
15.4.3 Excitation and Dynamics of PPSs *385*
15.5 Two-Dimensional Moving Bright CPSs *387*
15.6 Summary *389*
Acknowledgments *389*
References *390*

16 Data Methods and Computational Tools for Characterizing Complex Cavity Dynamics *395*
J. Nathan Kutz, Steven L. Brunton, and Xing Fu
16.1 Introduction *395*
16.2 Data Methods *396*
16.2.1 Dimensionality-Reduction: Principal Components Analysis *397*
16.2.2 Search Algorithms and Library Building *398*
16.2.3 Sparse Measurements and Compressive Sensing *400*
16.2.4 Sparse Representation and Classification *401*
16.3 Adaptive, Equation-Free Control Architecture *402*

16.4 Prototypical Example: Self-Tuning Mode-Locked Fiber Lasers *403*
16.4.1 Governing Equations *404*
16.4.2 Jones Matrices for Waveplates and Polarizers *404*
16.4.3 Performance Monitoring and Objective Function *405*
16.4.4 Sparse Representation for Birefringence Classification *405*
16.4.5 Self-Tuning Laser *406*
16.5 Broader Applications of Self-Tuning Complex Systems *409*
16.5.1 Phased Array Antennas *409*
16.5.2 Coherent Laser Beam Combining *411*
16.5.3 Neuronal Stimulation *412*
16.6 Conclusions and Technological Outlook *413*
Acknowledgments *415*
References *415*

17 Conclusion and Outlook *419*
Philippe Grelu
References *421*

Index *423*

List of Contributors

Muhammad I. M. Abdul Khudus
University of Southampton
Optoelectronics Research Centre
Southampton
SO17 1BJ
UK

Thorsten Ackemann
University of Strathclyde
SUPA and Department of Physics
107 Rottenrow East
Glasgow G4 0NG
Scotland
UK

Nail Akhmediev
The Australian National University
Optical Sciences Group
Research School of Physics and Engineering
Acton ACT 2601
Australia

Alexander A. Apolonski
Institute of Automation and Electrometry
SB RAS
1 Koptyug Ave.
Novosibirsk 630090
Russia

and

Ludwig-Maximilians-Universitaet
Schellingstr. 4
Am Coulombwall 1
85748 Garching
Germany

and

Max-Planck-Institut fuer Quantenoptik
Hans-Kopfermann-Straße 1
85748 Garching
Germany

Sergey A. Babin
Institute of Automation and Electrometry
SB RAS
1 Koptyug Ave.
Novosibirsk 630090
Russia

and

Novosibirsk State University
2 Pirogova Str.
Novosibirsk 630090
Russia

Stéphane Barland
Université de Nice – CNRS
UMR 7335
Institut Non Linéaire de Nice
1361 route des lucioles
06560 Valbonne
France

Anastasia E. Bednyakova
Novosibirsk State University
2 Pirogova Str.
Novosibirsk 630090
Russia

and

Institute of Computational Technologies
SB RAS
6 Lavrentiev Ave.
Novosibirsk 630090
Russia

Gilberto Brambilla
University of Southampton
Optoelectronics Research Centre
Southampton
SO17 1BJ
UK

Neil G.R. Broderick
University of Auckland
Department of Physics
Science Centre
38 Princes Street
City Campus
92019 Auckland
New Zealand

Marc Brunel
Département Optique et Photonique
Institut de Physique de Rennes
Université de Rennes 1 – CNRS
UMR 6251
263 avenue du Général Leclerc
35042 Rennes Cedex
France

Steven L. Brunton
University of Washington
Department of Mechanical Engineering
Mechanical Engineering
Building 305
Seattle
WA 98195
USA

Wonkeun Chang
The Australian National University
Optical Sciences Group
Research School of Physics and Engineering
Acton ACT 2601
Australia

Yanne K. Chembo
FEMTO-ST Institute
CNRS & Université Bourgogne
Franche-Comté
Optics Department
15B Avenue des
Montboucons
25030 Besançon cedex
France

Sai Tac Chu
STC
Department of Physics and
Materials Science
City University of Hong Kong
Kowloon Tong
Hong Kong

Stéphane Coen
University of Auckland
Department of Physics
Science Centre
38 Princes Street
City Campus
92019 Auckland
New Zealand

Aurélien Coillet
Univ. Bourgogne Franche-Comté
Laboratoire ICB
U.M.R. 6303 C.N.R.S.
9, avenue A. Savary
F-21078 Dijon
France

Pere Colet
Consejo Superior de
Investigaciones Científicas
Instituto de Física
Interdisciplinar y Sistemas
Complejos, IFISC (CSIC-UIB)
Campus Universitat de les Illes
Balears
07122 Palma de Mallorca
Spain

Oleg A. Egorov
Friedrich-Schiller-Universitaet
Jena
Faculty of Physics and
Astronomy
Institute of Condensed Matter
Theory and Solid State Optics
Max-Wien-Platz 1
07743 Jena
Germany

Miro Erkintalo
University of Auckland
Department of Physics
Science Centre
38 Princes Street
City Campus
92019 Auckland
New Zealand

Mikhail P. Fedoruk
Novosibirsk State University
2 Pirogova Str.
Novosibirsk 630090
Russia

and

Institute of Computational
Technologies
SB RAS
6 Lavrentiev Ave.
Novosibirsk 630090
Russia

Xing Fu
University of Washington
Department of Applied
Mathematics
Lewis Hall 118
Seattle
WA 98195
USA

Lendert Gelens
Vrije Universiteit Brussel (VUB)
Applied Physics Research Group
Pleinlaan 2, 1050 Brussels
Belgium

and

University of Leuven
Laboratory of Dynamics in
Biological Systems
KU Leuven Department of
Cellular and Molecular Medicine
3000 Leuven
Belgium

and

Stanford University School of
Medicine
Department of Chemical and
Systems Biology
Stanford
CA 94305-5174
USA

Massimo Giudici
Université de Nice – CNRS
UMR 7335
Institut Non Linéaire de Nice
1361 route des lucioles
06560 Valbonne
France

Damià Gomila
Consejo Superior de
Investigaciones Científicas
Instituto de Física
Interdisciplinar y Sistemas
Complejos, IFISC (CSIC-UIB)
Campus Universitat de les Illes
Balears
07122 Palma de Mallorca
Spain

Michael L. Gorodetsky
M. V. Lomonosov Moscow State
University
Faculty of Physics
Moscow
Russia

Philippe Grelu
Univ. Bourgogne Franche-Comté
Laboratoire ICB
U.M.R. 6303 C.N.R.S.
9, avenue A. Savary
F-21078 Dijon
France

Tobias Herr
Centre Suisse d'Électronique et
de Microtechnique (CSEM)
Neuchâtel
Switzerland

Rand Ismaeel
University of Southampton
Optoelectronics Research Centre
Southampton
SO17 1BJ
UK

Julien Javaloyes
Universitat de les Illes Baleares
Departament de Física
C/ Valldemossa km 7.5
07122 Mallorca
Spain

Jesus Jimenez
University of Strathclyde
SUPA and Department of Physics
107 Rottenrow East
Glasgow G4 ONG
Scotland
UK

Vladimir L. Kalashnikov
Institut fuer Photonik
TU Wien
27 Gußhaus-Straße
1040 Vienna
Austria

Deborah M. Kane
Macquarie University
MQ Photonics Research Centre
Department of Physics and
Astronomy
Sydney 2109
Australia

Denis S. Kharenko
Institute of Automation and
Electrometry
SB RAS
1 Koptyug Ave.
Novosibirsk 630090
Russia

and

Novosibirsk State University
2 Pirogova Str.
Novosibirsk 630090
Russia

Tobias J. Kippenberg
EPFL
Laboratory of Photonics and
Quantum Measurements
Institute of Condensed Matter
Physics
CH-1015 Lausanne
Switzerland

Andrey Komarov
Russian Academy of Sciences
Institute of Automation and
Electrometry
Acad. Koptyug Pr. 1
630090 Novosibirsk
Russia

Konstantin Komarov
Russian Academy of Sciences
Institute of Automation and
Electrometry
Acad. Koptyug Pr. 1
630090 Novosibirsk
Russia

Hervé Leblond
Université d'Angers
Laboratoire de Photonique E.A.
4464
2 Bd Lavoisier
49045 Angers Cedex 01
France

Caroline Lecaplain
EPFL – Ecole Polytechnique
Fédérale de Lausanne
1015 Lausanne
Switzerland

and

Univ. Bourgogne Franche-Comté
Laboratoire ICB, U.M.R. 6303
C.N.R.S.
9 avenue A. Savary
21078 Dijon
France

Falk Lederer
Friedrich-Schiller-Universitaet
Jena
Faculty of Physics and
Astronomy
Institute of Condensed Matter
Theory and Solid State Optics
Max-Wien-Platz 1
07743 Jena
Germany

Timothy Lee
University of Southampton
Optoelectronics Research Centre
Southampton
SO17 1BJ
UK

Brent E. Little
Xi’an Institute of Optics and
Precision Mechanics of CAS
Xi’an
China

Manuel A. Matías
Consejo Superior de
Investigaciones Científicas
Instituto de Física
Interdisciplinar y Sistemas
Complejos, IFISC (CSIC-UIB)
Campus Universitat de les Illes
Balears
07122 Palma de Mallorca
Spain

Craig McIntyre
University of Strathclyde
SUPA and Department of Physics
Glasgow G4 ONG
Scotland
UK

Curtis R. Menyuk
University of Maryland
Computer Science and Electrical
Engineering Department
1000 Hilltop Circle
Baltimore
MD 21250
USA

Roberto Morandotti
Université du Québec
INRS-EMT
Centre Énergie Matériaux
Télécommunications
1650 boulevard Lionel-Boulet
Varennes (Québec)
J3X 1S2
Canada

David J. Moss
RMIT University
DJM
School of Electrical and
Computer Engineering
Melbourne
Victoria 3001
Australia

J. Nathan Kutz
University of Washington
Department of Applied
Mathematics
Seattle
WA 98195
USA

Yoann Noblet
University of Strathclyde
SUPA and Department of Physics
107 Rottenrow East
Glasgow G4 ONG
Scotland
UK

and

Macquarie University
MQ Photonics Research Centre
Department of Physics and
Astronomy
Sydney 2109
Australia

Gian-Luca Oppo
University of Strathclyde
SUPA and Department of Physics
107 Rottenrow East
Glasgow G4 ONG
Scotland
UK

Pedro Parra-Rivas
Vrije Universiteit Brussel (VUB)
Applied Physics Research Group
Pleinlaan 2, 1050 Brussels
Belgium

and

Universitat de les Illes Balears
Instituto de Física
Interdisciplinar y Sistemas
Complejos
IFISC (CSIC-UIB)
Campus Universitat de les Illes
Balears
07122 Palma de Mallorca
Spain

Alessia Pasquazi
University of Sussex
Department of Physics and
Astronomy
Falmer
Brighton BN1 9QH
UK

Pavel V. Paulau
Jade University of Applied
Sciences
Institut fuer Chemie und
Biologie des Meeres
Ofener Str. 16/19
26121 Oldenburg
Germany

Marco Peccianti
University of Sussex
Department of Physics and
Astronomy
Falmer
Brighton BN1 9QH
UK

Evgeniy V. Podivilov
Institute of Automation and Electrometry
SB RAS
1 Koptyug Ave.
Novosibirsk 630090
Russia

and

Novosibirsk State University
2 Pirogova Str.
Novosibirsk 630090
Russia

Neal Radwell
University of Glasgow
SUPA and Department of Physics and Astronomy
Kelvin Building
Glasgow G12 8QQ
UK

Guangyu Ren
University of Strathclyde
SUPA and Department of Physics
107 Rottenrow East
Glasgow G4 ONG
Scotland
UK

Marco Romanelli
Université de Rennes 1 – CNRS
UMR 6251
Département Optique et Photonique
Institut de Physique de Rennes
263 avenue du Général Leclerc
35042 Rennes Cedex
France

Mohamed Salhi
Université d'Angers
Laboratoire de Photonique E.A. 4464
2 Bd Lavoisier
49045 Angers Cedex 01
France

François Sanchez
Université d'Angers
Laboratoire de Photonique E.A. 4464
2 Bd Lavoisier
49045 Angers Cedex 01
France

Olga V. Shtyrina
Novosibirsk State University
2 Pirogova Str.
Novosibirsk 630090
Russia

and

Institute of Computational Technologies
SB RAS
6 Lavrentiev Ave.
Novosibirsk 630090
Russia

Giovanna Tissoni
Université de Nice – CNRS
UMR 7335
Institut Non Linéaire de Nice
1361 route des lucioles
06560 Valbonne
France

Joshua P. Toomey
Macquarie University
MQ Photonics Research Centre
Department of Physics and Astronomy
Sydney 2109
Australia

Marc Vallet
Université de Rennes 1 – CNRS UMR 6251
Département Optique et Photonique
Institut de Physique de Rennes
263 avenue du Général Leclerc
35042 Rennes Cedex
France

Stefan Wabnitz
University of Brescia
Department of Information Engineering
via Branze 38
25123 Brescia
Italy

Nan Yu
Jet Propulsion Laboratory
California Institute of Technology
4800 Oak Grove Drive
Pasadena 91109
USA

Foreword

Nonlinear optical cavity dynamics is an ever-expanding area of photonics, which this volume intends to picture at a propitious time when interactions between its topical branches have remarkably matured.

Thanks to the deep involvement of all the authors who accepted to share their foremost expertise in a thorough but didactical way, I believe that we have succeeded in bringing an impressive collection of intertwined knowledge to the Photonics community. I also wish to thank all contributors for their patience throughout the long process of book editing, knowing in particular that some chapters contain unpublished research works.

As any picture depending on timing and viewpoint, this book edition is certainly not comprehensive, let alone definitive. We had to place an upper boundary to the size of the volume, in order to keep it accessible, and managed to limit the possible frustration of some of our prolific contributors. I anticipate that ulterior advances in both fundamental and applied aspects of *nonlinear optical cavity dynamics* will be timely covered by subsequent reference books.

I hope that the overall enthusiasm of the authors will be shared by the readers, and I wish to thank the editorial and production teams at Wiley-VCH for being altogether interactive, friendly, and highly efficient.

28 October 2015
Dijon, France

Philippe Grelu

1
Introduction

Philippe Grelu

Light travels fast. Photons are its swift messengers. Designing an optical cavity is the appropriate answer to the necessity of enhancing the interaction time between photons and matter, through the recirculation of light amidst an optical medium of bounded size. The wave nature of light allows these multiple passes to interfere, and buildup at resonant wavelengths or frequencies. As a result, the nonlinear response of materials can be more easily awakened in optical cavities than in transmission experiments, as much as nonlinear effects can be sharply revealed through the microscopic wavelength ruler that is naturally embedded into a resonant optical cavity.

The science of photonics is diffusing continuously into all major sectors of the industry, from manufacturing and communications to medicine and environmental monitoring. Consequently, there is an increasing demand to develop efficient, compact, and cost-effective optical sources or devices to perform a wide range of tasks, which include high-speed spectroscopy and sensing, material processing, communication and data processing, and metrology. The optical cavity, either in its active – laser – or passive form, is becoming more and more an applicative node. The tremendous progress made in the field of semiconductor laser sources in the past decades makes a striking illustration. Currently, a wide range of other optical cavity designs show great promises, such as microresonators and fiber lasers. Thus, it is important to consider, in a newly unified way, the broad range of fast and ultrafast dynamics that now make a coherent conceptual frame for light generation and processing. This is the scope of this book, definitely grounded on fundamental considerations and also highlighting major applications.

The recirculation of light in the optical cavity produces a feedback mechanism, whose association with nonlinearity is conducive to the appearance of bistable behaviors. Thus, bistability is a generic feature of nonlinear optical cavities. As the optical nonlinearity can be of dispersive or dissipative nature – or rigorously, a combination of the two – various types of optical bistability can, accordingly, manifest [1]. Bistability is a fascinating property that naturally translates into the notion of information storage and manipulation. However, due to the scale of optical wavelengths, the density of optically stored information cannot compete with the memory density implemented in modern CMOS technology.

Nonlinear Optical Cavity Dynamics: From Microresonators to Fiber Lasers, First Edition.
Edited by Philippe Grelu.
© 2016 Wiley-VCH Verlag GmbH & Co. KGaA. Published 2016 by Wiley-VCH Verlag GmbH & Co. KGaA.

Thus, applicative motivations clearly shift toward the realization of optical buffer memories or arbitrary long delay lines, all-optical switches, and other advanced optical processing units. Recent technological breakthroughs in optical cavities, from microresonators to ultra-long fiber cavities, have entitled the exploration of nonlinear optical dynamics over unprecedented spatial and temporal orders of magnitude.

Indeed, the key advantage of optical technology lays in its potentially ultrahigh bandwidth, or equivalently, ultrafast transmission. As soon as the material nonlinearity response time is in the femtosecond to the picosecond range, as it is the case, for instance, with Kerr nonlinearity in most glass materials, the effects of nonlinearity and dispersion can combine to shape up short-to-ultrashort optical pulses. When the previous combination reaches a balance amid a single optical pulse, the latter becomes an optical soliton, which subsequently maintains its specific temporal waveform during propagation [2–3].

However, dealing with the arbitrarily long propagation distances that are accumulated through the succession of cavity round-trips, losses cannot be avoided. Several strategies can be implemented to compensate for these losses. In general, a coherent driving field can inject the cavity, either continuously or synchronously. Or, the cavity may include an incoherently pumped gain medium that makes it a laser system. In all cases, to maintain a given light state in the optical cavity, a balance between gain and losses should be reached. As soon as nonlinearity is involved in this dissipative balance, stable pulsed light states pertain to the general class of dissipative solitons [4]. The qualifier "dissipative" has to be understood in the broad dynamical sense attributed by Nicolis and Prigogine [5], and not as a mere synonym of a "lossy" system. Instead of remaining deceptive, dissipative systems, through the perpetual and bidirectional exchange of energy with their environment, can manifest conditions for self-organization. They have become during the past decade a fascinating area of research [4, 6]. Dissipative solitons are confined wave-packets of light whose existence and stability crucially depend on the energy balance. The dissipative soliton paradigm is underlying most of the chapters of the present volume, encompassing a myriad of possible dynamics, from stationary to pulsating and chaotic pulsed regimes.

Conceptually, the simplest nonlinear optical cavity scheme may correspond to a single transverse mode, coherently driven, cavity incorporating an ultrafast Kerr medium. It can then be considered as "the hydrogen atom" of nonlinear optical cavity dynamics. This statement obviously stands as long as polarization dynamics, thermal, and additional higher-order effects are not involved. In its distributed form, the optical cavity can be scaled from a compact microring to a kilometer-long fiber ring. Interestingly, going beyond the mean-field equation describing optical bistability, the stability analysis unveils the – parameter dependent – possibility of reaching various modulated and pulsating regimes. This underpins the existence of well-localized temporal cavity solitons, which can be considered as individual, addressable optical bits of information that travel round the optical cavity. Coen and Erkintalo discuss this topic extensively in Chapter 2, in correspondence with fiber ring cavity experiments.

For high-finesse-driven resonators, the Lugiato–Lefever equation (LLE) is a central dynamical model [7, 8]. It is used in several chapters, and chapter authors were allowed to retain their own derivation and notations for the reader's convenience. The solitary wave solutions of the LLE have been called *cavity solitons*, and they belong to the general class of dissipative solitons, as explained previously and reflected in Lugiato and Lefever's [7] seminal 1987 paper. Interestingly, the latter original study considered the spatiotemporal dynamics of optical cavities with high Fresnel numbers, namely, the possibility to form transverse patterns and spots – spatial cavity solitons. This readily increases the complexity of the nonlinear optical cavity system: not only from the theoretical point of view, where complex two-dimensional transverse structures, such as vortices, can form without having an equivalent in the purely temporal case but also – and mostly – because it is extremely difficult to realize a homogeneous wide-aperture cavity. Then, losing the translational symmetry, the spatial cavity solitons are set to move transversally, sensing the gradients of their local environments, until they become pinned by defects.

In active media, laser light can be generated with versatile underlying dynamics, from stationary to pulsating and chaotic ones. Emphasizing on ultrafast dynamics, the vital arena for the information technology, we find the soliton as a common conceptual keyword, thriving into its modern developments with the closely related denominations of dissipative solitons and cavity solitons.

Broad-area vertical-cavity surface emitting lasers (VCSELs) make an advantageous technological platform to experiment cavity solitons [9]. They benefit from the compactness and high nonlinearity of grown semiconductor structures. It is also possible to combine their optical gain with a particular feedback mechanism, to circumvent the necessity of an external coherent driving transverse wave. Such a design allows the observation of specific cavity solitons, namely, laser cavity solitons. As can be expected, the use of a semiconductor material increases the complexity of the underlying theoretical description, involving a set of coupled nonlinear equations for the carrier density along with the intracavity optical field. It is also particularly interesting to study the interactions between neighboring laser cavity solitons, and their coherence properties. All these points are addressed in Chapter 3, by Ackemann *et al.*, maturing a thorough expertise about complex spatiotemporal dynamics. A challenging perspective is to find experimental conditions where cavity solitons localized both transversally and in the time domain, namely, laser light bullets, could manifest. Until now, stable light bullets that can be manipulated remain the holy grail of nonlinear optics [10, 11].

Semiconductor laser cavities are characterized by a short gain relaxation time of the order of a nanosecond or less. By extending the cavity length, with a delay line in air, one may shift the laser dynamical regime from class B to class A. Now, let us consider a single transverse-mode semiconductor laser. When the gain relaxation lifetime becomes much shorter than the cavity round-trip time, and by using a suitable saturable absorber, it is possible to modelock the extended semiconductor laser cavity with multiple independent pulses. Because these pulses do not interact, when sufficiently separated, they can be considered as “localized structures,” a particular class of dissipative solitons, making a laser analog of the temporal cavity solitons described in Chapter 1. Similarly, these laser temporal cavity solitons can be manipulated as independent information bits. This is the main subject of Chapter 4, by Barland *et al.*

In general, any extended optical cavity will experimentally feature some amount of spatial inhomogeneity and drift. These two additional effects can lead to a wide range of bifurcations, including excitable behavior. Interestingly, an analogy can be made between the transverse spatial case, and the longitudinal temporal case, when the spatial inhomogeneity is replaced by the periodic injection of driving pulses. When the injection period does not precisely coincide with the cavity fundamental repetition frequency, an equivalent drift source also appears. These fundamental explorations of nonlinear cavity dynamics, relevant for systems ranging from broad-area VCSELs to microresonators and frequency comb generation, are developed in Chapter 5 by Parra-Rivas *et al.*

Frequency combs establish a modern workhorse for high-precision spectral measurements that can be performed in a record time [12–14]. Driven by the perspective of developing compact, efficient, and reliable frequency comb generators, the research on microresonators has expanded tremendously during the past 10 years. One has to realize the major gaps, technological as well as conceptual ones, needed to progress from the observation of optical bistability [15], usually dominated by slow thermal nonlinearities, to the efficient cascading of four-wave mixing, exploiting the ultrafast Kerr nonlinearity of the optical material [16], and nowadays, to the study and control of the coherence properties of the generated frequency combs.

It is remarkable that the latest research trends have brought closer several scientific communities that used to thrive quite separately. This is particularly true concerning the communities of optical microresonators, of nonlinear dynamics, and of mode-locked lasers. As the reader may have guessed, this recent movement represents a major motivation to encompass, as much as possible, the joined expertise into a single book volume. Also, it is quite conspicuous that the concept of a dissipative soliton represents a major thread linking all these current researches. The cross-fertilization between various areas is also represented by the alternation of spectral and temporal pictures, or temporal and spatial pictures, that are put in vivid correspondence.

Chapters 6 and 7 successively unveil the major developments in the area of microresonators designed for frequency comb generation. Chapter 6, by Herr *et al.*, unfolds the recent history of the progresses made, from experimental and fundamental points of view, which lead to the mastering of frequency comb generation in specifically shaped, ultrahigh quality factor, crystalline microresonators. The focus is then on the particular experimental conditions and parameters that allow the multiple frequency lines to lock in order to promote the formation of temporal dissipative solitons that circulate round the laser-driven microresonator. Despite being based on completely different technological platforms, with around five orders of magnitude difference between their respective sizes, driven microresonators and fiber ring cavities behave similarly, as attested by the common use of the LLE to reveal the most salient temporal dynamics. Naturally, this huge dimension gap initially made scientific languages to develop relatively apart: whereas it is natural to describe the microresonator dynamics in terms of spectral modes that are well resolved with any standard optical spectrum analyzer, the real-time observation of pulsed structures is challenging, due to their high repetition rate. The picture is opposite for long fiber cavities, which also feature a much lower finesse: the tightly packed, weakly modulated, spectral modes remain generally unresolved, but the low cavity repetition rate makes the direct observation of the temporal structures in the making a natural scope, despite the gigahertz bandwidth limitation of the analyzing electronics. After recalling the equivalence between the spectral and temporal formalisms, Chapter 7 by Coillet *et al*. takes on the solid grounds of the temporal modeling of driven-microresonator dynamics to explore the wide range of dynamical properties of frequency combs, backed by comparisons with experimental results, which includes Turing patterns, bright and dark solitons, as well as higher-order pulsations and chaotic states. The latter are shown to support the transient formation of optical rogue waves, which are extreme-wave events ubiquitous in highly dimensional nonlinear systems [17].

Although the technological platforms of fiber cavities and microresonators may seem a world apart, there is an original research at their crossroad, which is represented by microfiber, nanofiber, and microcoil resonators. As a prerequisite, this has implied during the past decade, the transformation of artisanship skills to automated procedures, in order to routinely produce high-quality submicron-diameter optical fibers drawn from optical fibers of standard diameters. That said, microfibers represent an easily accessible and particularly versatile technological platform [18], which is able to test a wide range of concepts of integrated nonlinear optics, such as frequency conversion, pulse shaping, and nonlinear switching. Chapter 8, by Abdul Khudus *et al*., reviews all these prospects in the light of both experimental and numerical explorations.

The crossroad between microresonators and fiber lasers represents a different recent conjunction. Although it is known that both platforms can be used separately to generate optical frequency combs, it would be highly desirable to combine the technological connectivity and the dynamical self-organization that are naturally available in fiber lasers with the multi-gigahertz frequency range spacing of comb lines that are intrinsic to microresonators. Pasquazi *et al*. relate this endeavor in Chapter 9. The authors explain the advantages and constraints inherent to the association of a long and a short cavity, aimed at processing distinct tasks for the establishment of a high-harmonic laser mode locking, and emphasize on the stability features of the demonstrated pulsed sources.

For passively mode-locked fiber lasers, harmonic mode locking is just one among the myriads of multipulse dynamics that can be experimented. Owing to the general efficiency of fiber lasers, to the scalability of their pulsed dynamics, and to the availability of intense pump modules, the number of ultrashort pulses that can coexist in a fiber laser cavity can be varied from a few to thousands. In contrast to the situation in passive-driven resonators (Chapter 2) and to some specific class-A lasers (Chapter 4), multiple pulses in mode-locked fiber lasers always interact in a manifested way, which can become dramatic for some cavity parameter settings. This topic is thoroughly developed in Chapter 10 by Sanchez *et al*., and explained in the light of dissipative soliton dynamics. Remarkable collective behaviors include soliton crystals, which could represent an alternative way to obtain stable frequency combs and high-harmonic mode locking, and complex soliton dynamics such as soliton rain and dissipative optical rogue waves (DRWs). A bridge is established among DRWs, chaotic pulse bunching, and noise-like pulse emission, which are denominations of chaotic dynamics well represented in the arena of short-pulse fiber laser dynamics.

In Chapter 11, Chang and Akhmediev build a noteworthy bridge between rogue waves and another category of short-pulse chaotic dynamics: exploding solitons. Exploding solitons are remarkable states linked to the existence of strange attractors [19]. In addition, chaotic dynamics in highly-dimensional nonlinear systems are conducive to rogue wave formations [17]. The authors having a foremost expertise in both topics quite naturally anticipate and demonstrate numerically the existence of a significant overlap between DRW and exploding soliton dynamics, using a passively mode-locked laser propagation model.

The area of short-pulse fiber lasers is extremely dynamic [20–22]. The recent dissipative soliton paradigm [23] applied to mode-locked lasers has allowed relaxing several of the previously implied cavity design constraints, notably concerning the sign of the chromatic dispersion, and the amount of acceptable losses of the fiber laser cavity. Such renewed freedom has promoted a lot of creative cavity design, including all-normal-dispersion chirped-pulsed lasers [24], and soliton–similariton mode-locked lasers [25] as prominent illustrations. One clear objective is now to obtain optimized pulse features – in terms of pulse energy, optical bandwidth, or pulse duration – out of all-fibered laser oscillators. The analysis of the current pulse energy limitations of mode-locked fiber lasers, and the possibilities to circumvent them, are explored in detail in Chapter 12 by Babin *et al*.

Beyond representing a complication for experiments and modeling alike, polarization introduces a smart degree of freedom to the dynamics, which can dispel some fundamental impossibility. For example, we all know that, by using polarization components and a nonreciprocal element such as a Faraday rotator, the principle of reversible ray tracing does not hold any longer, which is very useful to design the optical isolators and circulators that are ubiquitous in laser and optical communication technology. Involving polarization and vector systems, in general, the dynamical domains multiply. For instance, using birefringent fibers, parameters can be found to trigger modulation instability (MI) in the normal dispersion regime, through simple propagation experiments [26, 27], whereas scalar MI necessitates an anomalous dispersion regime. In the light of the previous chapters, there is a recurrent observation: as soon as the space of parameters expands, new dynamical breaches appear, such as MI in driven, normally dispersive resonators – by virtue of the detuning extra degree of freedom [28], and bright dissipative soliton pulses in normally dispersive laser cavity – by virtue of the dissipative terms [29].

Involving polarization dynamics can have far-reaching consequences for laser systems. Indeed, for instance, dispersive (crossed-Kerr effect) and/or dissipative (crossed gain saturation) contributions can initiate short-pulse dynamics in the absence of known (scalar) saturable absorber in the laser cavity [30]. To address this topic, the most instructive route begins with a journey through vectorial solid-state lasers, where the piecewise cavity design allows controlling and modeling well all the anisotropies. This is presented by Brunel *et al.*, in Chapter 13. Although disconcertingly simple linear physics is sufficient to understand the onset of self-pulsing at specific beat frequencies, the pulse shaping definitely involves the presence of crossed nonlinearities. Subsequently combinations of anisotropy, saturable absorption, and frequency-shifted feedback lead to various illustrations of synchronization mechanisms among the vector cavity modes.

The modeling of vector fiber ring lasers is more challenging, as the fiber anisotropies are not uniformly distributed, and not precisely known, in the experiment. However, vector pattern formations and complex self-pulsing dynamics are found to abound in fiber laser experiments, even without any explicit saturable absorber element, with an underlying perspective of chaos synchronization [31]. Wabnitz *et al.*, in Chapter 14, present the recent exploration of these vector dynamics, and put forward universal distributed vector equations as phenomenological models allowing to picture qualitatively well the experimentally observed dynamics.

Egorov and Lederer, in Chapter 15, review the nonlinear dynamics of a markedly different vector laser system: the strong coupling between excitons and photons in a driven quantum-well semiconductor microcavity. Exciton-polaritons are half-light, half-matter quantum quasi-particles that have attracted considerable attention during the past few years [32, 33]. Numerical investigations demonstrate how the nonlinear coupling can form stable localized exciton-polaritons collective states, namely, cavity polariton solitons, which can be of different types and spatial dimensionality.

Almost all nonlinear dynamical systems involved in this volume are of quasi-infinite dimensionality – being modeled by partial derivative equations. This explains the great diversity of the nonlinear dynamics that can be found in these systems, from localized solitons to pattern formation, and from stationary to pulsating and chaotic evolutions. However, when considering practical applications, it may become vital to develop efficient and reliable automated procedures of surveillance and control of these complex dynamical systems. This is the focus of Chapter 16, by Kutz *et al.*, where essential dimensionality-reduction methods, sparse representation, and data-driven machine learning strategies are presented.

To conclude this introductory chapter, I am particularly grateful to all the eminent specialists, representing various aspects of nonlinear optical cavity dynamics, who have contributed to this volume. They have allowed me to gather key contributions that illustrate the diversity of dynamics as well as the strong analogies and cross-fertilization between topics that used to thrive more independently, spanning from mode-locked lasers to driven cavities, miniature and microcavities for frequency comb generation, to spatially extended cavities and spatiotemporal cavity solitons. Considering also the vital soaring of photonics in our industries and its growing impact on our societies, with the potential of nonlinear optical cavity dynamics in particular to perform ultrafast light engineering and analysis, I hope that this monograph will serve as a valuable reference guide for photonics researchers and graduate students as well as a source of inspiration for photonics engineers.

References

1. Gibbs, H.M. (1984) *Optical Bistability: Controlling Light with Light*, Academic Press.
2. Akhmediev, N. and Ankiewicz, A. (1997) *Solitons, Nonlinear pulses and beams*, Springer.
3. Kivshar, Y.S. and Agrawal, G.P. (2003) *Optical solitons: from fibers to photonic crystals*, Academic Press.
4. Akhmediev, N. and Ankiewicz, A. (eds) (2005) *Dissipative Solitons*, Lecture Notes in Physics, vol. **661**, Springer, Berlin.
5. Nicolis, G. and Prigogine, I. (1977) *Self-Organization in Nonequilibrium Systems: From Dissipative Structures to Order through Fluctuations*, John Wiley & Sons, Inc.
6. Akhmediev, N. and Ankiewicz, A. (eds) (2008) *Dissipative Solitons: From Optics to Biology and Medicine*, Springer.
7. Lugiato, L.A. and Lefever, R. (1987) Spatial dissipative structures in passive optical systems. *Phys. Rev. Lett.*, **58**, 2209–2212.
8. Lugiato, L., Prati, F., and Brambilla, M. (2015) *Nonlinear Optical Systems*, Cambridge University Press.
9. Barland, S. *et al.* (2002) Cavity solitons as pixels in semiconductor microcavities. *Nature*, **419**, 699–702.
10. Firth, W.J. and Scroggie, A.J. (1996) Optical bullet holes: robust controllable localized states of a nonlinear cavity. *Phys. Rev. Lett.*, **76**, 1623–1626.
11. Wise, F. and Di Trapani, P. (2002) The hunt for light bullets spatio-temporal solitons. *Opt. Photonics News*, **13**, 28–32.
12. Cundiff, S.T. and Ye, J. (2003) Colloquium: femtosecond optical frequency combs. *Rev. Mod. Phys.*, **75**, 325–342.
13. Horiuchi, N. and Hänsch, T.W. (2011) The impact of frequency combs. *Nat. Photonics*, **5**, 193.
14. Schliesser, A., Picqué, N., and Hänsch, T.W. (2012) Mid-infrared frequency combs. *Nat. Photonics*, **6**, 440–449.
15. Braginsky, V.B., Gorodetsky, M.L., and Ilchenko, V.S. (1989) Quality factor and nonlinear properties of optical whispering-gallery modes. *Phys. Lett. A*, **137**, 393–397.
16. Del'Haye, P., Schliesser, A., Arcizet, O., Wilken, T., Holzwarth, R., and Kippenberg, T. (2007) Optical frequency comb generation from a monolithic microresonator. *Nature*, **450**, 1214–1217.
17. Akhmediev, N. and Pelinovsky, E. (eds) (2010) Rogue waves – towards a unifying concept. Special Issue of *Eur. Phys. J. Spec. Top.*, **185**, pp. 1–266.
18. Brambilla, G. (2010) Optical fibre nanowires and microwires: a review. *J. Opt.*, **12**, 043001.
19. Akhmediev, N., Soto-Crespo, J.M., and Ankiewicz, A. (2005) in *Nonlinear Waves: Classical and Quantum Aspects*, NATO Science Series II: Mathematics, Physics and Chemistry, vol. **153**, Springer, pp. 45–60.

20. Delavaux, J.-M., Grelu, P., Pu, W., and Ilday, F.Ö. (eds) (2014) Special issue on short-pulse fiber lasers. *Opt. Fiber Technol.*, **20** (6), 561.
21. Okhotnikov, O. (ed) (2012) *Fiber Lasers*, Wiley-VCH Verlag GmbH & Co. KGaA.
22. (2013) Nat. Photonics Focus Issue on Fiber Lasers, **7** (11), 841–882.
23. Grelu, P. and Akhmediev, N. (2012) Dissipative solitons for mode-locked lasers. *Nat. Photonics*, **6** (2), 84–92.
24. Chong, A., Renninger, W.H., and Wise, F.W. (2007) All-normal dispersion femtosecond fiber laser with pulse energy above 20 nJ. *Opt. Lett.*, **32**, 2408–2410.
25. Oktem, B., Ülgüdür, C., and Ilday, F.Ö. (2010) Soliton–similariton laser. *Nat. Photonics*, **4**, 307–311.
26. Wabnitz, S. (1988) Modulational polarization instability of light in a nonlinear birefringent dispersive medium. *Phys. Rev. A*, **38** (4), 2018.
27. Rothenberg, J.E. (1990) Modulational instability for normal dispersion. *Phys. Rev. A*, **42**, 682(R).
28. Haelterman, M., Trillo, S., and Wabnitz, S. (1992) Additive-modulation-instability ring laser in the normal dispersion regime of a fiber. *Opt. Lett.*, **17** (10), 745–747.
29. Soto-Crespo, J.M., Akhmediev, N.N., Afanasjev, V.V., and Wabnitz, S. (1997) Pulse solutions of the cubic–quintic complex Ginzburg–Landau equation in the case of normal dispersion. *Phys. Rev. E*, **55**, 4783.
30. Javaloyes, J., Mulet, J., and Balle, S. (2006) Passive mode locking of lasers by crossed-polarization gain modulation. *Phys. Rev. Lett.*, **97**, 163902.
31. García-Ojalvo, J. and Roy, R. (2001) Spatiotemporal communication with synchronized optical chaos. *Phys. Rev. Lett.*, **86**, 5204.
32. Amo, A. *et al.* (2009) Collective fluid dynamics of a polariton condensate in a semiconductor microcavity. *Nature*, **457**, 291.
33. Amo, A. *et al.* (2011) Polariton superfluids reveal quantum hydrodynamic solitons. *Science*, **332**, 1167.

2
Temporal Cavity Solitons in Kerr Media

Stéphane Coen and Miro Erkintalo

2.1
Introduction

Solitons are self-reinforcing waves that propagate without changing their shape [1]. Rigorously speaking, they arise as localized solutions of integrable nonlinear systems [2]. It is in this context that Zabusky and Kruskal [3], observing the particle-like properties of solitons, first coined the term in 1965. Over the decades, the soliton concept has, however, been extended far beyond integrable systems, particularly in physics, where localized waves with characteristics resembling "ideal" solitons often occur even in highly complex nonintegrable systems (see, e.g., [4] and references therein). Significantly, such solitary waves can also manifest themselves in systems that are, not only nonintegrable, but also nonconservative, that is, dissipative [5]. In these systems, the solitary waves arise due to mechanisms related to self-organization phenomena [6], and the term "dissipative soliton" has been introduced to collectively capture their essence [5, 7, 8]. They are also known as localized dissipative structures (LDSs) or as spots, oscillons, and filaments in various other fields, including chemistry, granular matter, hydrodynamic, or gas discharges [9–12].

Solitons, both conservative and dissipative, have been extensively studied in optics, where they can be realized experimentally relatively easily, and in many different settings [4, 13–15]. Broadly, they manifest themselves either as beams in space or pulses in time, respectively, referred to as *spatial* and *temporal* solitons (we note that hybrid spatiotemporal solitons, also known as light bullets, are also possible [16, 17]). In conservative systems, optical solitons arise through a single balance, whereby nonlinearity arrests the diffractive (or dispersive) spreading of the spatial beam (temporal pulse) [14]. By contrast, in dissipative optical systems (many of which are considered in this book), a second balance is simultaneously at play, through which the losses suffered by the solitons as they propagate are compensated by some form of gain or external driving or forcing [5]. This double balancing act makes dissipative solitons unique attracting states for given external parameters.

Nonlinear Optical Cavity Dynamics: From Microresonators to Fiber Lasers, First Edition.
Edited by Philippe Grelu.
© 2016 Wiley-VCH Verlag GmbH & Co. KGaA. Published 2016 by Wiley-VCH Verlag GmbH & Co. KGaA.

In this chapter, we focus on a particular class of dissipative optical solitons, known as cavity solitons (CSs) [18, 19]. They are solitons existing in *passive* nonlinear resonators, and for which the loss compensating mechanism is based on a coherent external forcing. CSs can be further distinguished as *spatial* and *temporal* CSs, and the latter is our main focus here. Although similarities exist, we must insist that such CSs are fundamentally different from the dissipative solitons supported by laser cavities [20]. CSs can persist indefinitely without any active gain—the cavity can be purely lossy—or in laser cavities operated below threshold, and more importantly the external coherent forcing breaks the phase rotation symmetry traditionally present in lasers [20]. This gives unique properties to CSs which we discuss later. For those reasons, analogies between mode-locked laser solitons and CSs are usually misleading. We must also note that the cavity solitons discussed here should not be confused with the "laser cavity solitons" reported in [21], and which constitute yet another class of dissipative solitons.

Although many nonlinearities can support optical solitons, and CSs in particular, the simplest is arguably the third-order Kerr nonlinearity, which gives rise to a change in the material refractive index that is proportional to the intensity of light [22]. An optical wave with transverse or longitudinal intensity gradients thus creates a refractive index variation acting as a lens, capable of arresting diffraction and/or chromatic dispersion [14]. In conservative systems, such "Kerr" solitons are only stable in one dimension; it is well-known that in two or three dimensions they undergo a catastrophic collapse [23]. This is no longer the case for dissipative systems, however, and in passive cavities stable two-dimensional Kerr cavity solitons have been theoretically identified [24]. Quoting Firth and Weiss, it must, therefore, be clear that CSs are not simply "solitons in a box" [19]: the cavity boundary conditions actively contribute to their stability and existence.

Interest in CSs stems from the fact that they can be individually addressed—turned on and off and even moved around—and that several of them can simultaneously and independently coexist. For that reason, they have early on been proposed as ideal bits in all-optical buffers or optical array processors [25]. Their history starts with the work of McLaughlin *et al.* [26] and Rosanov and Khodova [27] and is well-documented [28–30]. Although they have been extensively investigated since the early 1990s, the majority of these studies have been conducted in the context of two-dimensional spatial nonlinear optics, where the CSs manifest themselves as self-localized beams persisting in the transverse plane of spatially diffractive cavities. Such spatial CSs have been experimentally observed in semiconductor microcavities with a saturating nonlinearity in 2002 [31]. More recent experiments, starting in 2010, have focused on one-dimensional temporal CSs, that is, pulses of light that recirculate in a passive loop of nonlinear optical material coherently driven by a continuous wave (CW) beam [32]. Most temporal studies are based on single- mode optical fiber loops [32–35] and, therefore, deal with purely one-dimensional, instantaneous Kerr, cavity solitons. These constitute the most paradigmatic example of CSs and indeed the pure passive Kerr cavity has been dubbed the "hydrogen atom" of nonlinear cavities [19]. More recently, Kerr temporal CSs have also been observed in monolithic microresonators [36–38] in the context of broadband frequency comb generation.

Temporal CSs hold several advantages over their spatial counterparts. In particular, the performance of spatial CS systems is typically hindered by unavoidable material defects and inhomogeneities in the transverse plane of the nonlinear cavities [31, 39–42]. Temporal CSs are immune to any such defects: as they all circulate around the same optical path, they all experience the same averaged material environment [20]. In other words, translation symmetry is essentially ideal (as discussed later, interactions between temporal CSs slightly break that symmetry [43], but the same occurs for spatial CSs). Integration with existing telecommunication technologies is also more natural.

In this chapter, we give a brief overview of the properties and dynamics of one-dimensional Kerr CSs. We focus, in particular, on implementations involving temporal CSs in fiber cavities, yet we do note that one-dimensional Kerr-like CSs have also been observed experimentally in *spatial* systems using liquid crystals [44]. In this context, we also emphasize that all dynamics and experiments that are specific to two-dimensional spatial CSs are wholly beyond the scope of our discussion; the keen reader is referred to one of the excellent reviews that have been published on the topic [28–30].

2.2
Mean-Field Equation of Coherently Driven Passive Kerr Resonators

Temporal cavity solitons can be understood as localized, nonperiodic steady-solutions of the mean-field equation that describes the dynamics of light in nonlinear optical cavities. We begin by briefly (and heuristically) recalling the physical origins of this equation, considering as a particular example a coherently driven optical fiber resonator (see Figure 2.1). A CW driving field E_{in} (which can be taken real without loss of generality) with power $P_{\text{in}} = |E_{\text{in}}|^2$ acts as the pump, and is coherently added to the light wave circulating in the resonator through a coupler with power transmission coefficient θ. The remaining port of the coupler is used to extract the output field. The intracavity field $E^{(m+1)}(z = 0, \tau)$ at the beginning of the $(m + 1)$th roundtrip can be related to the field $E^{(m)}(z = L, \tau)$ at the end of the mth roundtrip as

$$E^{(m+1)}(z = 0, \tau) = \sqrt{\theta}\, E_{\text{in}} + \sqrt{1-\theta}\, E^{(m)}(z = L, \tau)\, e^{i\phi_0}\ , \tag{2.1}$$

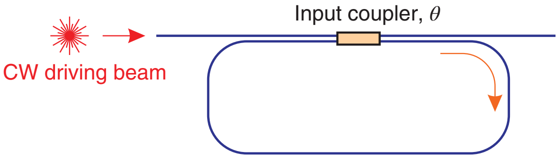

Figure 2.1 Schematic of a CW-driven nonlinear, passive, optical fiber ring cavity.

where τ is the fast time that describes the temporal profile of the intracavity field in a reference frame traveling at the group velocity of the driving field, L the roundtrip length of the resonator, z the spatial coordinate along the resonator, and ϕ_0 is the linear phase accumulated by the intracavity field with respect to the driving field over one roundtrip. Denoting as β_0 the propagation constant of the fiber mode at the driving beam angular frequency ω_0, we have $\phi_0 = \beta_0 L$.

Assuming that the fiber only supports a single spatial mode and neglecting polarization effects, the evolution of the field through one roundtrip of the resonator is governed by the well-known nonlinear Schrödinger equation (NLSE) [45],

$$\frac{\partial E(z,\tau)}{\partial z} = -\frac{\alpha_\mathrm{i}}{2}E - i\frac{\beta_2}{2}\frac{\partial^2 E}{\partial \tau^2} + i\gamma|E|^2 E\,. \tag{2.2}$$

where α_i is the linear absorption coefficient of the fiber (and represents the *internal* cavity loss), β_2 is the group-velocity dispersion coefficient, and $\gamma = n_2\omega_0/(cA_\mathrm{eff})$ is the nonlinearity coefficient with n_2 the nonlinear refractive index, c the speed of light in vacuum, and A_eff the effective modal area of the fiber spatial mode.

The infinite-dimensional map given by Eqs. (2.1) and (2.2) describes completely the nonlinear cavity dynamics. However, for low-loss (high finesse) resonators ($\alpha_\mathrm{i}L, \theta \ll 1$), the equations can be combined into a single partial differential equation that is more amenable to theoretical analysis. In this limit, the cavity photon lifetime is large with respect to the roundtrip time t_R. The intracavity field can thus be assumed to vary only slightly over the course of one roundtrip, so that Eq. (2.2) can be trivially integrated (with a first-order Euler step) and subsequently combined with the boundary conditions Eq. (2.1) (for more details, we refer to [46]). The resulting equation for the mean intracavity field E has the form of an externally driven NLSE,

$$t_\mathrm{R}\frac{\partial E(t,\tau)}{\partial t} = \left[-\alpha - i\delta_0 - iL\frac{\beta_2}{2}\frac{\partial^2}{\partial \tau^2} + i\gamma L|E|^2\right]E + \sqrt{\theta}\,E_\mathrm{in}\,. \tag{2.3}$$

Here, the continuous variable t measures the *slow time* of the cavity and describes how the intracavity field evolves over subsequent roundtrips. It can be linked to the roundtrip index m as $E(t = mt_\mathrm{R}, \tau) = E^{(m)}(0, \tau)$. To avoid any ambiguity, τ is then referred to as the *fast time*. The coefficient $\alpha = (\alpha_\mathrm{i}L + \theta)/2$ represents the total cavity losses, lumping together internal losses, and output coupling (more generally, other losses such as splice loss or intracavity component losses can be added as well). Strictly speaking, it is half the percentage of the total roundtrip power losses, and the cavity finesse can then be expressed as $\mathcal{F} \simeq \pi/\alpha$. The parameter $\delta_0 = 2\pi l - \phi_0$ describes the phase detuning of the driving field with respect to the closest cavity resonance (with order l and angular frequency ω_l). At first order (neglecting chromatic dispersion), it can also be expressed in terms of the angular frequencies of the lth cavity resonance and that of the driving beam as $\delta_0 = t_\mathrm{R}(\omega_l - \omega_0)$. We must note that with the change of variable $E \to Ee^{-i\delta_0 t/t_\mathrm{R}}$, the detuning term in the above-mentioned equation can be eliminated provided that the driving term is replaced by $E_\mathrm{in}e^{i\delta_0 t/t_\mathrm{R}} = E_\mathrm{in}e^{i(\omega_l-\omega_0)t}$. Equation (2.3) is, therefore, also known as the *AC-driven* NLSE [47].

It is convenient to write Eq. (2.3) in normalized units as

$$\frac{\partial E(t,\tau)}{\partial t} = \left[-1 + i(|E|^2 - \Delta) - i\eta\frac{\partial^2}{\partial \tau^2}\right] E + S. \tag{2.4}$$

Here, we have introduced the normalized detuning $\Delta = \delta_0/\alpha$ and driving strength $S = E_{\text{in}}(\gamma L\theta/\alpha^3)^{1/2}$, while η is the sign of the dispersion coefficient β_2. To avoid notational clutter, we have, however, used the same symbols for the intracavity field E, slow-time t, and fast-time τ as in the dimensional variant Eq. (2.3). The normalization we use is such that [32],

$$t \to \alpha\frac{t}{t_R}, \qquad \tau \to \tau\sqrt{\frac{2\alpha}{|\beta_2|L}}, \qquad E \to E\sqrt{\frac{\gamma L}{\alpha}}\ . \tag{2.5}$$

Equation (2.4) represents the mean-field model of a nonlinear Kerr resonator. Its simplicity stems from the equation being uni-dimensional and having only two external controllable parameters, both real, respectively, S and Δ. In that sense, it can be seen as the paradigmatic model of nonlinear resonators. Equation (2.4) was first studied by Lugiato and Lefever in the context of spatially diffractive cavities [48], and for this reason it is often referred to as the "Lugiato-Lefever" equation (LLE). The LLE was extended to the temporal domain by Haelterman *et al.*, who used it to describe the formation of temporal modulation instability patterns in fiber ring resonators [49]. More recently, it has found extensive applications in the modeling of optical frequency combs in monolithic Kerr microresonators [50]. The resemblance of Eq. (2.4) with reaction-diffusion equations is also clear, therefore justifying the analogy between CSs and self-organized LDSs found, for example, in chemistry and developmental biology [6, 51].

2.3

Steady-State Solutions of the Mean-Field Equation

One-dimensional temporal CSs correspond to temporally localized, steady-state solutions of Eq. (2.4). To best appreciate their essence, however, we first need to discuss briefly the other types of steady-state solutions supported by the Kerr cavity.

The simplest stationary ($\partial E/\partial t = 0$) solutions of Eq. (2.4) are homogeneous ($\partial E/\partial \tau = 0$). They satisfy the well-known cubic equation of dispersive optical bistability [46]:

$$X = Y^3 - 2\Delta Y^2 + (\Delta^2 + 1)Y, \tag{2.6}$$

where $X = |S|^2$ and $Y = |E|^2$ represent, respectively, the CW driving and intracavity powers. As illustrated in Figure 2.2a, the steady-state curve (Y vs. X) is single-valued for $\Delta < \sqrt{3}$, whereas it assumes the typical S-shape characteristics of hysteresis for $\Delta > \sqrt{3}$. That hysteresis is associated with optical bistability; indeed, the middle branch of the steady-state curve is unconditionally homogeneously

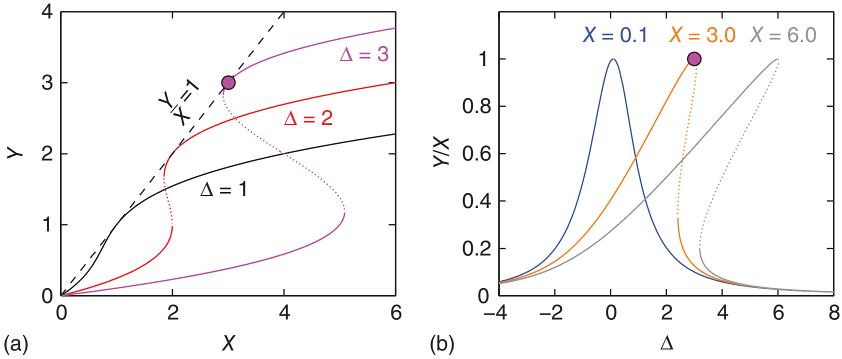

Figure 2.2 Optical bistability of the homogeneous state. (a) Intracavity power Y versus driving power X for various values of the detuning Δ. (b) Corresponding response but versus Δ, for fixed values of X (normalized to X for clarity). The circle corresponds to the peak of the resonance at $X = Y = \Delta = 3$. Dotted parts are unstable.

unstable. Equation (2.6) is a second-order equation in the detuning Δ, which can be trivially solved, leading to

$$\Delta = Y \pm \sqrt{\frac{X}{Y} - 1}\,. \tag{2.7}$$

This equation is illustrated in Figure 2.2b and can be interpreted as the resonance of the ring cavity tilted under the influence of the Kerr nonlinearity (the linear resonance would peak at $\Delta = 0$). Together with Figure 2.2a, these are simply different cross-sections of the intracavity power response, $Y = Y(X, \Delta)$. We note that, with our units, the peak of the (nonlinear) resonance in Figure 2.2b satisfies $X = Y = \Delta$ (and $Y \leq X$ for all Δ). The corresponding point in Figure 2.2a is found where a straight line passing through the origin is tangent to the S-shaped response (maximum intracavity build-up factor).

Although the lower and upper branches of the homogeneous bistable response are stable to *homogeneous* perturbations, they can exhibit an instability against *periodic* perturbations [49]. This corresponds to the ubiquitous modulation instability (MI) so common with nonlinear waves, whereby a weak periodic perturbation grows atop a plane wave (or CW) background [52, 53]. In optical fibers, MI normally only occurs in the anomalous dispersion regime [45]. However, because of the extra degree of freedom provided by the boundary conditions [49, 54], MI in passive cavities exists both for anomalous ($\eta = -1$) and normal ($\eta = +1$) dispersion. Another important difference is that, in passive cavities, the growing MI pattern is eventually stabilized by the dissipation, so that *stationary* periodic pattern solutions can exist (in contrast to the Fermi-Pasta-Ulam recurrence observed in conservative systems [55, 56]). This is directly related to the well-known Turing patterns and other periodic patterns and stripes that commonly occur in nature [57], including, for example, in vegetation [58] and animal coats [51].

In the mean-field limit, the small signal amplitude gain λ of the MI-generated spectral sidebands is given by Haelterman *et al.* [49]

$$\lambda = -1 + \sqrt{4Y(\Delta - \eta\Omega^2) - (\Delta - \eta\Omega^2)^2 - 3Y^2}\ , \tag{2.8}$$

where Y is the power of the CW background [satisfying Eq. (2.6)] and Ω is the angular frequency of the modulation. We must have $\mathrm{Re}(\lambda) > 0$ for MI to occur. In terms of power threshold, a necessary condition in all cases is that the CW intracavity power $Y \geq 1$. This in turn implies that the absolute minimum *driving* power required for intracavity MI is $X \geq 1$ (for $X = 1$, MI would precisely occur at the peak of the tilted CW resonance, where $\Delta = 1$). In addition, for $\Delta > 2$, MI in the anomalous dispersion regime requires $Y > \Delta/2$, which makes the entire upper branch of the homogeneous response unstable while the lower one is stable. Slightly, the opposite occurs for normal dispersion, where the extra condition is $Y < \Delta/2$. In that case, MI only occurs at the end of the CW lower branch [59].

An example of the emergence of a steady-state intracavity MI pattern is illustrated in Figure 2.3, which was obtained by numerically integrating Eq. (2.4) with a standard split-step Fourier algorithm [45]. Here, we consider the anomalous dispersion regime ($\eta = -1$), and we have chosen $X = 2.5$ and $\Delta = 1.5$. As $\Delta < \sqrt{3}$, the homogeneous response is monostable: Eq. (2.6) yields a single real root, $Y = 2$, which is the power of the CW intracavity field before MI emerges as seen in Figure 2.3. Over time, it can be seen how that CW wave evolves into a steady pattern consisting of a periodic train of pulses.

In the anomalous dispersion regime, we must also stress that the MI pattern solution emerges supercritically from the homogeneous state when $\Delta < 41/30$, while the bifurcation becomes subcritical for $\Delta > 41/30$ [48, 60]. In the latter case, a periodic pattern can, therefore, coexist with a stable CW solution (the lower branch when bistability of the homogeneous state is present) over a certain

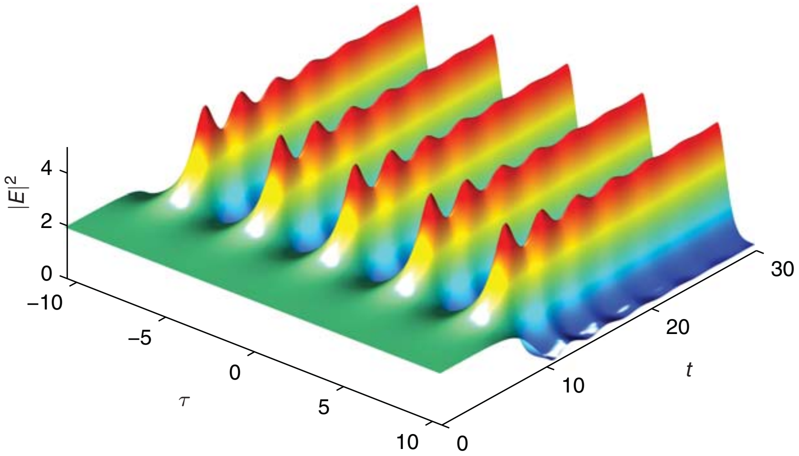

Figure 2.3 Spontaneous emergence of a periodic pattern through MI from a CW background power level $Y = 2$ with $X = 2.5$ and $\Delta = 1.5$ (anomalous dispersion).

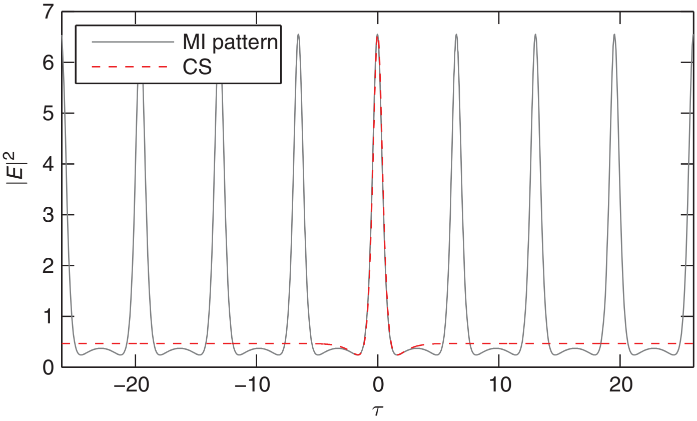

Figure 2.4 Illustration of how the CS solution results from the coexistence of the CW and patterned solution in different parts of the cavity. Both solutions are calculated for the same parameters, $X = 3$ and $\Delta = 2.8$ (anomalous dispersion).

range of parameters. It is this coexistence that underpins the existence of cavity solitons [61, 62]. Specifically, CSs can be understood as localized structures that correspond to the periodic MI pattern over some finite range in τ connected on both sides by fronts with the CW solution [63]. This is illustrated in Figure 2.4. Both the patterned MI and the localized CS solutions shown correspond to steady states of Eq. (2.4) with $\eta = -1$, $X = 3$, and $\Delta = 2.8$. The situation is a bit different in the normal dispersion regime where both the upper and lower CW states can be simultaneously stable. Under certain conditions, two fronts connecting these states can stably lock together forming what has been called autosolitons [27]. This can lead in particular to dark localized structures [64]. Higher-order dispersion also further enriches the landscape of solutions (see, e.g., [65–67]). In the following sections, however, we restrict our discussion to the anomalous dispersion regime, which is where most experimental results on temporal CSs have been obtained.

2.4
Existence and Characteristics of One-Dimensional Kerr Cavity Solitons

The existence and stability of one-dimensional Kerr CSs has been investigated by many groups [32, 47, 64, 68], and for an in-depth analysis we refer, in particular, to [47]. Here, we focus on parameters relevant to experiments involving temporal CSs. These experiments typically are performed in the $\Delta > \sqrt{3}$ regime where the CW solutions exhibit bistability.

Figure 2.5 gives an example of where CSs exist in the (X, Δ) parameter space. More specifically, we have plotted here the peak power of the CSs (red curve labeled "CS") (a) versus the driving power X for a fixed detuning value $\Delta = 2.5$,

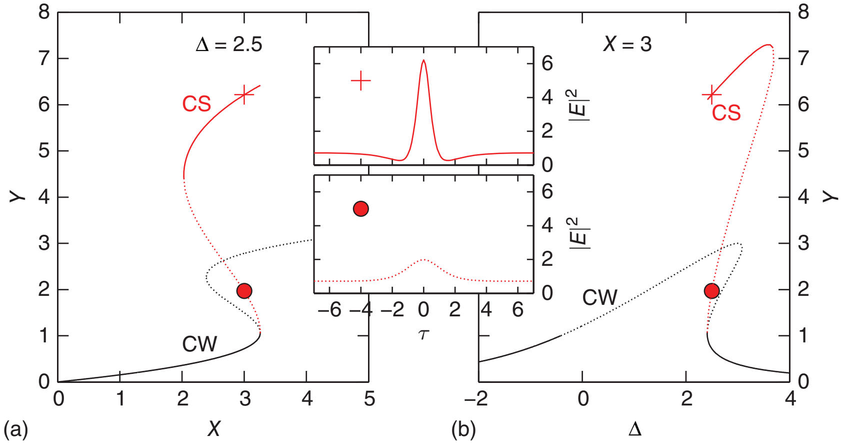

Figure 2.5 Existence and stability charts of CS (red) solutions superimposed on the CW response (black). Dotted parts are unstable. (a) Peak intracavity power as a function of driving power X for a fixed detuning $\Delta = 2.5$. (b) Same as (a) but versus Δ, for a fixed driving power, $X = 3$. The middle insets show temporal intensity profiles of stable (top) and unstable (bottom) CSs that exist for the same parameters ($X = 3$, $\Delta = 2.5$) and indicated in the main plots with the cross and the solid circle, respectively.

and (b) versus the detuning for a fixed driving power $X = 3$. These curves are superimposed with the CW bistable response (black curve labeled "CW") and Figure 2.5 can, therefore, be seen as an extension of Figure 2.2. All the unstable solutions appear dotted: the middle CW branch, the upper CW branch [through MI, wherever $Y > \max(1, \Delta/2)$], and the lower part of the CS branch.

As seen in Figure 2.5, the CS branch emerges from the homogeneous (CW) response at the CW up-switching point [for $X = 3.26$ in (a) and for $\Delta = 2.41$ in (b)]. CSs are initially unstable, very broad, and with a low peak power above the CW background (they tend to be infinitely wide when approaching the CW up-switching point). The temporal intensity profile of such a solution is illustrated in the lower inset of Figure 2.5 [and corresponds to the filled circle in panels (a) and (b)]. The CS branch eventually folds, approximately when $\Delta = \pi^2 X/8$ (valid in the limit of large X) [47], and CSs are typically stable from here. A corresponding typical temporal intensity profile is shown in the upper inset [crosses in (a) and (b)] and reveals the well-documented characteristic presence of dips around the main peak [19, 32].

In both insets, it is clear that the CSs are superimposed on (or connected with) a CW background, which corresponds to the lower state CW solution (the smallest solution of Eq. (2.6), $Y = 0.72$ for the profiles shown in insets). The necessary presence of this background is easy to understand: far from the CS peak, the intracavity field must correspond to one of the *stable* solutions of the LLE (2.3). It cannot be zero as $E = 0$ is not a solution of Eq. (2.3) when $X > 0$. This requirement on the CW background also explains why CSs cease to exist beyond the CW up-switching point [for $X > 3.26$ in (a) and for $\Delta < 2.41$ in (b)].

To be complete, we must also mention that for higher values of the detuning ($\Delta \gtrsim 3.3$, not shown in Figure 2.5), a Hopf bifurcation occurs. In this case, the end of the upper CS branch is unstable, and CSs in this regime exhibit a breathing behavior (limit cycle) [33, 67, 69]. For even larger values of the parameters, the dynamics becomes more complex, and eventually chaotic [33, 69]. Another important consideration worth pointing out is that CSs on the lower (unstable) branch have only one unstable eigenmode. They, therefore, act as quasi-attractors during transients, and CSs being written or erased dwell close to it before eventually moving away [24, 29, 32, 70].

Figure 2.5 makes clear that, for given external parameters X and Δ, CSs do not form continuous families of solutions such as (conservative) NLSE solitons. Rather, CSs are unique, fixed attracting states whose characteristics are completely and uniquely determined by the parameters. This is similar to other kind of dissipative solitons, including those in mode-locked lasers. A significant difference exists, however, with (active) laser cavities in that pulses in lasers compete for the same material gain, which creates strong long-range coupling between each unit simultaneously existing in the cavity. Kerr CSs in contrast are not subject to any material gain, and as a consequence several can simultaneously and independently circulate in the same cavity without competition. In particular, whether no, one, or several CSs (all with the same characteristics) are present in the cavity, the driving power required would stay the same.

This explains why CSs can be individually addressed, that is, independently turned on (or "written") and off ("erased") without affecting others, which is one of their key features. This can be achieved by applying localized perturbations on the intracavity field. Figure 2.6 illustrates these dynamics using numerical simulations of the LLE (2.4). Here, we have started the simulation from a zero initial condition and, at $t = 50$, we have abruptly added a localized perturbation

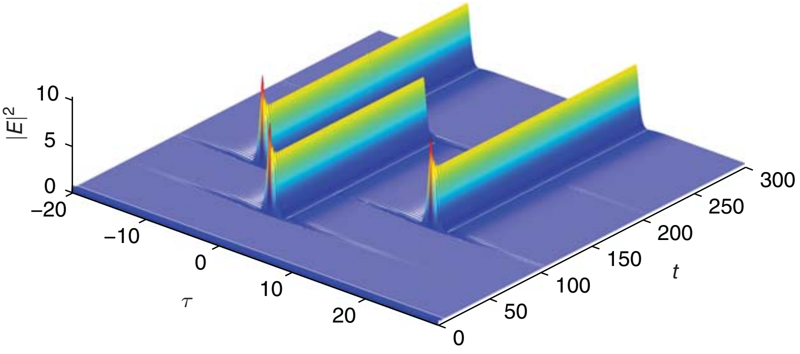

Figure 2.6 Numerical simulation illustrating individual addressing of CSs. Starting from an empty cavity, the field first converges to the steady-state CW solution. At $t = 50$, a pulse at $\tau = 0$ is superimposed on the background, exciting a single CS. At $t = 100$, two further CSs are similarly excited at $\tau = -8$ and $\tau = +15$. At $t = 200$, the first CS is erased using a perturbation with a π phase shift relative to that used for excitation.

in the form of a hyperbolic secant pulse to the intracavity field so as to create a single CS. Using similar means, we create at a later time, $t = 100$, two more CSs, asymmetrically positioned around the first one. At $t = 200$, we then erase the first CS by adding to the intracavity field the same perturbation as for writing but phase shifted by π. At each writing and erasing step, we must note that the CSs that are not being addressed are unaffected. During the whole simulation, we maintain the driving power and the detuning constant, $X = 3$ and $\Delta = 3$.

The mutual independence of CSs also makes it possible to move them around without disturbing them. In fact, this stems from the translation symmetry (in τ) of the LLE (2.4). This implies that CSs are neither stable nor unstable to perturbations that shift their position: if they are shifted, they will stay put at their new position and there will not be any restoring force to bring them back to their original position. This is associated with the existence of a neutral translation mode with zero eigenvalue for the CS solutions [30, 70]. For a stable CS, this is the only mode that is nondamped and, therefore, the effect of any perturbation will be to shift the CS position (provided the perturbation overlaps with the neutral mode). In particular, any gradient in the cavity or driving beam parameters will induce motion of the CSs.

Gradients can be present accidentally, such as in planar cavity experiments with spatial CSs, where the cavity is usually not perfectly planar [31]. These defects are very hard to avoid, but temporal CSs are immune to this since each temporal CS continuously samples the entire cavity and only sees the average environment [20]. Gradients can also be introduced artificially by modulating the intensity or phase of the driving beam, either in space or in time for spatial and temporal CSs, respectively. In that case, CSs will eventually be trapped at the positions where the gradient vanishes [62, 71]. These gradients can, therefore, be used to easily manipulate the CSs and this is referred to as the CS "plasticity." Several experiments with spatial CSs have demonstrated these concepts [31, 39, 41, 72], which have also been used to design delay lines and probe the defects of optical structures [40, 73]. More recently, they were implemented with temporal CSs, and simultaneous independent manipulation of multiple temporal CSs has been reported, thereby demonstrating a fully reconfigurable optical buffer [74]. Finally, gradients can arise from the decaying tails of other nearby CS. This can lead to relative motion of two CSs that are sufficiently close to each other. Since the CS field decays exponentially, such interactions typically occur only for separations smaller than a few characteristic soliton widths [28, 75–77].

2.5
Original Experimental Observation of Temporal Kerr Cavity Solitons

Temporal CSs were first observed experimentally in 2010 by Leo *et al.* using the experimental setup depicted in Figure 2.7 [32]. Their passive Kerr cavity was constructed entirely out of standard single-mode silica fiber, and had a total length of about 380 m, which resulted in a roundtrip time of 1.85 μs. The fiber

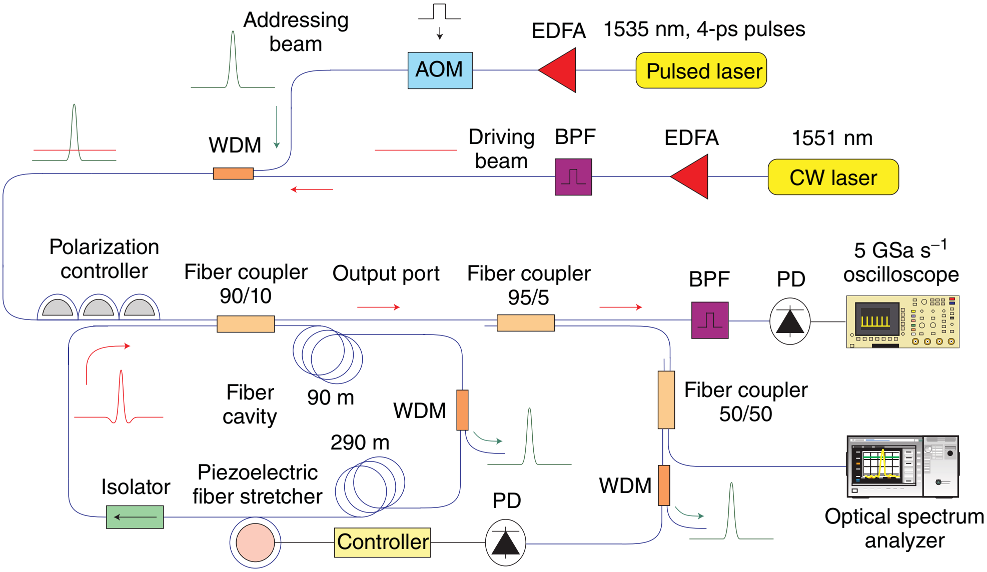
Addressing beam
AOM
EDFA
1535 nm, 4-ps pulses
Pulsed laser
WDM
Driving beam
BPF
EDFA
1551 nm
CW laser
Polarization controller
Fiber coupler 90/10
Output port
Fiber coupler 95/5
BPF
PD
5 GSa s^{-1} oscilloscope
Fiber cavity
90 m
WDM
290 m
Fiber coupler 50/50
Isolator
Piezoelectric fiber stretcher
PD
WDM
Controller
Optical spectrum analyzer

Figure 2.7 Experimental setup used for the first observation of temporal CSs by Leo *et al.* EDFA, Erbium-doped fiber amplifier; BPF, bandpass filter; PD, photodiode (adapted from [32]).

was laid in a ring configuration and closed on itself with a 90/10 fiber coupler, arranged such that 90% of the intracavity power was recirculated. The resonator also incorporated an optical fiber isolator—to prevent the build-up of stimulated Brillouin scattering [45, 78]—and a wavelength-division multiplexer (WDM) through which the pulses used to excite CSs were coupled out of the cavity (as explained later). Overall, the cavity had total losses (including the 90/10 coupler) of 26%, corresponding to a high finesse of 24 and to 22-kHz-wide linear (cold) resonances.

To coherently drive the resonator, it is necessary that the spectral linewidth of the driving laser is narrower than that of the cavity resonances (or equivalently that the driving laser coherence time is larger than the cavity photon lifetime). In [32], this was achieved using a distributed feedback fiber laser with an ultra-narrow 1-kHz linewidth. The laser was operating at 1551 nm wavelength and its power was amplified to 225 mW before it was launched into the cavity as the driving field. The intracavity field was diagnosed spectrally and temporally through the fourth port of the 90/10 coupler. Because the cavity resonance frequencies (and to a lesser extent the driving laser frequency) are generally sensitive to environmental perturbations, it is necessary to actively stabilize the cavity phase detuning Δ. In the setup shown in Figure 2.7, this was achieved by sending part of the extracted output power to a servo-controller so as to drive a piezoelectric fiber stretcher that actuated the cavity length (and thereby the resonance frequencies). Once the driving beam was turned on, the servo-controller was adjusted such that the intracavity field was locked to the lower level within the CW bistable regime.

To excite temporal CSs, amplified 4 ps addressing pulses from a 1535 nm wavelength mode-locked laser (with a 10 MHz repetition rate) were mixed with the driving beam (through another WDM) before its launch into the cavity. An acousto-optic modulator (AOM) was used to either pick a single addressing pulse or to encode a desired binary data sequence onto the 10 MHz pulse train. Inside the resonator, the addressing pulses excited CSs by interacting incoherently with the 1551 nm CW intracavity field through cross-phase modulation [45]. Specifically, CS excitation occurs because the addressing pulses locally perturb the phase of the CW background. This perturbation—provided it is strong enough—eventually reshapes into a CS [79, 80]. The intracavity WDM was used to extract the addressing pulses 100 m down from the input coupler to avoid excitation of multiple CSs that would occur due to the walk-off between the addressing pulses and the CW intracavity field. It must be clear that addressing pulses need only to interact *once* with the intracavity field to excite CSs. The rest of the time, the addressing laser is totally blocked by the AOM while the temporal CSs persist by themselves. Another important point to highlight is that the temporal CSs are created at the wavelength of the driving field and are coherent with it.

Figure 2.8 is the first record of a temporal CS as reported in [32]. It shows the temporal intensity profile of the steady-state cavity output, recorded with a 5 GSa s^{-1} oscilloscope, after a single addressing pulse was launched into the cavity. A periodic train of pulses with a temporal separation that coincides with the 1.85 μs cavity roundtrip time can clearly be seen. This implies that a single pulse was persistently circulating in the resonator. Significantly, the measurement was taken 1 s after the addressing pulse had left the cavity, during which the intracavity pulse had already completed more than half a million roundtrips. Recalling

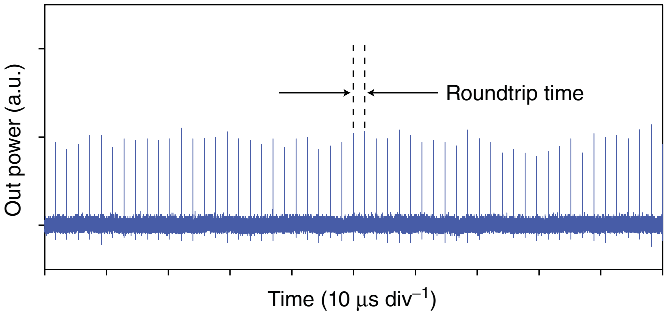

Figure 2.8 Original 2010 observation of an isolated temporal CS in the form of an oscilloscope recording (linear scale) of the light intensity at the cavity output. The delay between subsequent pulses matches the 1.85-μs cavity roundtrip time and confirmed the presence inside the cavity of a single persistent pulse circulating repeatedly, only sustained by the CW driving beam (adapted from [32]).

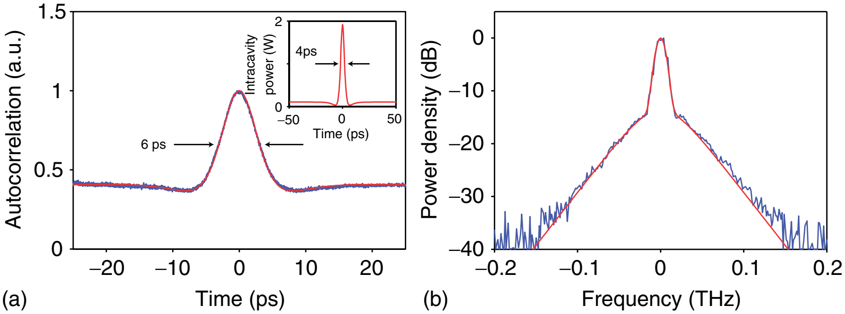

Figure 2.9 (a) Experimental (blue) intensity autocorrelation trace of the intracavity pulse observed by Leo *et al.* It is compatible with a 4-ps-long temporal CS, as revealed by its comparison with a numerically simulated trace (red) that corresponds to the temporal intensity profile of the CS shown in the inset. (b) Experimental (blue) and simulated (red) optical spectra. The simulated spectrum corresponds to the CS shown in the inset in (a) (adapted from [32]).

that the cavity had total roundtrip losses of 26%, this unequivocally highlights that the pulse was continuously extracting energy from the CW driving, balancing all the losses it experienced. Such an energy balance is a characteristic feature of CSs, and of dissipative solitons in general. The authors of [32] also measured the spectral and temporal characteristics of the intracavity pulses. Results of these measurements are shown in Figure 2.9, together with numerical simulations (red lines). Agreement is excellent and, in particular, both sets of results suggest that the pulses have a duration of 4 ps. The fact that these measurements were also performed after the pulses had traversed hundreds of thousands of roundtrips strongly indicates that nonlinearity is arresting dispersion-induced spreading. Indeed, with the parameters used in the experiment, a linearly propagating 4 ps pulse would be expected to double its duration half way through a single roundtrip.

Taken all together, the observations reported here strongly suggest that the pulse circulating in the cavity was a temporal CS. For final confirmation, the authors also convincingly demonstrated that the pulses could be individually addressed and that several of them could simultaneously coexist. This was achieved by using the AOM to encode a particular binary-coded data sequence onto the addressing beam. The 15-bit long data sequence was selected to correspond to the acronym “ULB” of the Université Libre de Bruxelles, [32] authors’ institution. Each letter was represented by its ordinal position in the alphabet ($U = 21$, $L = 12$, $B = 2$) coded on five bits. Figure 2.10 shows the stored data stream at the cavity output after a storage time exceeding a second. As can clearly be seen, the cavity output repeats the addressing bit-stream without degradation. This result proves without doubt that several pulses can be independently excited at different positions along the cavity, thereby further confirming that they are genuine temporal CSs.

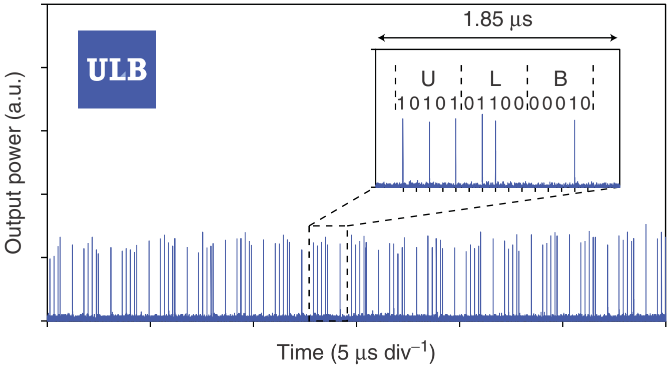

Figure 2.10 The acronym of ULB (Université Libre de Bruxelles) encoded with temporal CSs as a 15-bit data stream. Each letter is represented with five bits by its ordinal position in the alphabet (U = 21, L = 12, B = 2) (adapted from [32]).

2.6
Interactions of Temporal CSs

Similar to all solitons [13], Kerr CSs interact when sufficiently close to each other, which places limitations as to how densely they can be stored. In a pure Kerr medium, the interaction strength is expected to decay exponentially with CS separation [81], such that non-negligible interactions only manifest themselves for solitons separated by a few characteristic widths [43, 75]. Leo *et al.* made a preliminary investigation of such interactions in their seminal work of 2010 [32]. Two temporal CSs were excited in close proximity by using a pair of addressing pulses whose relative delay could be tuned. For small separations of 25 ps or less, it was found that only a single CS persisted after the writing process. Either only one had actually been excited, or two were excited but subsequently attracted and merged—numerical simulations revealed that this depended sensitively on initial conditions. In contrast, when the addressing pulses were separated by 30 ps, the two CSs repelled, increasing their separation to 39 ps after freely propagating for about 1 s in the cavity. The repulsion was found to weaken with a larger initial separation of 40 ps, yet, quite unexpectedly, appeared to strengthen again when the addressing pulses were separated by 60 ps. Interestingly, such a separation corresponded to more than 10 soliton widths, and clearly the observations do not fit with an exponential interaction law. Unfortunately, at the time, the cavity detuning could not be kept locked for more than one second [32], which prevented the dynamical mechanisms behind such long-range interactions to be fully unveiled.

This was, however, achieved in a subsequent experiment conducted by Jang *et al.* by using a slightly different experimental design [34]. Specifically, instead of adjusting the cavity length to stabilize the cavity phase detuning (as was done by Leo *et al.* [32]), Jang *et al.* actuated the frequency of the driving laser. Because this approach could work over a larger excursion of the environmental parameters, it rendered the stabilization system much more robust. Combined with the fact that the cavity was about four times shorter (100 m long, or a cavity roundtrip time of about 0.5 μs), temporal CSs could be routinely supported for periods in excess of 30 min. These experiments revealed that temporal CSs in fiber rings could interact even when separated by hundreds of soliton widths. Note that the duration of the temporal CSs in Jang *et al.*'s experiment was only 2.6 ps, mainly due to the shorter cavity length [34].

Again, the interactions were studied by launching two temporal CSs in the cavity with a predefined initial separation and by observing their evolution. Three representative measurements are shown in Figure 2.11 for initial separations of 100 ps (38 soliton widths), 1500 ps (577 soliton widths), and 1800 ps (692 soliton widths). Here, the plots have been obtained by vertically concatenating successive oscilloscope traces of the cavity output intensity recorded at 1 frame per second. Interactions can clearly be seen for all cases. For the smallest separation of 100 ps (Figure 2.11a), the temporal CSs repel each other until they reach a stable separation of about 420 ps. When the initial separation is 1500 ps (Figure 2.11b), the solitons were found to attract one another until the same stationary separation of 420 ps was reached. When the initial separation was increased even further, the interaction was found to become repulsive again but no stable separation was observed (Figure 2.11c).

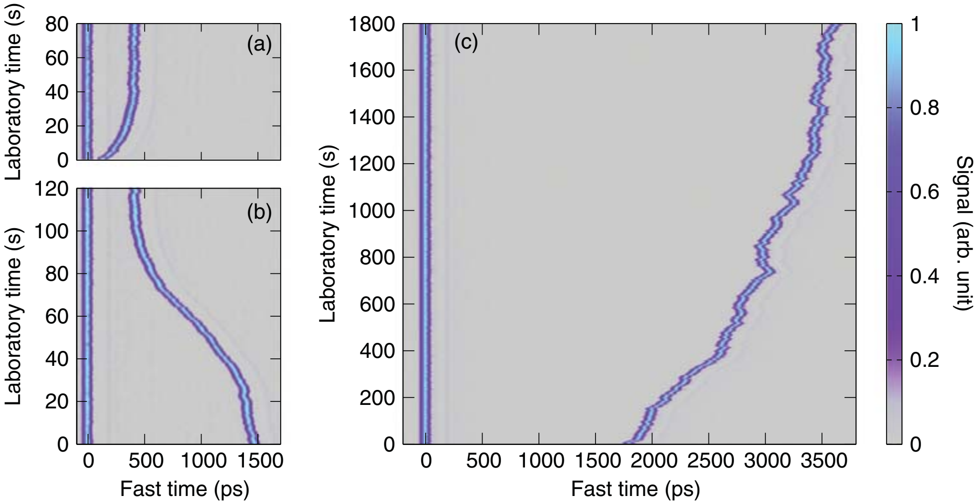

Figure 2.11 Color plots made up of successive oscilloscope measurements at the cavity output showing the temporal evolution of two temporal CSs as they interact. (a) For an initial separation of 100 ps (38 soliton widths), the interaction is repulsive until a stable separation of 420 ps is attained. (b) An attractive interaction is observed when the initial separation is increased to 1500 ps (577 soliton widths), eventually leading to the same final separation of 420 ps. (c) For an initial separation of 1800 ps, the interaction is very weakly repulsive (adapted from [34]).

The interactions reported by Jang *et al.* [34] display some quite remarkable characteristics. First, they occur over extremely long ranges, indicating a highly nonlocal underlying mechanism. Second, the timescales involved are remarkably long for an optical system. Indeed, the measurements in Figure 2.11c span a 30-min period during which the picosecond CSs travel around the cavity 3.6 billion times, for a total distance of 360 million kilometers, or 2.4 astronomical units. Yet over that vast distance, the two CSs only shift their relative position by less than 2 ns, equivalent to a change of 40 cm in spatial separation, 12 orders of magnitude smaller than the distance traveled. Such displacement corresponds to half an attosecond per cavity roundtrip, that is, much smaller than the carrier wavelength. It is in some sense simply spectacular that such a small displacement can coherently accumulate over billions of roundtrips despite the environmental noise. This result, therefore, highlights the robustness and stability of solitons as never before.

The physical mechanism giving rise to these long-range, ultraweak interactions between the temporal CSs was found to be electrostriction [34]. Specifically, thanks to its time-dependent intensity profile, a temporal CS generates transverse acoustic waves that perturb the fiber refractive index [82]. Figure 2.12a shows the calculated impulse response of that perturbation, δn. It consists of short spikes (1-2 ns in duration) occurring every 21 ns. These correspond to increasing orders of echoes, that is, back-and-forth reflections of the acoustic wave from the fiber cladding-coating boundary back into the fiber core region [83]. In between the spikes, the response remains negligible due to the absence of overlap between the optical mode trapped inside the fiber core and the acoustic wave traveling in the cladding. When two temporal CSs co-propagate, the trailing CS can temporally overlap with the refractive index perturbation created by the leading one. Because the perturbation is time-varying, it can give rise to a shift in the instantaneous frequency of the trailing CS. Specifically, if $d\delta n/dt > 0$ (respectively, <0), the trailing temporal CS is red-shifted (blue-shifted) with respect to the leading one. Because the experiment was performed in the anomalous dispersion regime [45], this frequency shift translates into a smaller (larger) group velocity, resulting in an effective repulsion (attraction) between the CSs. It is only when $d\delta n/dt = 0$ that the two CSs travel at the same group velocity and do not move with respect to each other. In other words, the trailing CS is attracted to the closest peak of the refractive index perturbations, where it may sit stably. Figure 2.12b shows a close-up of the first spike of the acoustic impulse response plotted in Figure 2.12a, and highlights the ranges of repulsion and attraction inferred from the previous analysis. Very good qualitative agreement is observed between this predicted behavior and the experimental observations summarized in Figure 2.11.

To further confirm the acoustic origins of the observed interactions, the authors of [34] also explored the dynamics of a pair of temporal CSs whose initial separation was adjusted around 21 ns to match the first re-entrance of the acoustic wave into the fiber core. A zoom on the refractive index perturbation in this region is shown in Figure 2.13a. The two maxima signal that four different

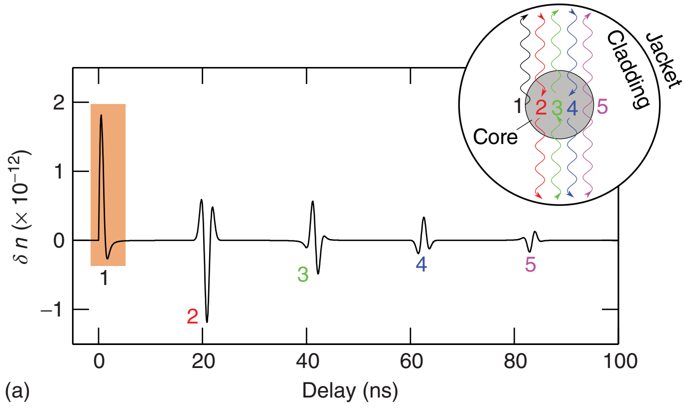

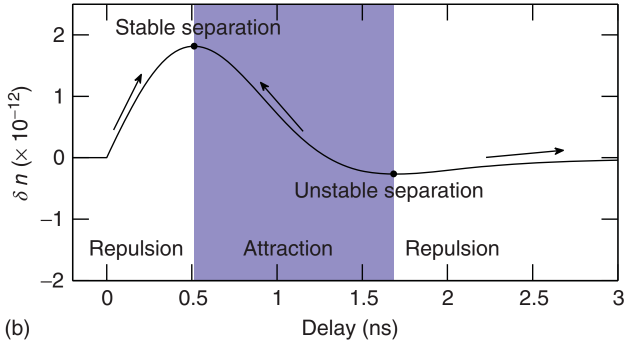

Figure 2.12 (a) Theoretical impulse response of the refractive index acoustic perturbation calculated for values pertinent to the experiment. Subsequent spikes (numbered 1-5) are separated by ~21 ns and arise from consecutive reflections of the acoustic wave from the fiber cladding-coating boundary, as schematically illustrated in the inset. (b) Close-up of the first peak of the acoustic response. Ranges of repulsion and attraction of a trailing temporal CS are highlighted. The maximum corresponds to a stable separation (adapted from [34]).

interaction regimes can be expected. By carefully controlling the initial temporal CS separation, experiments were performed in all four regimes. Results are shown in Figure 2.13b, with all the four distinct measurements juxtaposed on the same graph. (Note that for clarity only the trailing soliton is shown.) The observed interactions follow very well the expected trends. In particular, two stable states of 19.79 ns and 22.05 ns were observed, in good agreement with the two predicted refractive index maxima at 19.82 ns and 22.03 ns. The red solid lines in Figure 2.13b correspond to numerical calculations based on an extended mean-field equation (2.4) incorporating the acoustic response. Given the widely different timescales involved—picosecond temporal CSs, nanosecond acoustic response time, minutes of interactions—the agreement is excellent.

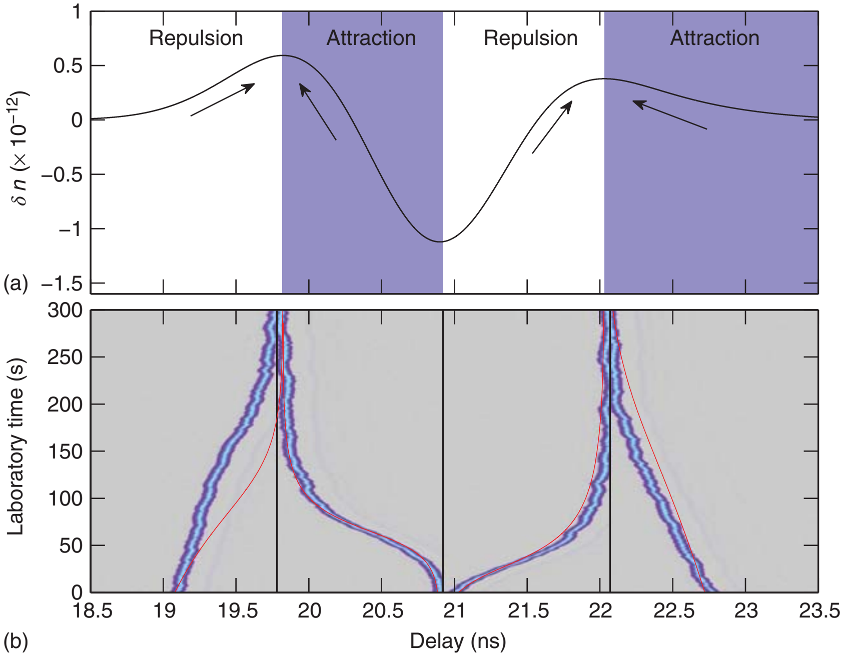

Figure 2.13 (a) Close-up of the first echo of the acoustic impulse response (see spike labeled 2 in Figure 2.12a). (b) Experimental color plot of the trailing cavity soliton in each of the regions highlighted in (a), as in Figure 2.11. The plot consists of the juxtaposition of four different independent measurements (separated by vertical lines) obtained for different initial separations between the two cavity solitons. Red curves are numerical simulations (adapted from [34]).

2.7
Breathing Temporal CSs

As was briefly mentioned in Section 2.4 of this chapter, for certain parameters the fixed-point CS solution loses its stability through a Hopf bifurcation, giving rise to a small-amplitude limit cycle. At this point, the CSs exhibit breathing (or oscillatory) behavior in their duration, shape, and energy. This has been theoretically known for a very long time, initially in the context of plasma physics [69], yet experimental demonstration was not reported until 2013 [33]. In these recent experiments, the authors employed a setup identical to that shown in Figure 2.7, but they systematically controlled the CW driving power as well as the cavity phase detuning so as to access the unstable breathing regime.

Experimental results are shown in Figure 2.14 for three different sets of pump-cavity parameters. In each case, the plots represent the evolution of the temporal CS energy over subsequent roundtrips. Figure 2.14a first shows the results obtained in [33] when the parameters were below the Hopf threshold. Some stochastic fluctuations are observed in the CS energy, yet these can be

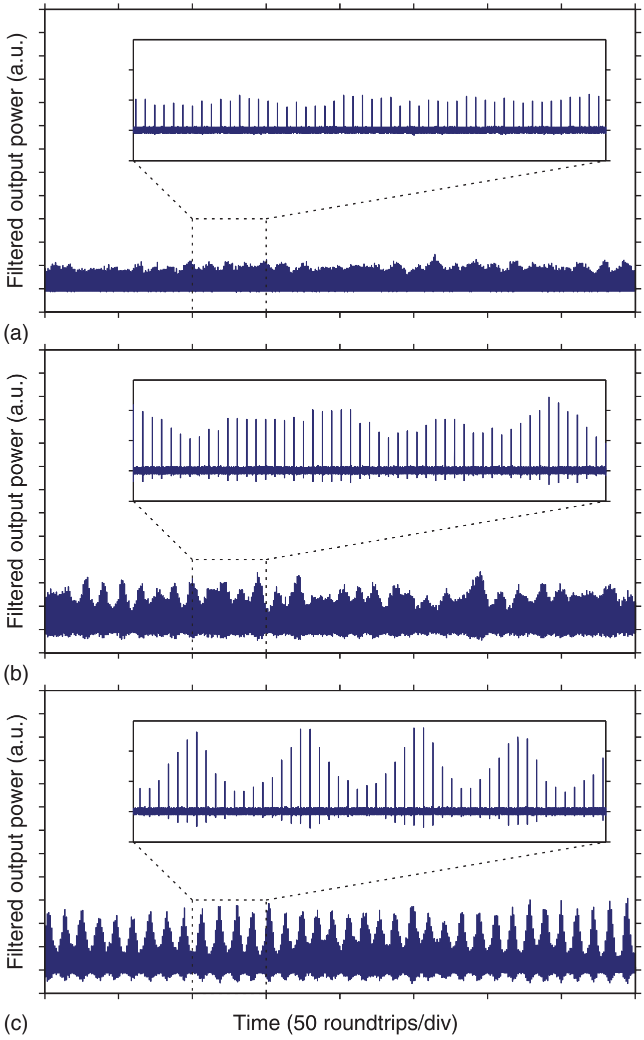

Figure 2.14 Oscilloscope traces (linear scaling) of temporal CSs (a) below [$X = 6.2$ and $\Delta = 3.8$], (b) near [$X = 7.3$ and $\Delta = 4.1$], and (c) beyond [$X = 8.5$ and $\Delta = 4.1$] the Hopf bifurcation point. In (c), the temporal CS appears to be breathing with a period of about 11 roundtrips. The delay between subsequent pulses in the output sequences shown is equal to the 1.85 μs cavity roundtrip time (adapted from [33]).

attributed to noise on the CW driving laser (amplified spontaneous emission in particular). Closer to the theoretically predicted Hopf threshold, the CS was seen to evolve irregularly and was very sensitive to the driving laser fluctuations (Figure 2.14b). This was interpreted (i) as a noisy precursor of the instability that can appear just below the Hopf threshold [84], and (ii) by remarking that, just above the threshold, the system converges very slowly to the limit cycle, leading to increased sensitivity to external fluctuations [33]. When the pump-cavity parameters move well-beyond the Hopf threshold, however, the system quickly converges to the limit cycle despite external noise. Experimental results in this regime are shown in Figure 2.14c, where a clear signature of a breathing behavior was observed.

2.8
Emission of Dispersive Waves by Temporal CSs

The simple mean-field LLE (2.4) is only approximatively valid as a model for fiber resonators. Indeed, it neglects many physical effects, including the acoustic wave perturbations described in Section 2.6 of this chapter. It also neglects the significant fact that the group-velocity dispersion coefficient β_2 of optical fibers is generally wavelength dependent. Although this latter approximation is well justified for the experiments described earlier, physical configurations exist where it loses validity. This is particularly the case for the Kerr microresonators used for the generation of optical frequency combs [36, 38, 85] (see also Chapter 6 of this book).

Wavelength-dependent group-velocity dispersion (GVD) can easily be included in the LLE model by adding terms with higher-order τ-derivatives proportional to the higher-order dispersion coefficients β_k $(k \geq 3)$, where $\beta_k = d^k\beta/d\omega^k|_{\omega=\omega_0}$ [50], with $\beta(\omega)$ the angular frequency-dependent propagation constant of the waveguide. Insofar as temporal CSs are concerned, it has been theoretically found that the dominant effects of wavelength-dependent GVD are twofold. First, the symmetry breaking introduced by the odd-order derivatives causes the CSs to propagate at a group-velocity slightly different from that of the CW driving field [66, 86, 87]. In other words, the CSs drift temporally in the reference frame of the driving beam and the repetition rate at which they exit the resonator is slightly different from the cavity free-spectral range. Second, it leads to the emission of resonant dispersive waves (DWs) at specific wavelengths across the zero-dispersion wavelength (ZDW)—a process that has been extensively examined with conservative solitons in single-pass fiber configurations [88–91]. DW emission ought to be exploited in microresonator Kerr frequency combs so as to generate octave spanning spectra with sufficient power in the wings for optimized f-$2f$ interferometry [38, 92].

DW emission was initially not observed in temporal CS experiments [32–34] because they were all performed in cavities constructed of standard telecommunications single-mode fiber, which has negligible higher-order dispersion coefficients at the used driving wavelength of 1550 nm (and for the relevant spectral bandwidths). DW emission by temporal CSs was first discussed in the numerical studies that followed, from 2013 onwards [50, 87, 93]. We must note that, in 2011, an octave-spanning comb spectrum obtained with a silicon-nitride microresonator was reported [94], and exhibited a spectral feature that, with the benefit of hindsight, looked suspiciously as due to DW emission (see [95] for a more in-depth theoretical analysis of that experiment). It was not recognized as such, however, because the fact that ultrashort temporal CSs and related MI patterns underlie Kerr comb generation was not appreciated at the time: even though it was already hinted in 2010 [32], it was only clearly established two years later [36, 37, 50].

An experimental evidence of DW emission clearly connected to temporal CSs has, however, been provided very recently by Jang *et al.* using a cavity constructed of two fibers with very different dispersion coefficients [35]. Significantly, in such a dispersion-managed system, the dynamics is governed by the average cavity dispersion coefficients [35, 86]. These could be systematically controlled in the experiment simply by adjusting the relative lengths of the two different fibers in the cavity, enabling exploration of CS dynamics in a regime where higher-order dispersion plays a significant role.

The experimental (red) and numerical (blue) results obtained in [35] for three different averaged cavity dispersions are shown in Figure 2.15. Clearly, almost perfect agreement is observed between numerics and experiments. The dashed vertical lines indicate the ZDW, that is, the wavelength at which the β_2 coefficient is zero, calculated from the averaged dispersion coefficients. Roughly speaking, the closer the ZDW is to the pump wavelength (the smaller the average dispersion), the more significant the higher-order dispersive corrections are. From the result shown in Figure 2.15a, it can be seen that when the ZDW was far from the pump wavelength, no spectral signatures of DWs were observed in the normal dispersion regime where they would be expected. We emphasize in particular that the weak peak observed at 1560 nm was not due to higher-order dispersion. Instead, it corresponds to a quasi-phase-matched so-called "Kelly" sideband that arose due to the periodic nature of the cavity constructed of two different fiber types. Similar sidebands have been extensively observed in mode-locked fiber lasers [96–98] and, more recently, in synchronously pumped passive cavities [99] and other periodic structures [100].

As the average dispersion was reduced to $-0.32\ \text{ps}^2\ \text{km}^{-1}$, such that the ZDW moved closer to the pump wavelength, the spectrum is clearly seen to develop a peak at 1541.1 nm in the normal dispersion regime (Figure 2.15b). The peak shifts slightly to 1541.4 nm and becomes more prominent (Figure 2.15c) for an even lower average dispersion of $-0.23\ \text{ps}^2\ \text{km}^{-1}$. This peak is a clear signature of DWs emitted by the circulating temporal CSs, and the trend observed as the dispersion was reduced is in full agreement with this conclusion. Indeed, it is well-known that moving the ZDW closer to the DW-generating pump results in the DW shifting spectrally closer to the pump and the amplification process becoming more effective [89, 90]. To further confirm that the spectral features corresponded to genuine DWs, the authors of [35] compared the experimentally observed DW frequencies with theoretical predictions approximated from recent results of Milián and Skryabin [87] using the phase-matching relation

$$\frac{\beta_3 L}{3!}Q^3 + \frac{\beta_2 L}{2!}Q^2 - VQ + [(2\gamma L P_0 - \delta_0) + i\alpha] = 0\ . \tag{2.9}$$

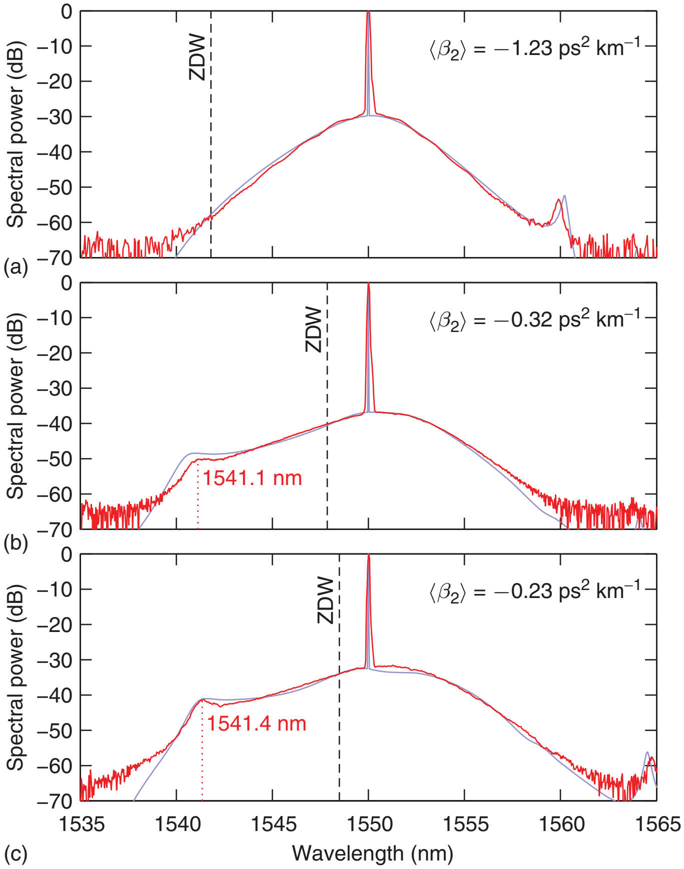

Figure 2.15 Experimental (red) and numerical (blue) spectra of temporal CSs for three different values of average cavity dispersion as shown. In each case, the black dashed line indicates the position of the ZDW while the red dotted line highlights the observed DW wavelength (adapted from [35]; parameters listed therein).

Here, Q is the (complex) angular frequency shift (with respect to the driving frequency ω_0) of the DW (the imaginary part represents the decay rate of the associated oscillating tail of the CSs), V is the drift velocity of the temporal CS (describing how much the CS drifts in time per roundtrip due to its altered group-velocity), and P_0 is the CW background power over which the CSs are superimposed. Using their experimental parameters, and estimating V from the shift in the center of mass of the spectra (spectral recoil [101]), the authors predicted DW emission at around 1540.9-1541.2 nm for Figure 2.15b, and 1541.3 nm for Figure 2.15c. (Note that the error for the first case arises from uncertainty in the CS drift velocity V—see [35] for more details.) These predictions are in very good agreement with the experiments, thereby confirming that the observed spectral features correspond to DWs emitted by the temporal CSs [35]. We note that this experiment also constitutes a strong evidence of the intimate connection that exists between temporal CSs and microresonator Kerr frequency combs.

2.9
Conclusion

In this chapter, we have given a brief overview of the dynamics of temporal cavity solitons in Kerr media, focusing in particular on results that have so far been observed in experiments based on optical fiber cavities. We have discussed in detail the experimental configurations where temporal CSs were first observed, and elaborated on the different classes of interactions they have been found to display. New results have recently appeared that are not discussed here [74, 80], however, and it is also necessary to emphasize that experimental investigations of temporal CSs is an endeavor that is far from complete. Indeed, many dynamical effects that can be theoretically predicted from the simple LLE model remain unexamined. Such is the case for example for bound states of temporal CSs [67, 102] as well as for a variety of dynamical instabilities that are predicted to manifest themselves for regions of the parameter space that are beyond current experimental configurations [33]. And of course, it is well-expected that more effects will be discovered, as time progresses, that are *not* included in a simple LLE-model, but that nevertheless have impact on temporal CS dynamics. Finally, we also mention in closing the exciting new paradigm of observing and studying temporal CSs in experiments involving monolithic microresonators [36, 38, 50, 68, 95]. We have here refrained ourselves from a detailed discussion on this topic, but have no doubt that experiments in this context will continue to bring forward new dynamical effects involving temporal CSs [93, 103–108].

References

1. Russell, J.S. (1845) On waves. *Report of the 14th meeting of the British Association for the Advancement of Science, York, September 1844*, John Murray, London, pp. 311–390, Plates XLVII-LVII.
2. Zakharov, V.E. and Shabat, A.B. (1972) Exact theory of two-dimensional self-focusing and one-dimensional self-modulation of wave in nonlinear media. *Sov. Phys. JETP*, **34** (1), 62–69.
3. Zabusky, N.J. and Kruskal, M.D. (1965) Interaction of “solitons” in a collisionless plasma and the recurrence of initial states. *Phys. Rev. Lett.*, **15** (6), 240–243, doi: 10.1103/PhysRevLett.15.240.
4. Segev, M. (1998) Optical spatial solitons. *Opt. Quantum Electron.*, **30** (7–10), 503–533, doi: 10.1023/A:1006915021865.
5. Akhmediev, N.N. and Ankiewicz, A. (eds) (2008) *Dissipative Solitons: From Optics to Biology and Medicine*, Lecture Notes in Physics, vol. **751**, Springer-Verlag, Berlin/Heidelberg.
6. Nicolis, G. and Prigogine, I. (1977) *Self-Organization in Nonequilibrium Systems: From Dissipative Structures to*

Order Through Fluctuations, John Wiley & Sons, Inc., New York.

7. Purwins, H.G., Bödeker, H., and Amiranashvili, S. (2010) Dissipative solitons. *Adv. Phys.*, **59** (5), 485–701, doi: 10.1080/00018732.2010.498228.
8. Grelu, P. and Akhmediev, N. (2012) Dissipative solitons for mode-locked lasers. *Nat. Photonics*, **6** (2), 84–92, doi: 10.1038/nphoton.2011.345.
9. Lee, K.J., McCormick, W.D., Ouyang, Q., and Swinney, H.L. (1993) Pattern formation by interacting chemical fronts. *Science*, **261** (5118), 192–194, doi: 10.1126/science.261.5118.192.
10. Wu, J., Keolian, R., and Rudnick, I. (1984) Observation of a nonpropagating hydrodynamic soliton. *Phys. Rev. Lett.*, **52** (16), 1421–1424, doi: 10.1103/PhysRevLett.52.1421.
11. Umbanhowar, P.B., Melo, F., and Swinney, H.L. (1996) Localized excitations in a vertically vibrated granular layer. *Nature*, **382** (6594), 793–796, doi: 10.1038/382793a0.
12. Astrov, Y. and Logvin, Y. (1997) Formation of clusters of localized states in a gas discharge system via a self-completion scenario. *Phys. Rev. Lett.*, **79** (16), 2983–2986, doi: 10.1103/PhysRevLett.79.2983.
13. Stegeman, G.I. and Segev, M. (1999) Optical spatial solitons and their interactions: universality and diversity. *Science*, **286** (5444), 1518–1523, doi: 10.1126/science.286.5444.1518.
14. Kivshar, Y.S. and Agrawal, G. (2003) *Optical Solitons: From Fibers to Photonic Crystals*, 1st edn, Academic Press, Amsterdam, Boston, MA.
15. Chen, Z., Segev, M., and Christodoulides, D.N. (2012) Optical spatial solitons: historical overview and recent advances. *Rep. Prog. Phys.*, **75** (8), 086 401, doi: 10.1088/0034-4885/75/8/086401.
16. Liu, X., Qian, L.J., and Wise, F.W. (1999) Generation of optical spatiotemporal solitons. *Phys. Rev. Lett.*, **82** (23), 4631–4634, doi: 10.1103/PhysRevLett.82.4631.
17. Minardi, S., Eilenberger, F., Kartashov, Y.V., Szameit, A., Röpke, U., Kobelke, J., Schuster, K., Bartelt, H., Nolte, S., Torner, L., Lederer, F., Tünnermann, A., and Pertsch, T. (2010) Three-dimensional light bullets in arrays of waveguides. *Phys. Rev. Lett.*, **105** (26), 263 901/1-4, doi: 10.1103/PhysRevLett.105.263901.
18. Lugiato, L.A. (2003) Introduction to the feature section on cavity solitons: an overview. *IEEE J. Quantum Electron.*, **39** (2), 193–196, doi: 10.1109/JQE.2002.807195.
19. Firth, W.J. and Weiss, C.O. (2002) Cavity and feedback solitons. *Opt. Photonics News*, **13** (2), 54–58.
20. Firth, W. (2010) Temporal cavity solitons: buffering optical data. *Nat. Photonics*, **4** (7), 415–417, doi: 10.1038/nphoton.2010.142.
21. Tanguy, Y., Ackemann, T., Firth, W.J., and Jäger, R. (2008) Realization of a semiconductor-based cavity soliton laser. *Phys. Rev. Lett.*, **100** (1), 013 907/1-4, doi: 10.1103/PhysRevLett.100.013907.
22. Boyd, R.W. (2003) *Nonlinear Optics*, 2nd edn, Academic Press.
23. Silberberg, Y. (1990) Collapse of optical pulses. *Opt. Lett.*, **15** (22), 1282–1284, doi: 10.1364/OL.15.001282.
24. Firth, W.J., Harkness, G.K., Lord, A., McSloy, J.M., Gomila, D., and Colet, P. (2002) Dynamical properties of two-dimensional Kerr cavity solitons. *J. Opt. Soc. Am. B*, **19** (4), 747–752, doi: 10.1364/JOSAB.19.000747.
25. McDonald, G. and Firth, W. (1990) All-optical switching in a nonlinear resonator. *J. Mod. Opt.*, **37** (4), 613–626, doi: 10.1080/09500349014550701.
26. McLaughlin, D.W., Moloney, J.V., and Newell, A.C. (1983) Solitary waves as fixed points of infinite-dimensional maps in an optical bistable ring cavity. *Phys. Rev. Lett.*, **51** (2), 75–78, doi: 10.1103/PhysRevLett.51.75.
27. Rosanov, N.N. and Khodova, G.V. (1990) Diffractive autosolitons in nonlinear interferometers. *J. Opt. Soc. Am. B*, **7** (6), 1057–1065, doi: 10.1364/JOSAB.7.001057.
28. Firth, W.J. (2001) Theory of cavity solitons, in *Soliton-Driven Photonics*, NATO Science Series, vol. **31** (eds A.D. Boardman and A.P. Sukhorukov),

Springer-Verlag, The Netherlands, pp. 459–485.

29. Ackemann, T. and Firth, W.J. (2005) Dissipative solitons in pattern-forming nonlinear optical systems: cavity solitons and feedback solitons, in *Dissipative Solitons*, Lecture Notes in Physics, vol. **661**, Springer-Verlag, Berlin/Heidelberg, pp. 55–100.

30. Ackemann, T., Firth, W.J., and Oppo, G.L. (2009) Fundamentals and applications of spatial dissipative solitons in photonic devices, in *Advances in Atomic, Molecular, and Optical Physics*, Advances in Atomic Molecular and Optical Physics, vol. **57**, Chapter 6 (eds E. Arimondo, P.R. Berman, and C.C. Lin), Academic Press, pp. 323–421.

31. Barland, S., Tredicce, J.R., Brambilla, M., Lugiato, L.A., Balle, S., Giudici, M., Maggipinto, T., Spinelli, L., Tissoni, G., Knodl, T., Miller, M., and Jäger, R. (2002) Cavity solitons as pixels in semiconductor microcavities. *Nature*, **419** (6908), 699–702, doi: 10.1038/nature01049.

32. Leo, F., Coen, S., Kockaert, P., Gorza, S.P., Emplit, Ph., and Haelterman, M. (2010) Temporal cavity solitons in one-dimensional Kerr media as bits in an all-optical buffer. *Nat. Photonics*, **4** (7), 471–476, doi: 10.1038/nphoton.2010.120.

33. Leo, F., Gelens, L., Emplit, Ph., Haelterman, M., and Coen, S. (2013) Dynamics of one-dimensional Kerr cavity solitons. *Opt. Express*, **21** (7), 9180–9191, doi: 10.1364/OE.21.009180.

34. Jang, J.K., Erkintalo, M., Murdoch, S.G., and Coen, S. (2013) Ultraweak long-range interactions of solitons observed over astronomical distances. *Nat. Photonics*, **7** (8), 657–663, doi: 10.1038/nphoton.2013.157.

35. Jang, J.K., Erkintalo, M., Murdoch, S.G., and Coen, S. (2014) Observation of dispersive wave emission by temporal cavity solitons. *Opt. Lett.*, **39** (19), 5503–5506, doi: 10.1364/OL.39.005503.

36. Herr, T., Brasch, V., Jost, J.D., Wang, C.Y., Kondratiev, N.M., Gorodetsky, M.L., and Kippenberg, T.J. (2014) Temporal solitons in optical microresonators. *Nat. Photonics*, **8** (2), 145–152, doi: 10.1038/nphoton.2013.343.

37. Saha, K., Okawachi, Y., Shim, B., Levy, J.S., Salem, R., Johnson, A.R., Foster, M.A., Lamont, M.R.E., Lipson, M., and Gaeta, A.L. (2013) Modelocking and femtosecond pulse generation in chip-based frequency combs. *Opt. Express*, **21** (1), 1335–1343, doi: 10.1364/OE.21.001335.

38. Brasch, V., Herr, T., Geiselmann, M., Lihachev, G., Pfeiffer, M.H.P., Gorodetsky, M.L., and Kippenberg, T.J. (2014) Photonic chip based optical frequency comb using soliton induced Cherenkov radiation, arXiv e-print 1410.8598 [physics].

39. Pedaci, F., Genevet, P., Barland, S., Giudici, M., and Tredicce, J.R. (2006) Positioning cavity solitons with a phase mask. *Appl. Phys. Lett.*, **89** (22), 221 111/1-3, doi: 10.1063/1.2388867.

40. Pedaci, F., Tissoni, G., Barland, S., Giudici, M., and Tredicce, J. (2008) Mapping local defects of extended media using localized structures. *Appl. Phys. Lett.*, **93** (11), 111 104/1-3, doi: 10.1063/1.2977603.

41. Cleff, C., Gütlich, B., and Denz, C. (2008) Gradient induced motion control of drifting solitary structures in a nonlinear optical single feedback experiment. *Phys. Rev. Lett.*, **100** (23), 233 902/1-4, doi: 10.1103/PhysRevLett.100.233902.

42. Caboche, E., Pedaci, F., Genevet, P., Barland, S., Giudici, M., Tredicce, J., Tissoni, G., and Lugiato, L.A. (2009) Microresonator defects as sources of drifting cavity solitons. *Phys. Rev. Lett.*, **102** (16), 163 901/1-4, doi: 10.1103/PhysRevLett.102.163901.

43. Wabnitz, S. (1993) Suppression of interactions in a phase-locked soliton optical memory. *Opt. Lett.*, **18** (8), 601–603, doi: 10.1364/OL.18.000601.

44. Odent, V., Taki, M., and Louvergneaux, E. (2011) Experimental evidence of dissipative spatial solitons in an optical passive Kerr cavity. *New J. Phys.*, **13** (11), 113 026/1-13, doi: 10.1088/1367-2630/13/11/113026.

45. Agrawal, G.P. (2006) *Nonlinear Fiber Optics*, 4th edn, Academic Press.

46. Haelterman, M., Trillo, S., and Wabnitz, S. (1992) Dissipative modulation instability in a nonlinear dispersive ring cavity. *Opt. Commun.*, **91** (5–6), 401–407, doi: 10.1016/0030-4018(92)90367-Z.

47. Barashenkov, I.V. and Smirnov, Y.S. (1996) Existence and stability chart for the AC-driven, damped nonlinear schrödinger solitons. *Phys. Rev. E*, **54** (5), 5707–5725, doi: 10.1103/PhysRevE.54.5707.

48. Lugiato, L.A. and Lefever, R. (1987) Spatial dissipative structures in passive optical systems. *Phys. Rev. Lett.*, **58** (21), 2209–2211, doi: 10.1103/PhysRevLett.58.2209.

49. Haelterman, M., Trillo, S., and Wabnitz, S. (1992) Additive-modulation-instability ring laser in the normal dispersion regime of a fiber. *Opt. Lett.*, **17** (10), 745–747, doi: 10.1364/OL.17.000745.

50. Coen, S., Randle, H.G., Sylvestre, T., and Erkintalo, M. (2013) Modeling of octave-spanning Kerr frequency combs using a generalized mean-field Lugiato-Lefever model. *Opt. Lett.*, **38** (1), 37–39, doi: 10.1364/OL.38.000037.

51. Murray, J.D. (1993) *Mathematical Biology*, Biomathematics Texts, vol. **19**, 2nd edn, Springer-Verlag, Berlin/Heidelberg, New York.

52. Zakharov, V.E. and Ostrovsky, L.A. (2009) Modulation instability: the beginning. *Physica D*, **238** (5), 540–548, doi: 10.1016/j.physd.2008.12.002.

53. Dudley, J.M., Dias, F., Erkintalo, M., and Genty, G. (2014) Instabilities, breathers and rogue waves in optics. *Nat. Photonics*, **8** (10), 755–764, doi: 10.1038/nphoton.2014.220.

54. Coen, S. and Haelterman, M. (1997) Modulational instability induced by cavity boundary conditions in a normally dispersive optical fiber. *Phys. Rev. Lett.*, **79** (21), 4139–4142, doi: 10.1103/PhysRevLett.79.4139.

55. Van Simaeys, G., Emplit, Ph., and Haelterman, M. (2001) Experimental demonstration of the Fermi-Pasta-Ulam recurrence in a modulationally unstable optical wave. *Phys. Rev. Lett.*, **87** (3), 033 902/1-4, doi: 10.1103/PhysRevLett.87.033902.

56. Akhmediev, N.N. (2001) Nonlinear physics: déjà vu in optics. *Nature*, **413** (6853), 267–268, doi: 10.1038/35095154.

57. Turing, A.M. (1952) The chemical basis of morphogenesis. *Philos. Trans. R. Soc. Lond. B*, **237** (641), 37–72.

58. Lejeune, O. and Tlidi, M. (1999) A model for the explanation of vegetation stripes (tiger bush). *J. Veg. Sci.*, **10** (2), 201–208, doi: 10.2307/3237141.

59. Coen, S. and Haelterman, M. (1999) Competition between modulational instability and switching in optical bistability. *Opt. Lett.*, **24** (2), 80–82, doi: 10.1364/OL.24.000080.

60. Scroggie, A.J., Firth, W.J., McDonald, G.S., Tlidi, M., Lefever, R., and Lugiato, L.A. (1994) Pattern formation in a passive Kerr cavity. *Chaos, Solitons Fractals*, **4** (8-9), 1323–1354, doi: 10.1016/0960-0779(94)90084-1.

61. Tlidi, M., Mandel, P., and Lefever, R. (1994) Localized structures and localized patterns in optical bistability. *Phys. Rev. Lett.*, **73** (5), 640–643, doi: 10.1103/PhysRevLett.73.640.

62. Firth, W.J. and Scroggie, A.J. (1996) Optical bullet holes: robust controllable localized states of a nonlinear cavity. *Phys. Rev. Lett.*, **76** (10), 1623–1626, doi: 10.1103/PhysRevLett.76.1623.

63. Coullet, P., Riera, C., and Tresser, C. (2000) Stable static localized structures in one dimension. *Phys. Rev. Lett.*, **84** (14), 3069–3072, doi: 10.1103/PhysRevLett.84.3069.

64. Godey, C., Balakireva, I.V., Coillet, A., and Chembo, Y.K. (2014) Stability analysis of the spatiotemporal Lugiato-Lefever model for Kerr optical frequency combs in the anomalous and normal dispersion regimes. *Phys. Rev. A*, **89** (6), 063 814/1-21, doi: 10.1103/PhysRevA.89.063814.

65. Tlidi, M., Mussot, A., Louvergneaux, E., Kozyreff, G., Vladimirov, A.G., and Taki, M. (2007) Control and removal of modulational instabilities in low-dispersion photonic crystal fiber cavities. *Opt. Lett.*, **32** (6), 662–664, doi: 10.1364/OL.32.000662.

66. Tlidi, M., Bahloul, L., Cherbi, L., Hariz, A., and Coulibaly, S. (2013) Drift of dark cavity solitons in a photonic-crystal fiber resonator. *Phys. Rev. A*, **88** (3), 035 802, doi: 10.1103/PhysRevA.88.035802.
67. Parra-Rivas, P., Gomila, D., Leo, F., Coen, S., and Gelens, L. (2014) Third-order chromatic dispersion stabilizes Kerr frequency combs. *Opt. Lett.*, **39** (10), 2971–2974, doi: 10.1364/OL.39.002971.
68. Coen, S. and Erkintalo, M. (2013) Universal scaling laws of Kerr frequency combs. *Opt. Lett.*, **38** (11), 1790–1792, doi: 10.1364/OL.38.001790.
69. Nozaki, K. and Bekki, N. (1985) Chaotic solitons in a plasma driven by an RF field. *J. Phys. Soc. Jpn.*, **54** (7), 2363–2366, doi: 10.1143/JPSJ.54.2363.
70. Maggipinto, T., Brambilla, M., Harkness, G.K., and Firth, W.J. (2000) Cavity solitons in semiconductor microresonators: existence, stability, and dynamical properties. *Phys. Rev. E*, **62** (6), 8726–8739, doi: 10.1103/PhysRevE.62.8726.
71. McDonald, G.S. and Firth, W.J. (1990) Spatial solitary-wave optical memory. *J. Opt. Soc. Am. B*, **7** (7), 1328–1335, doi: 10.1364/JOSAB.7.001328.
72. Taranenko, V.B., Staliunas, K., and Weiss, C.O. (1997) Spatial soliton laser: localized structures in a laser with a saturable absorber in a self-imaging resonator. *Phys. Rev. A*, **56** (2), 1582–1591, doi: 10.1103/PhysRevA.56.1582.
73. Pedaci, F., Barland, S., Caboche, E., Genevet, P., Giudici, M., Tredicce, J.R., Ackemann, T., Scroggie, A.J., Firth, W.J., Oppo, G.L., Tissoni, G., and Jäger, R. (2008) All-optical delay line using semiconductor cavity solitons. *Appl. Phys. Lett.*, **92** (1), 011 101/1-3, doi: 10.1063/1.2828458.
74. Jang, J.K., Erkintalo, M., Coen, S., and Murdoch, S.G. (2014) Temporal tweezing of light: trapping and manipulation of temporal cavity solitons. *Nat. Communications*, **6**, 7370, doi: 10.1038/ncomms8370.
75. Brambilla, M., Lugiato, L.A., and Stefani, M. (1996) Interaction and control of optical localized structures. *Europhys. Lett.*, **34** (2), 109–114.
76. Ramazza, P.L., Benkler, E., Bortolozzo, U., Boccaletti, S., Ducci, S., and Arecchi, F. (2002) Tailoring the profile and interactions of optical localized structures. *Phys. Rev. E*, **65** (6), 066 204/1-4, doi: 10.1103/PhysRevE.65.066204.
77. Tlidi, M., Vladimirov, A.G., and Mandel, P. (2003) Interaction and stability of periodic and localized structures in optical bistable systems. *IEEE J. Quantum Electron.*, **39** (2), 216–226, doi: 10.1109/JQE.2002.807193.
78. Coen, S. and Haelterman, M. (2001) Continuous-wave ultrahigh-repetition-rate pulse-train generation through modulational instability in a passive fiber cavity. *Opt. Lett.*, **26** (1), 39–41, doi: 10.1364/OL.26.000039.
79. McDonald, G.S. and Firth, W.J. (1993) Switching dynamics of spatial solitary wave pixels. *J. Opt. Soc. Am. B*, **10** (6), 1081–1089, doi: 10.1364/JOSAB.10.001081.
80. Jang, J.K., Erkintalo, M., Murdoch, S.G., and Coen, S. (2015) Writing and erasing of temporal cavity solitons by direct phase modulation of the cavity driving field, arXiv e-print 1501.05289 [nlin, physics:physics].
81. Gordon, J.P. (1983) Interaction forces among solitons in optical fibers. *Opt. Lett.*, **8** (11), 596–598, doi: 10.1364/OL.8.000596.
82. Dianov, E.M., Luchnikov, A.V., Pilipetskii, A.N., and Prokhorov, A.M. (1992) Long-range interaction of picosecond solitons through excitation of acoustic waves in optical fibers. *Appl. Phys. B*, **54** (2), 175–180, doi: 10.1007/BF00331891.
83. Jaouën, Y. and du Mouza, L. (2001) Transverse Brillouin effect produced by electrostriction in optical fibers and its impact on soliton transmission systems. *Opt. Fiber Technol.*, **7** (3), 141–169, doi: 10.1006/ofte.2000.0353.
84. Wiesenfeld, K. (1985) Noisy precursors of nonlinear instabilities. *J.*

Stat. Phys., **38** (5–6), 1071–1097, doi: 10.1007/BF01010430.

85. Kippenberg, T.J., Holzwarth, R., and Diddams, S.A. (2011) Microresonator-based optical frequency combs. *Science*, **332** (6029), 555–559, doi: 10.1126/science.1193968.
86. Leo, F., Mussot, A., Kockaert, P., Emplit, Ph., Haelterman, M., and Taki, M. (2013) Nonlinear symmetry breaking induced by third-order dispersion in optical fiber cavities. *Phys. Rev. Lett.*, **110** (10), 104 103/1-5, doi: 10.1103/PhysRevLett.110.104103.
87. Milián, C. and Skryabin, D.V. (2014) Soliton families and resonant radiation in a micro-ring resonator near zero group-velocity dispersion. *Opt. Express*, **22** (3), 3732–3739, doi: 10.1364/OE.22.003732.
88. Wai, P.K.A., Menyuk, C.R., Lee, Y.C., and Chen, H.H. (1986) Nonlinear pulse propagation in the neighborhood of the zero-dispersion wavelength of monomode optical fibers. *Opt. Lett.*, **11** (7), 464–466, doi: 10.1364/OL.11.000464.
89. Akhmediev, N. and Karlsson, M. (1995) Cherenkov radiation emitted by solitons in optical fibers. *Phys. Rev. A*, **51** (3), 2602–2607, doi: 10.1103/PhysRevA.51.2602.
90. Erkintalo, M., Xu, Y.Q., Murdoch, S.G., Dudley, J.M., and Genty, G. (2012) Cascaded phase matching and nonlinear symmetry breaking in fiber frequency combs. *Phys. Rev. Lett.*, **109** (22), 223 904/1-5, doi: 10.1103/PhysRevLett.109.223904.
91. Webb, K.E., Xu, Y.Q., Erkintalo, M., and Murdoch, S.G. (2013) Generalized dispersive wave emission in nonlinear fiber optics. *Opt. Lett.*, **38** (2), 151–153, doi: 10.1364/OL.38.000151.
92. Wang, S., Guo, H., Bai, X., and Zeng, X. (2014) Broadband Kerr frequency combs and intracavity soliton dynamics influenced by high-order cavity dispersion. *Opt. Lett.*, **39** (10), 2880–2883, doi: 10.1364/OL.39.002880.
93. Lamont, M.R.E., Okawachi, Y., and Gaeta, A.L. (2013) Route to stabilized ultrabroadband microresonator-based frequency combs. *Opt. Lett.*, **38** (18), 3478–3481, doi: 10.1364/OL.38.003478.
94. Okawachi, Y., Saha, K., Levy, J.S., Wen, Y.H., Lipson, M., and Gaeta, A.L. (2011) Octave-spanning frequency comb generation in a silicon nitride chip. *Opt. Lett.*, **36** (17), 3398–3400, doi: 10.1364/OL.36.003398.
95. Erkintalo, M. and Coen, S. (2014) Coherence properties of Kerr frequency combs. *Opt. Lett.*, **39** (2), 283–286, doi: 10.1364/OL.39.000283.
96. Kelly, S.M.J. (1992) Characteristic sideband instability of periodically amplified average soliton. *Electron. Lett.*, **28** (8), 806–807, doi: 10.1049/el:19920508.
97. Smith, N., Blow, K., and Andonovic, I. (1992) Sideband generation through perturbations to the average soliton model. *IEEE J. Lightwave Technol.*, **10** (10), 1329–1333, doi: 10.1109/50.166771.
98. Dennis, M. and Duling, I.N.I. (1994) Experimental study of sideband generation in femtosecond fiber lasers. *IEEE J. Quantum Electron.*, **30** (6), 1469–1477, doi: 10.1109/3.299472.
99. Luo, K., Xu, Y., Erkintalo, M., and Murdoch, S.G. (2015) Resonant radiation in synchronously pumped passive Kerr cavities. *Opt. Lett.*, **40** (3), 427–430, doi: 10.1364/OL.40.000427.
100. Conforti, M., Trillo, S., Mussot, A., and Kudlinski, A. (2015) Parametric excitation of multiple resonant radiations from localized wavepackets, arXiv e-print 1502.02266 [nlin, physics:physics].
101. Skryabin, D.V., Luan, F., Knight, J.C., and Russell, P.St.J. (2003) Soliton self-frequency shift cancellation in photonic crystal fibers. *Science*, **301** (5640), 1705–1708, doi: 10.1126/science.1088516.
102. Parra-Rivas, P., Gomila, D., Matías, M.A., Coen, S., and Gelens, L. (2014) Dynamics of localized and patterned structures in the Lugiato-Lefever equation determine the stability and shape of optical frequency combs. *Phys. Rev. A*, **89** (4), 043 813/1-12, doi: 10.1103/PhysRevA.89.043813.
103. Hansson, T., Modotto, D., and Wabnitz, S. (2014) Mid-infrared soliton and

Raman frequency comb generation in silicon microrings. *Opt. Lett.*, **39** (23), 6747–6750, doi: 10.1364/OL.39.006747.

104. Hansson, T. and Wabnitz, S. (2014) Bichromatically pumped microresonator frequency combs. *Phys. Rev. A*, **90** (1), 013 811/1-7, doi: 10.1103/PhysRevA.90.013811.

105. Del'Haye, P., Beha, K., Papp, S.B., and Diddams, S.A. (2014) Self-injection locking and phase-locked states in microresonator-based optical frequency combs. *Phys. Rev. Lett.*, **112** (4), 043 905/1-6, doi: 10.1103/PhysRevLett.112.043905.

106. Papp, S.B., Del'Haye, P., and Diddams, S.A. (2013) Parametric seeding of a microresonator optical frequency comb. *Opt. Express*, **21** (15), 17 615-17 624, doi: 10.1364/OE.21.017615.

107. Wen, Y.H., Lamont, M.R.E., Kloumann, I.M., Strogatz, S.H., and Gaeta, A.L. (2014) Self-organization in soliton modelocked parametric frequency combs, arXiv e-print 1412.0119 [nlin].

108. Del'Haye, P., Coillet, A., Loh, W., Beha, K., Papp, S.B., and Diddams, S.A. (2014) Phase steps and hot resonator detuning in microresonator frequency combs, arXiv e-print 1405.6972 [physics].

3

Dynamics and Interaction of Laser Cavity Solitons in Broad-Area Semiconductor Lasers

Thorsten Ackemann, Jesus Jimenez, Yoann Noblet, Neal Radwell, Guangyu Ren, Pavel V. Paulau, Craig McIntyre, Gian-Luca Oppo, Joshua P. Toomey, and Deborah M. Kane

3.1

Introduction

Laser solitons (LS) or laser cavity solitons are a special class of dissipative solitons in a system out of equilibrium where cavity losses are counterbalanced by the energy input of the pumping. We will refer to a laser emitting temporally or spatially localized structures due to nonlinear processes (and not by linear boundary conditions) as a cavity soliton laser. Cavity solitons and cavity soliton lasers found a lot of sustained interest over more than two decades. This is partially due to the fact that pulse shaping in certain mode-locked lasers is related to soliton dynamics [1–4] and thus has important applicative aspects. Since a laser can operate through pumps with low temporal and spatial coherence (or even completely incoherent sources such as electrical pumping) cavity soliton lasers may be easier to operate than cavity soliton schemes relying on coherent driving. From the fundamental point of view, LS combine self-localization with the phase symmetry of a self-sustained oscillator. As a consequence LS have two Goldstone modes, location (spatial phase) and the optical phase that they can choose freely. In addition, LS can – within the limitations of the cavity setup – choose frequency and polarization, the latter providing potentially a third Goldstone mode in an isotropic system. We will explore some of the consequences of these degrees of freedom in this chapter, as well as point out limitations in real implementations.

The complex Ginzburg–Landau equation (GLE) is the archetypical equation describing the nonlinear dynamics of active dissipative systems. It is known that the GLE supports soliton solutions although they are typically unstable [5–7]. One established way towards stabilization is the extension of the GLE to a quintic nonlinearity [8, 9], leading to the cubic–quintic Ginzburg–Landau equation (CQGLE) that can describe the dynamics of spatial as well as temporal LS (see, e.g., [10] for a review). The temporal case was recently reviewed in [3] and is covered in other chapters of this book in lasers and coherently driven

Nonlinear Optical Cavity Dynamics: From Microresonators to Fiber Lasers, First Edition.
Edited by Philippe Grelu.
© 2016 Wiley-VCH Verlag GmbH & Co. KGaA. Published 2016 by Wiley-VCH Verlag GmbH & Co. KGaA.

configurations [11–15]. We will be looking instead at spatial LS. As the coefficients of the CQGLE are complex, soliton formation and stabilization can be either due to dispersive nonlinearities (imaginary part), that is, nonlinear phase and frequency shifts, or nonlinear gain and losses (real part). In optics, spatial LS started with the latter, being observed in early examples of dye lasers or photorefractive oscillators containing saturable absorbers [16–19]. Pioneering theory was done by Rosanov and coworkers [20–22]. Dispersive extensions of the GLE models were developed [6, 23], but not applied to lasers until recently [24].

Following the demonstration of cavity solitons in driven semiconductor microcavities [25], interest is shifted to semiconductor laser systems. They constitute compact, robust, fairly inexpensive, and energy efficient devices with the potential to interface to modern photonic networks. The first semiconductor cavity soliton laser was based on a vertical-cavity surface-emitting laser (VCSEL) with frequency-selective feedback (FSF) relying on dispersive effects [26, 27]. A realization based on saturable absorption followed soon afterwards [28]. Both configurations used broad-area but otherwise fairly standard VCSELs. Later, dedicated devices with a monolithic integration of gain and absorbers were implemented [29]. For reviews about much of this work, we refer to [30, 31] and a special issue of the European Physics Journal D [32].

In this contribution, we will review the main properties of LS in the VCSEL with FSF, explore more complex phenomena related to the Goldstone modes and how LS interact with imperfections due to spatial disorder. We will provide an introduction to the devices and the setup in Section 3.2. In Section 3.3, we will present evidence of the dispersive mechanism at the base of the existence of LS followed by the relevance of spatial disorder in pinning LS to preferred positions. In Section 3.4, we will review the model and explain the theoretical interplay between the Goldstone modes of location and phase during LS interaction. We will find in Section 3.5 that the experimental observations are different as the LS are pinned by disorder. This leads to frequency- and phase-locking between LS at different locations. We will demonstrate a connection to the archetypical Adler-model and thus establish a link between soliton physics and synchronization dynamics, both being important research topics of nonlinear and complexity science in their own rights. In Section 3.6, we will look at the transient switch-on dynamics of LS as well as giving an outlook on asymptotic dynamic states. We will find that solitons can operate on multiple longitudinal cavity modes and demonstrate self-pulsing indicating that these modes are at least partially phase-locked. This has relevance for spatio-temporal cavity solitons or cavity light bullets where self-localization occurs in all three space dimensions. Stable 3D self-localization appears to be the holy grail of nonlinear photonics in spite of significant efforts and intermediate achievements [33–36].

3.2
Devices and Setup

3.2.1
Devices

The devices under study are broad-area VCSELs. These are high finesse semiconductor plano-planar microcavities characterized by a short cavity length (≈ 1.2 μm) and a wide transverse aperture (tens to hundreds of micrometer). This results in a high Fresnel number and thus the coexistence of many transverse modes. Though this constitutes a limit on applications requiring high beam quality, it makes them ideal devices to investigate self-organized spatial laser structures and LS. A scheme of the device is shown in Figure 3.1a. It is based on three InGaAs quantum wells (QW) in between GaAs barriers as gain medium leading to emission in the 970–980 nm spectral range. The gain region is sandwiched by AlGaAs spacer layers defining a one-wavelength long cavity. This cavity is closed by high reflectivity AlGaAs/GaAs distributed Bragg reflectors (DBR), which are p- and n-doted, respectively, to allow for current injection. Optical and current confinement is provided by an oxide aperture. We investigated devices with apertures between 80 and 200 μm, most results (and all reported here) were obtained in devices with 200 μm diameter. Current injection is via a circular, disk-shaped contact on the top p-mirror. This ensures a fairly homogeneous current injection (there is still an enhancement at the device perimeter of about 10–20% [37]) as the current has about 200 μm of propagation path in the substrate to disperse to the ring-shaped contact at the bottom n-side. The emission window is anti-reflection (AR) coated. Figure 3.1b shows an optical

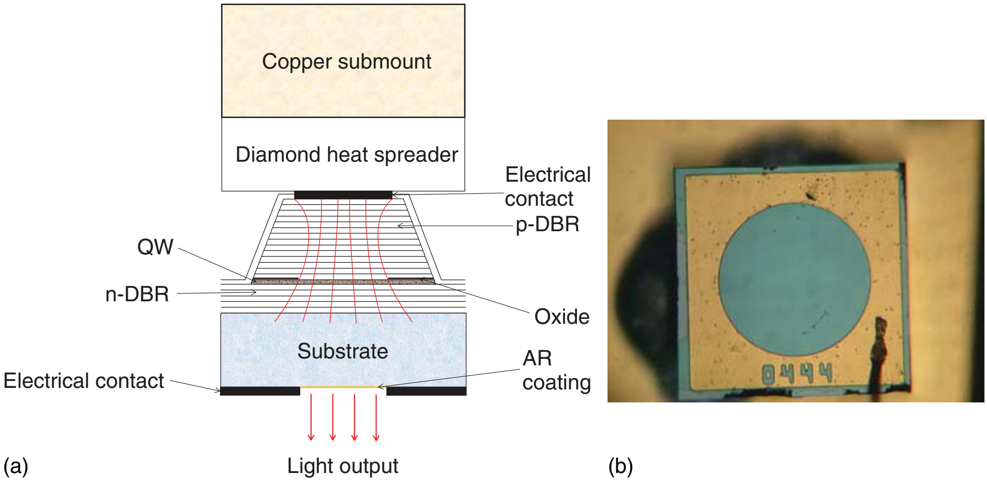

Figure 3.1 (a) Scheme of VCSEL. (b) Microscope image of emission window of a VCSEL with 106 μm circular aperture.

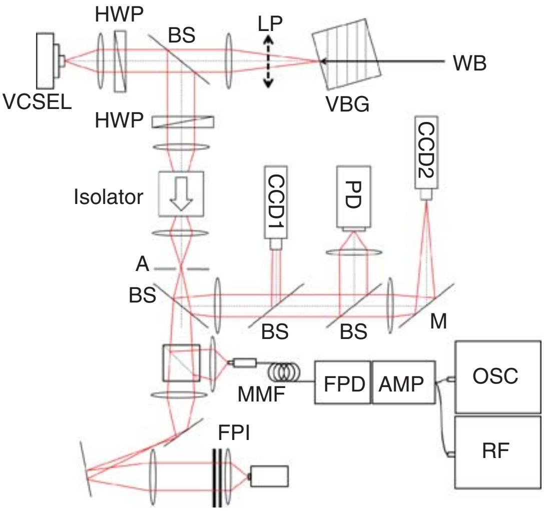

Figure 3.2 Experimental setup. VCSEL, vertical-cavity surface-emitting laser; BS, beam splitter; VBG, volume Bragg grating; HWP, half-wave plate; LP, linear polarizer; WB, external writing beam; A, aperture; M, mirror; PD, photo diode; CCD2, CCD camera in near field image plane of VCSEL; CCD1, CCD camera in far field image plane of VCSEL; FPI, Fabry–Perot interferometer; MMF, multimode fibre; FPD, fast photodetector; AMP, RF-amplifier; OSC, single-shot digitizing oscilloscope; RF, electrical spectrum analyzer for RF analysis.

image of the emission window and n-contact. This geometry is enabled by the fact that the GaAs substrate is transparent for the laser radiation at 980 nm and is referred to as bottom-emitting. Efficient heat sinking is enabled via a diamond heat sink soldered on the p-contact. Technical and performance aspects of these lasers are discussed in [38–40].

3.2.2
Experimental Setup

The experimental setup is shown in Figure 3.2. Details can be found in [41–43]. The VCSEL is mounted on a temperature controlled submount. Its emission is collimated by an aspheric lens with an effective focal length of $f_1 = 8$ mm. It is then refocused with a plano-convex lens of $f_2 = 50$ mm onto the frequency-selective element closing the external cavity. The lens configuration corresponds to a telescope focused to infinity, that is, the cavity is self-imaging allowing for self-localization. In first investigations [26, 27, 44], a diffraction grating was used as frequency-selective element, but we are using now glass volume Bragg gratings (VBG) [41] as they are more selective and “wrong” components are transmitted and not reinjected in the VCSEL with changed angles. VBG 1 has a peak reflectivity of greater than 99% at 981 nm and a bandwidth of 0.2 nm (full width half maximum, FWHM), VBG 2 a peak reflectivity of about 95% at 978 nm and a bandwidth of slightly larger than 0.1 nm (FWHM).

The Fresnel reflection from a wedged beam sampler (front uncoated, back AR-coated) is used for output coupling. The cavity is isolated from the detection setup by an optical isolator. After the isolator, there is an intermediate image plane with a movable circular aperture A by which we can select only a part of the VCSEL aperture for analysis. The output intensity distributions are analyzed by charge-coupled device cameras (CCD) after suitable optics, in near field (CCD2) and far field (CCD1). The total output power is monitored by an amplified, slow photodetector (PD). The optical spectrum is monitored by a confocal scanning Fabry–Perot interferometer (FPI) with a free spectral range (FSR) of 10 GHz and a finesse of 40–80 depending on alignment.

For fast time-resolved measurements, another part of the output is coupled to a multimode fiber and then to amplified fast photodetectors. The first option is a pin-detector (FPD) with a 3 dB frequency bandwidth of 12 GHz (New Focus 1544-B), which is then amplified further by a 15 dB amplifier (AMP) with 15 GHz bandwidth (Picosecond Pulse Labs 5867). An alternative detector is an avalanche photodiode (APD) with a 3 dB cutoff frequency of 1.1 GHz and variable gain (New Focus 1647). These signals are monitored on single-shot oscilloscopes with 12–18 GHz analog bandwidth (LeCroy and Tektronix digital signal analyzer) and a sampling rate of at least 40 Gb s^{-1}, digitally filtered at 10 GHz to reduce noise.

The polarization isotropy is broken by uncontrolled intrinsic polarization anisotropies in the VCSEL microcavity and by the intra-cavity beam sampler, as its reflection for s-polarization is about 10%, but only about 1% for p-polarization. We find that the solitons have slightly different, though similar, polarization axes [41] and use a half-wave plate to maximize the signal through the optical isolator. For the purposes of this review we can assume a quasi-scalar situation. However, nontrivial polarization effects are currently under investigation. For some of the investigations on fast dynamics, we force the LS to work on vertical polarization by inserting a linear polarizer (LP) and a half-wave plate (HWP) into the cavity. Though this introduces additional losses, we gain signal-to-noise ratio on the fast photodetectors as the outcoupling is much higher for vertically polarized light. There is no principle difference in soliton properties with and without these additional polarization-selective elements.

3.3
Basic Observations and Dispersive Optical Bistability

3.3.1
Basic Observation of Spatial Solitons

Figure 3.3 show the light–current characteristic (LI-curve) of the device. It is characterized by abrupt transitions between different emission states. The laser is not lasing across the whole aperture but on small localized spots. Increasing the

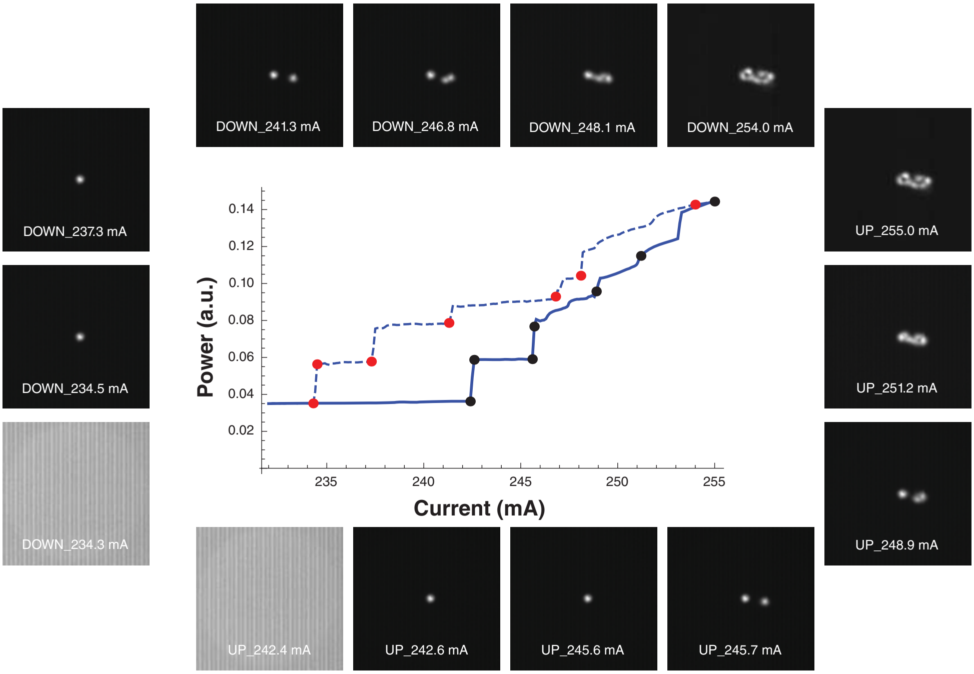

Figure 3.3 Light–current characteristic and near field emission structures from the VCSEL. The dots in the LI-curve denote the points were the images were taken. The current values are also in insets. The images are displayed in a linear gray scale with white denoting high intensity. All images are obtained at the same gain and filter settings of CCD2, but each image is scaled to obtain maximum contrast within the image. Hence the images containing only spontaneous emission are dominated by RF-interference. Submount temperature, 44 °C, VBG 2; displayed area, 208 × 208 μm^2.

current, additional spots appear at different locations or a spot changes to more complex structures as double-peaked clusters and rings. The single-humped spots are the fundamental LS. A detailed characterization can be found in [41]. They have a size of 5–7 μm (1/e^2 – radius). Within experimental accuracy, they are diffraction-limited, that is, have a high spatial coherence. Note that the spatial coherence of a dissipative soliton is expected to be imperfect as the phase profile is not flat (see Figure 3.6a), but the effect is too small to be reliably measured. With a high resolution FPI with an FSR of 1 GHz their linewidth is measured to be a few megahertzs [41], that is, LS have also a high temporal coherence. Hence, each of these spots is a small microlaser stabilized by solitonic effects.

Obviously, the LS are bistable, one or two LS can coexist with the nonlasing solution. The approximately ring-shaped structures were identified as vortex solitons by interference measurements [45, 46]. They can be interpreted as high-order solitons. They can coexist with fundamental LS and the non-lasing state. Increasing the current further, more LS are emerging, preferentially at perimeter of the existing emission, and LS give way to spatially extended, off-axis lasing states. Examples and details can be found in [41, 47, 48]. The details of the structures encountered on the upper branch depend on the current value at which the up-scan is stopped and reversed. This indicates that the hysteresis loops of the different structures are heavily interwoven. Within the coexistence range of the nonlasing state and the LS, one can switch LS on and off per external control beams [26, 27, 41]. This external control beam or writing beam (WB) is derived from a single-mode tunable laser and is injected via the VBG (see Figure 3.2). This possibility to manipulate LS makes them attractive for optical information processing [49, 50].

3.3.2
Interpretation as Dispersive Optical Bistability

If one repeats the LI-curves for different submount temperatures, one obtains data like the ones displayed in Figure 3.4. The first important observation is that the switch-on and the switch-off currents increase strongly with decreasing submount temperature. Other tendencies observed are that the LS power at switch-off and switch-on increases with switching current (decreasing temperature) and that the width of the hysteresis loop widens. The details of these amplitude changes are currently under investigation. The LI-curves at high temperature (50 °C) are actually continuous, that is, do not show bistability any more.

For a quantitative investigation of the switch-on and switch-off points we are plotting these thresholds against the submount temperature in Figure 3.5a. The thresholds drop approximately linearly with temperature. Fitting yields a slope of $-19.1\ \mathrm{mA\,K^{-1}}$ for the switch-on thresholds and $-17.9\ \mathrm{mA\,K^{-1}}$ for the switch-off thresholds. The small discrepancy is due to the widening of the hysteresis loops as mentioned earlier. From other measurements without feedback, we know how

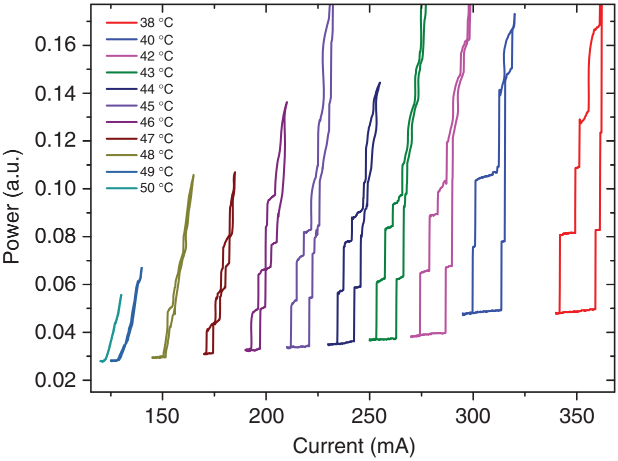

Figure 3.4 LI-curves obtained for different submount temperatures (in legend). The temperature parameter for the particular LI-curves decreases from left (50 °C) to right (38 °C) via the steps given by the values in the legend. Other parameters: VBG 2.

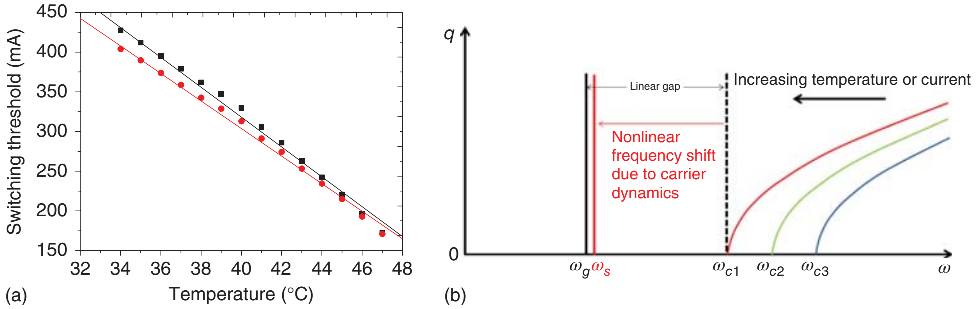

Figure 3.5 (a) Switch-on (black squares) and switch-off thresholds (red circles) in dependence on submount temperature. The straight lines are linear fits to the data. (b) Illustration of mechanism for soliton-switch-on. The transverse wavenumber of the resonances is plotted against frequency. ω_g denotes the frequency of the VBG reflection peak. It is nearly independent of transverse wavenumber for the purpose of these considerations, hence the VBG characteristic is shown as a straight line. ω_{ci} represents the longitudinal resonance frequency of the VCSEL for a certain set of parameters. All high-order VCSEL modes are at higher frequencies. For increasing current or increasing submount temperature the resonance red-shifts from ω_{c3} to ω_{c1}. Alternatively, one can think of the different lines as dispersion curves at different spatial locations in the VCSEL at a certain temperature and current, shifted by disorder. ω_s is the final LS frequency.

much the wavelength of the cavity resonance shifts with submount temperature ($d\lambda_c/dT \approx 0.066$ nm K^{-1}) and with current ($d\lambda_c/dI \approx 0.0035$ nm mA^{-1}). From that one estimates a heating rate of the device by ohmic losses as $dT/dI \approx 0.053$ K mA^{-1}. The inverse is $dI/dT \approx 18.9$ mA K^{-1}. This is very close to the rate measured for the change in switch-on current and still very close to the rate of change of the switch-off current. This allows to conclude that the active zone of the VCSEL actually switches always at approximately the same temperature, independent of gain.

This behavior can be explained by the scheme in Figure 3.5b. Initially, the longitudinal resonance of the VCSEL is at higher frequency than the reflection peak of the VBG. Increasing the submount temperature or increasing the current red-shifts it so that it moves closer to the VBG resonance. If the gap is small enough, the carrier related intrinsic optical nonlinearity of the VCSEL takes over. A small fluctuation increasing emission intensity leads to a decrease in carrier number due to stimulated emission. Semiconductor lasers are characterized by a strong phase–amplitude coupling, their refractive index n increases with decreasing carrier number. In the simplest description by Henry's α-factor, one assumes a linear relationship [51]. As the cavity resonance is given by $\omega_c \sim c/(\text{Ln})$, an increase in refractive index decreases the cavity resonance. Hence the VCSEL resonance moves closer to the grating frequency, the losses of the system become smaller and due to positive feedback intensity will increase further and abrupt switching takes place. In the terminology of optical bistability [52] this mechanism corresponds to dispersive optical bistability. Switching due to these relatively fast nonlinearity (the carrier response time is about 1 ns) can take place if the thermal tuning (either by temperature or by current) decreased the gap between VCSEL and VBG resonance sufficiently. This argument explains the occurrence of bistability. In principle, a plane wave high-amplitude state could exist but it is unstable due to the self-focusing (again mediated via the α-factor) stabilizing the LS. The conditions for bistability were worked out in detail for the plane-wave case in [53–55]. For some other aspects of the nonlinear dynamics of semiconductor lasers with FSF we refer to, for example, [53, 56, 57].

If the temperature of the submount is too high (in our case at about 50 °C), the VCSEL resonance overshoots the VBG resonance before threshold is reached. In that case the switch-on is similar to the one of a normal laser, that is, not abrupt but continuous (see leftmost part of Figure 3.4). Emission takes place at increasing mode order as the VBG sweeps through the dispersion curve of the VCSEL [48].

In a homogeneous system one expects that LS could exist at any location and would have the same threshold for switch-on (actually, as LS demand a hard excitation to switch-on, lasing should not start before the whole laser crosses threshold). Figure 3.3 clearly demonstrates that this is not the case. The LS are pinned at certain locations. These locations depend on device and can be changed slightly, but only slightly, by alignment of the VBG [41]. Different LS have also slightly different frequencies, though the spread is small, for example, about 0.1 nm for the first four LS obtained with VBG 1 [41]. This is due to uncontrolled fluctuations in the expitaxial growth process, which cause a variation of resonance conditions across the pumped aperture of the device. Since translation is a Goldstone mode of a soliton, it will couple to all spatially inhomogeneous perturbations and the LS will move until it reaches a local extremum of the perturbation, where the gradient vanishes [18, 50, 58, 59] (see also the review in this book [60]). This leads first to a pinning of the solitons at certain positions generally referred as either traps or defects. This was investigated in detail in coherently driven semiconductor microcavities [61, 62] and by some of the authors in the VCSEL with FSF [47]. In addition, this will also lead to a spread in LS thresholds as the detuning condition between VBG and VCSEL frequency for switch-on will be reached at different currents at different locations (Figure 3.5b). Unfortunately, it turns out that monolayer fluctuations are enough to affect LS behavior significantly and this poses a severe obstacle to develop devices that exploit the potentially massive parallelism offered by the coexistence of many LS in a single broad-area cavity soliton laser.

3.3.3
Comparison to Absorptive Case

The results obtained here are phenomenologically very similar to results on spatial LS obtained using saturable absorption as a mechanism to stabilize the nonlasing state. An experiment performed by Genevet *et al.* [28] (see also the review in [11]) at the Institut Nonlinear de Nice uses a VCSEL of identical design as the ones used here as the gain medium, biased above transparency but below threshold. The VBG is replaced by a nominally identical VCSEL structure biased below transparency, that is, the VCSEL acts as resonantly enhanced saturable absorber. The resonances of the two devices are aligned by current tuning. Bistable spots are observed, which can be controlled by an external writing beams. These are the fundamental solitons. They can be sustained if the finesse of the external cavity is high enough after the losses in the absorber are saturated. In the terminology of optical bistability [52] this mechanism corresponds to absorptive optical bistability. Outside the LS, the unsaturated losses are so high that the nonlasing solution is stable. Thus, the stabilization of the background required to stabilize the unstable GLE solitons discussed in [5–7] can be achieved by saturable absorption or saturable nonlinear index changes in the same devices using different settings.

Apart from fundamental LS, high-order vortex solitons are found [63]. The location of the spots are pinned and different spots are typically mutually incoherent [64]. This demonstrates the importance of spatial disorder also in the absorptive case.

3.4
Modelling of LS and Theoretical Expectations in Homogenous System

3.4.1
Model Equations

A theoretical model for the VCSEL with FSF based on a system of coupled partial differential rate equations for the intra-cavity optical field E and carrier density N was developed by some of the authors in [65]:

$$\partial_t E = -(1 + i\theta)E + i\nabla^2 E + \sigma(1 - i\alpha)(N - 1)E + \frac{2\sqrt{T_1}}{(T_1 + T_2)}F \tag{3.1}$$

$$\partial_t N = -\gamma[N - J + |E|^2(N - 1)] \tag{3.2}$$

$$F(t) = \mathrm{e}^{-i\delta\tau_f}\hat{G}(t - \tau_f/2)\ [-\sqrt{1 - T_1}F(t - \tau_f) + \sqrt{T_1}E(t - \tau_f)] \tag{3.3}$$

In Eq. (3.1), θ is the detuning of the VCSEL cavity with respect to the carrier reference frequency (taken as the VBG frequency), σ is a coupling constant, α is the linewidth enhancement factor, and T_1 and T_2 are the transmittivities of the VCSEL mirrors. The Laplacian operator describes diffraction. F is the feedback field. Time is scaled to the lifetime of the intra-cavity field, space is normalized to the square root of the diffraction parameter [66]. For a low-loss VCSEL, where losses are dominated by the output coupling, the time scale is of the order of 10 ps, while the spatial scale is around 4 μm (see also [66]). In Eq. (3.2), J is the injection current normalized to the value at transparency, $\gamma \approx 0.01$ is the normalized carrier decay rate.

In Eq. (3.3), δ is the external cavity carrier field detuning and τ_f the external round-trip time. Note that the inclusion of the feedback field delayed by one round-trip allows for the description of light propagation in the external cavity beyond the typical Lang–Kobayashi [67] approximation of a single round-trip in the external cavity, with only minor additional computational costs [65, 68]). The operator $\hat{G}$ describes the frequency-selective operation of the Bragg reflector on the field envelope and is taken to be

$$\hat{G}(t)\ \{h(t)\} = \frac{r_g}{2\zeta} \int_{t-2\zeta}^{t} e^{i\Omega_g(t'-t)}\ h(t')\ dt', \tag{3.4}$$

where Ω_g is the grating central frequency relative to the reference (carrier) frequency (shifted to zero in the following), ζ the inverse of the filter bandwidth and r_g the overall reflection coefficient. Note that this description neglects the transverse wavevector dependence of the reflector response.

Solutions of Eqs. (3.1–3.3) were analyzed in [65]. Under suitable operating conditions, a range of currents opens up where extended modes determined by the grating can lase but where the off-state is also stable. In this region of bistability between lasing and non-lasing states it is possible to observe LS in 2D as well as 1D [65].

Spatial inhomogeneities, such as those associated to uncontrolled fluctuations in the VCSEL growth process, can be introduced in the model by considering spatial dependence on the model parameters. In particular one can consider in Eq. (3.1) a spatially dependent detuning, that is $\theta = \theta(x)$ for a 1D system. We will refer to this model as "semiconductor class B model" as it includes the carrier dynamics.

In a series of papers [24, 69–72], Paulau *et al.* investigated the properties and bifurcation structure of LS in simpler class A models, in which the carrier dynamics was eliminated. The simplest model based on this scenario, which captures the basic features of a semiconductor laser with feedback, consists of a cubic complex GLE linearly coupled to an additional linear filter equation (GLE-F) [23, 72]

$$\begin{aligned} \frac{\partial E}{\partial t} &= g_0 E + g_2 |E|^2 E - i\frac{\partial^2}{\partial x^2}E + F + in(x)E, \\ \frac{\partial F}{\partial t} &= -\lambda F + \tilde{\sigma} E. \end{aligned} \tag{3.5}$$

g_0 describes linear gain and detuning, g_2 nonlinear gain saturation and frequency shifts (the ratio $\mathrm{Im}(g_2)/\mathrm{Re}(g_2)$ corresponds to the α-factor of semiconductor lasers discussed above), $\tilde{\sigma}$ the feedback strength and λ the bandwidth of the feedback. Finally, $n(x)$ describes spatial variations of the linear detuning due to local variations in the optical length of the cavity. The time and space coordinates (t, x) are scaled to 1 ns and 40 μm, respectively, that is, the normalized scalings cannot be compared directly between the class-B and the GLE-F model, but they refer to similar physical scales, after the scalings are undone.

As indicated before, for $n(x) = 0$, Eq. (3.5) has an analytical soliton solution of chirped-sech type [6, 23, 24]:

$$E = E_{\max}[\cosh(Kx)]^{-1-i\beta} e^{i\omega t} \tag{3.6}$$

where the amplitude $E_{\max}$, the inverse width K, the chirp β and the frequency ω are expressed through system parameters. The physical interpretation of the stabilization of LS in Eq. (3.5) is that the linear filter renders the background off-resonant thus suppressing lasing but the nonlinear frequency shift allows lasing in high-amplitude, resonant states (cf. to the discussion of Figure 3.5).

The field amplitude decays exponentially in the wings of the soliton (see Figure 3.6a below for a particular example). The crucial difference between the dissipative soliton given by Eq. (3.6) and an analogous conservative soliton is the nonzero value of β leading to the dependence of the phase on x as illustrated in Figure 3.6a. Far from the centre, the phase changes linearly with distance and hence repeats with a period of $P = 2\pi/(K\beta)$. Only with a moderate to large absolute value of chirp the soliton phase changes significantly within the soliton width x_0. Recall that an NLSE soliton has flat phase, that is, zero chirp: in tendency, the chirp increases with the ratio of nonlinear gain to nonlinear dispersion. Figure 3.6a and c illustrate this for parameters corresponding to α-factors of 0.5 and 1.

3.4.2
Interaction of Laser Solitons in a Homogenous System

In this subsection we consider the pairwise interaction of LS found in the GLE-F model, Eq. (3.5). We consider first the ideal case with translational invariance ($n(x) = 0$), where a single soliton has two Goldstone modes, location and phase. We chose a superposition of two solutions of the type given in Eq. (3.6), with the maximum of one LS at x_1, and the maximum of the other LS at $x_2 > x_1$ as initial conditions for the evolution. We also chose random initial phases ϕ_1 and ϕ_2. The two LS will mutually interact by providing a perturbation to each other.

The results of the interaction can be visualized nicely in the "interaction plane," introduced in [74] and spanned by polar coordinates $L = |x_2 - x_1|$ and $\Phi = \phi_2 - \phi_1$. It is presented in Figure 3.6b, which depicts key trajectories and fix points. It is characterized by a series of foci close to $\Phi \approx \pi/2$ corresponding to moving bound states, and two series of saddles with $\Phi = 0$ and $\Phi = \pi$ representing stationary bound states. The interaction phase space diagram of our GLE-F looks qualitatively similar to that of the CQGLE [75, 76]. We conclude that this kind of weak-interaction scenario is qualitatively independent from the mechanism of soliton stabilization (quintic nonlinearity or linear filter), although details as soliton width and interaction strength are affected by the details of the nonlinearity quantitatively, of course. Indeed the foci were observed experimentally in fibre lasers [77, 78] (see the review in this book [14]). As these solutions are moving one can expect that the pinning due to spatial disorder provides an obstacle for their observation and indeed no indications were seen in the experiment.

Hence we turn our attention to the saddles. The stable and unstable manifolds of the saddles coincide with the Goldstone modes of the single soliton. The horizontal manifolds correspond to the soliton translation mode, while the vertical manifolds to that of the local phase. Note that neighboring saddles have opposite stability properties with respect to phase and translation. The light-gray (white) shading in Figure 3.6b shows the regions where the active tangential

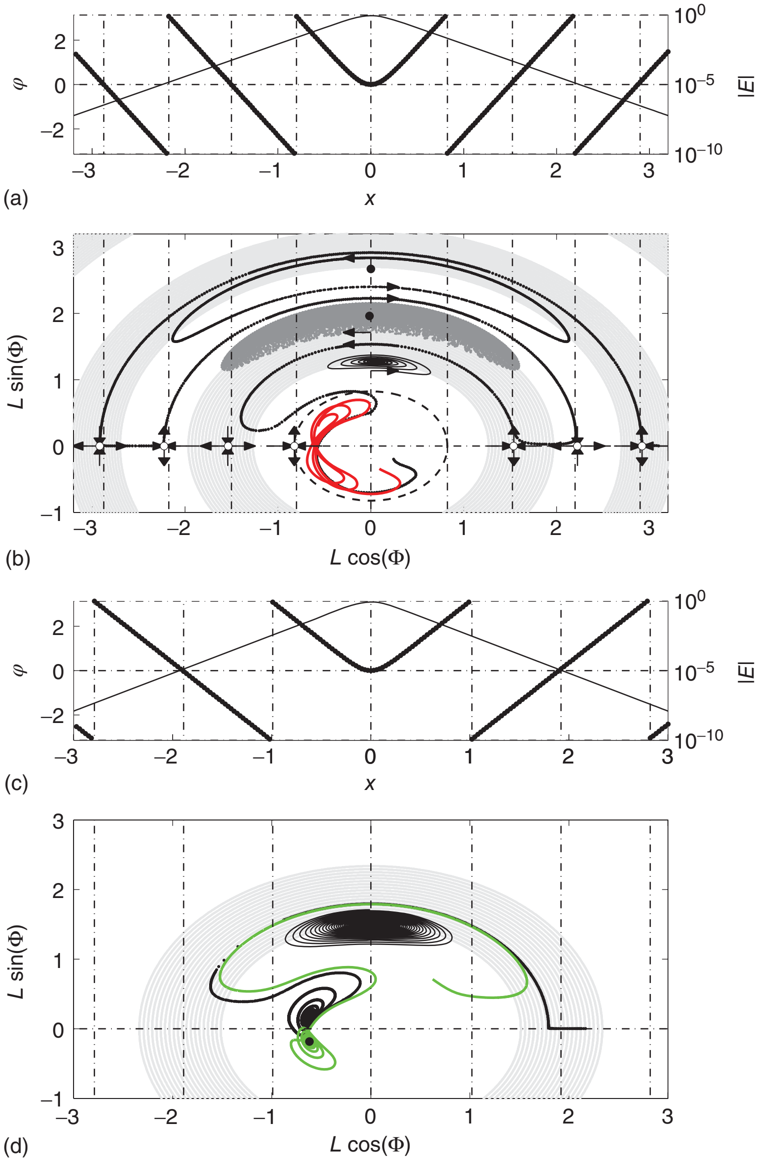
(a)
φ
2
0
−2
−3
−2
−1
0
1
2
3
x
10^0
10^{-5}
10^{-10}
|E|
(b)
L sin(Φ)
3
2
1
0
−1
L cos(Φ)
(c)
φ
x
|E|
(d)
L sin(Φ)
L cos(Φ)

Figure 3.6 (a,c) Profile of the soliton field from Eq. (3.6) for the parameters listed at the end of the caption and (a) $\alpha = 0.5$, (c) $\alpha = 1.0$. Dots show the phase (left vertical axis); solid line shows the amplitude distribution (right vertical axis, semi-logarithmic scale). (b, d) "interaction plane" of two LCS (b) $\alpha = 0.5$, (d) $\alpha = 1.0$). The arrows indicate the direction of motion of the system along any trajectory. The dark-gray shaded region is a dense spiral. Black dots near $\Phi = \pi/2$ are foci, while the white dots (along $\Phi = 0$ and $\Phi = \pi$) are saddle points. The vertical dash-dotted lines link subplots (a) and (b), and confirm that the saddles have the same spatial period as the phase of an isolated soliton. The shading is explained in the text. In (b), the red line crossing the horizontal axis around $L \cos \Phi \approx -0.63$ indicates the existence of two unstable foci above and below the horizontal axis. The two solitons finally merge into one. In (d), these two foci are stable, see the black and green lines. Parameters: $g_0 = (-4, 28)$, $\lambda = 2.71$, $\tilde{\sigma} = 162.6$, (a, b) $g_2 = (-96, -48)$ (see [72]), (c, d) $g_2 = (-96, -96)$ ((a, b) adapted from [73]).

components are directed counterclockwise (clockwise) in the upper half-plane (the sense of rotation is inverted in the lower half-plane that is not shown). It is clear that the location of the saddles is strongly determined by the chirped phase of the individual LS, which leads to intensity oscillations in their mutual interference profile [75, 79].

For very small values of L, the description as a pair of separate, weakly interacting, LS becomes questionable and typically soliton merging takes place. There are indications for one unstable focus ($L \cos \Phi \approx -0.7$, red line, quite strongly shifted from $\Phi \approx \pi/2$) and we suspect the existence of another saddle at $L \cos \Phi \approx 0.8$.

For increasing absolute value of the imaginary part of g_2 (increasing α-factor of the semiconductor laser) the phase profile of the solitons becomes flatter (Figure 3.6c) and the saddles move to higher distances in the interaction plane (Figure 3.6d). The additional foci at $L \cos \Phi \approx -0.7$ become stable. Figure 3.6d is only intended to display basic tendencies; it obviously does not constitute a thorough investigation. Since experimentally relevant α-parameters are between 2 and 9, the saddles are expected to be further out, corresponding to weak LS interactions so that the guidance provided by diagrams like this becomes questionable. Nevertheless, one can infer from the interaction diagram that pinning the relative position of LS via traps can lead to the stabilization of position-unstable saddles and thus make phase-locking of the stationary state with relative phases close to 0 or π possible. Some further details, including those about soliton interaction in the class B model, can be found in [73].

3.5
Phase and Frequency Locking of Trapped Laser Cavity Solitons

3.5.1
Basic Observation

As argued in Section 1.3.2, typically different LS are mutually incoherent due to disorder. As a consequence, the far field of several LS is the incoherent sum of the far field of the single LS and single-humped as a consequence. However, for certain combinations of current values and minute alignment of the retro-reflection angle of the VBG, a pronounced and beautiful interference pattern appears in the far field indicating that they are phase-locked. This is illustrated in detail in Figure 3.7 for two LS 25 μm apart. Blocking one of the LS using the aperture A in the intermediate image plane (see Figure 3.2) yields the image of the other LS (LS1) in near and far field displayed in Figure 3.7a. Blocking LS1, yields the image of LS2, spatially shifted in near field but approximately identical in far field as both LS are emitting along the optical axis (Figure 3.7b). This is very different, if both LS are detected together (Figure 3.7c), now the far field shows a highly modulated fringe pattern.

A Gaussian profile modulated by a sine-wave is fitted to this cut,

$$y = y_0 + A \exp \left[\frac{-(\theta - \theta_0)^2}{2w^2} \right] \left[\frac{1 + M \sin(F(\theta - \theta_0) + P)}{1 + M} \right]. \tag{3.7}$$

Here y_0 is the offset, A is the amplitude, x_0 is the peak centre, w is the width, M is the modulation depth or fringe visibility, F is the frequency of the sine modulation, and P its phase. The fringe spacing F is inversely related to the LS distance in near field, the fringe phase P is related to the locking dynamics. In this case we extract a visibility of 0.91 and a period of 49 mrad.

The existence of this fringe pattern confirms phase-locking over the integration time of the CCD, that is, milliseconds. Once achieved, phase-locking is actually quite robust and can last for minutes, up to hours, depending on parameters. The optical spectra of the LS shown in the lower panels of Figure 3.7 confirm that the LS are single mode and that the central frequencies coincide within the resolution of the measurement. As the finesse in this implementation is only 45 and LS1 couples less well to the MM fibre than LS2, this is a fairly weak statement. Indeed, we typically see that during the time needed to shift the aperture A and to take the spectra, the LS frequencies shift, but the important point is that they shift together, that is, the locking is more robust than the frequency perturbations, for example, by temperature fluctuations and drifts and some vibrations.

3.5.2
Experiments on Locking Phase

For a more detailed investigation, it is necessary to control the detuning between the different LS. As the disorder in the VCSEL resonance is frozen, this is only possible via the external cavity. Tilting the VBG by small angles (much smaller than the LS width in Fourier space) changes the differential external cavity length and thus the feedback phase (the term $-i\delta\tau_f$ in Eq. (3.3)). It is well known that this changes the operating frequency of a semiconductor laser with feedback [55, 67]. This tilt is implemented via a computer-controlled piezo-electrical transducer. For details we refer to [73].

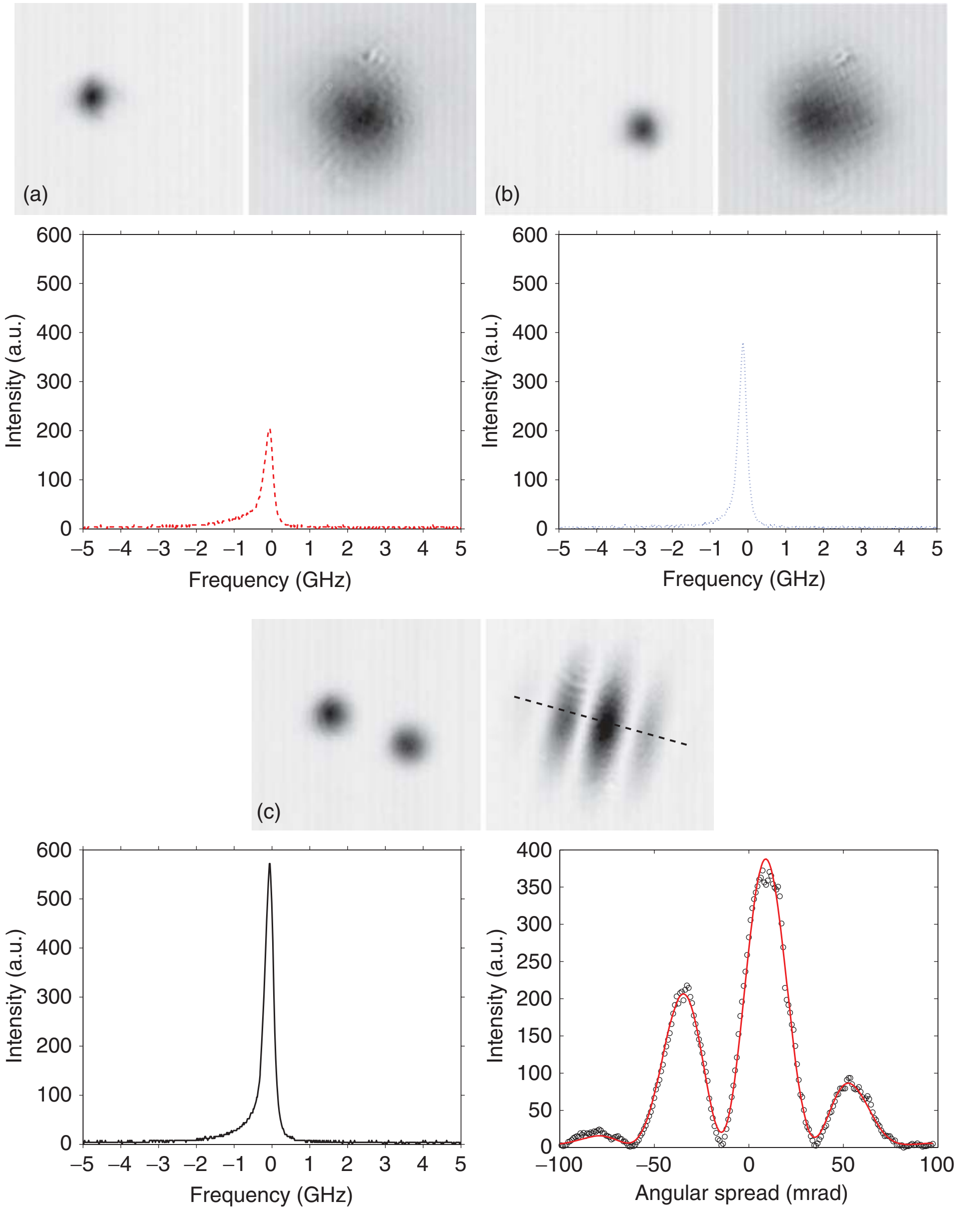

Figure 3.7 Emission of (a) LS1 alone, (b) LS2 alone, and (c) both detected together. The left panel shows the near field, the right panel the far field (both in an inverse gray scale with black denoting highest intensity), the lower panel the optical spectrum. The lower right panel of (c) shows a cut through the far field distribution orthogonal to the fringes with a fit to Eq. (3.7). Other parameters: $T = 36$ °C, current $I = 328.6$ mA, VBG 2.

Results for a typical pair of LS are summarized in Figure 3.8. A detailed discussion can be found in [73, 80]. Figure 3.8c shows that the transition to locking is quite abrupt and that the fringes shift with detuning within the locking region (within a fringe visibility higher than 0.5), that is, the locking phase changes. The quantitative analysis in Figure 3.8a indicates that this variation is nearly linear over most of the range. The width of the locking range is close to π. If the direction of the scan of the tilt is reversed (see the blue dashed line in panel (a)) the locking phase shadows the one obtained in the up-scan, that is, there is no discernible hysteresis. As we will discuss in the theoretical sections, these features are fingerprints of the Adler locking. The noise of the fringe phase is considerably smaller in the region corresponding to complete locking than in the partially locked regions. For even larger tilts (not achievable with the PZT), the two LCS are completely unlocked and their phases random. Modulations depths of about 5% are due to noise in the images.

Figure 3.8b illustrates the evolution of the frequencies of LCS in optical spectra. All spectral lines are shifted due to the change of feedback phase due to the tilt of the VBG. The differential frequency shift in the external cavity is about 30 MHz over the whole diagram, the resulting frequency shift between LS is expected to be even smaller and hence cannot be resolved with the FPI (Finesse 80, frequency resolution about 130 MHz). Hence the differential frequency shift of the two LS can only be inferred from its indirect effect via stabilization and destabilization of external cavity modes and the resulting possibility of locking and unlocking. When comparing panel (b) to panels (a) and (c) one observes that when the fringe visibility is high, the two LCS operate on a single frequency (region within dashed lines in panel (b)).

There is a jump in the common operation frequency of the LS by one FSR slightly after 15 MHz, where the fringe visibility is nearly maintained. This indicates that the two LS do a common mode jump retaining phase and frequency locking. Outside the locking region the two LS operate on two different external cavity modes (with a frequency separation of 1.23 GHz between two adjacent modes). In this region the fringe visibility is rather low (below 0.25) and the locking is very weak. Some residual coupling via side-modes is probably responsible for this residual partial locking. As indicated, for higher tilts, the visibility drops to a background given by noise on the order of 5% or less.

We have obtained a variety of different dynamical behaviors for LCS pairs with different distances ranging from 25 to 80 μm. They all share the common feature of a region of nearly complete locking in which the phase is evolving approximately linearly with detuning. The locking is dominantly anti-phase (π locking phase) and the locking phase varies by nearly π over the locking range. We will interpret these observations below as a manifestation of the Adler-scenario. The observed variations in dynamics are expected since important parameters are associated to background disorder that cannot be controlled by the operator.

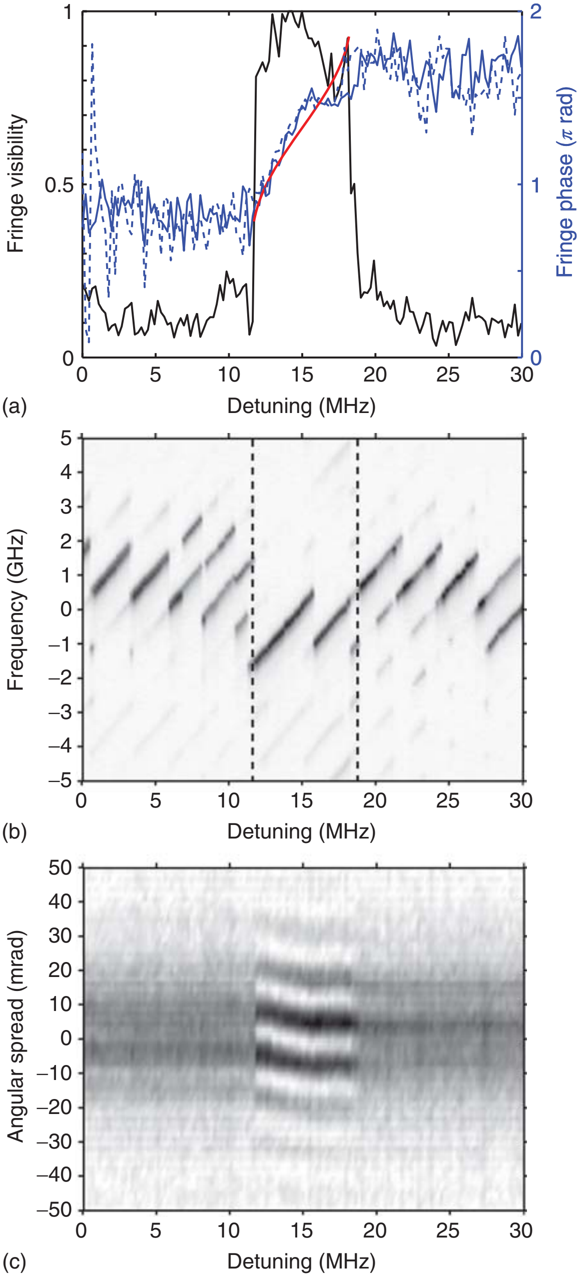
Fringe visibility
1
0.5
0
Fringe phase (π rad)
2
1
0
0
5
10
15
20
25
30
(a)
Detuning (MHz)
Frequency (GHz)
5
4
3
2
1
0
−1
−2
−3
−4
−5
0
5
10
15
20
25
30
(b)
Detuning (MHz)
Angular spread (mrad)
50
40
30
20
10
0
−10
−20
−30
−40
−50
0
5
10
15
20
25
30
(c)
Detuning (MHz)

Figure 3.8 (a) Fringe visibility (black) and fringe phase (blue curves) as a function of the tilt angle that changes the difference between the feedback phases for two LS, 79 µm apart. This difference is converted to a frequency scale by multiplying it by the free spectral range of the external cavity thus providing the change of the relative detuning between the two LCS in the external cavity. The zero of this detuning scale is arbitrary. The solid and dashed blue curves are obtained for scanning the tilt back and forth. The sigmoid red curve in the central, locked region is a superimposed Adler curve, Eq. (3.8), scaled and shifted appropriately. (b) Evolution of frequencies, the frequency distribution is obtained from the optical spectra recorded by the FPI. (c) Cut through far field intensity distribution orthogonal to fringe orientation. Other parameters: temperature 69 °C, current $I = 373$ mA, VBG 1 (adapted from [73, 80]).

3.5.3
Adler Locking: Theory

Strong disorder will freeze the translational degrees of freedom and hence the remaining degree of freedom from the interaction diagram (Figure 3.6) is the phase. Though amplitude dynamics might be also relevant, we can attempt to describe the system by an Adler equation [81], the archetypical equation describing synchronization between coupled oscillators. For our case it can be written in the form

$$\frac{d\Phi}{dt} = \Delta\omega - \epsilon \sin(\Phi), \tag{3.8}$$

where $\Delta\omega$ is the trap-detuning (which is zero for $n_1 = n_2$), and ϵ is a coupling constant. In-phase and anti-phase solutions are selected for $\Delta\omega = 0$, depending on the sign of the coupling. For positive ϵ, the stable final state is $\Phi = 0$, for negative ϵ it is $\Phi = \pi$. It is obvious from the results presented in Figure 3.6 that the distance between traps affects both the magnitude and sign of the coupling in our system. Corresponding terms appear in the perturbation analysis of the CQGLE [75]. The survival of the (slightly modified) $\pi/2$-states for weak perturbations, followed by a transition to in- or anti-phase locking was also observed numerically for the CQGLE with regular modulations [82, 83]. For details of the transformation of the flow from the homogeneous system to the disordered one we refer to [73], here we present only the final result that for traps of sufficient depths, the locking phase follows very accurately the Adler prediction in both the class B and the GLE-F model, if the detuning between LS is changed via adjusting the trap depth (Figure 3.9). In addition a curve (red line in Figure 3.8a) whose shape is determined by the Adler equation (but suitably scaled and shifted) is giving a reasonable agreement with the experimental data. Similar measurements were done for laterally coupled solid-state lasers in the 1990s (e.g., [84, 85]) but apparently the whole scenario of the phase change with detuning was never measured before experimentally.

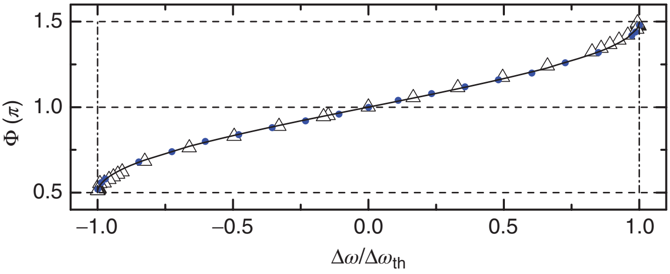

Figure 3.9 Locked phase differences Φ of pinned LCS for different frequency detunings (controlled by the potential depths n_1 and n_2) from integration of Eq. (3.5) (dots, LCS separation of 5.3 soliton widths) and the Eqs. (3.1–3.3) (triangles, LCS separation of 4 soliton widths). The solid line refers to the Adler equation (3.8) (adapted from [73, 80]).

Figure 3.10 provides further details of the comparison with experiment using the class B model. The left column shows the interference fringes in far field. They are highly modulated in the locking region (a,d). The symmetry of the fringe pattern changes from (a) to (b), which is due to the change of the locking phase from π to 1.5π (c,f). The spectrum is single-mode (b,c). Outside the locking region, the fringe visibility drops (g), but some modulation survives (g). This is due to the fact that the phase dynamics is not strictly linear, but correlations remain due to the remnants of the fixed point (i). The spectrum is multi-peaked, the main peaks are offset but the LS share sidebands (h), presumingly via four-wave mixing processes. If the detuning is increased further, the LS are essentially uncoupled, the phase dynamics is linear (l), the far field essentially structure-less (j), and the spectra dominated by two peaks representing the two LS (k). This is in quite good agreement with experimental observation within the locking range and is expected to shed also some light on the partial locking observed outside the locking range, but a detailed comparison is not possibly as the calculations are done for a much shorter cavity length, that is, a much larger longitudinal mode separation so that only a single external cavity mode participates in the dynamics.

In summary, we demonstrated that nonlinear frequency- and phase-locking can overcome the disorder induced desynchronization of LS. The observed scenario is qualitatively explained by a pure phase model, the Adler equation. These results provide an interesting link between solitons and LS as one important subfield of nonlinear science to the field of synchronization dynamics of coupled oscillators [86], one other very important subfield of nonlinear and complexity science.

3.6
Dynamics of Single Solitons

Finally, we turn our attention to another source for rich dynamics in cavity soliton lasers compared to coherently driven systems, which is that lasers have the

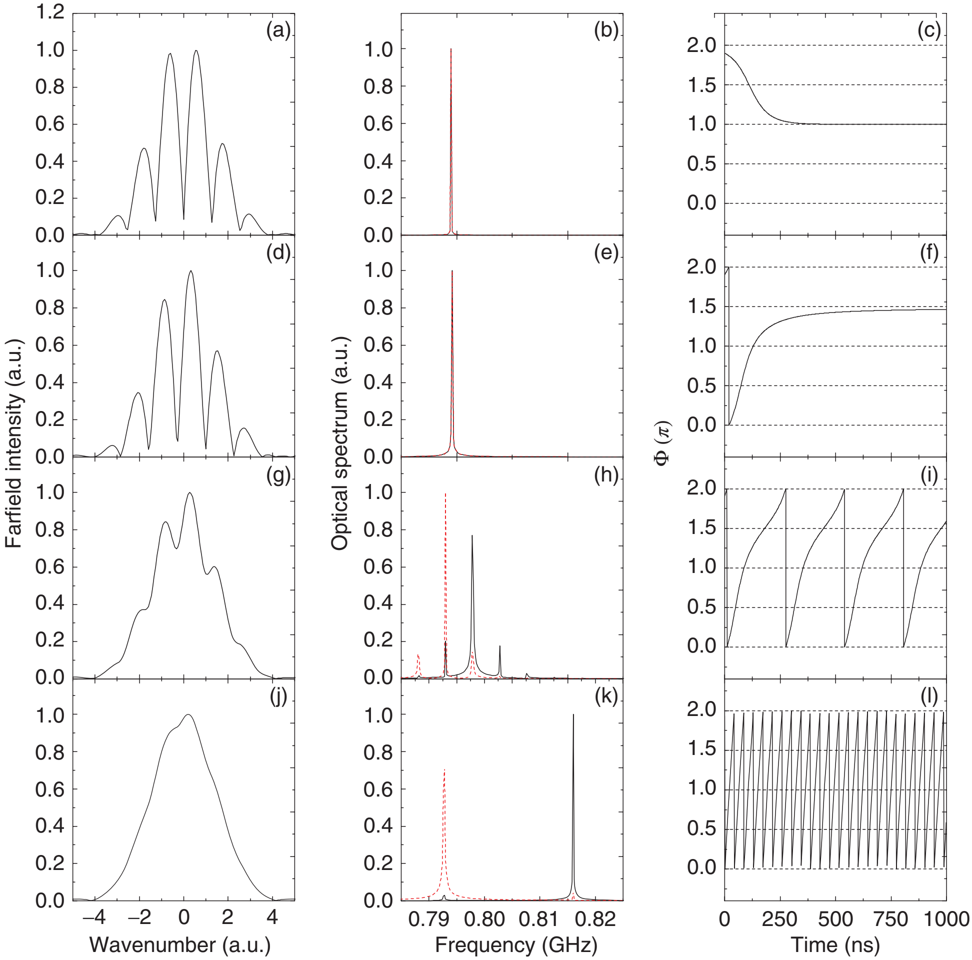

Figure 3.10 Far field images (a, d, g, and j) averaged over 2 μs, optical spectra (b, e, h, and k) for a time window of 5 μs and evolution of the phase difference (c, f, i, and l) for $\delta\omega/\delta\omega_{\text{th}} = 0$ (a–c), 0.99 (d–f), 2.0 (g–i), and 7.5 (j–l). In (b) and (e) the spectral peaks (dashed and solid lines) of the LS overlap. The simulations have been done using Eqs. (3.1)–(3.3) with LCS of initial separation of 4 soliton widths and an initial phase difference of 1.85π (c)–(f), 1.95π (i), and 0 (l).

freedom to choose frequency within the bandwidth of the gain and cavity. We will look at manifestations of this in the transient dynamics after switch-on and in the asymptotic state. For some of these measurements, the second telescope lens in the external cavity (Figure 3.2) is replaced by a lens with focal length $f_2 = 30$ mm to achieve a shorter cavity and a higher pulse repetition rate. As also the intra-cavity polarizer changes the cavity round-trip time, we give the values for the specific realizations in the figure captions.

3.6.1
Transient Dynamics

First, we are investigating the transient dynamics after switch-on of the LS as it has also relevance for possible applications in all-optical processing. Details can be found in [27, 87, 88]. The perturbation (WB) to induce the switch-on is provided by the beam of an external tunable laser, which is gated by an acousto-optical modulator (AOM). Best results are obtained if the WB is tuned about 40 GHz higher than the LS frequency. This indicates that the excitation takes place first at the "cold" VCSEL resonance (ω_{c1} in Figure 3.5b) and then cascades through the gap towards the VBG frequency. This interpretation is supported by the numerical simulations in [87]. The required switch-on power depends on the distance of the bias point to the spontaneous switch-on point.

The results for a particular bias current are shown in Figure 3.11a. The minimum peak power required is approximately constant for pulse durations larger than 100 ns and increases drastically for shorter pulse lengths. Figure 3.11b analyzes the minimum pulse energy needed for switch-on. It confirms that the switching energy increases approximately linearly with pulse length for pulses longer than 100 ns, that is, in this regime switch-on requires surpassing a power threshold as indicated before by panel (a). Below pulse length of 50 ns the required energy flattens off. A horizontal line would imply constant switching energy, also referred to as area law.

These dependencies are nicely reproduced in numerical simulations [87], though the transition from constant required peak power to a higher energy requirement at short pulse length is less pronounced and occurs only below about 15 ns in the simulations. LS can be switched on for pulse lengths down to 1.5 ns.

If the APD detector is replaced by the fast 12-GHz photodetector, it becomes apparent that there is fast pulsing during the first tens of nanoseconds of the switch-on process (Figure 3.12a). The period of the pulses typically corresponds to the cavity round-trip time (here 1.05 ns). Their duration is in the 100–150 ps range indication phase-correlation and mode-locking between several external cavity modes. A time–frequency spectrogram shows the presence of strong harmonics confirming anharmonic dynamics (Figure 3.12b). This clearly indicates that during this transient temporal structures of sub-cavity length are propagating along the cavity axis, that is, there are light "bullets" propagating in the cavity, or at least bullet components, as we cannot quantify the modulation depth accurately, though it seems to be high. These pulses die out within a few tens of nanoseconds after the end of the WB pulse and the time series becomes either cw (single longitudinal mode operation) or shows weak noise oscillations indicating the presence of weak sidemodes. These are typically not on adjacent external cavity modes but at frequencies of 4–5 GHz, which might be due to the fact that the corresponding sidemodes are enhanced by relaxation oscillations. Numerical simulations are in good agreement with these observations and indeed confirm a large modulation depth during the initial pulsing (Figure 3.12c and d).

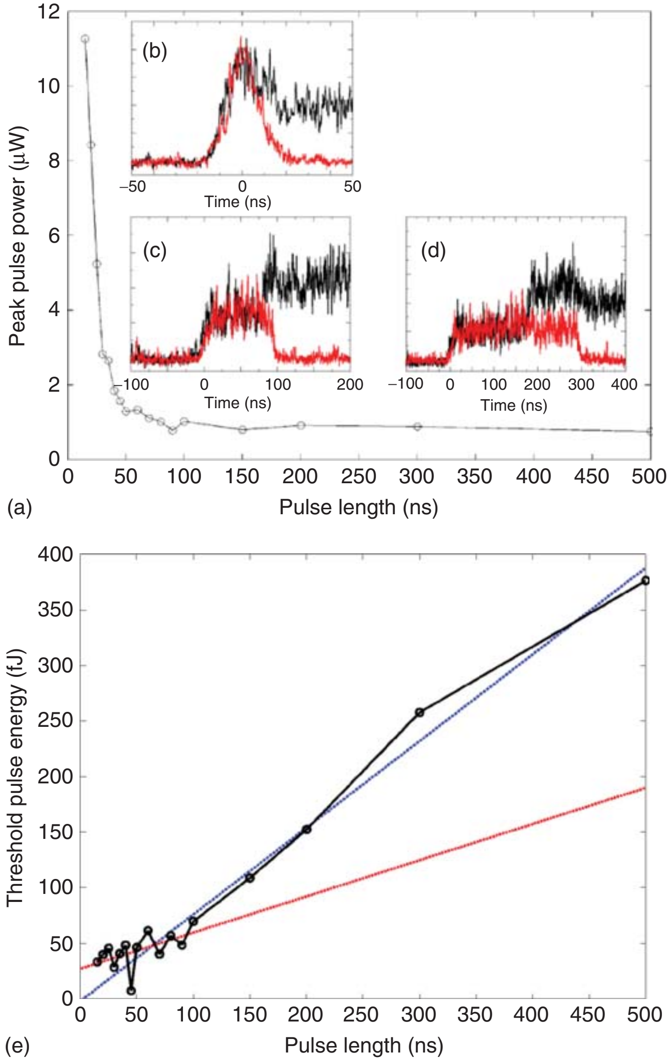

Figure 3.11 (a) Minimum peak pulse power required to switch on a LCS for varying pulse lengths. Insets: time trace of switch-on events for pulse length of (b) 15 ns (AOM limit), (c) 100 ns, and (d) 300 ns pulse. The red line corresponds to the WB pulse and the black line shows the response of the LCS. The LCS always switches to the same power. (e) Minimum energy required to switch a CS on for varying pulse lengths. The lower linear fit (red) is for all pulses shorter than and including 100 ns, the upper linear fit (blue) is for all pulses longer than and including 100 ns. Cavity round trip time 0.606 ns, VBG 1, bias current 3 mA below the spontaneous switch-on threshold. Data taken with APD ((a, c, d) adapted from [87], (e) Figure 4 of [87], with kind permission from Springer Science and Business Media).

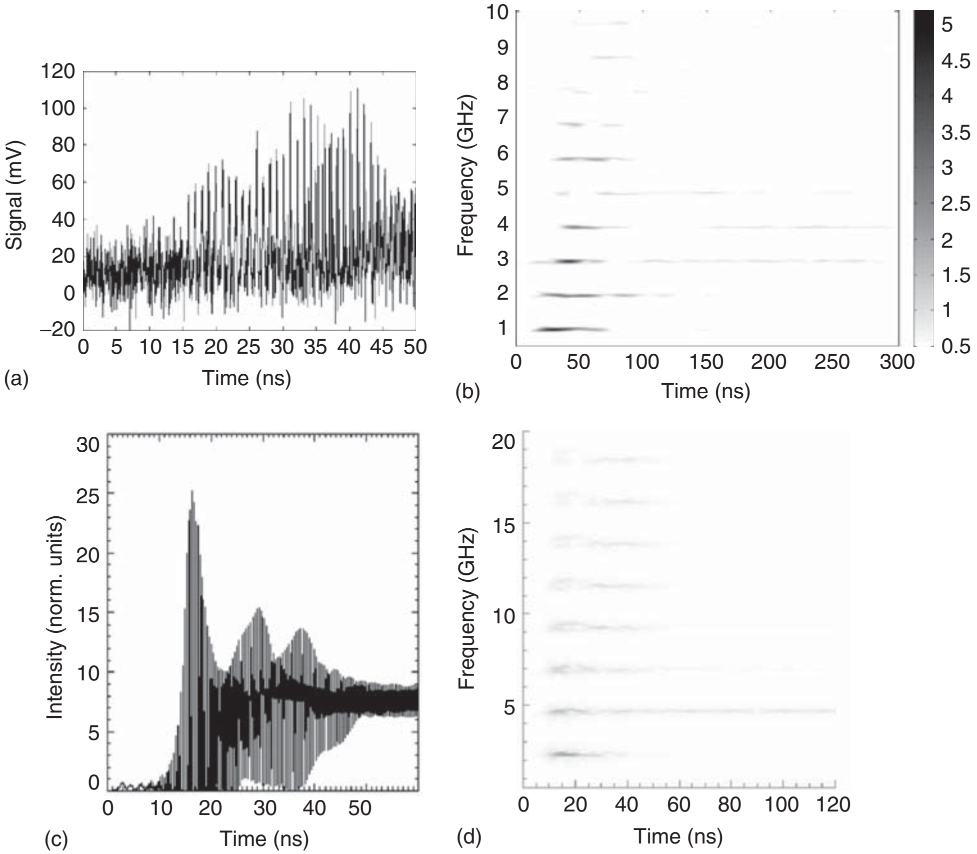

Figure 3.12 (a, b) Switch-on transient of an LS initiated by a 50 ns pulse of 4.8 times minimum threshold power monitored with an AC-coupled fast pin-photo detector. Cavity round-trip time: 1.05 ns, VBG 1. (c, d) Numerical simulation of a switch-on transient of a CS initiated by a 20 ns pulse of 2.3 times minimum threshold power. (a, c) Initial transient regime with strong pulsing. (b, d) Time-frequency spectrogram of intensity time series. Cavity round-trip time: 0.41 ns. ((b) adapted from [87], (c,d) adapted from [88]).

To summarize, these experiment demonstrate LS control with fairly low energy requirements (hundreds of femtojoule), fairly short pulses and delay times. However, the transients usually last a longer time, typically tens of nanoseconds. Long transients (actually extending up to 600 ns) pulsing at the cavity round-trip period (there 4 ns) is also observed in the VCSEL cavity soliton lasers based on saturable absorption [89]. In monolithic CSL based on saturable absorption [29, 90] the switch-on transient also takes a tens of nanoseconds and involves pulsations, probably related to Q-switching instabilities. Hence it appears that the coupled carrier-light dynamics in semiconductor CSL induces a certain tendency to a long self-pulsating transient. In that sense, systems biased below threshold, that is, amplifiers supporting cavity solitons, have actually superior performance, settling down in a few nanoseconds [91].

As we discuss in more detail below, the occurrence of the fast pulsations indicating mode-locking is extremely intriguing from a principal point of view, because it indicates a route to achieve spatio-temporal solitons or light bullet in a nonlinear cavity.

3.6.2
Outlook on Asymptotic Dynamics

Figure 3.13 gives an overview on optical spectra and radio-frequency (RF) spectra in the asymptotic regime. The system can be either single-mode (not shown, [41]), or emit on a dominant mode with weak side-modes (Figure 3.13, middle and lower rows). This leads to oscillating dynamics, but the modulation depth is typically so small that it is buried in detector noise and can only be recovered by a spectral analysis either by a numerical Fourier transform of the time domain signal or an electrical spectrum analyzer (right column). The oscillations can be resolved in numerical simulations [88, 92]. As indicated already in the discussion of the transients, the main frequency is typically not at the cavity-round trip frequency, but at harmonics and also the side-modes in the optical spectra are not adjacent but a few FSR apart (Figure 3.13, middle and lower rows). This is might be related to relaxation oscillations coloring the gain spectrum.

For certain combinations of currents and device temperature, a strong excitation of many modes in the optical spectrum is observed, which is usually associated also with strong peaks in the RF-spectrum at the fundamental cavity round-trip frequency or the first harmonic (Figure 3.13, upper row). Preferred regions of strong dynamics are in the vicinity of switching events between different longitudinal modes, but a systematic characterization of the possible scenarios was not achieved, yet. A corresponding tendency was observed in preliminary numerical simulations, at least for short cavities [65]. It is known in general that the external cavity modes in lasers with FSF are destabilized by Hopf bifurcations, at least for increasing current [54].

Figure 3.14 gives a more detailed analysis of one realization of particularly strongly pronounced dynamics. The time series shows irregular pulses (Figure 3.14a). The shortest features are quite short, for example, the central spike in Figure 3.14a has an FWHM of 80 ps, at the bandwidth limit of our detection system. Accordingly, a lot of higher harmonics are present in the RF-spectrum (Figure 3.14d) and a large number of side-modes with significant amplitude in the optical spectrum (Figure 3.14b). Furthermore, the time–frequency spectrogram in Figure 3.14c demonstrates that the dynamics is stationary in a statistical sense on long time scales. This seems to constitute an intriguing example of a chaotic LS, that is, a LS in the regime of "coherence collapse" well known for conventional semiconductor lasers with feedback [93, 94]. Further work is required to verify this and to provide a detailed characterization.

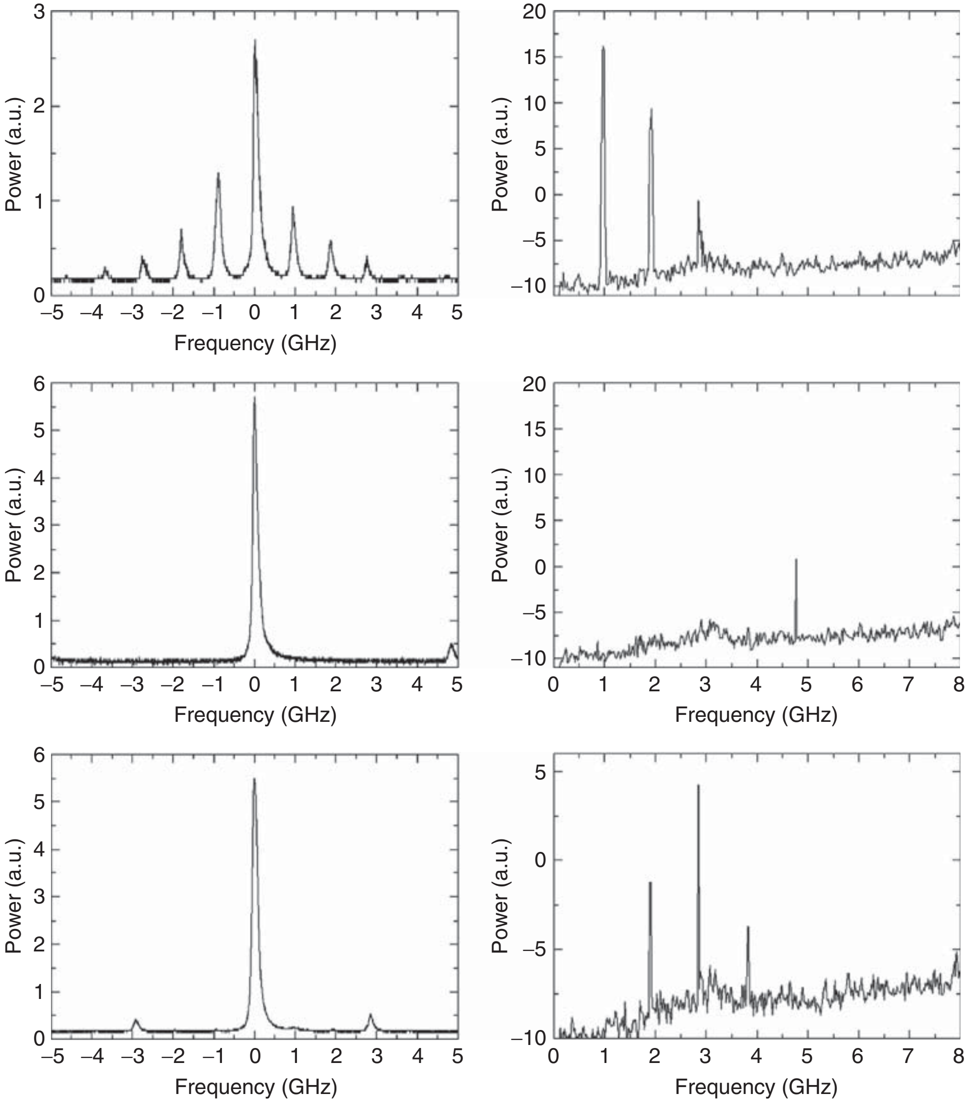

Figure 3.13 Examples for possible dynamical states characterized by time averaged optical spectra (left column) and RF-spectra (right column) for three different LCS and currents. Parameters: VBG 1, cavity round-trip time 1.05 ns.

The fact that the pulsing is irregular indicates that the phases between the different external cavity modes are not locked but vary quite randomly. However, in very narrow parameter regions we observed in short cavities (0.6 ns round-trip time) also the intriguing possibility of very pronounced fairly stable pulsing at the fundamental repetition frequency or the first harmonic. Preliminary results were presented in [42, 95] and analyzed by means of the permutation entropy in [96].

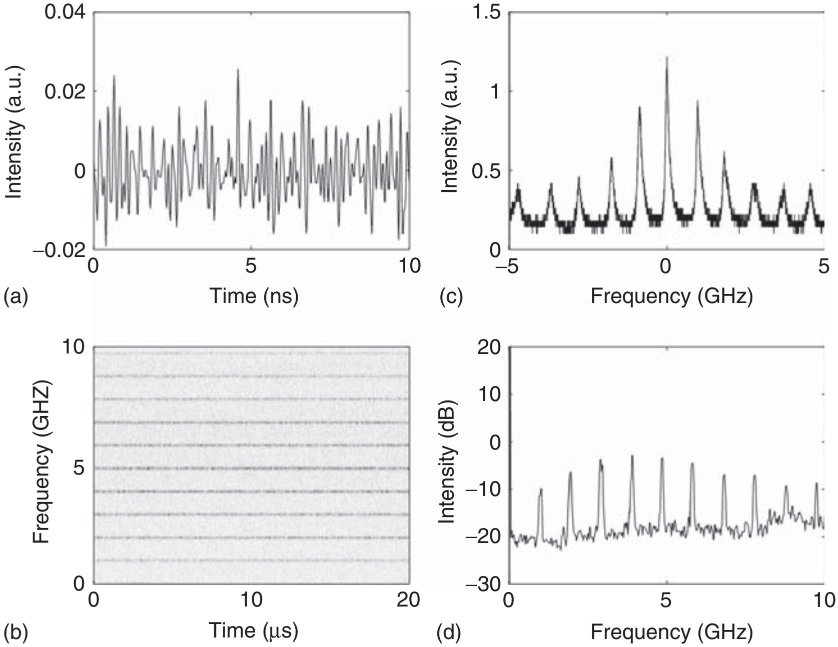

Figure 3.14 (a) Snapshot of temporal dynamics. (b) Time–frequency spectrogram of the intensity time series (note the change of scale compared to (a)!). (c) Time-averaged optical spectrum. (d) Time-averaged RF spectrum. Parameters: VBG 1, cavity round-trip time 1.05 ns.

This indicates the possibility of mode-locked LS. A proper characterization of this regime is currently ongoing.

Figure 3.15 provides an introduction to the analysis of the dynamics by means of permutation entropy (PE). This method to analyze nonlinear time series was introduced in [97] and applied to semiconductor lasers with feedback in [96, 98–100]. It consists of looking at sequences of the relative amplitude of points in the time series and assigning a unique symbol to each observed pattern. The number of points in each pattern D dictates how many possible unique patterns there are and is limited by the number of points N in the complete time series ($D! << N$). Changing the delay τ between points used in the patterns changes the time scale on which the complexity is assessed. Scanning through the complete time series and counting the occurrence of each unique pattern generates a probability distribution. The PE is then the normalized Shannon entropy of this symbol distribution. A PE of 0 indicates a completely regular time series, a PE of 1 high complexity, either because of stochastic noise or high-dimensional chaotic dynamics or a mixture of both. Details can be found in [97, 99].

Figure 3.15 demonstrates that the dynamics is fairly complex with distinct structures at different delay times. The background shows a high PE close to 1, which is possibly influenced by detector and amplifier noise in between the spikes. At

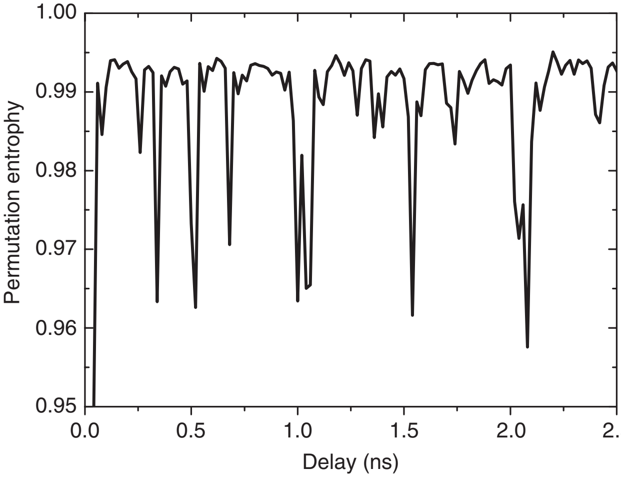

Figure 3.15 Permutation entropy versus delay for $D = 5$ pattern length of time series in Figure 3.14.

the round-trip time, harmonics and sub-harmonics as well as mixing frequencies, the dynamics becomes more regular. This means that the spiking is more "regular" and repetitive at the cavity frequencies, though irregular overall. This is found in other studies of semiconductor lasers with feedback [100]. The small peak within the trough corresponding to the round-trip time (less pronounced in the sub-harmonic) was shown in [96] to provide evidence of a fairly regular recurrence of pulses at the round-trip time but with amplitude and timing jitter leading to an increase of apparent complexity. This feature is strongly enhanced in the time series of the LS displaying fairly stable self-pulsing [96].

3.7
Summary and Outlook

In this chapter, we discussed LS in a VCSEL with FSF. They manifest themselves as small spots of coherent emission – microlasers – inside a much broader pumped area. Their shape, stability and bistability are mainly due to dispersive nonlinearities, that is, the amplitude – phase coupling in semiconductors. In real devices, LS are pinned to spatial defects introduced during the epitaxial growth process and show a variety of threshold values due to the disorder in the spatial distribution of the defects. These spatial variations presently limit the applicability of LS in large scale all-optical processing, but enable intriguing studies of synchronization dynamics.

We demonstrated frequency- and phase-locking of LS where the locked phase follows the Adler scenario. The sensitivity of spatial LS to disorder is larger compared to temporal LS due to the fact that a temporal LS explores all the cavity and thus all LS are experiencing the same (average) environment, whereas spatial LS only "sample" the local environment and thus disorder. "Local" perturbations can be introduced to temporal CSL by modulating parameters and indeed a change of bound states from the $\pi/2$ moving states to in- and anti-phase locked states was observed numerically in CQGLE with regular modulations [82, 83]. However, we are not aware of investigations about frequency locking or frequency unlocking which should occur in the presence of irregular modulations. A long-term vision is to study the synchronization dynamics of large ensembles of LS. Since it is not currently possible to modify the disorder within the VCSEL layer structure itself, one needs to find other possibilities to influence and shape the disorder parameters. Some of us demonstrated some time ago that the bistability loops of individual LS can be shifted by local injection of a WB thus changing the refractive index at that location [101]. We anticipate that this injection will also influence the detuning condition between different LS and thus will enable to control to a certain degree the locking dynamics. Adaptive control over the whole aperture should be possible with a high-quality spatial light modulator.

One interesting aspect of the locking dynamics is that the mechanism of LS coupling is only partially understood in the experiment. Since we observe locking at quite large distances between LS (up to about 100 μm), the coupling via the LS tails in the active medium (generally assumed in the theoretical treatment) cannot be the only mechanism responsible. Possible candidates are deviations from the self-imaging condition in the external cavity leading to nonlocal feedback. This provided the motivation for the studies of the dependence of extended laser states on length detunings in [48]. We have preliminary indication that these deviations do enhance LS coupling. Note that a similar scheme was used in a very nice experiment to control coupling strengths between thousands of microlasers (not LS) in [102]. We also going to look at the point spread function of our lens system to assess whether lens aberrations are enhancing coupling.

The degrees of freedoms provided by the external cavity enhance the dynamics of LS to levels that are even richer than the complex behavior of the CQGLE (e.g., soliton explosions [15, 103]). For example, we mentioned irregular dynamics resembling coherence collapse in a semiconductor laser. Even more intriguing are indications of fairly stable mode-locking [88, 96], which are currently under investigation. Mode-locked spatial LS would correspond to spatio-temporal solitons, often referred to as light bullets. These have been fascinating but elusive objects in nonlinear photonics for decades. As early as 1990 it was realized that simultaneous spatio-temporal compression can be obtained, but that stable localization would be difficult to achieve as solitons in Kerr media are unstable in more than one dimension [104]. Saturation might stabilize solitons [105] but the corresponding parameter ranges seem to be very difficult to reach experimentally. Possible remedies are to use discrete systems [106], and indeed very nice experiments in fibre arrays [34, 35] display 3D discrete solitons although they remain long-term unstable. As the dissipative dynamics of a cavity counteracts the Kerr collapse of 2D spatial solitons (see e.g., [107]), it seems attractive to look at cavity configurations, that is, searching for cavity light bullets. Indeed cavity light bullets were found in a model of a driven cavity with a two-level nonlinearity [108]. Recent work predicts spatio-temporal LS in a solid-state laser [36]. Note that (passive) mode-locking of spatial LS will provide solitonic states self-localized in all three dimensions, that is, spatio-temporal solitons or bullets. However, to achieve arbitrary configurations of soliton sequences along the cavity axis (as demonstrated in [12, 109] for temporal solitons in driven cavities and analogous to the control of spatial LS in transverse space within the limits imposed by disorder) puts stringent requirements on the time scale of gain dynamics with respect to the cavity round-trip time [4, 11]. We are confident that coming years will see very interesting developments in the field of cavity soliton bullets.

Acknowledgments

We are grateful to R. Jäger (Ulm Photonics) to supply the devices, to Y. Tanguy for his initial experimental contributions, to W.J. Firth for numerous fruitful discussions and collaboration and to A. Scroggie, P. Colet, D. Gomila, A. Vladimirov, N.A. Loiko, B.A. Malomed and N.N. Rosanov for theoretical collaboration and discussions in some stage of the investigations. The Strathclyde group gratefully acknowledges support of CONACYT for J. Jimenez, the EPSRC doctoral training account for Y. Noblet and N. Radwell, the Royal Society (London) for supporting the collaboration between the Australian and British group and the EU for initial support via the STREP FunFACS. The Macquarie group was supported by the Australian Research Council (Linkage Project LP100100312), Sirca Technology Pty Ltd, Macquarie University, the Science and Industry Endowment Fund (RP 04-174).

References

1. Paschotta, R., Häring, R., Garnache, A., Hoogland, S., Tropper, A.C., and Keller, U. (2002) Soliton-like pulse-shaping mechanism in passively mode-locked surface-emitting semiconductor lasers. *Appl. Phys. B*, **75**, 445–451.
2. Kieu, K., Renninger, W.H., Chong, A., and Wise, F.W. (2009) Sub-100 fs pulses at watt-level powers from a dissipative-soliton fiber laser. *Opt. Lett.*, **34**, 593.
3. Grelu, P. and Akhmediev, N. (2012) Dissipative solitons for mode-locked lasers. *Nat. Photonics*, **6**, 84–92.
4. Marconi, M., Javaloyes, J., Balle, S., and Giudici, M. (2014) How lasing localized structures evolve out of passive mode locking. *Phys. Rev. Lett.*, **112**, 223 901.
5. Hocking, L.M. and Stewartson, K. (1972) Nonlinear response of a marginally unstable plane parallel flow to a 2-dimensional disturbance. *Proc. R. Soc. London, Ser. A*, **326**, 289.
6. Pereira, N.R. and Stenflo, L. (1977) Nonlinear Schrödinger equation including growth and damping. *Phys. Fluids*, **20**, 1733–1734.
7. Bélanger, P.A., Gagnon, L., and Paré, C. (1989) Solitary pulses in an amplified nonlinear dispersive medium. *Opt. Lett.*, **14**, 943–945.
8. Thual, O. and Fauve, S. (1988) Localized structures generated by subcritical instabilities. *J. Phys. France*, **49**, 1829–1833.

9. Fauve, S. and Thual, O. (1990) Solitary waves generated by subcritical instabilities in dissipative systems. *Phys. Rev. Lett.*, **64**, 282–284.
10. Akhmediev, N. and Ankiewicz, A. (2005) *Dissipative Solitons in the Complex Ginzburg–Landau and Swift–Hohenberg Equations*, Lecture Notes in Physics, Springer-Verlag, Berlin, pp. 1–17.
11. Barland, S., Giudici, M., Javaloyes, J., and Tissoni, G. (2015) *Localized States in Semiconductor Microcavities, from Transverse to Longitudinal Structures and Delayed Systems*, John Wiley & Sons.
12. Coen, S. (2016) *Dynamics of one-dimensional Kerr cavity solitons*, John Wiley & Sons.
13. Kippenberg, T.J. (2016) *Monolithic Micro-Resonators for Frequency Comb Generation*, John Wiley & Sons.
14. Sanchez, F., Leblond, H., and Grelu, P. (2016) *Collective Dissipative Soliton Dynamics in Passively Mode-Locked Fiber Lasers*, John Wiley & Sons.
15. Chang, W. and Akhmediev, N. (2016) *Exploding Solitons and Rogue Waves in Optical Cavities*, John Wiley & Sons.
16. Bazhenov, V.Y., Taranenko, V.B., and Vasnetsov, M.V. (1992) WTA-dynamics in large aperture active cavity with saturable absorber. *Proc. SPIE*, **1806**, 14–21.
17. Saffman, M., Montgomery, D., and Anderson, D.Z. (1994) Collapse of a transverse-mode continuum in a self-imaging photorefractively pumped ring resonator. *Opt. Lett.*, **19**, 518–520.
18. Taranenko, V.B., Staliunas, K., and Weiss, C.O. (1997) Spatial soliton laser: localized structures in a laser with a saturable absorber in a self-imaging resonator. *Phys. Rev. A*, **56**, 1582–1591.
19. Slekys, G., Staliunas, K., and Weiss, C.O. (1998) Spatial localized structures in resonators with saturable absorber. *Opt. Commun.*, **149**, 113–116.
20. Rosanov, N.N. and Fedorov, S.V. (1992) Diffractive switching waves and autosolitons in a laser with saturable absorption. *Opt. Spectrosc.*, **72**, 782–787.
21. Rozanov, N.N., Federov, A.V., Fedorov, S.V., and Khodova, G.V. (1995) Particle-like light structure in a wide-aperture laser with saturable absorption. *J. Exp. Theor. Phys.*, **80**, 199–207.
22. Rosanov, N.N., Fedorov, S.V., and Shatsev, A.N. (2005) Curvilinear motion of multivortex laser–soliton complexes with strong and weak coupling. *Phys. Rev. Lett.*, **95**, 053 903.
23. Atai, J. and Malomed, B.A. (1998) Exact stable pulses in asymmetric linearly coupled Ginzburg–Landau equations. *Phys. Lett. A*, **246**, 412–422.
24. Firth, W.J. and Paulau, P.V. (2010) Soliton lasers stabilized by coupling to a resonant linear system. *Eur. Phys. J. D*, **59**, 13–21.
25. Barland, S., Tredicce, J.R., Brambilla, M., Lugiato, L.A., Balle, S., Giudici, M., Maggipinto, T., Spinelli, L., Tissoni, G., Knödel, T., Miller, M., and Jäger, R. (2002) Cavity solitons as pixels in semiconductors. *Nature*, **419**, 699–702.
26. Tanguy, Y., Ackemann, T., Firth, W.J., and Jäger, R. (2008) Realization of a semiconductor-based cavity soliton laser. *Phys. Rev. Lett.*, **100**, 013 907.
27. Tanguy, Y., Ackemann, T., and Jäger, R. (2007) Characteristics of switching in a semiconductor based cavity-soliton laser. *Opt. Express*, **15**, 16-773–16-780.
28. Genevet, P., Barland, S., Giudici, M., and Tredicce, J.R. (2008) Cavity soliton laser based on mutually coupled semiconductor microresonators. *Phys. Rev. Lett.*, **101**, 123 905.
29. Elsass, T., Gauthron, K., Beaudoin, G., Sagnes, I., Kuszelewicz, R., and Barbay, S. (2010) Control of cavity solitons and dynamical states in a monolithic vertical cavity laser with saturable absorber. *Eur. Phys. J. D*, **59**, 91–96.
30. Ackemann, T., Oppo, G.L., and Firth, W.J. (2009) Fundamentals and applications of spatial dissipative solitons in photonic devices. *Adv. At. Mol. Opt. Phys.*, **57**, 323–421.
31. Barbay, S., Kuszelewicz, R., and Tredicce, J.R. (2011) Cavity solitons in VCSEL devices. *Adv. Opt. Technol.*, **2011**, 628 761.
32. Kuszelewicz, R., Barbay, S., Tissoni, G., and Almuneau, G. (2010) Editorial on

dissipative optical solitons. *Eur. Phys. J. D*, **59**, 1–2.

33. Wise, F.W. and Di Trapani, P. (2002) The hunt for light bullets–spatiotemporal solitons. *Opt. Photonics News*, **13** (2), 28–32.
34. Minardi, S., Eilenberger, F., Kartashov, Y., Szameit, A., Röpke, U., Kobelke, J., Schuster, K., Bartelt, H., Nolte, S., Torner, L., Lederer, F., Tünnermann, A., and Pertsch, T. (2010) Three-dimensional light bullets in arrays of waveguides. *Phys. Rev. Lett.*, **105**, 263 901.
35. Eilenberger, F., Prater, P., Minardi, S., Geiss, R., Röpke, U., Kobelke, J., Schuster, K., Bartelt, H., Nolte, S., Tünnermann, A., and Pertsch, T. (2013) Observation of discrete, vortex light bullets. *Phys. Rev. X*, **3**, 041 031.
36. Renninger, W.H. and Wise, F.W. (2014) Spatiotemporal soliton laser. *Optica*, **1**, 101–104.
37. Michalzik, R., Grabherr, M., and Ebeling, K.J. (1998) High-power VCSELs: modeling and experimental characterization. *Proc. SPIE*, **3286**, 206–219.
38. Grabherr, M., Jäger, R., Miller, M., Thalmaier, C., Herlein, J., and Ebeling, K.J. (1998) Bottom-emitting VCSELs for high-CW optical output power. *IEEE Photonics Technol. Lett.*, **10**, 1061–1063.
39. Grabherr, M., Miller, M., Jäger, R., Michalzik, R., Martin, U., Unold, H.J., and Ebeling, K.J. (1999) High-power VCSEL's: single devices and densely packed 2-D-arrays. *IEEE J. Sel. Top. Quantum Electron.*, **5**, 495–502.
40. Miller, M., Grabherr, M., King, R., Jäger, R., Michalzik, R., and Ebeling, K.J. (2001) Improved performance of high-power VCSELs. *IEEE J. Sel. Top. Quantum Electron.*, **7** (2), 210–216.
41. Radwell, N. and Ackemann, T. (2009) Characteristics of laser cavity solitons in a vertical-cavity surface-emitting laser with feedback from a volume Bragg grating. *IEEE J. Quantum Electron.*, **45**, 1388–1395.
42. Radwell, N. (2010) Characteristics of a cavity soliton laser based on a VCSEL with frequency selective feedback. PhD thesis. SUPA and Department of Physics, University of Strathclyde.
43. Noblet, Y. (2014) Frequency modified feedback in external cavity laser systems. PhD thesis. SUPA and Department of Physics, University of Strathclyde.
44. Tanguy, Y., Radwell, N., Ackemann, T., and Jäger, R. (2008) Characteristics of cavity solitons and drifting excitations in broad-area vertical-cavity surface-emitting lasers with frequency-selective feedback. *Phys. Rev. A*, **78**, 023 810.
45. Jimenez, J., Noblet, Y., Paulau, P.V., Gomila, D., and Ackemann, T. (2013) Observation of laser vortex solitons in a self-focusing semiconductor laser. *J. Opt.*, **15**, 044 011.
46. Paulau, P.V., Gomila, D., Colet, P., Loiko, N.A., Rosanov, N.N., Ackemann, T., and Firth, W.J. (2010) Vortex solitons in lasers with feedback. *Opt. Express*, **18**, 8859–8866.
47. Ackemann, T., Radwell, N., Noblet, Y., and Jäger, R. (2012) Disorder mapping in VCSELs using frequency-selective feedback. *Opt. Lett.*, **37**, 1079–1081.
48. Noblet, Y. and Ackemann, T. (2012) Analysis of spatial emission structures in vertical-cavity surface-emitting lasers with feedback of a volume Bragg grating. *Phys. Rev. A*, **85**, 05 381.
49. McDonald, G.S. and Firth, W.J. (1990) Spatial solitary-wave optical memory. *J. Opt. Soc. Am. B*, **7**, 1328–1335.
50. Firth, W.J. and Scroggie, A.J. (1996) Optical bullet holes: robust controllable localized states of a nonlinear cavity. *Phys. Rev. Lett.*, **76**, 1623–1626.
51. Henry, C.H. (1982) Theory of the linewidth of semiconductor lasers. *IEEE J. Quantum Electron.*, **18**, 259–264.
52. Lugiato, L.A. (1984) Theory of optical bistability. Progress in Optics XXI, pp. 70–216.
53. Giudici, M., Giuggioli, L., Green, C., and Tredicce, J.R. (1999) Dynamical behavior of semiconductor lasers with frequency selective optical feedback. *Chaos, Solitons Fractals*, **10**, 811–818.
54. Naumenko, A., Loiko, N.A., Sondermann, M., Jentsch, K.F., and Ackemann, T. (2006) Abrupt turn-on and hysteresis in a VCSEL with

frequency-selective optical feedback. *Opt. Commun.*, **259**, 823–833.

55. Naumenko, A.V., Loiko, N.A., and Ackemann, T. (2007) Analysis of bistability conditions between lasing and nonlasing states for a vertical-cavity surface-emitting laser with frequency-selective optical feedback using an envelope approximation. *Phys. Rev. A*, **76**, 023 802.
56. Fischer, A.P.A., Yousefi, M., Lenstra, D., Carter, M.W., and Vemuri, G. (2004) Filtered optical feedback induced frequency dynamics in semiconductor lasers. *Phys. Rev. Lett.*, **92**, 023 901.
57. Erzgräber, H., Krauskopf, B., and Lenstra, D. (2007) Bifurcation analysis of a semiconductor laser with filtered optical feedback. *SIAM J. Appl. Dyn. Syst.*, **6**, 1–28.
58. Rosanov, N.N. (1991) Switching waves, autosolitons, and parallel digital-analogous optical computing. *Proc. SPIE*, **1840**, 130–143.
59. Schäpers, B., Ackemann, T., and Lange, W. (2001) Characteristics and possible applications of localized structures in an optical pattern-forming system. *Proc. SPIE*, **4271**, 130–137.
60. Parra-Rivas, P., Gomila, D., Gelens, L., Matias, M., and Colet, P. (2015) *Dynamics of Dissipative Solitons in Presence of Inhomogeneities and Drift*, John Wiley & Sons.
61. Pedaci, F., Barland, S., Caboche, E., Genevet, P., Giudici, M., Tredicce, J.R., Ackemann, T., Scroggie, A.J., Firth, W.J., Oppo, G.L., Tissoni, G., and Jäger, R. (2008) All-optical delay line using semiconductor cavity solitons. *Appl. Phys. Lett.*, **92**, 011 101.
62. Pedaci, F., Tissoni, G., Barland, S., Giudici, M., and Tredicce, J.R. (2008) Mapping local defects of extended media using localized structures. *Appl. Phys. Lett.*, **93**, 111 104.
63. Genevet, P., Barland, S., Giudici, M., and Tredicce, J.R. (2010) Bistable and addressable localized vortices in semiconductor lasers. *Phys. Rev. Lett.*, **104**, 223 902.
64. Genevet, P., Turconi, M., Barland, S., Giudici, M., and Tredicce, J.R. (2010) Mutual coherence of laser solitons in coupled semiconductor resonators. *Eur. Phys. J. D*, **59**, 109–114.
65. Scroggie, A.J., Firth, W.J., and Oppo, G.L. (2009) Cavity soliton laser with frequency selective feedback. *Phys. Rev. A*, **80**, 013 829.
66. Spinelli, L., Tissoni, G., Brambilla, M., Prati, F., and Lugiato, L.A. (1998) Spatial solitons in semiconductor microcavities. *Phys. Rev. A*, **58**, 2542–2559.
67. Lang, R. and Kobayashi, K. (1980) External optical feedback effects on semiconductor injection laser properties. *IEEE J. Quantum Electron.*, **16**, 347–355.
68. Giudici, M., Balle, S., Ackemann, T., Barland, S., and Tredicce, J.R. (1999) Effects of optical feedback on vertical-cavity surface-emitting lasers: experiment and model. *J. Opt. Soc. Am. B*, **16**, 2114–2123.
69. Paulau, P.V., Scroggie, A.J., Naumenko, A., Ackemann, T., Loiko, N.A., and Firth, W.J. (2007) Localized traveling waves in vertical-cavity surface-emitting lasers with frequency-selective optical feedback. *Phys. Rev. E*, **75**, 056 208.
70. Paulau, P.V., Gomila, D., Ackemann, T., Loiko, N.A., and Firth, W.J. (2008) Self-localized structures in vertical-cavity surface-emitting lasers with external feedback. *Phys. Rev. E*, **78**, 016 212.
71. Paulau, P.V., Gomila, D., Colet, P., Matías, M., Loiko, N.A., and Firth, W.J. (2009) Drifting instabilities of cavity solitons in vertical-cavity surface-emitting lasers with frequency-selective feedback. *Phys. Rev. A*, **80**, 023 808.
72. Paulau, P.V., Gomila, D., Colet, P., Malomed, B.A., and Firth, W.J. (2011) From one- to two-dimensional solitons in the Ginzburg–Landau model of lasers with frequency-selective feedback. *Phys. Rev. E*, **84**, 036 213.
73. Ackemann, T., Oppo, G.L., Paulau, P.V., McIntyre, C., Noblet, Y., Colet, P., and Firth, W.J. (2013) *Frequency- and Phase Locking of Laser Cavity Solitons*, Progress in Optical Science and Photonics, Springer-Verlag, New York, pp. 49–87.

74. Akhmediev, N., Ankiewicz, A., and Soto-Crespo, J.M. (1997) Multi-soliton solutions of the complex Ginzburg–Landau equation. *Phys. Rev. Lett.*, **79**, 4047–4050.

75. Turaev, D., Vladimirov, A.G., and Zelik, S. (2007) Chaotic bound state of localized structures in the complex Ginzburg–Landau equation. *Phys. Rev. E*, **75**, 045 601(R).

76. Zavyalov, A., Iliew, R., Egorov, O., and Lederer, F. (2009) Discrete family of dissipative soliton pairs in mode-locked fiber lasers. *Phys. Rev. A*, **79**, 053 841.

77. Grelu, P., Belhache, F., Gutty, F., and Soto-Crespo, J.M. (2002) Phase-locked soliton pairs in a stretched-pulse fiber laser. *Opt. Lett.*, **27**, 966–968.

78. Soto-Crespo, J.M., Akhmediev, N., Grelu, P., and Belhache, F. (2003) Quantized separations of phase-locked soliton pairs in fiber lasers. *Opt. Lett.*, **28**, 1757–1759.

79. Malomed, B.A. (1991) Bound solitons in the nonlinear Schrödinger–Ginzburg–Landau equation. *Phys. Rev. A*, **44**, 6954–6957.

80. Paulau, P.V., McIntyre, C., Noblet, Y., Radwell, N., Firth, W.J., Colet, P., Ackemann, T., and Oppo, G.L. (2012) Adler synchronization of spatial laser solitons pinned by defects. *Phys. Rev. Lett.*, **108**, 213 904.

81. Adler, R. (1946) A study of locking phenomena in oscillators. *Proc. IRE*, **34**, 351–357.

82. Chang, W., Akhmediev, N., and Wabnitz, S. (2009) Effect of an external periodic potential on pairs of dissipative solitons. *Phys. Rev. A*, **80**, 013 815.

83. He, Y.J., Malomed, B.A., Mihalache, D., Liu, B., Huang, H.C., Yang, H., and Wang, H.Z. (2009) Bound states of one-, two-, and three-dimensional solitons in complex Ginzburg–Landau equations with a linear potential. *Opt. Lett.*, **34**, 2976–2979.

84. Fabiny, L., Colet, P., Roy, R., and Lenstra, D. (1993) Coherence and phase dynamics of coupled solid-state lasers. *Phys. Rev. A*, **47**, 4287–4296.

85. Möller, M., Forsmann, B., and Lange, W. (1999) Amplitude instability in coupled Nd:YVO_4 microchip lasers. *Chaos, Solitons Fractals*, **10**, 825–830.

86. Pikovsky, A., Rosenblum, M., and Kurths, J. (2001) *Synchronization–A Universal Concept in Nonlinear Sciences*, Cambridge Nonlinear Science Series, vol. **12**, Cambridge University Press, Cambridge.

87. Radwell, N., McIntyre, C., Scroggie, A.J., Oppo, G.L., Firth, W.J., and Ackemann, T. (2010) Switching spatial dissipative solitons in a VCSEL with frequency-selective feedback. *Eur. Phys. J. D*, **59**, 121–131.

88. Ackemann, T., Radwell, N., McIntyre, C., Firth, W.J., and Oppo, G.L. (2010) Self-pulsing dynamics in a cavity soliton laser, in *Proceedings of SPIE*, Semiconductor Lasers and Laser Dynamics IV, vol. **7720** (eds K. Panajotov, M. Sciamanna, A.A. Valle, and R. Michalzik), SPIE, p. 772007.

89. Genevet, P., Barland, B., Giudici, M., and Tredicce, J.R. (2009) Stationary localized structures and pulsing structures in a cavity soliton laser. *Phys. Rev. A*, **79**, 033 819.

90. Elsass, T., Gauthron, K., Beaudoin, G., Sagnes, I., Kuszelewicz, R., and Barbay, S. (2010) Fast manipulation of laser localized structures in a monolithic vertical cavity with saturable absorber. *Appl. Phys. B*, **98**, 327–331.

91. Hachair, X., Furfaro, L., Javaloyes, J., Giudici, M., Balle, S., Tredicce, J., Tissoni, G., Lugiato, L., Maggipinto, T., and Brambilla, M. (2005) Cavity-solitons switching in semiconductor microcavities. *Phys. Rev. A*, **72**, 013-815-1–4.

92. McIntyre, C. (2013) Dynamics and interactions of cavity solitons in photonic devices. PhD thesis. SUPA and Department of Physics, University of Strathclyde.

93. Petermann, K. (1995) External optical feedback phenomena in semiconductor lasers. *IEEE J. Sel. Top. Quantum Electron.*, **1**, 480–489.

94. Fischer, I., Tartwijk, G.H.Mv., Levine, A.M., Elsässer, W., Göbel, E., and Lenstra, D. (1996) Fast pulsing and chaotic itinerancy with a drift in the coherence collapse of semiconductor lasers. *Phys. Rev. Lett.*, **76**, 220 – 223.

95. Ackemann, T., Radwell, N., McIntyre, C., Oppo, G.L., and Firth, W.J. (2010) Self pulsing solitons: a base for optically controllable pulse trains in photonic networks? 12th International Conference on Transparent Optical Networks (ICTON), IEEE, p. Th.B1.1.

96. Toomey, J.P., Kane, D.M., and Ackemann, T. (2014) Complexity in pulsed nonlinear laser systems interrogated by permutation entropy. *Opt. Express*, **22**, 17-840 – 17-853.

97. Bandt, C. and Pompe, B. (2002) Permutation entropy: a natural complexity measure for time series. *Phys. Rev. Lett.*, **88**, 174 102.

98. Tiana-Alsina, J., Torrent, M.C., Rosso, O.A., Masoller, C., and Garcia-Ojalvo, J. (2010) Quantifying the statistical complexity of low-frequency fluctuations in semiconductor lasers with optical feedback. *Phys. Rev. A*, **82**, 013 819.

99. Soriano, M.C., Zunino, L., Rosso, O.A., Fischer, I., and Mirasso, C.R. (2011) Time scales of a chaotic semiconductor laser with optical feedback under the lens of a permutation information analysis. *IEEE J. Quantum Electron.*, **47**, 252 – 261.

100. Toomey, J.P. and Kane, D.M. (2014) Mapping the dynamic complexity of a semiconductor laser with optical feedback using permutation entropy. *Opt. Express*, **22**, 1713 – 1725.

101. Radwell, N., Rose, P., Cleff, C., Denz, C., and Ackemann, T. (2010) Compensation of spatial inhomogeneities in a cavity soliton laser using a spatial light modulator. *Opt. Express*, **18**, 23-121 – 23-132.

102. Nixon, M., Ronen, E., Friesem, A.A., and Davidson, N. (2013) Observing geometric frustration with thousands of coupled lasers. *Phys. Rev. Lett.*, **110**, 184 102.

103. Cundiff, S.T., Soto-Crespo, J.M., and Akhmediev, N. (2002) Experimental evidence for soliton explosions. *Phys. Rev. Lett.*, **88**, 073 903.

104. Silberberg, Y. (1990) Collapse of optical pulses. *Opt. Lett.*, **15**, 1282 – 1284.

105. Soto-Crespo, J.M., Grelu, P., and Akhmediev, N. (2006) Optical bullets and “rockets” in nonlinear dissipative systems and their transformations and interactions. *Opt. Express*, **14**, 4013 – 4025.

106. Mihalache, D., Mazilu, D., Lederer, F., and Kivshar, Y.S. (2008) Spatiotemporal dissipative solitons in two-dimensional photonic lattices. *Phys. Rev. E*, **78**, 056 602.

107. Firth, W.J. and Lord, A. (1996) Two-dimensional solitons in a Kerr cavity. *J. Mod. Opt.*, **43**, 1071 – 1077.

108. Brambilla, M., Maggipinto, T., Patera, G., and Columbo, L. (2004) Cavity light bullets: three-dimensional localized structures in a nonlinear optical resonator. *Phys. Rev. Lett.*, **93**, 203 901.

109. Leo, F., Coen, S., Kockaert, P., Gorza, S.P., Emplit, P., and Haelterman, M. (2010) Temporal cavity solitons in one-dimensional Kerr media as bits in an all-optical buffer. *Nat. Photonics*, **4**, 471 – 476.

4

Localized States in Semiconductor Microcavities, from Transverse to Longitudinal Structures and Delayed Systems

Stéphane Barland, Massimo Giudici, Julien Javaloyes, and Giovanna Tissoni

4.1

Introduction

Localized structures (LS) are confined states appearing in nonlinear dissipative systems having sufficiently large spatial extension. They are characterized by a correlation range much shorter than the size of the system and are intrinsically bistable; hence, they can be individually addressed. LS may form when two different solutions coexist for the same values of the parameters. Although more complex scenarios exist, the most common case consists of the coexistence of a homogeneous and a modulated solution [1, 2]. Spatial LS have been widely observed in nature in systems such as granular media [3], gas discharges [4], semiconductor devices [5], reaction–diffusion systems [6], fluids [7], convective systems [8], and optical cavities [9–13]. In the case of weakly dissipative systems, LS may be interpreted as dissipative solitons [14, 15], but it is important to stress that the compensation between nonlinearities and the spreading effect (diffraction or group velocity dispersion), which is often considered the defining ingredient for conservative solitons, is not required for the existence of LS. In particular, in the strongly dissipative case, the interaction of fronts may provide a completely different mechanism for the stability of localized states [9, 16]. And LS can be observed even in the presence of nonlinearities that *favor* the spreading effect.

In this contribution, we are interested in LS formed in semiconductor optical cavities, which are compact devices, widely used in optoelectronics, and characterized by a rather fast although not instantaneous (between 0.1 and 1 ns) responding medium. LS in these resonators maybe used as bit units, thus enabling competitive applications in information processing [17–20]. Spatial LS appearing in the transverse section of broad-area vertical-cavity surface-emitting lasers (VCSEL) have been explored widely in the last 10 years (see reviews [12, 21–23]). VCSEL can be fabricated with transverse section larger than 200 micron and cavity length of the order of few microns, thus ensuring the condition of large aspect ratio required for transverse LS [24]. The second condition, namely

Nonlinear Optical Cavity Dynamics: From Microresonators to Fiber Lasers, First Edition.
Edited by Philippe Grelu.
© 2016 Wiley-VCH Verlag GmbH & Co. KGaA. Published 2016 by Wiley-VCH Verlag GmbH & Co. KGaA.

coexistence of two different spatial solutions, has been implemented using two different approaches.

The first one is based on injection of a coherent and homogeneous electromagnetic field inside the VCSEL resonator [25, 26]. The resonator is kept above transparency but slightly below threshold, thus behaving as an amplifier medium. LS appear for rather tight tuning conditions (less than 15 GHz) between the cavity resonance and the injection field frequency. This scheme is based on passive morphogenesis, since the resonator output results from a modification of the injected field that imposes the LS phase. This situation has been described theoretically in several papers [27, 28] and, in this context, LS were named *cavity solitons*. The system is described by two equations, one for the field evolution inside the cavity, the second for the carrier's evolution. Several experiments have been built in order to give evidence of applications to information processing of LS. By encoding an information bit in the form of a single peak LS, it has been proven that these bits can be optically addressed to form a two-dimensional array of data, which can be reconfigured [29] and operated as shift register [29–31].

The second scheme for LS generation is based on a localized *lasing* response of the broad-area resonator and does not require an externally injected field, thus preserving phase symmetry. Hence, LS are generated out of the vacuum (active morphogenesis) with independent phase and frequency. Bistability is implemented by coupling the amplifier VCSEL resonator with a frequency selective mirror [32] (further developments are reviewed in this book by Ackemann *et al.*) or with a saturable absorber resonator [33], or by designing a monolithic cavity containing both amplifying and absorbing media [34]. The bifurcation sequence leading to complex LS (in this case, also called *laser solitons*) has been described theoretically in [9, 35], showing a rich variety of complex LS appearing, including multihumped structures and localized vortices. The specific case of a semiconductor laser with an intracavity saturable absorber has been theoretically and numerically studied in [36–38].

Recent works have addressed the question whether the concept of LS can be extended to the *time domain*, where localization occurs in the propagation direction of the electromagnetic field, thus leading to localized light pulses [39–42]. In this case, the notion of extended system requires that the resonator round-trip τ be much larger than the (slowest) system timescale, a condition that is not generally fullfilled in mode-locked fiber or semiconductor lasers. Coexistence of different solutions in the time domain (temporal patterns), for example, a stationary one together with an oscillating one, gives the second necessary condition for temporal localized structures. A first observation of temporal cavity solitons has been revealed in a Kerr fiber injected by a coherent beam [39]. Encoding the information bit using single-pulse temporal cavity solitons has been demonstrated and it has shown several advantages with respect to the spatial case. In particular, the temporal system is not affected by local inhomogeneities, as it is the case for the transverse section of the VCSEL [43, 44].

In this chapter, we describe some recent progress on different forms of localization along the propagation direction in semiconductor-based resonators. There are several motivations for this analysis in particular in semiconductor systems. For instance, implementation of LS in fast responding and compact devices is a promising approach toward applications of LS for information encoding and process. In addition to processing information, temporal LS in an arbitrarily long cavity lead to laser pulses at an arbitrarily low repetition rate, providing reconfigurable pulse patterns, which may be very useful for applications that necessitate pulses on demands such as broadband spectroscopy, LIDAR applications, and in astronomy.

In addition, implementation of temporal localization using devices that are known to host spatial LS may pave the way to the generation and control of spatiotemporal localized structures, that is, light bullets (LB) [45–48]. We underline that, contrary to spatiotemporal LB in conservative media [49], dissipative LBs would preserve the bistability property of bidimensional or purely temporal LS. Besides the fundamental interest, LB present attractive application perspectives in the ultrafast digital information processing where their use could reach terahertz in terms of bandwidth [50]. Despite the efforts made, experimental observations of LB have not been reported until the end of 2010 when nonlinear propagation of a spatiotemporal soliton was observed in a waveguide array [51]. Unfortunately, these solitons are very fragile and they decay after propagating twice the characteristic length of linear propagation, which makes them difficult to be exploitable for applications. The possibility of implementing spatiotemporal localized structures is very interesting for circumventing the problems encountered so far with propagative solitons in waveguides. As explained earlier, LS stability does not necessarily rely on sensitive balance of nonlinearities and spreading effects, as it is the case for conservative solitons in waveguides. Moreover, because LS are dissipative structures, they are attractors toward which the system spontaneously evolves from a large set of initial conditions. Initial seeding is, therefore, not as critical as for conservative solitons.

Another appealing reason for analyzing localization along the propagation direction in semiconductor systems is the interesting comparison that it enables between spatially extended and delayed dynamical systems [52, 53]. Indeed, while transverse forms of localization in semiconductor media can take place in the bulk of the system provided the device is sufficiently broad, the analysis of phenomena taking place along the propagation direction in semiconductor microcavities also enables fascinating configurations in which the nonlinear interaction is confined in a small spatial region of an otherwise much larger system. In these cases, such as distant-coupled microcavities [54–56], multimode lasers [57, 58], or optical feedback systems [59–61], detailed or prototypical models (still infinite dimensional as for spatially extended systems) will include delayed terms instead of or in addition to partial derivatives. This reflects the fact that most of the beam propagation takes place in air, where group velocity dispersion and nonlinearities are not expected to play any role at the time scales and power level that are typical of semiconductor laser operation. In spite of this, the recent demonstration of coarsening dynamics in bistable systems with delay [53] has shown the existence of coupling mechanisms to a large extent equivalent to those found in spatially extended systems, which calls for an analysis of short pulses (much shorter than the round-trip time) in terms of self-localized wave packets. The origin of their stability must, however, be different than the well-known compensation between group velocity dispersion and self-phase modulation.

In addition to considering essentially delayed dynamical systems, we consider forms of localization in which optical power may not play a crucial role at all. In contrast to usual conservative or dissipative, propagative or transverse solitons or LS, which are in general described as bumps or holes of optical power, we focus on the field phase. In most cases, it is considered as slaved to the intensity dynamics (in the case of systems with coherent forcing, broken phase symmetry) or it is a neutral mode for localized states (in laser systems) and its impact is mostly in the interaction of neighboring LS (see [62] and the chapter about “Dynamics and interactions of laser cavity solitons in broad-area semiconductor lasers” in this book [63]) or dissipative solitons [64, 65]. Here, on the contrary, we analyze dissipative solitary waves whose stability is intrinsically based on phase dynamics.

In Section 4.2, we review past and recent results in semiconductor lasers with saturable absorber systems in extended cavities from space to time domain. In Section 4.3, we review recent experiments based on different nonlinear elements (bistable and excitable) enclosed in a feedback loop that demonstrate the existence of front pinning and topological phase solitons.

4.2
Lasing Localized States

Lasing localized structures are localized states built from the spontaneous emission noise of the system, which do not require an external driving field. They were first predicted by Rosanov and coauthors [9, 66] using two-level equations for a laser with saturable absorber and received the name of “autosolitons.” Because they appear in a phase invariant system, besides being individually addressable, these LS have their individual phase and frequency, and they may appear in complex forms as ring structures with a screw dislocation at their center (localized vortex solitons). Their bifurcation diagram was explored in one dimension [35], showing a very different behavior with respect to the homoclinic snaking observed in driven cavities for conventional LS [67, 68].

4.2.1
Transverse Localized States in Coupled Microcavities

We have experimentally implemented laser solitons using two nominally identical coupled 980-nm broad-area (200 μm diameter) VCSELs [24], one (L_1) biased above transparency while the second (L_2) is operated in the (saturable) absorbing regime [33]. The two devices are placed one in front of the other, as shown

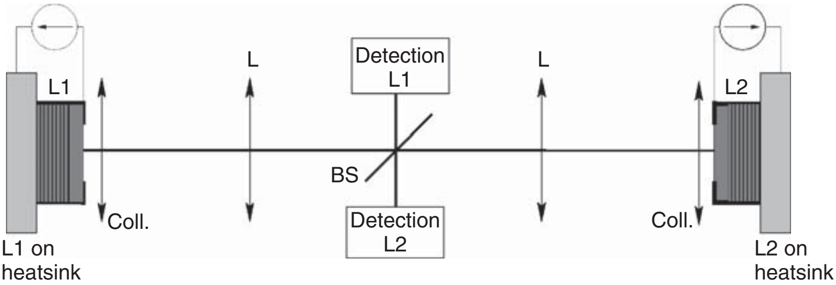

Figure 4.1 Experimental setup: two semiconductor lasers (L_1 and L_2) are imaged onto each other. A 20% reflection beam splitter is inserted in the center of the cavity to extract two output beams from the system. Two output beams are directed on CCD cameras and to a detector monitoring a small portion of the transverse section of L_1. A narrow (<15μm) tunable beam is used as an external optical perturbation for LS addressing (from [33]).

in Figure 4.1, forming a compound cavity where the near-field emission of L_1 is imaged onto L_2 near-field plane and vice versa. This self-imaging configuration virtually eliminates diffraction in the compound cavity, which is several tens of centimeters long, hence maintaining a large Fresnel number.

Both VCSELs are thermally controlled and individually biased. For suitable temperature and current settings (I_{L_1} and I_{L_2}), both VCSEL cavity resonances are close enough to enable interaction between the two devices. A complete description of the parameter space where this interaction occurs is presented in [54]. Within an interval of cavity detuning values, the system is locally bistable between a non-lasing and a lasing states, due to the saturation of the absorption in L_2. This is observed while monitoring the local intensity emitted by the system and sweeping the cavity detuning (which is varied by changing I_{L_1}). For a critical value of detuning, we observe a sudden jump in the emitted intensity from background level to a high level, corresponding to the formation of a bright single-peak structure in the transverse section. Bistability between the two states is evidenced by hysteresis when sweeping back the detuning value. The spectral emission of this bright single-peak structure reveals a well-pronounced peak red-detuned as compared with the spontaneous emission broad peak observed for the lower state. Considering the whole transverse section of L_1 (or L_2), several of these single-peak localized lasing structures appear at different positions. An interferometric analysis [55, 69], reveals that each one of these structures has its own lasing frequency with a linewidth of few megahertz. As in many experiments realized using similar VCSEL microcavities, the position where localized structures spontaneously form depends both on the system's inhomogeneities and on the precise alignment conditions [43].

Once the bistable region is identified, lasing LS may be addressed individually by using a narrow addressing beam. In the absence of an driving beam that may serve as reference, the addressing of laser LS is necessarily incoherent. Different kinds of perturbations have been analyzed numerically [70] and experimentally

[71]. Besides these simple states, higher-order lasing LS have also been observed and the coherence of distant LS and higher-order LS have been analyzed in [55] (see also [63] in this volume). Of particular interest are higher-order LS that host a phase defect. This defect is the signature of an optical *vortex*, where light is twisted like a corkscrew around its axis of travel [72]. In our case, the vortex is associated to a localized structure, hence we call it a localized vortex soliton [73].

It is interesting to note that bistability as coexistence between stationary states is the most common case for the observation of localized states, but nonstationary LS have also been observed in the same experiment such as excitable LS [74] and pulsing LS [54]. In the former case, excitability resulted from spatial inhomogeneities and gradients as in [75], while in the latter, the nonstationary behavior resulted from the interaction of many longitudinal modes of the coupled cavity. However, static yet nonstationary localized states have been observed numerically in models of semiconductor laser with saturable absorber, which did not include these specific ingredients [76]. An example of chaotic dynamics of laser LS is shown in Figure 4.2.

4.2.2
Time-Localized Structures in Passive Mode-Locked Semiconductor Laser

Passive mode-locking (PML) is a fascinating self-organized collective phenomenon where the longitudinal modes of a laser cavity lock in phase [77, 78], leading to narrow pulse emission in the laser intensity output. The larger the number of modes experiencing phase locking, the narrower is the pulse width, while the repetition rate, in the case of fundamental PML, is given by the resonator-free

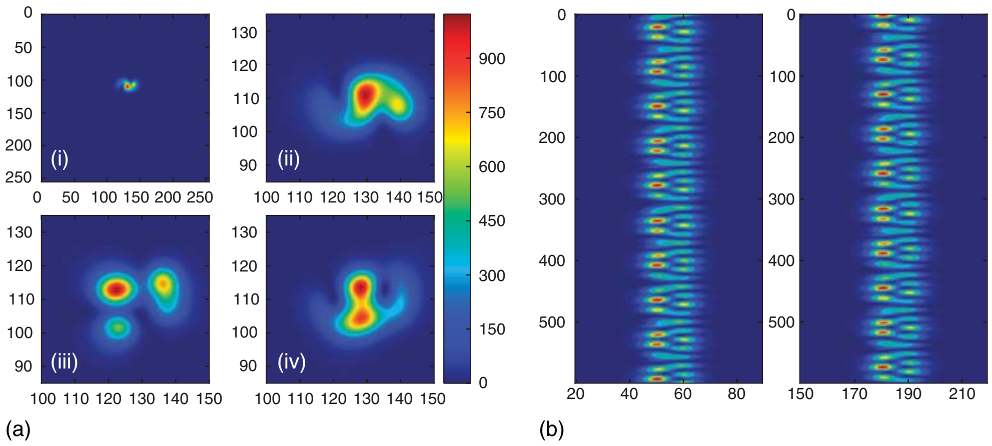

Figure 4.2 (a) Instantaneous field intensity of a chaotic laser LS observed in the model of [37]: (i) view of the full spatial extension of the system; (ii–iv) snapshots of the spatial region containing the chaotic LS. (b) Temporal evolution of a cut along the horizontal axis across two chaotic LS. Each LS is in a chaotic regime (from [76]).

spectral range. From a theoretical point of view, PML is successfully described via the seminal Haus' master equation, which combines the nonlinear Schroëdinger equation with dynamical nonlinear gain and losses [77]. In fiber [79] and in Ti:sapphire lasers [80], the gain recovery time (Γ^{-1}) and the absorption recovery time are, respectively, much slower and faster than the propagation time; and the Haus equation can be approximated by the subcritical cubic–quintic complex Ginzburg–Landau equation where the slowly evolving net gain is replaced by a constant. This constant must be determined self-consistently with the number of PML pulses per round-trip, which may be one (fundamental PML) or N_h (Nth order harmonic PML). The stability of these different emission states is described by the so-called background stability criterion of PML [81], which states that a pulsating solution is stable only if the losses are larger than the gain during the whole interval between pulses. Accordingly, the net gain constant of a stable solution must be negative, thus imposing a well-defined value for N_h once the values of the pump level and of the round-trip time are fixed. Usually, for a given value of these parameters, only one N_h PML is stable notwithstanding a small region of bistability in the transition region between operations at harmonic number N_h and $N_h + 1$ [82]. The PML pulses are often interpreted as dissipative solitons, see [79] for a review, and they are sometimes studied as perturbed nonlinear Schroëdinger conservative solitons.

The question we address in this section is whether mode-locking pulses exhibit the properties of temporal LS. In fiber or Ti:sapphire lasers, the gain recovery time is so large ($\Gamma^{-1} = 10$ ms in doped fibers) that, unless considering unrealistic resonator lengths, the limit described in the Section 4.1 $\Gamma\tau \gg 1$, required for the existence of LS cannot be achieved. This was exactly the main drawback of the fiber laser systems proposed in the 1990s as storage ring for information bits [83]. Gain level needed to be adjusted as a function of the number of pulses in the cavity, thus preventing from storing an arbitrary sequence of bits at a fixed gain level [84].

It is worth noting that LS can be instead successfully implemented in injected Kerr fiber resonators [39], where no carrier dynamics is associated with intensity-localized pulses. Our analysis is devoted to the realization of lasing temporal localized states in semiconductor devices for the reasons detailed in the Section 4.1. In semiconductor laser, PML is obtained by combining two elements, a laser amplifier providing gain and a saturable absorber acting as a pulse-shortening element. Under appropriate conditions, the different dynamical properties of the absorption and of the gain favor pulsed emission by creating a limited time window for amplification around an intensity pulse [85, 86]. In semiconductor lasers, the above-described limit can be easily implemented because $\Gamma^{-1} \approx 1$ ns and an external cavity may provide round-trip time values (τ) such that $\Gamma\tau \gg 1$. However, this situation has never been deeply explored because it implies that, after an intensity pulse, the gain recovers eventually overcoming the losses before the pulse return at the next round-trip. According to the background stability criterion, this has been always perceived as detrimental for fundamental mode-locking stability.

The result of our analysis shows instead that, for suitable parameters of the saturable absorber, in the limit $\Gamma\tau \gg 1$, both the fundamental mode-locked and the trivial off solutions are stable for current values below the laser threshold. The stability of the latter provides a stable background between pulses, which then become fully localized, that is, independent on cavity size. This enables the coexistence of a large quantity of stable solutions, each of them being characterized by a different number of pulses per round-trip (ranging from 0 to N_h, N_h being the largest number of pulses compatible with the cavity size) with different arrangements. In this situation, the PML pulses exhibit the properties of LS and they can be addressed as independent bits by injecting optical pulses.

We analyze theoretically PML in semiconductor laser with an external cavity closed by a saturable absorber mirror by using the delay differential equation model described in [87]. This model generalizes Haus' model as it encompasses both the pulsating and steady regimes and it allows to study the bifurcation sequence leading to fundamental mode-locking solution as a function of pumping current. The model equation and parameter values can be found in [88].

As explained earlier, the common settings for achieving PML in semiconductor lasers are based on the condition $\tau \leq \Gamma^{-1}$. In this situation, the bifurcation diagram leading to mode-locking as a function of laser pumping current is plotted in Figure 4.3a. At the lasing threshold $g_0 = g_{\text{th}}$, the off solution (not shown) becomes linearly unstable; a stable continuous wave (CW) solution bifurcates from the off state but it becomes unstable as g_0 is slightly increased. At that point, the fundamental PML solution emerges from it through a supercritical Andronov–Hopf bifurcation. Keeping on increasing the pumping current, this solution bifurcates (not shown in Figure 4.3a) toward increasing order harmonic mode-locking solutions. The same occurs for current values above laser threshold, if the cavity length is increased. These changes lead to an increasing number of pulses N_h in a single round-trip, such that the newfound value of N_h becomes again compatible with the background stability criterion.

The scenario described here radically changes for a long cavity; see Figure 4.3b. The Andronov–Hopf bifurcation originating the PML state becomes subcritical, hence the PML solution may exist below its bifurcation point, where it coexists with the CW solution. For even longer cavities, the breadth of the folded fundamental PML solution extends below the lasing threshold, where it coexists with the off solution; see Figure 4.3c. Interestingly, during this folding phenomenon, the fundamental PML branch eventually disconnects from the CW solution. It entails that PML appears for long delays as a saddle-node bifurcation of limit cycles instead of a nascent Andronov–Hopf bifurcation of the CW solution making this scenario out of the reach of any weakly nonlinear analysis.

The change in dynamical scenario that occurs in Figure 4.3c has a profound consequence on the fundamental mode-locked solutions, which becomes stable even in the limit $\Gamma\tau \gg 1$. The stability of the off solution engenders that, after the PML pulse, losses are larger than the gain even when the gain has fully recovered within the round-trip time. In other words, the PML pulse, whose duration τ_p is given by $\tau_p \sim 3\Gamma^{-1}$, becomes temporally localized. Moreover, a very large

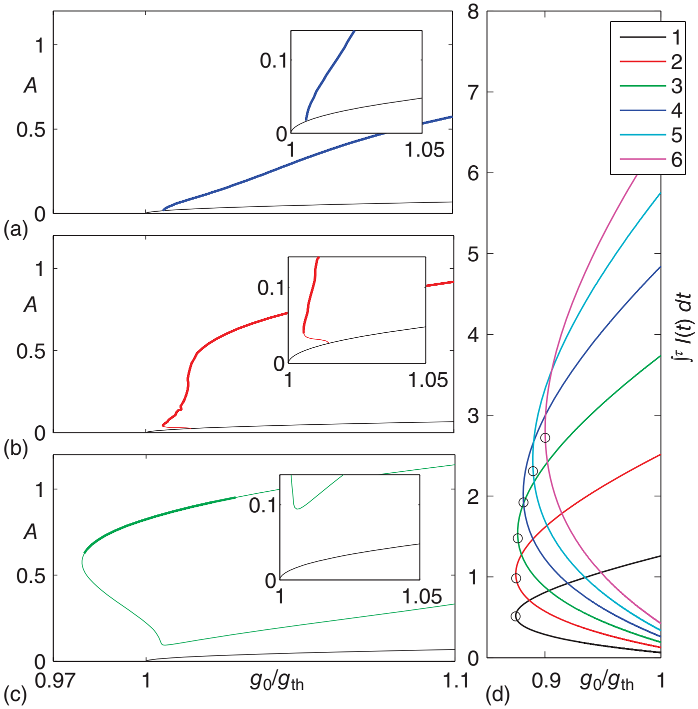

Figure 4.3 Panels (a–c) depict the bifurcation scenario as a function of the gain for different values of the delay: (a) $\tau = 1.2\Gamma^{-1}$, (b) $\tau = 2\Gamma^{-1}$, and (c) $\tau = 4\Gamma^{-1}$. The fundamental PML solution is plotted with the color line and its stability domain is indicated with a thicker line. The CW solution is plotted with the thin black line and its stability domain is not indicated. Panel (d) shows, for $\tau = 16\Gamma^{-1}$, the folding of several PML solutions having a different number of equally separated pulses per round-trip, while the folding point g_{sn} is represented by a circle (from [88]).

number of pulsing solutions with different number of pulses per round-trip and different arrangements become stable for the same parameter values. We reconstructed analytically some of these solutions using New's approximation [81] for $\tau = 16\Gamma^{-1}$ and restricting our analysis to equally spaced pulses solutions; see Figure 4.3d. Clearly, all these branches of solutions extend well below the laser threshold, where they are all stable together with the off solution. The multistability evidenced by Figure 4.3d suggests, in analogy to spatial LS [2, 20], that the harmonic mode-locked solution of maximal order that exists below threshold becomes *fully decomposable*, since essentially any pulse of this solution can be set on or off.

We give evidence of this property by imposing an arbitrary sequence of pulses within the laser cavity and examining the stability of the resulting configuration (Figure 4.4). Each pulse optically injected triggers the emission of a lasing LS, whose shape stabilizes after a short transient. A single localized pulse is not affected by a neighboring pulse, provided that their time separation is sufficiently

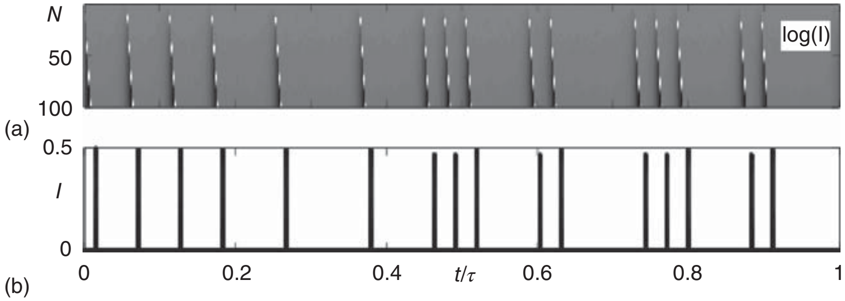

Figure 4.4 Evolution over $N = 100$ round-trips of a bit pattern written optically by injecting 1ps light pulses in the cavity (a) and detail over a single period (b). Parameters as in Figure 4.3 with $\tau = 200\Gamma^{-1}$. The bit sequence is 10101010010001001110011000111001100 (from [88]).

large, that is, $\Delta t \gtrsim \tau_p$. As shown in Figure 4.4, the device acts as an all-optical buffer with a bit rate limited by the size of the LS, that is, approximately 1Gb s^{-1} for typical semiconductor parameters.

The results of this theoretical analysis are confirmed by an experiment based on a VCSEL coupled to a distant semiconductor-based resonant saturable absorber mirror (RSAM). The setup is similar to the one shown in Figure 4.1, except for having replaced the VCSEL used as a saturable absorber by a commercial RSAM; see [88, 89] for details. We have obtained PML when the RSAM and the VCSEL are placed one in the Fourier plane of the other. This working condition is obtained by imaging the VCSEL near-field profile onto the front focal plane of the aspheric lenses placed in front of the RSAM, while the RSAM is placed onto the back focal plane of this lens.

In order to match the conditions predicted by the theory for observing LS, we chose an RSAM with reflectivity that increases from 1% to 60% when saturated. We set the cavity round-trip time at $\tau = 15.4$ ns, corresponding to a free spectral-range of 65 MHz and to $\tau \sim 50\Gamma^{-1}$. Moreover, we biased the VCSEL below threshold.

In these conditions, the system exhibits several emission states coexisting for the same values of bias current, as shown in Figure 4.5. These states consist of pulse trains having different number of pulses per round-trip (from 0 to 19). In these emission states, the individual pulses may appear grouped (Figure 4.5b) or equally separated (Figure 4.5c). The zero pulse emission (not shown in Figure 4.5) has the same intensity level of the intensity between the pulses and it corresponds to the off state. The laser pulses are regularly emitted at the fundamental repetition rate of 65 MHz (see Figure 4.5a), which is, to the best of our knowledge, the smallest repetition rate ever obtained with a PML semiconductor laser. The pulse width is below the bandwidth limit of our detection system (12 ps rise time), while the corresponding spectral emission consists of a peak having a width of 0.12 nm (FWHM). All these regimes coexist for a wide range of the VCSEL current J. The multistability of our system is depicted in Figure 4.5e where we classify the

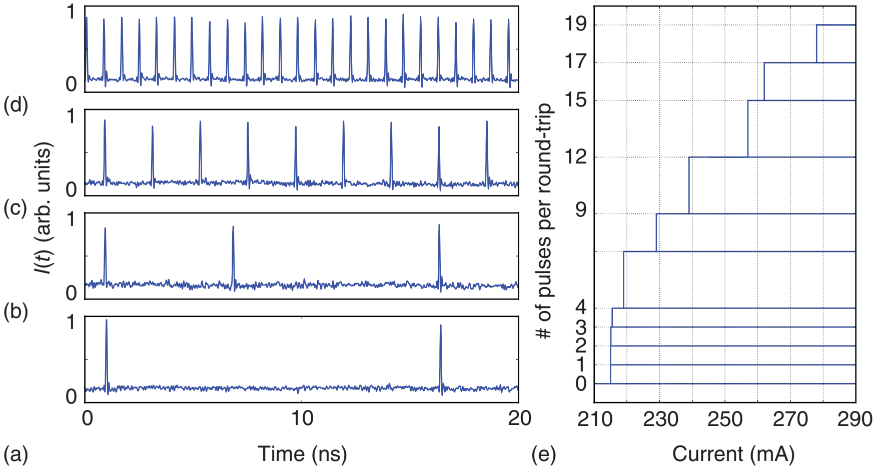

Figure 4.5 (a)–(d) Coexisting time output traces ($J = 290\,\text{mA}$). (e) Experimentally obtained bifurcation diagram for the number of pulses per round-trip. The stability of each solution is indicated by the solid horizontal lines (from [88]).

different solutions in terms of the number of pulses per round-trip. Figure 4.3e is obtained increasing the parameter J from $J = 210\,\text{mA}$, where only the steady off solution is stable, up to the value where it loses its stability ($J = 600\,\text{mA}$) and then decreasing it down to $J = 290\,\text{mA}$ where a periodic emission with 19 pulses per round-trip appears, corresponding to the highest order harmonic mode-locking solution that can be fitted in our cavity round-trip (Figure 4.5d). Scanning down J makes solution with decreasing number of pulses spontaneously appearing and, at every transition, we increase J to explore the branch stability up to $J = 290\,\text{mA}$. All-optical addressing of the LS shown in Figure 4.5 is the topic of ongoing research in our laboratory. Nevertheless, nucleation of a single pulse from the off state, as well as the switch between different emission states, can be observed when perturbing mechanically the system. Yet this kind of perturbation does not allow any control of the switching; it may lead to the nucleation of several pulses at the same time with random positions within the cavity.

4.3
Localized States in Nonlinear Element with Delayed Retroaction

In Section 4.2, we have shown that different kinds of temporal localized states can exist in mode-locked systems in which most of the propagation can be represented by delay terms. A complementary vision can be built by analyzing perhaps simpler systems in which a long delay term is simply added to a nonlinear element with a simple and well-defined phase space structure (see Fig. 4.6) and no spatial degrees of freedom. In this section, we analyze the formation of different kinds of localized states that appear in this conceptual setting, based on two well-defined phase space structures: the first one is that of two coexisting stable fixed points (a bistable system) and the second one consists of two neighboring fixed points (one stable and one unstable) sitting on a strongly attracting circle (and excitable system).

4.3.1
Front Pinning in Bistable System with Delay

Localized states in weakly dissipative systems can often be described as slightly perturbed soliton solutions of the corresponding conservative system [15, 90]. On the contrary, in strongly out-of-equilibrium systems, other mechanisms based on the stability of interacting fronts may be invoked [16]. In spatially extended systems admitting two coexisting stable homogeneous states, it is clear that any single front connecting these two states will not be stationary unless the two states are equivalently stable, that is, at the Maxwell point. On the contrary, a pair of fronts connecting one state to the other and back may be stable even outside of the Maxwell point, provided the connection is not monotonous [16]. This mechanism has been often invoked about the stability of LS in bistable laser systems [9]. Another possible mechanism (even for the stability of one single front) exists when one of the states is spatially modulated [2]. In this case, there is a nonzero energy cost associated with the motion of the front since this motion must happen in discrete steps whose size is defined by the spatial wavelength of the pattern. Although this mechanism may extend beyond simple periodically modulated states and may not even require the stability of the modulated state, the simplest case is probably that of two stable and coexisting homogeneous, with the addition of a spatial periodic forcing to one of them [91–93]. Starting from a situation of vanishing forcing where fronts move such that the system ends up in one single state covering the whole spatial extension, a gradual increase of the forcing leads to a pinning transition for the fronts, which end up being locked at discrete positions set by the spatial period of the forcing. Building on the stability of these fronts, many localized states consisting of pairs of fronts connecting the homogeneous state to itself after an integer number of (spatial) oscillations can be created. Their existence is well described by two (for even and odd number of oscillations) homoclinic connections undergoing sequences of saddle-node bifurcations corresponding to a larger and larger number of periods included in the structure. Due to the snake-like shape of these branches, this phenomenon has received the name of homoclinic snaking, and in the optical context it has been analyzed experimentally in liquid crystal light valve [93] and semiconductor microcavities with coherent forcing [94].

As mentioned in the Section 4.1 of this chapter, a parallel has been drawn between instabilities arising in spatially extended systems and delayed dynamical systems [95] and this parallel has been given formal grounds [52]. Provided a suitable spatiotemporal representation is chosen by defining the (real) time t as $t = \sigma + n\tau$ (with $\sigma \in [0, \tau]$ and $n \in \mathbb{N}$) and considering σ as a spatial variable and n as a discrete time, comoving Lyapunov exponents can be defined and computed in a delay dynamical systems and the existence of convective type instabilities in delay dynamical systems can be established. However, this analysis was limited to Hopf instabilities and thus does not extend to the case of coexisting attractors and their eventual connection as happens for patterns and localized states. Nevertheless, the interesting observation that delayed systems can show a dynamics very reminiscent to spatially extended systems has been recently extended to the case of bistable systems [53]. In that paper, the authors show that for suitable parameters the system with delay preserves its bistable character and then analyze the dynamics of the system in this range and in the comoving reference frame. Starting from random initial condition, the system will evolve toward homogeneous state via motion of fronts that move apart at constant speed provided they are separate enough not to interact. These observations, also backed by numerical simulations on a prototypical bistable model with the addition of delay, are in excellent analogy with spatially extended bistable systems.

Starting from that observation, the question of the eventual pinning of these fronts is obvious [96]: can the fronts that move at constant velocity in the absence of any “spatial” modulation in delayed systems be pinned to some “spatial trapping” as observed in spatially extended systems? This question has been partially addressed using the bistable system with delay already used in [53].

The experiment is based on a VCSEL. These devices can have near-perfect cylindrical symmetry, which sometimes leads to complex polarization behavior (see for instance [97]). In particular, some of these devices may admit two coexisting linear polarization states for one single pump parameter value. We observe this bistable response measured as the coexistence of a zero and a nonzero state of intensity transmitted through a polarizing beam splitter. In order to apply a controlled feedback, the intensity value transmitted through the polarizing beam splitter is monitored by a photodetector whose voltage is recorded by a digital acquisition board. This sequence of voltage values is then shifted in time and applied back after adequate scaling to the pump current of the VCSEL. Care is taken to keep the feedback small enough that it does not spoil the polarization bistability of the device. The delay is chosen to be much larger than the typical time scales of the system and the parameters are set such that the system is bistable. Following the initial idea of considering the fast time scale within one delay as a space-like variable and the number of delays as a discrete time, we analyze the dynamics in space – time diagrams as shown in Figure 4.6. Starting at time $n = 100$ from an initial condition in which all the system is in one state except for a small region, the left and right fronts will move apart, eventually leading to one state covering the whole system. At time $n = 378$, however, a periodic forcing is applied along the (pseudo-) spatial dimension. In practice, it consists of a time-periodic modulation of the transfer function of the feedback loop, small enough to keep the system in the bistable regime. The first effect of this modulation is to block the motion of the fronts, halting the coarsening process, in a very similar fashion to the pinning that is observed in spatially extended systems [92].

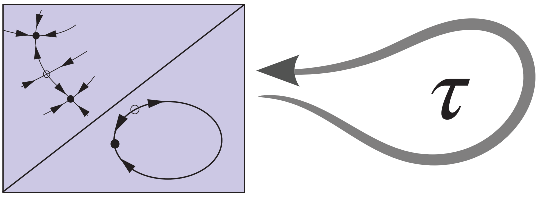

Figure 4.6 Several forms of localized states may be formed within a delayed retroaction loop applied to a nonlinear element that is either bistable or excitable, in the absence of any actual spatial degree of freedom.

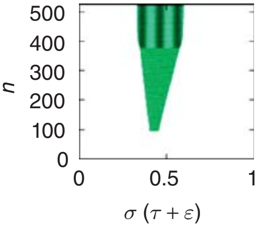

Figure 4.7 Laser intensity through the polarizer (dark green is high intensity). In a spatiotemporal representation, the horizontal scale is a fast time scale related to the delay and the vertical scale is discrete time in units of delay (see [53, 96]). In that comoving reference frame, fronts move apart at constant speed until "spatial" forcing is applied, which pins the fronts (from [96]).

Once this pinning is obtained, the existence of many kinds of localized states can be demonstrated easily by either specifying adequate initial conditions of applying perturbations in specific positions of the space – time diagram (Figure 4.8a). At this point, it is interesting to note that in the absence of delayed feedback the modulation itself would have changed the fixed points of Figure 4.7 in limit cycles. When adding the delay term, however, the phase space structure has become much more

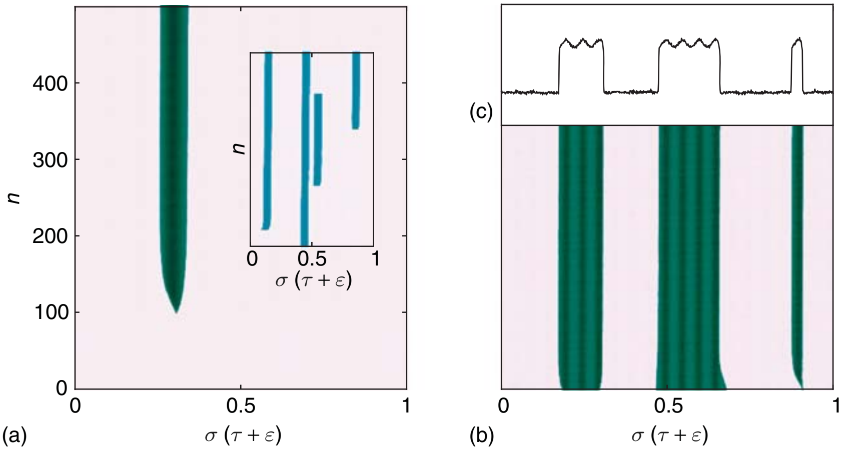

Figure 4.8 Many localized states can be formed in a bistable system with delayed feedback. (a) Evolution from the initial condition (a tiny spatial region in the "green" state) to a stable localized state. Inset: many localized states enclosing each a single maximum can coexist. (b, c) Different kinds of localized states can coexist, the size of each of them is a multiple of the period of the forcing in pseudospace (from [96]).

complex. Indeed, each kind of localized state (with one, two, or more maxima) is actually a limit cycle coexisting with many others, a transition which may be related to a homoclinic snaking scenario [98]. In addition, the many superpositions of these limit cycles corresponding to neighboring but independent localized states are also stable limit cycles.

In spite of the remarkable similarity between the results shown in Figure 4.8 and the observations realized in unidimensional spatially extended systems (see, e.g., [91–93]), one fundamental difference emerges between the two systems, and it is related to the lack of reversibility symmetry $\sigma \to -\sigma$ in pseudospace, which is a direct consequence of the *temporal* nature of this variable.

In fact, even if the drift term generically present in delayed systems [52] can be abstracted away by choosing an adequate set of coordinate (discussed at least in [52, 53, 96]), the rising and falling fronts are of different nature since they are two different heteroclinic connections between the states of the system (leaving and attaining an attractor along different directions in phase space). This asymmetry is clearly visible in Figure 4.8c, in which the rising and falling fronts connect to the oscillatory solution in markedly different positions with respect to the forcing. This translates in the unpinning transition that leads to destabilization of localized states, as shown in Figure 4.9. In symmetric spatially extended systems, the unpinning of the front is known to happen via a saddle-node bifurcation leading to an oscillating velocity of the fronts that will lead to one state covering the whole system. In the present case, the unpinning transition occurs separately for the rising and falling fronts as shown in Figure 4.9.

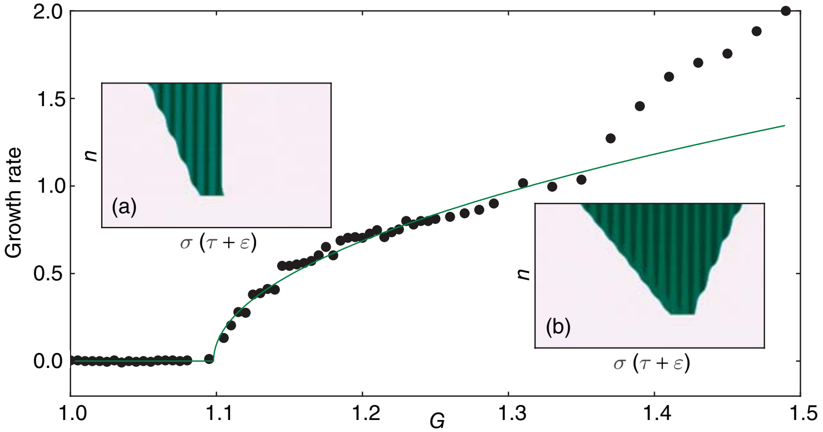

Figure 4.9 The pinning region (in which the front velocity is zero) is delimited by saddle-node bifurcations leading to oscillatory velocity of the front around a nonzero value. When the asymmetry between the states is increased the *left* front unpins first, while the right front is still locked to the forcing (a). Upon further increase, the *right* front finally also unpins (from [96]).

One important feature of this experimental system is that the delayed retroaction is implemented electronically by applying to the VCSEL a bias current that depends (linearly) on the emitted power. In this case, the optical phase completely disappears from the physics of the system, and the feedback term is real. This translates into the purely prototypical modeling used in [96], which is based on a bistable real system and yet reproduces very well the experimental findings.

Whether bidimensional structures could be observed in such systems is an open question [99].

4.3.2
Topological Dissipative Solitons in Excitable System with Delay

As we have seen in the previous sections, bistable systems either spatially extended or with delay can host localized states. An interesting alternative configuration is that of an *excitable* system with delay. In the following, we describe these localized states and relate them to dissipative phase solitons observed in a multimode laser with coherent forcing [100, 101]. A system is said to be excitable when it responds to external perturbations with an all-or-nothing response depending on whether the perturbation has overcome a well-defined threshold. This dynamics was first described in biology [102] but the phase space structures that may lead to this (and other neural cell) behavior(s) (see, e.g., [103] for a review) can of course be found in many other domains and in particular in nonlinear optical dynamical systems. Three main phase space structures are known to lead to excitable behavior, and all of them have been observed in laser systems [104–106]. The one that we consider here is the vicinity in parameter space of a saddle-node on invariant circle bifurcation, which is a very generic feature of forced oscillators and has been predicted to happen in a laser with coherent optical injection in [107]. In this context, excitability may be found when a laser is locked to an external forcing in the case of weak forcing, weak detuning, and far from laser threshold, that is, when the dynamics of the system can be simply reduced to purely phase (θ) dynamics and described by the Adler [108] equation $\partial_t\theta = \Delta - \sin\theta$, where Δ is the detuning scaled by the strength of the forcing. When stationary solutions exist and are close to each other (i.e., $|\Delta|$ slightly smaller than unity), any sufficiently large perturbation applied to the system will trigger a response, which consists of the relative phase between laser and forcing going a full 2π rotation before the laser locks again to the forcing. This bifurcation has been observed in [109] and the phase rotations have been measured explicitly in [110], but it is only very recently that the actual response of the system to external perturbations has been studied [111–113], putting in evidence an excitability threshold and the unicity of the response for any sufficiently large perturbation. This response is analyzed in Figure 4.10. In the inset, the response of the system to increasing phase jumps is depicted for four different phase jump heights, illustrating the "all or nothing" response of the system. The excitability threshold (which is expected to be perfectly defined in a strictly deterministic

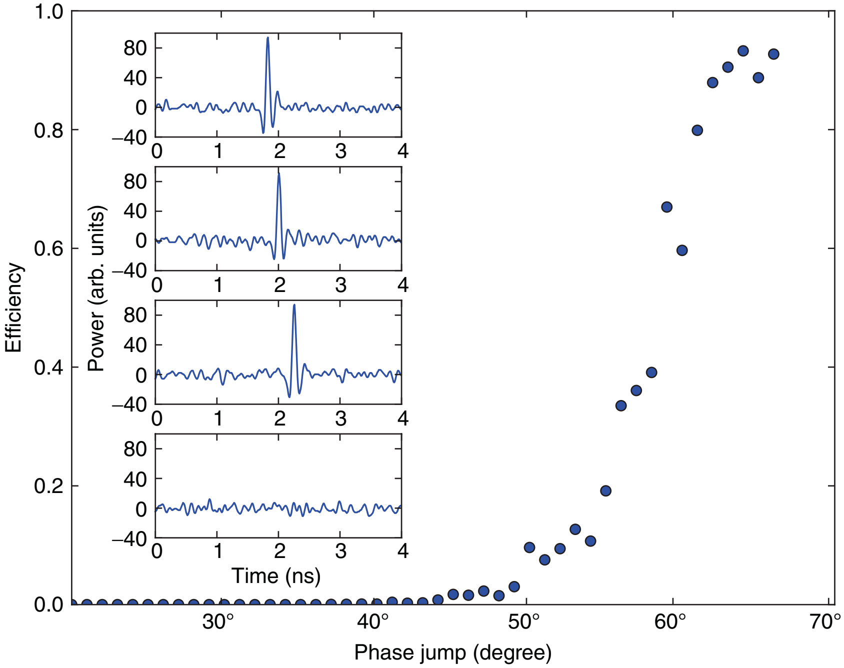

Figure 4.10 Response to external perturbations of an injection-locked semiconductor laser close to the unlocking transition in the excitable regime. For any perturbation beyond some threshold (here about 60° phase jumps), all responses are identical (insets). Each 2π phase rotation translates into a small intensity pulse (10–20% of the continuous level) due to interference with the forcing beam (from [111]).

system) is characterized experimentally by analyzing the efficiency of the perturbation depending on its size over many realizations. The efficiency abruptly raising from 0 to 1 shows the existence of the threshold, which is blurred by noise as studied analytically in a physically different but dynamically equivalent context in [114].

The clear phase space structure of this system (two fixed points sitting next to each other on a strongly attractive circle) can then be used as a nonlinear element for the implementation of the concept shown on Figure 4.7 by adding a simple delayed feedback term to the experimental system [115]. This can be done by adding to the initial experimental system (a semiconductor laser with coherent external forcing) a partially reflective feedback mirror. In this case, an external perturbation can trigger a 2π phase excursion but the small intensity pulse that is emitted is reinjected into the nonlinear element after a time corresponding to the propagation of the pulse in the feedback loop. This pulse is then regenerated by the nonlinear element, leading to a periodic orbit consisting of periodic emission of 2π phase rotations. As in Section 4.3.1, the dynamics of the system is better visualized in the comoving reference frame, as shown in Figure 4.11.

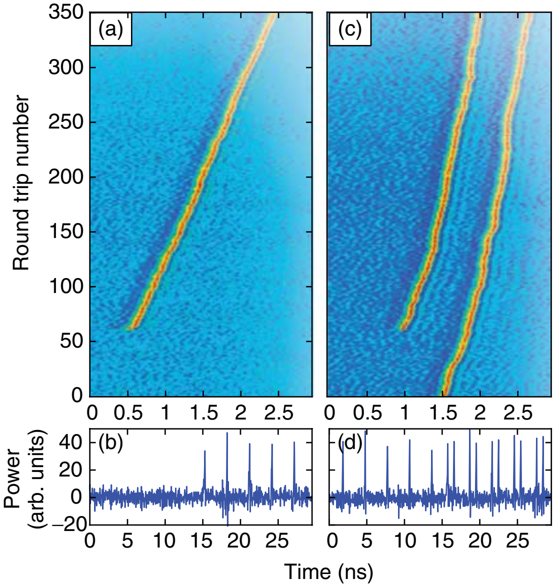

Figure 4.11 An injection locked semiconductor laser close to the unlocking transition with the addition of delayed feedback can produce periodic emission of 2π relative phase rotations. The use of the delay term as a spatial-like variable suggests the use of the available "space" to store information in the configuration of mutually independent phase bits. (a, b) A second phase bit has been nucleated by a phase perturbation, without impacting the pre-existing phase bit. (a, c) Spatiotemporal representation; (b, d) corresponding time traces (from [115]).

The fact that several of these pulses can coexist stably without perturbing each other naturally calls for an interpretation in terms of *localized states along the feedback dimension*. Due to their discrete nature of well-defined phase rotations, which can be nucleated and cancelled at will (see [115]), they can be expected to operate as *phase bits* or Φ-bits in optical coherent communication systems. More precisely, the experimental results in [115] show that a sequence of bit can be written and *reconfigured* by applying phase perturbations to the system, which therefore acts as a fully reconfigurable optical memory for incoming phase patterns.

This interpretation is strongly backed in [115] by a theoretical analysis along two directions. The first one consists of the analysis of the stability of these solutions, and the second one of the analytical connection of the delay differential equation used for modeling and a diffusion-like partial differential equation. In [115], the authors begin from the following equation in which one recognizes the simplest possible (Class-A) laser model with the addition of constant forcing and a delayed feedback term for the optical field amplitude E:

$$\frac{dE}{dt} = (1 + i\alpha)(1 - |E|^2)\,E + Y + i\Delta E + \eta e^{-i\Omega} E(t - \tau), \tag{4.1}$$

where time has been scaled to the photon lifetime in the VCSEL cavity times the excess pumping above threshold. α and Δ stand for the linewidth enhancement factor and the detuning between the solitary laser frequency and the injected field. The delayed retroaction is characterized by a delay τ, an amplitude η, and a phase Ω. Both the laser field amplitude E and the forcing amplitude Y have been rescaled to the one of the solitary laser and Y is chosen to be real. The relative simplicity of the model allows for Floquet analysis of the stability of periodic solutions with periodicity close to τ, realized by reconstruction of the monodromy operator $\mathcal{M}$, which describes the evolution of a perturbation after a full period. A histogram of the eigenvalues of $\mathcal{M}$ (i.e., of the Floquet multipliers) has been computed (building on [116, 117]) and is shown in Figure 4.12.

The Floquet multipliers close to unity correspond of course to neutral modes, which are neither damped nor amplified. A trivial one is associated with the translation of the periodic solution within the feedback loop, that is, one pulse single can be indifferently at any position within the loop. The number of Floquet multipliers close to unity scales such as the number of Φ-bits present within one period, and the eigenvectors associated with these eigenvalues are *relative translation* of one Φ-bit with respect to the others. This, together with the coexistence of all the solutions shown in Figure 4.12, confirms their nature of localized states since they interact only at short distance.

As in Section 4.3.1, we note that the phase space structure of the original system (essentially a circle holding two fixed points) has been notably complicated by the addition of the delay term. Each single pulse travelling in the feedback loop is now a limit cycle, and the superposition of many of them is again a limit cycle. How all these limit cycles emerge and to which extent they all (stably) coexist is an open

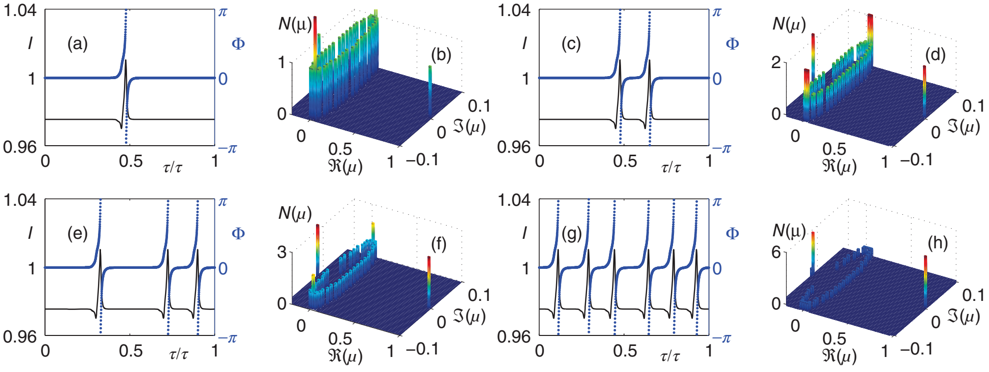

Figure 4.12 Analysis of model (4.1). Temporal traces (a,c,e,g) for the output intensity $I = |A|^2$ and phase $\Phi = \arg(A)$ and histogram $N(\mu)$ of the Floquet multipliers μ (b,d,f,h) in the cases of 1,2,3, and 6 Φ-bits. One notices that the number of neutral modes located in the vicinity of $\mu = 1$ increases linearly with the number of Φ-bits. After [115].

question, especially since some form of global coupling may be expected in delayed systems just as in propagative systems. In front of this situation, some insight can be gained by trying to push the analogy between delayed and spatially extended systems in this situation.

This analysis is performed in details in [115] and we refer the reader to this reference for some of it, but the most crucial point, which is the connection between a delay differential system and a spatially extended system is reproduced here since this connection is essential to this chapter. The initial model (4.1) can be reduced (via multiple time scale analysis and adiabatic elimination of the amplitude variable, which appears to be worked down to the slower phase dynamics) to a new delay differential equation describing the evolution of the relative phase of the laser with respect to the forcing, which reads

$$\frac{d\theta}{dt'} = \Delta' - \sin\theta + \chi \sin(\theta(t' - \tau') - \theta - \psi). \tag{4.2}$$

In Eq. (4.2), t' and τ' are time and delay terms essentially rescaled by the strength of the injection term. The few parameters left are Δ' the detuning of the forcing with respect to the free running laser and the feedback strength χ, delay τ', and phase ψ.

Assuming that interesting solutions of the system are periodic orbits whose period is close to τ'[1], one has $\theta(t' - \tau') - \theta < 1$ and, therefore, Eq. (4.2) can be expanded as

$$\frac{d\theta}{dt'} = (\Delta' - \sin\theta) - \chi \sin\psi + \chi\cos\psi(\theta(t'-\tau') - \theta)\frac{\chi\sin\psi}{2}(\theta(t'-\tau') - \theta)^2 + \cdots . \tag{4.3}$$

Following the procedure outlined in [52], it is possible analyze this equation further by introducing two time scales $u_1 = \epsilon t'$ and $u_2 = \epsilon^2 t'$, the chain rule being $d_{t'} \rightarrow \epsilon\partial_{u_1} + \epsilon^2\partial_{u_2}$. The fundamental point of the analysis lies in the way the delayed contribution to Eq. (4.3) is expanded as

$$\theta(t' - \tau') = \theta(\epsilon u_1 + \epsilon v, \epsilon^2 u_2 - \epsilon^2\tau'). \tag{4.4}$$

One notes that in this expansion the evolutions of θ (besides a drift term in u_1) are described by the slow time u_2, which implies that the solution only evolves slowly from one round-trip to the next.

Expanding the delayed term up to second order leads to

$$\theta(t' - \tau') - \theta \sim \left(\epsilon v\frac{\partial\theta}{\partial u_1} + \frac{(\epsilon v)^2}{2}\frac{\partial^2\theta}{\partial u_1^2} - \epsilon^2\tau'\frac{\partial\theta}{\partial u_2}\right), \tag{4.5}$$

$$(\theta(t' - \tau') - \theta)^2 \sim (\epsilon v)^2\left(\frac{\partial\theta}{\partial u_1}\right)^2 + \mathcal{O}(\epsilon^3), \tag{4.6}$$

---

[1] Actually experiments indicate some deviation with respect to τ but no analysis of the evolution of this period with parameters has been performed.

which eventually yields the following modified *overdamped* sine-Gordon equation with a tilt (also found in spatially extended forced oscillators in excitable regime [107] and a quadratic velocity contribution

$$\frac{\partial \theta}{\partial \xi} = \sin \overline{\theta} - \sin \theta + \frac{\partial^2 \theta}{\partial x^2} + \tan \psi \left(\frac{\partial \theta}{\partial x} \right)^2 . \tag{4.7}$$

Thanks to this analysis, the localized states observed experimentally and numerically in a delayed system based on an excitable element enclosed in a delayed feedback loop can be interpreted as dissipative solitons forming in the pseudospace $x = u_1 \epsilon^{-1} \sqrt{2\chi \cos \psi}$ (i.e., a fast time), which evolve slowly over time ξ defined as $\xi = u_2 \epsilon^{-2} / (1 + \tau' \chi \cos \psi)$.

In Eq. (4.7), we defined the equilibrium value $\sin \overline{\theta} = \Delta' - \sin \theta$. We also identified the drift velocity, that is, the deviation of the period with respect to the time delay as $v = 1/(\chi \cos \psi)$. Such a removal is done in such a way that the resulting localized structures become steady solutions of the resulting PDE, at least in the limit $\overline{\theta} = \psi = 0$.

Interestingly enough, searching directly for periodic solutions of Eq. (4.2) and imposing self-consistency relations yields an identical expression for the deviation of the period T with respect to the time delay, that is, $T = \tau + 1/(\chi \cos \psi)$.

We found the spatial kinks profiles of Eq. (4.7) that in the limit $\overline{\theta} = \psi = 0$ reads as $\theta(x) = 4 \arctan(\exp\ (x))$, to match very well the numerical solution of the DDE defined in Eq. (4.2). In particular, the temporal extend of the kink is proportional to $1/\sqrt{2\chi}$, which is quite intuitive. The larger the amplitude of the feedback term, the faster the rise time of the kink homoclinic orbit. The small deviations between the shape of the orbits of the DDE and of the PDE can be attributed to the influence of the higher-order spatial derivative that were neglected in the derivation of Eq. (4.2). In this respect, the larger the feedback, the smallest the drift and the influence of such higher-order derivative leading to an improvement of the agreement between the temporal and spatial profiles.

The very strong parallel between spatially extended and delay systems can be studied further by analyzing a complementary experiment based on a strongly multimode ring laser with coherent forcing, where a reduction of the dynamics to a single phase variable also leads to an overdamped sine-Gordon-like equation [118]. In this case, the system does not consist anymore of (zero-dimensional) phase-locked oscillator with addition of delayed retroaction. Instead, it is a distributed oscillator with spatial degrees of freedom (evidenced by its multimode character [57]) under coherent forcing. In this case and even when the dynamics cannot be reduced to a single phase equation, dissipative solitons consisting of 2π relative phase rotations embedded in phase locked regions can emerge from chaotic areas as shown in Figure 4.13 and analyzed in [100, 101].

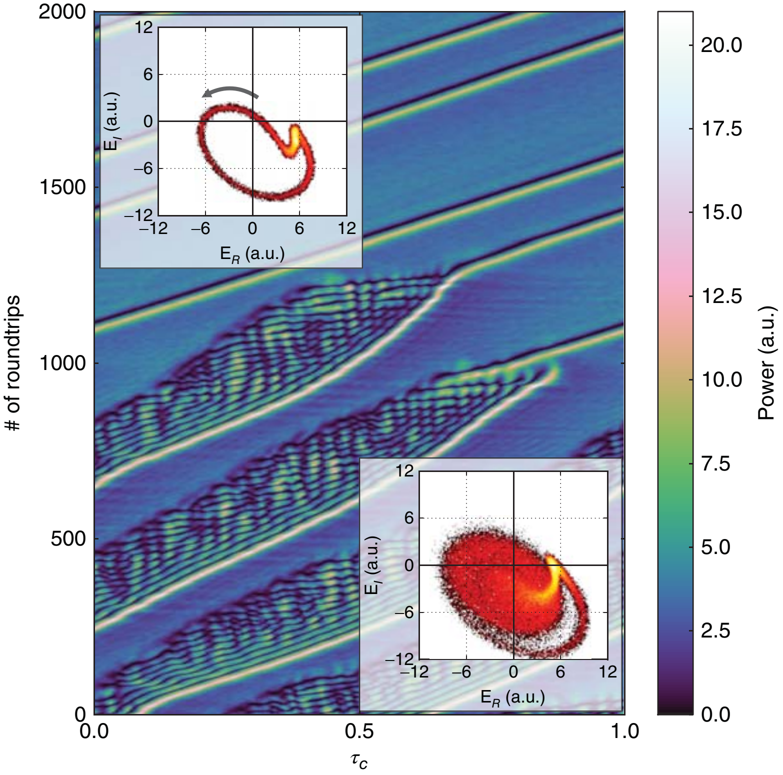

Figure 4.13 A multimode ring laser with coherent forcing can host nondispersive wave packets consisting of 2π phase rotations embedded in a uniformly locked domain (from [101]).

4.4
Conclusion and Outlook

In this chapter, we have reviewed some recent work about spatially localized states in the transverse section of semiconductor microcavities and discussed current approaches to localized states along the propagation direction in propagative and delay semiconductor systems. Although the identification between phenomena observed in the transverse and longitudinal directions is far from obvious and complete, many common features have been found. For instance, the analysis of mode-locked regimes and their relation to temporal localized states shows obvious similarities with lasing localized structures in the transverse dimension of lasers with saturable absorber. Similarly, the front pinning phenomenon that has been evidenced in a bistable VCSEL with the addition of optoelectronic feedback suggests that in this system without phase symmetry (the optoelectronic feedback implies that optical intensity instead of field is the relevant variable) the homoclinic snaking mechanism might be responsible for the formation of localized states. However, the lack of parity symmetry in the pseudo-spatial dimension of the feedback system leads to a yet undocumented splitting of the unpinning transition in parameter space. We note that this broken parity symmetry may in fact not be restricted to delayed systems and probably applies not only to propagative but also to most transverse systems. Finally, the dissipative topological solitons that form as stable self-sustained 2π phase rotations in a single mode laser with coherent forcing and delayed feedback bear strong analogies with excitable waves theoretically predicted in the transverse section of broad area lasers with coherent forcing.

In addition, we have presented novel kinds of optical localized states whose existence is fundamentally not based on the intensity or amplitude of the electric field but instead on the optical phase. Besides their physical interest, this may also confer them very interesting properties for optical communications. In fact, the well-known properties of localized states (discreteness, robustness, plasticity, bistability, finite interaction distance, etc.) also apply to these new localized states but they do not require particularly high power density, which may be promising in terms of energy-efficient applications. But most importantly, optical communications are now becoming *coherent*, with information encoded in the phase of light instead of intensity. In this context, the analysis of phase-localized states bears great promise since it can be expected to bring many of the previously envisioned applications of dissipative solitons to the realm of coherent communications.

Acknowledgements

We thank all the coauthors of the papers that we discuss in this chapter, in particular, the past and present PhD students at INLN whose work has been fundamental to the realization of all the experiments described here, namely Dr. Patrice Genevet, Dr. Margherita Turconi, M. Mathias Marconi, M. Bruno Garbin, and M. François Gustave. Finally, S.B. and M.G. address particular thanks to Prof. Jorge Tredicce.

References

1. Fauve, S. and Thual, O. (1990) Solitary waves generated by subcritical instabilities in dissipative systems. *Phys. Rev. Lett.*, **64**, 282–284, doi: 10.1103/PhysRevLett.64.282.
2. Coullet, P., Riera, C., and Tresser, C. (2000) Stable static localized structures in one dimension. *Phys. Rev. Lett.*, **84** (14), 3069–3072.
3. Umbanhowar, P.B., Melo, F., and Swinney, H.L. (1996) Localized excitations in a vertically vibrated granular layer. *Nature*, (382), 793–796, doi: 10.1038/382793a0.
4. Astrov, Y.A. and Purwins, H.G. (2001) Plasma spots in a gas discharge system: birth, scattering and formation of molecules. *Phys. Lett. A*, **283** (5–6), 349–354, doi: 10.1016/S0375-9601(01)00257-2.
5. Niedernostheide, F.J., Arps, M., Dohmen, R., Willebrand, H., and Purwins, H.G. (1992) Spatial and spatio-temporal patterns in pnpn

semiconductor devices. *Phys. Status Solidi B*, **172** (1), 249–266, doi: 10.1002/pssb.2221720123.

6. Lee, K.J., McCormick, W.D., Pearson, J., and Swinney, H.L. (1994) Experimental observation of self-replicating spots in a reaction–diffusion system. *Nature*, **369**, 215–218, doi: 10.1038/369215a0.
7. Wu, J., Keolian, R., and Rudnick, I. (1984) Observation of a nonpropagating hydrodynamic soliton. *Phys. Rev. Lett.*, **52**, 1421–1424, doi: 10.1103/PhysRevLett.52.1421.
8. Moses, E., Fineberg, J., and Steinberg, V. (1987) Multistability and confined traveling-wave patterns in a convecting binary mixture. *Phys. Rev. A*, **35**, 2757–2760, doi: 10.1103/PhysRevA.35.2757.
9. Rosanov, N.N. (2002) *Spatial Hysteresis and Optical Patterns*, Springer-Verlag, Berlin, Heidelberg, New York.
10. Lugiato, L. (2003) Introduction to the feature section on cavity solitons: an overview. *IEEE J. Quantum Electron.*, **39** (2), 193–196, doi: 10.1109/JQE.2002.807195.
11. Mandel, P. and Tlidi, M. (2004) Transverse dynamics in cavity nonlinear optics (2000-2003). *J. Opt. B: Quantum Semiclassical Opt.*, **6** (9), R60, http://stacks.iop.org/1464-4266/6/i=9/a=R02.
12. Ackemann, T., Firth, W., and Oppo, G.L. (2009) Fundamentals and applications of spatial dissipative solitons in photonic devices, in *Advances in Atomic Molecular and Optical Physics*, vol. **57** (eds E. Arimondo, P. Berman, and C.C. Lin), Academic Press, pp. 323–421, doi: 10.1016/S1049-250X(09)57006-1.
13. Descalzi, O., Clerc, M., Residori, S., and Assanto, G. (2011) *Localized States in Physics: Solitons and Patterns: Solitons and Patterns*, Springer-Verlag.
14. Malomed, B.A. (1987) Evolution of nonsoliton and “quasi-classical” wavetrains in nonlinear Schrödinger and Korteweg-de Vries equations with dissipative perturbations. *Physica D*, **29** (1), 155–172.
15. Fauve, S. and Thual, O. (1990) Solitary waves generated by subcritical instabilities in dissipative systems. *Phys. Rev. Lett.*, **64** (3), 282–284, doi: 10.1103/PhysRevLett.64.282.
16. Coullet, P. (2002) Localized patterns and fronts in nonequilibrium systems. *Int. J. Bifurcation Chaos*, **12** (11), 2445–2457.
17. Rozanov, N.N. and Khodova, G.V. (1988) Autosolitons in bistable interferometers. *Opt. Spectrosc.*, **65**, 449–450.
18. Tlidi, M., Mandel, P., and Lefever, R. (1994) Localized structures and localized patterns in optical bistability. *Phys. Rev. Lett.*, **73**, 640–643, doi: 10.1103/PhysRevLett.73.640.
19. Firth, W.J. and Scroggie, A.J. (1996) Optical bullet holes: robust controllable localized states of a nonlinear cavity. *Phys. Rev. Lett.*, **76**, 1623–1626, doi: 10.1103/PhysRevLett.76.1623.
20. Coullet, P., Riera, C., and Tresser, C. (2004) A new approach to data storage using localized structures. *Chaos*, **14**, 193–201.
21. Kuszelewicz, R., Barbay, S., Tissoni, G., and Almuneau, G. (2010) Editorial on dissipative optical solitons. *Eur. Phys. J. D*, **59** (1), 1–2.
22. Barbay, S., Kuszelewicz, R., and Tredicce, J. (2011) Cavity solitons in VCSEL devices. *Adv. Opt. Technol.*, **2011**, 628761.
23. Lugiato, L.A., Prati, F., Brambilla, M., Columbo, L., Barland, S., Tissoni, G., Aghdami, K.M., Kheradmand, R., Tajalli, H., and Vahed, H. (2013) Cavity solitons, in *Without Bounds: A Scientific Canvas of Nonlinearity and Complex Dynamics*, Understanding Complex Systems (eds R.G. Rubio, Y.S. Ryazantsev, V.M. Starov, G.X. Huang, A.P. Chetverikov, P. Arena, A.A. Nepomnyashchy, A. Ferrus, and E.G. Morozov), Springer-Verlag, Berlin, Heidelberg, pp. 395–404, doi: 10.1007/978-3-642-34070-3_33.
24. Grabherr, M., Jager, R., Miller, M., Thalmaier, C., Herlein, J., Michalzik, R., and Ebeling, K. (1998) Bottom-emitting VCSEL’s for high-cw optical output power. *IEEE Photonics Technol. Lett.*, **10** (8), 1061–1063, doi: 10.1109/68.701502.
25. Barland, S., Tredicce, J.R., Brambilla, M., Lugiato, L.A., Balle, S., Giudici, M.,

Maggipinto, T., Spinelli, L., Tissoni, G., Knodl, T., Miller, M., and Jager, R. (2002) Cavity solitons as pixels in semiconductor microcavities. *Nature*, **419** (6908), 699–702, doi: 10.1038/nature01049.

26. Hachair, X., Barland, S., Furfaro, L., Giudici, M., Balle, S., Tredicce, J.R., Brambilla, M., Maggipinto, T., Perrini, I., Tissoni, G., and Lugiato, L. (2004) Cavity solitons in broad area VCSELs below threshold. *Phys. Rev. A*, **69**, 043817.
27. Brambilla, M., Lugiato, L.A., Prati, F., Spinelli, L., and Firth, W.J. (1997) Spatial soliton pixels in semiconductor devices. *Phys. Rev. Lett.*, **79** (11), 2042–2045.
28. Spinelli, L., Tissoni, G., Brambilla, M., Prati, F., and Lugiato, L.A. (1998) Spatial solitons in semiconductor microcavities. *Phys. Rev. A*, **58** (3), 2542–2559.
29. Pedaci, F., Barland, S., Caboche, E., Genevet, P., Giudici, M., Tredicce, J.R., Ackemann, T., Scroggie, A.J., Firth, W.J., Oppo, G.L., Tissoni, G., and Jäger, R. (2008) All-optical delay line using semiconductor cavity solitons. *Appl. Phys. Lett.*, **92** (1), 011101, doi: 10.1063/1.2828458.
30. McIntyre, C., Yao, A.M., Oppo, G.L., Prati, F., and Tissoni, G. (2010) All-optical delay line based on a cavity soliton laser with injection. *Phys. Rev. A*, **81** (1), 013 838, doi: 10.1103/PhysRevA.81.013838.
31. Prati, F., Tissoni, G., McIntyre, C., and Oppo, G.L. (2010) Static and dynamic properties of cavity solitons in VCSELs with optical injection. *Eur. Phys. J. D*, **59** (1), 139–147.
32. Tanguy, Y., Ackemann, T., Firth, W.J., and Jäger, R. (2008) Realization of a semiconductor-based cavity soliton laser. *Phys. Rev. Lett.*, **100**, 013 907, doi: 10.1103/PhysRevLett.100.013907.
33. Genevet, P., Barland, S., Giudici, M., and Tredicce, J.R. (2008) Cavity soliton laser based on mutually coupled semiconductor microresonators. *Phys. Rev. Lett.*, **101**, 123 905, doi: 10.1103/PhysRevLett.101.123905.
34. Elsass, T., Gauthron, K., Beaudoin, G., Sagnes, I., Kuszelewicz, R., and Barbay, S. (2010) Control of cavity solitons and dynamical states in a monolithic vertical cavity laser with saturable absorber. *Eur. Phys. J. D*, **59** (1), 91–96, doi: 10.1140/epjd/e2010-00079-6.
35. Vladimirov, A.G., Fedorov, S.V., Kaliteevskii, N.A., Khodova, G.V., and Rosanov, N.N. (1999) Numerical investigation of laser localized structures. *J. Opt. B: Quantum Semiclassical Opt.*, **1** (1), 101–106, doi: 10.1088/1464-4266/1/1/019.
36. Bache, M., Prati, F., Tissoni, G., Kheradmand, R., Lugiato, L., Protsenko, I., and Brambilla, M. (2005) Cavity soliton laser based on VCSEL with saturable absorber. *Appl. Phys. B*, **81** (7), 913–, doi: 10.1007/s00340-005-1997-9.
37. Prati, F., Caccia, P., Tissoni, G., Lugiato, L., Mahmoud Aghdami, K., and Tajalli, H. (2007) Effects of carrier radiative recombination on a VCSEL-based cavity soliton laser. *Appl. Phys. B*, **88** (3), 405, doi: 10.1007/s00340-007-2711-x.
38. Tissoni, G., Aghdami, K., Prati, F., Brambilla, M., and Lugiato, L. (2011) Cavity soliton laser based on a VCSEL with saturable absorber, in *Localized States in Physics: Solitons and Patterns* (eds O. Descalzi, M. Clerc, S. Residori, and G. Assanto), Springer-Verlag, Berlin, Heidelberg, pp. 187–211, doi: 10.1007/978-3-642-16549-8_10.
39. Leo, F., Coen, S., Kockaert, P., Gorza, S., Emplit, P., and Haelterman, M. (2010) Temporal cavity solitons in one-dimensional Kerr media as bits in an all-optical buffer. *Nat. Photonics*, **4** (7), 471–476, doi: 10.1038/nphoton.2010.120.
40. Herr, T., Brasch, V., Jost, J.D., Wang, C.Y., Kondratiev, N.M., Gorodetsky, M.L., and Kippenberg, T.J. (2014) Temporal solitons in optical microresonators. *Nat. Photonics*, **8** (2), 145–152, doi: 10.1038/nphoton.2013.343.
41. Tlidi, M. and Gelens, L. (2010) High-order dispersion stabilizes dark dissipative solitons in all-fiber cavities. *Opt. Lett.*, **35** (3), 306–308, doi: 10.1364/OL.35.000306.

42. Tlidi, M., Bahloul, L., Cherbi, L., Hariz, A., and Coulibaly, S. (2013) Drift of dark cavity solitons in a photonic-crystal fiber resonator. *Phys. Rev. A*, **88**, 035 802, doi: 10.1103/PhysRevA.88.035802.

43. Pedaci, F., Tissoni, G., Barland, S., Giudici, M., and Tredicce, J. (2008) Mapping local defects of extended media using localized structures. *Appl. Phys. Lett.*, **93**, 111 104.

44. Prati, F., Tissoni, G., Lugiato, L.A., Aghdami, K.M., and Brambilla, M. (2010) Spontaneously moving solitons in a cavity soliton laser with circular section. *Eur. Phys. J. D*, **59** (1), 73–79.

45. Wise, F. and Trapani, P.D. (2002) Spatiotemporal solitons. *Opt. Photonics News*, **13** (2), 28–32.

46. Brambilla, M., Maggipinto, T., Patera, G., and Columbo, L. (2004) Cavity light bullets: three-dimensional localized structures in a nonlinear optical resonator. *Phys. Rev. Lett.*, **93** (20), 203 901, http://link.aps.org/abstract/PRL/v93/e203901.

47. Columbo, L., Perrini, I.M., Maggipinto, T., and Brambilla, M. (2006) 3D self-organized patterns in the field profile of a semiconductor resonator. *New J. Phys.*, **8**, 312.

48. Jenkins, S.D., Prati, F., Lugiato, L.A., Columbo, L., and Brambilla, M. (2009) Cavity light bullets in a dispersive Kerr medium. *Phys. Rev. A*, **80** (3), 033 832, doi: 10.1103/PhysRevA.80.033832.

49. Majus, D., Tamošauskas, G., Gražulevičiūtė, I., Garejev, N., Lotti, A., Couairon, A., Faccio, D., and Dubietis, A. (2014) Nature of spatiotemporal light bullets in bulk Kerr media. *Phys. Rev. Lett.*, **112** (19), 193 901.

50. McLeod, R., Wagner, K., and Blair, S. (1995) (3+ 1)-dimensional optical soliton dragging logic. *Phys. Rev. A*, **52** (4), 3254.

51. Minardi, S., Eilenberger, F., Kartashov, Y.V., Szameit, A., Röpke, U., Kobelke, J., Schuster, K., Bartelt, H., Nolte, S., Torner, L. et al. (2010) Three-dimensional light bullets in arrays of waveguides. *Phys. Rev. Lett.*, **105** (26), 263 901.

52. Giacomelli, G. and Politi, A. (1996) Relationship between delayed and spatially extended dynamical systems. *Phys. Rev. Lett.*, **76** (15), 2686.

53. Giacomelli, G., Marino, F., Zaks, M.A., and Yanchuk, S. (2012) Coarsening in a bistable system with long-delayed feedback. *Europhys. Lett.*, **99** (5), 58 005.

54. Genevet, P., Barland, S., Giudici, M., and Tredicce, J.R. (2009) Stationary localized structures and pulsing structures in a cavity soliton laser. *Phys. Rev. A: At. Mol. Opt. Phys.*, **79** (3), 033819, doi: 10.1103/PhysRevA.79.033819.

55. Genevet, P., Turconi, M., Barland, S., Giudici, M., and Tredicce, J.R. (2010) Mutual coherence of laser solitons in coupled semiconductor resonators. *Eur. Phys. J. D*, **59** (1), 109, doi: 10.1140/epjd/e2010-00138-0.

56. Columbo, L., Gil, L., and Genevet, P. (2010) Theoretical description of the transverse localised structures in a face to face VCSEL configuration. *Eur. Phys. J. D*, **59** (1), 97–107, doi: 10.1140/epjd/e2010-00142-4.

57. Tierno, A., Gustave, F., and Barland, S. (2012) Class a mode-locked semiconductor ring laser. *Opt. Lett.*, **37** (11), 2004–2006, http://ol.osa.org/abstract.cfm?URI=ol-37-11-2004.

58. Tierno, A., Barland, S., and Gil, L. (2013) Oscillating directional domains in a ring semiconductor laser. *IEEE J. Sel. Top. Quantum Electron.*, **19** (4), 1800108, doi: 10.1109/JSTQE.2013.2242850.

59. Tanguy, Y., Ackemann, T., Firth, W.J., and Jäger, R. (2008) Realization of a semiconductor-based cavity soliton laser. *Phys. Rev. Lett.*, **100** (1), 013 907, doi: 10.1103/PhysRevLett.100.013907.

60. Tanguy, Y., Radwell, N., Ackemann, T., and Jäger, R. (2008) Characteristics of cavity solitons and drifting excitations in broad-area vertical-cavity surface-emitting lasers with frequency-selective feedback. *Phys. Rev. A*, **78** (2), 023 810, doi: 10.1103/PhysRevA.78.023810.

61. Radwell, N. and Ackemann, T. (2009) Characteristics of laser cavity solitons in a vertical-cavity surface-emitting laser with feedback from a volume bragg grating. *IEEE J. Quantum*

Electron., **45** (11), 1388–1395, doi: 10.1109/JQE.2009.2027134.

62. Vahed, H., Kheradmand, R., Tajalli, H., Tissoni, G., Lugiato, L.A., and Prati, F. (2011) Phase-mediated long-range interactions of cavity solitons in a semiconductor laser with a saturable absorber. *Phys. Rev. A*, **84** (6), 063 814.
63. Ackemann, T., Jimenez, J., Noblet, Y., Radwell, N., Ren, G., Paulau, P., McIntyre, C., Oppo, G., Toomey, J., and Kane, D. (2015) Dynamics and interactions of laser cavity solitons in broad-area semiconductor lasers, in *Nonlinear Optical Cavity Dynamics* (ed. P. Grelu), Wiley-VCH Verlag GmbH.
64. Grelu, P., Belhache, F., Gutty, F., and Soto-Crespo, J.M. (2002) Phase-locked soliton pairs in a stretched-pulse fiber laser. *Opt. Lett.*, **27** (11), 966–968.
65. Akhmediev, N., Soto-Crespo, J., Grapinet, M., and Grelu, P. (2005) Dissipative soliton interactions inside a fiber laser cavity. *Opt. Fiber Technol.*, **11** (3), 209–228.
66. Rosanov, N. and Fedorov, S. (1992) Diffraction switching waves and autosolitons in a laser with saturable absorption. *Opt. Spectrosc.*, **72**, 782.
67. McSloy, J.M., Firth, W.J., Harkness, G.K., and Oppo, G.L. (2002) Computationally determined existence and stability of transverse structures. II. Multipeaked cavity solitons. *Phys. Rev. E*, **66** (4), 046 606.
68. Burke, J. and Knobloch, E. (2007) Homoclinic snaking: structure and stability. *Chaos*, **17** (3), 037102.
69. Genevet, P., Columbo, L., Barland, S., Giudici, M., Gil, L., and Tredicce, J.R. (2010) Multistable monochromatic laser solitons. *Phys. Rev. A*, **81** (5), 053 839, doi: 10.1103/PhysRevA.81.053839.
70. Mahmoud Aghdami, K., Prati, F., Caccia, P., Tissoni, G., Lugiato, L., Kheradmand, R., and Tajalli, H. (2008) Comparison of different switching techniques in a cavity soliton laser. *Eur. Phys. J. D*, **47** (3), 447, doi: 10.1140/epjd/e2008-00069-3.
71. Turconi, M., Giudici, M., and Barland, S. (2014) Response of laser-localized structures to external perturbations in coupled semiconductor microcavities. *Philos. Trans. R. Soc. London, Ser. A*, **372** (2027), 20140 004.
72. Desyatnikov, A.S., Kivshar, Y.S., and Torner, L. (2005) Optical vortices and vortex solitons. *Prog. Opt.*, **47**, 219–319.
73. Genevet, P., Barland, S., Giudici, M., and Tredicce, J.R. (2010) Bistable and addressable localized vortices in semiconductor lasers. *Phys. Rev. Lett.*, **104**, 223 902, doi: 10.1103/PhysRevLett.104.223902.
74. Turconi, M., Giudici, M., and Barland, S. (2013) Drift-induced excitable localized states. *Phys. Rev. Lett.*, **111** (23), 233 901, doi: 10.1103/PhysRevLett.111.233901.
75. Parra-Rivas, P., Gomila, D., Matías, M.A., and Colet, P. (2013) Dissipative soliton excitability induced by spatial inhomogeneities and drift. *Phys. Rev. Lett.*, **110** (6), 064 103, doi: 10.1103/PhysRevLett.110.064103.
76. Vahed, H., Prati, F., Turconi, M., Barland, S., and Tissoni, G. (2014) Periodic and chaotic solitons in a semiconductor laser with saturable absorber. *Philos. Trans. R. Soc. London, Ser. A*, **372** (2027), 20140 016.
77. Haus, H.A. (2000) Mode-locking of lasers. *IEEE J. Sel. Top. Quantum Electron.*, **6**, 1173–1185.
78. Gordon, A. and Fischer, B. (2002) Phase transition theory of many-mode ordering and pulse formation in lasers. *Phys. Rev. Lett.*, **89**, 103-901–3.
79. Grelu, P. and Akhmediev, N. (2012) Dissipative solitons for mode-locked lasers. *Nat. Photonics*, **6** (2), 84–92, doi: 10.1038/nphoton.2011.345.
80. Lederer, M.J., Luther-Davies, B., Tan, H.H., Jagadish, C., Akhmediev, N.N., and Soto-Crespo, J.M. (1999) Multipulse operation of a ti:sapphire laser mode locked by an ion-implanted semiconductor saturable-absorber mirror. *J. Opt. Soc. Am. B*, **16** (6), 895–904, doi: 10.1364/JOSAB.16.000895.
81. New, G. (1974) Pulse evolution in mode-locked quasi-continuous lasers. *IEEE J. Quantum Electron.*, **10** (2), 115–124, doi: 10.1109/JQE.1974.1145781.

82. Tang, D., Man, W., and Tam, H. (1999) Stimulated soliton pulse formation and its mechanism in a passively mode-locked fibre soliton laser. *Opt. Commun.*, **165** (4), 189–194.
83. Moores, J., Hall, K., LePage, S., Rauschenbach, K., Wong, W., Haus, H., and Ippen, E. (1995) 20-GHz optical storage loop/laser using amplitude modulation, filtering, and artificial fast saturable absorption. *IEEE Photonics Technol. Lett.*, **7** (9), 1096–1098.
84. Moores, J.D., Wong, W.S., and Haus, H.A. (1994) Stability and timing maintenance in soliton transmission and storage rings. *Opt. Commun.*, **113** (1), 153–175.
85. Haus, H.A. (1975) Theory of mode locking with a fast saturable absorber. *J. Appl. Phys.*, **46**, 3049–3058.
86. Haus, H.A. (1975) Theory of mode locking with a slow saturable absorber. *IEEE J. Quantum Electron.*, **11**, 736–746.
87. Vladimirov, A.G. and Turaev, D. (2005) Model for passive mode locking in semiconductor lasers. *Phys. Rev. A*, **72**, 033 808, doi: 10.1103/PhysRevA.72.033808.
88. Marconi, M., Javaloyes, J., Balle, S., and Giudici, M. (2014) How lasing localized structures evolve out of passive mode locking. *Phys. Rev. Lett.*, **112** (22), 223 901.
89. Marconi, M., Javaloyes, J., Balle, S., and Giudici, M. (2015) Passive mode-locking and tilted waves in broad-area vertical-cavity surface-emitting lasers. *IEEE J. Sel. Top. Quantum Electron.*, **21** (1), 1–9, doi: 10.1109/JSTQE.2014.2346614.
90. Nozaki, K. and Bekki, N. (1984) Solitons as attractors of a forced dissipative nonlinear Schrödinger equation. *Phys. Lett. A*, **102** (9), 383–386, doi: 10.1016/0375-9601(84)91060-0.
91. Haudin, F., Elías, R.G., Rojas, R.G., Bortolozzo, U., Clerc, M.G., and Residori, S. (2009) Driven front propagation in 1d spatially periodic media. *Phys. Rev. Lett.*, **103** (12), 128 003, doi: 10.1103/PhysRevLett.103.128003.
92. Haudin, F., Elías, R.G., Rojas, R.G., Bortolozzo, U., Clerc, M.G., and Residori, S. (2010) Front dynamics and pinning–depinning phenomenon in spatially periodic media. *Phys. Rev. E*, **81** (5), 056 203.
93. Haudin, F., Rojas, R.G., Bortolozzo, U., Residori, S., and Clerc, M.G. (2011) Homoclinic snaking of localized patterns in a spatially forced system. *Phys. Rev. Lett.*, **107** (26), 264 101.
94. Barbay, S., Hachair, X., Elsass, T., Sagnes, I., and Kuszelewicz, R. (2008) Homoclinic snaking in a semiconductor-based optical system. *Phys. Rev. Lett.*, **101** (25), 253 902, doi: 10.1103/PhysRevLett.101.253902.
95. Giacomelli, G., Meucci, R., Politi, A., and Arecchi, F.T. (1994) Defects and spacelike properties of delayed dynamical systems. *Phys. Rev. Lett.*, **73** (8), 1099–1102, doi: 10.1103/PhysRevLett.73.1099.
96. Marino, F., Giacomelli, G., and Barland, S. (2014) Front pinning and localized states analogues in long-delayed bistable systems. *Phys. Rev. Lett.*, **112** (10), 103 901, doi: 10.1103/PhysRevLett.112.103901.
97. Ackemann, T. and Sondermann, M. (2001) Characteristics of polarization switching from the low to the high frequency mode in vertical-cavity surface-emitting lasers. *Appl. Phys. Lett.*, **78** (23), 3574–3576.
98. Barton, D.A., Krauskopf, B., and Wilson, R.E. (2007) Homoclinic bifurcations in a neutral delay model of a transmission line oscillator. *Nonlinearity*, **20** (4), 809.
99. Yanchuk, S. and Giacomelli, G. (2014) Pattern formation in systems with multiple delayed feedbacks. *Phys. Rev. Lett.*, **112** (17), 174 103, doi: 10.1103/PhysRevLett.112.174103.
100. Gustave, F., Columbo, L., Giudici, M., Mouane, O., Brambilla, M., Prati, F., Tissoni, G., Kelleher, B., Tykalewicz, B., and Barland, S. (2014) Topological dissipative solitons in semiconductor lasers, in *Advanced Photonics*, Optical Society of America, p. 2, doi: 10.1364/NP.2014.NM2A.1.
101. Gustave, F., Columbo, L., Tissoni, G., Brambilla, M., Prati, F., Kelleher, B., Tykalewicz, B., and Barland, S. (2015)

Dissipative phase solitons in semiconductor lasers. *Phys. Rev. Lett.*, **115**, 043902.

102. Hodgkin, A.L., Huxley, A.F., and Katz, B. (1952) Measurement of current–voltage relations in the membrane of the giant axon of loligo. *J. Physiol.*, **116** (4), 424.
103. Izhikevich, E.M. (2006) *Dynamical Systems in Neuroscience*, MIT Press.
104. Plaza, F., Velarde, M.G., Arecchi, F.T., Boccaletti, S., Ciofini, M., and Meucci, R. (1997) Excitability following an avalanche-collapse process. *Europhys. Lett.*, **38** (2), 85, http://stacks.iop.org/0295-5075/38/i=2/a=085.
105. Giudici, M., Green, C., Giacomelli, G., Nespolo, U., and Tredicce, J.R. (1997) Andronov bifurcation and excitability in semiconductor lasers with optical feedback. *Phys. Rev. E*, **55**, 6414.
106. Barland, S., Piro, O., Giudici, M., Tredicce, J.R., and Balle, S. (2003) Experimental evidence of van der Pol–Fitzugh–Nagumo dynamics in semiconductor optical amplifiers. *Phys. Rev. E*, **68**, 036 209.
107. Coullet, P., Daboussy, D., and Tredicce, J.R. (1998) Optical excitable waves. *Phys. Rev. E*, **58** (5), 5347–5350.
108. Adler, R. (1946) A study of locking phenomena in oscillators. *Proc. IRE*, **34** (6), 351–357.
109. Goulding, D., Hegarty, S.P., Rasskazov, O., Melnik, S., Hartnett, M., Greene, G., McInerney, J.G., Rachinskii, D., and Huyet, G. (2007) Excitability in a quantum dot semiconductor laser with optical injection. *Phys. Rev. Lett.*, **98** (15), 153 903, doi: 10.1103/PhysRevLett.98.153903.
110. Kelleher, B., Goulding, D., Baselga Pascual, B., Hegarty, S.P., and Huyet, G. (2010) Phasor plots in optical injection experiments. *Eur. Phys. J. D*, **58** (2), 175–179, doi: 10.1140/epjd/e2010-00063-2.
111. Turconi, M., Garbin, B., Feyereisen, M., Giudici, M., and Barland, S. (2013) Control of excitable pulses in an injection-locked semiconductor laser. *Phys. Rev. E*, **88** (2), 022 923.
112. Garbin, B., Turconi, M., Giudici, M., Tissoni, G., Feyereisen, M., and Barland, S. (2013) Control of excitable pulses in a laser with optical injection. Laser Dynamics and Nonlinear Photonics, 2013 6th" Rio De La Plata" Workshop on, pp. 1–3.
113. Garbin, B., Goulding, D., Hegarty, S.P., Huyet, G., Kelleher, B., and Barland, S. (2014) Incoherent optical triggering of excitable pulses in an injection-locked semiconductor laser. *Opt. Lett.*, **39** (5), 1254–1257, doi: 10.1364/OL.39.001254.
114. Pedaci, F., Huang, Z., van Oene, M., Barland, S., and Dekker, N.H. (2010) Excitable particles in an optical torque wrench. *Nat. Phys.*, **7** (3), 259–264, doi: 10.1038/nphys1862.
115. Garbin, B., Javaloyes, J., Tissoni, G., and Barland, S. (2014) Topological solitons as addressable phase bits in a driven laser. arXiv preprint arXiv:1409.6350.
116. Pérez-Serrano, A., Javaloyes, J., and Balle, S. (2011) Longitudinal mode multistability in Ring and Fabry-Pérot lasers: the effect of spatial hole burning. *Opt. Express*, **19** (4), 3284–3289, doi: 10.1364/OE.19.003284.
117. Lehoucq, R. and Sorensen, D. (1996) Deflation techniques for an implicitly restarted Arnoldi iteration. *SIAM J. Matrix Anal. Appl.*, **17** (4), 789–821, doi: 10.1137/S0895479895281484.
118. Longhi, S. (1998) Nonlinear travelling pulses in laser injection locking. *Quantum Semiclassical Opt.*, **10** (4), 617–635, doi: 10.1088/1355-5111/10/4/005.

5

Dynamics of Dissipative Solitons in Presence of Inhomogeneities and Drift

Pedro Parra-Rivas, Damià Gomila, Lendert Gelens, Manuel A. Matías, and Pere Colet

5.1

Introduction

Nonlinear spatially extended systems can self-organize in response to external driving, leading to the formation of spatial structures. Those structures can extend over the whole spatial domain, but can also be localized in space. This is an emergent phenomenon and the properties of the resulting patterns are universal and independent of the microscopic details of the system. The field of pattern formation in extended systems driven out of equilibrium has attracted a lot of interest over the years, see [1, 2].

Recently, it has also been shown that the equations describing cavity configurations [3–6] or delayed systems [7–9] with no transverse degrees of freedom in nonlinear optics can be recast to partial differential equations equivalent to those used to study one dimensional spatially extended systems. In this case, the spatial coordinate is replaced by a fast time scale, and a second slow time scale plays the role of the usual time describing the evolution of the field. Often, the resulting partial differential equation is of complex Ginzburg–Landau type [3, 7, 8, 10], showing typical pattern formation phenomena.

Particularly interesting is the formation of localized structures, known in this context as cavity solitons (CSs) or dissipative solitons (DSs). These DSs are spots of higher or lower field intensity than their stable homogeneous background. As coherent structures, DSs have emergent dynamical properties. For instance, regardless of their physical origin, they all move following the same law under the action of gradients, they all interact with each other following a potential characterized by the shape of their tails, they can be created by localized perturbations over a certain threshold, and so on. Sometimes understanding these general dynamical properties of DSs provides a better insight into the behavior of the system under study than focusing on the microscopic details that give rise to the formation of the DSs.

In this chapter, we explain precisely how DSs behave under the action of a drift and when interacting with an inhomogeneity of the medium. The interplay between these two ingredients induces dynamical regimes, such as oscillations

Nonlinear Optical Cavity Dynamics: From Microresonators to Fiber Lasers, First Edition.
Edited by Philippe Grelu.
© 2016 Wiley-VCH Verlag GmbH & Co. KGaA. Published 2016 by Wiley-VCH Verlag GmbH & Co. KGaA.

and excitable behavior, in which the structure of DSs is preserved [1]. The effects of inhomogeneities and drift are present in many optical, chemical, and fluid systems. On the one hand, in optical systems, the drift can be produced by misalignments of mirrors [11, 12], nonlinear crystal birefringence [13, 14], parameter gradients [15], or by the effects of high orders of light dispersion [16]. Inhomogeneities, on the other hand, can originate from imperfections in the mirrors of an optical cavity, or be generated by bubbles of a material with different absorption coefficient or refraction in optical fibers [17].

The chapter is organized as follows: in Section 5.2, we present the general theory about how different DS dynamics are induced by inhomogeneities and drift. For this purpose, we use the prototypical Swift–Hohenberg equation (SHE) [18]. In Section 5.3, we report on the mechanism that leads to excitable dynamics. Later, in Section 5.4, we discuss the modeling of fiber cavities in terms of the Lugiato–Lefever model. In Section 5.5, we then discuss the effect of periodic pumping in ring cavities, and in Section 5.6, we compare the the general results from Sections 5.2 and 5.3 with those obtained for the Lugiato–Lefever model to describe fiber cavities and microresonators. Finally, a summary of the chapter is given in Section 5.7.

5.2
General Theory: Swift–Hohenberg Equation with Inhomogeneities and Drift

We start our analysis considering the prototypical SHE. This is a generic amplitude equation describing pattern formation close to a Turing instability in a large variety of systems [2]. For a real field u in one spatial dimension, the SHE can be written as

$$\partial_t u = -(\partial_x^2 + k_0^2)^2 u + ru + au^2 - u^3, \tag{5.1}$$

where k_0 is a characteristic wave number of the system, and r and a are the linear and nonlinear growth rates. For systems with periodic boundary conditions, Eq. (5.1) has gradient dynamics, meaning that the equation can be written as

$$\partial_t u = -\delta_u F, \tag{5.2}$$

where $\delta_u F$ is the functional derivative of the Lyapunov functional F given by

$$F = \int_0^L dx \left(-\frac{1}{2} ru^2 + \frac{1}{2} \left(\left(\partial_x^2 + k_0^2 \right) u \right)^2 - \frac{1}{3} au^3 + \frac{1}{4} u^4 \right), \tag{5.3}$$

with L being the size of the system. Along any trajectory $u(x, t)$, the Lyapunov potential F decreases until reaching a local minimum, that is, a steady state. As a consequence, Hopf bifurcations are not allowed and, therefore, the system cannot display dynamical regimes.

The homogeneous steady states (HSSs) of the SHE are $u_s = 0$, and $u_s = \frac{1}{2g} \left(a \pm \sqrt{a^2 + 4g(r - k_0^4)} \right)$. The linear stability analysis of the HSSs under the effect of finite wavelength perturbations

$$u(x,t) = u_s + \epsilon \exp\ (\Gamma t + ikx), \tag{5.4}$$

leads to the dispersion relation

$$\Gamma(k) = r + 2au_s - 3u_s^2 - (k_0^2 - k^2)^2. \tag{5.5}$$

HSSs undergo a Turing instability if the maximum $\Gamma(k)$ becomes positive when varying the parameter r. The critical value of k at which that happens will be labeled as k_c. The zero HSS $u_s = 0$ becomes first Turing unstable at $r = 0$ for perturbations with critical wave number $k_c = \pm k_0$. For $a < \sqrt{27/38}$, this instability leads to a supercritical pattern, while for $a > \sqrt{27/38}$ the pattern emerges subcritically [19]. For $r > 0$, the zero HSS is unstable to perturbations whose wave number is within two ranges, one centered at k_0 and the other at $-k_0$. The two ranges are larger as r increases and at $r = k_0^4$ they merge forming a single broad instability range that includes $k = 0$. Therefore, for $r \geq k_0^4$ the zero HSS is also unstable to homogeneous perturbations.

For $a < \sqrt{27/38}$, together with the subcritical pattern, two sets of DSs, one with even and one with odd number of peaks, unfold from the $r = 0$ bifurcation point forming what is known as homoclinic snaking [19]. Since the SHE is invariant under translations there is no preferred spatial location for DSs, they can be formed anywhere and are neutrally stable against perturbations that push them in any direction. In order to satisfy the condition for subcriticality in what follows, we assume $a = 1.2$. We also set the value $k_0^2 = 0.5$.

We now proceed to analyze the different dynamics that appear when spatial inhomogeneities and drift are involved. We model the drift by a gradient term $c\partial_x$, being c the drift strength, and the spatial inhomogeneity $b(x)$ by a single Gaussian profile of height h, and half-width σ located at x_0, typically in the center of the system,

$$b(x) = h \exp\ \left(-\left(\frac{x - x_0}{\sigma} \right)^2 \right). \tag{5.6}$$

Moreover, we will consider that the gain of the system is limited to a finite spatial region such that any DS that travels to the boundary is absorbed and disappears. More precisely, we use a super-Gaussian gain profile, given by

$$r(x) = r_0 - 1 + \exp\ \left(-\left(\frac{x - x_0}{\epsilon} \right)^{18} \right), \tag{5.7}$$

so that the system has an effective size $L = 2\epsilon$. Adding those elements, we have

$$\partial_t u = ru + au^2 - u^3 - (\partial_x^2 + k_0^2)^2 u - c\partial_x u. \tag{5.8}$$

The gain profile $r(x)$ has a flat maximum at x_0 where it takes the value r_0. Here, we assume $r_0 = -0.2$ within the region of existence of DSs. We also consider $\epsilon = 94.0842$ and choose $\sigma = 2.045$ (roughly half the width of a DS) so that only DSs with a single maximum are triggered. In what follows, the drift strength c and the strength of the inhomogeneity h are the control parameters of the system.

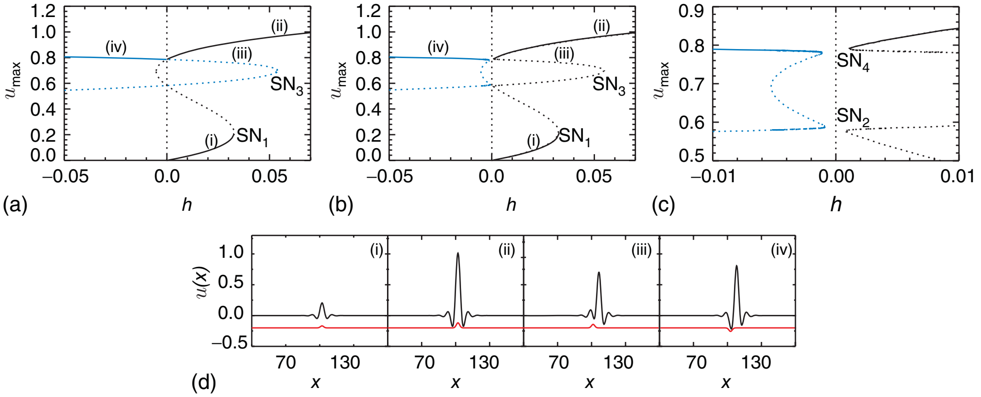

Figure 5.1 (a) Bifurcation diagram showing the maximum of the steady state as a function of h for $c = 0$. (b) Bifurcation diagram when the reflection symmetry is weakly broken, for $c = 0.0015$. (c) Zoom of (b) showing the reconnection of the branches. (d) Main solutions corresponding to the labels in (a).

We first consider the presence of a spatial inhomogeneity without drift ($c = 0$ and $h \neq 0$). The spatial inhomogeneity breaks the translational invariance of the system and, as a consequence, the DSs are now pinned at a fixed location given by the inhomogeneity. Despite the fact that the translational invariance is broken, the system still has a reflection symmetry around the center of the inhomogeneity, x_0. Figure 5.1a shows the bifurcation diagram of the DSs. In this diagram, we plot the maximum value of the field, $u_{\max}$, as a function of the control parameter h. Each branch corresponds to a different type of steady-state solution of the system whose spatial profile is shown in Figure 5.1d. The steady states (i), (ii), and (iv) are the main attractors of the system. They correspond to the fundamental solution (a low bump corresponding to the deformation of the trivial solution), a high amplitude DS pinned at its center, and a DS pinned in the first oscillation of its tail, respectively. For completeness and because it will prove to be useful in the following sections, we also show the spatial profile of the unstable solution corresponding to the branch label with (iii). Due to the translational symmetry breaking, a transcritical bifurcation takes place at $h = 0$, where branches (ii) and (iv) interchange their stability. Physically, for $h > 0$ the spatial inhomogeneity corresponds to a bump, while for $h < 0$ it is a hole. DSs tend to sit at the inhomogeneity maximum; thus, for $h > 0$ DSs are centered at the hole. Decreasing h, at $h = 0$, this location becomes unstable, and for $h < 0$, the DS shifts its position until the hole coincides with the first minimum of its tail. Branch (iv) corresponds to pinned DSs whose maximum is at the right of the defect. There is also a degenerated branch with the maximum at the left.

When both inhomogeneity and drift are taken into account ($c \neq 0$ and $h \neq 0$), the reflection symmetry around x_0 is broken and the pinned state experiences a force in the direction of the drift. The competition between the inhomogeneity pinning the DS to a fixed position and the drift trying to pull it out leads to the appearance of a very rich dynamical scenario as it was shown in [18]. Resulting from the breaking of the reflection symmetry, the bifurcation diagram is modified as shown in Figure 5.1b for a weak symmetry breaking. As a result, the transcritical bifurcations become imperfect so that the branches at negative values of h split from the ones at positive values of h. Each transcritical bifurcation leads to two saddle-node bifurcations, one at each side of $h = 0$, which reconnect the branches of the corresponding side, as can be seen in Figure 5.1b, and more in detail in the zoom displayed in panel (c) of the same figure. In what follows, we focus on the part of the parameter space corresponding to $h > 0$. Saddle-node bifurcations SN_1 and SN_3 are already present for $c = 0$. Saddle-node bifurcations SN_2 and SN_4 are born for $c \neq 0$ from the transcritical bifurcations involving, respectively, the middle and upper branches in Figure 5.1a.

As c increases, SN_2 and SN_4 move away from $h = 0$. The overall bifurcation diagram stretches as shown in Figure 5.2a for $c = 0.05$. In fact, for that value of c, the saddle-node bifurcation SN_4 has already encountered a saddle-node separatrix-loop codimension 2 bifurcation after which it has become a saddle-node on the invariant circle (SNIC) bifurcation [18]. As a consequence, branches (ii) and (iii) are now reconnected via this SNIC bifurcation in which a cycle consisting of the periodic emission of DS from the inhomogeneity is created. This emission generates a sequence of equal-spaced drifted solitons called train of solitons [18]. This train of solitons is shown in Figure 5.3 for $c = 0.12$. Already for that value, SN_1 and SN_2 have collided in a cusp bifurcation and a Hopf bifurcation appears subcritically (see Figure 5.2b). We denote this bifurcation as H^+, where the symbol + stands for the subcritical character of the bifurcation [18]. In region I, one encounters only the fundamental solution. In region II, one has trains of solitons while the fundamental solution is unstable. In region V, there is coexistence of the fundamental solutions and trains of solitons. Finally, in regions III and IV, one encounters pinned DSs.

For larger values of c, the SNIC becomes a saddle-node out of the circle and another Hopf bifurcation appears, this time supercritically, labeled as H^-. Just after that, SN_3 and the new saddle-node disappear into another cusp bifurcation and a single monotonic branch of steady-state solutions remains as we can see in Figure 5.2c. From H^-, a stable limit cycle appears whose amplitude is plotted using + symbols. Within region II, for values of h under H^- but close to the bifurcation, the spatial inhomogeneity is large enough to prevent the advection of DSs, but small-amplitude oscillations of the DSs appear. When the value of h decreases, the effect of the advection becomes more important, generating a train of solitons that, when considering nonperiodic boundary conditions, disappear at the boundary of the system. The transition between both types of oscillatory regimes happens drastically through what it is called a canard explosion [18]. The trains of solitons cycle is stable all the way to a fold of cycle (FC) bifurcation, where it becomes unstable and disappear in H^+.

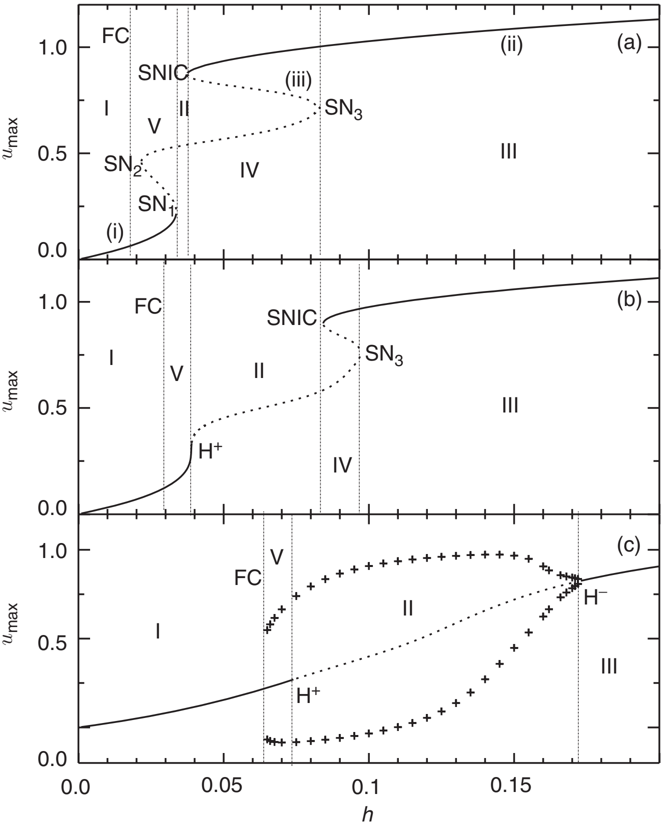

Figure 5.2 Bifurcation diagram as Figure 5.1 for (a) $c = 0.05$, (b) $c = 0.12$, and (c) $c = 0.4$. In (c), the crosses indicate the maximum and minimum values of the oscillatory DS at a given spatial location.

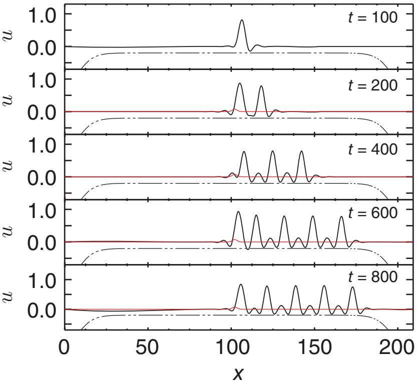

Figure 5.3 Train of solitons for $c = 0.12$ and $h = 0.075$, corresponding to the oscillatory region in Figure 5.2b.

5.3
Excitability Regimes

One of the most interesting aspects of this bifurcation scenario is that this pinning–depinning competition can lead to excitable behavior [20]. A system is said to be excitable if starting from a steady-state solution, perturbations below a certain threshold decay exponentially, while perturbations above this threshold induce a large response before going back to the steady state. Therefore, a threshold for the perturbations is one of the key ingredients in order to have excitability. The other ingredient is a reinjection mechanism in the phase space that allows the system to go back to the initial resting state. Here, that reinjection mechanism is provided by the drift and the boundary conditions are defined by the supergaussian (Eq. (5.7)).

In general, the presence of excitability is related with the emergence or disappearance of a limit cycle. In the literature, it is common to find a classification of the excitability depending on whether there is a divergence of the period of the cycle involved in the dynamics [21]. It is said that the excitability is of type I if the period diverges close to the bifurcation leading to the creation or destruction of the limit cycle, and of type II if the period remains finite when approaching the bifurcation. We discuss briefly these two kinds of bifurcations before showing the results for the system considered here.

Type I excitability is associated with two specific bifurcations, the saddle-loop (SL) and the SNIC. Both bifurcations involve a saddle, the stable manifold of which signals the threshold beyond which perturbations trigger an excitable excursion of the system [22]. At the SNIC, a saddle and a stable node located on top of a limit cycle collide and disappear, leading to an oscillatory behavior. Before the collision, the dynamics of the system is excitable. Although this bifurcation is local in (one-dimensional) flows on the circle, it has global characteristics in higher dimensional dynamical systems, so it is also termed as local–global bifurcation [23]. At the SL, also known as homoclinic bifurcation, a limit cycle collides with a saddle [23]; thus, this is a global bifurcation. Before the collision, the system has an oscillatory behavior. After the collision, the limit cycle is no longer present but its remnants determine the shape of the excitable excursions in phase space.

Approaching the SNIC or the SL from the oscillatory dynamics, the period of the cycle diverges, but it does so following different laws. For the SNIC, the divergence follows a power law [23]

$$T \propto (h - h_{\mathrm{SNIC}})^{-1/2}, \tag{5.9}$$

while for an SL the divergence is logarithmic [23, 24]

$$T \propto -\frac{1}{\lambda_1} \ln\,(h - h_{\mathrm{SL}}), \tag{5.10}$$

where λ_1 is the eigenvalue of the unstable localized eigenvector of the saddle [25]. One of the main differences between those two scaling laws is that the SNIC-mediated excitability is easier to observe than the SL one, because the inverse square-root scaling law occurs in a broader parameter range.

Type II excitability requires the presence of a suitable Hopf bifurcation nearby in parameter space. In this case, there is no saddle involved in the bifurcation and, therefore, there is no manifold that plays the role of threshold. In fact, the threshold is not precisely defined and it is referred to as a quasi-threshold [21]. For this kind of excitability, the period of the oscillations remains practically constant as one approaches the point where such oscillations are created or destroyed. The Hopf bifurcation leading to type II excitability can take place in two different ways, a subcritical Hopf bifurcation as H^+ or a supercritical Hopf as H^- followed by a canard explosion.

In our case, the DS will display excitability when the parameter values are such that the DS finds itself in regions I, III, and IV. In these regions, there is a stable steady state and by applying a sufficiently large perturbation, the system can be brought momentarily into the oscillatory region II. In this way, an excitable excursion exploring one loop of the cycle is triggered before returning to the original steady state. The perturbation can be induced by either suddenly changing the state of the system or by means of a transient parameter change [21]. Here, we consider transient parameter changes since they are typically easier to implement experimentally. We apply a perturbation in h for a short time in such a way that we modify the height of the spatial inhomogeneity for a short time. This can be done by just redefining the profile

$$b(x,t) = (h + \Delta h H(t,t_0))\exp\left(-\left(\frac{\mathrm{x}-\mathrm{x}_0}{\sigma}\right)^2\right), \tag{5.11}$$

with the step function $H(t, t_0)$ defined as

$$H(t,t_0) = \begin{cases} 1 & \text{if } 0 < t < t_0, \\ 0 & \text{if } t > t_0 \end{cases}.$$

For low values of c, type-I excitability is found close to the SNIC bifurcation such as the one appearing in Figure 5.2b. For high-amplitude pinned DSs arising for parameter values in region IV, a superthreshold perturbation that brings the system momentarily below the SNIC into region II triggers the unpinning of a DS leading to an excitable excursion. This excursion is shown in Figure 5.4a. The initial state corresponds to the parameters $c = 0.12$ and $h = 0.085$. Here, we apply a perturbation $\Delta h = -0.03$ in h during the time $\Delta t = 40$ that brings the system into the oscillatory regime. This perturbation is not enough to trigger a complete cycle but it does trigger the DS to be pulled out of the finite size domain due to the advection, such that the system goes back to the initial state. The divergence of the period of oscillations close to SNIC can be seen in Figure 5.5b.

For large values of c, type-II excitability can be found close to the Hopf bifurcations. One of the possible routes to excitability is related with the supercritical Hopf bifurcation H^- in the presence of a canard explosion. This is the case for the bifurcation diagram shown in Figure 5.2c. On the left of H^-, but very close to it, DSs exhibit small amplitude oscillations. However, moving further away from H^-, the inhomogeneity serves as a source of DSs, through a canard explosion, leading to a train of DSs [26]. This excursion is shown in Figure 5.4b.

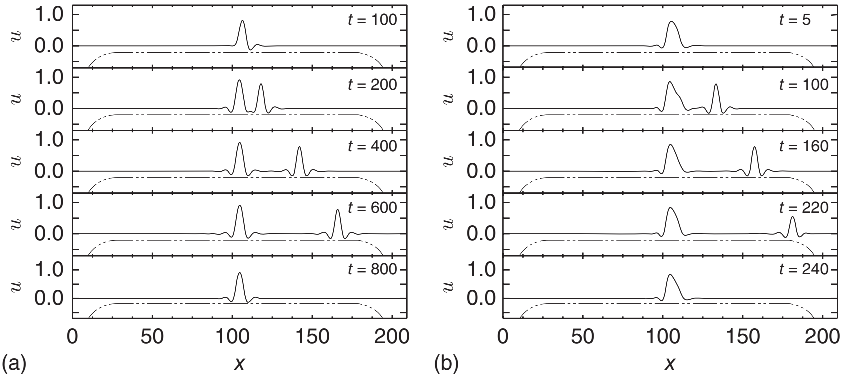

Figure 5.4 Excitable excursions of DSs. (a) A type-I excitable excursion for system parameters in region IV close to the SNIC bifurcation, $c = 0.12$ and $h = 0.085$ (see Figure 5.2b). (b) A type-II excitable excursion for system parameters in region III close to H^-, $c = 0.4$ and $h = 0.177$ (see Figure 5.2c). The parameters of the perturbation were $\Delta h = -0.03$ and $\Delta t = 40$.

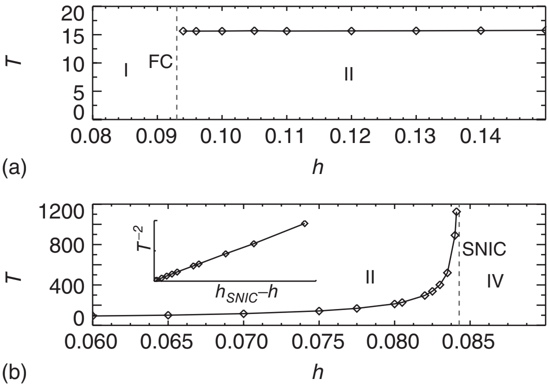

Figure 5.5 Scaling of the period for type II (a) at $c = 0.6$, and type I (b) at $c = 0.12$ excitability.

Excitability mediated by H^+ differs from the cases already discussed by the fact that here the initial and final states are not a high-amplitude DSs, but rather low bump solutions (the fundamental solution). This excitable excursion is shown in Figure 5.6 for $c = 0.6$ for which the shape of the bifurcation diagram is somehow similar to that shown in Figure 5.2c for $c = 0.4$. A superthreshold perturbation of the fundamental solution found for parameters in region I that brings momentarily the system into the oscillatory region II grows to generate a DS. The DS is then advected away and the system goes back to the resting state, namely to the fundamental solution. Approaching the threshold from the oscillatory side, the period of the oscillations remains practically constant as shown in Figure 5.5a. The concept of a quasi-threshold can be understood by looking at this specific case. If one

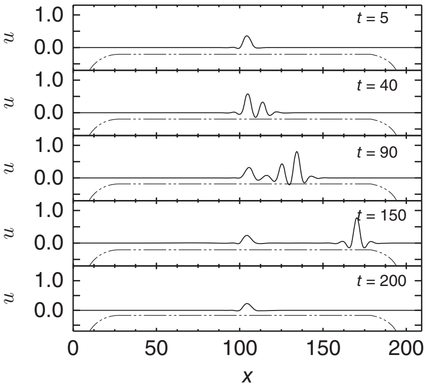

Figure 5.6 Excitable excursion of the fundamental solution in region I, close to the FC ($c = 0.6, h = 0.085$).

applies a perturbation that crosses FC but not H^+, the system will find itself in region V where there is bistability. The best way to avoid this situation is to consider system parameters for which the FC and the H^+ take place at close parameter values so that region V is small. For $c = 0.4$, as shown in Figure 5.2c, region V has still a substantial size. As c is increased region V narrows, and for $c = 0.6$, it is narrow enough so that if h is close to H^+ this kind of excitable excursions can be easily triggered as shown in Figure 5.6. Actually, the system is excitable even for $h = 0$, although in this case, very large perturbations are required.

5.4
Fiber Cavities and Microresonators: The Lugiato–Lefever model

In nonlinear optical cavities, DSs are known as CSs. More specifically, in fiber cavities and microresonators, they are temporal CSs. The interest in those structures has increased in the recent years. One of the main reasons is the recent discovery of the duality between temporal CSs and Kerr frequency combs (KFCs) in microresonators [4, 5, 27]. This duality allows us to understand the properties of Kerr combs through the study of temporal CSs [16, 28]. CSs have been observed experimentally in fiber cavity resonators where complex dynamical behavior has been found [29].

From a theoretical point of view, fiber cavities and microresonators can be described by the well-known Lugiato–Lefever equation [30]. Because the derivation is very similar for both systems, here we focus on a fiber cavity similar to the one shown in Figure 5.7a. The system consists of a fiber loop of length L, and a beam splitter with reflection and transmission coefficients R and T, respectively. The beam splitter is pumped by a continuous wave (CW) electromagnetic field of amplitude E_0 and frequency ω_0. We define the round-trip t_R of the cavity by $t_R = L/c$, where c is the speed of light in the fiber.

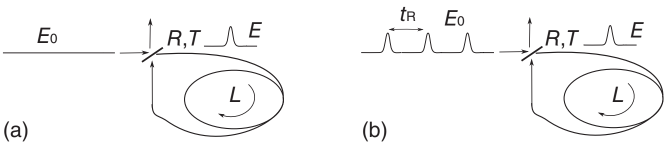

Figure 5.7 (a) A ring fiber cavity pumped by a continuous wave (CW) of frequency ω_0. (b) The same cavity but now pumped synchronously by pulses with a frequency $1/t_R$. Here, R and T are the reflection and transmission coefficients of the beam splitter, respectively. L is the length of the fiber and t_R is the round-trip time of the cavity.

Considering that the electromagnetic field propagates in a single spatial mode and maintains its polarization, we can disregard the transverse dependence and describe the dynamics in terms of a scalar field that depends only on the longitudinal coordinate along the ring axis z and the time s. Expanding in a Taylor series the propagation constant $\beta(\omega)$ about the center frequency of the driving field ω_0, we have

$$\beta(\omega) = \beta(\omega_0) + \beta_1(\omega - \omega_0) + \frac{1}{2}\beta_2(\omega - \omega_0)^2 + \mathcal{O}(3), \tag{5.12}$$

where β_k is the dispersion coefficient of order k,

$$\beta_k = \left.\frac{d^k\beta}{d\omega^k}\right|_{\omega=\omega_0}. \tag{5.13}$$

Neglecting the effect of third and higher-order dispersion, that is, $\beta_k = 0$ for $k \geq 3$ [31–33] and considering a change of variable to the moving reference frame at group velocity β_1^{-1} given by $\tau = s - \beta_1 z$, the propagation in the fiber can be described by the nonlinear Schrödinger equation (NLS) for the slowly varying complex amplitude $E(z, \tau)$ of the field

$$\partial_z E(z, \tau) = -\frac{\alpha_i}{2}E - i\frac{\beta_2}{2}\partial^2\tau E + i\gamma|E|^2E. \tag{5.14}$$

In Eq. (5.14), the parameter α_i corresponds to the linear absorption coefficient inside the fiber cavity, while γ is the nonlinear coefficient due to the Kerr effect in the resonator.

In order to fully describe the dynamics, besides the propagation equation (Eq. (5.14)), it is necessary to establish the boundary conditions relating the intracavity field at the end of round-trip m, $E^{(m)}(L, \tau)$, with the field at the beginning of the next round-trip, $E^{(m+1)}(0, \tau)$ and with the pump field E_0 that enters in the cavity through the beam splitter. Mathematically, this relation is given by

$$E^{(m+1)}(0, \tau) = \sqrt{T}E_0 + \sqrt{1 - T}E^{(m)}(L, \tau)e^{i\phi_0}, \tag{5.15}$$

where ϕ_0 is the linear phase accumulated by the intracavity field with respect to the pump field over one round-trip.

The set of equations, Eqs. (5.14) and (5.15), form an infinite-dimensional map that describes completely the dynamics of a ring fiber cavity of any size and shape. In the limit of low loss, we can consider that the intracavity field envelope varies slightly between consecutive round-trips. In these conditions, the previous infinite-dimensional map can be averaged to give the externally driven NLS equation [34]

$$t_R \frac{\partial E(t,\tau)}{\partial t} = -(\alpha + i\delta_0)E - i\frac{L\beta_2}{2}\frac{\partial^2 E}{\partial \tau^2} + i\gamma L|E|^2 E + \sqrt{T}E_0, \tag{5.16}$$

where $\alpha = (\alpha_i + T)/2$ accounts for the overall cavity losses and $\delta = 2\pi l - \phi_0$ is the cavity detuning, with l being the order of the cavity resonance closest to the driving field. The continuous variable t describes the slow time of the cavity and can be linked to the round-trip index as $E(t = mt_R, \tau) = E^{(m)}(z = 0, \tau)$. This variable t has a meaning only when its value is an integer of the round-trip time $t = mt_R$. Then, Eq. (5.16) describes the evolution of the cavity field at $z = 0$ round-trip after round-trip.

Finally, one can get rid of several parameters by introducing a dimensionless slow time $t' = \alpha t/t_R$, a dimensionless fast time $\tau' = \tau\sqrt{2\alpha/(L|\beta_2|)}$, a dimensionless complex field amplitude $u(t', \tau') = E(t, \tau)\sqrt{\gamma L/\alpha}$, and a dimensionless pump $u_0 = E_0\sqrt{\gamma LT/\alpha^3}$. In what follows, we drop the accents in the notation of t' and τ'. Then, Eq. (5.16) becomes the dimensionless mean-field Lugiato–Lefever equation [30, 35, 36]

$$\frac{\partial u}{\partial t} = -(1 + i\theta)u + i|u|^2 u + i\frac{\partial^2 u}{\partial \tau^2} + u_0, \tag{5.17}$$

where $\theta = \delta/\alpha$ is the effective dimensionless detuning. This equation has to be complemented with periodic boundary conditions for the τ coordinate. Therefore, the fast time coordinate τ can be viewed as a "spatial" coordinate.

The homogeneous steady states of Eq. (5.17), namely those whose amplitude does not depend on τ, correspond to CW emission and satisfy the well-known cubic equation for dispersive optical bistability

$$I_s^3 - 2\theta I_s^2 + (1 + \theta)I_s = I_0, \tag{5.18}$$

where $I_s = |u_s|^2$ is the intracavity field intensity and $I_0 = |u_0|^2$ is the pump field intensity.

For small detunings, $\theta < \sqrt{3}$, the implicit equation (5.18) has only one solution such that there is a single steady state I_s for a given pump I_0. For detuning $\theta > \sqrt{3}$, Eq. (5.18) has three solutions for I_s for a given value of the pump I_0. Two solutions are stable to homogeneous perturbations while the other is unstable, and thus the homogeneous solution is bistable.

In what follows, we consider $\theta < \sqrt{3}$ for which the homogeneous CW solution is monostable. In this situation, increasing I_0 the homogeneous CW solution of the Lugiato–Lefever equations can become unstable to perturbations of the form $u \approx e^{\lambda t + ik\tau}$. This is a modulational instability, which first takes place for perturbations with critical wave number $k_c = \sqrt{2 - \theta}$ when the intracavity field reaches the threshold value at $I_s = I_{\text{th}} = 1$. The modulational instability leads to a periodic solution in τ which, considering τ as a spatial coordinate, can be viewed as a pattern solution. This patterned solution can arise either supercritically (for

$\theta < 41/30$) or subcritically (for $\theta > 41/30$). In the subcritical case, the bistability between the homogeneous CW solution and the pattern allows the formation of stationary CSs [35]. These structures are stationary in the sense that the field amplitude $u(t, \tau)$ does not depend on the slow time t, and are cavity solitons in the sense that their profile in the τ coordinate is localized. The Lugiato–Lefever equation is invariant under translations in the coordinate τ, as a consequence CSs can arise at any location within the temporal domain $\tau \in [0, L_\tau]$.

In the following, we fix the values $\theta = 1.56$ and $u_0 = 1.1367$ just in the region of existence of a single CS and consider a τ-domain of length $L_\tau \approx 70$.

5.5
Periodically Pumped Ring Cavities

In the context of ring cavities, one of the ways in which inhomogeneities can arise corresponds to the scheme depicted in Figure 5.7b in which the input field is a periodic train of pulses $E_0(\tau)$ at a repetition frequency $1/t_R$ instead of a CW as considered earlier (Figure 5.7a). We assume that the duration of the pulses is much shorter than t_R. The periodic train of pulses can be generated, for instance, by a mode-locked laser. If the repetition frequency is precisely the inverse of the round-trip time, then at each roundtrip the pulse is added at the beam splitter to the electromagnetic wave circulating inside the fiber in a synchronous way. At every round-trip, the normalized background field u_0 is modified by the pump pulse, which can be seen as an inhomogeneity on the τ-space. The effect of this inhomogeneity on the dynamics of nonlinear waves after every round-trip can be modeled by a dimensionless input field of the form $u_0(\tau) = u_0 + b(\tau)$, where

$$b(\tau) = h \exp\left(-\left(\frac{\tau - \tau_0}{\sigma}\right)^2\right), \tag{5.19}$$

is a Gaussian pulse of height h and width σ. Here, we choose $\sigma = 0.2727$ around half of the width of the CS at half maximum and $\tau_0 = L_\tau/2$ in such a way that the inhomogeneity is centered in the τ-domain.

Introducing an input field of this form in the Lugiato–Lefever equation (5.17), the inhomogeneity $b(\tau)$ breaks the invariance under translations in the τ coordinate. As a result CSs, which without inhomogeneity can arise at arbitrary values of τ, are now pinned at a fixed value of τ set by the inhomogeneity.

Depending on the amplitude of the inhomogeneity, several pinned stationary states appear. In Figure 5.8, we show the bifurcation diagram by plotting, as a function of h, the energy of the states with respect to the homogeneous solution, which evaluated as the norm

$$\|u - u_s\|^2 = \frac{1}{L_\tau}\int_0^{L_\tau} (u(\tau) - u_s)(u(\tau) - u_s)^\dagger d\tau, \tag{5.20}$$

where u_s is the field homogeneous steady state and the superscript † stands for hermitic conjugate. The insets in Figure 5.8 show the typical profile of the field intensity along the coordinate τ for the different stationary states.

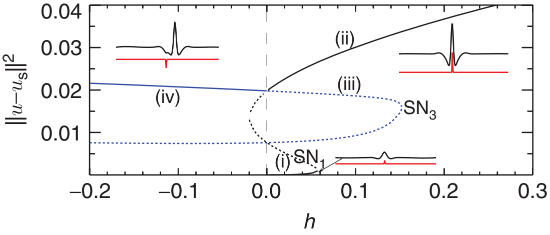

Figure 5.8 Bifurcation diagram of the different pinned states in function of h. The solid (dashed) lines represent the energy of the stable (unstable) states.

For pulses of low positive amplitude, there is a fundamental solution consisting of a practically homogeneous solution with a small bump at the pinning location (see the inset for branch (i) in Figure 5.8. On increasing the value of h, the system jumps to a regime of a high-amplitude CS pinned at its center, as shown for branch (ii) in Figure 5.8. On decreasing h, the branch of large-amplitude CS pinned at the center is stable all the way up to $h = 0$, where it encounters a transcritical bifurcation. For negative values of h, CSs pinned at the center are unstable while there are stable large-amplitude CSs pinned in the first oscillation of its tail (see branch (iv)). It is clear from this bifurcation diagram that the scenario is the same as the one predicted by the general theory described in Section 5.2 (compare Figure 5.8 with Figure 5.1a).

5.6
Effects of Drift in a Periodically Pumped Ring Cavity

There are a variety of sources of drift in fiber cavities or microresonators. For instance, any odd order term in the Taylor expansion of the chromatic dispersion (Eq. (5.12)) will break the $\tau \rightarrow -\tau$ symmetry in the Lugiato–Lefever equation introducing a preferred direction. As an example, one can consider cavities in which dispersion is compensated ($\beta_2 \approx 0$), and as a consequence, third-order dispersion effects need to be taken into account. In this situation, a suitable description requires an additional term $\sim \partial_\tau^3$ in Eq. (5.17) [28]. Another source of drift comes from pumping the ring cavity with a periodic train of pulses whose repetition frequency is not exactly the inverse of the cavity roundtrip time. If the time between input pulses does not match the roundtrip time, then in the fast time coordinate τ the location of the inhomogeneity τ_0 changes from pulse to pulse. For pulses with a fixed repetition rate, the inhomogeneity will drift at a constant velocity proportional to the detuning between the frequency of the pulses and the inverse of the cavity round-trip time.

Here, we model the effect of different sources of drift as a gradient term $-c\partial_\tau$, being c the drift strength [37]. Therefore, Eq. (5.17) becomes

$$\frac{\partial u}{\partial t} = -(1 + i\theta)u + i|u|^2 u + i\frac{\partial^2 u}{\partial \tau^2} - c\frac{\partial u}{\partial \tau} + u_0(\tau). \tag{5.21}$$

A similar extension of the Lugiato–Lefever equation has been derived to model pump pulses with arbitrary temporal shapes and durations, noninterferometric walk-off values and the combination of Kerr, Raman, shock, and non-linear gain effects [38]. We also note that Eq. (5.21) is similar to the AC-driven and damped nonlinear Schrödinger equation [39, 40].

As discussed earlier, the drift pushes the pinned CS and can detach it from the inhomogeneity. As discussed in Section 5.3, this competition allows the appearance of dissipative solitons excitability [18]. There is, however, an important difference with the ring cavities considered here, namely the boundary conditions. While in the general model discussed in Sections 5.2 and 5.3 we considered absorbing boundaries, here the geometry of the system implies periodic boundary conditions. Therefore, drifting CSs are reinjected in the cavity, and as a consequence, dynamical states that locally are equivalent to those encountered before, can lead to a different global behaviors.

Figure 5.9 shows how the diagram in Figure 5.8 deforms when increasing c. The overall structure is qualitatively the same as the one found for the SHE (compare this figure with Figure 5.2). In region I, for small values of the pinning amplitude h, the system takes the fundamental solution, similar to the inset shown in Figure 5.8 for branch (i). In region III, for large values of h, the only solution of the system is the large-amplitude soliton, similar to that shown for branch (ii) in Figure 5.8.

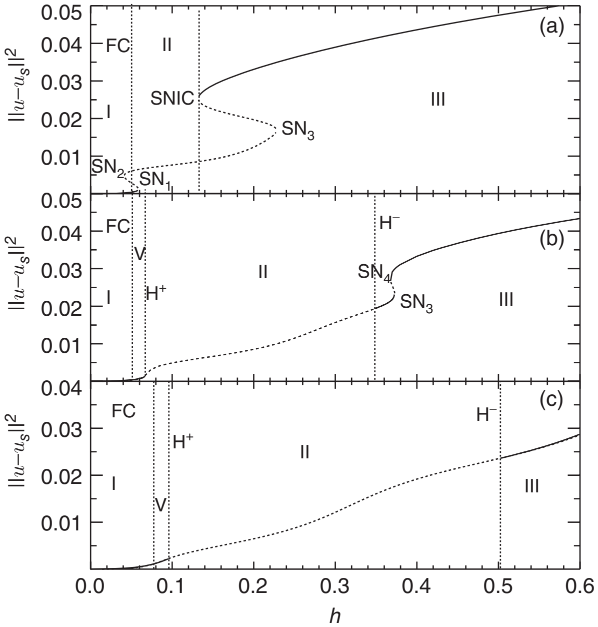

Figure 5.9 Bifurcation diagrams as in Figure 5.8 for (a) $c = 0.025$, (b) $c = 0.06$, and (c) $c = 0.1$.

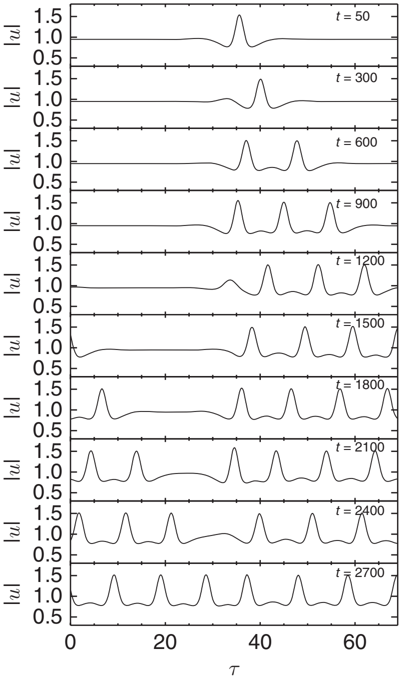

Figure 5.10 Train of solitons taking over the whole τ-domain for $h = 0.07$ and $c = 0.25$.

For small values of c, decreasing h from region III one encounters a SNIC bifurcation in which a limit cycle is created (Figure 5.9a). The limit cycle corresponds to a train of solitons emitted periodically at the inhomogeneity. In the general case considered before the train of solitons emitted at the inhomogeneity travelled until reaching the boundary where it was absorbed. Here, since the boundaries are periodic, the train of solitons is re-injected. An example of such dynamics is shown in Figure 5.10, in particular notice the reinjection of the soliton at time $t \approx 1200$. At the final state, the train of solitons invades the whole τ-domain. In parameter space, the train of solitons solutions exist over a fairly large range of values of h (region II) until the limit cycle collides with an unstable limit cycle at an FC similar to that for the SHE.

As c is increased (see Figure 5.9b for $c = 0.06$), saddle-node bifurcations SN_1 and SN_2 collide in a cusp bifurcation and a subcritical Hopf bifurcation H^+ appears. The SNIC bifurcation becomes a saddle-node, labeled as SN_4, and a there is also a subcritical Hopf bifurcation H^-. Regions I, II, and III are still present. We note that within region II, close to H^-, since the bifurcation is supercritical the amplitude of the oscillations is small. However, as h is decreased and one goes deeper into region II the system undergoes a canard explosion similar to that discussed in Section 5.2 and the amplitude of the oscillations suddenly increases, leading the periodic emission of a train solitons. As h is further decreased, this dynamical regime generating a train of solitons persists all the way until encountering the FC, where it collides with an unstable limit cycle born at the subcritical Hopf bifurcation H^+. Region II, where trains of solitons are the only solution, extends from the Hopf H^+ to the Hopf H^-. In the small region V, there is coexistence of the fundamental solution and the train of solitons solution.

Finally, on increasing the value of c further, all saddle-node bifurcations disappeared and only the supercritical H^- and a subcritical H^+ Hopf bifurcations remained as shown in Figure 5.9c for $c = 0.1$.

Similar to that for the SHE considered in Sections 5.2 and 5.3, the system admits a stable steady state for parameter values within regions I, III, or IV and a temporary perturbation can bring it momentarily into region II, thus triggering an excitable CS excursion. The perturbation can be either in the amplitude of the pump pulses h or in the drift strength c. There is a substantial difference, however, due to the boundary conditions. Absorbent boundaries ensure the return of the system into the unperturbed state after the transient, and therefore we can properly say that the system undergoes an excitable excursion. Here, the system is periodic and, therefore, the CS once generated never disappears. Instead, it travels continuously along the ring. Thus, even when the local behavior at the inhomogeneity is the same, the global outcome is different. To illustrate these differences, we consider the scenario depicted in Figure 5.9c. Here, as in Figure 5.2c, we have two steady states, one is the fundamental solution with a small-amplitude bump for low values of h (regions I and V) and the other is a pinned CS on the inhomogeneity for high values of h (region III). Figure 5.11a shows the dynamics of the ring cavity after a suitable above-threshold perturbation is applied to the fundamental solution. This can be compared with Figure 5.6 for the SHE with absorbent boundaries. Similarly, Figure 5.11b shows the dynamics of the ring cavity after a perturbation applied to the pinned CS, which can be compared with Figure 5.4b. As shown in the top three panels of these figures, the perturbation triggers the emission of a CS at the inhomogeneity, which is then drifted away. Up to this point, the dynamics of the CS in a ring cavity is essentially the same as that of DSs in the SHE. The main difference arises when the DS or the CS approaches the domain boundary. The CS re-enters the system on the opposite side due to the periodicity (namely it propagates continuously on the ring) while the DS was absorbed. As a result of this, the CS arrives at the inhomogeneity after a roundtrip and interacts with it. In the case of the fundamental state, the interaction between the drifting CS and the inhomogeneity is weak and the CS just passes over the inhomogeneity (see panels in Figure 5.11a and the spatiotemporal dynamics shown in Figure 5.12a). In the case of a perturbation of a pinned CS, since h is larger, the interaction between the drifting CS and the inhomogeneity is stronger and as a consequence the drifting soliton is trapped at the inhomogeneity. However, the incoming soliton generates a perturbation that brings the system momentarily into region II and thus a new CS is again emitted [37] (see Figures 5.11b and 5.12b). This process is repeated over and over, such that this kind of dynamics resembles a Newton cradle.

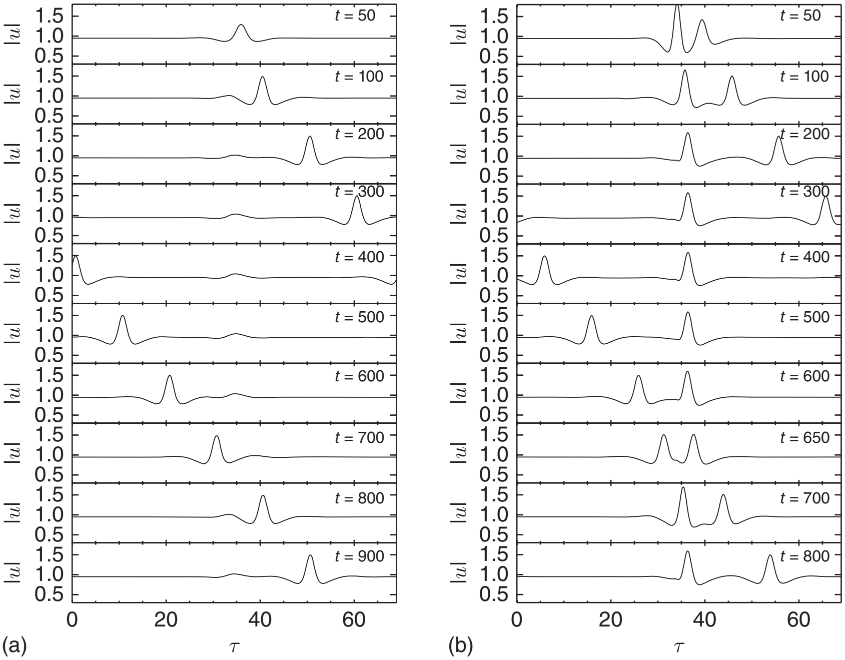

Figure 5.11 Evolution of the CS after a suitable perturbation of the steady state in the LLE model for a ring cavity that brings the system momentarily into region II. For panels on (a) an initial perturbation with $\Delta h = 0.04$ is applied over a time $\Delta t = 30$ to the fundamental solution $h = 0.07$ and $c = 0.1$ (region I). Panels on (b) correspond to the application of a perturbation $\Delta h = -0.3$ over $\Delta t = 30$ to the pinned CS for parameter values $h = 0.6$ and $c = 0.1$ (region III).

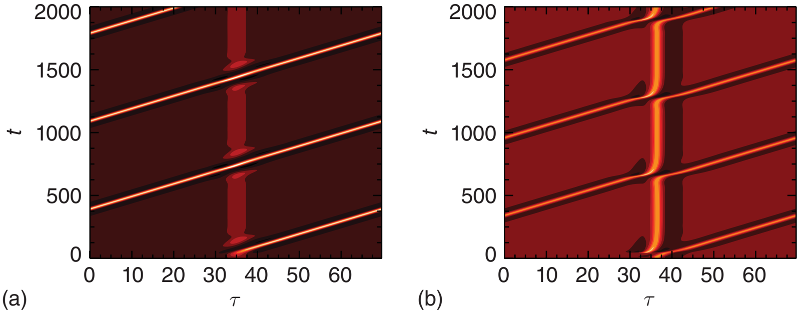

Figure 5.12 Spatiotemporal evolution after a perturbation of the fundamental steady state (a) and the pinned CS (b) for the same parameter values as in Figure 5.11.

5.7
Summary

We have discussed the dynamics of DSs subject to a drift and interacting with a system inhomogeneity. In general, one finds that the competition between the pinning and the pulling can lead to oscillatory dynamics and to type I and type II excitable behavior. Similar dynamical regimes are encountered in two completely different systems such as the SHE and the LLE, which confirms the generic nature of the scenario discussed here. The main gradients are (a) dissipative soliton solutions with oscillatory tails, (b) inhomogeneities, which exert a force that can pin the soliton, and (c) a drift, which pulls the soliton and can depin it.

As discussed in Section 5.1, inhomogeneities and drift are naturally present in many systems. In particular, in fiber cavities and microresonators, they are unavoidable due to imperfections in the fabrication process, material properties, and higher-order chromatic light dispersion. Furthermore, drift can also be induced by a mismatch between the periodicity of a train of input pulses and the cavity round-trip time, providing a mechanism to experimentally control the effective drift of the system, which can be used as a tool to explore different dynamical regimes.

In the context of fiber cavities and microresonators, periodic boundary conditions lead to the emission of a train of solitons from the inhomogeneity. These trains of solitons lie at the basis of Kerr frequency comb generation. Therefore, the dynamical instabilities of cavity solitons induced by imperfections of the microresonator can be particularly relevant for applications relying on stable frequency combs.

Acknowledgments

We acknowledge financial support from MINECO, Spain, and FEDER under projects FIS2012-30634 (INTENSE@COSYP) and TEC2012-36335 (TRIPHOP), from the Research Foundation—Flanders, from the research council of the VUB, by the Belgian American Educational Foundation, from the Belgian Science Policy Office (BelSPO) under Grant No. IAP 7-35, and from Comunitat Autònoma de les Illes Balears.

References

1. Walgraef, D. (1997) *Spatio-Temporal Pattern Formation*, Springer-Verlag, New York.
2. Cross, M. and Greenside, H. (2009) *Pattern Formation and Dynamics in Nonequilibrium Systems*, Cambridge University Press, Cambridge.
3. Grelu, P. and Akhmediev, N. (2012) Dissipative solitons for mode-locked lasers. *Nat. Photonics*, **6**, 84–92, doi: 10.1038/nphoton.2011.345.
4. Chembo, Y.K. and Menyuk, C.R. (2013) Spatiotemporal Lugiato–Lefever formalism for Kerr-comb generation

in whispering-gallery-mode resonators. *Phys. Rev. A*, **87**, 053 852, doi: 10.1103/PhysRevA.87.053852.

5. Coen, S., Randle, H.G., Sylvestre, T., and Erkintalo, M. (2013) Modeling of octave-spanning Kerr frequency combs using a generalized mean-field Lugiato–Lefever model. *Opt. Lett.*, **38**, 37–39, doi: 10.1364/OL.38.000037.
6. Coen, S. and Erkintalo, M. (2013) Universal scaling laws of Kerr frequency combs. *Opt. Lett.*, **38**, 1790–1792, doi: 10.1364/OL.38.001790.
7. Giacomelli, G. and Politi, A. (1996) Relationship between delayed and spatially extended dynamical systems. *Phys. Rev. Lett.*, **76**, 2686–2689, doi: 10.1103/PhysRevLett.76.2686.
8. Wolfrum, M. and Yanchuk, S. (2006) Eckhaus instability in systems with large delay. *Phys. Rev. Lett.*, **96**, 220 201, doi: 10.1103/PhysRevLett.96.220201.
9. Marino, F., Giacomelli, G., and Barland, S. (2014) Front pinning and localized states analogues in long-delayed bistable systems. *Phys. Rev. Lett.*, **112**, 103 901, doi: 10.1103/PhysRevLett.112.103901.
10. Yanchuk, S. and Giacomelli, G. (2014) Pattern formation in systems with multiple delayed feedbacks, *Phys. Rev. Lett.*, **112**, 174103, doi: 10.1103/PhysRevLett.112.174103.
11. Santagiustina, M., Colet, P., San Miguel, M., and Walgraef, D. (1997) Noise-sustained convective structures in nonlinear optics. *Phys. Rev. Lett.*, **79**, 3633–3636, doi: 10.1103/PhysRevLett.79.3633.
12. Louvergneaux, E., Szwaj, C., Agez, G., Glorieux, P., and Taki, M. (2004) Experimental evidence of absolute and convective instabilities in optics. *Phys. Rev. Lett.*, **92**, 043 901, doi: 10.1103/PhysRevLett.92.043901.
13. Ward, H., Ouarzazi, M.N., Taki, M., and Glorieux, P. (1998) Transverse dynamics of optical parametric oscillators in presence of walk-off. *Eur. Phys. J. D*, **3**, 275–288, doi: 10.1007/s100530050175.
14. Santagiustina, M., Colet, P., San Miguel, M., and Walgraef, D. (1998) Walk-off and pattern selection in optical parametric oscillators. *Opt. Lett.*, **23**, 1167–1669, doi: 10.1364/OL.23.001167.
15. Schapers, B., Ackemann, T., and Lange, W. (2003) Properties of feedback solitons in a single-mirror experiment. *IEEE J. Quantum Electron.*, **39**, 227–237, doi: 10.1109/JQE.2002.807211.
16. Parra-Rivas, P., Gomila, D., Leo, F., Coen, S., and Gelens, L. (2014) Third-order chromatic dispersion stabilizes Kerr frequency combs. *Opt. Lett.*, **39**, 2971–2974, doi: 10.1364/OL.39.002971.
17. Kozyreff, G. and Gelens, L. (2011) Cavity solitons and localized patterns in a finite-size optical cavity. *Phys. Rev. A*, **84**, 023 819, doi: 10.1103/PhysRevA.84.023819.
18. Parra-Rivas, P., Gomila, D., Matías, M.A., and Colet, P. (2013) Dissipative soliton excitability induced by spatial inhomogeneities and drift. *Phys. Rev. Lett.*, **110**, 064 103, doi: 10.1103/PhysRevLett.110.064103.
19. Burke, J. and Knobloch, E. (2006) Localized states in the generalized Swift-Hohenberg equation. *Phys. Rev. E*, **73**, 056 211, doi: 10.1103/PhysRevE.73.056211.
20. Gomila, D., Matías, M.A., and Colet, P. (2005) Excitability mediated by localized structures in a dissipative nonlinear optical cavity. *Phys. Rev. Lett.*, **94**, 063 905, doi: 10.1103/PhysRevLett.94.063905.
21. Izhikevich, E.M. (2007) *Dynamical Systems in Neuroscience: The Geometry of Excitability and Bursting*, MIT Press, Cambridge, MA.
22. Jacobo, A., Gomila, D., Matías, M.A., and Colet, P. (2008) Effects of a localized beam on the dynamics of excitable cavity solitons. *Phys. Rev. A*, **78**, 053 821, doi: 10.1103/PhysRevA.78.053821.
23. Strogatz, S.H. (1994) *Nonlinear Dynamics and Chaos*, Addison-Wesley, Reading, MA.
24. Gaspard, P. (1990) Measurement of the instability rate of a far-from-equilibrium steady state at an infinite period bifurcation. *J. Phys. Chem.*, **94**, 1–3, doi: 10.1021/j100364a001.
25. Gomila, D., Jacobo, A., Matías, M.A., and Colet, P. (2007) Phase-space structure of two-dimensional excitable localized structures. *Phys. Rev. E*, **75**, 026 217, doi: 10.1103/PhysRevE.75.026217.

26. Bold, K., Edwards, C., Guckenheimer, J., Guharay, S., Hoffman, K., Hubbard, J., Oliva, R., and Weckesser, W. (2003) The forced van der Pol equation II: canards in the reduced system. *SIAM J. Appl. Dyn. Syst.*, **2**, 570–608, doi: 10.1137/S1111111102419130.
27. Kippenberg, T.J., Holzwarth, R., and Diddams, S.A. (2011) Microresonator-based optical frequency combs. *Science*, **332**, 555–559, doi: 10.1126/science.1193968.
28. Parra-Rivas, P., Gomila, D., Matías, M.A., Coen, S., and Gelens, L. (2014) Dynamics of localized and patterned structures in the Lugiato–Lefever equation determine the stability and shape of optical frequency combs. *Phys. Rev. A*, **89**, 043 813, doi: 10.1103/PhysRevA.89.043813.
29. Leo, F., Gelens, L., Emplit, P., Haelterman, M., and Coen, S. (2013) Dynamics of one-dimensional Kerr cavity solitons. *Opt. Express*, **21**, 9180–, doi: 10.1364/OE.21.009180.
30. Lugiato, L.A. and Lefever, R. (1987) Spatial dissipative structures in passive optical systems. *Phys. Rev. Lett.*, **58**, 2209–2211, doi: 10.1103/PhysRevLett.58.2209.
31. Gelens, L., Van der Sande, G., Tassin, P., Tlidi, M., Kockaert, P., Gomila, D., Veretennicoff, I., and Danckaert, J. (2007) Impact of nonlocal interactions in dissipative systems: towards minimal-sized localized structures. *Phys. Rev. A*, **75** (6), 063 812, doi: 10.1103/PhysRevA.75.063812.
32. Gelens, L., Gomila, D., Van der Sande, G., Danckaert, J., Colet, P., and Matías, M.A. (2008) Dynamical instabilities of dissipative solitons in nonlinear optical cavities with nonlocal materials. *Phys. Rev. A*, **77** (3), 033 841, doi: 10.1103/PhysRevA.77.033841.
33. Tlidi, M. and Gelens, L. (2010) High-order dispersion stabilizes dark dissipative solitons in all-fiber cavities. *Opt. Lett.*, **35**, 306–308, doi: 10.1364/OL.35.000306.
34. Haelterman, M., Trillo, S., and Wabnitz, S. (1992) Dissipative modulation instability in a nonlinear dispersive ring cavity. *Opt. Commun.*, **91**, 401–407, doi: 10.1016/0030-4018(92)90367-Z.
35. Gomila, D., Scroggie, A.J., and Firth, W.J. (2007) Bifurcation structure of dissipative solitons. *Physica D*, **227**, 70–77, doi: 10.1016/j.physd.2006.12.008.
36. Lugiato, L.A. (2003) Introduction to the feature section on cavity solitons: an overview. *IEEE J. Quantum Electron.*, **39**, 193–196, doi: 10.1109/JQE.2002.807195.
37. Parra-Rivas, P., Gomila, D., Matías, M.A., Colet, P., and Gelens, L. (2014) Effects of inhomogeneities and drift on the dynamics of temporal solitons in fiber cavities and microresonators. *Opt. Express*, **22**, 30943–30954, doi: 10.1364/OE.22.030943.
38. Schmidberger, M., Novoa, D., Biancalana, F., Russell, P., and Joly, N. (2014) Multistability and spontaneous breaking in pulse-shape symmetry in fiber ring cavities. *Opt. Express*, **22**, 3045–3053, doi: 10.1364/OE.22.003045.
39. Barashenkov, V. and Smirnov, Y.S. (1996) Existence and stability chart for the ac-driven, damped nonlinear Schrödinger solitons. *Phys. Rev. E*, **54**, 5707–5725, doi: 10.1103/PhysRevE.54.5707.
40. Barashenkov, I.V. and Zemlyanaya, E.V. (2011) Travelling solitons in the externally driven nonlinear Schrödinger equation. *J. Phys. A: Math. Theor.*, **44**, 465 211, doi: 10.1088/1751-8113/44/46/465211.

6
Dissipative Kerr Solitons in Optical Microresonators

Tobias Herr, Michael L. Gorodetsky, and Tobias J. Kippenberg

6.1
Introduction to Optical Microresonator Kerr-Frequency Combs

Ultra high-quality factor (Q) optical whispering-gallery mode resonators have long been considered promising for their nonlinear optical properties since their discovery by Braginsky *et al.* [1] in 1989. Early works included the observation of bistability, thermal nonlinearity [2], Kerr-nonlinearity at cryogenic temperature [3], stimulated Raman- [4] and Brillouin-scattering [5], electro-optic effect [6, 7], as well as second [8] and third [9] harmonic generation. In particular, the third-order Kerr-nonlinearity can give rise to parametric oscillations in an optical microresonator. In this four-photon process, two pump photons are converted to one signal and one idler photon (i.e., degenerate four-wave mixing) where the photonic energy is conserved. These parametric oscillations (sometimes called hyperparametric to distinguish them from three-photon oscillations associated with the second-order optical nonlinearity), despite being well-known in nonlinear optics for decades [10], were observed in ultra high-Q toroidal fused silica and crystalline resonators only in 2004 [11, 12]. These studies demonstrated the dramatic reduction of threshold power for nonlinear optical oscillation owing to the $1/Q^2$ scaling of the threshold [1].

In 2007, it was discovered [13] that Kerr-nonlinear optical microresonators can give rise to optical frequency-comb [14, 15] generation. The surprising cascade and mode proliferation associated with four-wave mixing (FWM) was demonstrated to lead to a broadband series of optical lines equidistantly spaced in the optical frequency domain that is an optical frequency comb. The discovery of these so-called microresonator *Kerr-combs* established optical microresonators as tools for precision frequency metrology, a connection not made before. Such frequency-comb spectra are conventionally derived from mode-locked femtosecond lasers (Figure 6.1). In this way, Kerr-combs broke with the conventional dogma, in the frequency metrology community, that an optical frequency comb requires a mode-locked pulsed laser source. Different from conventional mode-locked laser-based combs, regular microresonator Kerr-combs are not pulsed in the time domain. By comparing the comb spectrum from a microresonator

Nonlinear Optical Cavity Dynamics: From Microresonators to Fiber Lasers, First Edition.
Edited by Philippe Grelu.
© 2016 Wiley-VCH Verlag GmbH & Co. KGaA. Published 2016 by Wiley-VCH Verlag GmbH & Co. KGaA.

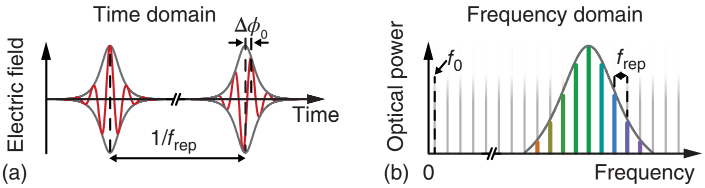

Figure 6.1 Time- and frequency-domain picture of mode-locked laser-based frequency combs. A periodic train of pulses with a pulse repetition rate f_{rep} (a) corresponds to a comb spectrum of equidistant lines in the frequency domain (b). The line spacing is given by f_{rep}. The offset f_0 of the frequency-comb spectrum relates to the carrier–envelope phase shift $\Delta\phi_0$ between two consecutive pulses via $f_0 = f_{rep} \cdot \Delta\phi_0/(2\pi)$. The two parameters f_{rep} and f_0 fully define all comb frequencies $f_n = n \cdot f_{rep} + f_0$.

with a conventional mode-locked fiber laser comb, the equidistance of the comb lines could be proven at the level of 1 part in 10^{17}. Since this work the field of microresonator Kerr-combs has increased substantially. In the subsequent years, Kerr-combs have been demonstrated in a variety of platforms, including crystalline resonators [16], CMOS compatible platforms such as silicon nitride (Si_3N_4) [17–19], Hydex glass [20], as well as aluminum nitride [21] or diamond [22]. In addition to allowing for miniaturization and chip-scale integration of frequency-comb oscillators, microresonator-based Kerr-combs enable to attain wide comb-line spacings in the technologically relevant 10–100 GHz range [23, 24], which is not easily accessible using mode-locked laser frequency combs. Such large mode spacing is of particular interest in coherent telecommunication [25], spectrometer calibration for astronomy [26, 27], low-noise microwave [28, 29], and arbitrary optical waveform generation [30]. Optical temporal dissipative Kerr cavity solitons, predicted theoretically [31–33] and first realized experimentally in optical fibers [34], have played a decisive role in allowing to overcome noise processes associated with comb formation in microresonators. As detailed later, dissipative Kerr solitons (DKS) provide a deterministic way to generate broadband, coherent, and spectrally smooth optical frequency combs, which are in addition amenable to an analytical theory and numerical simulation. These developments, along with the experimental generation of single soliton states in crystalline resonators [35, 36] and integrated Si_3N_4 resonators [37], make microresonators suitable for precision frequency metrology and many related applications. Owing to the pulsed nature of the solitons (in contrast to the earlier Kerr-combs), microresonators can now provide equivalent counterparts to mode-locked laser regarding the time-domain properties. This allows using methods of spectral transfer and broadening as well as self-referencing techniques [38–40] that have been developed for mode-locked laser-systems. In this way, temporal dissipative solitons in microresonators provide a route to synthesize absolute optical frequencies from an RF or microwave signal and the opportunity to use microresonators for counting the cycles of light.

6.2
Resonator Platforms

Parametric frequency conversion in Kerr-nonlinear microresonators, first observed in toroidal fused silica and crystalline microresonators, has now been observed in a wide variety of geometries and platforms, including microspheres [41, 42] and integrated, planar ring-type resonators, such as those based on Si_3N_4 [43]. The work presented in this chapter on dissipative Kerr soliton generation has been carried out with crystalline magnesium fluoride MgF_2 resonators and Si_3N_4 integrated microrings, which are briefly described in the following sections.

6.2.1
Ultra High-Q (MgF_2) Crystalline Microresonators

The first microresonator platform in which temporal DKS have been observed experimentally [35] were crystalline resonators made from magnesium fluoride (MgF_2). Crystalline optical resonators were first introduced in [44], and further development demonstrated that polishing of crystalline materials can lead to exceptionally high Q-factors (exceeding 10^{11} [45, 46]). This method, therefore, extended the ultra high-Q attained with surface reflow methods [1, 47] to crystalline materials. Figure 6.2 shows an ultra high-Q crystalline resonator made from an MgF_2 cylindrical preform, which is prestructured with protrusions using precision diamond turning. After prestructuring, a series of polishing steps using diamond films and slurries are used to attain a low roughness surface finish and ultra high-Q optical modes. To excite the whispering-gallery modes, evanescent optical coupling via a tapered optical fiber can be used [48, 49]. This is possible as the refractive index of MgF_2 is lower than that of fused silica fibers. The use of thin tapered fiber for coupling is feasible despite the large volume of the employed (typically millimeter scale) resonators, due to the exceptionally high-Q, which reduces the necessary coupling rates required for critical coupling. Typically, the

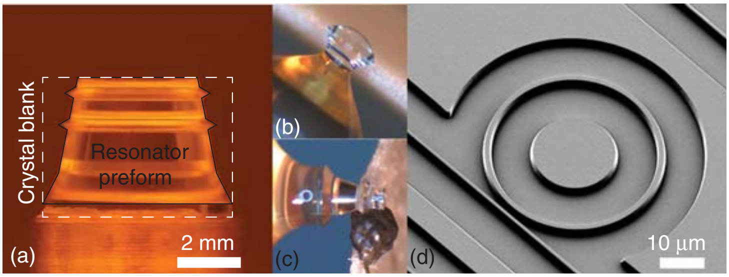

Figure 6.2 Microresonator platforms. (a) Diamond-turned magnesium fluoride resonator containing two protrusions that confine high-Q optical whispering-gallery modes. (b) Manually shaped and polished resonator. (c) Polishing of a diamond-turned preform. (d) Scanning electron micrograph of a silicon nitride microresonator before applying the fused silica cladding.

resonance width is in the range of 50 – 500 kHz corresponding to Q values of 10^8 to several 10^9. The nonlinear frequency conversion threshold is reached at optical powers below 1 mW. For soliton generation, pump powers of the order of 10 mW are typical.

6.2.2
Integrated Photonic Chip Microring Resonators

From a future application perspective, microresonator platforms that are amenable to wafer-scale processing can be advantageous. A key challenge in this context is attaining sufficiently high-Q for efficient nonlinear parametric frequency conversion. One platform that is particularly well suited is based on silicon nitride (Si_3N_4) waveguides embedded in fused silica, which is a material already used in the microelectronic industry (part of the CMOS process) and is well suited for integrated photonic waveguides. Its refractive index of $n \approx 2$ enables tight optical confinement waveguides and microring resonators and the high bandgap ($\sim 3\,$eV) mitigates two (or higher-order) photon absorption in the telecommunication band. While the achieved Q-factors ($\sim 10^6$) in integrated devices are still many orders of magnitude below that of polished crystalline resonators, higher Kerr-nonlinearity and tighter optical confinement lead to high effective nonlinearities that are almost three orders of magnitude larger than in crystalline resonators. This has enabled parametric oscillations to be accessible with pump powers of $\sim 100\,$mW as demonstrated first in [18, 50]. Subsequent work demonstrated low-phase-noise comb operation [51] via nonlinear synchronization, as detailed later. In addition, Si_3N_4 microresonators were the first microresonator platform that allowed for the observation of soliton-induced Cherenkov radiation [52] (or dispersive wave emission), that is, the dynamics of solitons in the presence of higher-order dispersion [53]. Fabrication of the resonators proceeds by lithography, etching, and a final encapsulation technique in which the waveguides are clad with fused silica. The image of a final (but not yet clad resonator) is shown in Figure 6.2. Coupling to and from the chip is achieved with inverse tapered waveguides, adiabatically converting the mode spot diameter from a tight nanophotonic waveguide mode to a large area mode that can be excited with a lensed single-mode optical fiber.

6.3
Physics of the Kerr-comb Formation Process

In a simplified picture, the Kerr-comb formation in microresonators starts with an initial degenerate FWM process, generating a pair of sidebands symmetrically spaced in frequency around the pump laser in the resonances adjacent to the pumped resonance. In this process, the free spectral range (FSR) defines the frequency spacing of the sidebands from the pump laser. A subsequent cascade of nondegenerate four-wave mixing processes generates a large series of sidebands in frequency steps corresponding to the initially defined line spacing. The bandwidth of the comb is limited by the dispersion of the resonator that causes a mismatch between the optical sidebands and the resonance frequencies. This mismatch increases with the spectral distance to the pump wavelength. While it explains well the early results of Kerr-frequency-comb generation with typically terahertz-line spacing and moderate bandwidth, this picture had to be refined when attempting broader optical bandwidth and narrower line spacing (less than 50 GHz) in toroidal [54], crystalline [16], and integrated Si_3N_4 resonators [17, 55, 56]. Here, unexpected noise phenomena were observed in the form of broad optical lines, high amplitude noise, and loss of coherence. These phenomena appeared to be independent of the chosen microresonator platform. Indeed, the origin of this noise can be explained by the universal properties of the comb formation mechanism [51]. While in early microresonator comb experiments, due to the wide line spacing, the mode proliferation occurred indeed on adjacent resonators modes, the latter is typically not the case in resonators with narrow FSR. Here, the first pair of primary sidebands generated by the initial FWM process can occur in resonances that are widely separated from the pump (by multiple FSR). The process is depicted schematically in Figure 6.3. Using the nonlinear coupled mode equations, as introduced in the following section, one can show that the mode spacing between the primary modes is essentially defined by the (normalized) ratio of second-order dispersion parameter and resonance width. If the resonator has a comparatively narrow FSR, then the initial sidebands are separated by a frequency interval Δ that encompasses a high number of FSR intervals. Further four-wave mixing can fill up the unpopulated resonances by formation of secondary sidebands separated by a smaller frequency spacing δ. In other words, subcombs with δ-line spacing form around the Δ-spaced primary lines. As, however, the primary spacing Δ is not guaranteed to be an integer multiple of the secondary spacing δ, the generated lines cannot generally form a consistent comb, which manifests itself in the previously mentioned noise. This hypothesis of comb formation has been experimentally tested in [51] using a fiber laser frequency comb as a reference to reconstruct the frequency components of the Kerr-comb. Another key finding of this work is that in contrast to the early model of comb formation, more than one single comb line can occupy a given resonance (cf. Figures 6.3 and 6.4).

Despite these noise processes, regimes have been found where broadband coherent Kerr-combs can be generated. The first observed transition to such a regime of low phase noise was presented in [51]. Here, the subcombs defined by Δ and δ can be synchronized by changing the pump laser frequency and power so that Δ and δ become commensurate. Once close enough to the commensurate state, nonlinear synchronization and locking sets in and creates a phase coherent optical frequency comb [51] (albeit not pulsed in the time domain). Such synchronization has been experimentally observed and studied by reconstruction of the frequencies of the Kerr-comb lines as shown in Figure 6.5. Once the Kerr-comb falls into such a synchronized state it remains stable against fluctuations in the pump laser parameters and can be used for further experiments.

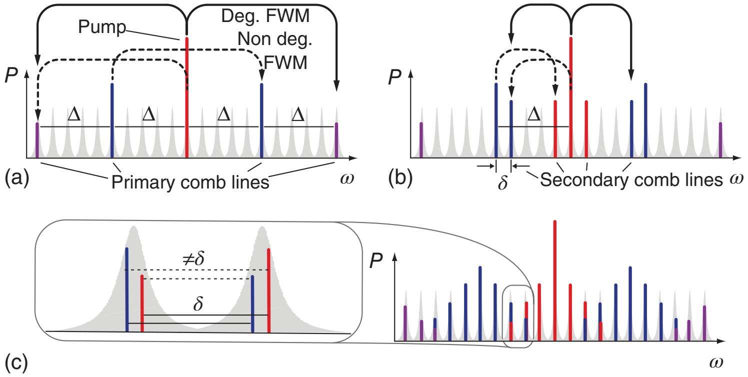

Figure 6.3 Universal Kerr-comb formation processes. (a) Formation of primary sidebands. (b) Formation of subcombs. (c) Overlap between inconsistent subcombs can lead to multiple lines per cavity resonance and explains noise phenomena in Kerr-combs.

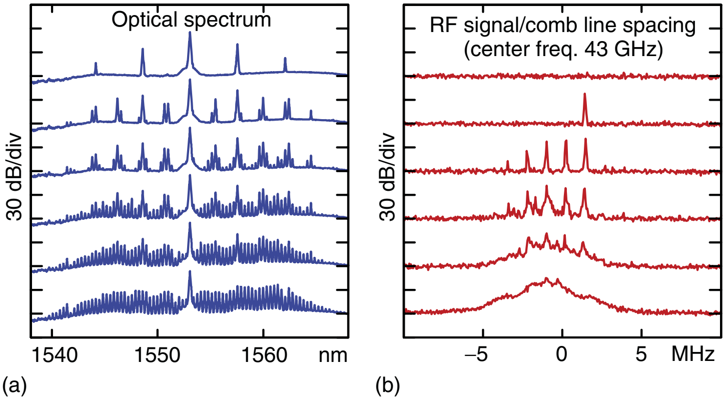

Figure 6.4 Kerr-comb formation and noise. (a) Formation of the optical spectrum as the laser is tuned into resonance and the intracavity power increases. (b) Comb-line spacing measured as the radio frequency (RF) beat note between neighboring comb lines. Multiple and broad beat notes indicate multiple and inconsistent line spacings present in the comb spectrum.

Later experiments have revealed that the nonlinear locking process can be captured by the Adler equation, which is known from injection locking of lasers [57]. Kerr combs driven into a low-phase noise, coherent state have been used in applications, such as coherent communications [25], where they are used to provide a multitude of data channels from a single laser, enabling terabit per second data-communication. Yet, despite the promising prospects a central missing element has been ways to reliably achieve such low-phase-noise combs, with smooth spectral envelope. A surprising discovery has been made in 2012 [35, 58], when it was demonstrated that the generated subcombs can not only undergo nonlinear synchronization, but moreover can seed the formation of

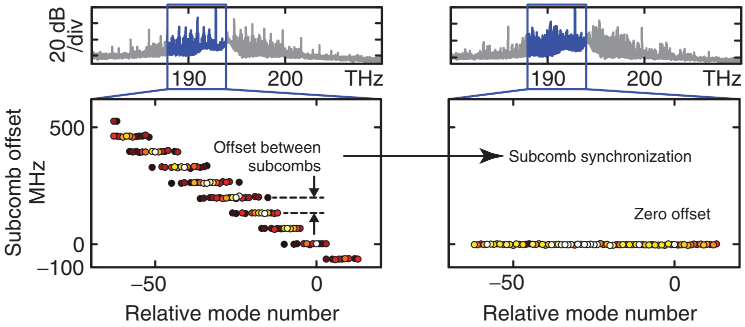

Figure 6.5 Subcomb synchronization in an Si_3N_4 optical microresonator achieved by changing the pump laser wavelength.

temporal dissipative Kerr solitons in optical microresonators. This discovery provides not only an opportunity to study temporal dissipative solitons in microresonators, but moreover a powerful tool to generate low-phase-noise combs with broad spectral bandwidth that can be used in a variety of applications. Before turning to soliton formation, we review first the basic formalism describing Kerr-nonlinearity-driven parametric oscillations.

6.3.1
Nonlinear Coupled Mode Equations

The theoretical analysis of parametric oscillations, frequency comb and soliton formation is a complex nonlinear mathematical problem for which several approaches have been proposed [11, 42, 59–62]. Besides description in the time domain, the modal expansion approach in the frequency domain [63, 64] has proven particularly useful in the context of microresonators as it allows easily to take into account particularities in the mode structure. The system of equations describing the dynamics of each optical mode A_m in the slowly varying envelope approximation can be obtained from the nonlinear wave equation in conjunction with the quantum Langevin equations:

$$\begin{aligned}\frac{\partial A_m}{\partial t} &= -\frac{\kappa_m}{2}A_m + \delta_{m,m_0}\sqrt{\frac{\kappa_{\mathrm{ex,m}}P_{\mathrm{in}}}{\hbar\omega_0}}e^{-i(\omega_p-\omega_0)t}\\ &\quad + ig\sum_{m',m'',m'''}\Lambda_m^{m'm''m'''}D_m^{m'm''}A_{m'}A_{m''}A^*_{m'''}e^{-i(\omega'_m+\omega''_m-\omega'''_m-\omega_m)t}\\ &\quad + \sqrt{\kappa_{i,m}}\delta s_{i,m} + \sqrt{\kappa_{\mathrm{ex,m}}}\delta s_{\mathrm{ex},m},\end{aligned} \tag{6.1}$$

Here, κ_m denotes the cavity decay rate of mode m with eigenfrequency ω_m and $\hbar$ is the reduced Planck constant. The cavity decay rate is composed of intrinsic ($\kappa_{i,m}$) and external coupling ($\kappa_{\mathrm{ex,m}}$) loss rates such that the total loss rate is $\kappa_m = \kappa_{i,m} + \kappa_{\mathrm{ex,m}} = \frac{\omega_m}{Q_m}$, where Q_m is the loaded quality-factor of mode m. One mode (m_0, ω_0) is driven by a classical field with optical power P_{in} and frequency ω_p. The terms $\delta s_{i,m}$ and $\delta s_{\mathrm{ex,m}}$ designate quantum Langevin input noises with commutation relations $[\delta s_j(t), \delta s_j^\dagger(t')] = \delta(t-t')$ and with zero mean ($\langle \delta s_j(t) \rangle = 0$). The summation over the nonlinear interaction terms is made over all azimuthal indices for the nearly equidistant set of fundamental whispering-gallery eigenmodes, satisfying the following conservation relation: $m' + m'' - m''' = m$, where $\mathcal{D}_m^{m'm''}$ is the degeneracy factor: $\mathcal{D}_m^{m'\neq m''} = 2$ in case of cross-phase modulation and nondegenerate four-wave mixing, and $\mathcal{D}^{m'm'} = 1$ for self-phase modulation and hyperparametric generation. We neglect processes where one of the frequencies is significantly smaller ($\omega_m = \omega_{m'} - \omega_{m''} - \omega_{m'''}$) or larger than other frequencies ($\omega_m = \omega_{m'} + \omega_{m''} + \omega_{m'''}$), as it is the case for third-harmonic generation (when in the degenerate case $\mathcal{D}_{3m'}^{m'm'} = 1/3$). The intermodal coupling factor is given by

$$\Lambda_m^{m'm''m'''} = \frac{\int \mathbf{e}_{m'}\mathbf{e}_{m''}\mathbf{e}^*_{m'''}\mathbf{e}^*_m dV}{\int |\mathbf{e}_0|^4 dV} \frac{\chi^{(3)}(\omega_m = \omega_{m'} + \omega_{m''} - \omega_{m'''})}{\chi^{(3)}(\omega_0 = \omega_0 + \omega_0 - \omega_0)}, \tag{6.2}$$

where $\mathbf{e}_m$ is the vector electric field distribution of the mode m and $\chi^{(3)}$ describes the third-order Kerr-nonlinearity. This factor is analytically different from that obtained in [62–64].1) The effective nonlinear volume of the modes is given by

$$V_m = \frac{(\int |\mathbf{e}_m|^2 dV)^2}{\int |\mathbf{e}_m|^4 dV}, \tag{6.3}$$

The latter may be found from the field distribution of the cavity eigenmodes. The modes are normalized such that $|A_m|^2$ corresponds to the number of photons in a given cavity mode. The nonlinear coupling constant g (that is the Kerr frequency shift per photon) is defined as in [59]:

$$g = \frac{3\hbar\omega_0^2 \chi^{(3)}(\omega_0)}{4\epsilon_0 n^4(\omega_0) V_0} = \frac{\hbar\omega_0^2 c n_2(\omega_0)}{n^2(\omega_0) V_0}. \tag{6.4}$$

Here, ϵ_0 denotes the dielectric constant, and n and n_2 are the refractive nonlinear optical indices. A seeding via input noises is important for numerical simulations to initiate the comb; however, it is not required in further analytical considerations as their means vanish.

For the calculation of the field distribution and eigenfrequencies in crystalline resonators, we do not use the modes of a sphere as proposed in [63, 64] but asymptotic solutions obtained for a spheroid [66–68], producing better approximations for the wide range of geometries, or eigenfrequencies obtained

---

1) The authors of [62–64] overlooked in the derivation that the nonlinear polarization is time dependent and cannot be simply taken out from the time derivative in wave equation [65]. This omission leads to unphysical asymmetry in Λ over mode indices and loss of precise degeneracies important for analytical considerations, but usually plays negligible role in numerical simulations of narrow combs when $\Lambda \simeq 1$.

via COMSOL finite element modeling. From these approximations, as well as from Sellmeier's equation for the resonator material one can determine V_m and eigenfrequencies ω_m to find second- and higher-order dispersions. The latter can be approximated by

$$\omega_\mu \approx \omega_0 + D_1\mu + \frac{1}{2!}D_2\mu^2 + \frac{1}{3!}D_3\mu^3, \tag{6.5}$$

where $\mu = m - m_0$. The parameter D_2 is related to the second-order group velocity dispersion (GVD) β_2 ($\beta_j = \frac{\partial^j \beta}{\partial\omega^j}$) via $D_2 = -\frac{c}{n}D_1^2\beta_2$, and D_3 relates to the third-order dispersion via $D_3 = -\frac{c}{n}D_1^3\beta_3 + 3\frac{c^2}{n^2}D_1^3\beta_2^2 \approx -\frac{c}{n}D_1^3\beta_3$.

It is convenient to remove the explicit time dependence in the nonlinear equations with the substitution $A_\mu = \tilde{A}_\mu e^{i(\omega_\mu - \omega_p - \mu D_1)t}$, where $D_1/(2\pi)$ is the mode spacing of the comb at the pump wavelength. Moreover, the pump term is written as $F = \sqrt{\frac{\kappa_c P_{in}}{\hbar\omega_0}}$. In this new basis, the oscillations of each optical mode are considered not around eigenfrequencies but around nearest frequencies on an equidistant D_1 spaced-grid:

$$\begin{aligned}\frac{\partial\tilde{A}_\mu}{\partial t} = & -\left[i(\omega_\mu - D_1\mu - \omega_p) + \frac{\kappa_\mu}{2}\right]\tilde{A}_\mu + \delta_{\mu 0}F \\ & + ig\sum_{\mu',\mu'',\mu'''}\Lambda_\mu^{\mu'\mu''\mu'''}\tilde{A}_{\mu'}\tilde{A}_{\mu''}\tilde{A}^*_{\mu'+\mu''-\mu}.\end{aligned} \tag{6.6}$$

If L pairs of sidebands and the pump are considered, then the total number of nonlinear terms in all $2L + 1$ equations is $\frac{1}{3}(L+1)(8L^2 + 7L + 3)$.

It is possible to get some useful conservation laws for this set of equations. Calculating the evolution of the total number of photons in the comb $\frac{dN}{dt} = \sum_{\mu=-L}^{L}\frac{dN_\mu}{dt}$, with $\frac{dN_\mu}{dt} = \frac{dA_\mu}{dt}A_\mu^* + \frac{dA_\mu^*}{dt}A_\mu$ and assuming symmetry: $\Lambda_\mu^{\mu'\mu''\mu'''} + \Lambda_{\mu'''}^{\mu'\mu''\mu'''} = \Lambda_{\mu'}^{\mu\mu'''\mu''} + \Lambda_{\mu''}^{\mu\mu'''\mu'}$, we find that most of the terms in the sum cancel each other:

$$\frac{dN}{dt} + \sum_{\mu=-L}^{L}\kappa_\mu N_\mu = (FA_0^* + F^*A_0), \tag{6.7}$$

which in case of $\kappa_\mu = \kappa$ simplifies to

$$\frac{dN}{dt} + \kappa N = 2|F||A_0|\cos\phi_0, \tag{6.8}$$

where ϕ_0 is the phase difference between F and A_0. This master equation for the whole optical spectrum may be useful, for example, for the analysis of the steady states.

In a similar way, one may find

$$\sum_{\mu=-L}^{L}\mu\left(\frac{dN_{+\mu}}{dt} - \frac{dN_{-\mu}}{dt}\right) = -\sum_{\mu=-L}^{L}\mu(\kappa_{+\mu}N_{+\mu} - \kappa_{-\mu}N_{-\mu}), \tag{6.9}$$

which in the case of steady state means that the "center of mass" (i.e., the frequency center of photonic energy) of the spectrum is conserved and coincides with the pump frequency as each four-wave mixing process follows this conservation law.

In the following analysis, we use further simplifications, assuming equal parameters for all comb lines ($\kappa_m = \kappa$, $\Lambda_m^{m'm''m'''} = 1$) and renumbering comb lines with index μ, starting from the central driven mode m_0, that is, $\mu = m - m_0$. In this case, it is possible to write the equations in a dimensionless way, as suggested in [59]:

$$\begin{aligned}
a_\mu &= \tilde{A}_\mu \sqrt{2g/\kappa},\\
f &= \sqrt{8g/\kappa^3}|F_p|,\\
\zeta_\mu &= 2(\omega_\mu - \mu D_1 - \omega_p)/\kappa \approx \zeta_0 + D_2\mu^2/\kappa,\\
\tau &= \kappa t/2,
\end{aligned} \tag{6.10}$$

$$\frac{\partial a_\mu}{\partial \tau} = -[1 + i\zeta_\mu]a_\mu + i\sum_{\mu',\mu''} a_{\mu'}a_{\mu''}a^*_{\mu'+\mu''-\mu} + \delta_{0\mu}f, \tag{6.11}$$

In this form, all frequencies, detunings, and magnitudes are measured in units of cavity resonance width so that $|a_\mu|^2 = 1$ corresponds to the nonlinear mode pulling of one cavity resonance width (thresholds for both single-mode bistability and degenerate oscillations).

6.3.2
Degenerate Hyperparametric Oscillations

An analytic solution of the complete nonlinear system with many comb lines in general case is hardly possible. It is possible, however, to resolve equations for an arbitrary set of modes if only degenerate processes caused by the pump as well as nonlinear mode pulling effects corresponding to cross- and self-phase modulation are taken into account. These effects are dominating as long as the energy in each of the optical lines is small compared with the intracavity pump power and when due to strong second-order dispersion the resonator modes are far enough from equidistance lines to suppress nondegenerate four-wave mixing.

The following set of reduced equations qualitatively describes the processes of initial comb formation, including widely spaced primary lines, switching between initially excited modes, chaotic behavior, and noisy RF signals with many frequencies:

$$\begin{aligned}
\frac{\partial a_0}{\partial \tau} &= -[1 + i\zeta_0]a_0 + i(2\tilde{N} - |a_0|^2)a_0 + 2i\sum_{\mu=1}^{L} a_\mu a_{-\mu}a_0^* + f,\\
\frac{\partial a_\mu}{\partial \tau} &= -[1 + i\zeta_\mu]a_\mu + i(2\tilde{N} - |a_\mu|^2)a_\mu + ia^*_{-\mu}a_0^2,
\end{aligned} \tag{6.12}$$

where according to the normalization $\tilde{N} = 2gN/\kappa$. The reduced model was compared with the full numeric model integrated using the Runge–Kutta scheme. It shows good agreement concerning the initially generated sidebands and qualitative agreement of the comb in the noisy, chaotic regime.

With the substitution $a_\mu = \alpha_\mu e^{-i\phi_\mu}$, $\psi_\mu = 2\phi_0 - \phi_\mu - \phi_{-\mu}$, it is possible to search for steady-state solutions with $\dot{\alpha}_\mu = 0$ and $\dot{\phi}_\mu \equiv \delta\tilde{\omega}_\mu = \text{const}$. One may obtain a steady state from the resulting equations when $\dot{\phi}_0 = 0$ and $\dot{\psi}_\mu = 0$, so that $\dot{\phi}_\mu = -\dot{\phi}_{-\mu}$ and $\delta\tilde{\omega}_\mu = -\delta\tilde{\omega}_{-\mu} = D_3\mu^3/(3\kappa) + \cdots$. Splitting the Eq. (6.12) into real and imaginary parts, we get

$$\begin{aligned}
&\alpha_0\left(1 + 2\sum_{\mu=1}^{L} \alpha_\mu\alpha_{-\mu}\sin\psi_\mu\right) = f\cos\phi_0,\\
&\left(\zeta_0 - 2\tilde{N} - 2\sum_{\mu=1}^{L} \alpha_\mu\alpha_{-\mu}\cos\psi_\mu + \alpha_0^2\right)\alpha_0 = f\sin\phi_0,\\
&\alpha_{\pm\mu} - \alpha_{\mp\mu}\alpha_0^2\sin\psi_\mu = 0,\\
&\tilde{\zeta}_\mu\alpha_\mu - (2\tilde{N} - \alpha_\mu^2)\alpha_\mu - \alpha_{-\mu}\alpha_0^2\cos\psi_\mu = 0,
\end{aligned}\tag{6.13}$$

where

$$\tilde{\zeta}_\mu = (\zeta_\mu - 2\dot{\phi}_\mu/\kappa).\tag{6.14}$$

From the third equation, we find that $\alpha_\mu = \alpha_{-\mu}$ and $\psi_\mu \equiv \psi = \arcsin(1/\alpha_0^2)$. Substituting this into the first and second equations of Eq. (6.13), we obtain

$$\begin{aligned}
&\tilde{N} = f\alpha_0\cos\phi_0,\\
&\left[\zeta_0 - 2\tilde{N} + \alpha_0^2 + (\tilde{N} - \alpha_0)\sqrt{1 - 1/\alpha_0^4}\right]\alpha_0 = f\sin\phi_0.
\end{aligned}\tag{6.15}$$

The first equation of Eq. (6.15) also follows from the master equation (6.8). Adding both equations squared, we get the system

$$\begin{aligned}
&[\zeta_0 - \tilde{N}(2 + \cos\psi) + \alpha_0^2(1 + \cos\psi)]^2\alpha_0^2 + \tilde{N}^2/\alpha_0^2 = f^2,\\
&\tilde{\zeta}_\mu + \alpha_\mu^2 - 2\tilde{N} = \tilde{\zeta}_{\mathrm{nl}} = \alpha_0^2\cos\psi.
\end{aligned}\tag{6.16}$$

It follows that $\tilde{\zeta}_{\mathrm{nl}}$, which determines the detuning of the new nonlinear effective eigenfrequency from the frequency of oscillations, does not depend on μ. This means that in the steady state an equidistant comb may be formed if the dispersion of each mode is compensated by nonlinear pulling with appropriate amplitude distribution of each excited comb line. This nonlinear dispersion compensation is possible due to the fact that self-phase modulation is two times smaller than cross-phase modulation and is an essential mechanism for comb formation [41, 69].

The last equation of Eq. (6.16) may be summed over all excited lines to get

$$\tilde{N} = \frac{\zeta_\Sigma - \alpha_0^2 + 2L\sqrt{\alpha_0^4 - 1}}{4L - 1},\tag{6.17}$$

where $\zeta_\Sigma = \sum_{\mu=-L}^{L}\tilde{\zeta}_\mu = (2L+1)\zeta_0 + d_2\sum_\mu \mu^2$ (where $d_2 = D_2/\kappa$). If excited comb lines are filling all resonator modes in some interval without omissions the summation may be done analytically. If substituted in the first equation of Eq. (6.16), we can finally get an equation for the pump mode magnitude α_0^2 ready for numerical analysis. Substituting $\beta = \alpha_0^2 - \sqrt{\alpha_0^4 - 1}$, $\alpha_0^2 = \frac{\beta^2+1}{2\beta}$ then transforms the final equation to a rational sixth-order equation. Further analysis of these equations may reveal the properties of the low-noise, low-populated combs observable in experiments.

6.3.3
Primary Sidebands

A particular case of the reduced model is a three-mode system for which all the nonlinear terms are in fact considered, that is, the model is complete. This system can describe the threshold for primary sideband hyperparametric oscillations at a μ times FSR frequency separation from the pump that can be softly excited when the pump is gradually tuned into resonance starting from infinite detuning ($\omega_0 < \omega_p$ for $D_2 > 0$).

The three-mode system and its stability was analyzed in detail using numerical analysis of the nonlinear equations [59] or stability analysis of the linearized equations [63]. Both approaches lead to the same equation following from the reduced model when $L = 1$:

From the nonlinear resonance condition and condition for the first sideband to emerge ($\alpha^2_{\mu,\mathrm{th}} = 0, \tilde{N} = \alpha_0^2$), we obtain

$$\begin{aligned}&(\zeta_0 - \alpha_0^2)^2\alpha_0^2 + \alpha_0^2 = f^2,\\ &\zeta_0 + d_2\mu^2 = 2\alpha_0^2 - \sqrt{\alpha_0^4 - 1}.\end{aligned} \tag{6.18}$$

It follows the equation determining the possibility to excite the mode μ:

$$\begin{aligned}&\zeta_0 = \alpha_0^2 - \sqrt{f^2/\alpha_0^2 - 1},\\ &\sqrt{f^2/\alpha_0^2 - 1} - d_2\mu_{\mathrm{th}}^2 + \alpha_0^2 - \sqrt{\alpha_0^4 - 1} = 0,\end{aligned} \tag{6.19}$$

or using the smallest possible $\alpha_0^2 = 1$ when the radical is real:

$$\mu_{\mathrm{th}} = \left\lfloor \sqrt{(1 + \sqrt{f^2 - 1})/d_2} \right\rfloor . \tag{6.20}$$

Alternatively, this can be rewritten in physical terms [51] as

$$\mu_{\mathrm{th}} = \left\lfloor \sqrt{\frac{\kappa}{D_2}(1 + \sqrt{\frac{P_{\mathrm{in}}}{P_{\mathrm{th}}} - 1)}} \right\rfloor . \tag{6.21}$$

The threshold power P_{th} corresponds to $|a_{0,\mathrm{th}}| = 1$. The minimum obtainable μ_{th} for $P_{\mathrm{in}} = P_{\mathrm{th}}$ is given by

$$\mu_{\mathrm{th}} = \sqrt{\frac{D_2}{\kappa}}. \tag{6.22}$$

and depends only on the ratio of cavity decay rate κ to second-order cavity dispersion D_2.

Note that the threshold $\alpha_{0,\mathrm{th}} = 1$, determining the first sideband to appear when tuning the pump into resonance at a given power (also found in [63]), however, does not correspond to a minimum of input power when hyperparametric generation may start. This minimum, numerically calculated in [59] may be found explicitly as $\alpha_{\mathrm{in,min}} = 2/\sqrt{3}$.

6.4
Dissipative Kerr Solitons in Optical Microresonators

The formation of stable temporal DKS circulating in a continuous-wave (CW)-driven microresonator with Kerr-nonlinearity is a remarkable form of optical self-organization. It requires, similarly to the Kerr-combs described earlier, a medium with focusing third-order nonlinearity and anomalous group velocity dispersion. Fundamentally different from the above-described Kerr-combs, the formation of temporal dissipative Kerr solitons implies a stable pulsed time-domain waveform where the pulse properties are fully determined by the experimental parameters. The ultrashort soliton pulse duration, typically in the femtosecond regime, implies broadband optical frequency-comb spectra that show the same wide-line spacing that is known from the previous Kerr-combs. Importantly, however, the soliton-based comb spectra do not suffer from the inconsistent subcomb formation and associated noise processes that are often observed in Kerr-combs. Before the observation in a microresonator, temporal dissipative solitons had already been observed in a several hundred meter long, CW-driven fiber cavity, where additional short-laser pulses had been used to stimulate the soliton formation [34]. In this context, it was speculated that temporal dissipative solitons could be formed in a microresonator as well. (Note: the possibility of solitons circulating in a dielectric sphere was already proposed in [70].) Moreover, it was pointed out in earlier studies [71, 72] that the theoretical formalism so far used by researchers to describe microresonators and fiber cavities, that is, the nonlinear coupled mode equations and the Lugiato–Lefever equation, respectively, can be mapped onto each other. From a historical perspective, it is thus interesting to note that after the first reports on microresonator Kerr-combs in 2007 [13], it took 5 years to enter the regime of dissipative Kerr solitons in a microresonator. One reasons for this is the particular thermal behavior of a microresonator system that had long masked this regime (cf. Section 6.6). Moreover, the approach of stimulating solitons using laser pulses that is successfully used with long-fiber cavities cannot easily be transferred to microresonators due to their much higher finesse (i.e., difficulty of coupling the pulse into the resonator). Before presenting experimental observations, the following section establishes the theoretical formalism that allows describing dissipative Kerr soliton in a microresonator (Figure 6.6).

6.4.1
Analytical Theory of Dissipative Kerr Solitons

To describe the internal field in a nonlinear microresonator, the following master equation may be used when the third- and higher-order dispersion terms are neglected [61, 71]:

$$\frac{\partial A}{\partial t} - i\frac{1}{2}D_2\frac{\partial^2 A}{\partial \phi^2} - ig|A|^2A = -\left(\frac{\kappa}{2} + i(\omega_0 - \omega_p)\right)A + \sqrt{\frac{\kappa\eta P_{\mathrm{in}}}{\hbar\omega_0}}. \tag{6.23}$$

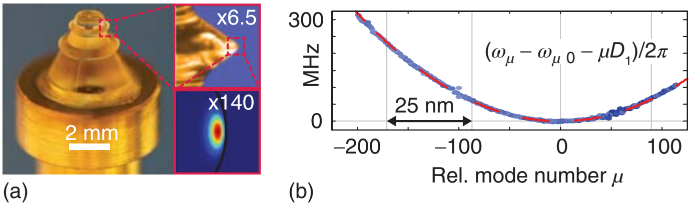

Figure 6.6 Crystalline resonator for temporal dissipative Kerr soliton generation. (a) Crystalline MgF$_2$ resonator and simulated mode profile. (b) Measured anomalous group velocity dispersion for the resonator shown in panel (a). The dispersion of a resonator can be quantified in terms of the deviation of its resonance frequencies ω_μ from an equidistant frequency grid $\omega_0 + \mu D_1$, where $D_1/(2\pi)$ is the FSR at the pump wavelength. An anomalous group velocity dispersion corresponds to a parabolic curve as shown in (b).

Here, $A(\phi, t) = \sum_\mu A_\mu e^{i\mu\phi - i(\omega_\mu - \omega_p)t}$ is the slowly varying field amplitude and $\phi \in [0, 2\pi]$ is the angular coordinate inside the resonator with periodic boundary conditions, $\eta = \kappa_{\mathrm{ex}}/\kappa$ is the coupling efficiency with critical coupling corresponding to $\eta = 1/2$. Transforming Eq. (6.23) to its dimensionless form gives

$$i\frac{\partial \Psi}{\partial \tau} + \frac{1}{2}\frac{\partial^2 \Psi}{\partial \theta^2} + |\Psi|^2\Psi = (-i + \zeta_0)\Psi + if. \tag{6.24}$$

Here, $\theta = \phi\sqrt{\frac{1}{2d_2}}$ is the dimensionless longitudinal coordinate, $\Psi(\tau, \phi) = \sum a_\mu(\tau)e^{i\mu\phi}$ is the waveform, and $d_2 = D_2/\kappa$ is the dimensionless dispersion. Equation (6.24) is identical to the Lugiato–Lefever equation [31], where a transversal coordinate is used instead of a longitudinal one in our case. It is important to note here, that though we used throughout the chapter the term *temporal* to differentiate DCS from better known spacial cavity solitons in nonlinear Fabry-Perot etalons, this term may also be confusing. For temporal dissipative solitons in fibers and fiber loop resonators in equations time is usually considered as a “fast” variable, describing the form of the pulse, while the coordinate along propagation is describing slow variations. In the case of WGM microresonators the opposite mapping is more convenient with “slow” time variation averaged over many roundtrips and fast mapped azimuthal angular coordinate. This equation may also be considered as a driven, damped nonlinear Schrödinger equation (NLS) [32]. Analytical solutions of the NLS in the form of bright soliton are known only in case of zero dissipation [73]. An approximate solution for the dissipative soliton may be found using Lagrangian perturbation approach [74, 75]. First, we introduce Lagrangian density so that the variation of it over Ψ^* (Landau–Euler equation) leads to an unperturbed NLS equation:

$$\frac{\delta \mathcal{L}}{\delta \Psi^*} \equiv \frac{\partial \mathcal{L}}{\partial \Psi^*} - \frac{\partial}{\partial \tau}\frac{\partial \mathcal{L}}{\partial \Psi^*_\tau} - \frac{\partial}{\partial \theta}\frac{\partial \mathcal{L}}{\partial \Psi^*_\theta} = 0, \tag{6.25}$$

$$\mathcal{L} = \frac{i}{2}\left(\Psi^*\frac{\partial \Psi}{\partial \tau} - \Psi\frac{\partial \Psi^*}{\partial \tau}\right) - \frac{1}{2}\left|\frac{\partial \Psi}{\partial \theta}\right|^2 + \frac{1}{2}|\Psi|^4 - \zeta_0|\Psi|^2, \tag{6.26}$$

Now taking into account the perturbed equation (Eq. 6.24), we introduce the dissipative function:

$$\begin{aligned}\frac{\delta \mathcal{L}}{\delta \Psi^*} &= \mathcal{R},\\ \mathcal{R} &= -i\Psi + if,\end{aligned} \tag{6.27}$$

The equations that need to be solved are the following:

$$\begin{aligned}\frac{\partial L}{\partial r_i} - \frac{d}{d\tau}\frac{\partial L}{\partial \dot{r}_i} &= \int \left(\mathcal{R}\frac{\partial \Psi^*}{\partial r_i} + \mathcal{R}^*\frac{\partial \Psi}{\partial r_i} \right) d\theta,\\ L &= \int \mathcal{L} d\theta.\end{aligned} \tag{6.28}$$

where r_i are different possibly time-dependent collective coordinates. Using the ansatz of a stationary ($\frac{\partial\Psi}{\partial\tau} = 0$) soliton $Be^{i\varphi_0}\mathrm{sech}(B\theta)$ (exact for unperturbed case when $B = \sqrt{2\zeta_0}$) with $r_1 = B$ and $r_2 = \varphi_0$ [33], we get

$$L = -2B\frac{\partial\phi_0}{\partial\tau} + \frac{1}{3}B^3 - 2B\zeta_0. \tag{6.29}$$

This yields

$$\frac{d\boldsymbol{B}}{d\tau} = -2B + \pi f \cos\varphi_0, \tag{6.30}$$

$$\frac{d\phi_0}{d\tau} = \frac{1}{2}B^2 - \xi_0. \tag{6.31}$$

This leads to the stationary parameters of the soliton attractor [33]:

$$B = \sqrt{2\xi_0}, \tag{6.32}$$

$$\cos\varphi_0 = \frac{2B}{\pi f} = \frac{\sqrt{8\xi_0}}{\pi f}, \tag{6.33}$$

$$\zeta_0^{\max} = \frac{\pi^2 f^2}{8}. \tag{6.34}$$

An approximate single-soliton solution that accounts for a flat CW background is then given by

$$\Psi = \Psi_0 + \Psi_1 \simeq \Psi_0 + Be^{i\varphi_0}\mathrm{sech}(B\theta), \tag{6.35}$$

The constant CW background Ψ_0 may be found by substituting Ψ_0 into Eq. (6.24) as the lowest branch [32] of the solution of

$$(|\Psi_0|^2 - \zeta_0 + i)\Psi_0 = if, \tag{6.36}$$

which, eventually, results for $\zeta_0 > \sqrt{3}$ (bistability criterion) and large enough detunings $f^2 < \frac{2}{27}\zeta_0(\zeta_0^2 + 9)$ in

$$|\Psi_0|^2 = \frac{2}{3}\zeta_0 - \frac{2}{3}\sqrt{\zeta_0^2 - 3}\cos\left(\frac{1}{3}\arccos\left(\frac{2\zeta_0^3 + 18\zeta_0 - 27f^2}{2(\zeta_0^2 - 3)^{2/3}}\right)\right),$$

$$\Psi_0 = \frac{if}{|\Psi_0|^2 - \zeta_0 + i} \simeq \frac{f}{\zeta_0^2} - i\frac{f}{\zeta_0}. \tag{6.37}$$

Extending Eq. (6.35) to the case of multiple solitons inside the resonator gives

$$\Psi(\phi) \simeq \Psi_0 + \left(\frac{4\zeta_0}{\pi f} + i\sqrt{2\zeta_0 - \frac{16\zeta_0^2}{\pi^2 f^2}}\right)\sum_{j=1}^{K} \operatorname{sech}\left(\sqrt{\frac{\zeta_0}{d_2}}(\phi - \phi_j)\right). \tag{6.38}$$

This ansatz automatically translates to discrete possible states (steps) in nonlinear resonant response. These steps are an important signature of soliton Kerr combs and are observed in the experiments (see Section 6.5). The height of steps in the intracavity power can be found by averaging the waveform amplitude (Eq. (6.38)) squared over one round-trip for different numbers K of solitons:

$$\begin{aligned}\overline{|\Psi|^2} &= |\Psi_0|^2 + K\frac{1}{2\pi}\int_0^{2\pi}(\Psi_1^2 + \Psi_0\Psi_1^* + \Psi_1\Psi_0^*)d\phi \\ &\simeq \frac{f^2}{\zeta_0^2} + K\frac{2}{\pi}\sqrt{d_2\zeta_0}.\end{aligned} \tag{6.39}$$

The Fourier transform of a hyperbolic secant soliton is again a hyperbolic secant:

$$\Psi(\mu) = \mathrm{FT}\left[\sqrt{2\zeta_0}\operatorname{sech}\left(\sqrt{\frac{\zeta_0}{d_2}}\phi\right)\right] = \sqrt{d_2/2}\operatorname{sech}\left(\frac{\pi\mu}{2}\sqrt{\frac{d_2}{\zeta_0}}\right). \tag{6.40}$$

Using the relation for the optical frequency $\omega = \omega_p + \mu D_1$ and the time $t = \phi/D_1$, the spectral envelopes and the soliton waveform can be rewritten as

$$\Psi(\omega - \omega_p) = \sqrt{d_2/2}\operatorname{sech}((\omega - \omega_p)/\Delta\omega) \text{ with } \Delta\omega = \frac{2D_1}{\pi}\sqrt{\frac{\zeta_0}{d_2}}. \tag{6.41}$$

and

$$\Psi(t) = \sqrt{2\zeta_0}\operatorname{sech}(t/\Delta t), \text{ with } \Delta t = \frac{1}{D_1}\sqrt{\frac{d_2}{\zeta_0}}. \tag{6.42}$$

The minimal possible soliton duration can be found by using $\zeta_0^{\max}$ (Eq. (6.33)) in the above-mentioned equation for Δt:

$$\Delta t_{\min} = \frac{1}{\pi D_1}\sqrt{\frac{\kappa D_2 n_0^2 V_{\mathrm{eff}}}{\eta P_{\mathrm{in}}\omega_0 c n_2}}. \tag{6.43}$$

This equation can be recast in the form of the group velocity dispersion $\beta_2 = \frac{-n_0}{c}D_2/D_1^2$, the nonlinear parameter $\gamma = \frac{\omega}{c}\frac{n_2}{\mathcal{A}_{\mathrm{eff}}}$ (for Simplicity, we assume critical coupling $\eta = 1/2$ and on resonant pumping):

$$\Delta t_{\min} = \frac{2}{\sqrt{\pi}} \sqrt{\frac{-\beta_2}{\gamma \mathcal{F} \mathcal{P}_{\text{in}}}}, \tag{6.44}$$

where $\mathcal{F} = \frac{D_1}{\kappa}$ denotes the finesse of the cavity. Note that the values $\Delta\omega$ and Δt need to be multiplied by a factor of $2\,\text{arccosh}(\sqrt{2}) = 1.763$ to yield the full-width half-maximum (FWHM) of the sech^2-shaped power spectrum and pulse intensity, respectively.

For the time bandwidth product (TBP), we find $\Delta t \Delta\omega = 2/\pi$ or, when considering the FWHM of spectral and temporal power (in units of hertz and second), TBP = 0.315.

In the case of K multiple solitons inside the cavity, there is a more structured optical spectrum Ψ_k, resulting from interference of single soliton spectra $\Psi_j(\mu)$, where the relative phases of these spectra are determined by the positions ϕ_j of individual solitons: $\Psi_K(\mu) = \Psi(\mu) \sum_{j=1}^{K} e^{i\mu\phi_j}$. The line-to-line variations can be high; however, the overall averaged spectrum still follows the single soliton shape and is proportional to $\sqrt{K}\Psi(\mu)$.

6.5
Signatures of Dissipative Kerr Soliton Formation in Crystalline Resonators

The generation of temporal dissipative solitons in microresonators is associated with several characteristic signatures that can already be observed during a transient generation of the solitons. Here, transient generation refers to the situation where the pump laser is scanned (with increasing wavelength) through the resonance of the microresonator. The described signatures are particularly useful from a practical perspective as they allow for rapid sample characterization. Depending on the detuning during the laser scan the system can enter different nonlinear regimes including, parametric sideband generation with Turing patterns [76], Kerr-comb formation, breather solitons [77], and stable temporal dissipative soliton generation. One signature, though not unambiguously connected to soliton formation, is a transition from high-intensity noise and high-phase-noise (related to Kerr-subcomb formation) to a low-noise state. While scanning the laser, the noise can be monitored by, for example, recording the intensity noise in the generated spectrum or by detecting the beat note signal between the generated optical lines as shown in Figure 6.7b.

A more unique and easily observable signature of soliton formation in optical microresonators is the occurrence of discontinuous staircase-like steps in the transmitted pump-laser power while the laser is continuously scanned across the optical resonance (cf. Figure 6.7a) [35].[2] When operating a microresonator a

---

[2] Discontinuous steps can also be observed (typically with a higher signal-to-noise ratio) in the power of the nonlinearly generated light.

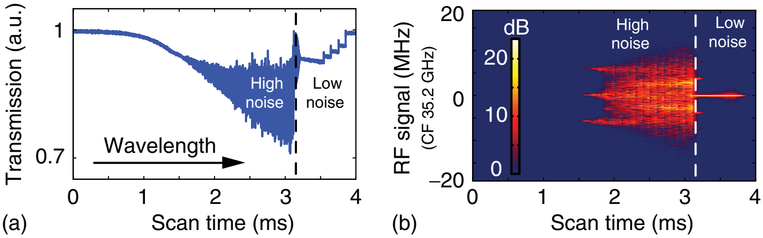

Figure 6.7 Signatures of soliton formation. (a) A staircase-like step structure in the pump laser transmission indicates the formation of several DKS in the microresonator. High intensity noise is apparent in the transmission signal before soliton formation. (b) The formation of the solitons is associated with a transition to low noise. This is evidenced here by the transition of a broad RF beat note (cf. Figure 6.4) to a single narrowband signal. CF, center frequency.

lower pump laser transmission implies a higher average intracavity power. The emergence of the steps may be explained by referring to the cavity bistability curve that describes the power inside the cavity in dependence of the pump laser detuning. When approaching the cavity resonance from the blue detuned side (laser frequency is higher than the resonance frequency and correspondingly laser wavelength is shorter than the resonance wavelength) the intracavity power will increase. This increase of intracavity power will then, due to the Kerr-nonlinearity, effectively shift the resonance frequency toward longer wavelength. As the laser detuning is further decreased the intracavity power will steadily increase (upper branch on the bistability curve), until the highest possible power is reached at the point of effective zero-detuning. Beyond this point (now effectively red-detuned), the intracavity power will steeply drop to a much lower value (lower branch on the bistability curve) as the Kerr-nonlinear resonance shift vanishes (cf. Figure 6.8a). Exactly at this transition to red detuning, temporal dissipative Kerr solitons can emerge from the noisy intracavity waveform (cf. Figure 6.9). In this case, the formation of a high-peak-power soliton pulse will cause an additional Kerr-frequency shift such that the part of the pump light that sees the soliton pulse (i.e., copropagating with the soliton inside the cavity) follows now a second bistability curve (Figure 6.8b). The result is a second power drop at a larger detuning when the soliton vanishes.

The combined signal of power drops occurring at different laser detunings leads to the overall staircase-like step structure in the transmitted power. If a higher number of soliton pulses is generated, a series of multiple steps can be observed (during a rapid scan not all solitons disappear at the exact same detuning). The exact number of generated solitons differs from one laser scan to the other as the solitons emerge from a noisy state. It is interesting to note that the transition to effective red-detuning has not been considered in previous work as it is usually associated with only low intracavity power [78]. Section 6.6 describes how stable operation in the soliton regime can be achieved despite the steps in the intracavity power that can affect the resonator temperature.

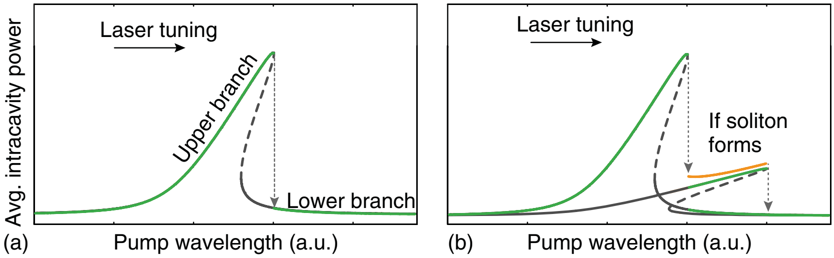

Figure 6.8 Stability of soliton states: considering only the Kerr-nonlinear resonance shift the intracavity power can be described by bistability curves where the upper branch solution corresponds to high and the lower branch solution to low intracavity power. When tuning into the resonance with decreasing optical frequency (increasing wavelength) the intracavity power follows the upper branch of the Kerr-bistability curve. After the transition to a soliton state, the major fraction of the pump light is described by the lower branch of the bistability curve. The fraction of the pump light that propagates with the soliton inside the microresonator experiences a larger phase shift and is effectively blue detuned on the upper branch of another bistability curve. The extend of the "soliton bistability curve" toward longer wavelength depends on the peak power of the solitons (i.e., the maximal nonlinear phase shift), the relative height of the curve depends on the relative fraction of the pump light that is affected by the high-peak-power soliton. The overall intracavity power can be inferred by adding the bistability curves resulting in the black curve.

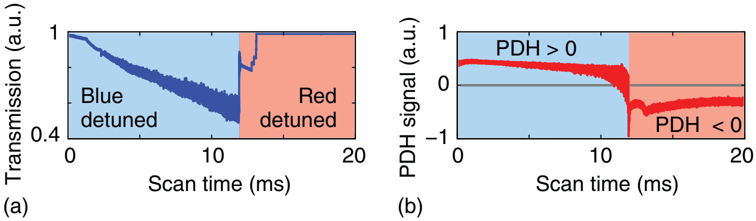

Figure 6.9 Laser detuning and soliton formation. (a) The transmitted power and a series of steps associated with multiple temporal cavity solitons. The background shading indicates the laser detuning that is derived from a Pound–Drever-Hall (PDH) error signal shown in (b). The soliton formation coincides with the transition to red detuning (indicated by a sign change in the PDH error signal). Note that the additional Kerr-frequency shift due to the high-peak-power soliton does not significantly impact the PDH error signal as its relative contribution is small.

6.6
Laser Tuning into the Dissipative Kerr Soliton States

For stable operation of a microresonator system, thermal self-locking [79, 80] is a widely used method. Here, the resonator self-locks itself thermally to the pump laser frequency. Besides being a simple and convenient method, this allows for a fixed pump laser frequency during steady-state operation (instead of a pump laser that follows drifts in the resonator). This is advantageous for frequency comb operation, where the pump laser constitutes one of the comb lines that should remain fixed in frequency. The mechanism of thermal self-locking is somewhat analogous to the Kerr-nonlinear bistability curve and gives rise to a so-called thermal triangle, which is known from the earliest reports of whispering-gallery mode microresonators [1, 2]. In a resonator with positive thermo-refractive coefficient (as in MgF_2 or Si_3N_4), thermal locking is achieved by blue detuned pumping. In this regime, an increase of pump wavelength (or equivalently a decrease of resonance wavelength) implies a higher intracavity power and higher rate of absorptive heating. As a consequence of this heating and mostly due to the thermo-optic effect, the resonance wavelength shifts toward longer wavelength thus stabilizing the relative detuning between pump laser and resonator. Exactly this behavior is present during a soliton state. This can be seen, for example, in Figure 6.7 where (within a particular soliton state) an increase in pump wavelength causes an increase in intracavity power (decrease of transmission).

In order to stably reach the regime of thermal locking of a soliton state, it is important that the transition to the soliton state does not induce a change of the resonator temperature (despite the fact that the intracavity power changes), which would directly destabilize the system. One solution to this problem is to tune the pump laser from a far-blue detuned position into the soliton state with a tuning speed chosen such that the “integrated absorptive heating” over the tuning time corresponds to the heating rate in the soliton state. In this case, the temperature does not change significantly when the soliton state is reached. Thermal locking then ensures the stable operation of the soliton state (for many hours), without actuation on the pump laser frequency, as illustrated in Figure 6.10. It is important to note that the solitons emerge from intrinsic noise present in the cavity before reaching the soliton state. As a consequence, the initial number of solitons generated via the laser tuning method varies randomly from shot to shot. However, the experimental conditions can often be adjusted such that a certain number of solitons (e.g., one soliton) are generated with high probability. The maximal number of soliton that can be generated via the laser tuning method is related to the dispersion of the cavity and grows with the applied pump power [35]. For typical parameters, only a few, maximally up to approximately 10 or 20, solitons are generated. As the exact number depends on a random process, the electronically controlled laser tuning method is usually repeated several times until it yields the desired number of solitons. Note that the laser tuning method does not require an additional external stimulation (e.g., a laser pulse), as it is the case in fiber cavities. The following section characterizes the solitons generated via the described laser tuning method.

6.7
Simulating Soliton Formation in Microresonators

Dissipative Kerr solitons in a microresonator can be simulated by integrating the coupled mode equation (6.11) in time similar to work related to Kerr-combs by Chembo *et al.* [62–64]. We use an adaptive Runge–Kutta method of the fifth

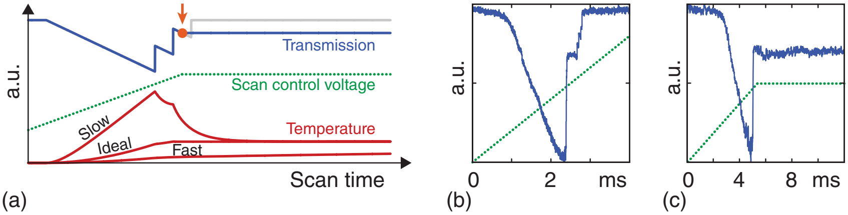

Figure 6.10 Generation of stable solitons via laser tuning. (a) Illustration of laser transmission, scan control voltage (corresponding to pump wavelength), and resonator temperature for slow, ideal, and fast laser tuning speed. In the ideal case, the resonator temperature does not change once the desired soliton state is reached and the laser scan can be stopped for stable operation. (b) Regular scan of the pump laser over a resonance showing a "soliton step." (c) The laser tuning method allows to stop the laser scan once the soliton is generated. Once generated in this manner, the soliton circulates stably inside the microresonator.

order, which together with a transformed system of equations without trigonometric functions and explicit time dependence allows achieving fast simulation. The simulation of hundreds of optical lines allows for accurate modeling of realistic experimental systems. This includes in particular the beat note between the optical lines (i.e., the repetition rate), the envelope of the optical spectrum as well as instant amplitudes, phases and frequencies of all modes. The sum of the nonlinear mixing terms is efficiently calculated in the Fourier-domain [81]. An additional self-steepening term is added when simulating broad combs in Si_3N_4 rings to better model the behavior of few-cycle pulses [82]. In simulations, similar to the experiment, solitons can be generated via tuning the pump laser into resonance. The number of generated solitons depends on the noisy intracavity waveform preceding the soliton state. To allow for deterministic simulations of a certain number of solitons, the respective number of sech-pulses can be seeded as an initial waveform while the simulation is started directly with a detuning that allows for stable solitons. It is worthwhile noting that the underlying coupled mode equations readily allow for the simulation of complex and irregular mode structures as often encountered in real microresonators (cf. Section 6.9). Based on our simulations, we developed an open-source graphical user interface using MATLAB [83] that allows numerical simulation of Kerr-comb and soliton generation in microresonators (Figure 6.11).

6.8
Characterization of Temporal Dissipative Solitons in Crystalline Microresonators

The ability to stably tune into soliton states as described in the Section 6.6 allows for characterization of the solitons' spectral and temporal properties in crystalline microresonators MgF_2. Precisely as predicted by theory, the single soliton state has a sech-squared spectral envelope from which a pulse duration in the femtosecond regime can be inferred. The latter can be confirmed via

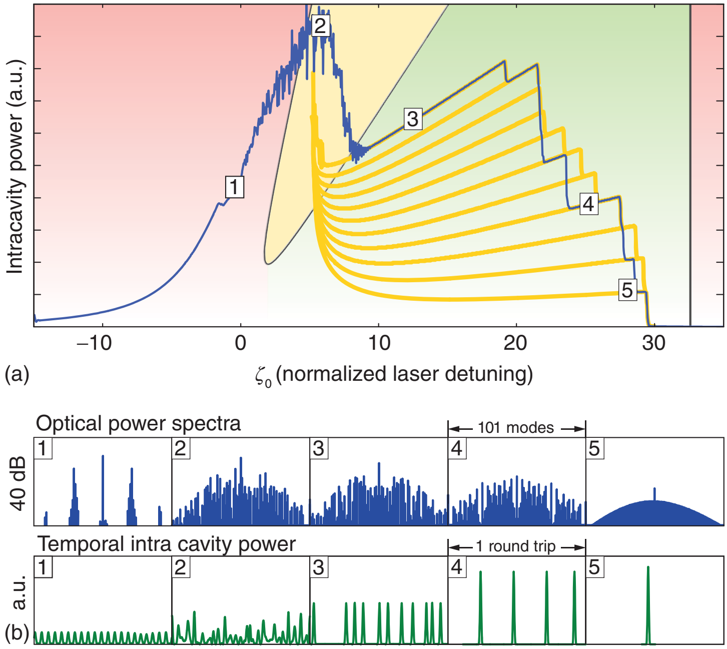

Figure 6.11 Numerical simulations of dissipative Kerr soliton formation in a crystalline microresonator. (a) Intracavity power (corresponding to the transmission signal in Figure 6.7a when mirrored horizontally) during a simulated laser scan (101 simulated modes) over a resonance in a microresonator. The step features are clearly visible. The light gray lines trace out all possible states of the system during the scan. The unshaded area corresponds to the area where DKSs can exist, the light shaded area allows for breather solitons with a time variable, oscillating envelope; no solitons can exist in the dark shaded area. (b) Optical spectrum and intracavity intensity for different detuning values (1–5) in the laser scan.

direct temporal characterization. Here, frequency-resolved optical gating using a nonlinear Michelson-interferometer (SHG-FROG) [84] is used (cf. Figure 6.12). This method also allows for the reconstruction of the complex pulse envelope [85]. The high pulse repetition rate inherent to microresonators allows the FROG interferometer delay to extend over several pulse round-trip times, that is, consecutive pulses can be cross correlated.

Besides stable single solitons, also stable multisoliton states can be generated using the laser tuning method. Figure 6.13 compares the optical spectra and SHG-FROG traces of a single and two different multisoliton states. A salient feature of multisoliton states is the modulated spectral envelope arising from the interference of the individual soliton. Based on the spectral envelope, the relative positions of the solitons can be reconstructed (cf. Section 6.11). Once a multisoliton state is generated inside the cavity, the envelope pattern does not change over several hours, implying that the temporal separation between the solitons in the microresonator does not change on this time scale.

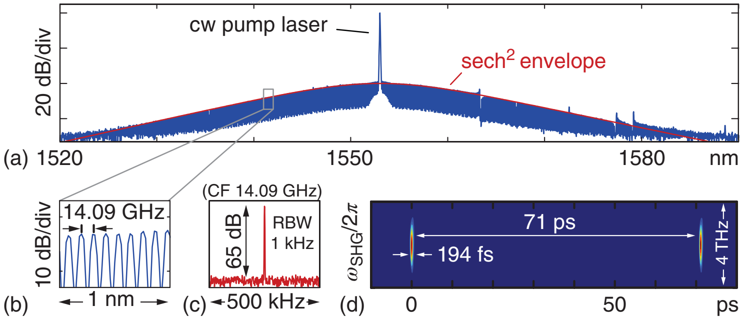

Figure 6.12 Characteristics of a Dissipative Kerr soliton in a crystalline resonator. (a) Optical spectrum showing the characteristic sech-squared envelope. (b) Magnified part of the spectrum, resolving the individual comb lines of which it is composed. (c) The low-noise radio frequency beat note at 14.09 GHz corresponds to the comb line spacing and the soliton pulse repetition rate. (d) SHG-FROG trace revealing femtosecond pulse duration. The pulse to pulse separation of 71 ps corresponds to the pulse repetition rate of 14.09 GHz and the pulse duration of 194 fs can be inferred (in agreement with the spectral width). RBW, resolution bandwidth; CF, center frequency).

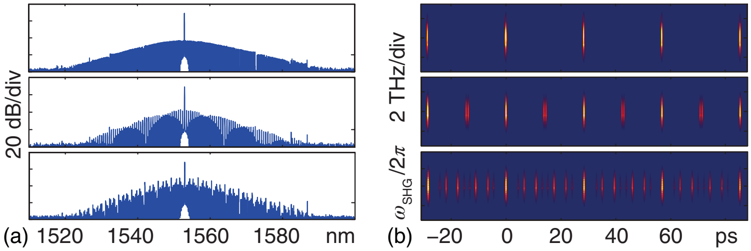

Figure 6.13 Spectral and temporal characterization of multisoliton states in a crystalline resonator. (a) Optical spectra of a single soliton (top) and two multisoliton states (middle, bottom). (b) SHG-FROG traces corresponding to (a).

6.9
Resonator Mode Structure and Soliton Formation

The generation of bright dissipative Kerr solitons requires a focusing nonlinearity and an anomalous group velocity dispersion (GVD), that is, a linear (*neglecting higher order terms*) growth of the resonator's FSR with the mode number. In this case the growth of the FSR can be compensated by nonlinear mode pulling, that is, nonlinear optical shifts of the resonance frequency. In principle, most microresonators fulfill this requirement in the (near-)infrared spectral regime. As opposed to optical fiber systems, microresonators, however, can exhibit a rich and complex optical mode structure. Some modes are affected by higher-order dispersion or are even characterized by normal GVD. Moreover, fabrication defects and asymmetries can lead to modal coupling and distortions of the mode

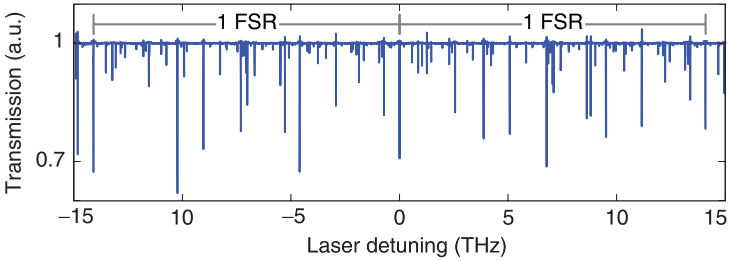

Figure 6.14 Transmission spectrum of an MgF$_2$ crystalline microresonator with an FSR of approximately 14.09 GHz. The upward transmission spikes (values > 1) result from cavity-ringdown. Frequency-comb-assisted diode laser spectroscopy ensures precise calibration of the laser detuning (megahertz level).

spectrum due to avoided mode crossings. While dissipative Kerr solitons are a single-mode phenomenon, the structure of the respective mode family can be altered by the presence of other modes. The understanding of the impact and influence of the mode structure is a decisive step in understanding DKS in optical microresonators. In Reference [36] this is studied experimentally and with the help of the numerical tools described in Section 6.7. First, the mode structure of the microresonator is precisely measured using frequency-comb-assisted diode laser spectroscopy [86]. Figure 6.14 shows a fraction of the recorded transmission spectrum of a crystalline resonator, revealing several mode families. The full data set is represented in Figure 6.15a. Individual mode families and their dispersion can be extracted from the full data set. An example of a mode family with almost perfect anomalous GVD is shown in Figure 6.15b, top. In contrast, Figure 6.15b, bottom shows a another mode family where the globally anomalous GVD is locally modified by two avoided mode crossing. While in the first case solitons can be generated, this is not possible in the latter. The hypothesis that avoided mode crossing (if they occur in the spectral vicinity of the pumped mode) inhibits soliton formation is confirmed by numerical simulation [36]. Moreover, strong higher-order dispersion can prevent soliton formation. Importantly, moderate contribution of higher-order dispersion and avoided mode crossings further away from the pump wavelength do not inhibit soliton formation but manifest themselves in the optical spectrum as qualitatively illustrated in Figure 6.16. Indeed, similar structures can be observed in the experimentally generated soliton spectra, that is, in Figure 6.12.

6.10
Using Dissipative Kerr solitons to Count the Cycles of Light

The observation of temporal solitons in microresonators, and the associated generation of ultrashort femtosecond optical pulses, provides an opportunity to count the cycles of light using an optical microresonator, that is, to link phase coherently

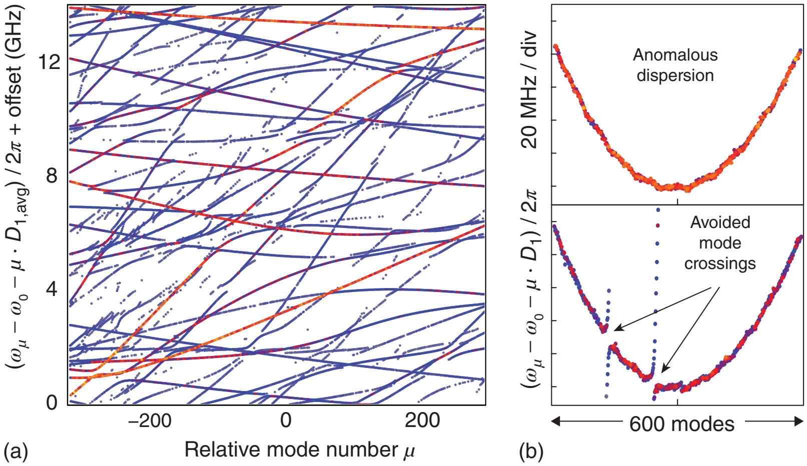

Figure 6.15 Mode structure of an MgF_2 resonator with an FSR of 14.09 GHz. (a) Two-dimensional Echelle-type representation where for all measured mode families the deviation $\omega_\mu - \omega_0 - \mu \cdot D_{1,\mathrm{avg}}$ of the resonance frequency ω_μ from an equidistant $D_{1,\mathrm{avg}}$-spaced frequency grid ($D_{1,\mathrm{avg}}$ is an approximate average FSR of all modes) is shown (plus some offset) in function of the mode number μ. Dots forming a continuous line represent a particular mode family. Different free spectral ranges correspond to different slopes of the lines, whereas dispersion and variation of the FSR show as curvature and bending of the lines. The dispersion can be strongly affected by mode crossings. (b) Two mode families have been extracted from the data set shown in (a). The upper one is characterized by an anomalous dispersion, the lower one exhibits two avoided mode crossings that induce deviations from the anomalous dispersion.

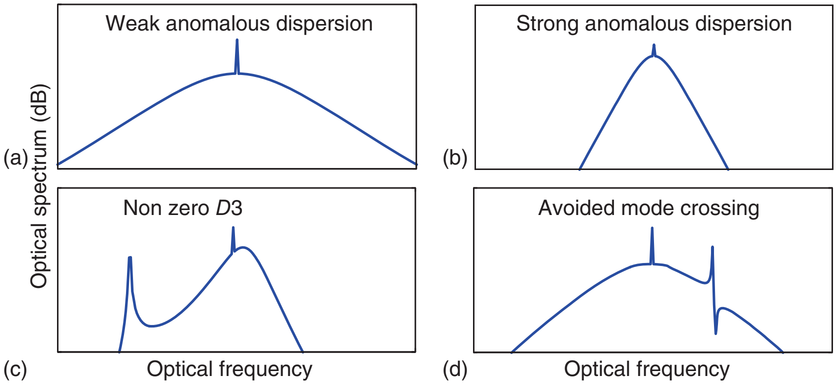

Figure 6.16 Mode structure and spectral envelope. (a) Typical sech-squared envelope for the case of weak (a) and strong anomalous dispersion (b). (c) Higher-order dispersion (such as non zero D_3) leads to an asymmetric spectrum, dispersive wave emission (cf. Section 6.11) and a shift of the spectral soliton peak intensity away from the pump laser (soliton recoil). (d) Avoided mode crossings manifest themselves in a characteristic spectrally local variation of the spectrum.

an optical laser frequency to the radio frequency domain. In order to achieve such a radio to optical frequency link [87] self-referencing has to be employed; a process where the comb's offset frequency f_0 (cf. Figure 6.1) is measured. To this end, an optical spectrum of sufficient spectral span is required that spans either a full octave when using the $1f-2f$ self-referencing technique or 2/3 of an octave for the $2f-3f$ self-referencing method [14, 38, 39] (cf. Figure 6.17). While the soliton spectrum generated in a crystalline resonator is not sufficiently broad by itself, the short pulse duration enables (after power amplification in an erbium-doped fiber amplifier) spectral broadening [88] in highly nonlinear optical fiber. Figure 6.18a

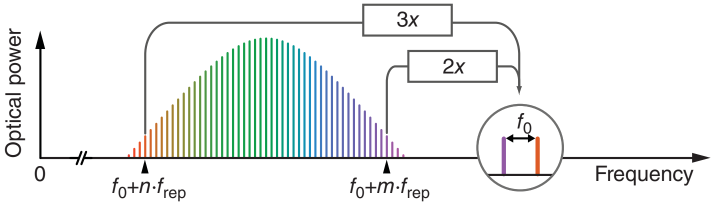

Figure 6.17 Illustration of $2f-3f$ self-referencing. If the frequency-comb spectrum spans more than two-thirds of an octave, the second and third harmonics of blue and red wings of the spectrum can be overlapped. The difference frequency beat note between the two harmonics yields the comb's offset frequency f_0.

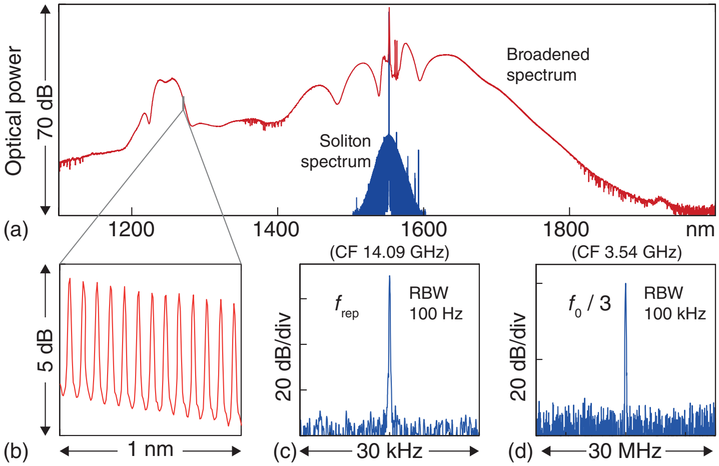

Figure 6.18 Counting the cycles of light by self-referencing a soliton-based frequency comb. (a) Soliton spectrum and nonlinearly broadened spectrum. The broadened spectrum spans more than two-thirds of an octave and allows for $2f-3f$ self-referencing. (b) Magnified part of the broadened spectrum. The line spacing is the same as for the soliton spectrum (14.09 GHz). (c) Pulse repetition rate beat note measured via direct photodetection of the comb spectrum. (d) Offset frequency signal measured via a modified $2f-3f$ self-referencing technique, where two transfer lasers are used for signal enhancement (see [89] for details). RBW, resolution bandwidth; CF, center frequency.

shows a soliton spectrum that has been broadened in this way [89]. Here, $2f-3f$ self-referencing is implemented allowing for detection of the soliton comb's offset frequency f_0 (cf. Figure 6.18d). Together, with the comb line spacing (i.e., the pulse repetition rate) f_{rep} that can be readily measured via direct photodetection (cf. Figure 6.18c), the frequencies constituting the soliton comb are fully defined. In this way, the dissipative Kerr soliton allows linking optical frequencies (e.g., the pump laser wavelength or any other comb line) to the radio (or microwave) frequencies f_0 and f_{rep}.

6.11
Temporal Solitons and Soliton-Induced Cherenkov Radiation in an $\mathrm{Si_3N_4}$ Photonic Chip

The discovery of temporal solitons in crystalline resonators, as described in the previous chapters not only enables generating coherent optical frequency combs in a reliable manner, but also opened the ability to use time-domain broadening methods to achieve a coherent link from the RF (or microwave) domain to the optical frequency domain. A key emerging research question has been whether solitons can also be generated in other microresonator platforms. One particularly promising platform for applications are $\mathrm{Si_3N_4}$ integrated microresonators. This platform allows for the integration of coupling waveguide and resonators on a microchip. Indeed, it was demonstrated that by carefully optimizing the fabrication process, the influence of detrimental avoided mode crossings can be strongly reduced, enabling the generation of DKS in $\mathrm{Si_3N_4}$ microresonators [37]. Here, as in the case of crystalline resonators, the soliton formation is indicated by discrete steps in the resonator transmission. Similar to the method described earlier in detail in Section 6.6 a suitable laser scan allows for stable and thermally locked solitons in $\mathrm{Si_3N_4}$ microresonators. Figure 6.19 shows the generation of a single-soliton state in an $\mathrm{Si_3N_4}$ microresonator. The bandwidth of the generated spectrum is much wider than what has been observed in crystalline resonators. As an immediate consequence, higher-order dispersion terms become relevant; indeed, the third-order dispersion causes the temporal soliton to emit what is known as *Soliton–Cherenkov* radiation [52] (or dispersive wave), that is, a radiative tail in the time domain. It is important to note that the process can also be understood in the frequency domain as successive FWM [90]. Dispersive wave formation has been predicted particularly for $\mathrm{Si_3N_4}$ resonators, where for a coherent spectrum a spectrally sharp dispersive wave is expected [91], as it is indeed the case (cf. Figure 6.19). For a resonator with third-order dispersion (i.e., non-zero D_3), this occurs approximately near the mode number $\mu \approx -3\frac{D_2}{D_3}$ (three times the distance of the zero dispersion point from the pump wavelength, $\mu \approx -\frac{D_2}{D_3}$) [37].

It is important to note that unlike the case of a soliton propagating along an optical fibers where the dispersive wave is generally incoherent with the soliton (i.e., propagating at a velocity different from the soliton's velocity), the

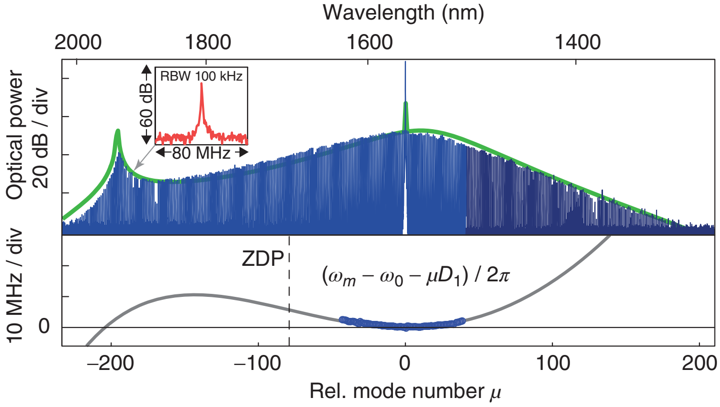

Figure 6.19 Single temporal soliton generation in an Si_3N_4 microresonator. The upper panel shows the single soliton spectrum that covers a spectral bandwidth of 2/3 of an octave. The black line in the background is the spectral envelope obtained by the simulation described in Section 6.7. The lower panel shows the measured dispersion (dots) free of avoided mode crossing and the dispersion over the full-spectral span as obtained through finite element simulation. The dispersive wave forms at the wavelength of approximately 1.9 micron where the phase-matching condition $\omega_\mu - \omega_0 - \mu \cdot D_1 \approx 0$ is fulfilled. The zero dispersion point (ZDP) is marked by a vertical, dashed line. The inset in the upper panel shows a heterodyne beat note between the dispersive wave and an external laser. Its narrow width proves the coherence of the dispersive wave.

coherence can be maintained in case of the microresonator owing to the periodic boundary conditions. This is similar to the coherence of the dispersive wave in supercontinua that are generated by a periodic train of ultrashort pulses. At the same time, the presence of a dispersive wave can also occur in the case of a high-noise, nonsoliton state. The presence of a dispersive wave, therefore, is not a proof of a coherent temporal soliton state [92]. Note that the coherence of the spectrum in Figure 6.19 has been verified by recording the soliton pulse repetition rate beat note at 190 GHz as well as the heterodyne beat notes of the soliton spectrum with external CW lasers at various wavelengths (including the dispersive wave spectral region). Based on the spectral width, a soliton pulse duration of approximately 30 fs can be estimated.

It is also possible to generate multiple solitons in the Si_3N_4 microresonators. As in the case of the crystalline resonators, once a multisoliton state is generated, the modulation of the spectral envelope, resulting from the interference of the solitons, remains stable for hours. The spectral envelope function $I(\mu)$ of this interference is given by

$$I(\mu) = \left| \sum_{j=1}^{N} \exp(i\phi_j \mu) \right|^2 ,$$

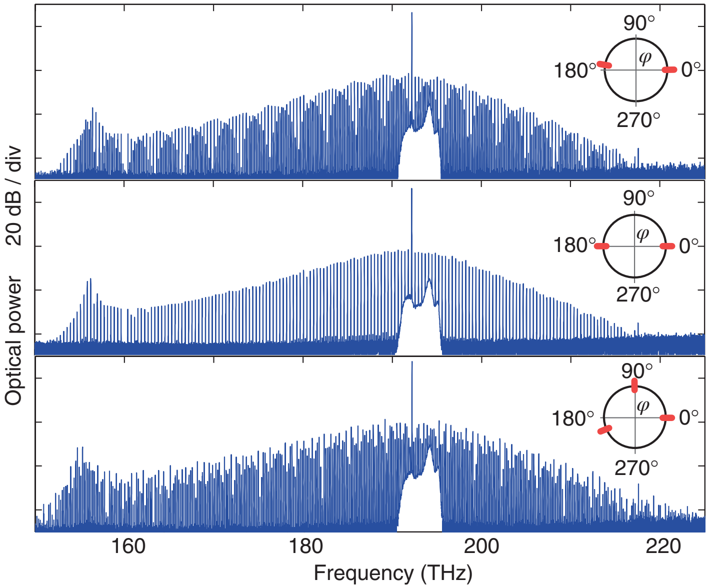

Figure 6.20 Generation of multisoliton states and soliton-induced Cherenkov radiation in an Si_3N_4 microresonator. The characteristic spectral modulations occur due to the interference of solitons at different positions in the microresonators as indicated in the insets.

where ϕ_j corresponds to the relative angular position of the j^{th} soliton. From the envelope of the spectrum, the single soliton spectrum and the relative positions of the solitons can be reconstructed as shown in Figure 6.20.

6.12
Summary

The observation and stable generation of dissipative Kerr solitons in optical microresonators provides a major impetus to the field of microresonator frequency combs. It provides a long-sought method for the generation of widely spaced frequency combs, with smooth spectral envelope and with low phase noise. In addition, soliton-induced Cherenkov radiation provides a method to increase the bandwidth and transfer the coherence of the comb into the normal GVD regime. Together with the ability to accurately predict the comb performance via numerical simulations, this implies that the synthesis of octave spanning frequency comb spectra directly from a CW laser using a microresonator is a possibility. Solitons in microresonators may make frequency-comb metrology ubiquitous by enabling compact comb generators that exhibit mode spacings in the 10 – 100 GHz regime. Potential applications include frequency metrology (i.e., frequency measurements), data transfer, microwave signal generation, spectroscopy, optical sampling, and arbitrary optical waveform generation.

References

1. Braginsky, V.B., Gorodetsky, M.L., and Ilchenko, V.S. (1989) Quality-factor and nonlinear properties of optical whispering-gallery modes. *Phys. Lett. A*, **137** (7–8), 393–397.
2. Ilchenko, V.S. and Gorodetsky, M.L. (1992) Thermal nonlinear effects in optical whispering gallery microresonators. *Laser Phys.*, **2** (2), 1004–1009.
3. Treussart, F., Ilchenko, V.S., Roch, J.-F., Hare, J., Lefèvre-Seguin, V., Raimond, J.-M., and Haroche, S. (1998) Evidence for intrinsic {K}err bistability of high-{Q} resonators in suprafluid helium. *Eur. Phys. J. D*, **1**, 235–238.
4. Spillane, S.M., Kippenberg, T.J., and Vahala, K.J. (2002) Ultralow-threshold {R}aman laser using a spherical dielectric microcavity. *Nature*, **415** (6872), 621–623.
5. Grudinin, I.S., Matsko, A.B., and Maleki, L. (2009) Brillouin lasing with a {C}a{F}_2 whispering gallery mode resonator. *Phys. Rev. Lett.*, **102**, 43902.
6. Cohen, D.A., Hossein-Zadeh, M., and Levi, A.F.J. (2001) High-Q microphotonic electro-optic modulator. *Solid-State Electron.*, **45**, 1577–1589.
7. Ilchenko, V.S., Savchenkov, A.A., Matsko, A.B., and Maleki, L. (2003) Whispering-gallery-mode electro-optic modulator and photonic microwave receiver. *J. Opt. Soc. Am. B: Opt. Phys.*, **20**, 333–342.
8. Ilchenko, V.S., Savchenkov, A.A., Matsko, A.B., and Maleki, L. (2004) Nonlinear optics and crystalline whispering gallery mode cavities. *Phys. Rev. Lett.*, **92** (4), 43903.
9. Carmon, T. and Vahala, K.J. (2007) Visible continuous emission from a silica microphotonic device by third-harmonic generation. *Nat. Phys.*, **3** (6), 430–435.
10. Klyshko, D.N. (1988) *Photons and Nonlinear Optics*, Gordon and Breach Science Publishers.
11. Kippenberg, T.J., Spillane, S.M., and Vahala, K.J. (2004) Kerr-nonlinearity optical parametric oscillation in an ultrahigh-Q toroid microcavity. *Phys. Rev. Lett.*, **93** (8), 83904.
12. Savchenkov, A.A., Matsko, A.B., Strekalov, D., Mohageg, M., Ilchenko, V.S., and Maleki, L. (2004) Low threshold optical oscillations in a whispering gallery mode CaF2 resonator. *Phys. Rev. Lett.*, **93**, 243905.
13. Del'Haye, P., Schliesser, A., Arcizet, O., Wilken, T., Holzwarth, R., and Kippenberg, T. (2007) Optical frequency comb generation from a monolithic microresonator. *Nature*, **450**, 1214–1217.
14. Udem, Th., Holzwarth, R., and Hänsch, T.W. (2002) Optical frequency metrology. *Nature*, **416**, 233–237.
15. Cundiff, S.T. and Ye, J. (2003) Colloquium: Femtosecond optical frequency combs. *Rev. Mod. Phys.*, **75** (1), 325–342.
16. Savchenkov, A.A., Matsko, A.B., Ilchenko, V.S., Solomatine, I., Seidel, D., and Maleki, L. (2008) Tunable optical frequency comb with a crystalline whispering gallery mode resonator. *Phys. Rev. Lett.*, **101** (9), 93902.
17. Foster, M.A., Levy, J.S., Kuzucu, O., Saha, K., Lipson, M., and Gaeta, A.L. (2011) Silicon-based monolithic optical frequency comb source. *Opt. Express*, **19** (15), 14233–14239.
18. Levy, J.S., Gondarenko, A., Foster, M.A., Turner-Foster, A.C., Gaeta, A.L., and Lipson, M. (2010) CMOS-compatible multiple-wavelength oscillator for on-chip optical interconnects. *Nat. Photonics*, **4** (1), 37–40.
19. Razzari, L., Duchesne, D., Ferrera, M., Morandotti, R., Chu, S., Little, B.E., and Moss, D.J. (2010) CMOS-compatible integrated optical hyper-parametric oscillator. *Nat. Photonics*, **4** (1), 41–45.
20. Moss, D.J., Morandotti, R., Gaeta, A.L., and Lipson, M.L. (2013) New CMOS-compatible platforms based on silicon nitride and Hydex for nonlinear optics. *Nat. Photonics*, **7**, 597–563.
21. Jung, H., Xiong, C., Fong, K.Y., Zhang, X., and Tang, H.X. (2013) Optical frequency comb generation from aluminum nitride microring resonator. *Opt. Lett.*, **38** (15), 2810–2813.
22. Hausmann, B.J.M., Bulu, I., Venkataraman, V., Deotare, P., and

Loncar, M. (2014) Diamond nonlinear photonics. *Nat. Photonics*, **8** (5), 369–374.

23. Del'Haye, P., Arcizet, O., Schliesser, A., Holzwarth, R., and Kippenberg, T.J. (2008) Full stabilization of a microresonator-based optical frequency comb. *Phys. Rev. Lett.*, **101** (5), 053903.
24. Johnson, A.R., Okawachi, Y., Levy, J.S., Cardenas, J., Saha, K., Lipson, M., and Gaeta, A.L. (2012) Chip-based frequency combs with sub-100 GHz repetition rates. *Opt. Lett.*, **37** (5), 875–877.
25. Pfeifle, J., Brasch, V., Lauermann, M., Yu, Y., Wegner, D., Herr, T., Hartinger, K., Schindler, P., Li, J., Hillerkuss, D., Schmogrow, R., Weimann, C., Holzwarth, R., Freude, W., Leuthold, J., Kippenberg, T.J., and Koos, C. (2014) Coherent terabit communications with microresonator Kerr frequency combs. *Nat. Photonics*, **8** (5), 375–380.
26. Steinmetz, T., Wilken, T., Araujo-Hauck, C., Holzwarth, R., Hänsch, T.W., Pasquini, L., Manescau, A., D'Odorico, S., Murphy, M.T., Kenitscher, T., Schmidt, W., and Udem, T. (2008) Laser frequency combs for astronomical observations. *Science*, **321**, 1335–1337.
27. Murphy, M.T., Udem, T., Holzwarth, R., Sizmann, A., Pasquini, L., Araujo-Hauck, C., Dekker, H., D'Odorico, S., Fischer, M., Hansch, T.W., and Manescau, A. (2007) High-precision wavelength calibration of astronomical spectrographs with laser frequency combs. *Mon. Not. R. Astron. Soc.*, **380** (2), 839–847.
28. Savchenkov, A.A., Rubiola, E., Matsko, A.B., Ilchenko, V.S., and Maleki, L. (2008) Phase noise of whispering gallery photonic hyper-parametric microwave oscillators. *Opt. Express*, **16** (6), 4130–4144.
29. Li, J., Lee, H., Chen, T., and Vahala, K.J. (2012) Low-pump-power, low-phase-noise, and microwave to millimeter-wave repetition rate operation in microcombs. *Phys. Rev. Lett.*, **109** (23), 233901.
30. Jiang, Z., Huang, C.B., Leaird, D.E., and Weiner, A.M. (2007) Optical arbitrary waveform processing of more than 100 spectral comb lines. *Nat. Photonics*, **1** (8), 463–467.
31. Lugiato, L.A. and Lefever, R. (1987) Spatial dissipative structures in passive optical systems. *Phys. Rev. Lett.*, **21**, 2209–2211.
32. Barashenkov, I.V. and Smirnov, Yu.S. (1996) Existence and stability chart for the AC-driven, damped nonlinear Schrödinger solitons. *Phys. Rev. E*, **54** (5), 5707–5725.
33. Wabnitz, S. (1993) Suppression of interactions in a phase-locked soliton optical memory. *Opt. Lett.*, **18** (8), 601–603.
34. Leo, F., Coen, S., Kockaert, P., Gorza, S.-P.P., Emplit, P., and Haelterman, M. (2010) Temporal cavity solitons in one-dimensional Kerr media as bits in an all-optical buffer. *Nat. Photonics*, **4** (7), 471–476.
35. Herr, T., Brasch, V., Jost, J.D., Wang, C.Y., Kondratiev, N.M., Gorodetsky, M.L., and Kippenberg, T.J. (2013) Temporal solitons in optical microresonators. *Nat. Photonics*, **8** (2), 145–152.
36. Herr, T., Brasch, V., Jost, J.D., Mirgorodskiy, I., Lihachev, G., Gorodetsky, M.L., and Kippenberg, T.J. (2014) Mode spectrum and temporal soliton formation in optical microresonators. *Phys. Rev. Lett.*, **113** (12), 123901.
37. Brasch, V., Herr, T., Geiselmann, M., Lihachev, G., Pfeiffer, M.H.P., Gorodetsky, M.L., and Kippenberg, T.J. (2014) Photonic chip based optical frequency comb using soliton induced Cherenkov radiation. arXiv, 1410.8598.
38. Reichert, J., Holzwarth, R., Udem, T., and Hänsch, T.W. (1999) Measuring the frequency of light with mode-locked lasers. *Opt. Commun.*, **172**, 59–68.
39. Telle, H.R., Steinmeyer, G., Dunlop, A.E., Stenger, J., Sutter, D.H., and Keller, U. (1999) Carrier-envelope offset phase control: a novel concept for absolute optical frequency measurement and ultrashort pulse generation. *Appl. Phys. B: Lasers Opt.*, **69** (4), 327–332.
40. Ramond, T.M., Diddams, S.A., Hollberg, L., and Bartels, A. (2002) Phase-coherent link from optical to microwave frequencies by means of the broadband continuum from a 1-GHz Ti:sapphire femtosecond oscillator. *Opt. Lett.*, **27** (20), 1842.

41. Agha, I.H., Okawach, Y., Foster, M.A., Sharping, J.E., and Gaeta, A.L. (2007) Four-wave-mixing parametric oscillations in dispersion-compensated high-{Q} silica microspheres. *Phys. Rev. A*, **76**, 43837.

42. Agha, I.H., Okawachi, Y., and Gaeta, A.L. (2009) Theoretical and experimental investigation of broadband cascaded four-wave mixing in high-Q microspheres. *Opt. Express*, **17** (18), 16209–16215.

43. Turner, A.C., Foster, M.A., Gaeta, A.L., and Lipson, M. (2008) Ultra-low power parametric frequency conversion in a silicon microring resonator. *Opt. Express*, **16** (7), 4881–4887.

44. Ilchenko, V.S., Yao, X.S., and Maleki, L. (2000) Microsphere integration in active and passive photonics devices, in *Laser Resonators III*, Proceedings of the Society of Photo-Optical Instrumentation Engineers (SPIE), vol. **3930** (eds A.V. Kudryashov and A.H. Paxton), SPIE, pp. 154–162.

45. Savchenkov, A.A., Ilchenko, V.S., Matsko, A.B., and Maleki, L. (2004) Kilohertz optical resonances in dielectric crystal cavities. *Phys. Rev. A*, **70** (5), 051804.

46. Savchenkov, A.A., Matsko, A.B., Ilchenko, V.S., and Maleki, L. (2007) Optical resonators with ten million finesse. *Opt. Express*, **15**, 6768.

47. Armani, D.K., Kippenberg, T.J., Spillane, S.M., and Vahala, K.J. (2003) Ultra-high-{Q} toroid microcavity on a chip. *Nature*, **421**, 925–928.

48. Knight, J.C., Cheung, G., Jacques, F., and Birks, T.A. (1997) Phase-matched excitation of whispering-gallery-mode resonances by a fiber taper. *Opt. Lett.*, **22** (15), 1129–1131.

49. Spillane, S.M., Kippenberg, T.J., Painter, O.J., and Vahala, K.J. (2003) Ideality in a fiber-taper-coupled microresonator system for application to cavity quantum electrodynamics. *Phys. Rev. Lett.*, **91** (4), 43902.

50. Levy, J.S., Gondarenko, A., Foster, M.A., Turner-Foster, A.C., Gaeta, A.L., Lipson, M., and Gaeta, A.L. (2009) Monolithically integrated multiple wavelength oscillator on silicon. arXiv:0907.1077.

51. Herr, T., Hartinger, K., Riemensberger, J., Wang, C.Y., Gavartin, E., Holzwarth, R., Gorodetsky, M.L., and Kippenberg, T.J. (2012) Universal formation dynamics and noise of Kerr-frequency combs in microresonators. *Nat. Photonics*, **6**, 480–487.

52. Akhmediev, N. and Karlsson, M. (1995) Cherenkov radiation emitted by solitons in optical fibers. *Phys. Rev. A*, **51** (3), 2602–2607.

53. Brasch, V., Chen, Q.-F., Schiller, S., and Kippenberg, T.J. (2014) Radiation hardness of high-Q silicon nitride microresonators for space compatible integrated optics. arXiv, 1406.0297.

54. Del'Haye, P., Herr, T., Gavartin, E., Gorodetsky, M.L., Holzwarth, R., and Kippenberg, T.J. (2011) Octave spanning tunable frequency comb from a microresonator. *Phys. Rev. Lett.*, **107** (6), 063901.

55. Ferdous, F., Miao, H., Leaird, D.E., Srinivasan, K., Wang, J., Chen, L., Varghese, L.T., and Weiner, A.M. (2011) Spectral line-by-line pulse shaping of on-chip microresonator frequency combs. *Nat. Photonics*, **5**, 770–776.

56. Okawachi, Y., Saha, K., Levy, J.S., Wen, Y.H., Lipson, M., and Gaeta, A.L. (2011) Octave-spanning frequency comb generation in a silicon nitride chip. *Opt. Lett.*, **36** (17), 3398–3400.

57. Del'Haye, P., Beha, K., Papp, S.B., and Diddams, S. (2014) Self-injection locking and phase-locked states in microresonator-based optical frequency combs. *Phys. Rev. Lett.*, **112** (4), 043905.

58. Herr, T., Brasch, V., Jost, J.D., Wang, C.Y., Kondratiev, N.M., Gorodetsky, M.L., and Kippenberg, T.J. (2012) Mode-locking in an optical microresonator via soliton formation. arXiv, 1211.0733.

59. Matsko, A.B., Savchenkov, A.A., Strekalov, D., Ilchenko, V.S., and Maleki, L. (2005) Optical hyperparametric oscillations in a whispering-gallery-mode resonator: threshold and phase diffusion. *Phys. Rev. A*, **71**, 33804.

60. Maleki, L., Ilchenko, V.S., Savchenkov, A.A., Liang, W., Seidel, D., and Matsko, A.B. (2010) High performance, miniature hyper-parametric microwave photonic oscillator. Frequency Control Symposium (FCS), 2010 IEEE International, pp. 558–563.

61. Matsko, A.B., Savchenko, A.A., Liang, W., Ilchenkko, V.S., Seidel, D., and Maleki, L. (2011) Mode-locked Kerr frequency combs. *Opt. Lett.*, **36**, 2845–2847.

62. Chembo, Y.K., Strekalov, D.V., and Yu, N. (2010) Spectrum and dynamics of optical frequency combs generated with monolithic whispering gallery mode resonators. *Phys. Rev. Lett.*, **104** (10), 103902.

63. Chembo, Y.K.K. and Yu, N. (2010) Modal expansion approach to optical-frequency-comb generation with monolithic whispering-gallery-mode resonators. *Phys. Rev. A*, **82** (3), 33801.

64. Chembo, Y.K. and Yu, N. (2010) On the generation of octave-spanning optical frequency combs using monolithic whispering-gallery-mode microresonators. *Opt. Lett.*, **35** (16), 2696–2698.

65. Boyd, R.W. (2007) *Nonlinear Optics*, 3rd edn, Academic Press.

66. Gorodetsky, M.L. and Fomin, A.E. (2007) Eigenfrequencies and Q factor in the geometrical theory of whispering-gallery modes. *Quantum Electron.*, **37** (2), 167–172.

67. Gorodetsky, M.L. (2011) *Optical Microresonators with Giant Quality-Factor*, Fizmatlit, Moscow. (in Russian).

68. Demchenko, Y.A. and Gorodetsky, M.L. (2013) Analytical estimates of eigenfrequencies, dispersion, and field distribution in whispering gallery resonators. *J. Opt. Soc. Am. B: Opt. Phys.*, **30** (11), 3056–3063.

69. Bao, C.Y. and Yang, C.X. (2013) Quantitative analysis of the mode-pulling effect in microcomb generation based on the modal expansion method. *J. Opt. Soc. Am. B: Opt. Phys.*, **30**, 3243–3248.

70. Whitten, W.B., Barnes, M.D., and Ramsey, J.M. (1997) Propagation of short optical pulses in a dielectric sphere. *J. Opt. Soc. Am. B: Opt. Phys.*, **14**, 3424–3429.

71. Matsko, A.B., Savchenkov, A.A., Liang, W., Ilchenko, V.S., Seidel, D., and Maleki, L. (2009) Whispering gallery mode oscillators and optical comb generators. Proceedings of the 7th Symposium Frequency Standards and Metrology, pp. 539–558.

72. Chembo, Y.K. and Menyuk, C.R. (2013) Spatiotemporal Lugiato-Lefever formalism for Kerr-comb generation in whispering-gallery-mode resonators. *Phys. Rev. A*, **87** (5), 053852.

73. Zakharov, V.E. and Shabat, A.B. (1972) Exact theory of two-dimensional self-focusing and one-dimensional self-modulation of waves in nonlinear media (differential equation solution for plane self focusing and one dimensional self modulation of waves interacting in nonlinear media). *Sov. Phys. JETP*, **34**, 62–69.

74. Anderson, D. (1983) Variational approach to non-linear pulse-propagation in optical fibers. *Phys. Rev. A*, **27** (6), 3135–3145.

75. Mertens, F.G., Quintero, N.R., and Bishop, A.R. (2010) Nonlinear Schroedinger equation with spatiotemporal perturbations. *Phys. Rev. E*, **81** (1 Pt 2), 016608.

76. Coillet, A., Balakireva, I., Henriet, R., Saleh, K., Larger, L., Dudley, J.M., Menyuk, C.R., and Chembo, Y.K. (2013) Azimuthal turing patterns, bright and dark cavity solitons in Kerr combs generated with whispering-gallery-mode resonators. *IEEE Photonics J.*, **5** (4), 6100409.

77. Matsko, A.B., Savchenko, A.A., and Maleki, L. (2012) On excitation of breather solitons in an optical microresonator. *Opt. Lett.*, **37** (23), 4856–4858.

78. Carmon, T., Yang, L., and Vahala, K.J. (2004) Dynamical thermal behavior and thermal selfstability of microcavities. *Opt. Express*, **12**, 4742–4750.

79. Carmon, T., Schwefel, H.G.L., Yang, L., Oxborrow, M., Stone, A.D., and Vahala, K.J. (2008) Static envelope patterns in composite resonances generated by level crossing in optical toroidal microcavities. *Phys. Rev. Lett.*, **100** (10), 103905.

80. Li, J., Diddams, S., and Vahala, K.J. (2014) Pump frequency noise coupling into a microcavity by thermo-optic locking. *Opt. Express*, **22** (12), 14559–14567.

81. Hansson, T., Modotto, D., and Wabnitz, S. (2014) On the numerical simulation of Kerr frequency combs using coupled mode equations. *Opt. Commun.*, **312**, 134–136.

82. Lamont, M.R.E., Okawachi, Y., and Gaeta, A.L. (2013) Route to stabilized ultrabroadband microresonator-based frequency combs. *Opt. Lett.*, **38** (18), 3478–3481.

83. Lihachev, G.V., Herr, T., Kippenberg, T.J., and Gorodetsky, M.L. (2009) Tool for simulation of Kerr frequency combs. Microresonator Frequency Combs and Applications, Ascona, Switzerland. (code: http://www.rqc.ru/groups/gorodetsky/combgui.htm (accessed 13 August 2015)).

84. Kane, D.J. and Trebino, R. (1993) Characterization of arbitrary femtosecond pulses using frequency-resolved optical gating. *IEEE J. Quantum Electron.*, **29** (2), 571–579.

85. Kane, D.J. (2008) Principal components generalized projections: a review. *J. Opt. Soc. Am. B*, **25** (6), A120–A132.

86. Del'Haye, P., Arciezt, O., Gorodetsky, M.L., Holzwarth, R., and Kippenberg, T.J. (2009) Frequency comb assisted diode laser spectroscopy for measurement of microcavity dispersion. *Nat. Photonics*, **3**, 529–533.

87. Diddams, S.A., Jones, D.J., Ye, J., Cundiff, S.T., Hall, J.L., Ranka, J.K., Windeler, R.S., Holzwarth, R., Udem, T., and Hänsch, T.W. (2000) Direct link between microwave and optical frequencies with a 300 THz femtosecond laser comb. *Phys. Rev. Lett.*, **84**, 5102–5105.

88. Dudley, J.M., Genty, G., and Coen, S. (2006) Supercontinuum generation in photonic crystal fiber. *Rev. Mod. Phys.*, **78** (4), 1135–1184.

89. Jost, J.D., Herr, T., Lecaplain, C., Brasch, V., Pfeiffer, M.H.P., and Kippenberg, T.J. (2014) Microwave to optical link using an optical microresonator. arXiv, 1411.1354.

90. Erkintalo, M., Xu, Y.Q., Murdoch, S.G., Dudley, J.M., and Genty, G. (2012) Cascaded phase matching and nonlinear symmetry breaking in fiber frequency combs. *Phys. Rev. Lett.*, **109** (22), 223904.

91. Coen, S., Randle, H.G., Sylvestre, T., and Erkintalo, M. (2013) Modeling of octave-spanning Kerr frequency combs using a generalized mean-field Lugiato–Lefever model. *Opt. Lett.*, **38** (1), 37–39.

92. Erkintalo, M. and Coen, S. (2014) Coherence properties of Kerr frequency combs. *Opt. Lett.*, **39**, 283–286.

7
Dynamical Regimes in Kerr Optical Frequency Combs: Theory and Experiments

Aurélien Coillet, Nan Yu, Curtis R. Menyuk, and Yanne K. Chembo

7.1
Introduction

Kerr optical frequency combs are sets of equidistant spectral components generated through pumping an ultra-high-quality factor whispering gallery mode (WGM) resonator with a continuous-wave (CW) laser. Owing to the Kerr nonlinearity, the photons originating from the pump are transferred through four-wave mixing (FWM) to neighboring cavity eigenmodes. Depending on the pump power, laser frequency, and chromatic dispersion of the cavity, this cascaded hyperparametric process can generate as much as several hundred oscillating modes, which will be the spectral components of the Kerr comb.

An important challenge is to understand the complex light-matter interactions leading to the comb formation.

A first approach uses the concept of modal expansion [1–3], which relies on large sets of coupled nonlinear ordinary differential equations ruling the temporal dynamics of each eigenmode. The second approach is based on the fact that since light propagates circumferentially inside the resonator, it can be treated as if it was propagating along an unfolded trajectory with periodic boundary conditions [4–7]. In this case, it can be shown that the system obeys a spatiotemporal partial differential equation known as the Lugiato–Lefever equation (LLE), which is a nonlinear Schrödinger equation (NLSE) with damping, detuning, and driving [8]. The variable of the LLE is the overall intracavity field, which is the sum of the modal fields described by the modal model. Equivalence between the modal and the spatiotemporal formalisms has been demonstrated, and both approaches enable us to understand Kerr combs from complementary standpoints: the modal approach is more useful when only few modes are involved (e.g., threshold phenomena), while the spatiotemporal formalism is suitable when a very large number of modes has to be accounted for [3]. In the latter case, the LLE formalism enables us to investigate Kerr combs as the spectral signature of dissipative patterns or localized structures in WGM resonators [9].

Previous studies have shown that above a given threshold, Kerr combs can be excited and yield permanent states featuring an all-to-all coupling amongst the

Nonlinear Optical Cavity Dynamics: From Microresonators to Fiber Lasers, First Edition.
Edited by Philippe Grelu.
© 2016 Wiley-VCH Verlag GmbH & Co. KGaA. Published 2016 by Wiley-VCH Verlag GmbH & Co. KGaA.

excited modes. Various dynamical states can be thereby obtained, and they can be stationary (Turing rolls, solitons), pulsating (breathers), and even chaotic. It is noteworthy that the phase-locked states are particularly relevant for a wide spectrum of applications [10–17].

Our objective in this contribution is to present a synthetic overview of the various dynamical states in Kerr combs, in either the anomalous or normal group-velocity dispersion regime. We focus on the role of the parameters that are the most easily accessible at the experimental level, namely, the pump power and the laser detuning relatively to the cavity resonance.

The chapter is structured as follows. In the next section, we present the system under study, and briefly discuss the main parameters of interest. In Section 7.3, the modal and spatiotemporal formalisms are introduced. Both approaches are routinely used today to investigate the dynamical properties of Kerr combs. We also perform a stability analysis that enables us to unveil the bifurcation mechanisms that are taking place when the externally controllable parameters (laser power and frequency) are continuously tuned. The various dynamical states are explored in Section 7.4, where we discuss the main features of nontrivial solutions such as Turing rolls, solitons, and chaos. The last section concludes this chapter.

7.2
The System

Kerr frequency combs are generated from the nonlinear interaction between the light of a CW laser and the matter of a dielectric optical resonator [1]. As such, a typical experimental setup is displayed in Figure 7.1: the light of a narrow-linewidth laser is amplified and coupled to a high-Q resonator, using either a tapered fiber, the frustrated total internal reflexion of a dielectric prism, or an angle-cleaved optical fiber. The new frequencies generated by FWM in the resonator are coupled out and then further processed or analyzed, using, for example, a spectrum analyzer.

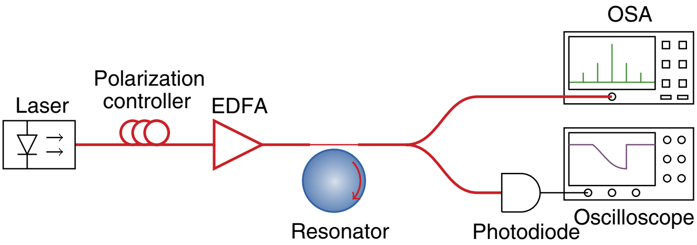

Figure 7.1 Typical experimental setup for the generation of Kerr frequency combs in WGM resonators. The light of a CW-laser is amplified and coupled to the high-Q resonator via the evanescent field of a tapered fiber. The output of the same fiber is used to monitor the optical spectrum or to further process the generated comb.

The key component for the generation of Kerr combs is, therefore, the optical resonator, and its parameters are crucial for the efficient generation of a broadband and stable comb. First of all, its Q-factor has to be high (at least $> 10^5$, preferably $> 10^8$), so that the generation of new frequencies can be achieved at reasonably low optical powers. The best candidates for the generation of Kerr combs are resonators based on WGM in which photons are propagating on a closed path, undergoing total internal reflections on the surface of a convex dielectric material. Many different optical WGM resonators have been developed in the past decade, with various shapes (cylinders, spheres, toroid, disks) and materials (glasses or crystals). Figure 7.2 shows 2 examples of such resonators, a crystalline disk resonator and a planar, integrated resonator. Among them, fluoride crystals such as magnesium fluoride (MgF_2) and calcium fluoride (CaF_2) are particularly attractive because of their exceptional transparency over a large frequency range. These readily available materials can be shaped into WGM resonators using a low-investment grinding-and-polishing method. The last polishing steps must yield a smooth surface with nanometer-scale roughness, so that light can be efficiently trapped. Using these techniques, it is possible to achieve Q factors as high as 10^{11} with CaF_2 crystals [18]. An infrared photon coupled in such a resonator will remain stored in the cavity for a time $\tau_{\text{ph}} = Q_0/\omega_0 \sim 100\ \mu s$, where ω_0 is its angular frequency. It should be noted that the coupling of light inside and outside the resonator decreases this photon lifetime, and the total, or *loaded* Q-factor, is the combination of the *intrinsic* and *coupling* (or extrinsic) Q-factors: $1/Q_{\text{tot}} = 1/Q_0 + 1/Q_{\text{ext}}$.

An optical resonator is also characterized by the frequency difference between two consecutive resonances, its *free-spectral range* (FSR). A resonator's FSR is fixed by its size and refractive index through the relation $\Delta\omega_{\text{FSR}} = c/(an_g)$, where c is the speed of light in vacuum, a is the principal radius of the resonator, and n_g its group velocity index. The size of WGM resonators may vary from a few microns to tens of millimeters, corresponding to an FSR in the gigahertz and terahertz ranges. Since the refractive index of the WGM slightly depends on the wavelength, the resonator's FSR is not strictly equidistant, and this dispersion is yet another characteristic that will play an important role in the generation of Kerr combs.

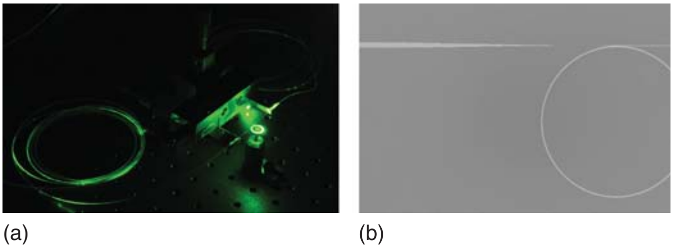

Figure 7.2 Examples of WGM resonators manufactured at the FEMTO-ST Institute. (a) Photograph of a crystalline whispering-gallery disk coupled with a tapered fiber. (b) Scanning electron microscope image of a planar, integrated resonator, and tapered coupling waveguide.

7.3
The Models

Two different approaches have been proposed to theoretically describe the generation of wideband Kerr frequency combs [3, 6, 7]. The first model is based on a modal expansion of the intracavity optical field, where each comb mode is described by its own ordinary differential equation [2, 3]. This model can be derived in a straightforward manner from Maxwell's equations, and it is particularly suitable to determine the threshold for the spontaneous generation of Kerr combs. This Fourier-domain theoretical description can be used as the starting point to derive a spatiotemporal formalism based on the 1D Lugiato–Lefever equation [4–7]. This latter model is more appropriate when studying spatially localized structures, such as solitons and breathers. These two complementary theoretical models are further described in the two following sections.

7.3.1
Modal Expansion Model

A WGM resonator can only trap light for a discrete number of optical frequencies, its eigenmodes. Although several families of these eigenmodes exist, each characterized by a specific polarization and transverse distribution, we focus only on one of them. In this mode family, each mode is defined by an integer wave number ℓ, corresponding to the ratio between the optical length of the cavity and the wavelength of the mode. If we denote the pumped mode as ℓ_0, the eigenfrequencies of the modes can be expanded in a finite Taylor series:

$$\omega_\ell = \omega_{\ell_0} + \sum_{n=1}^{N} \frac{\zeta_n}{n!}(\ell - \ell_0)^n, \tag{7.1}$$

where ω_{ℓ_0} is the eigenfrequency at $\ell = \ell_0$. Most of the time, it is generally not necessary to go beyond $N = 2$ or 3. The first Taylor coefficient $\zeta_1 = d\omega/d\ell = \Delta\omega_{\mathrm{FSR}}$ is the free spectral range of the resonator, and the coefficient $\zeta_2 = d^2\omega/d\ell^2$ is the second-order dispersion coefficient. For perfectly equidistant resonant modes, the coefficient ζ_2 and all the subsequent Taylor coefficients are null. The dispersion is normal when $\zeta_2 < 0$ and anomalous when $\zeta_2 > 0$.

We are assuming that only a single transverse mode propagates in the cavity. We may then write the total electric field in the cavity as

$$\mathbf{E}(\mathbf{r}, t) = \sum_{\ell} \frac{1}{2}\, \mathcal{A}_\ell(t)\, \mathrm{e}^{i\omega_\ell t} \Upsilon_\ell(\mathbf{r}) + \text{c.c.} \tag{7.2}$$

where $\Upsilon_\ell(\mathbf{r})$ is the spatial mode profile of the ℓth azimuthal mode, and the fields have been normalized such that $|\mathcal{A}_\ell|^2$ is equal to the number of photons in the ℓth mode. It has been shown that the slowly varying envelopes $\mathcal{A}_\ell$ of the modes are governed by the following system of equations [3]:

$$\begin{aligned}\frac{d\mathcal{A}_\ell}{dt} = &-\frac{1}{2}\Delta\omega_\ell \mathcal{A}_\ell \\ &- ig_0 \sum_{m,n,p} \Lambda_\ell^{mnp} \mathcal{A}_m \mathcal{A}_n^* \mathcal{A}_p e^{i(\omega_m-\omega_n+\omega_p-\omega_l)t} \delta(m-n+p-\ell) \\ &+ \frac{1}{2}\Delta\omega_\ell \mathcal{F}_0 e^{i(\Omega_0-\omega_\ell)t} \delta(\ell-\ell_0),\end{aligned} \tag{7.3}$$

where $\delta(x)$ denotes the usual Kronecker function that equals 1 for $x = 0$ and 0 elsewhere. The mode bandwidth $\Delta\omega_\ell$ is defined as the inverse of the photon lifetime for the ℓth mode: $\Delta\omega_\ell = 1/\tau_{\mathrm{ph},\ell} = \omega_\ell/Q_{\mathrm{tot},\ell}$. The FWM gain is $g_0 = n_2 c\hbar\omega_{\ell_0}^2/n_0^2 V_0$, where n_2 is the nonlinear coefficient of the refraction index, $\hbar$ is Planck's constant, and V_0 is the effective mode volume. The parameter Λ_ℓ^{mnp} describes the nonlinear mode overlap. The parameter $\mathcal{F}_0$ is proportional to the amplitude of the pump laser field, while Ω_0 is its angular frequency, assumed to be close to the pumped resonance frequency ω_{ℓ_0}, so that the frequency detuning $\sigma = \Omega_0 - \omega_{\ell_0}$ is of the order of the loaded linewidth.

The modal expansion approach enables to understand many interesting features related to Kerr combs. For instance, it allows to determine the threshold value of the intracavity pump power above which the comb can be excited. Under the simplifying assumption of degenerate linewidths ($\Delta\omega_\ell \equiv \Delta\omega_{\ell_0}$) and overlap integrals ($\Lambda_\ell^{mnp} \equiv 1$), this threshold explicitly yields

$$|\mathcal{A}_0|_{\mathrm{th}}^2 = \frac{1}{2}\frac{\Delta\omega_{\ell_0}}{g_0} \tag{7.4}$$

in terms of number of intracavity photons. This threshold value is a theoretical minimum under which no Kerr comb can be generated. The effective threshold power, though, has generally the same order of magnitude, and it is set by other parameters such as frequency detuning and overall dispersion.

7.3.2
Spatiotemporal Model

The optical path of a WGM cavity can be seen as a circle of radius a, on which the optical field is distributed. The intracavity field would then be described by the slowly varying envelope $\mathcal{A}(\theta, t)$, where $\theta \in [-\pi, \pi]$ is the azimuthal angle along the circumference of the cavity. In this framework, the total field $\mathcal{A}(\theta, t)$ corresponds to the sum of the different modal components $\mathcal{A}_\ell(t)$:

$$\mathcal{A}(\theta, t) = \sum_\ell \mathcal{A}_\ell(t) e^{[i(\omega_\ell-\omega_{\ell_0})t - i(\ell-\ell_0)\theta]}. \tag{7.5}$$

Using the approximation of degenerated modal linewidths and transverse profiles, and combining Eqs. (7.5) and (7.3), we can derive a partial differential equation for $\mathcal{A}(\theta, t)$. We apply the transformation $\theta \to \theta - \zeta_1 t$ to this equation, so that the reference frame is rotating with the light. Finally, this equation can be rewritten in the laboratory frame in the form of the normalized, one-dimensional LLE [6]

$$\frac{\partial \psi}{\partial \tau} = -(1 + i\alpha)\psi + i|\psi|^2\psi - i\frac{\beta}{2}\frac{\partial^2 \psi}{\partial \theta^2} + F, \tag{7.6}$$

where the field envelope and time have been rescaled so that $\psi = (2g_0/\Delta\omega)^{1/2}\mathcal{A}^*$ and $\tau = \Delta\omega t/2$. The dimensionless parameters of this normalized equation are the frequency detuning $\alpha = -2\sigma/\Delta\omega$, the cavity second-order dispersion $\beta = -2\zeta_2/\Delta\omega$, and the external excitation $F = (2g_0/\Delta\omega)^{1/2}\mathcal{F}_0^*$. In this dimensionless form, the threshold intracavity power calculated is simply $|\psi|^2_{\text{th}} = 1$.

The LLE is a variant of the well-known NLSE that includes three additional terms: a damping term accounting for the losses in the cavity, the detuning between the input laser and the pumped mode, and the driving of the pump laser. As such, the LLE can benefit from the extensive methods developed for the NLSE, for instance, in terms of efficient simulations using the split-step Fourier method, or for the inclusion of additional effects such as -steepening, higher-order dispersion terms, and Raman scattering. The two-dimensional variant of the LLE has also been extensively studied since its first derivation [8], providing insight into the various dynamical features that can be expected in the one-dimensional case.

7.3.3
Stability Analysis

Using the LLE, we can now investigate the dynamical characteristics of Kerr-comb generation. In particular, we focus on the stability analysis of the steady-state solutions, and we determine the regions of the parameter space where frequency combs can be generated. Among those parameters, the second-order dispersion plays an unique role, since the nonlinear dynamics will differ significantly depending on its sign. Kerr-comb generation was earlier thought to be impossible in normal regimes of dispersion ($\beta > 0$), but later on, a few experimental demonstrations have been reported [9, 19, 20]. In contrast, many different comb states have been reported in the anomalous regime of dispersion [1, 21–23]. The two remaining parameters, the pump laser detuning and power are the most accessible to the experiments, and will, therefore, be the control parameters of the two-dimensional stability map.

The steady-state equilibria ψ_e are obtained from Eq. (7.6) by setting all the derivatives to zero, and it is found that they obey the nonlinear algebraic equation

$$F^2 = \left[1 + (\rho - \alpha)^2\right]\rho \equiv G(\alpha, \rho), \tag{7.7}$$

with $\rho = |\psi_e|^2$ being the intracavity optical power. This cubic polynomial equation in ρ has one, two, or three real-valued solutions depending on the parameters α and F. By looking for the local extrema of the G function, we find that Eq. (7.7) can have more than one solution only for $|\alpha| \geq \sqrt{3}$. In this case, the solutions are

$$\rho_\pm(\alpha) = \frac{2\alpha \pm \sqrt{\alpha^2 - 3}}{3}, \tag{7.8}$$

and the corresponding pumping parameters are

$$
\begin{aligned}
F_\pm^2(\alpha) &= G(\alpha, \rho \mp (\alpha)) \\
&= \frac{2\alpha \mp \sqrt{\alpha^2 - 3}}{3}\left[1 + \left(\frac{\sqrt{\alpha^2 - 3} \pm \alpha}{3}\right)^2\right].
\end{aligned}
\tag{7.9}
$$

For $\alpha > \sqrt{3}$ and $F^2 \in]F_-^2(\alpha), F_+^2(\alpha)[$, the system will, therefore, have three different steady-state solutions. It can be shown that the extremal solutions are always stable, while the intermediate one is unstable [24]: this is the well-known phenomenon of bistability in a nonlinear resonance [25]. In Figure 7.3, the $F_\pm^2$ dependency on the detuning α are represented as thick lines, encompassing the region where the system has three steady-state solutions.

Since the LLE describes the intracavity field in a rotating frame of reference, a stable and stationary Kerr comb corresponds to τ-independent but θ-dependent solution. In order to study the appearance of such solutions close to the steady-state states ψ_e, we only set the temporal derivative in Eq. (7.6) to zero and separate the real and imaginary components:

$$
\frac{\partial^2 \psi_r}{\partial \theta^2} = \frac{2}{\beta}\left[\left(\psi_r^2 + \psi_i^2 - \alpha\right)\psi_r - \psi_i\right], \tag{7.10}
$$

$$
\frac{\partial^2 \psi_i}{\partial \theta^2} = \frac{2}{\beta}\left[\left(\psi_r^2 + \psi_i^2 - \alpha\right)\psi_i - \psi_r - F\right], \tag{7.11}
$$

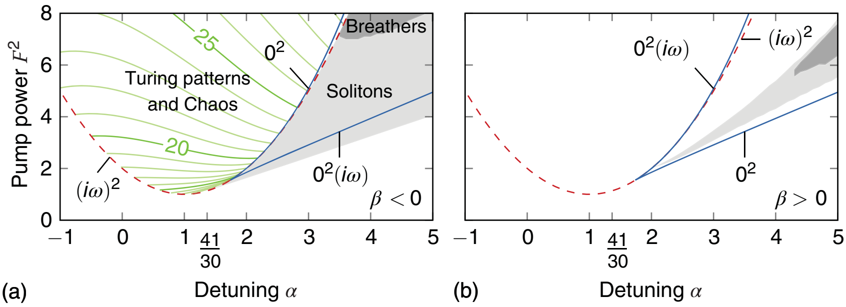

Figure 7.3 Stability map of the LLE in the (a) anomalous ($\beta < 0$) and (b) normal ($\beta > 0$) dispersion regimes. The dashed line in both cases corresponds to the threshold value $|\psi|^2_{\text{th}} = 1$. Between the two thick lines, the Lugiato–Lefever equation has three steady-state solutions, two of which are stable. In the anomalous case, Turing patterns can be found above threshold when the detuning is smaller than $\alpha = 2$, and the lines indicate the iso-values of the roll pattern. Numerical simulations show that bright solitons (breathers) can be excited in the light gray (dark gray) area. Since it can be generated for pump powers below the bifurcation line, the soliton is a subcritical structure. In the normal dispersion regime, dark solitons (breathers) can also be generated in the light gray (dark gray) area. The critical value $\alpha = 41/30$ separates supercritical (or soft) from subcritical (or hard) excitation of the comb [24]. The bifurcation lines 0^2, $0^2(i\omega)$, and $(i\omega)^2$ correspond to a structural change of the Jacobian eigenvalues, as explained in Table 7.1.

Table 7.1 Nomenclature and pictograms for the various sets of eigenvalues

Eigenvalues and reversible spatial bifurcations in the Lugiato–Lefever model			
Nomenclature	Eigenvalues ($\lambda_{1,2}; \lambda_{3,4}$)	Pictogram	Bifurcation
Takens–Bogdanov	$(\pm a; 0)$	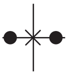	0^2
Takens–Bogdanov–Hopf	$(0; \pm ib)$	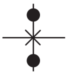	$0^2(i\omega)$
Hamiltonian–Hopf	$(\pm ia; \pm ia)$	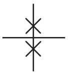	$(i\omega)^2$

A set of four eigenvalues is attached to each equilibrium, and some classified bifurcations are attached to certain configurations of eigenvalues. A dot stands for one eigenvalue, and a cross corresponds to a set of two degenerated eigenvalues. These bifurcation lines are displayed in Figure 7.3.

where $\psi = \psi_r + i\psi_i$. By introducing the variable $\phi_{r,i} = \partial\psi_{r,i}/\partial\theta$, we can transform these second-order equation into the following first-order system:

$$\frac{\partial\psi_r}{\partial\theta} = \phi_r, \tag{7.12}$$

$$\frac{\partial\phi_r}{\partial\theta} = \frac{2}{\beta}(\psi_r^3 + \psi_i^2\psi_r - \alpha\psi_r - \psi_i), \tag{7.13}$$

$$\frac{\partial\psi_i}{\partial\theta} = \phi_i, \tag{7.14}$$

$$\frac{\partial\phi_i}{\partial\theta} = \frac{2}{\beta}(\psi_r^2\psi_i + \psi_i^3 - \alpha\psi_i + \psi_r - F). \tag{7.15}$$

In the vicinity of a steady-state equilibrium $\psi_\mathrm{e} = \psi_{\mathrm{e},r} + i\psi_{\mathrm{e},i}$, this system can be linearized to yield the following Jacobian matrix:

$$\mathsf{J}_\mathrm{e} = \begin{bmatrix} 0 & 1 & 0 & 0 \\ \frac{2}{\beta}(3\psi_{\mathrm{e},r}^2 + \psi_{\mathrm{e},i}^2 - \alpha) & 0 & \frac{2}{\beta}(2\psi_{\mathrm{e},r}\psi_{\mathrm{e},i} - 1) & 0 \\ 0 & 0 & 0 & 1 \\ \frac{2}{\beta}(2\psi_{\mathrm{e},r}\psi_{\mathrm{e},i} + 1) & 0 & \frac{2}{\beta}(\psi_{\mathrm{e},r}^2 + 3\psi_{\mathrm{e},i}^2 - \alpha) & 0 \end{bmatrix}. \tag{7.16}$$

The eigenvalues of this Jacobian matrix reveal where the system will undergo substantial changes; spatial bifurcations can potentially occur where the real or imaginary parts of the eigenvalues vanish. These eigenvalues obey the characteristic equation

$$\lambda^4 - \frac{4}{\beta}(2\rho - \alpha)\lambda^2 + \frac{4}{\beta^2}\left(3\rho^2 - 4\alpha\rho + \alpha^2 + 1\right) = 0 \tag{7.17}$$

which is quadratic in λ^2. The four eigenvalues will, therefore, always be either pairwise opposite (when real-valued) or pairwise conjugate (when complex). Since

Eq. (7.17) depends on ρ, there are four eigenvalues for each steady-state solution. The nature (complex, real, or pure imaginary) of the eigenvalues is partially decided by the sign of the discriminant $\Delta = 16(\rho^2 - 1)/\beta^2$. The curve $\rho = 1$ will, therefore, play an important role in the bifurcation diagram; it is represented as a dashed line in Figure 7.3.

Table 7.1 displays the various eigenvalue configurations leading to bifurcations in the system. The nomenclature labels them as 0^2 (Takens–Bogdanov), $0^2(i\omega)$ (Takens–Bogdanov–Hopf), and $(i\omega)^2$ (Hamiltonian–Hopf) bifurcations [26].

7.4
Dynamical States

The previous stability and bifurcation analysis shows that the parameter space can be divided into specific areas where different behaviors of the system are expected. This section is devoted to the study of the different comb states that can be generated in these various zones.

7.4.1
Primary Combs

In the anomalous regime of dispersion, one of the most common experimental combs consists of spectral lines separated by an integral multiple of the FSR. These "primary combs" are often generated at pump frequencies slightly higher than the resonance frequency, corresponding to negative α detunings. In the bifurcation diagram of Figure 7.3a, the generation of such combs is, therefore, due to the $(i\omega)^2$ bifurcation corresponding to the line $\rho = 1$ located on the left side of the plane (dashed line). The spatial counterpart is an oscillating pattern with the same number of "rolls" as the line spacing of the comb (in multiples of the FSR). Such structures are referred to as *Turing patterns* (or simply *rolls* in our case), after Alan Turing's work on morphogenesis [27], and can be found in many different nonlinear systems. This bifurcation is also often referred to as *modulational instability*, especially in nonlinear fiber optics, where the dynamics is governed by the nonlinear Schrödinger equation, which is closely related to the LLE from a dynamical point of view.

For the sake of simplicity, we focus on the case $\alpha < \sqrt{3}$, where the $\rho = 1$ bifurcation is the only one that can occur in the system. The threshold pump power for this bifurcation is obtained by setting $\rho = |\psi_{\text{th}}|^2 = 1$ in Eq. (7.7):

$$F_{\text{th}}^2 = 1 + (1 - \alpha)^2. \tag{7.18}$$

It can be shown that Turing rolls emerge in the system from a supercritical bifurcation (soft excitation) when $\alpha < 41/30$, and a subcritical bifurcation (hard excitation) when $\alpha > 41/30$ [8, 28–30]. In the supercritical case, the unique equilibrium ψ_{e} is stable when the external excitation is lower than the threshold $F < F_{\text{th}}$, and unstable when $F > F_{\text{th}}$. Above the threshold F_{th}, the sidemodes

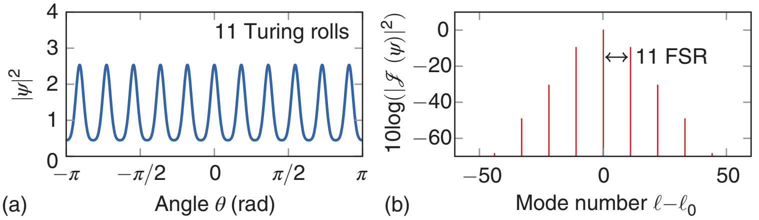

Figure 7.4 (a) Stationary spatiotemporal distribution of the optical power and (b) optical spectrum of a supercritical Turing patterns (or "primary comb") generated from small amplitude noise. The parameters used in this simulation are $\alpha = -0.5$, $\beta = -0.05$, and $F^2 = 5$.

experience a positive gain, and grow to reach a significant amplitude as the pump power increases. Hence, the steady-state equilibrium ψ_e and the Turing pattern can never be simultaneously stable. A numerical simulation of a Turing pattern is displayed in Figure 7.4, with detuning $\alpha = -0.5$, dispersion $\beta = -0.05$, and pump power $F^2 = 5 > F^2_{\text{th}} = 3.25$. The subcritical case occurs when $\alpha > 41/30$, and similar to the supercritical case, the steady-state ψ_e is unstable above threshold. However, a Turing pattern can be stable in a small range of pump power *below* the threshold power F^2_{th}. Hence, in this region, stable comb and steady-state solutions can coexist, creating bistability and inducing hysteresis, since the dynamical state of the system will not be the same if the excitation is adiabatically increased or decreased.

Due to the 2π-periodicity of the θ variable, the number of rolls in the Turing pattern must be an integer. To find this integer, it is necessary to analyze the stability of the system when the steady-state equilibrium ψ_e is perturbed by $\delta\psi(\theta, \tau)$. Applying this perturbation to the LLE leads to the linearized equation:

$$\frac{\partial}{\partial\tau}[\delta\psi] = -(1 + i\alpha)\delta\psi + 2i|\psi_e|^2\delta\psi + i\psi_e^2\delta\psi^* - i\frac{\beta}{2}\frac{\partial^2}{\partial\theta^2}[\delta\psi]. \tag{7.19}$$

We can decompose the perturbation as a sum of the modal contributions:

$$\delta\psi(\theta, \tau) = \sum_l \delta\psi_l(\tau)e^{il\theta}, \tag{7.20}$$

where $l = \ell - \ell_0$ is the eigennumber of the mode with respect to the pumped mode. Inserting this ansatz into Eq. (7.19) and projecting along a given mode l' leads to two equations for each modal perturbation:

$$\begin{bmatrix} \delta\dot{\psi}_l \\ \delta\dot{\psi}^*_{-l} \end{bmatrix} = \begin{bmatrix} \mathcal{M} & \mathcal{N} \\ \mathcal{N}^* & \mathcal{M}^* \end{bmatrix} \begin{bmatrix} \delta\psi_l \\ \delta\psi^*_{-l} \end{bmatrix}, \tag{7.21}$$

where the overdot stands for the derivative with respect to the dimensionless time τ, and

$$\mathcal{M} = -(1 + i\alpha) + 2i|\psi_e|^2 + i\frac{\beta}{2}l^2, \tag{7.22}$$

$$\mathcal{N} = i\psi_e^2. \tag{7.23}$$

The eigenvalues of the matrix in Eq. (7.21) define whether a small perturbation in the modes $\pm l$ will grow or decay with time. The largest value of the real part of the eigenvalues can be interpreted as a gain, and its expression is

$$\Gamma(l) = \mathrm{Re}\left\{ -1 + \sqrt{\rho^2 - \left(\alpha - 2\rho - \frac{1}{2}\beta l^2\right)^2} \right\}, \tag{7.24}$$

where $\rho = |\psi_\mathrm{e}|^2$. At threshold, the intracavity power is $\rho = 1$, and the gain of one mode reaches $\Gamma = 0$. From this expression, we can deduce that the two modes $\pm l_\mathrm{th}$ that satisfy

$$l_\mathrm{th} = \sqrt{\frac{2}{\beta}(\alpha - 2)}, \tag{7.25}$$

will grow. Above threshold, several modes can experience a positive gain, and the modes for which the gain is maximal are referred to as the maximum gain modes. They are found through the solution of the equation $\partial\Gamma/\partial l = 0$, which yields

$$l_\mathrm{mgm} = \sqrt{\frac{2}{\beta}(\alpha - 2\rho)}. \tag{7.26}$$

For a given dispersion parameter β, one can draw the curves where l_mgm is constant and integer. The case where $\beta = -0.0125$ is represented as gray lines in Figure 7.3a. When the system is pumped above threshold, two symmetric spectral sidebands are created on each side of the pump. These spectral sidebands are most likely the ones that experience the largest gain, namely $\pm l_\mathrm{mgm}$. Just above threshold, only two sidebands are generated; however, when the pump power is increased, new higher-order modes are generated at eigennumbers $\pm k l_\mathrm{mgm}$, where k is an integer number. In the time domain, the modulation that was sinusoidal close to the threshold gradually morphs into a train of sharp pulses as the pump power is increased. This increased excitation also leads to an outwards shift of the maximum gain mode l_mgm, and sudden increase in the line spacing can occur. A few examples of experimental Turing patterns with different number of rolls are presented in Figure 7.5a. They were obtained in a $\mathrm{MgF_2}$ resonator with different mode families, associated with different mode profiles and Q-factors, and, therefore, different normalized dispersion parameters β. The simulations of Figure 7.5b reproduce accurately the experimental results, especially the relative amplitudes of the lines, representative of the anharmonicity of the temporal signal.

Many applications of Kerr combs rely on the fixed relationship between the optical phases of the different spectral lines. In the case of Turing patterns, this relationship is not trivial, and a theoretical investigation is needed to shed more light on the phase-locking mechanism. This task can, however, hardly be performed using the LLE, and a modal decomposition of the field appears more appropriate [31]:

$$\psi(\theta, \tau) = \sum_l \psi_l(\tau) \mathrm{e}^{il\theta}. \tag{7.27}$$

This decomposition allows direct access to the modal phases $\phi_l(\tau) = \arg[\psi_l(\tau)]$ of the slowly varying modal amplitude $\psi_l(\tau)$. Substituting this ansatz in the LLE

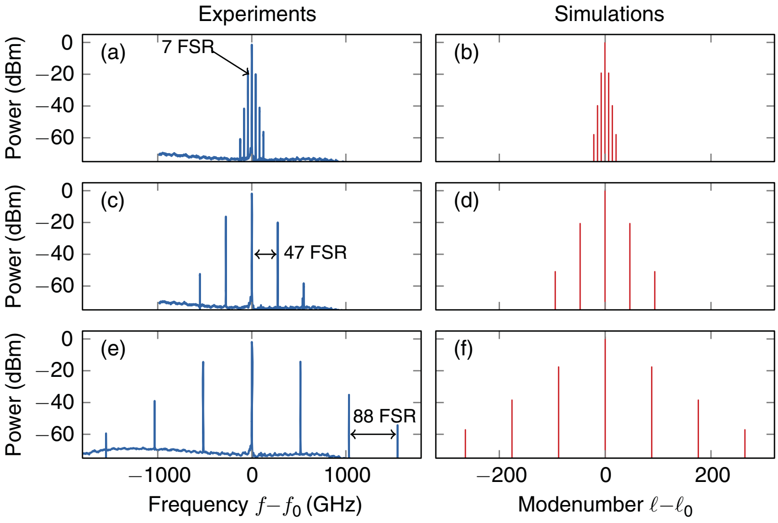

Figure 7.5 (a, c, e) Three experimental primary combs corresponding to Turing patterns with different mode spacings. (b, d, f) Corresponding numerical simulations. The parameters used are (b) $\beta = -0.03$, $\alpha = 1.27$, and $F^2 = 1.075$; (d) $\beta = -0.003$, $\alpha = -1.3$, and $F^2 = 6.4$; (f) $\beta = -0.001$, $\alpha = -1.87$, and $F^2 = 14$.

yields the following system of ordinary differential equations:

$$\frac{d\psi_l}{d\tau} = \left[-(1+i\alpha) + i\frac{\beta}{2}l^2\right]\psi_l + \delta(l)F + i\sum_{m,n,p}\delta(m-n+p-l)\psi_m\psi_n^*\psi_p. \tag{7.28}$$

Note that this system of equations is similar to the modal description presented in Section 7.3.1. Above threshold, and after a transient regime characterized by modal competition, two symmetric spectral lines are generated at modes $\pm L$ close to the maximum gain modes $\pm l_{\text{mgm}}$. As explained earlier, if the gain is sufficient, new sidemodes at $\pm kL$ are generated through cascaded FWM, k being a positive integer. This cascading effect can be seen on the phases of the generated sidemodes, as represented in Figure 7.6a, c, e. After the transient dynamics, the various modal phases $\varphi_l = \phi_l - \phi_0$ with respect to the pump reach a time-independent value. This asymptotic value is reached for the modes close to the pump, and the comb progressively becomes phase-locked. However, the asymptotic value depends on the initial condition, as shown in Figure 7.6b, where the evolution of φ_1 is shown for different noisy initial conditions. By focusing on the interaction between neighboring modes, we can show that their phases are linked by a fixed relationship.

In the stationary regime, the three consecutive modes $(k-1)L$, kL, and $(k+1)L$ interact nonlinearly and as a consequence, their phases become locked according to [32]:

$$\xi_k = \phi_{(k-1)L} - 2\phi_{kL} + \phi_{(k+1)L} = \text{constant}. \tag{7.29}$$

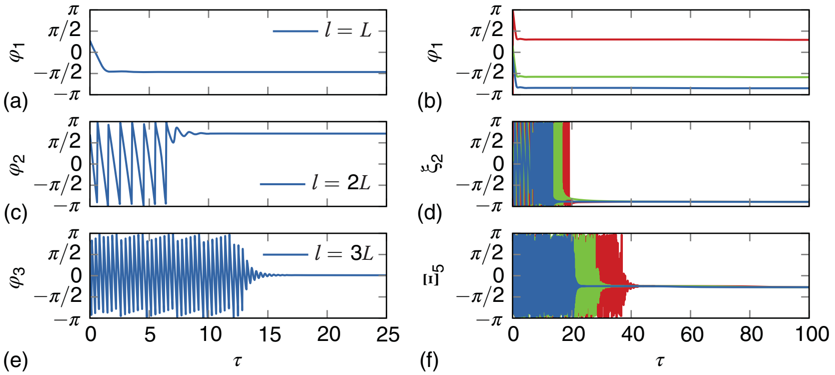

Figure 7.6 (a, c, e) Time evolution of the relative phases of the first three modes of a primary comb. After a delay increasing with the mode number, the relative phases reach a constant value, the Kerr comb becoming phase-locked. (b) Evolution of the relative phase of the first excited modes for three different initial conditions. The asymptotic value depends on the initial condition. Evidence of triplet phase locking (d) ξ_2, and global phase locking (f) Ξ_5.

This constant does not depend on the initial condition, but only on the parameters α, β, F, L, and k, as can be seen in Figure 7.6d. This relationship remains valid for all k, as well as for any linear combination of ξ_k. If we consider $2N + 1$ excited modes in a primary comb (we recall that this is the spectral counterpart of a Turing pattern), the following global phase relationship can be derived [31]:

$$\begin{aligned}\Xi_N &= \frac{1}{2}\sum_{k=-N+1}^{k=N-1}\left[1-(-1)^{N+k}\right]\xi_k \\ &= \phi_{-NL} + 2\sum_{k=-N+1}^{k=N-1}(-1)^{N+k}\phi_{kL} + \phi_{NL} \\ &= \text{constant}. \end{aligned} \tag{7.30}$$

The temporal evolution of Ξ_N is displayed in Figure 7.6f for $N = 5$, and its asymptotic value is indeed independent of the initial condition.

So far, we have discussed the generation of Turing patterns in the anomalous regime of dispersion. In optical fibers, the scalar modulational instability is known to occur only in this dispersion regime, and not for a normal dispersion. In the case of Kerr combs, the cavity detuning introduces a new degree of freedom, and Turing patterns can be generated under some particular conditions [19, 33]. In the bifurcation map of Figure 7.3b, the bifurcation that could lead to the generation of Turing patterns is the $(i\omega)^2$ (or Hamiltonian–Hopf) line corresponding at $\rho = 14$ for $\alpha > 2$ (dashed thin line) [24]. As in the anomalous case, the pump threshold is given by $F_{\text{th}}^2 = 1 + (\alpha - 1)^2$. However, numerical simulations show that Turing patterns in the normal regime of dispersion are observed only for large detunings, even though the theory predicts that they arise for $\alpha > 2$. In contrast to the anomalous case, Turing patterns in the normal regime of dispersion are generated where the LLE has three steady-state solutions. For detunings slightly above $\alpha = 2$, and above threshold, these three solution $\rho_{1,2,3}$ are very close to one another, and a moderate perturbation is likely to make the system go from one stable solution to the other. Starting with small amplitude noise around the smallest steady-state solution ρ_1 above threshold will, therefore, lead to the growth of Turing rolls; however, once the maxima of these rolls reach the intermediate and unstable steady-state level ρ_2, the system will quickly evolve to the upper steady-state ρ_3. In order to generate stable normal Turing patterns, the detuning has to be high enough so that the amplitude difference between the two steady-state solutions ρ_1 and ρ_2 is compatible with the stabilization of the Turing rolls. Numerical simulations show that a primary comb can be generated spontaneously from low-amplitude noise for detunings greater than 8.

The number of rolls in the normal Turing patterns can be determined using the same approach as for the anomalous dispersion regime. This analysis shows that the number of rolls at threshold ($\rho = 1$) is given by $l_{\text{th}} = \sqrt{2(2-\alpha)/\beta}$, while above threshold ($\rho > 1$), the maximum gain mode is $l_{\text{mgm}} = \sqrt{2(2\rho-\alpha)/\beta} \geq l_{\text{th}}$.

7.4.2
Solitons

Contrary to Turing patterns, which fill entirely the cavity, a *soliton* is a localized structure since it does not feel the boundaries when they are at a distance significantly larger than its pulse width. Its existence in anomalous dissipative systems such as nonlinear optical cavities is a well-known topic [34–39]. In such systems, its stability is due to a double balance between four influences: its shape is mostly defined by the interplay between the nonlinearity and anomalous dispersion, while its amplitude mainly results from the competition between the gain and the cavity losses.

For our system, which is governed by the LLE and for an anomalous dispersion, the bifurcation that leads to the formation of soliton is the $0^2(i\omega)$ one, corresponding to the lower limit of the bistability area. The region of the parameter space where solitons occur can be determined using numerical simulations of the LLE, and is shown in light gray in Figure 7.3a. In this region, the steady-state is such that $\rho < 1$, and both the soliton and the flat-state are solutions of the LLE. In contrast to the case of supercritical Turing patterns, it is difficult to excite a soliton starting from noise. Instead, an optical pulse is the easiest way to excite them, and convergence to the soliton solution is achieved, provided width and energy are close enough to those of the soliton. For instance, the soliton displayed in Figure 7.7a was excited using a Gaussian pulse with amplitude and width similar to the final soliton. Its spectrum shown in Figure 7.7b has a single-FSR spacing and displays hundreds of mode-locked modes. Indeed, the phase differences between two adjacent modes $\phi_k - \phi_{k-1}$ is stationary and close to zero, except around the pump mode. As expected, the spectral extension of this comb is larger for smaller dispersion amplitude $|\beta|$. Such solitons have also been observed in recent experiments [22].

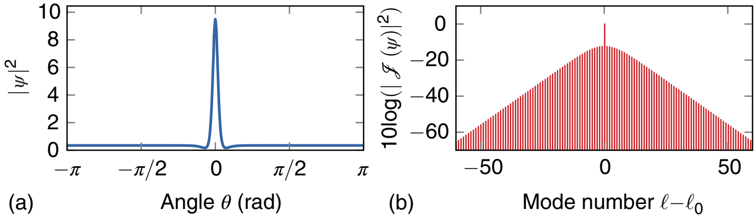

Figure 7.7 (a) Spatiotemporal distribution of the intracavity field and (b) corresponding optical spectrum for a bright soliton in the anomalous regime of dispersion. The parameters used are $\alpha = 4$, $\beta = -0.05$, $F^2 = 5$, and the initial intracavity field envelope is $\psi_0 = 1 + 1.5\exp(-(\theta/0.1)^2)$.

For subcritical structures, the final stationary state does largely depend on the initial condition. Solitons are an example of such structures where higher energy initial conditions can lead to the growth of multiple-peaked solutions that are referred to as *soliton molecules*. These molecules can be considered as a limited number of pulses carved out of a subcritical Turing pattern. It can be shown that the number of solitons in a molecule is governed by a snaking bifurcation [40–42].

If the excitation is increased and for relatively large detunings, a soliton can be destabilized and evolve into a *breather*, that is, a soliton whose amplitude varies periodically in time. The dark gray area in Figure 7.3a represents the parameter-space region where breathers can be obtained, and was determined through numerical simulations [24, 43–45]. The breathing period is very low compared with the cavity round-trip time, and it is of the order of the photon lifetime. The maximal and minimal amplitudes of a breather are displayed in Figure 7.8a, and their spatiotemporal distribution is shown in Figure 7.8b.

In the normal regime of dispersion, one can also generate a localized structure in the form of a *dark soliton* [46], which can be seen as a hole in a finite background. Two examples of such solitons are shown in Figure 7.9a, c, and their spectra in Figure 7.9b, d. Numerical simulations show that such solitons can appear in the bistable region of the parameter-space, in the light gray region of Figure 7.3b. The continuous background of the dark soliton actually corresponds to the upper

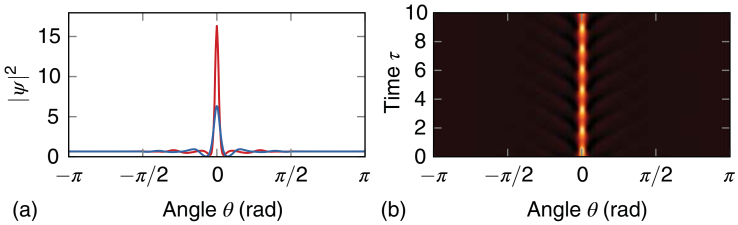

Figure 7.8 (a) Intracavity intensity profiles of a bright breather in the anomalous regime of dispersion, at two different evolution times. (b) Spatiotemporal distribution of the field intensity of the bright breather. The parameters used are $\alpha = 4$, $\beta = -0.05$, and $F^2 = 8$, and the initial intracavity field envelope is $\psi_0 = 0.5 + 1.5\exp(-(\theta/0.1)^2)$.

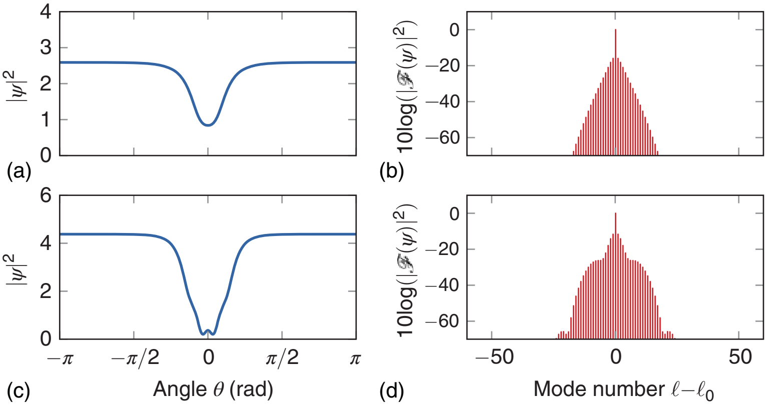

Figure 7.9 Spatiotemporal distribution of the (a,c) intracavity field and (b,d) corresponding optical spectrum for two dark solitons in the normal regime of dispersion. The parameters for the first soliton are $\alpha = 2.5$, $\beta = 0.05$, $F^2 = 2.61$, and the initial intracavity field envelope is $\psi_0 = 1.5 - \exp[-(\theta/0.9)^2]$. For the second soliton, the parameters are unchanged except for $\alpha = 4$ and $F^2 = 5$.

steady-state solution ρ_3 while the dip is close to the lower stable solution ρ_1, where we note that the intermediate solution ρ_2 is unstable. As it is the case for a bright soliton, the dark soliton cannot easily be excited from noise alone, and an appropriate initial condition must be used. If this condition is not met, the system will either evolve toward the lower or the upper steady-state solutions. Despite this relatively stringent requirement, dark solitons have been reported by several groups [9, 20], and an example is provided in Figure 7.10 with its numerical counterpart. When the excitation and detuning are progressively increased, the shape of the dark soliton is modified, as shown in Figure 7.9c. Accordingly, the corresponding spectrum (Figure 7.9d) becomes wider and more intricate. At higher excitations, the dark soliton can also evolve to a *dark soliton breather*, in a similar fashion to the bright soliton breather. In this case, the amplitude of the dip changes with a period in the order of the photon lifetime, as shown in Figure 7.11. These breathers only occur in the dark gray area of Figure 7.3b.

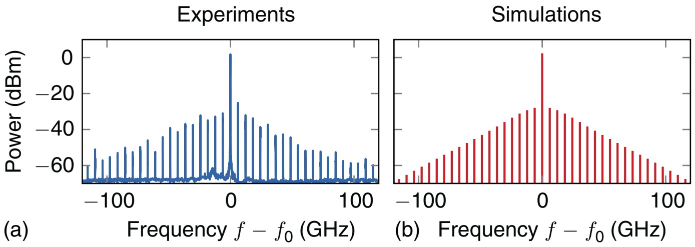

Figure 7.10 (a) Experimental frequency comb obtained in a CaF$_2$ resonator with Q-factor around 1×10^9 and FSR 6 GHz. (b) Numerical simulation of the spectrum of a dark soliton.

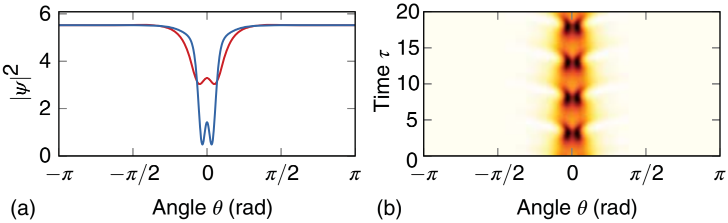

Figure 7.11 (a) Intensity profiles of a dark breather at two different evolution times where it reaches its maximum and minimum amplitudes. (b) Spatiotemporal distribution of the optical intensity of the dark breather, in the normal regime of dispersion. $\alpha = 5$, $\beta = 0.05$, $F^2 = 7$, and the initial intracavity field envelope is $\psi_0 = 2.2 - 2\exp[-(\theta/0.3)^2]$.

7.4.3
Chaos

From a theoretical point of view, it is well known that chaos can potentially arise in any nonlinear system with more than three degrees of freedom. The LLE satisfies these conditions, since it is highly nonlinear and has an infinite number of dimensions. These necessary conditions are, however, not sufficient to insure that a chaotic behavior can be found at high excitation in the system. The normal dispersion case of the LLE is one such example. As it can be seen in Figure 7.3b, the regions in the $\alpha - F^2$ plane where nontrivial solutions can be excited are well defined, with finite boundaries. In contrast, the stability map in the anomalous dispersion regime (Figure 7.3a) shows that the previously discussed structures can evolve at higher excitations, leading to chaotic behaviors through various bifurcations [2, 45, 47, 48]. This evolution can be investigated using numerical simulations: the system is simulated for durations one hundred times longer than the photon lifetime τ_{ph} so that its whole dynamics is explored. The extrema of the 100 last intensity profiles are recorded and plotted as a function of the control parameter, the external driving F^2. By varying adiabatically the value of F^2 and using each previous final state as the initial condition of the following iteration, one obtains the bifurcation diagrams presented in Figure 7.12. Note that, in this figure, the starting value for the F^2 parameter is indicated with a dashed gray segment, and the bifurcation diagram is obtained by decreasing and increasing the control parameter from this starting point.

Based on this figure, we can identify at least two different routes to chaos. If the detuning α is below $\sqrt{3}$, the stable nontrivial structure in the cavity at low excitations is a Turing pattern. The route to chaos will, therefore, start by the destabilization of this patterns. Figure 7.12a displays the bifurcation diagram of the system for $\alpha = -1$. In this case, the initial condition is low-amplitude noise for $F^2 = 5.5$, just above the $(i\omega)^2$ bifurcation. At this pump power, the system quickly evolves to a stable Turing pattern, as the presence of two extrema suggest. Since the detuning α is below $41/30$, this Turing pattern is supercritical and disappears when the excitation is decreased below the threshold. When the control

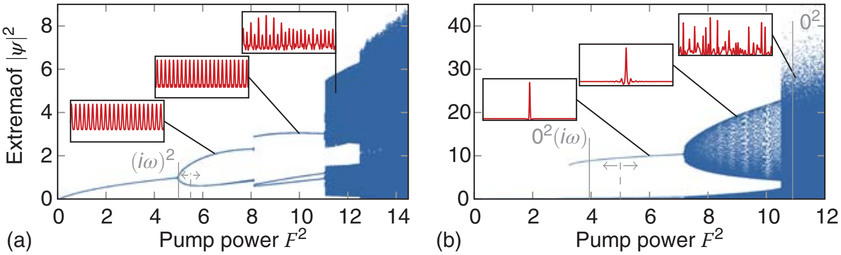

Figure 7.12 Anomalous dispersion bifurcation diagrams for two different detunings (a) $\alpha = -1$ and (b) $\alpha = 4$, when the pump power F^2 is increased. For $\alpha = -1$, the first bifurcation $(i\omega)^2$ leads to the formation of Turing patterns with an integer number of rolls (22). For higher pump powers, this structure evolves to a different number of rolls, 23 in this case. For higher gains, the amplitude of each roll oscillates, and finally, a chaotic regime is reached. In the case $\alpha = 4$, the initial condition is a Gaussian pulse leading to the formation of a soliton just above the bifurcation (dashed gray line). This soliton is stable at excitations lower than the bifurcation limit, revealing its subcritical nature. With higher pump power, the soliton evolves into a bright breather, and ultimately, the system becomes chaotic in the vicinity of the 0^2 bifurcation.

parameter is increased, the system shows a first qualitative change for $F^2 \sim 8$: the number of Turing rolls abruptly changes from 22 to 23. We have indeed previously shown in Eq. (7.26) that the maximum gain mode number depends on the intracavity power. For the second bifurcation occurring at $F^2 \sim 11$, the Turing patterns become unstable and start oscillating in time. In the Fourier domain, this corresponds to the apparition of new spectral lines in between the primary comb's lines. In experiments, this particular comb is often referred to as the *secondary comb*. Finally, as the pump power is increased again, the systems reach a chaotic state with peaks of diverse amplitudes fluctuating rapidly.

When $\alpha > \sqrt{3}$, the stable structure of interest is the bright cavity soliton discussed in Section 7.4.2. The starting point of the corresponding bifurcation will thus be a stable soliton just above the bifurcation threshold. In the example of Figure 7.12b, the detuning is $\alpha = 4$, and the starting excitation is $F^2 = 5$. The subcritical nature of the soliton can be verified on this diagram, since the excitation has to be significantly lower than the $0^2(i\omega)$ bifurcation threshold for the soliton to disappear. When this excitation is higher, the soliton evolves into a breather whose amplitude increases as the pump power is increased. Finally, in the vicinity of the 0^2 bifurcation, the system explodes into a chaotic behavior where many new peaks with fluctuating amplitudes are generated.

This latter chaotic regime presents interesting characteristics. Indeed, when the simulation time is long enough, some pulses reach highly peaked amplitude before vanishing. To shed some light on this phenomenon, a statistical study has been performed. Figure 7.13a, c, and e displays the snapshots of the intracavity intensity distribution when the highest wave of the simulation appears. The parameters used for these simulations correspond to the bifurcation diagram of Figure 7.12b, with the detuning being kept constant at $\alpha = 4$ and pump powers

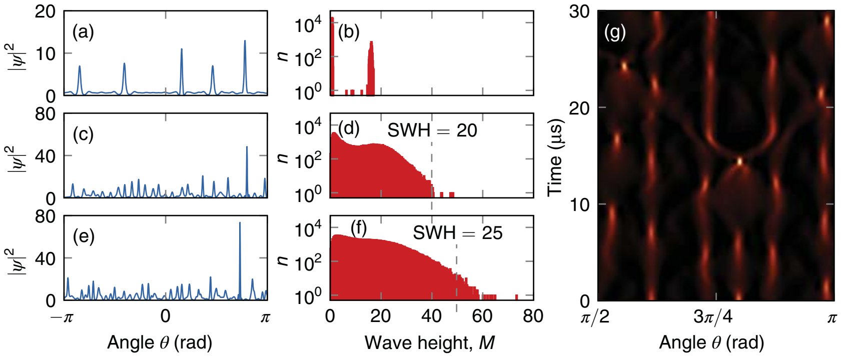

Figure 7.13 (first column) Spatial distribution of the optical intensity when the highest wave occurs for different pump powers: (a) $F^2 = 8$, (c) 10, and (e) 20. The second column represents the number of events recorded for each wave height bin during the simulation time. (g) Spatiotemporal distribution of the field when the highest wave occurs at $F^2 = 10$.

$F^2 = 8$, 10, and 20. The second column of Figure 7.13 displays the statistical distribution of the wave heights $\max(|\psi(\theta,\tau)|^2)$ for the same parameters. For $F^2 = 8$, the high-amplitude noise initial condition leads to the generation of a few breathers, and their maximal amplitudes are all approximately identical. The associated histogram indeed shows a sharp peak for local maxima around 15, and another peak slightly above 0 corresponding to the small pedestals next to the breathers. In the cases $F^2 = 10$ and $F^2 = 20$, and starting from the same initial condition, the system evolves quickly to chaos, with many pulses filling the cavity with various maximum amplitudes. As the spatial traces of Figure 7.13c and d show, some waves clearly stand above the others. In both cases, the histogram shows that the probability density function (PDF) varies continuously. Of greater interest, the tail for intense events shows an exponential decay except for some very rare waves with relatively high amplitudes [49]. Those events qualify for the appellation of *rogue waves*. Rogue (or "freak") waves are rare events of relatively high amplitudes that were first investigated in hydrodynamics, where their fascinating nature and disastrous consequences have drawn noticeable attention [50]. Later research showed that rogue waves may be found in various nonlinear systems such as Bose–Einstein condensates, superfluid helium, plasma waves, and pulse propagation in nonlinear optical fibers and lasers [51–53].

A convenient way to characterize a rogue wave is to calculate the significant wave height (SWH), defined as the mean amplitude of the highest third of the waves. It is convenient to consider that a wave can be qualified as rogue if its height is at least two times larger than the SWH. This limit has been added to the histograms of Figure 7.13d and f as dashed gray lines, and some waves are indeed higher than this limit. Rogue waves also have to appear and disappear quickly. The spatiotemporal representation of Figure 7.13g focuses on the highest wave of the $F^2 = 10$ simulation. One can see that the highest wave is a very localized and rare event. This same representation also advocates for the interpretation of rogue waves as a collision between breathers. Before the maximum amplitude event, three breathers are present in the cavity close the one to the other, while after this event, only two of them remain.

Drawing analogous bifurcation diagrams for the experimental system is difficult. On one hand, the picosecond range of the optical pulse widths makes it hard to detect the maxima of the temporal signal. On the other hand, increasing the pump power for a fixed detuning is also a challenge because of thermal nonlinearities that shift the resonance frequencies. However, increasing the detuning at a fixed pump power is rather easy, and one can monitor the generated comb using an optical spectrum analyzer. This series of experiments was performed on a MgF_2 disk resonator with Q-factor higher than 10^9 and the resulting optical spectra are shown in the first column of Figure 7.14. For pump wavelengths

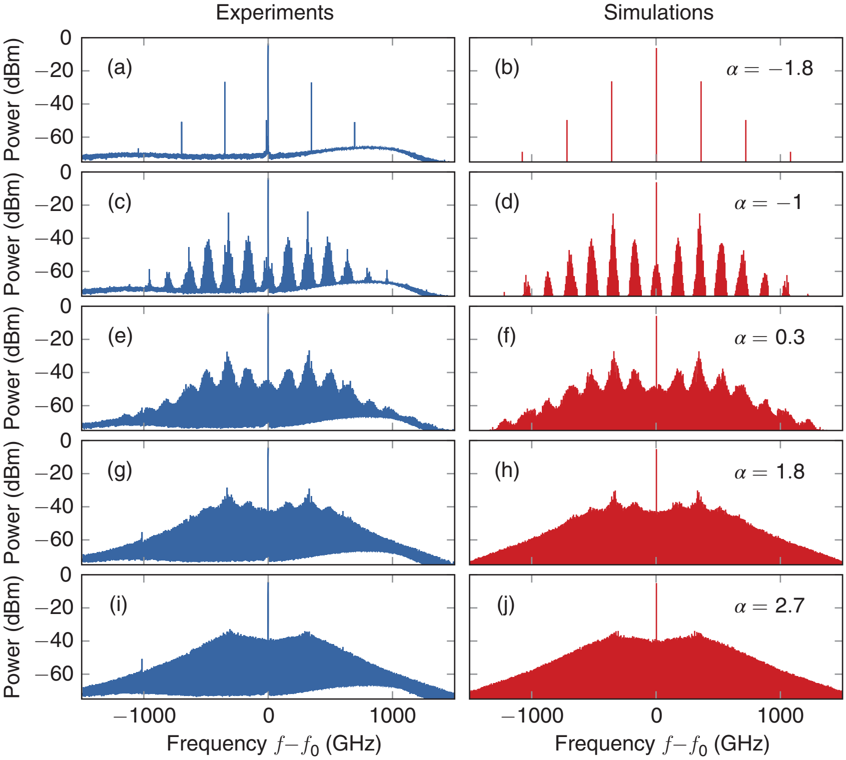

Figure 7.14 Comparison between experiments and simulations for several regimes of Kerr combs. In the experiments (first column), the pump power is kept constant while the laser frequency is progressively decreased (α is increased). For the numerical simulations (second column), the excitation is kept constant at $F^2 = 12$, the dispersion is $\beta = 2.2 \times 10^3$ and the detuning is progressively increased. The excellent agreement between the experimental results and numerical simulations over different regimes proves the relevance of the LLE model to describe the generation of Kerr frequency combs.

smaller than the resonance's (detuning $\alpha < 0$), the system spontaneously evolves toward a Turing pattern when the threshold is crossed, and its spectrum is the primary comb of Figure 7.14a. Increasing the detuning leads to the appearance of new spectral components between the primary comb: these new lines constitute the secondary comb of Figure 7.14c, corresponding to oscillations of the Turing pattern in the temporal domain. Figure 7.14e, g, and i are different chaotic regimes obtained for higher detunings. One can note that the shape of the comb is reminiscent of the secondary comb, and these features gradually disappear as the pump wavelength is increased. This progression can be compared with numerical simulations in which the excitation is kept constant while the detuning is increased. The results of these simulations are presented in the second column of Figure 7.14, and the parameters used in this case are $F^2 = 12$ and $\beta = 2.2 \times 10^3$. The agreement between the experimental and numerical results is excellent: it covers a dynamical range of 80 dB on more than 300 modes. Furthermore, it remains valid for a wide range of detunings and comb regimes, especially in the chaotic regimes [45]. This agreement validates the use of the LLE as an appropriate model for Kerr-comb generation, and shows that the two different routes to chaos identified earlier lead to distinct optical spectra. The chaotic comb of Figure 7.14f was simulated for a detuning below $\sqrt{3}$, in the Turing pattern region, while the one of Figure 7.14j was obtained in the soliton regime, with $\alpha = 2.7 > \sqrt{3}$.

7.5
Conclusion

In this chapter, we have investigated the main dynamical regimes resulting from Kerr-comb generation.

We have presented the two main formalisms used to understand these combs from a theoretical standpoint, namely the modal and the spatiotemporal formalisms. We have also performed a bifurcation analysis that enabled us to outline the structural changes that the system undergoes when externally controllable parameters (laser frequency and power) are tuned.

We have shown that in the regime of anomalous dispersion, dissipative structures such as Turing rolls arise in the system through a super- or subcritical pitchfork bifurcation, which is here intrinsically associated with a Hamiltonian–Hopf spatial bifurcation. We have also determined the threshold power and the number of rolls when this solution is excited. Our work also permits to understand the formation of solitons as subcritical structures. Other solutions such as soliton breathers or spatiotemporal chaos have also been investigated. Nontrivial solutions in the normal dispersion regime include dark cavity solitons, and also Turing rolls, but these solutions are much more difficult to excite than in the anomalous dispersion regime.

An important challenge for future work will be to investigate other effects such as higher-order nonlinearity and dispersion, Raman, Brillouin, and Rayleigh effects [6, 54–57]. It will also be necessary to gain higher control of the various dynamical states in order to fine-tune the spectral features of the combs for a large range of potential applications [23, 58–61].

7.6
Acknowledgements

Y.K. Chembo acknowledges support from the European Research Council (ERC) through the StG NextPhase and PoC Versyt, from the *Centre National d'Etudes Spatiales* (CNES) through the project SHYRO, from the *Région de Franche-Comté*, and from the Labex ACTION. The authors also thank the colleagues who have contributed to this research work, at either the theoretical of experimental level: I.V. Balakireva, R. Henriet, K. Saleh, R. Salut, C. Godey, M. Haragus, and L. Larger.

References

1. Savchenkov, A.A., Matsko, A.B., Strekalov, D., Mohageg, M., Ilchenko, V.S., and Maleki, L. (2004) Low threshold optical oscillations in a whispering gallery mode CaF_2 resonator. *Phys. Rev. Lett.*, **93**, 243 905, doi: 10.1103/PhysRevLett.93.243905.
2. Chembo, Y.K., Strekalov, D.V., and Yu, N. (2010) Spectrum and dynamics of optical frequency combs generated with monolithic whispering gallery mode resonators. *Phys. Rev. Lett.*, **104**, 103 902, doi: 10.1103/PhysRevLett.104.103902.
3. Chembo, Y.K. and Yu, N. (2010) Modal expansion approach to optical-frequency-comb generation with monolithic whispering-gallery-mode resonators. *Phys. Rev. A*, **82**, 033 801, doi: 10.1103/PhysRevA.82.033801.
4. Agha, I.H., Okawachi, Y., and Gaeta, A.L. (2009) Theoretical and experimental investigation of broadband cascaded four-wave mixing in high-Q microspheres. *Opt. Express*, **17** (18), 16-209–16-215, doi: 10.1364/OE.17.016209.
5. Matsko, A.B., Savchenkov, A.A., Liang, W., Ilchenko, V.S., Seidel, D., and Maleki, L. (2011) Mode-locked Kerr frequency combs. *Opt. Letters*, **36** (15), 2845–2847, doi: 10.1364/OL.36.002845.
6. Chembo, Y.K. and Menyuk, C.R. (2013) Spatiotemporal Lugiato-Lefever formalism for Kerr-comb generation in whispering-gallery-mode resonators. *Phys. Rev. A*, **87**, 053 852, doi: 10.1103/PhysRevA.87.053852.
7. Coen, S., Randle, H.G., Sylvestre, T., and Erkintalo, M. (2013) Modeling of octave-spanning Kerr frequency combs using a generalized mean-field Lugiato–Lefever model. *Opt. Lett.*, **38** (1), 37–39, doi: 10.1364/OL.38.000037.
8. Lugiato, L.A. and Lefever, R. (1987) Spatial dissipative structures in passive optical systems. *Phys. Rev. Lett.*, **58**, 2209–2211, doi: 10.1103/PhysRevLett.58.2209.
9. Coillet, A., Balakireva, I., Henriet, R., Saleh, K., Larger, L., Dudley, J., Menyuk, C., and Chembo, Y. (2013) Azimuthal turing patterns, bright and dark cavity solitons in Kerr combs generated with whispering-gallery-mode resonators. *IEEE Photonics J.*, **5** (4), 6100409–, doi: 10.1109/JPHOT.2013.2277882.
10. Kippenberg, T.J., Holzwarth, R., and Diddams, S.A. (2011) Microresonator-based optical frequency combs. *Science*, **332** (6029), 555–559, doi: 10.1126/science.1193968.
11. Ferdous, F., Miao, H., Leaird, D.E., Srinivasan, K., Wang, J., Chen, L., Varghese, L.T., and Weiner, A.M. (2011) Spectral line-by-line pulse shaping of on-chip microresonator frequency combs.

Nat. Photonics, **5** (12), 770–776, doi: 10.1038/nphoton.2011.255.

12. Savchenkov, A.A., Matsko, A., Liang, W., Ilchenko, V., Seidel, D., and Maleki, L. (2011) Kerr combs with selectable central frequency. *Nat. Photonics*, **5** (5), 293–296, doi: 10.1038/nphoton.2011.50.
13. Papp, S.B. and Diddams, S.A. (2011) Spectral and temporal characterization of a fused-quartz-microresonator optical frequency comb. *Phys. Rev. A*, **84**, 053 833, doi: 10.1103/PhysRevA.84.053833.
14. Del'Haye, P., Papp, S.B., and Diddams, S.A. (2012) Hybrid electro-optically modulated microcombs. *Phys. Rev. Lett.*, **109**, 263 901, doi: 10.1103/PhysRevLett.109.263901.
15. Herr, T., Hartinger, K., Riemensberger, J., Wang, C.Y., Gavartin, E., Holzwarth, R., Gorodetsky, M.L., and Kippenberg, T.J. (2012) Universal formation dynamics and noise of Kerr-frequency combs in microresonators. *Nat. Photonics*, **6** (7), 480–487, doi: 10.1038/nphoton.2012.127.
16. Wang, C.Y., Herr, T., Del'Haye, P., Schliesser, A., Hofer, J., Holzwarth, R., Hänsch, T.W., Picqué, N., and Kippenberg, T.J. (2013) Mid-infrared optical frequency combs at 2.5 μm based on crystalline microresonators. *Nat. Commun.*, **4**, 1345–, doi: 10.1038/ncomms2335.
17. Coillet, A., Henriet, R., Phan Huy, K., Jacquot, M., Furfaro, L., Balakireva, I., Larger, L., and Chembo, Y.K. (2013) Microwave photonics systems based on whispering-gallery-mode resonators. *J. Vis. Exp.*, (78), e50 423–, http://www.jove.com/video/50423.
18. Savchenkov, A.A., Matsko, A.B., Ilchenko, V.S., and Maleki, L. (2007) Optical resonators with ten million finesse. *Opt. Express*, **15** (11), 6768–6773, doi: 10.1364/OE.15.006768.
19. Matsko, A.B., Savchenkov, A.A., and Maleki, L. (2012) Normal group-velocity dispersion Kerr frequency comb. *Opt. Lett.*, **37** (1), 43–45, doi: 10.1364/OL.37.000043.
20. Liang, W., Savchenkov, A.A., Ilchenko, V.S., Eliyahu, D., Seidel, D., Matsko, A.B., and Maleki, L. (2014) Generation of a coherent near-infrared Kerr frequency comb in a monolithic microresonator with normal GVD. *Opt. Lett.*, **39** (10), 2920–2923, doi: 10.1364/OL.39.002920.
21. Del'Haye, P., Schliesser, A., Arcizet, O., Wilken, T., Holzwarth, R., and Kippenberg, T.J. (2007) Optical frequency comb generation from a monolithic microresonator. *Nature*, **450** (7173), 1214–1217, doi: 10.1038/nature06401.
22. Herr, T., Brasch, V., Jost, J.D., Wang, C.Y., Kondratiev, N.M., Gorodetsky, M.L., and Kippenberg, T.J. (2014) Temporal solitons in optical microresonators. *Nat. Photonics*, **8** (2), 145–152, doi: 10.1038/nphoton.2013.343.
23. Grudinin, I.S., Baumgartel, L., and Yu, N. (2012) Frequency comb from a microresonator with engineered spectrum. *Opt. Express*, **20** (6), 6604–6609, doi: 10.1364/OE.20.006604.
24. Godey, C., Balakireva, I.V., Coillet, A., and Chembo, Y.K. (2014) Stability analysis of the spatiotemporal Lugiato–Lefever model for Kerr optical frequency combs in the anomalous and normal dispersion regimes. *Phys. Rev. A*, **89**, 063 814, doi: 10.1103/PhysRevA.89.063814.
25. Gibbs, H. (1985) *Optical Bistability: Controlling Light with Light*, Quantum Electronics Series, Academic Press, http://books.google.com/books?id=1dVhGQAACAAJ.
26. Haragus, M. and Iooss, G. (2011) *Local Bifurcations, Center Manifolds, and Normal Forms in Infinite-Dimensional Dynamical Systems*, Universitext, Springer-Verlag London, Ltd., London; EDP Sciences, Les Ulis, doi: 10.1007/978-0-85729-112-7.
27. Turing, A.M. (1952) The chemical basis of morphogenesis. *Philos. Trans. R. Soc. London, Ser. B*, **237** (641), 37–72, doi: 10.1098/rstb.1952.0012.
28. Miyaji, T., Ohnishi, I., and Tsutsumi, Y. (2010) Bifurcation analysis to the Lugiato–Lefever equation in one space dimension. *Physica D*, **239** (23-24), 2066–2083, doi: http://dx.doi.org/10.1016/j.physd.2010.07.014.

29. Kozyreff, G. (2012) Localized turing patterns in nonlinear optical cavities. *Physica D*, **241** (10), 939–946.

30. Matsko, A.B., Savchenkov, A.A., Ilchenko, V.S., Seidel, D., and Maleki, L. (2012) Hard and soft excitation regimes of Kerr frequency combs. *Phys. Rev. A*, **85**, 023 830, doi: 10.1103/PhysRevA.85.023830.

31. Coillet, A. and Chembo, Y. (2014) On the robustness of phase locking in Kerr optical frequency combs. *Opt. Lett.*, **39** (6), 1529–1532, doi: 10.1364/OL.39.001529.

32. Matsko, A.B., Savchenkov, A.A., Strekalov, D., Ilchenko, V.S., and Maleki, L. (2005) Optical hyperparametric oscillations in a whispering-gallery-mode resonator: threshold and phase diffusion. *Phys. Rev. A*, **71**, 033 804, doi: 10.1103/PhysRevA.71.033804.

33. Hansson, T., Modotto, D., and Wabnitz, S. (2013) Dynamics of the modulational instability in microresonator frequency combs. *Phys. Rev. A*, **88**, 023 819, doi: 10.1103/PhysRevA.88.023819.

34. Lugiato, L. (2003) Introduction to the feature section on cavity solitons: an overview. *IEEE J. Quantum Electron.*, **39** (2), 193–196, doi: 10.1109/JQE.2002.807195.

35. Akhmediev, N. and Ankiewicz, A. (2008) *Dissipative Solitons: From Optics to Biology and Medicine*, Lecture Notes in Physics, Springer-Verlag, Berlin, Heidelberg, doi: 10.1007/978-3-540-78217-9.

36. Scroggie, A., Firth, W., McDonald, G., Tlidi, M., Lefever, R., and Lugiato, L. (1994) Pattern formation in a passive Kerr cavity. *Chaos, Solitons Fractals*, **4** (8-9), 1323–1354, doi: http://dx.doi.org/10.1016/0960-0779(94)90084-1, special Issue: Nonlinear Optical Structures, Patterns, Chaos.

37. Santagiustina, M., Colet, P., San Miguel, M., and Walgraef, D. (1997) Noise-sustained convective structures in nonlinear optics. *Phys. Rev. Lett.*, **79**, 3633–3636, doi: 10.1103/PhysRevLett.79.3633.

38. Firth, W.J., Harkness, G.K., Lord, A., McSloy, J.M., Gomila, D., and Colet, P. (2002) Dynamical properties of two-dimensional Kerr cavity solitons. *J. Opt. Soc. Am. B*, **19** (4), 747–752, doi: 10.1364/JOSAB.19.000747.

39. Gomila, D., Matías, M.A., and Colet, P. (2005) Excitability mediated by localized structures in a dissipative nonlinear optical cavity. *Phys. Rev. Lett.*, **94**, 063 905, doi: 10.1103/PhysRevLett.94.063905.

40. Woods, P. and Champneys, A. (1999) Heteroclinic tangles and homoclinic snaking in the unfolding of a degenerate reversible hamiltonian-hopf bifurcation. *Physica D*, **129** (3–4), 147–170, doi: http://dx.doi.org/10.1016/S0167-2789(98)00309-1.

41. Knobloch, J. and Wagenknecht, T. (2005) Homoclinic snaking near a heteroclinic cycle in reversible systems. *Physica D*, **206** (1–2), 82–93, doi: http://dx.doi.org/10.1016/j.physd.2005.04.018.

42. Gomila, D., Scroggie, A., and Firth, W. (2007) Bifurcation structure of dissipative solitons. *Physica D*, **227** (1), 70–77, doi: http://dx.doi.org/10.1016/j.physd.2006.12.008.

43. Matsko, A.B., Savchenkov, A.A., and Maleki, L. (2012) On excitation of breather solitons in an optical microresonator. *Opt. Lett.*, **37** (23), 4856–4858, doi: 10.1364/OL.37.004856.

44. Leo, F., Gelens, L., Emplit, P., Haelterman, M., and Coen, S. (2013) Dynamics of one-dimensional Kerr cavity solitons. *Opt. Express*, **21** (7), 9180–9191, doi: 10.1364/OE.21.009180.

45. Coillet, A. and Chembo, Y.K. (2014) Routes to spatiotemporal chaos in Kerr optical frequency combs. *Chaos*, **24** (1), 013113–, doi: http://dx.doi.org/10.1063/1.4863298.

46. Kivshar, Y.S. and Luther-Davies, B. (1998) Dark optical solitons: physics and applications. *Phys. Rep.*, **298** (2-3), 81–197, doi: http://dx.doi.org/10.1016/S0370-1573(97)00073-2.

47. Matsko, A.B., Liang, W., Savchenkov, A.A., and Maleki, L. (2013) Chaotic dynamics of frequency combs generated with continuously pumped nonlinear microresonators. *Opt. Lett.*, **38** (4), 525–527, doi: 10.1364/OL.38.000525.

48. Haelterman, M., Trillo, S., and Wabnitz, S. (1992) Low dimensional modulational chaos in diffractive nonlinear cavities. *Opt. Commun.*, **93** (5-6), 343–349, doi: http://dx.doi.org/10.1016/0030-4018(92)90198-Z.

49. Coillet, A., Dudley, J., Genty, G., Larger, L., and Chembo, Y.K. (2014) Optical rogue waves in whispering-gallery-mode resonators. *Phys. Rev. A*, **89**, 013 835, doi: 10.1103/PhysRevA.89.013835.

50. Solli, D.R., Ropers, C., Koonath, P., and Jalali, B. (2007) Optical rogue waves. *Nature*, **450** (7172), 1054–1057, doi: 10.1038/nature06402.

51. Akhmediev, N., Dudley, J.M., Solli, D.R., and Turitsyn, S.K. (2013) Recent progress in investigating optical rogue waves. *J. Opt.*, **15** (6), 060 201, doi: 10.1088/2040-8978/15/6/060201.

52. Kibler, B., Fatome, J., Finot, C., Millot, G., Dias, F., Genty, G., Akhmediev, N., and Dudley, J.M. (2010) The peregrine soliton in nonlinear fibre optics. *Nat. Phys.*, **6** (10), 790–795, 10.1038/nphys1740.

53. Lecaplain, C., Grelu, P., Soto-Crespo, J.M., and Akhmediev, N. (2012) Dissipative rogue waves generated by chaotic pulse bunching in a mode-locked laser. *Phys. Rev. Lett.*, **108**, 233 901, doi: 10.1103/PhysRevLett.108.233901.

54. Tlidi, M., Bahloul, L., Cherbi, L., Hariz, A., and Coulibaly, S. (2013) Drift of dark cavity solitons in a photonic-crystal fiber resonator. *Phys. Rev. A*, **88**, 035 802, doi: 10.1103/PhysRevA.88.035802.

55. Colet, P., Matías, M.A., Gelens, L., and Gomila, D. (2014) Formation of localized structures in bistable systems through nonlocal spatial coupling. I. General framework. *Phys. Rev. E*, **89**, 012 914, doi: 10.1103/PhysRevE.89.012914.

56. Gelens, L., Matías, M.A., Gomila, D., Dorissen, T., and Colet, P. (2014) Formation of localized structures in bistable systems through nonlocal spatial coupling. II. The nonlocal Ginzburg-Landau equation. *Phys. Rev. E*, **89**, 012 915, doi: 10.1103/PhysRevE.89.012915.

57. Parra-Rivas, P., Gomila, D., Leo, F., Coen, S., and Gelens, L. (2014) Third-order chromatic dispersion stabilizes Kerr frequency combs. *Opt. Lett.*, **39** (10), 2971–2974, doi: 10.1364/OL.39.002971.

58. Chembo, Y.K. and Yu, N. (2010) On the generation of octave-spanning optical frequency combs using monolithic whispering-gallery-mode microresonators. *Opt. Lett.*, **35** (16), 2696–2698, doi: 10.1364/OL.35.002696.

59. Grudinin, I.S., Baumgartel, L., and Yu, N. (2013) Impact of cavity spectrum on span in microresonator frequency combs. *Opt. Express*, **21** (22), 26-929–26-935, doi: 10.1364/OE.21.026929.

60. Lamont, M.R.E., Okawachi, Y., and Gaeta, A.L. (2013) Route to stabilized ultrabroadband microresonator-based frequency combs. *Opt. Lett.*, **38** (18), 3478–3481, doi: 10.1364/OL.38.003478.

61. Coen, S. and Erkintalo, M. (2013) Universal scaling laws of Kerr frequency combs. *Opt. Lett.*, **38** (11), 1790–1792, doi: 10.1364/OL.38.001790.

8
Nonlinear Effects in Microfibers and Microcoil Resonators

Muhammad I. M. Abdul Khudus, Rand Ismaeel, Gilberto Brambilla, Neil G. R. Broderick, and Timothy Lee

8.1
Introduction

The tapering of optical fibers down to micron diameters (or less) has long been used to fabricate a wide range of devices such as evanescent field sensors or fused fiber couplers, and the linear properties of such devices are well known. However, in the early 2000s it was realized that such optical micro- and nanofibers (OMNs) could easily be manipulated in the third dimension to form a variety of novel resonators that combine the advantages of nanophotonics with the integrability of standard optical components. Early examples of these include loop [1–3] and knot [4–7] resonators in which a fiber is bent or knotted to create a simple loop resonator with an extremely high-Q factor due to the low intrinsic loss of silica. Then, in 2004, Sumetsky [8] introduced the optical microcoil resonator (OMR), which is essentially a helical coil of micron diameter optical fiber as shown in Figure 8.1. Since then, there have been a large number of studies on the linear and nonlinear properties of such OMRs, and in this chapter, we discuss some of our work focusing on their nonlinear aspects, while noting that significant progress has also been achieved in exploiting such resonators for sensing applications.

Figure 8.1 shows that optical OMN resonators consist of a single unbroken length of fiber, so where is the cavity? In fact, due to the wave nature of light there is an evanescent field outside the coils, which means that light can couple from one section of the OMN to another. Vitally, light from one OMN section can couple to the section beneath it returning light to where it started. For the OMR, this continuous coupling means that such a helical coil forms a novel resonator – an intrinsically three-dimensional structure for which no 2D analog exists.

The other obvious fact that can be seen from Figure 8.1 is that OMN resonators are all-pass devices; that is, in the absence of loss, all of the light that enters the cavity must leave it. Along with other all-pass devices, this means that all of the important information is contained in the phase of the light as it exits the cavity. More practically, OMN resonators and in particular OMRs can be shown to be highly dispersive due to the fact that there are multiple paths that light can

Nonlinear Optical Cavity Dynamics: From Microresonators to Fiber Lasers, First Edition.
Edited by Philippe Grelu.
© 2016 Wiley-VCH Verlag GmbH & Co. KGaA. Published 2016 by Wiley-VCH Verlag GmbH & Co. KGaA.

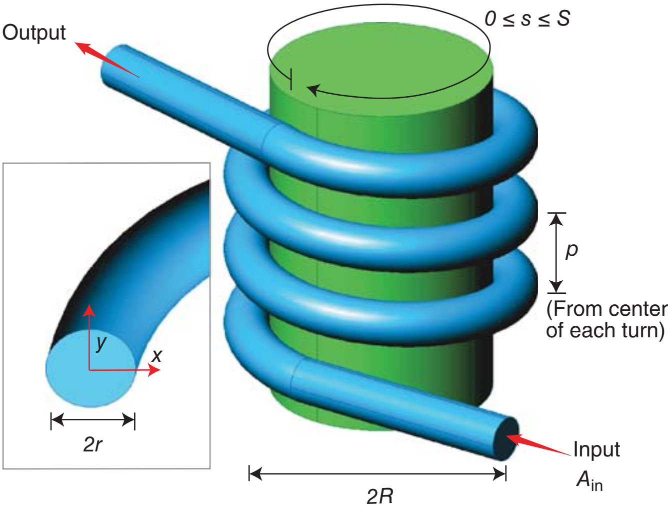

Figure 8.1 Uniform microcoil formed by wrapping microfiber around a rod. Inset shows the local x–y fiber axes (from: [9]).

take to get from the input to the output – there is the usual way going around the resonator, the short way involving jumping from one coil to the higher one and a long-way whereby the light couples predominantly to the coil below thus significantly extending the time spent in the resonator.

In the lossless case, proof that it is in fact a resonator is shown by the existence of solutions in which the input and output intensities are zero but there is a nonzero intensity everywhere else in the OMR (the question of how to excite such a cavity mode is an exercise left to the reader). It is shown in the subsequent sections that once one introduces nonlinearities into the cavity, the behavior becomes more interesting with the OMRs becoming bistable devices in a manner similar to other optical cavities.

In addition to this work on the geometrical manipulation of OMNs, there has been a renewed investigation into the fundamentals of light propagation in such nanofibers. While in essence this work is a re-discovery of the exact solutions for a step-index waveguide (i.e., going beyond the weakly guiding approximation) it has lead to the remarkable discovery that such fibers are intrinsically more nonlinear than expected [10], something that has been verified experimentally using soft-glass photonic crystal fibers [11]. This increase in the nonlinearity, which is due to the nontransverse mode-profile of the electric field, means that OMNs have in recent years attracted significant attention for a range of nonlinear applications including pulse shaping [12], supercontinuum generation [13–16], second-harmonic generation (SHG) [17, 18], and third-harmonic generation (THG) [12, 19–24]. In addition, OMNs have the advantage that the dispersion can be easily tuned by varying the diameter of the fiber, which also allows multimodal phase matching for THG [25, 26]. Finally, unlike many other nanophotonic devices, coupling to OMNs is trivial since at the end of the tapered section the fiber remains a standard single-mode fiber and if the transition region is sufficiently long then all of the light in the fundamental mode of the standard fiber will be coupled into the fundamental mode of the OMN.

8.2
Linear Optical Properties of Optical Microfibers

Here, we give a brief discussion of the linear properties of optical microfibers. Such OMNs are drawn from standard step-index fibers; however, in essence the presence of the core can be ignored since if the original dimensions are shrunk by a factor of 100 or so then the core perturbation is of subwavelength size. Hence, the OMN is modeled as a step-index fiber with a core of pure silica and a cladding of air. As there is an extremely large index mismatch between the core and cladding (of approximately $\Delta n = 0.4$), the exact analytic solutions for step-index fibers need to be used when solving for the supported modes. Following the analysis in Snyder and Love [27], there are three distinct family of modes, categorized in accordance with the directions of their electric and magnetic field vectors:

1) Hybrid (HE, EH) modes – all three components of the electric and magnetic field vectors are nonzero.
2) Transverse electric (TE) modes – $E_z = 0$.
3) Transverse magnetic (TM) modes – $H_z = 0$

The number of modes can be visualized by plotting the effective index n_{eff} of the modes against OMN diameter, D, as shown in Figure 8.2. For an operating

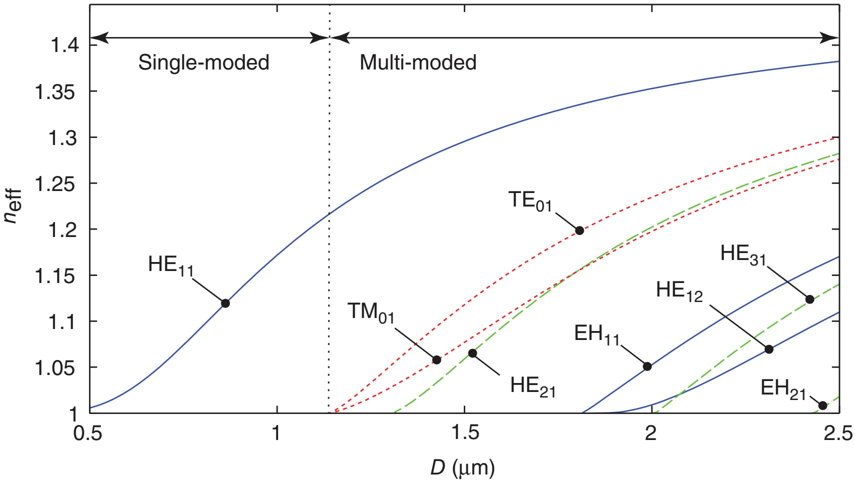

Figure 8.2 Mode dispersion curves showing the effective index (n_{eff}) of various modes with changing OMN diameter for a wavelength of $\lambda = 1.55$ μm.

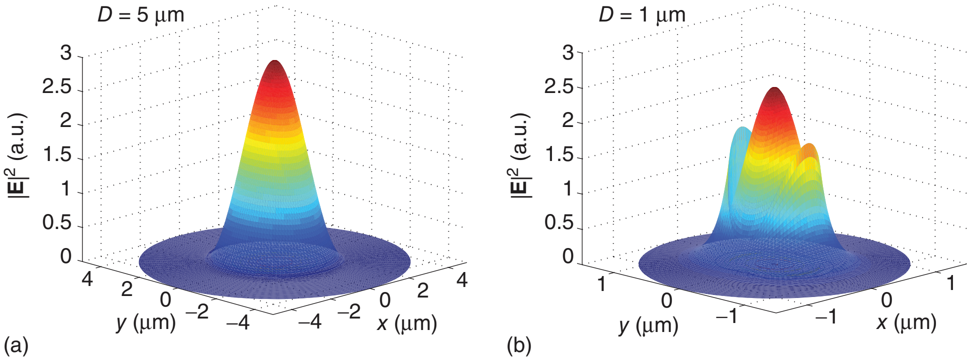

Figure 8.3 Mode field intensity $|\mathbf{E}|^2$ profiles of the fundamental HE_{11} mode for a silica OMN with a core diameter D of (a) 5 μm and (b) 1 μm. $\lambda = 1.55$ μm.

wavelength of 1.55 μm, for example, OMNs become multimoded for diameters D larger than $\simeq 1.1$ μm. The onset diameter of the multimode regime decreases as expected with wavelength and thus fibers that are single-moded at one wavelength will in general be multimoded at shorter wavelengths. It is this behavior that is exploited for modal phase-matching of THG as explained later.

In OMNs, the spatial distribution of the fundamental mode is no longer well approximated by a Gaussian as in the weakly guiding approximation. This is illustrated in Figure 8.3, where the fundamental mode of an OMN at two different diameters is shown. Note that for the 1 μm diameter field the discontinuity of the electric field can be clearly seen. This is due to the interface conditions for Maxwell's equations, which require continuity of **D** rather than **E** at the boundary. In Figure 8.3b, only one of the two degenerate quasi-linearly polarized modes is plotted which accounts for the lack of circular symmetry. Alternatively, left- and right-handed circularly polarized modes can be defined, which would properly reflect the symmetry of the fiber.

Two other parameters of the OMN are of interest, namely η, the fraction of the power in the core, and γ, the effective nonlinearity, which is related to the mode's effective area. The effective nonlinearity is plotted in Figure 8.4a for two different wavelengths. The effective area also closely tracks the power in the core with A_{eff} becoming increasingly large for both large and small diameters. There is thus an optimal core diameter if one wishes to maximize the nonlinearity [11]. The percentage of power that resides in the core should be high for nonlinear applications (and Y is maximal around a diameter of 0.7 μm for silica in air when $\lambda = 1.0$ μm) while it needs to be low for sensing applications where most of the power should be in the air. For OMN resonators, however, a compromise is needed since while high nonlinearities are required for nonlinear applications there still needs to be a substantial evanescent fraction so that light can couple from one core to the other. It should be noted that in Figure 8.4 the peak values of $\gamma = 0.09\ \mathrm{m}^{-1}\mathrm{W}^{-1}$ and $\gamma = 0.34\ \mathrm{m}^{-1}\mathrm{W}^{-1}$ for $\lambda = 1.55$ μm and $\lambda = 1.0$ μm, respectively, are nearly

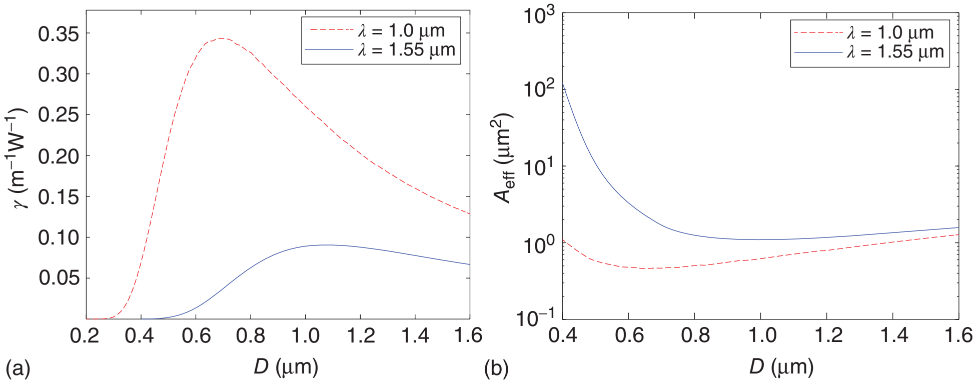

Figure 8.4 (a) Effective nonlinearity γ of OMNs and (b) effective modal area A_{eff} versus microfiber diameter D for the fundamental mode at $\lambda = 1.0$ μm and $\lambda = 1.55$ μm.

two orders of magnitude larger than those of conventional single-mode fibers at the same wavelengths. We can thus expect to see nonlinear effects at much lower power levels or shorter lengths than in standard fibers.

8.3
Linear Properties of Optical Microcoil Resonators

Using the basic linear properties of optical microfibers discussed earlier, it is possible to analyze the behavior of resonators fabricated from them. The crucial fact to realize is that if two microfibers are in contact then light can couple from one fiber to the other. Hence, couplers can be formed simply by placing two OMNs in contact with one another. Moreover, this coupling can be either restricted to a localized region as in a micro-knot resonator or it can occur along the entire length of the device as in a microcoil resonator. In this section, we briefly recap the linear properties of microcoil resonators. Following the analysis of Sumetsky [8], light propagating round a uniform microcoil with n turns in the linear regime is described by the following set of equations:

$$-i\frac{d}{ds}\begin{pmatrix} A_1 \\ A_2 \\ A_3 \\ \vdots \\ A_{n-1} \\ A_n \end{pmatrix} = \begin{pmatrix} 0 & \kappa & 0 & 0 & \cdots & 0 & 0 \\ \kappa & 0 & \kappa & 0 & \cdots & 0 & 0 \\ 0 & \kappa & 0 & \kappa & \cdots & 0 & 0 \\ \vdots & \vdots & \vdots & \vdots & \cdots & \vdots & \vdots \\ 0 & 0 & \cdots & 0 & \kappa & 0 & \kappa \\ 0 & 0 & 0 & \cdots & 0 & \kappa & 0 \end{pmatrix}\begin{pmatrix} A_1 \\ A_2 \\ A_3 \\ \vdots \\ A_{n-1} \\ A_n \end{pmatrix} \tag{8.1}$$

where $A_k(s)$ is the slowly varying amplitude of the electric field in the kth turn at a distance s round the coil and κ is the usual coupling constant between two adjacent waveguides. Since at the end of each loop the output of the kth turn must equal the input of the $k+1$th turn, this implies that

$$\begin{pmatrix} A_1(0) \\ A_2(0) \\ A_3(0) \\ \vdots \\ A_{n-1}(0) \\ A_n(0) \end{pmatrix} = \begin{pmatrix} 0 & 0 & 0 & \cdots & 0 & 0 \\ e^{i\beta S} & 0 & 0 & \cdots & 0 & 0 \\ 0 & e^{i\beta S} & 0 & \cdots & 0 & 0 \\ \vdots & \vdots & \vdots & \cdots & \vdots & \vdots \\ 0 & 0 & 0 & \cdots & 0 & 0 \\ 0 & 0 & 0 & \cdots & e^{i\beta S} & 0 \end{pmatrix} \begin{pmatrix} A_1(S) \\ A_2(S) \\ A_3(S) \\ \vdots \\ A_{n-1}(S) \\ A_n(S) \end{pmatrix} + \begin{pmatrix} A_1(0) \\ 0 \\ 0 \\ \vdots \\ 0 \\ 0 \end{pmatrix} \tag{8.2}$$

where β is the propagation constant of the mode and S is the length of each turn (see Figure 8.1). The input to the coil is given by $A_1(0)$ while the output is given by $A_n(S)e^{i\beta S}$. The transmission coefficient is defined as

$$T = A_n(S)e^{i\beta S}/A_1(0). \tag{8.3}$$

Note that for a lossless system $|T| = 1$ while one can describe the effects of loss through an imaginary propagation constant $\beta = 2\pi/\lambda + i\alpha$ where α represents the loss. Figure 8.5b shows a typical transmission spectrum for a lossy OMR with eight turns and with $\kappa = 5\ \mathrm{mm}^{-1}$ and $S = 1$ mm. Introducing loss into the system not only makes the model more realistic but also provides a useful guide to understanding the resonant behavior of the OMR. In the lossy case, resonances lead to light having a longer effective path length and so experiences more loss leading to a drop in transmission.

It is possible to solve Eqs. (8.1) and (8.2) as follows. Rewriting Eq. (8.2) in vector form gives

$$\mathbf{A}(0) = B\mathbf{A}(S) + \mathbf{A}_{\text{in}} \tag{8.4}$$

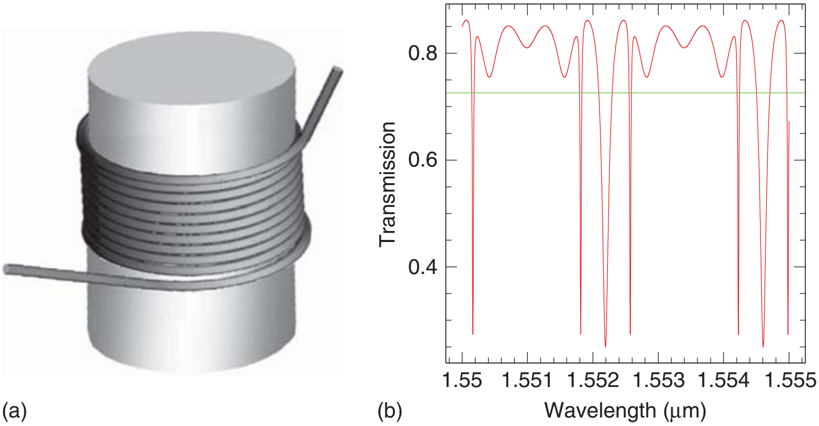

Figure 8.5 (a) Schematic of a microcoil resonator taken from [8]. (b) Transmission spectrum for a lossy OMR with eight coils. The loss is 0.02 $dB\ \mathrm{mm}^{-1}$ while the coupling strength is $3\ \mathrm{mm}^{-1}$. The green line shows the expected transmission for a straight microfiber with the same length and loss (from [28]).

while the solution of Eq. (8.1) is given by

$$\mathbf{A}(S) = K(S)\mathbf{A}(0) \tag{8.5}$$

where $\mathbf{A}$ is a column vector of the amplitudes A_k and $K(S)$ is the formal matrix exponent of the coupling matrix in Eq. (8.1). Equations (8.4) and (8.5) can be solved simultaneously giving

$$\mathbf{A}(S) = [I - K(S)B]^{-1}K(S)\mathbf{A}_{\text{in}} \tag{8.6}$$

$$\mathbf{A}(0) = [I - BK(S)]^{-1}\mathbf{A}_{\text{in}} \tag{8.7}$$

$$\mathbf{A}(s) = K(s)[I - BK(S)]^{-1}\mathbf{A}_{\text{in}}. \tag{8.8}$$

From these solutions, the other parameters of interest such as the transmission, the group velocity (the derivative of the phase of the transmitted light), and dispersion can all be found. In Figure 8.5b, the transmission is compared with that of an identical length of straight fiber with the same loss (given by the green line). Immediately, one can then see the regions of interest – note that there are distinct regions where the group velocity is significantly less than unity (corresponding to regions of high loss) and also regions where the loss is reduced indicating that light is coupling out of the resonator faster than expected. The regions of slow light can be understand as corresponding to resonances of the microcoil, that is, slow light occurs near the values of β and κ for which

$$\det(I - BK(S)) = 0. \tag{8.9}$$

At these points, resonator modes exist (defined by $A_1(0) = A_n(S) = 0$ and $|\mathbf{A}| > 0$), which store energy indefinitely in the OMR. It should be noted that the so-called critical coupling values exist for κ as a function of the loss α such that at particular wavelengths the transmission is identically zero. These values for critical coupling are useful since they correspond to a maximum intensity in the resonator and so can be used to optimize nonlinear effects such as harmonic generation.

It should be noted that in the preceding analysis we assume that the fibers are circularly symmetric and that the input light is linearly polarized. Such assumptions are not necessary, and we have previously examined polarization effects such as Berry phase magnification in microcoil resonators [9] but for the sake of brevity we do not include them here. We also note that considerable work has been done on optimizing the linear properties of OMRs for sensing applications and again those interested in such devices can consult the relevant literature [29]. Instead, we now look at the nonlinear properties of OMRs.

8.4
Bistability in Nonlinear Optical Microcoil Resonators

As discussed earlier, optical microfibers are highly nonlinear due to the tight confinement of light and thus it is expected that this will carry over to microcoil resonators. Following the standard derivation for light propagating in coupled nonlinear waveguides in the nonlinear regime, light evolves around the coil according to

$$\frac{dA_1}{ds} = -\alpha A_1 + i\gamma |A_1(s)|^2 A_1(s) + i\kappa A_2(s), \tag{8.10a}$$

$$\frac{dA_k}{ds} = -\alpha A_k + i\gamma |A_k(s)|^2 A_k(s) + i\kappa [A_{k-1}(s) + A_{k+1}(s)], \tag{8.10b}$$

$$\frac{dA_n}{ds} = -\alpha A_n + i\gamma |A_n(s)|^2 A_n(s) + i\kappa A_{n-1}(s), \tag{8.10c}$$

where γ is the nonlinear coefficient discussed previously and is proportional to the appropriate element of the χ^3 susceptibility tensor. $A_k(s)$ represents the slowly varying amplitude of the light in the kth turn as before. Here, the loss α is explicitly included in the equations. Again the boundary conditions given by Eq. (8.2) hold. Renormalizing the field amplitudes by $A_k \rightarrow 1/\sqrt{\gamma} A_k$ sets the effective nonlinear coefficient to unity, which is done in the following numerical simulations. Writing the formal solution to Eq. (8.10a) as $\mathbf{A}(S) = N(\mathbf{A})\mathbf{A}(0)$, the self-consistent solutions obey

$$\mathbf{A}(0) = BN(\mathbf{A})\mathbf{A}(0) + \mathbf{A}_{\text{in}}, \tag{8.11}$$

where B is given by Eq. (8.2). In the nonlinear regime, analytic solutions do not exist and so the set of equations must be solved numerically.

It should be noted that the case of a single loop coil was studied by Ogusu [30] who found that in the nonlinear regime the coil exhibited bistability and hysteresis. Similarly, it is well known that lossy ring resonators also demonstrate bistable behavior in the nonlinear regime (e.g., see [31]). Hence, it is to be expected that the nonlinear OMR will also exhibit bistable behavior and hysteresis. This is indeed what is found as shown in Figure 8.6a, which shows the bistable behavior for a microcoil resonator with three turns for a variety of wavelengths. Here, the loss

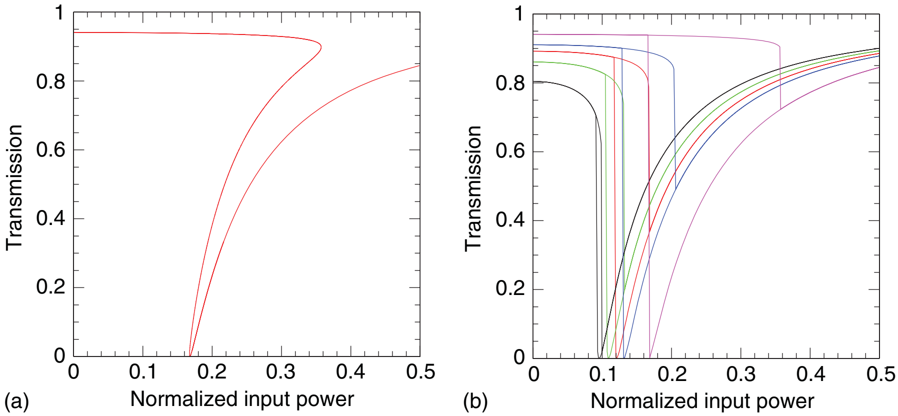

Figure 8.6 Nonlinear response of a three turn microcoil resonator. (a) Full solution (both stable and unstable branches) as a function of the input power. (b) Hysteresis curves for the resonator for a range of wavelengths (from [28]).

was 0.02 *dB* mm^{-1} and the diameter of the turns was 1 mm, while the coupling coefficient was chosen so that in the linear regime the transmission is identically zero at $\lambda = 1.530$ μm (i.e., we are in the critical coupling regime). Although having zero transmission is not necessary, it does maximize the contrast between the high and low transmission states.

In Figure 8.6a, the middle branch of the solution is unstable and thus the light will switch from one branch to the other if the power is increased or decreased. Since the power at which this switching will occur is different depending on whether the power is increased or decreased, the OMR will exhibit hysteresis in its transmission. Several hysteresis curves are plotted in Figure 8.6b for the same parameters as in Figure 8.6a but for a range of different wavelengths. It can be seen that there is a considerable range of both switching depths and the width of the hysteresis window available.

8.4.1
Broken Microcoil Resonators

An interesting feature of an OMR is that transmission is still possible if the fiber is broken at one or several points. This is due to the fact that there are always multiple paths for light to get from one point in the resonator to another depending on where it couples from one coil to the next. The attraction of this is that it makes it possible to tailor the response of the OMR after it has been made by cutting it in appropriate places. This affects both the linear and nonlinear responses of the resonator in a dramatic fashion as seen in Figure 8.7.

To obtain these figures, the same equations as previously discussed were solved; only the boundary conditions were altered to reflect the fact that the input to one of the turns was zero. Note that for the second figure (the nonlinear response curve) the wavelength has been fixed to lie on the long wavelength

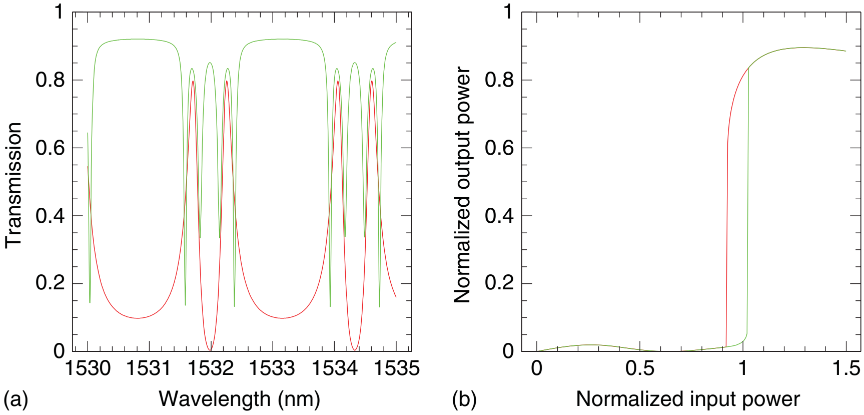

Figure 8.7 (a) Linear transmission spectrum for a broken OMR (red line) and unbroken OMR (green line). (b) The nonlinear response for a broken OMR for both increasing (green line) and decreasing (red line) input power (from [32]).

side of a transmission dip in Figure 8.7a. A qualitative understanding of the nonlinear behavior of the resonator can be gained by realizing that the Kerr effect, to its lowest order, has the effect of increasing the propagation constant for a fixed wavelength. Thus, as the power increases, we would expect that the transmission spectrum would rigidly move to longer wavelengths. So using the linear transmission function in Figure 8.7a, we can see that if we fix the input wavelength to be on the long wavelength side of one of the transmission minima, then in the nonlinear regime we would expect the transmission to first decrease and then increase, and indeed this is what we find when we solve Eqs. (8.10a) and (8.10b) in the nonlinear regime. Figure 8.7b shows the nonlinear transfer function for the broken microcoil resonator as the input power is increased (red curve) or decreased (green curve) for a wavelength of 1532.1 nm.

Such a square nonlinear transfer function has potential applications for noise-reduction in some communications systems, for example, [32]. We have also looked at the stability in the time domain of the upper branch and have found that depending on the precise parameters the solutions can be stable or unstable. Surprisingly, in the unstable case, the periodic nature of the transmission of the coil leads to time periodic solutions, which evolve to have abrupt transitions between states of high and low intensities. However, long before this shock wave formation occurs the bandwidth of the output has expanded to the point where the slowly varying envelope approximation that allows the coupled mode equations to be written down breaks down and so more refined approximations will need to be used.

8.4.2
Polarization Effects in Nonlinear Optical Microcoil Resonators

Along with our work looking at the linear polarization effects in OMRs we have also conducted a theoretical study of what happens in the nonlinear regime [33]. Here, the behavior is complicated by the fact that each turn has two independent polarizations propagating in them and so the coupling can occur not only from one turn to another but also from one polarization to another. This is due to the intrinsically three-dimensional nature of such resonators, which means that the fiber can rotate its orientation as it coils around allowing the local x and y polarizations to couple. This geometry is shown in Figure 8.8.

In this case, the dynamics are more complicated and only a flavor of them is given here. Typical examples are shown in Figure 8.9. As before, we can see hysteresis and bistable behavior for both the x and y polarizations and also more complicated switching dynamics [33], which become particularly interesting when the fiber birefringence is chosen such that the x and y resonances are spectrally close together as in Figure 8.9a. In this case, the pump interacts with both resonances in turn as the input power is ramped up and down, leading to the two distinct regimes of bistability shown in Figure 8.9b and c. Although only one polarization (either x or y) is on resonance and recirculated within each of the hysteresis loops, the nonlinear switching is clearly observed in the transmissions of both polarizations. In

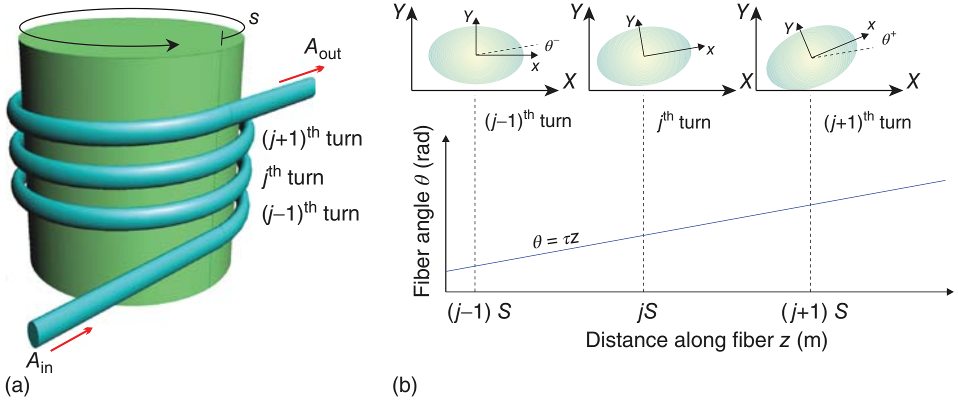

Figure 8.8 (a) The microcoil geometry and (b) a cross section of three adjacent turns and the local (x, y) axes when the birefringent fiber is twisted, shown here for a linear rotation $\theta(z) = \tau z$, which permits cross-polarization coupling (from [33]).

this way, we are able to design a more specific nonlinear response for a given input polarization by selecting an appropriate birefringence and fiber twist, in addition to the geometric parameters of the OMR itself.

8.4.3
Possible Experimental Verification

So far, we have examined theoretically the effects of a Kerr nonlinearity on optical microcoil resonators. In general, we have normalized the power so that the effective nonlinearity can be set equal to unity for convenience of simulation. However, we now wish to discuss the practicality of such devices.

First, it should be noted that the state of the art in fabrication is restricted to OMRs with three turns at most. This is not a serious limitation since the nonlinear effects described here do not depend critically upon the number of turns. Rather, the number of turns serves to make the linear transmission spectrum more complicated and so would require narrower sources to probe them. Instead, the major problem is thermal effects in the microfibers. The bistability arises due to the interplay between loss and self-phase modulation due to the stored energy in the resonator (recall that in the lossless case all of the light exits the resonator). The effect of the loss will be to heat up the microfiber, and this in turn will alter the refractive index and so detune the light from resonance. A quick back of the envelope calculation suggests that near a resonance where the loss is high, thermal effects will dominate due to the small volume of silica. Indeed, such thermal nonlinearities have been reported in microfiber knot resonators [34], where hysteresis was attributed to thermal phase shifts. This would make it very hard to differentiate between thermal effects and those from a pure Kerr nonlinearity in practice.

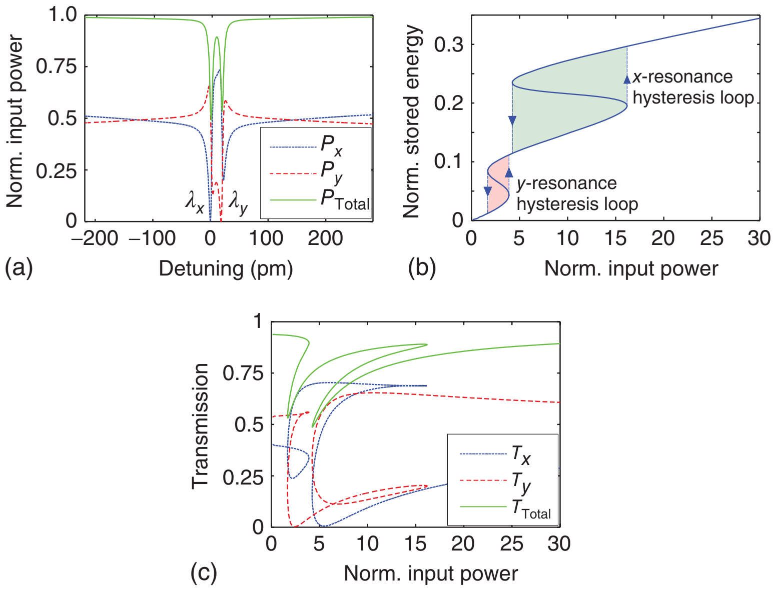

Figure 8.9 (a) Linear transmission spectrum for a coil with a weak birefringence of $B = 1 \times 10^{-5}$. (b) The energy stored in the OMR against the input power, showing the double nonlinear hysteresis loops for a pump wavelength red-detuned by $\delta\lambda = 6$ pm from the *y* resonance. (c) The nonlinear transmission characteristic (from [33]).

If one wanted to observe such Kerr-mediated switching, one possibility would be to actively stabilize the temperature of the OMR, which could be done relatively easily since the large surface area to volume ratio of such microfibers means that they cool extremely quickly. The other distinguishing characteristic of the Kerr nonlinearity would be its speed, compared with the much slower thermal effect, and so by quickly ramping the power up and down it could be possible to observe a Kerr-mediated hysteresis loop.

8.5
Harmonic Generation in Optical Microfibers and Microloop Resonators

Perhaps surprisingly, as the diameter of optical microfibers decreases new nonlinear effects can be observed. The most striking of these is harmonic generation with observations of both SHG and THG having been reported in the literature [17, 19]. Here, we report our work looking at such effects in both straight microfibers and in resonators.

Unlike the effects of self-phase modulation, THG (and indeed SHG) requires that the fundamental pump and harmonic waves be in phase for efficient energy transfer. However, due to the underlying dispersion of the medium this can almost never be achieved and so such effects are rarely seen and in general do not have a

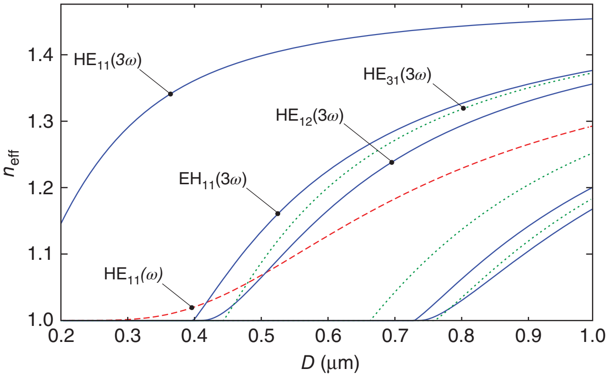

Figure 8.10 Effective index curves for the fundamental $\mathrm{HE}_{11}(\omega)$ mode at $\lambda = 1.064$ μm (red dashed line) and third-harmonic hybrid modes for azimuthal order $\nu = 1, 3$ (solid blue and dotted green lines). Phase-matching points occur where the pump and harmonic curves intersect.

high efficiency. In OMNs, however, the possibility exists for phase-matching to be achieved between the fundamental mode at one wavelength and a different mode at the shorter wavelength.

The main requirement for this to occur is that the effective refractive index, n_{eff}, of the pump with frequency ω in mode M is equal to the effective index of light at the third-harmonic frequency (3ω) in mode N, that is, $n_{\mathrm{eff}}(\omega, M) = n_{\mathrm{eff}}(3\omega, N)$. Since we have the freedom to choose the modes M and N for the interactions and also as the effective index is a strong function of the microfiber diameter, there are almost always points where the phase-matching requirements are satisfied.

As an example, we plot in Figure 8.10 the effective indices for the fundamental mode at $\lambda = 1064$ nm and a number of higher-order modes at the third harmonic as a function of the microfiber diameter. It can be clearly seen that there are a variety of intersection points between the different modes' n_{eff} curves and at these diameters THG is possible. In the next section, we discuss briefly the theory behind THG and then look at some early experimental results.

8.5.1
Mathematical Modeling and Efficiency of Third Harmonic Generation

To model THG, we start with the usual coupled mode equations for the slowly varying envelopes of the electric field at the pump and third harmonic [20, 35]:

$$\begin{aligned}\frac{\partial A_1}{\partial z} &= -\alpha_1 A_1 + in^{(2)}k_1[(J_1|A_1|^2 + 2J_2|A_3|^2)A_1\\ &\quad + J_3 A_1^{*2} A_3 \mathrm{e}^{i\delta\beta z}] \qquad (8.12)\end{aligned}$$

$$\begin{aligned}\frac{\partial A_3}{\partial z} &= -\alpha_3 A_3 + in^{(2)}k_1[(6J_2|A_1|^2 + 3J_5|A_3|^2)A_3\\ &\quad + J_3^* A_1^3 \mathrm{e}^{-i\delta\beta z}] \qquad (8.13)\end{aligned}$$

Table 8.1 Mathematical expressions and physical interpretations of the J_n nonlinear overlap integrals.

J_n	Mathematical expression	Physical interpretation
J_1	$\frac{1}{3}\oiint_{A_{\mathrm{NL}}}[2\lvert\mathbf{F}_1\rvert^4+\lvert\mathbf{F}_1^2\rvert^2]dA$	Self-phase modulation (SPM) of pump field
J_2	$\frac{1}{3}\oiint_{A_{\mathrm{NL}}}[\lvert\mathbf{F}_1\rvert^2\lvert\mathbf{F}_3\rvert^2+\lvert\mathbf{F}_1\cdot\mathbf{F}_3\rvert^2+\lvert\mathbf{F}_1\cdot\mathbf{F}_3^*\rvert^2]dA$	Cross-phase modulation (XPM) between pump and harmonic fields
J_3	$\oiint_{A_{\mathrm{NL}}}(\mathbf{F}_1^*\cdot\mathbf{F}_3)(\mathbf{F}_1^*\cdot\mathbf{F}_1^*)dA$	Nonlinear coupling between pump and harmonic fields
J_5	$\frac{1}{3}\oiint_{A_{\mathrm{NL}}}[2\lvert\mathbf{F}_3\rvert^4+\lvert\mathbf{F}_3^2\rvert^2]dA$	SPM of harmonic field

a) $\mathbf{F}_1$ and $\mathbf{F}_3$ represent the normalized electric field vectors of pump and harmonic modes, respectively.

where A_1 and A_3 are amplitudes of the pump and harmonic waves, respectively, α_n is the loss at a particular wavelength, $k_1 = 2\pi/\lambda$ is the propagation constant of the pump in vacuum, $n^{(2)}$ the nonlinear refractive index, $\delta\beta = \beta(3\omega) - 3\beta(\omega)$ is the detuning and J_n the various modal overlap coefficients, explained in detail later. In the absence of loss, these equations can be solved exactly [35–37]; however, when the effects of loss are included, they need to be solved numerically. In general, the parameter of interest is the conversion efficiency $\eta = \frac{|A_3(L)|^2}{|A_1(0)|^2}$, where L is the length of the system.

In Eqs. (8.12) and (8.13), the parameters J_i relate to various overlap integrals between the modes as defined in Table 8.1. These overlap integrals can be evaluated using the exact solutions for the higher-order modes once the core diameter has been specified. Of the different overlap integrals the crucial one is J_3, which determines the rate at which energy can flow from one field to the other. In particular, it can be identically zero for modes with different symmetries, which restricts the choice of diameter.

The main effect of the J_1 and J_2 coefficients, which relate to the self- and cross-phase modulation terms of the equations is to shift the phase-matching requirements from $\delta\beta = 0$ to $\delta\beta = -3(2J_2 - J_1)k_1 n^{(2)} P_0$ for maximal conversion efficiency, where P_0 is the input pump power. Thus, in Figure 8.10, the diameter should be chosen not at the point where the curves intersect but very slightly offset. If this criteria is achieved then the energy flows consistently from one field to the other, otherwise the power would oscillate rapidly between the fundamental and the third harmonic. This can be seen in Figure 8.11.

In the absence of loss and provided that the correct phase-matching is achieved, the conversion efficiency can be made as large as possible simply by increasing the length of the microfiber. Practically, however, there are severe constraints to achieving this since the uniformity of the microfiber is critical and the highest efficiency achieved thus far is only a meager $\eta = 0.4\%$, and was accomplished via broadband conversion with a pump at 1.55 μm [23]. The use of a broadband pump

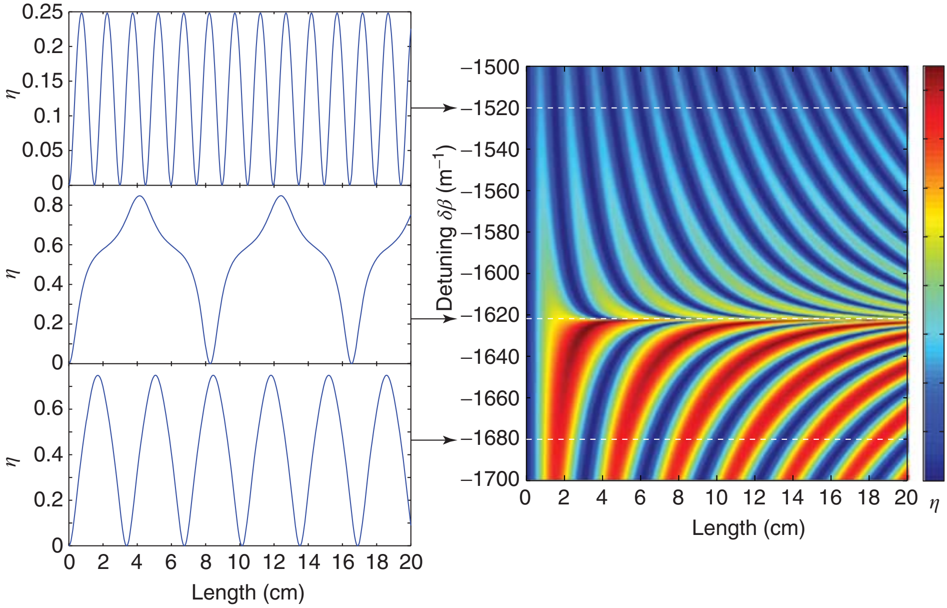

Figure 8.11 The effect of detuning $\delta\beta$ on THG conversion efficiency η in an OMN. The insets detail the evolution of efficiency η along the taper for different $\delta\beta$. Here, $\lambda = 1.064$ μm and $P_0 = 1$ kW.

ensured that there was always some frequency for which phase-matching was possible and also it was found that the harmonic generation occurred predominately in the transition region where the diameter was rapidly reducing. The combination of a changing diameter and a broadband pump meant that there was always a combination of the two that allowed phase-matching.

A recent study on the effect of intrinsic surface roughness has shown that for periodic surface waves with an amplitude of 0.2 nm, the highest possible η is reduced by 50% in a 1 mm OMN [38]. Interestingly, η is not dependent upon the period of the surface wave, but is strongly affected by its amplitude, as well as where the surface wave is located vis-á-vis the ideal detuning value. As measured experimentally with profilometers, the surface diameter fluctuation itself has a random component, resulting in a statistically Gaussian distribution of diameters. With this in mind, a "realistic" fiber was assumed to have a longitudinal diameter with a Gaussian noise distribution given by the spectral density:

$$S_z(\kappa) = \frac{k_B T_g}{4\pi\gamma_s\kappa} \coth\left(\frac{\kappa W}{2}\right) \tag{8.14}$$

where k_B is the Boltzmann's constant, γ_s the surface tension, W the OMN perimeter, and T_g the glass transition temperature. The resulting efficiencies for three different surface tensions are reproduced in Figure 8.12, where it can be seen that, in general, η increases rapidly up to a point and then stops growing, with

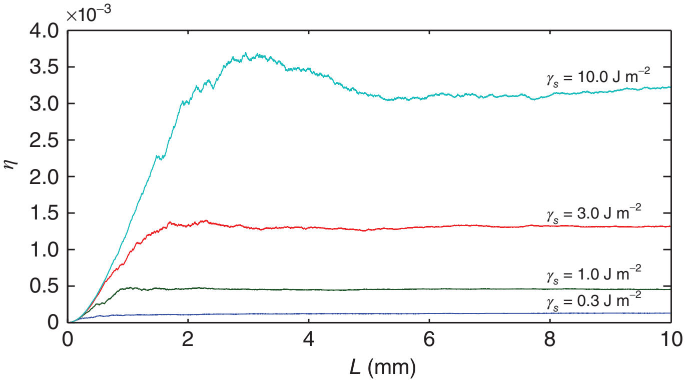

Figure 8.12 THG efficiency η dependence on the random surface fluctuations, for four different surface tension values γ_s. Here, T_g = 1400 °C, and the RMS radius is 383.2 nm, with λ = 1.55 μm (adapted from [38]).

higher surface tension resulting in higher η. This behavior results from the fact that the transfer of energy happens both ways, and due to the random nature of the detuning, an equilibrium is quickly established where equal amounts of energy are transferred between the two wavelengths.

Despite the seemingly low efficiencies resulting from physical constraints, it is possible to increase the overall efficiency by reconfiguring the OMN into a loop resonator, as explored in the following section.

8.5.2
Third Harmonic Generation in Microloop Resonators

One way to overcome the thermodynamic limitations on the efficiency of THG is to place the microfiber inside a cavity. This allows you to reduce the physical length of the microfiber while keeping a long effective interaction length. This technique does not require long tapers, as the optical path is considerably increased by the resonator finesse, and thus benefits from a reduced surface and diameter nonuniformity.

A THG loop resonator can be described in two separate parts (Figure 8.13): the coupling region where the two segments of the OMN couple via the coupling coefficient $\kappa_\omega(s)$, and the loop region, where THG primarily occurs. In the case of a perfectly uniform OMN, THG can be assumed to take place throughout the entirety of the loop; otherwise in a realistic model the OMN diameter uniformity is far from ideal because of intrinsic surface roughness and so phase-matching is assumed to take place only over a short section within the loop.

Modeling THG in a resonator is conceptually the same as the earlier model, only now the number of equations is doubled since there are two propagating fields in the loop. With this in mind, we can write down the following equations for the

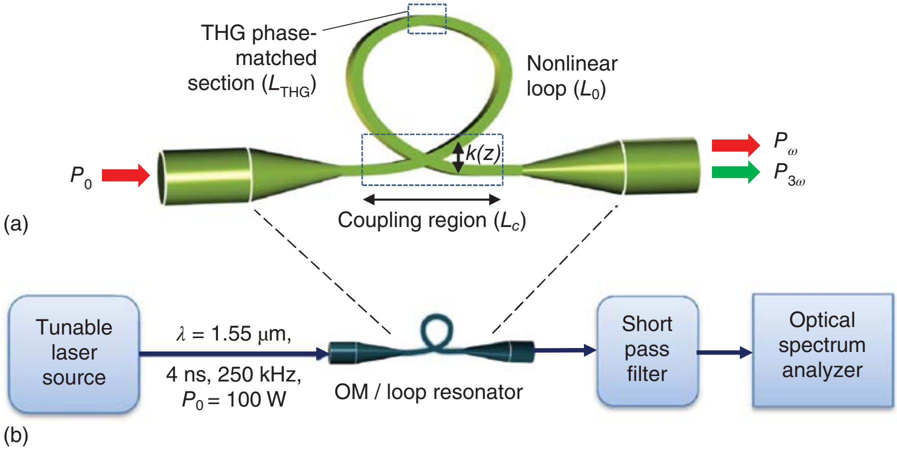
THG phase-matched section (L_{THG})
Nonlinear loop (L_0)
P_0
k(z)
P_ω
$P_{3\omega}$
(a)
Coupling region (L_c)
Tunable laser source
λ = 1.55 μm,
4 ns, 250 kHz,
P_0 = 100 W
OM / loop resonator
Short pass filter
Optical spectrum analyzer
(b)

Figure 8.13 (a) Schematic of the OMN loop resonator and (b) the experimental implementation used to generate and detect the third harmonic (from [39]).

slowly varying amplitudes for the fundamental F_i and third harmonic fields T_i:

$$\frac{dF_1}{ds} = -\alpha_\omega F_1 + i\kappa_\omega(s)F_2 + in^{(2)}k_1[(J_1|F_1|^2 + 2J_2|T_1|^2)F_1 + J_3(F_1^*)^2 T_1 e^{i\delta\beta s}] \tag{8.15a}$$

$$\frac{dT_1}{ds} = -\alpha_{3\omega} T_1 + i\kappa_{3\omega}(s)T_2 + in^{(2)}k_1[(6J_2|F_1|^2 + 3J_5|T_1|^2)T_1 + J_3^*(F_1)^3 e^{-i\delta\beta s}] \tag{8.15b}$$

In the coupling region of the loop, we write similar equations for F_2 and T_2, the amplitudes in the adjacent segment of microfiber. Again, we are primarily interested in the efficiency η evaluated at the output of the coupling region of length L_c:

$$\frac{P_{3\omega}}{P_0} = \left|\frac{T_2(L_c)}{F_1(0)}\right|^2 \tag{8.16}$$

and which is strongly dependent on the coupling geometry of the loop. The dominant factor in the increased conversion efficiency is the increase in intensity inside the resonator. The maximum enhancement takes place when critical coupling $K_c = \kappa_c L_c = \pi(2m+1)/2$ for $m \geq 1$ is achieved since this gives the largest internal field [39]. Typical results from our numerical simulations are shown in Figure 8.14.

Figure 8.14a shows the output pump power P_ω when its wavelength λ_P is detuned from the resonant wavelength λ_R: the figure shows both the linear spectrum (where nonlinear effects are neglected) and the nonlinear case (which considers all significant nonlinear effects). While in the linear case the graph is symmetric and the pump power falls to its minimum at the resonance

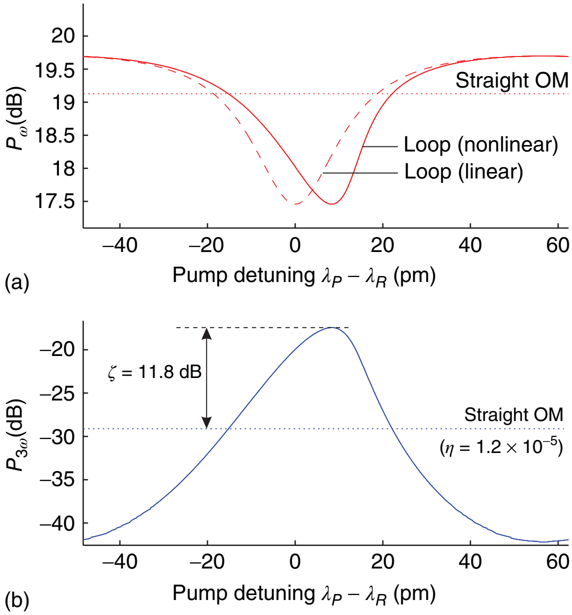

Figure 8.14 (a) Simulated output-pump power and (b) third-harmonic power from a silica loop resonator against pump detuning from resonance (solid lines). The dashed line indicates the linear resonance spectrum, and dotted lines represent the output from an equivalent nonlinear length of straight OMN. P_0 = 100 W (from [39]).

wavelength, in the nonlinear case an asymmetry is observed, and a resonant wavelength shift of +8 pm is noticed. These effects are primarily the result of the pump SPM-induced phase shift.

As expected, we see from Figure 8.14b that the third-harmonic power is enhanced the most for pump frequencies closest to the resonance. This is explored further in Figure 8.15, which shows the effects of (a) detuning and (b) coupling on THG efficiency, while a $\zeta \approx 12$ dB enhancement (relative to the harmonic power from an equivalent straight OMN) can be observed at resonance, off-resonance most of the pump bypasses the loop resulting in a considerable drop in efficiency [40, 41]. Similarly, close to critical coupling the greatest enhancement is observed with ζ increasing cubically with circulating power ratio P_{circ}/P_0 [41].

The experimental demonstration, performed in a 760-nm-diameter silica OMN configured into a 6-mm-diameter loop resonator with a full-width at half-maximum (FWHM) linewidth of 50 pm and $Q = 3.1 \times 10^4$, was carried out using a pump power of $P_0 = 100$ W to minimize pump spectral broadening and ensure that the pump linewidth (100 pm) can remain comparable to the resonance FWHM. The results of this can be seen in Figure 8.16.

The experimentally observed enhancement ($\zeta = 7.7$ dB) is similar but slightly lower than the theoretical value and this was attributed to scattering loss from

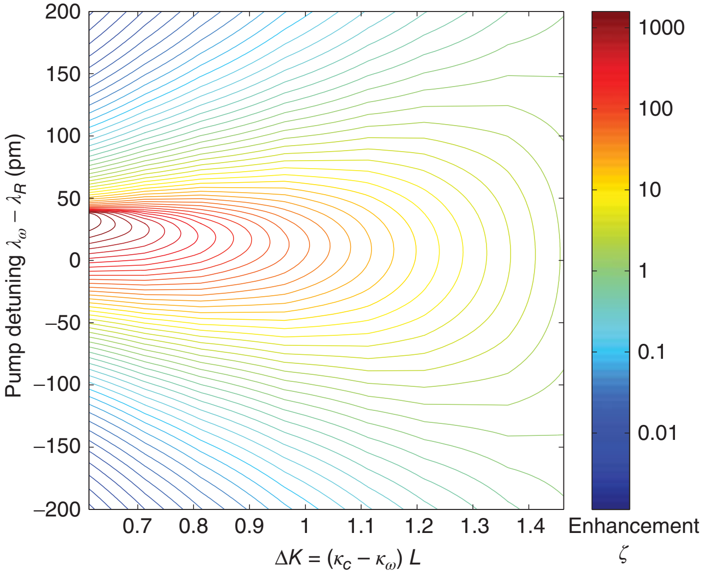

Figure 8.15 Theoretical enhancement η of the THG efficiency from a loop resonator against pump detuning from resonant wavelength $\lambda_\omega - \lambda_R$ and proximity to critical coupling ΔK (adapted from [41]).

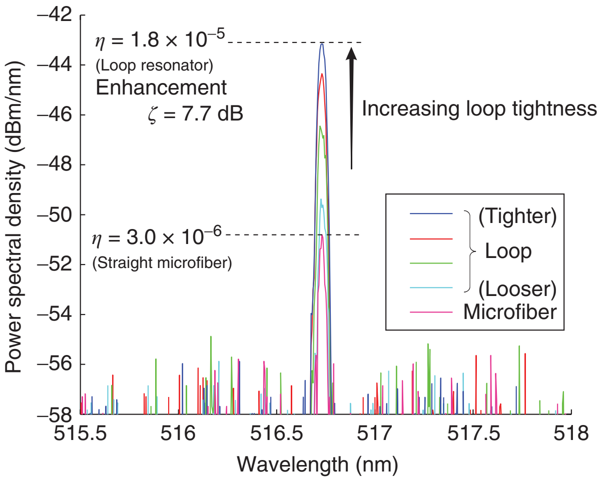

Figure 8.16 Experimental demonstration of enhanced third-harmonic generation in a loop resonator. The different colors show the effect of tightening the loop radius and thus increasing the coupling (from [39]).

the coupling region. It was also noted that the 3 dB THG linewidth of 50 pm was slightly larger than the original 45 pm linewidth recorded from the straight OMN, due to pump broadening in the loop [39]. While the absolute efficiency was still low it can be seen that cavity effects play an important role in the generation of third harmonic.

8.5.3
Second-Harmonic Generation

Despite the lack of a bulk electric dipole in silica glass due to its centrosymmetric structure, it is still possible to observe the second harmonic in optical microfibers. The bulk quadrupole and magnetic dipole moments lead to a nonzero second-order susceptibility χ^2, which permits the generation of the second harmonic [42, 43], as well as surface dipole contributions at the glass–air interface. The second effect is especially suitable to generate the second harmonic in silica OMNs because of the strong surface field and large surface-area-to-volume ratio.

SHG in silica OMNs was modeled [17] assuming that the second-order polarization is due to surface dipole and bulk multipole nonlinearities, incorporating a realistic description of the surface roughness. A model was also created assuming a typical tapered diameter profile [44]. As for THG, the efficiency is maximized by phase-matching the fundamental pump mode to a higher-order second-harmonic mode. The conversion can be, furthermore, enhanced by the large electric fields in a loop resonator, and we have experimentally demonstrated this [18].

Experiments were carried out on a 10 mm long OMN configured into a loop resonator with a diameter of 4 mm, which was subsequently tightened to 1 mm, and these results are shown in Figure 8.17. At a pump power of $P_0 = 90$ W, an efficiency enhancement of $\zeta = 5.7$ was recorded for the loop in comparison with the original

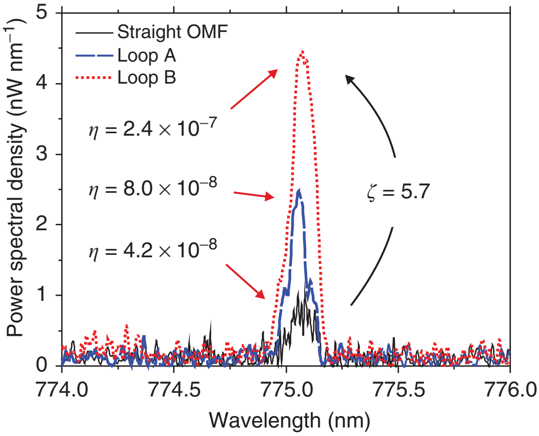

Figure 8.17 Experimentally measured second-harmonic spectra from a loop resonator recorded as its diameter was tightened from 4 mm (Loop A) to 1 mm (Loop B), showing a resonant efficiency enhancement compared with the original straight OMN (from [18]).

straight OMN case. The enhancement is lower than the theoretical value, possibly since the loop was not critically coupled (thus reducing the amplification of the pump field in the loop), or nonlinear pump broadening, which shifts some pump frequency components off resonance. This latter effect is particularly important as it relates to the trade-off between bandwidth and enhancement, since a higher Q resonance would increase the enhancement but only for a narrower range of frequencies. Nonetheless, even higher enhancements of the order of $\zeta \approx 30$ have been predicted for a loss of $\alpha = 10\ \mathrm{m}^{-1}$ and optimized coupling, which can be realistically achieved using current fabrication technology.

8.6
Conclusions and Outlook

In this chapter, we have discussed our work looking at various nonlinear processes in optical microfiber-based resonators. Central to our work is the microcoil resonator introduced by Sumetsky in 2004, which unlike most other optical resonators is an intrinsically three-dimensional structure giving it a wealth of interesting properties. Although we have not discussed it in detail here, such resonators have also been widely used as sensors both for measuring refractive index and also for magnetic fields. In the nonlinear regime, they demonstrate large amounts of hysteresis and can exhibit very interesting power transfer characteristics. However, experimental confirmation of such predictions is likely to be complicated due to thermal effects.

In contrast to self-phase modulation effects, enhanced harmonic generation (both second and third) has been experimentally demonstrated. Here, the limiting factor is the uniformity of the microfiber that alters the phase-matching along the length of the fiber. Also of interest is the possibility of using such resonators to produce one-third harmonic light (the inverse of THG). Such a source would have immediate applications for quantum information processing since in the single photon limit it would produce gigahertz states, for example. It would also provide a novel optical parametric amplifier for mid-IR wavelengths, since pumping with a $\lambda = 2\ \mu\mathrm{m}$ thulium fiber laser source, for example, would provide gain near 6 μm (a spectral region where conventional optical sources do not exist). Moreover, moving to longer wavelengths would substantially relax the fabrication tolerances required, allowing larger resonators with longer nonlinear interaction lengths to be created.

References

1. Sumetsky, M., Dulashko, Y., Fini, J.M., and Hale, A. (2005) Optical microfiber loop resonator. *Appl. Phys. Lett.*, **86**, 16 161108.
2. Xu, F., Pruneri, V., Finazzi, V., and Brambilla, G. (2008) An embedded optical nanowire loop resonator refractometric sensor. *Opt. Express*, **16**, 2 1062.
3. Ismaeel, R., Lee, T., Ding, M., Belal, M., and Brambilla, G. (2013) Optical microfiber passive components. *Laser Photonics Rev.*, **7**, 3 350.

4. Jiang, X., Yang, Q., Vienne, G., Li, Y., Tong, L., Zhang, J., and Hu, L. (2006) Demonstration of microfiber knot laser. *Appl. Phys. Lett.*, **89**, 14 143513.
5. Jiang, X., Song, Q., Xu, L., Fu, J., and Tong, L. (2007) Microfiber knot dye laser based on the evanescent-wave-coupled gain. *Appl. Phys. Lett.*, **90**, 23 233501.
6. Jiang, X., Tong, L., Vienne, G., Guo, X., Tsao, A., Yang, Q., and Yang, D. (2006) Demonstration of optical microfiber knot resonators. *Appl. Phys. Lett.*, **88**, 22 223501.
7. Xiao, L. and Birks, T.A. (2011) High finesse microfiber knot resonators made from double-ended tapered fibers. *Opt. Lett.*, **36**, 7 1098.
8. Sumetsky, M. (2004) Optical fiber microcoil resonators. *Opt. Express*, **12**, 10 2303.
9. Lee, T., Broderick, N.G.R., and Brambilla, G. (2011) Berry phase magnification in optical microcoil resonators. *Opt. Lett.*, **36**, 15 2839.
10. Afshar, V.S. and Monro, T.M. (2009) A full vectorial model for pulse propagation in emerging waveguides with subwavelength structures part I: Kerr nonlinearity. *Opt. Exp.*, **17**, 4 2298.
11. Afshar, V.S., Zhang, W.Q., Ebendorff-Heidepriem, H., and Monro, T.M. (2009) Small core optical waveguides are more nonlinear than expected: experimental confirmation. *Opt. Lett.*, **34**, 22 3577.
12. Coillet, A., Vienne, G., and Grelu, P. (2010) Potentialities of glass air-clad micro-and nanofibers for nonlinear optics. *J. Opt. Soc. Am. B*, **27**, 3 394.
13. Leon-Saval, S.G., Birks, T.A., Wadsworth, W.J., Russell, P.St.J., and Mason, M.W. (2004) Supercontinuum generation in submicron fibre waveguides. *Opt. Express*, **12**, 13 2864.
14. Brambilla, G., Koizumi, F., Finazzi, V., and Richardson, D.J. (2005) Supercontinuum generation in tapered bismuth silicate fibres. *Electron. Lett.*, **41**, 14 795.
15. Gattass, R.R., Svacha, G.T., Tong, L., and Mazur, E. (2006) Supercontinuum generation in submicrometer diameter silica fibers. *Opt. Express*, **14**, 20 9408.
16. Yeom, D.I., Mägi, E.C., Lamont, M.R., Roelens, M.A., Fu, L., and Eggleton, B.J. (2008) Low-threshold supercontinuum generation in highly nonlinear chalcogenide nanowires. *Opt. Lett.*, **33**, 7 660.
17. Lægsgaard, J. (2010) Theory of surface second-harmonic generation in silica nanowires. *J. Opt. Soc. Am. B*, **27**, 7 1317.
18. Gouveia, M.A., Lee, T., Ismaeel, R., Ding, M., Broderick, N.G.R., Cordeiro, C.M., and Brambilla, G. (2013) Second harmonic generation and enhancement in microfibers and loop resonators. *Appl. Phys. Lett.*, **102**, 20 201120.
19. Akimov, D.A., Ivanov, A.A., Naumov, A.N., Kolevatova, O.A., Alfimov, M.V., Birks, T.A., Wadsworth, W.J., Russell, P.St.J., Podshivalov, A.A., and Zheltikov, A.M. (2003) Generation of a spectrally asymmetric third harmonic with unamplified 30-fs Cr: forsterite laser pulses in a tapered fiber. *Appl. Phys. B*, **76**, 5 515.
20. Grubsky, V. and Savchenko, A. (2005) Glass micro-fibers for efficient third harmonic generation. *Opt. Express*, **13**, 18 6798.
21. Grubsky, V. and Feinberg, J. (2007) Phase-matched third-harmonic UV generation using low-order modes in a glass micro-fiber. *Opt. Commun.*, **274**, 2 447.
22. Wiedemann, U., Karapetyan, K., Dan, C., Pritzkau, D., Alt, W., Irsen, S., and Meschede, D. (2010) Measurement of submicrometre diameters of tapered optical fibres using harmonic generation. *Opt. Express*, **18**, 8 7693.
23. Lee, T., Jung, Y., Codemard, C.A., Ding, M., Broderick, N.G.R., and Brambilla, G. (2012) Broadband third harmonic generation in tapered silica fibres. *Opt. Express*, **20**, 8 8503.
24. Coillet, A. and Grelu, P. (2012) Third-harmonic generation in optical microfibers: from silica experiments to highly nonlinear glass prospects. *Opt. Commun.*, **285**, 16 3493.
25. Brambilla, G. (2010) Optical fibre nanowires and microwires: a review. *J. Opt.*, **12**, 4 043001.
26. Tong, L., Zi, F., Guo, X., and Lou, J. (2012) Optical microfibers and

nanofibers: a tutorial. *Opt. Commun.*, **285**, 23 4641.

27. Snyder, A.W. and Love, J.D. (1983) *Optical Waveguide Theory*, Chapman and Hall, Berlin.
28. Broderick, N.G.R. (2008) Optical snakes and ladders: dispersion and nonlinearity in microcoil resonators. *Opt. Express*, **16**, 20 16247.
29. Xu, F. and Brambilla, G. (2008) Demonstration of a refractometric sensor based on optical microfiber coil resonator. *Appl. Phys. Lett.*, **92**, 101126.
30. Ogusu, K. (1996) Dynamic behavior of reflection optical bistability in a nonlinear fiber ring resonator. *IEEE J. Quantum Electron.*, **32**, 1537.
31. Xu, Q. and Lipson, M. (2006) Carrier-induced optical bistability in silicon ring resonators. *Opt. Lett.*, **31**, 341.
32. Broderick, N.G.R. and Ng, T.N. (2009) Theoretical study of noise reduction of NRZ signals using nonlinear broken microcoil resonators. *IEEE Photonics Technol. Lett.*, **21**, 7 444.
33. Lee, T., Broderick, N.G.R., and Brambilla, G. (2012) Nonlinear polarisation effects in optical microcoil resonators with fibre twist and birefringence. *Opt. Commun.*, **285**, 23 4670.
34. Vienne, G., Li, Y., Tong, L., and Grelu, P. (2008) Observation of a nonlinear microfiber resonator. *Opt. Lett.*, **33**, 1500.
35. Armstrong, J.A., Bloembergen, N., Ducuing, J., and Pershan, P.S. (1962) Interactions between light waves in a nonlinear dielectric. *Phys. Rev.*, **127**, 6 1918.
36. Puell, H.B. and Vidal, C.R. (1978) Optimal conditions for nonresonant third harmonic generation. *IEEE J. Quantum Electron.*, **14**, 5 364.
37. Afshar, V.S., Lohe, M.A., Lee, T., Monro, T.M., and Broderick, N.G.R. (2013) Efficient third and one-third harmonic generation in nonlinear waveguides. *Opt. Lett.*, **38**, 3 329.
38. Khudus, M.I., Lee, T., Horak, P., and Brambilla, G. (2015) Effect of intrinsic surface roughness on the efficiency of intermodal phase matching in silica optical nanofibers. *Opt. Lett.*, **40**, 7 1318.
39. Ismaeel, R., Lee, T., Ding, M., Broderick, N.G.R., and Brambilla, G. (2012) Nonlinear microfiber loop resonators for resonantly enhanced third harmonic generation. *Opt. Lett.*, **37**, 24 5121.
40. Lee, T. (2013) Nonlinear properties of optical microfibers. PhD thesis. University of Southampton.
41. Lee, T., Broderick, N.G.R., and Brambilla, G. (2013) Resonantly enhanced third harmonic generation in microfiber loop resonators. *J. Opt. Soc. Am. B*, **30**, 3 505.
42. Guyot-Sionnest, P. and Shen, Y.R. (1988) Bulk contribution in surface second-harmonic generation. *Phys. Rev. B*, **38**, 12 7985.
43. Agrawal, G.P. (2007) *Nonlinear Fiber Optics*, Academic Press.
44. Richard, S. (2010) Second-harmonic generation in tapered optical fibers. *J. Opt. Soc. Am. B*, **27**, 8 1504.

9

Harmonic Laser Mode-Locking Based on Nonlinear Microresonators

Alessia Pasquazi, Marco Peccianti, David J. Moss, Sai Tac Chu, Brent E. Little, and Roberto Morandotti

9.1

Introduction

The complex interaction of gain, nonlinearity, and dispersion works naturally in passively mode-locked lasers [1–4] to form ultrashort pulses and governs the generation of solitary pulses in different regimes spanning from optical dissipative solitons to optical similaritons [5]. There is indeed considerable interest in pushing these systems toward high repetition rates for applications such as ultrafast optical clocks, metrology, high-speed communications, and many others.

Different designs and solutions have been proposed so far, from lasers based on extremely ultrashort cavities, to the exploration of multiple soliton regimes in dissipative systems [6]. In the former case, the high repetition rate is achieved by reducing the free spectral range (FSR) of the cavity. Conversely, the latter approach – mainly explored in fiber lasers – is based on the excitation of bursts of solitary pulses per round-trip [7] and requires efficient methods to stabilize and control the repetition rate of the train of pulses.

The first experimental evidence of these multisoliton regimes was reported in 1995, where Franco *et al.* [8] introduced the so-called modulational instability laser. Some success in controlling the properties of these lasers was achieved in 1997 by Yoshida and Nakazawa [9]. The modulation instability laser was refined by inserting a Fabry Perot (FP) filter in the laser cavity to force the laser to oscillate at a repetition rate equal to the FSR of the FP. In this case, the mode-locking mechanism relied on the nonlinear energy exchange between the main cavity modes (also addressed as "supermodes") selected by the filter. The bandwidth-limited gain (or alternatively, band-pass filtering) selects the central modes that exchange energy and phase via four-wave mixing, thus guaranteeing mutual phase-locking.

In 2002, Sylvestre *et al.* [10] demonstrated that these systems worked on a mode-locking principle introduced in 1998 by Quiroga-Teixeiro, named dissipative four-wave mixing (DFWM) [11]. Since the formulation of these pioneering works, the generation of high-repetition-rate pulse trains has been demonstrated by several groups using different approaches [12–15].

Nonlinear Optical Cavity Dynamics: From Microresonators to Fiber Lasers, First Edition.
Edited by Philippe Grelu.
© 2016 Wiley-VCH Verlag GmbH & Co. KGaA. Published 2016 by Wiley-VCH Verlag GmbH & Co. KGaA.

Compared with an ultrashort cavity pulsed laser, DFWM has the advantage of maintaining the narrow linewidths of long cavity fiber lasers (arising because the intrinsic phase noise related to the Schawlow and Townes [16] limit is smaller for longer cavities), while exploiting the large FSR of short cavities. Practically, however, this advantage was never realized since the stability of these lasers has proven elusive due to a significant limitation from the so-called "*supermode instability*" [13]. Achieving the required gain and nonlinearity requires that these lasers employ long fiber lengths – typically exceeding 50 – 100 m, which corresponds to an FSR of the main cavity of the order of only a few megahertz. For high repetition rates, even for quite high-Q (high quality) FP filters, each FP resonance passes a significant number of main cavity supermodes, allowing all of them to oscillate and mix randomly. Since all modes within the filter passband experience similar gain, they all grow – eventually filling a large fraction of the bandwidth of each FP line. Consequently, the stream of high-repetition-rate pulses is strongly deteriorated by the low-frequency noise arising from the beating of these (randomly phased) supermodes.

In 2012 [17 – 19], by taking advantage of the significant advances in high-Q-factor-integrated microresonators, we introduced the concept of filter-driven four-wave mixing (FD-FWM) based mode-locking. This approach is related to the DFWM laser concept but with the critical difference that the nonlinear optical processes that drive the lasing mechanism occur entirely within a high-Q microring resonator cavity [20, 21]. Here, both linear filtering and nonlinear mixing occur inside the ring resonator. This is in stark contrast to classic DFWM, where the nonlinear interaction occurs in the fiber and is then filtered separately by an FP filter. The advantage of this approach is twofold. First, the effective nonlinearity is increased by orders of magnitude due to the field enhancement, taking place in the resonances associated with the high-Q resonator. Second, the nonlinearity is *filter-driven*, meaning that it inherently suppresses any natural shifting of the spectral content of the modes outside the filter bandwidth, which in turn reduces the nonlinear losses. Both of these aspects contribute significantly to increase the efficiency of the FWM while sustaining the spectral comb lines, thereby reducing the operating pump threshold. Even more critically, this approach eliminates the need for long main cavity loops since no fiber-based (external) nonlinearities are required, and this in turn drastically reduces the number of main cavity modes per filter line. Because the amplitude stability of the laser depends directly on the ratio between the FSR of the main cavity and the resonator bandwidth – that is, the number of oscillating supermodes – this approach has enabled us to achieve stable oscillation behavior over a large range of operating conditions. As previously remarked, our laser possesses the excellent line width typical of the main cavity loop, while the frequency modes are directly selected by the microcavity nonlinear resonator. This design is, therefore, also insensitive to any thermally induced perturbation of the microresonator lines (intrinsic or extrinsic) since the lasing operation naturally follows the microresonator resonances, in contrast to externally pumped multiple wavelength optical parametric oscillator (OPO) sources [22 – 25] (Figure 9.1).

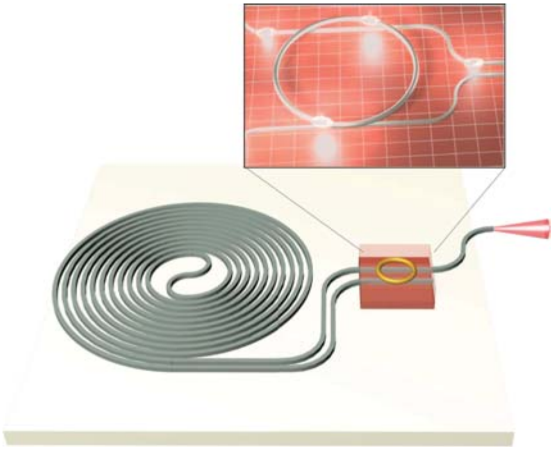

Figure 9.1 Sketch of the FD-FWM fiber laser: a nonlinear microcavity, here a microring resonator, is inserted in an active fiber loop.

9.2
Modeling

We performed numerical simulations involving the coupled equations of the field evolution $f(z_F,t)$ in the amplifying fiber and the field $a(z_R,t)$ evolving in the nonlinear ring:

$$\begin{aligned}
&\partial_z f\ (z_F,t) + \frac{n_F}{c}\ \partial_t f(z_F,t) + i\frac{\beta_F}{2}\partial_{tt} f(z_F,t)\\
&\quad = g(f)\left(1+\frac{\partial_{tt}}{\Omega^2}\right) f(z_F,t) - \alpha f(z_F,t),\\
&\partial_z a\ (z_R,t) + \frac{n_R}{c}\ \partial_t a(z_R,t) + i\frac{\beta_R}{2}\partial_{tt} a(z_R,t) + i\gamma\,|a(z_R,t)|^2 a(z_R,t) = 0,
\end{aligned} \tag{9.1}$$

where c is the light speed, z_F, z_R; n_F, n_R; and β_{2F}, β_{2R} are the propagation variable, refractive indices, and second-order dispersion in the fiber and in the ring, respectively, γ is the nonlinear coefficient in the ring, α is the absorption, and $g(f)$ is the saturable gain in the fiber expressed as

$$g(f) = G_0 e^{-\frac{1}{E_0}\int |f(z_F,t)|^2 dz_F}, \tag{9.2}$$

with G_0 and E_0 being the gain and saturation energy, respectively, and Ω regulates the gain bandwidth.

The equations represent the standard evolution of a pulse in a waveguide and are solved in time, over a propagation length L_R for the ring and L_F for the fiber, as indicated in Figure 9.2a. Such equations are coupled at the ring ports via the

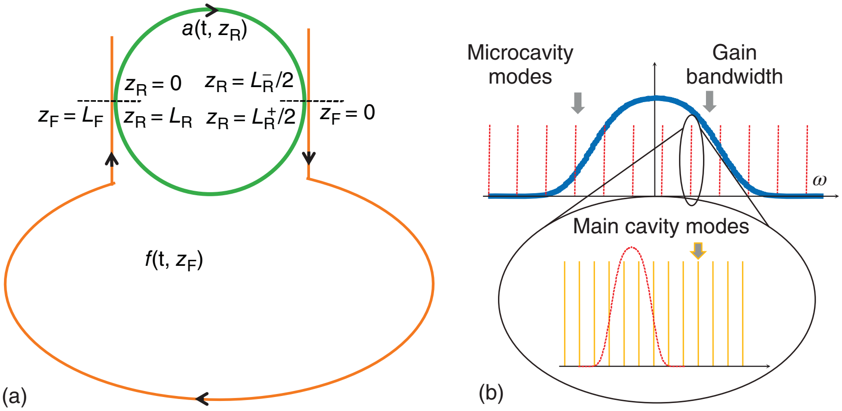

Figure 9.2 (a) Sketch of the propagation geometry used in the simulations. The field $a(z_R,t)$ [$f(z_F,t)$] propagates in the microresonator (fiber) over a length L_R [L_F]. The fields and $a(z_R,t)$ and $f(z_F,t)$ are coupled at the microresonator ports. (b) Summary of the numerical parameters used in the simulations, in the frequency space ω. The gain bandwidth (blue line) is controlled by the constant Ω. The position of the microcavity modes set (red continuous lines) is controlled by the parameter φ_{RC}. The position of the main cavity modes (inset, yellow lines) with respect to the microcavity resonances (red dashed curves) is regulated via the parameter φ_{MC}. The bandwidth of the microcavity resonances is controlled by adjusting the coefficients T and R.

relation

$$a(z_\mathrm{R}=0) = T\,a(z_\mathrm{R}=L_\mathrm{R})e^{i\varphi_{RC}} + Rf(z_\mathrm{F}=L_\mathrm{F})e^{i\varphi_{MC}}, \tag{9.3a}$$

$$\begin{aligned} a(z_\mathrm{R}=L_\mathrm{R}^+/2) &= Ta(z_\mathrm{R}=L_\mathrm{R}^-/2)e^{i\varphi_{RC}}, \\ f(z_\mathrm{F}=0) &= Ra(z_\mathrm{R}=L_\mathrm{R}^-/2)e^{i\varphi_{RC}}, \end{aligned} \tag{9.3b}$$

where T and R are the (real) transmission and reflection coefficients, with $T^2+R^2=1$. These coefficients regulate the microcavity resonances bandwidth, φ_MC regulates the position of the main cavity modes with respect to the ring modes, and finally φ_RC regulates the position of the ring modes with respect to the center of the gain bandwidth. Figure 9.2b sketches the different roles of the numerical parameters in the frequency space. The zero frequency here represents the center of the gain bandwidth.

Figures 9.3 and 9.4 report a set of simulations under different conditions. The simulations are performed for a 200 GHz repetition rate system, starting from noise and letting the system reach a stationary state. The operation is investigated for a main cavity with FSR: $\mathrm{FSR_{MC}}=12$ GHz. The lasing is investigated for different ratios of the microcavity resonance's full-width half-maximum ($\mathrm{FWHM_{RC}}$) over the main cavity FSR, $\mathrm{FWHM_{RC}/FSR_{MC}}=0.25$, 1.25, and 2.5, reported in top, central, and bottom panels, respectively, for both figures. The dispersion of the fiber is 42 $\mathrm{ps^2\,m^{-1}}$, while the microcavity is assumed to have a much smaller dispersion with respect to the main cavity and is zero in the simulations. Graphs displayed

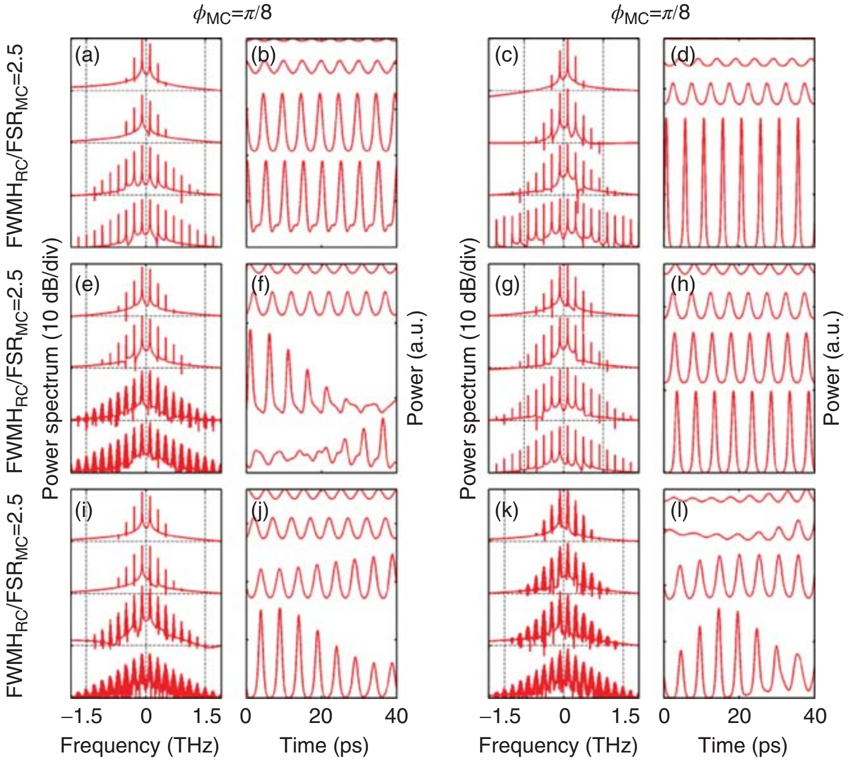

Figure 9.3 Simulations for an even symmetry of the microcavity modes with respect to the gain band. $\varphi_{RC} = \pi/2$ in all cases; $\varphi_{MC} = \pi/8$ for (a, b, e, f, i, j); and $\varphi_{MC} = 7\pi/8$ for (c, d, g, h, k, l). The lasing is investigated for different ratios of the ring lines FWHM over the main cavity FSR, $\mathrm{FWHM}_{RC}/\mathrm{FSR}_{MC} = 0.25$, 1.25, and 2.5 for the top, central, and bottom panels, respectively. The top–bottom curve for each panel is for growing cavity saturation powers (P_0, $2P_0$, $3P_0$, and $4P_0$, respectively). The main cavity has $\mathrm{FSR}_{RC} = 12$ GHz. Here, (a, c, e, g, i, k) report the power spectral densities and (b, d, f, h, j, l) report the temporal evolution of the intensity.

from top to bottom are for saturation powers P_0, $2P_0$, $3P_0$, and $4P_0$, respectively, where P_0 is the value chosen to obtain mode-locking on a sufficient number of microcavity modes. The parameter φ_{RC} is $\pi/2$. In this case, the resonances of the microcavity are evenly distributed with respect to the center of the gain bandwidth. The simulations are performed allowing the parameter φ_{MC} to vary from 0 to π. In this way, all the representative cases for the position of the main cavity modes with respect to the microcavity modes are spanned.

Figure 9.3 shows the spectral and temporal features in representative cases for the parameter φ_{RC}, while Figure 9.4 summarizes the results obtained in the whole range of parameters $\varphi_{MC} = [0\ \pi]$. Specifically, Figure 9.4 reports the optical bandwidth of the laser output (right side of the y-axis), defined as the FWHM of the optical spectrum and expressed in terms of the FSR of the microcavity. In this way,

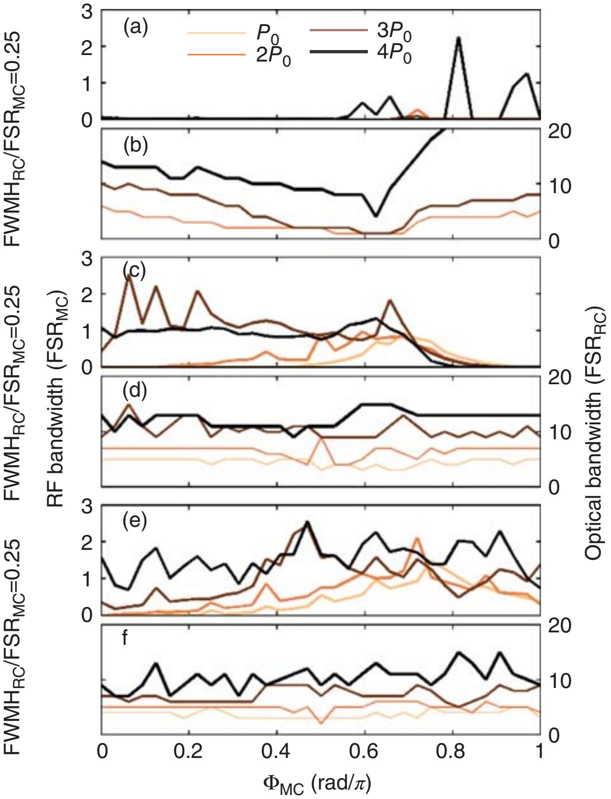

Figure 9.4 Simulation for an even symmetry of the microcavity modes with respect to the gain band. The parameter φ_{RC} is $\pi/2$ in all cases, while φ_{MC} varies as reported in the *x*-axis. The lasing is investigated for different ratios of the ring lines FWHM over the main cavity FSR, $\mathrm{FWHM}_{RC}/\mathrm{FSF}_{MC} = 0.25$, 1.25, and 2.5, top to down panels, respectively. Increasingly darker gray curves are for growing cavity saturation powers (P_0, $2P_0$, $3P_0$, and $4P_0$, respectively). The main cavity has FSR = 12 GHz. The RF spectrum bandwidth is reported on the left side *y*-axis (a, c, e), the optical spectrum bandwidth is reported on the right side *y*-axis (b, d, f).

this quantity expresses how many modes of the microcavities are excited during the mode-locking process; this value clearly increases with the saturation power in all the cases shown here. On the left side of the *y*-axis, the bandwidth of the radio frequency component is reported, calculated by filtering the spectrum of the output intensity for frequencies lower than the FSR of the microcavity (e.g., $f < 200$ GHz). This value is expressed in terms of the FSR of the main cavity and gives a direct measure of how many modes of the main cavity are resonating per microcavity resonance, or better, the number of modes minus one ($N - 1$). Such a value is close to zero for almost all the cases observed in panels (a, b) where the narrowest microcavity resonance case is used, showing that stable oscillations can be obtained when a single mode of the main cavity oscillates in a microcavity resonance. There is still a range of values for φ_{MC} where the system is stable in panels (c, d) and (e, f) but in several cases the radio frequency oscillation has a bandwidth larger than the FSR of the main cavity, showing that supermode instability is still occurring.

From simulations, we see that the supermode instability could be either induced or suppressed simply by optimizing the main cavity length. The parameter controlling the phase of the main cavity modes is φ_{MC}, which also determines the spectral position of the main cavity modes with respect to the resonances associated with the ring resonator. The cavity energy (relative to the gain saturation power) can also affect the stability, since it regulates the number of supermodes that oscillate – higher powers support more lines and hence can be less stable. The stability for the case of high-power configurations can be improved by decreasing the ratio of the microring linewidth versus the main cavity FSR. The set of stable conditions as a function of the phase delay φ_{MC} shrinks with the cavity energy.

Noticeably, this analysis shows a dependence of the laser instability on the relative phase of the main cavity modes. This was not observed in previous works, where the long external cavity length lasers yielded an unstable behavior only because of the high number of oscillating main cavity modes, and the phase of the individual supermodes played a negligible role. In contrast, the cavity phase of the short-length laser reported here is pivotal since it determines the precise alignment of the central two or three cavity modes relatively to the ring resonator mode, and this has a critical effect on how many supermodes oscillate.

9.3
Experiments

Figure 9.5 shows the central component of the laser, an integrated microring resonator with a Q factor of 1.2 million [19] (corresponding to a mode linewidth

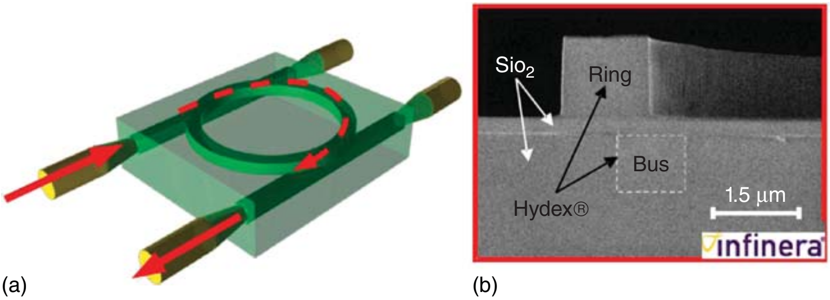

Figure 9.5 (a) Schematic of the central component – a monolithically integrated four-port high-Q ($Q = 1.2$ million) microring resonator (fiber pigtails not shown). (b) SEM picture of the ring cross-section before depositing the upper cladding of SiO$_2$. The waveguide core is made of high index (1.7) doped silica glass.

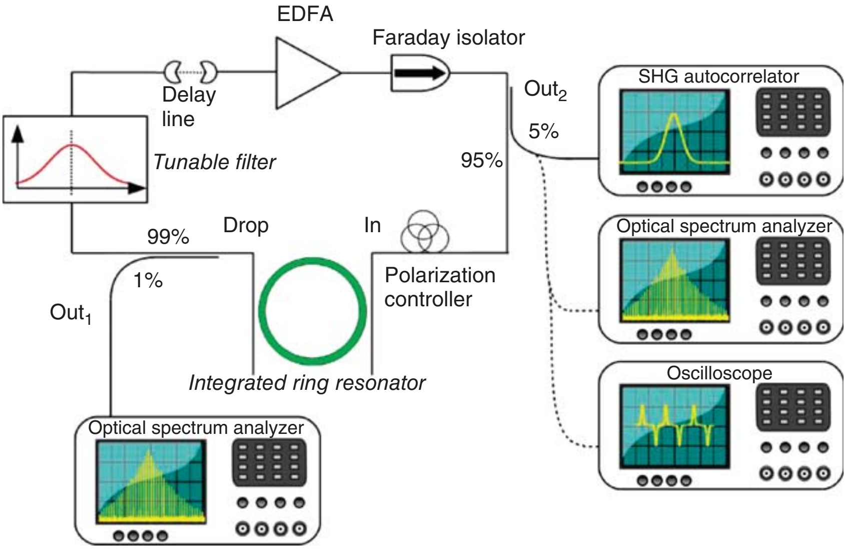

Figure 9.6 High-repetition-rate laser: sketch of the experimental setup.

of 160 MHz), fabricated in a CMOS compatible chip platform based on Hydex® [20, 21] waveguides having optical properties similar to silicon oxynitride. The waveguides possess a high effective nonlinearity ($\gamma = 220\,\mathrm{W}^{-1}\,\mathrm{km}^{-1}$) due to a combination of tight mode confinement and high intrinsic Kerr coefficient (n_2 is five times that of silica glass), as well as near optimum dispersion characteristics (small and anomalous) for nonlinear optics. Most significantly, the waveguides exhibit very low linear optical loss and negligible nonlinear optical loss (i.e., two photon absorption) up to $25\,\mathrm{GW\,cm}^{-2}$. All these factors make this platform particularly attractive for low-power nonlinear optics in the C-band.

Figure 9.6 shows the experimental setup. The microring resonator is embedded in a larger fiber loop cavity with the input and output bus waveguides of the resonator pigtailed to a standard single mode fiber (SMF) using integrated mode converters and V-groove technology, resulting in a coupling loss of <1.5 dB per facet. The fiber cavity loop contained an optical amplifier to provide , a Faraday isolator, a polarization controller, and a free-space delay line. In addition, we used a passband filter inserted in the fiber-loop with a bandwidth large enough to pass all of the oscillating lines, in order to control the central oscillating wavelength λ_0.

In order to investigate the dependence of the laser performance on the main cavity length, we conducted the experiments using two different main cavity configurations, each with an optical amplifier having a different length, and hence main cavity FSR. A delay line was employed to control the phase of the main cavity modes with respect to the ring modes. By adjusting the delay line of our system, we observed three main operation regimes: unstable, stable, and dual mode, described in detail later.

The optical amplifiers were either an ultrashort-length Er-doped fiber amplifier (EDFA from PriTel) or a more conventional (longer length) high-power erbium–ytterbium-doped fiber amplifier (EYDFA). The EYDFA had a maximum saturation output power of ∼3 W, and produced a main cavity FSR of 6.0 MHz, corresponding to a length of 18 m, while the short-length EDFA had a saturation output power of ∼35 mW and resulted in a cavity length of only 1.5 m, corresponding to a very large main cavity FSR of 68.5 MHz. This is much larger than what is achievable using conventional DFWM approaches that rely on nonlinear interactions in fibers. The FSR of the microresonator was 200.3 GHz, while the single resonances had an FWHM linewidth of 160 MHz at the lasing wavelengths. For the EYDFA-based laser, the band-pass filter in the fiber loop used to control the central oscillating wavelength was a 15-nm-wide Gaussian filter with ∼4 dB loss, whereas for the short-length laser a 5 nm wide filter was used, having a loss of 1.5 dB. For the short laser, a limited gain was available and so the low-loss, narrow bandwidth filter was chosen – also because the overall output bandwidth was much smaller than the EYDFA laser due to the lower available gain.

Figure 9.7 shows the experimentally observed pulse spectra and temporal profiles achieved via autocorrelation for the long laser cavity as a function of the output power. Figure 9.7a and b shows the spectra and second-order noncollinear autocorrelation traces for the longer high-power erbium–ytterbium amplifier as a function of power, up to a maximum of $P_{\text{in}} = 68$ mW measured at the input of the ring resonator port. The output power of the EYDFA-based laser was limited only by the damage threshold of the fiber pigtails to the chip. It is important to note that autocorrelation measurements average any laser fluctuations over long time scales, and hence can exhibit ultrashort-pulsed features without actually requiring a stable pulsed output. Hence, the key issue of laser stability can only be determined by comparing the experimental autocorrelation traces with the calculated traces (Figure 9.7b, green plots) for a fully stable and coherent system possessing the optical spectra in Figure 9.7a. A noncollinear second harmonic (SH) autocorrelation of an isolated pulse is background free. Conversely, the background of the autocorrelation of a coherent train of pulses is dependent on the pulse length versus repetition rate, but can be easily inferred from the optical spectrum analyzer (OSA) trace assuming that the lines in the spectra are fully coherent (all in-phase). The long cavity design shows a considerably higher background than the calculated traces, thus clearly pointing to an unstable laser operation [13]. To properly quantify the laser instability, we determined the laser amplitude noise by measuring the electrical radio frequency (RF) spectrum of the laser using a fast photodetector and a trans-impedance amplifier (bandwidth ∼200 MHz). Figure 9.7c and d shows the long timescale temporal output (measured with the 200 MHz detector) along with the RF spectra. In accordance with the large background measured in the autocorrelation traces in Figure 9.7b, the RF signal clearly shows a dramatic irregular pulsation. We observed temporal dynamics characterized by two temporal scales: (i) a fast scale due to the main cavity (MC) mode beating, as is clearly visible in the spectrum, showing two lateral wings around the FSR of the MC (6 MHz) and (ii) a slow scale, with modulation on

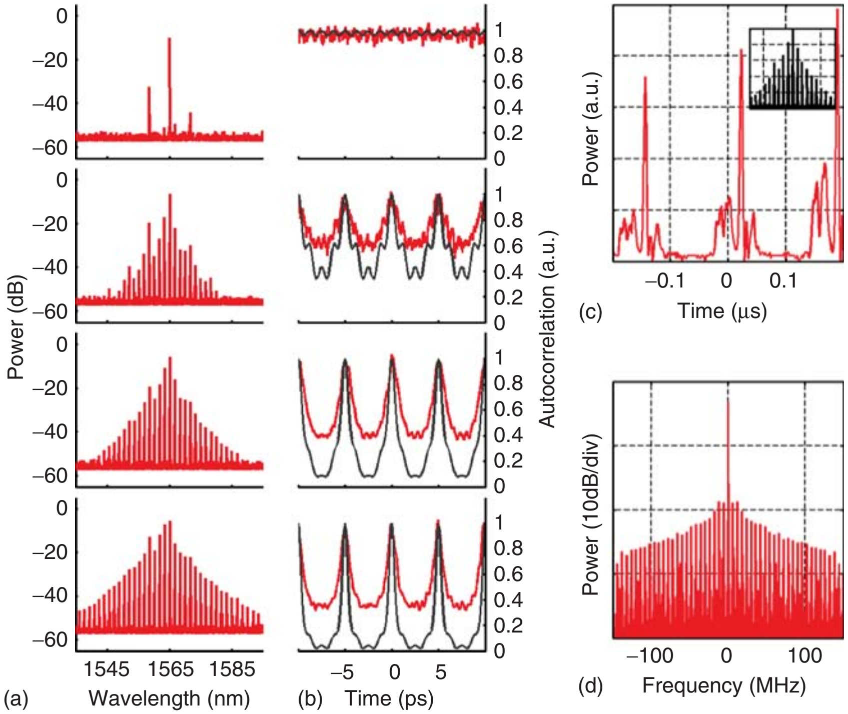

Figure 9.7 Experimental optical spectra and autocorrelation traces of the laser output, for different FSRs of the main cavity. (a,b) Laser emission for increasing (top to bottom) pump powers, achieved through the use of a long EYDFA, for 5.5, 28, 40, and 68 mW average powers at the ring input, respectively. In (b), the autocorrelation traces calculated starting from the experimental optical spectra for a fully stable-coherent and transform-limited system are also shown in green. These profiles are calculated considering each line of the experimental optical spectra perfectly monochromatic and in-phase with the others, thus yielding to a soliton output pulse with a width (FWHM) of 730 fs (duty cycle $\rho = 0.15$) for the highest excitation condition. The measured autocorrelation shows a considerable higher background (the peak-to-background ratio is 2.5 : 1 for the 68 mW case) than the expected autocorrelation (50 : 1). (c,d) Unstable oscillation condition for a main cavity FSR = 6 MHz. The average power in the ring was 68 mW (c) temporal modulation of the output intensity measured with a slow photodetector and (d) RF noise.

the order of 6 μs, indicating that the cavity is working in an unstable *Q*-switching regime due to the slow recovery time of the EYDFA gain – a common occurrence in fiber lasers [28]. Unstable behavior was observed for all settings of the delay line for the long cavity case. For the short EDFA, however, a strong variation in stability with the position of the delay line was observed. This is in agreement with the numerical analysis presented earlier, showing a strong dependence of the laser stability on the relative phase of the main cavity supermodes, especially in the case where the microcavity has a resonance bandwidth comparable with the FSR of the main cavity. We focus on each regime of operation in the sections that follow.

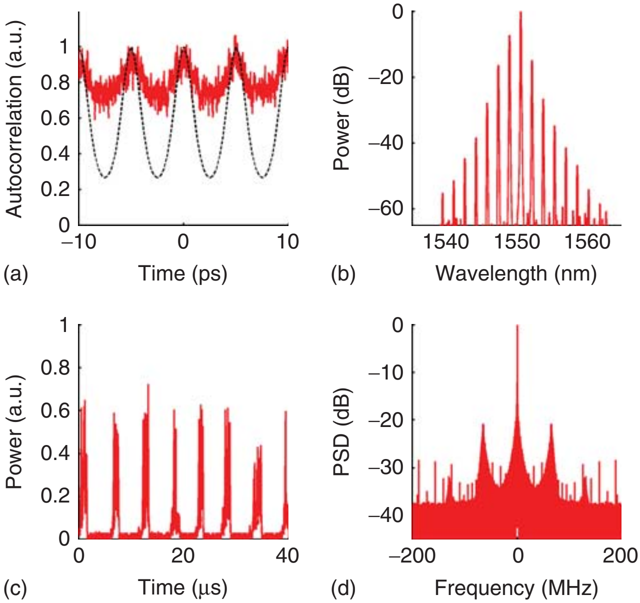

Figure 9.8 Unstable regime for the short-length cavity: optical (a,b) and radio-frequency (c,d) characterization of the laser output: (a) experimental autocorrelation trace (black) and (b) experimental optical spectrum. The autocorrelation trace for a fully coherent transform-limited system calculated from the spectrum in (b) is shown (dashed line) in (a). RF signal of the laser output in time (c) and spectrum (power spectral density (PSD)) (d). The RF signal also shows a pulsation due to the beating of the MC modes, as visible in the spectral components at 65 MHz in (d).

9.3.1
Short Cavity, Unstable Laser Oscillation

Figure 9.8 shows the results for the unstable pulsation of the laser. The data were obtained while driving the EDFA at the maximum available current, corresponding to approximately 16 mW at the input of the microring. Panel (a) reports the SH noncollinear autocorrelation where a periodic modulation at 200 GHz is visible with an extremely poor contrast, as already observed for the unstable operation. Panel (b) shows a comb-like spectrum spaced by the FSR of the microring (200 GHz), indicating that a fast modulation of the laser output is present, also confirmed by the 200 GHz periodic modulation of the signal in panel (a) obtained with an SH noncollinear autocorrelator (black). The autocorrelation calculated from the optical spectrum under the assumption of fully coherent pulses is also reported in (a) (dashed lines), showing the high background of the measured traces. The envelope signal recorded with a photodetector is reported in panels (c and d) in time and frequency, respectively.

While this configuration did display temporal instability as a result of supermode beating, it is qualitatively very different from the long-EYDFA configuration because of the widely different main cavity mode spacing relative to the ring resonator linewidth. The FSR of the short cavity laser was roughly 1/2 that of the ring resonator bandwidth, allowing at most only a few main cavity modes to oscillate, while the 6 MHz FSR of the long cavity laser was such that a very high number of cavity modes could be supported by the 160 MHz wide ring resonator linewidth, as clearly shown in Figure 9.7d. As in the previous cases, we observed a slow temporal modulation of the order of 6 μs, due to an unstable *Q*-switching regime.

9.3.2
Short Cavity, Stable Laser Oscillation

Figure 9.9a and b shows the spectra and autocorrelation traces for the short-length EDFA for pump powers up to a maximum of 15.4 mW at the ring input port. Since the short-length EDFA had a lower available gain (20 dB), the maximum spectral bandwidth that we could achieve was limited to seven or eight lasing modes of the 200 GHz FSR of the ring resonator. The calculated autocorrelation traces obtained

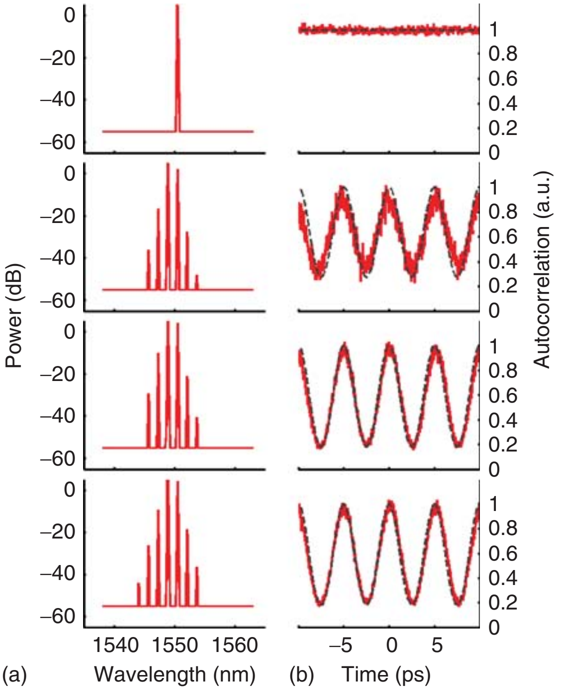

Figure 9.9 Experimental spectra and autocorrelation traces of the filter-driven mode-locked laser. (a,b) Same as Figure 9.7a and b for short-cavity laser emission. The average powers in the ring were, respectively, 7, 11.4, 15.2, and 15.4 mW (top–bottom).

for a fully stable and coherent system possessing the optical spectra in Figure 9.9a are reported in green, and show a perfect match to the experiment. This leads to an estimated transform-limited soliton pulse width FWHM of 2.3 ps (corresponding to a duty cycle of 0.46). In all cases, oscillation was self-starting and did not critically depend on the initial conditions.

This regime was obtained by adjusting the phase of the cavity modes relative to the ring resonator mode using a free-space delay line (Figure 9.6). By aligning one of the cavity modes to the center of the ring resonator mode, we were able to achieve lasing at a single cavity mode only. This completely eliminated any main cavity supermode beating and consequently gave rise to an extremely stable output, as reflected in both the temporal output and RF spectrum, reported in Figure 9.10, together with the optical spectra and autocorrelation traces. In this case, the RF signal exhibited a dominant DC component with a bandwidth <0.25 Hz (the resolution of our measurement system) as well as an out-of-band noise 55 dB lower than the DC peak. We estimate the ratio between the power of the DC component to the spectral noise (within the 200 MHz bandwidth) to be >31 dB, again limited by our measurement sensitivity – in our case by detection and sampling noise. For the unstable case, this is typically $\ll 0$ dB – which we estimate to be ~ -13 dB for the 6 MHz FSR main cavity.

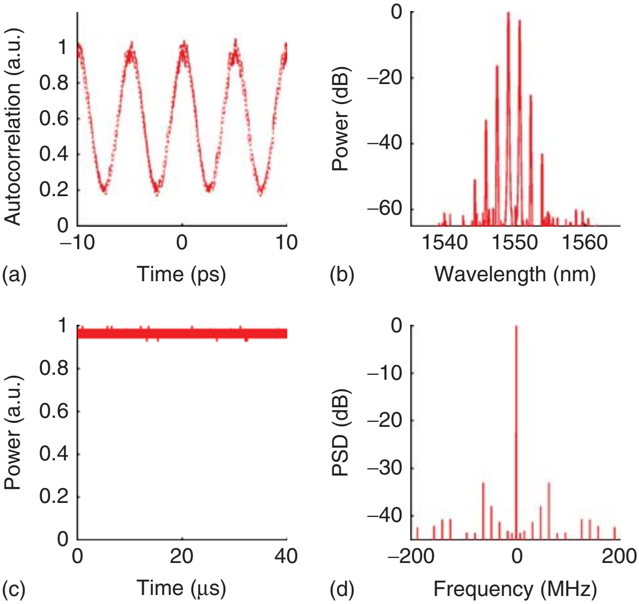

Figure 9.10 Stable regime for the short-length cavity: optical (a, b) and radio frequency (c, d) characterization of the laser output: (a) experimental autocorrelation trace (black) and (b) experimental optical spectrum. The autocorrelation trace for a fully coherent transform-limited system calculated from the spectrum in (b) is shown in dashed in (a). RF signal of the laser output in time (c) and spectrum (d).

To characterize the phase noise, we measured the linewidth of the oscillating lines by selecting each with a narrowband filter and then analyzing the output using a re-circulating delayed self-heterodyne interferometer (RDSHI) [26, 27, 29, 30] with a delay line of 5.8 km, and a modulation frequency of 6.5 MHz. We found that all of the observable emitted lines had a bandwidth much less than 100 kHz (standard deviation) – limited by environmental acoustic noise that we minimized but could not eliminate. This is consistent with our estimation of the intrinsic Lorentian contribution to the linewidth being <13 kHz and implies that ultimately, proper packaging, and acoustic isolation would significantly reduce the spectral linewidths.

9.3.3
Short Cavity, Dual-Line Laser Oscillation

Figure 9.11 summarizes another important operation regime of our system, possessing similar properties to the stable case of Figure 9.10 at the optical temporal scale: the autocorrelation (panel (a)) showed a stable pulsation consistent with the

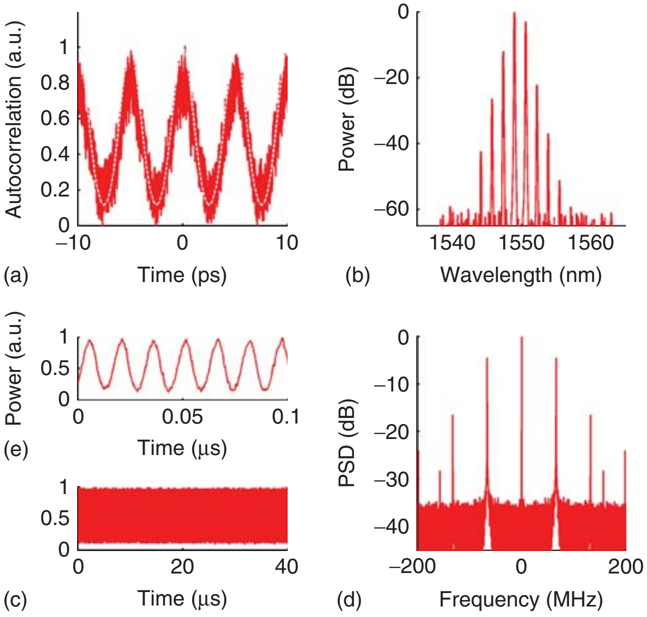

Figure 9.11 Dual-line regime for the short-length cavity: optical (a, b) and radio frequency (c, d) characterization of the laser output: (a) experimental autocorrelation trace (black) and (b) experimental optical spectrum. The autocorrelation trace for a fully coherent transform-limited system calculated from the spectrum in (b) is shown (dashed line) in (a). RF signal of the laser output in time (c) (inset in (e)) and spectrum (d).

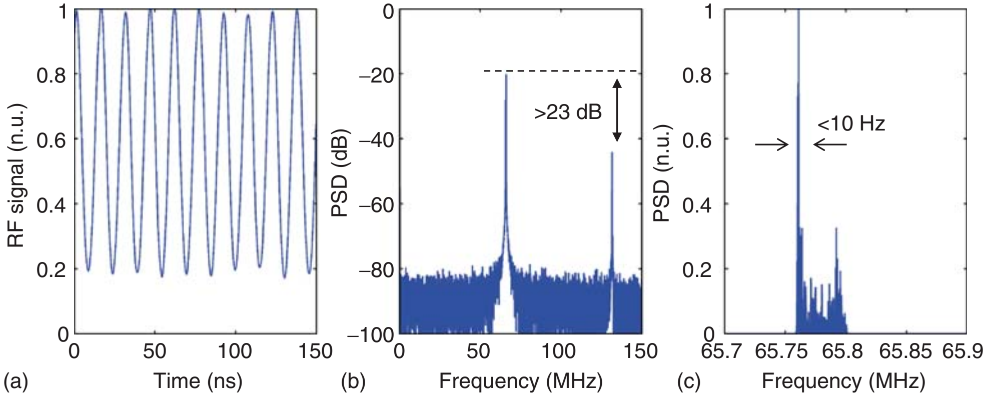

Figure 9.12 Dual-line regime for the short-length cavity: (a) experimental autocorrelation trace (black) and (a) RF signal output, over shorter time scale than Figure 9.11c. (b) RF spectrum showing the first and second harmonic at the main cavity FSR = 65 MHz. (c) RF spectrum around the 65 MHz oscillation.

calculated autocorrelation trace (dashed line) – again, obtained by assuming that the frequencies in the optical spectrum (panel (b) were in phase). Conversely, on the RF scale the temporal signal (panel (c)) along with its RF spectrum (panel (d)), showed a highly coherent beating at 65 MHz, indicating that two distinct modes of the MC were oscillating per microring resonator line. Using a filter, we verified that the beating originated from mode doublets that oscillated in every excited resonance. An inset of the RF data is reported in Figure 9.12.

These measurements indicate that the system was oscillating with two MC modes symmetrically distributed around a ring resonance peak: the laser oscillated in a stable mode-locking manner with an output spectrum consisting of a number of closely spaced MC mode doublets. The extinction ratio of the beating (Figures 9.11c and 9.12a) exceeds 80% and demonstrates a good balance of the two comb replica energies. The secondary peak at 130 MHz in Figure 9.11d is an SH of the RF beat frequency and has a negligible power level (−23 dB down from the main RF peak, as visible in Figure 9.12b).

Figure 9.12c shows the particularly narrow linewidth of the RF beat frequency, that is, <10 kHz.

This beating is related to the instantaneous frequency difference between the two oscillating comb replicas and so its spectrum is an accurate reflection of the dynamics of the line-to-line spacing of the MC modes. This confirms the instantaneous frequency locking between the MC oscillating lines. In addition, the measurement of the amplitude noise of this configuration gives important information on the phase stability of the system, since the line width of the AC peak at 65.8 MHz in Figure 9.12c, is a direct measurement of the stability of the FSR of the MC, which is better than 0.01% for the case presented here. This measurement reflects the very high stability of the ultrafast comb.

The RF modulation generated by the beating among the cavity modes was coherent with the 200 GHz optical pulse train. This is qualitatively very different from what is achievable by modulating a pulse train with an external modulator, for example. To the first order, the modulation can be thought of as a phase-locked loop (PLL) subcarrier since its frequency shifts with the repetition rate. Although it is not necessarily an integer fraction of the repetition rate, obtaining a locked subcarrier requires one to "read" the pulse train with a PLL, but in this case the repetition rate is well beyond the capability of standard detectors, at 200 GHz. Instead, in this case, the signal already carries the information that is useful, for example, to synchronize slower sources for time-division multiplexing applications.

9.4

Conclusions

In conclusion, we have reviewed our first results concerning a mode-locked laser based on a monolithic high-Q resonator.

We generated picosecond and subpicosecond optical pulses at a repetition rate of 200.8 GHz by exploiting a CMOS compatible microring resonator that forms the basis of a soliton laser. Our device operates via a new mechanism that we term *filter-driven four wave mixing* that allows us to obtain the first demonstration of stable emission from an DFWM-based passively mode-locked soliton laser. We achieve extremely stable, low RF-noise, operation with a record narrow optical linewidth of <100 kHz. Indeed, the use of a long main cavity guarantees better performances in terms of Schawlow–Townes noise. This is mostly reflected on the quality of the laser linewidth for high-repetition-rate operation.

These results also demonstrate the versatility of the DFWM scheme for different lengths of the main cavity. By adjusting the relative phase between the MC modes and the ring resonator, it is not only possible to eliminate all the low-frequency instabilities arising from supermode beating and EDFA gain switching, in order to obtain stable pulsation, but it is also possible to achieve stable oscillation of twin combs separated by the FSR of the MC.

Although the gain of the laser is still not integrated in the device, the laser produces optical pulses at 200 GHz directly on chip. The scheme allows the generation of a train of optical pulses always tuned to the resonances of the microring, hence the system is resilient to the thermal perturbations that usually have detrimental effect in the coupling of external laser sources. This is particularly important especially for integrated devices, where high-energy dissipation is expected on chip for a realistic high concentration of devices.

Finally, our new mechanism enables stable mode-locked lasing with negligible amplitude noise, and extrinsically limited phase noise, not constrained by the repetition rate, and it is designed to work with on chip resonators. This work may represent the first step toward a new generation of ultrastable, high repetition rate, optical pulsed sources.

References

1. Haus, H. (2000) Mode-locking of lasers. *IEEE J. Sel. Top. Quantum Electron.*, **6**, 1173–1185.
2. Fermann, M.E. and Hartl, I. (2009) Ultrafast fiber laser technology. *IEEE J. Sel. Top. Quantum Electron.*, **15**, 191–206.
3. Mollenauer, L.F. and Stolen, R.H. (1984) The soliton laser. *Opt. Lett.*, **9**, 105–108.
4. Lecaplain, C., Grelu, P., Soto-Crespo, J.-M., and Akhmediev, N. (2012) Dissipative rogue waves generated by chaotic pulse bunching in a mode-locked laser. *Phys. Rev. Lett.*, **108**, 233901.
5. Grelu, P. and Akhmediev, N. (2012) Dissipative solitons for mode-locked lasers. *Nat. Photonics*, **6**, 84–92 and references therein.
6. Akhmediev, N., Ankiewicz, A., and Soto-Crespo, J. (1997) Multisoliton solutions of the complex Ginzburg–Landau equation. *Phys. Rev. Lett.*, **79**, 4047–4051.
7. Arbel, D. and Orenstein, M. (1999) Self-stabilization of dense soliton trains in a passively mode-locked ring laser. *IEEE J. Quantum Electron.*, **35**, 977–982.
8. Franco, P. *et al.* (1995) Self-induced modulational-instability laser. *Opt. Lett.*, **20**, 2009–2011.
9. Yoshida, E. and Nakazawa, M. (1997) Low-threshold 115-GHz continuous-wave modulational-instability erbium-doped fiber laser. *Opt. Lett.*, **22**, 1409–1411.
10. Sylvestre, T. *et al.* (2002) Self-induced modulational instability laser revisited: normal dispersion and dark-pulse train generation. *Opt. Lett.*, **27**, 482–484.
11. Quiroga-Teixeiro, M. *et al.* (1998) Passive mode locking by dissipative four-wave mixing. *J. Opt. Soc. Am. B*, **15**, 1315–1325.
12. Schröder, J., Vo, T.D., and Eggleton, B.J. (2009) Repetition-rate-selective, wavelength-tunable mode-locked laser at up to 640 GHz. *Opt. Lett.*, **34**, 3902–3904.
13. Schröder, J. *et al.* (2008) Dynamics of an ultrahigh-repetition-rate passively mode-locked Raman fiber laser. *J. Opt. Soc. Am. B*, **25**, 1178–1189.
14. Sylvestre, T. *et al.* (2001) Demonstration of passive modelocking through dissipative four-wave mixing in fibre laser. *Electron. Lett.*, **37**, 881.
15. Zhang, S. *et al.* (2005) Passive mode locking at harmonics of the free spectral range of the intracavity filter in a fiber ring laser. *Opt. Lett.*, **30**, 2852–2854.
16. Schawlow, A.L. and Townes, C.H. (1958) Infrared and optical masers. *Phys. Rev.*, **112**, 1940–1949.
17. Peccianti, M. *et al.* (2012) Demonstration of a stable ultrafast laser based on a nonlinear microcavity. *Nat. Commun.*, **3**, 765.
18. Pasquazi, A. *et al.* (2012) Stable, dual mode, high repetition rate mode-locked laser based on a microring resonator. *Opt. Express*, **20**, 27355–27363.
19. Pasquazi, A. *et al.* (2013) Self-locked optical parametric oscillation in a CMOS compatible microring resonator: a route to robust optical frequency comb generation on a chip. *Opt. Express*, **21**, 13333–13341.
20. Ferrera, M. *et al.* (2009) Low power four wave mixing in an integrated, micro-ring resonator with Q = 1.2 million. *Opt. Express*, **17**, 14098–14103.
21. (a) Razzari, L. *et al.* (2009) CMOS-compatible integrated optical hyper-parametric oscillator. *Nat. Photonics*, **4**, 41–45; (b) Johnson, F.G. *et al.* (2003) Use of deuterated gases for the vapor deposition of thin films for lowloss optical devices and waveguides. US Patent 6614977 B2.
22. Del'Haye, P., Arcizet, O., Schliesser, A., Holzwarth, R., and Kippenberg, T.J. (2008) Full stabilization of a microresonator-based optical frequency comb. *Phys. Rev. Lett.*, **101**, 053903.
23. Grudinin, I.S., Yu, N., and Maleki, L. (2009) Generation of optical frequency combs with a CaF_2 resonator. *Opt. Lett.*, **34**, 878–880.
24. Kippenberg, T.J., Spillane, S.M., and Vahala, K.J. (2004) Kerr-nonlinearity optical parametric oscillation in an ultrahigh-Q toroid microcavity. *Phys. Rev. Lett.*, **93**, 083904.

25. Agha, I.H., Okawachi, Y., Foster, M.A., Sharping, J.E., and Gaeta, A.L. (2007) Four-wave-mixing parametric oscillations in dispersion-compensated high-Q silica microspheres. *Phys. Rev. A*, **76**, 043837.

26. Dawson, J.W., Park, N., and Vahala, K.J. (1992) An improved delayed self-heterodyne interferometer for linewidth measurements. *IEEE Photonics Technol. Lett.*, **4**, 1063–1066.

27. Mercer, L.B. (1998) 1/F frequency noise effects on self-heterodyne linewidth measurements. *J. Lightwave Technol.*, **9**, 485–493.

28. Haboucha, H. *et al.* (2008) Analysis of soliton pattern formation in passively mode-locked fiber lasers. *Phys. Rev. A*, **78**, 043806.

29. Okoshi, T., Kikuchi, K., and Nakayama, A. (1980) Novel method for high resolution measurement of laser output spectrum. *Electron. Lett.*, **16**, 630.

30. Linde, D. (1986) Characterization of the noise in continuously operating mode-locked lasers. *Appl. Phys. B*, **39**, 201–217.

10

Collective Dissipative Soliton Dynamics in Passively Mode-Locked Fiber Lasers

François Sanchez, Andrey Komarov, Philippe Grelu, Mohamed Salhi, Konstantin Komarov, and Hervé Leblond

10.1

Introduction

10.1.1

Dissipative Solitons and Mode-Locked Lasers

In the 1990s, the concept of optical solitons was gradually extended to nonconservative systems. Indeed, in addition to the balance between nonlinear self-compression and dispersion (or self-focusing and diffraction), when a second balance between nonlinear gain and losses occurs, stable localized electromagnetic structures may form and propagate. Such structures were called *dissipative solitons*, although not only losses, but also gain is required for their formation [1]. In optics, the terminology was introduced in the case of a Brillouin fiber laser [2], and then for an amplifying medium with group velocity dispersion [3]. Let us recall a recent definition of dissipative optical solitons [4]: “dissipative solitons are localized formations of an electromagnetic field that are balanced through an energy exchange with the environment in the presence of nonlinearity, dispersion and/or diffraction.” Consequently, fiber lasers appear as an excellent framework for the generation of dissipative solitons. They offer the possibility to vary the experimental parameters in large ranges, thus providing a great versatility in the operating conditions. In contrast to conservative solitons, bright dissipative solitons can form in both anomalous and normal dispersion regimes. For instance, although pulse broadening in normal dispersion cannot be balanced by self-compression, it can be compensated by a nonlinear gain, which replaces the energy flying out from the top of the pulse, and the help of gain dispersion, which clips off the chirped pulse tails. Although the gain/loss balance needs to be precisely satisfied for stationary solutions, a dissipative soliton involves a more global balance as it comes to dispersive effects. This view is also related to the existence of an internal energy flow within dissipative solitons, in correspondence to their nonuniform phase profiles [4]. Working on this paradigm enables to take benefit from the large dynamical evolution per round-trip generally implicit

Nonlinear Optical Cavity Dynamics: From Microresonators to Fiber Lasers, First Edition.
Edited by Philippe Grelu.
© 2016 Wiley-VCH Verlag GmbH & Co. KGaA. Published 2016 by Wiley-VCH Verlag GmbH & Co. KGaA.

in fiber lasers [5], and to find record high-energy pulse solutions. The latter is developed in the chapter from Babin *et al.* [6].

Nonlinear dissipation is a central feature of passive mode-locking, which requires a filtering mechanism penalizing low intensities and transmitting higher ones. This can be achieved in practice by using various physical effects. An efficient technique consists in inserting a localized fast saturable absorber in the cavity, such as a semiconductor saturable absorber mirror [7], carbon nanotubes [8], or graphene layers [9, 10]. Other mode-locking techniques peculiar to fiber lasers are based on nonlinear interferences, which utilize the optical Kerr effect. These are implemented in figure-of-eight lasers (F8L), either in the nonlinear optical loop mirror (NOLM) [11–13] or in the nonlinear amplifying loop mirror (NALM) configurations [14–16]. One of the most popular techniques is based on the nonlinear polarization evolution (NPE) resulting from the vectorial optical Kerr effect: nonlinear transmission is obtained thanks to an intracavity polarizer that transforms the nonlinear evolution of the polarization state into intensity-dependent losses [17–20].

From the point of view of mathematical physics, dissipative solitons are widely studied in the frame of the complex Ginzburg–Landau (CGL) equation. This nonlinear partial differential equation finds numerous applications in various domains of physics, such as superconductivity, Bose–Einstein condensation, particle physics, and nonlinear optics [21]. In the frame of mode-locked lasers, the cubic CGL equation is equivalent to the "Haus master equation" [22]. It can be derived as an average model in various cases, such as for a fiber ring laser mode-locked through the nonlinear polarization evolution [23] or for a figure-of-eight fiber laser [13]. However, the cubic CGL equation does not admit stable soliton solutions; consequently, quintic nonlinear terms were introduced to prevent the blow-up of the solutions [24, 25]. The cubic–quintic CGL equation could also be derived as an average model for mode-locked fiber lasers [26, 27]. Besides CGL models, more detailed modeling of the pulse propagation and its related dynamics involve the extensive numerical resolution of piecewise propagation equations [28–30]. Note that soliton propagation in periodic systems is a quite involved general problem [31]. In an intermediary approach, assumptions allow to treat part of the equations as a local operator applied periodically during propagation in the cavity [32]. There are also sets of averaged model equations that are more complicated than the CGL equation, such as a Swift–Hohenberg model derived from Maxwell–Bloch equations [33], and extended CGL equations including the mechanisms of gain depletion and relaxation [34–36].

10.1.2
Multiple Pulses and Their Interactions

A common feature to passively mode-locked lasers is the increase of the number of pulses per cavity round-trip when the pumping power increases. This has been observed since the early stage of fiber lasers [37], and occurs regardless of the mode-locking mechanism. By providing a clamping of the single-pulse energy, and a tendency to destabilize the pulse repetition rate, multiple pulsing is considered as detrimental to most applications. However, it can be used to increase the fundamental cavity repetition rate to ultrahigh frequencies, and it is a good framework for fundamental studies on collective dissipative soliton dynamics. The power threshold of multiple pulsing is highly dependent on the sign of the dispersion, on the spectral gain bandwidth and on the nonlinear losses that are associated with the saturable absorber. In general, multiple pulsing is accompanied by multistability and hysteresis phenomena [32, 38]. The existence of a single dynamical attractor guaranties that all pulses have the same field profile. Once several solitons are generated in the laser cavity, they can move, collide, and lead to a variety of patterns under the action of the interactions between them. A leading attractive interaction entails the formation of bound states [39], from soliton molecules [40, 41] to soliton crystals [42, 43], according to the number of pulses involved and to the uniformity of their distribution. On the contrary, a dominant repulsive interaction is conducive to harmonic mode-locking (HML), with pulses equally distributed all-along the laser cavity [44].

Soliton interaction was initially investigated in the frame of conservative solitons. In 1983, Gordon pointed out a direct soliton–soliton interaction [45] that can be repulsive or attractive depending on the phase difference between two neighbor solitons, and was later validated experimentally [46]. In the situation of dissipative solitons interacting in passively mode-locked fiber lasers, the mechanisms are more diverse and complex, while the interacting solitons share the same profile, in contrast to the conservative case. The existence of a direct short-range coherent interaction was predicted by Malomed [47], and the stability of bound states demonstrated by Akhmediev et al. [39]. Another coherent interaction uses dispersive waves associated with resonant soliton radiation [48], as a way to mediate soliton–soliton interaction over a longer range, typically of the order of 100 pulse widths [49]. Other long-range interaction mechanisms, whose ranges exceed 100 pulse widths, have been pointed out. The gain depletion and recovery dynamics results in a repulsive interaction leading to HML regime [50]. The acoustically induced long-range interaction in a passively mode-locked fiber laser can either trap solitons into bunches, or lead to equally spaced solitons [51]. Background noise fluctuations can statistically produce an effective long-range attractive interaction between pulses, in analogy with Casimir forces [52]. Recently, it was experimentally demonstrated that the external injection of a continuous wave (CW) into the fiber laser cavity favored HML [53]. Theoretical studies showed that the CW component could generate a long-range attractive or repulsive interaction among solitons [54, 55].

Although very different fiber laser configurations can be designed, we may wonder whether there is a specific cavity design leading to a specific collective dynamics. However, the studies reveal the existence of universal dynamical behaviors, with similar soliton patterns observed in various laser cavities, using different mode-locking schemes [4, 56]. First investigations involved few solitons, which allowed gaining fundamental insight into the interaction mechanisms. Much interest was concentrated on bound states consisting of phase-locked dissipative solitons, which appeared as a striking universal collective behavior [4, 39, 41].

The scaling up of the pumping power in fiber lasers has allowed a considerable increase in the number of coexisting solitons in passively mode-locked fiber lasers, from a few tens to several thousands, resulting in original complex pattern formation dynamics. Bound states consisting of hundreds of equidistant pulses, dubbed "soliton crystals," were experimentally reported and theoretically analyzed [35, 42]. The intriguing "soliton rain" dynamics involves a complex interplay between numerous dissipative solitons and a large noise background [57, 58]. Various soliton distributions presenting analogies with the states of matter have been pointed out [59]. HML has been generalized to the equal distribution of bound solitons [60], rain of solitons [58], and soliton crystals [61].

This chapter gives a comprehensive review of collective soliton dynamics in passively mode-locked fiber lasers. Section 10.2 introduces the multiple-pulsing properties occurring in ultrashort pulse fiber lasers. Theoretical and experimental results emphasize on multistability and hysteresis phenomena. In Section 10.3, we consider the formation of bound states obtained with high pumping power and involving hundreds of identical solitons, especially when the soliton distribution is analogous to the periodic arrangement of atoms in a crystal. We provide in Section 10.4 recent experimental developments of HML fiber lasers, pointing out the possibility to induce HML by an external continuous component. The recent interest for complex multisoliton dynamics is covered in Section 10.5. The soliton rain dynamics, which displays some analogy with the water cycle, is presented. Dynamics analogous to various states of matter, and chaotic multiple pulse dynamics, including noise-like pulses (NLP) and dissipative rogue waves are also reported. It is evidenced that all these complex soliton patterns, which do not depend on the exact mode-locking mechanism, possess a universal character.

10.2
Multistability and Hysteresis Phenomena

10.2.1
Multiple Pulsing

Multiple pulsing is a common behavior in passively mode-locked fiber lasers, found in most laser cavity configurations [15, 62–65]. Although multiple pulsing was observed and qualitatively understood from the early days of mode-locked fiber laser experiments, the clarification of its various mechanisms required subsequent investigations [30, 32, 66]. We recall that in multipulse steady-state operation, being dissipative solitons, all pulses in a laser cavity have identical profiles and energies. Typically, an experimentalist follows the evolution of the number of solitons as a function of the pumping power, and sees that pulses appear and disappear either one by one, or by multiples, within large hysteresis domains. When the pumping power is increased, one mechanism of additional pulse generation originates from the soliton shaping of dispersive waves [64, 65]. In this process, the energy content of the dispersive waves increases significantly, while the energy of the solitons remains roughly constant. When the amplitude of the dispersive waves becomes large enough, an instability develops so that dispersive wave interaction triggers the formation of an additional soliton. This mechanism is particularly salient in anomalous-dispersion fiber lasers. Combined with low-energy soliton pulses, it favors mode-locked regimes with numerous pulses per cavity round-trip. Multiple pulsing is also strongly determined by the mode-locking mechanism that is implemented. Notably, the use of NPE mode-locking displays a nonlinear transmission function that is periodic with respect to the nonlinear phase delay. Consequently, when the peak power increases beyond a turning point, the effective saturable absorber becomes overdriven, and the corresponding high-intensity pulse part may be strongly attenuated, leading to the breaking of the pulse and to the generation of an additional soliton.

10.2.2
Multistability Observations

Let us now illustrate the observation of multistability. The experimental setup, sketched in Figure 10.1, consists of a passively mode-locked Er-doped double-clad fiber (DCF) laser, which emits at 1.5 μm [67, 68]. The cavity comprises a double-clad Er:Yb-doped fiber amplifier pumped with two counter-propagating semiconductor lasers. The pumping light is injected using the V-groove technique, allowing the coupling of multiwatt pumps into the multimode pumping core. A polarization-independent optical isolator ensures unidirectional laser oscillation. Here, the DCF and the standard SMF fiber have anomalous dispersion ($\beta_2 < 0$). In order to manage the total cavity dispersion, a piece of dispersion-shifted fiber is inserted (DSF, $\beta_2 > 0$). The different fibers are combined so that the laser operates in the stretched-pulse regime, the total cavity dispersion being slightly positive or negative, according to the DCF length. Mode-locking is achieved by nonlinear polarization evolution occurring in the fibers combined with the transmission through a polarizing beam splitter. The latter is sandwiched between a set of waveplates, thus allowing the manual control of the nonlinear transfer function. The recording shown in Figure 10.2a demonstrates that, except in the first mode-locking step when two pulses are formed, pulses appear or disappear one by one within large ranges of hysteresis, when the pumping power is, respectively, increased or decreased.

In general, the pump threshold for pulse breaking and multiple pulsing is significantly increased when the laser operation is shifted into the normal dispersion regime. Indeed, by acquiring a large frequency chirp, which tends to reduce the pulse peak power and related nonlinearity impairments, the intracavity pulse is allowed to carry a significantly greater energy. However, multipulse emission was evidenced in a fiber cavity with a normal dispersion as large as 0.68 ps^2 [69]. Although solitons appeared and disappeared one by one, unstable regions were

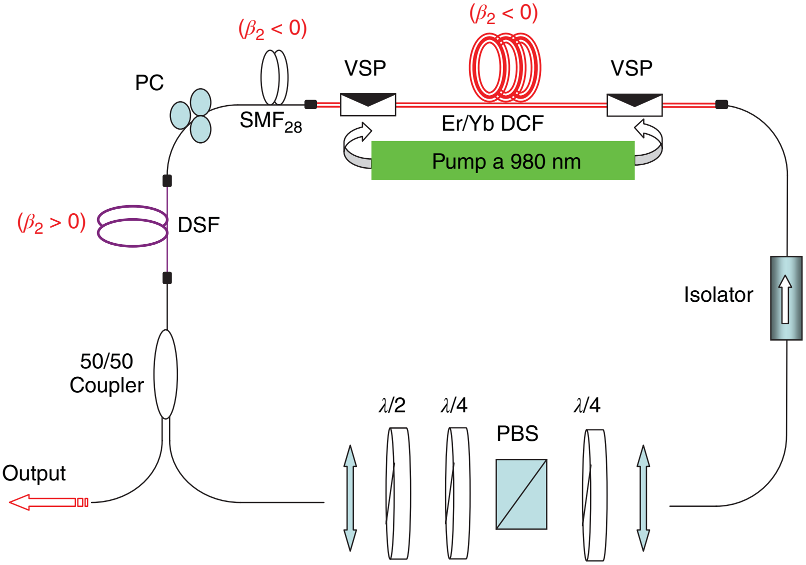

Figure 10.1 Experimental high-power fiber laser setup. PC, polarization controller; PBS, polarization beam-splitter; DSF, dispersion-shifted fiber; DCF, double-clad fiber; VSP, V-groove side pumping; SMF, standard single-mode fiber (from [67]).

identified in between successive N-soliton states, and attributed to the accumulation of an excessive pulse chirp. Even laser configurations reputed to operate in a wave-breaking-free regime, by favoring self-similar evolution, were found to promote multiple pulsing at a high pumping power [30].

10.2.3
Modeling Multiple Pulsing and Hysteresis

For a comprehensive description of the NPE mode-locking technique, it is necessary to start with a vector field model [23, 32, 70]. In the laser depicted in Figure 10.1, the field passes sequentially through a quarter-wave plate, a half-wave plate, the polarizer, and a quarter-wave plate. The orientation of the three waveplates is determined by the angles α_1, α_2, α_3, respectively (α_i is an angle of one eigenaxis of a corresponding plate with respect to the passing axis of the polarizer). The quarter-wave plate after the polarizer transforms a linear polarization into an elliptic one, so that NPE can take place. After propagation in the fibers, the direction of the elliptical polarization of the central part of the pulse can be rotated toward the passing axis of the polarizer by the half-wave plate. Then, this elliptical polarization of the central part of the pulse can be transformed into a linear one by the first quarter-wave plate. In this situation, the losses for the central part of the pulse are minimized while the wings undergo strong losses, hence producing an effective ultrafast saturable absorber effect. Starting with coupled equations for the two orthogonal field components, the

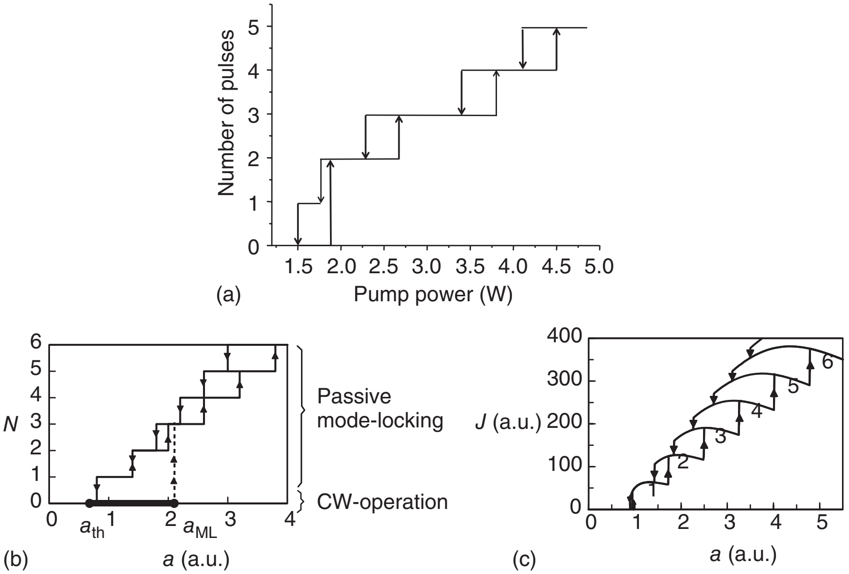

Figure 10.2 Multihysteresis of the lasing regime and number of mode-locked pulses: (a) Experimental evolution of the number of pulses N versus the pump power, in the normal dispersion regime with 0.0572 ps^2 (from [68]). (b) Numerical observation of the number N of pulses in steady-state operation versus the pumping level a in the normal dispersion regime (from [68]). (c) Dependence of the intracavity energy J on pumping a. Digits indicate the number of pulses in the cavity for the corresponding branch.

following effective scalar equation describing the evolution of the field amplitude in the fiber could be obtained [32]:

$$\frac{\partial E}{\partial Z} = (D_r + iD_i)\frac{\partial^2 E}{\partial \tau^2} + \left[G + iq|E|^2\right] E. \tag{10.1}$$

$E(Z,\tau)$ is the electric field amplitude, τ is a time coordinate expressed in units $\sqrt{|\beta_2|L/2}$ (β_2 is the second-order group-velocity dispersion and L is the total fiber length), $Z = z/L$ is the normalized propagation distance (the number of round-trips of the radiation in the cavity); D_r and D_i are, respectively, the effective averaged frequency dispersions for the gain–loss and the refractive index, and q is the Kerr nonlinearity coefficient. The amplification coefficient G is determined by

$$G = \frac{a}{1 + bJ}, \tag{10.2}$$

where $J = \int |E|^2 d\tau$ is the total intracavity energy, a is the pumping parameter, and b is the saturation one. In this model, all the physical effects taking place in the fibers are uniformly distributed over the entire cavity length. The relationship between the temporal distributions of the field before and after the nth pass of radiation through the polarizer is determined by the following scalar equation:

$$\begin{aligned} E_{n+1}(\tau) = -\eta \, & \left[\cos\left(pI_n + \alpha_0\right)\cos\left(\alpha_1 - \alpha_3\right)\right. \\ & \left. + i \sin\left(pI_n\left(\tau\right) + \alpha_0\right)\sin\left(\alpha_1 + \alpha_3\right)\right] E_n(\tau), \end{aligned} \tag{10.3}$$

where η is the transmission of the polarizer, $I(\tau) = |E(\tau)|^2$, and the parameters α_0, p are defined as $\alpha_0 = 2\alpha_2 - \alpha_1 - \alpha_3$, and $p = \sin(2\alpha_3)/3$.

This iterative procedure is repeated until a steady state is achieved. Figure 10.2b displays the evolution of the number N of identical pulses in the laser cavity, in the stationary regime, as a function of the pumping level a. While altering the pump level, pulses appear or annihilate one by one, except for the first mode-locking step, in good agreement with the experimental recording of Figure 10.2a. Thus, the laser operation is multistable: the number of pulses depends on the initial condition. The hysteresis loops tend to widen for higher pumping. The corresponding changes in the intracavity energy J versus the pump level are shown in Figure 10.2c, in qualitative agreement with experimental reports [37].

When other control parameters are used instead of the pumping power, the evolution of the number of pulses can be even more dramatic, with very pronounced hysteresis. For instance, altering the polarization controller orientation, a pulse fragmentation mechanism was observed in a fiber laser mode-locked through NPE, and numerically modeled [71].

10.3
Soliton Crystals

10.3.1
From Soliton Molecules to Soliton Crystals

When several pulses coexist inside the laser cavity, since they have virtually an infinite time to interact, even tiny forces acting between or upon them can be instrumental in generating specific pulse patterns. While in the following we restrict ourselves to the situation of passive mode-locking, we note that the external effective potentials produced by active phase modulation can lead to the formation of bound soliton states [72, 73]. Despite the denominations “soliton bound states” and “soliton molecules” are now used indifferently in the literature, there is still a nuance: molecules refer to particularly stable bound states, which are best exemplified by the self-phase-locked soliton-pair molecules [29]. The latter are made possible by phase sensitive interactions, which for dissipative systems were modeled in the frame of the CGL equation [39, 47]. Within a specific range of cavity parameters, two pulses interacting through their overlapping tails may bind at a fixed distance with a fixed relative phase. Theoretically, the potential to form a stationary soliton molecule is linked to the existence, in the dynamical system, of a point attractor whose detailed features vary with the cavity parameters.

Thus, soliton-pair molecules represent the central object of the collective dynamics of dissipative solitons, and have been found in diverse experimental configurations, emission wavelengths, and dispersion regimes. Similar soliton molecules can be formed when the interaction between pulses is mediated through a coherent wave—such as the resonant dispersive wave commonly radiated in fiber laser cavities [49]. In the latter, the reach of the interaction is considerably enhanced, allowing the binding of pulses at around 100 times their temporal width. This comes along with the multiplicity of attractors, constituting a periodic set of allowed pulse-to-pulse binding separations. Varying the cavity parameters, a Hopf-type bifurcation can take place, transforming the point attractor into a limit cycle attractor. Correspondingly, oscillating and vibrating soliton molecules can be found, strengthening further the “molecule analogy” [74].

As soon as three pulses interact, the number of scenarios becomes considerable. For instance, periodic pulse collisions resulting from the mutual exchange between a soliton pair and a third soliton can take place [75]. Even the study of three-soliton molecules becomes complex, with the possibility of forming different “isomers” of various allowed sequences for the pulse-to-pulse separations and phase differences [29, 76]. With hundreds of interacting soliton pulses, the amount of possible conformations becomes enormous. No wonder that specific conditions would preside over the regular spacing of pulses in such “macromolecules.” Since the temporal length of soliton macromolecules may become no longer negligible with respect to the response time of the gain medium, it is very likely that the slow gain dynamics impacts their distributions, entailing for instance a chirped train of pulses instead of a periodic pulse train inside of the soliton macromolecule [77]. Very strong soliton molecule attractors are required to resist the influence of the gain dynamics and other higher-order effects, so that the periodic binding of pulses is maintained over the whole macromolecule. A soliton macromolecule made of a periodic pulse train is analogous to a one-dimensional crystal. In such a case, even though the temporal periodicity may be too short to be directly measured by most photodetectors and oscilloscope settings, it will yield a clear signature on the optical autocorrelation trace as well as in the optical spectrum.

10.3.2
Soliton Crystal Experiments

The “soliton crystal” terminology was introduced by Mitschke in the case of a passive resonator [78, 79]. Here, in the context of the dissipative soliton molecules generated by passively mode-locked fiber lasers, we define it as a regular sequence of equidistant identical solitons with a constant phase relationship between adjacent pulses. Large soliton crystals, comprising hundreds of solitons, were first reported within the DCF laser configured as in Figure 10.1, operating in the anomalous dispersion regime [42]. The direct oscilloscope recording is shown in Figure 10.3a: since the electronic detection resolution is not sufficient to retrieve the internal structure of the pulse train, it displays a periodic square signal, whose

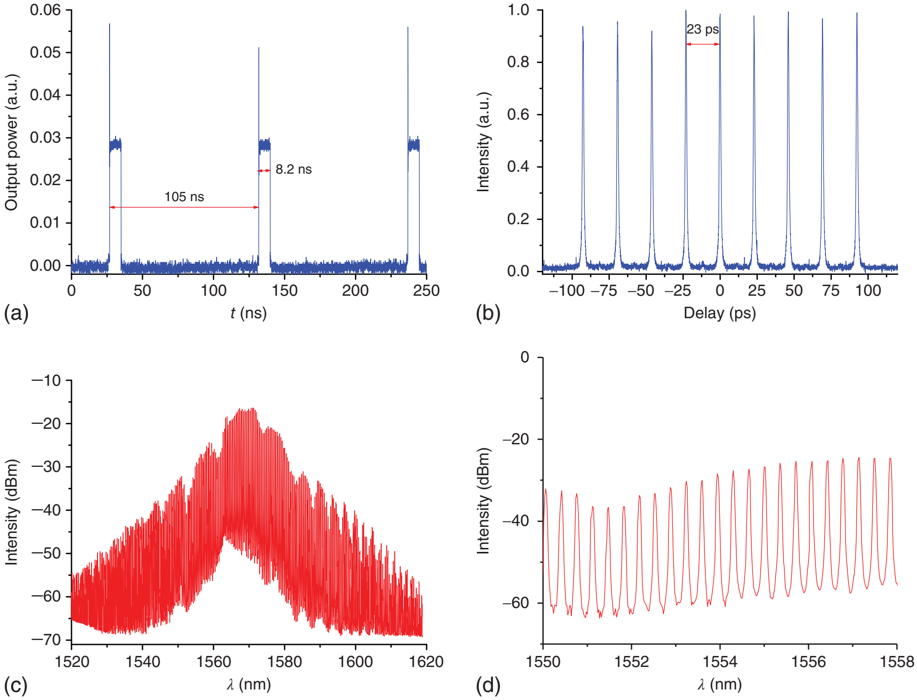

Figure 10.3 Experimental characterization of a soliton crystal: (a) direct laser output recording with a 12-GHz oscilloscope, (b) optical autocorrelation trace, (c) optical spectrum, and (d) spectral fringes of high contrast (from [42]).

period coincides with the cavity round-trip time. However, the autocorrelation trace shown in Figure 10.3b reveals the pulse train structure: the sharpness of the peaks and the absence of a continuous background prove the regularity of the periodic pulse pattern. This is corroborated by the optical spectrum, shown in Figure 10.3c and magnified in Figure 10.3d, which exhibits a fast modulation of high contrast that accounts for the periodic pulse structure along with the mutual coherence between pulses. The number of bound solitons in this structure is estimated to be 350. Soliton crystals belong to a universal class of soliton patterns, as they have also been observed in other laser configurations, such as in F8Ls, which are mode-locked through an NALM [56].

10.3.3
Modeling Soliton Crystal Formations

The experimental results clearly highlight different timescales: the pulse duration, the length of the train, and the round-trip time of the cavity. In addition, the gain relaxation is slow, with the lifetime of the upper lasing transition being much larger than the cavity round-trip time. This suggests undertaking a multiscale approach to understand the pulse pattern [80]. We first consider the spatially averaged gain g_0, which evolves according to

$$\frac{\partial g_0}{\partial \tau} = -\left(\frac{1}{\tau_g} - a\left\langle |E|^2 \right\rangle\right) g_0 + \Lambda, \tag{10.4}$$

where Λ is the pumping rate, τ_g is the gain relaxation time, and a is a coefficient related to stimulated emission. However, stimulated emission induces fast low-amplitude gain variations at the timescale of the pulse, which can be incorporated into the equation evolution for the electric field E, after following a procedure based on perturbative calculations and multiscale approach [23]. The resulting equation is a CGL equation with an integral term accounting for the fast gain dynamics:

$$\begin{aligned} i\frac{\partial E}{\partial Z} &= ig_1 E + \left(\frac{\beta_2}{2} + i\rho\right)\frac{\partial^2 E}{\partial \tau^2} + (B_r + iB_i)|E|^2 E \\ &\quad - GE\int_{-\infty}^{\tau} \left(|E|^2(t') - \langle |E|^2 \rangle\right) dt', \end{aligned} \tag{10.5}$$

where g_1 (positive) is an excess gain needed to compensate for nonlinear losses, and $G = g_0 a[\exp\ (2g_0L) - 1]/2g_0L$ is the linear gain. B_r and B_i represent the effective nonlinear index and nonlinear gain coefficients, respectively: they depend on the orientation angles of the intracavity phase plates, and can be largely altered by the rotation of a single-wave plate [23]. β_2 is the group velocity dispersion, and $\rho = g_0/\omega_g^2$, where ω_g is the spectral gain bandwidth. In numerical simulations, we used $\beta_2 = -0.002$ ps^2 m^{-1}, and $\omega_g/2\pi = 2.5$ ps^{-1}. The fast gain dynamics is involved in the periodic pulse train formation: the numerical solving of Eq. (10.5) demonstrates the evolution toward a stable steady-state pattern that is periodic in time, as displayed in Figure 10.4. Starting from a wide range of initial conditions, pulses acquire the same profile, then become phase-locked and get equally separated.

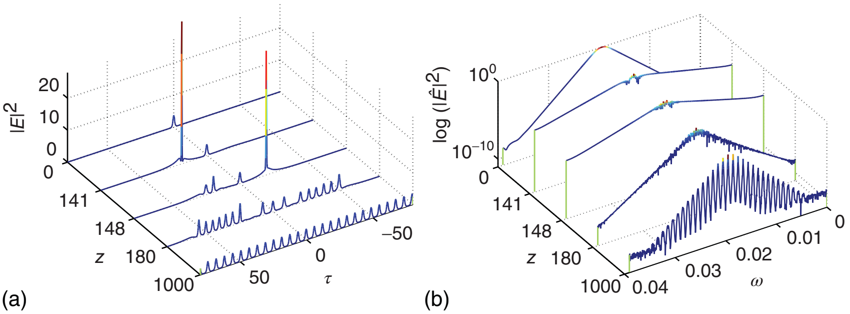

Figure 10.4 (a) Numerical simulation of the soliton crystal buildup: (a) optical intensity, and (b) optical spectrum, versus the round-trip number.

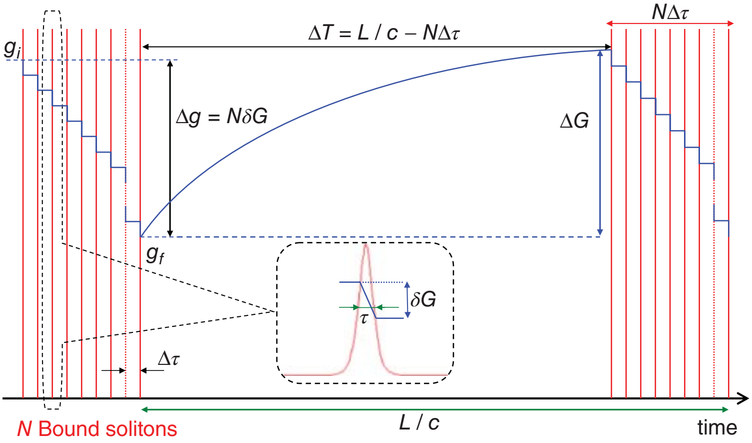

Figure 10.5 Schematics of the gain evolution during a cavity round-trip. Each of the *N* pulses takes off an amount of gain δG, and after the pulse train, pumping restores the amount ΔG (from [35]).

To understand the finite length of the pulse train observed in the experiments, we can invoke the role of the slow gain dynamics, as soon as the pumping rate contribution between subsequent pulses is weaker than the pump depletion after one pulse passing through the gain medium. This scenario is depicted in Figure 10.5: while each pulse slightly depletes the gain, the latter is recovered after the end of the pulse train, owing to the positive balance between pumping and relaxation in Eq. (10.4). This dynamical balance entails the finiteness of the pulse train, as the formation of subsequent pulses is expected to stop when the gain goes below some threshold. Within this description, the buildup of a soliton crystal filling the entire cavity seems precluded. This fact is consistent with the experimental reports so far, where the buildup of stable and compact laser soliton crystals did not lead to a cavity filling greater than 20% of the round-trip time. However, we know that there are other ranges of parameters that favor HML, where all pulses are equally distributed along the cavity [81]. We conjecture that certain regimes of soliton crystals should also be compatible with HML, hence providing the passively mode-locked fiber laser cavity with an unprecedented stability and ultrahigh repetition rate, in contrast to the usually strong timing jitter observed in harmonic passively mode-locked lasers.

It is important to note that similar soliton crystals of limited extension can be numerically obtained with the model presented in Section 10.2, which does not include the gain relaxation dynamics [43]. For a suitable orientation of the phase plates, the model predicts large binding energies between solitons. This results in the formation of particularly stable long trains of bound solitons, which nevertheless do not fill the entire numerical grid [82]. As the extent of the crystal increases with the pumping power, it may eventually fill the entire laser cavity, leading to harmonic passive mode-locking [43]. The repetition rate of the bound-state harmonic mode-locked laser is predicted to reach the terahertz repetition rate, in the case of tightly bound subpicosecond pulses.

10.3.4
Soliton Crystal Instability

Stimulated by the above predictions, power-scaling fiber laser experiments were conducted with a 40-dBm (maximum output power) DCF amplifier [61]. At a pumping power of 15 W, the laser delivered a soliton crystal containing as many as 930 solitons. However, when the pumping was increased to 25 W, the soliton crystal underwent a rapid dislocation. The final soliton distribution, shown in Figure 10.6, consists of 50 nearly equidistant soliton packets of approximately the same duration. Each packet is a small soliton crystal comprising around 50 solitons. The total number of solitons is, therefore, about 2500. So, in practice, it appears that a soliton crystal of very large extent suffers from an intrinsic instability. This observed instability tends to demonstrate that for large crystals, the gain relaxation dynamics cannot be ignored [50, 83]. In fact, for certain parameters, gain relaxation dynamics has been shown to directly impact the internal structure of soliton macromolecules, leading to chirped soliton trains, namely, soliton molecules where the separation between subsequent pulses increases along the pulse train [77]. However, recent experiments may provide a hint to circumvent the instability of long soliton crystals. Indeed, a small CW component frequently appears in the spectrum of harmonically mode-locked

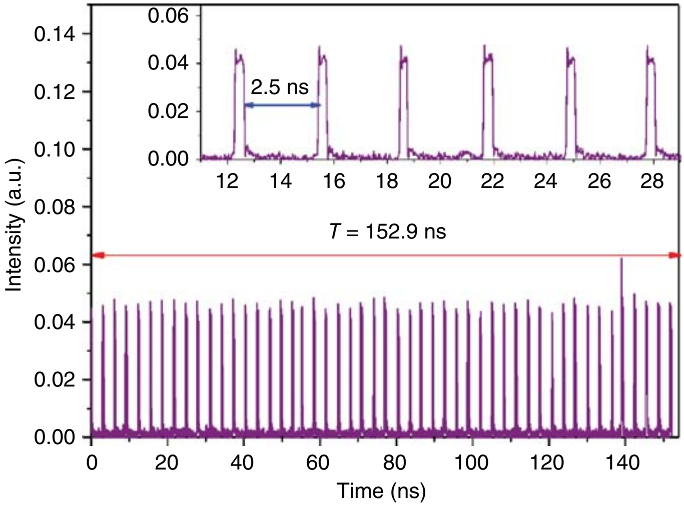

Figure 10.6 Harmonic soliton crystal mode-locking, obtained after dislocation of a long soliton crystal at a pump power of 25 W. Each square pulse of the inset is in fact a minicrystal of pulses (from [61]).

lasers. It is anticipated that this component could mediate the rearrangement of numerous solitons along the cavity [54, 55]. This topic is introduced in the following section.

10.4
Toward the Control of Harmonic Mode-Locking by Optical Injection

With solitons equally distributed along the whole fiber laser cavity, HML represents an attractive regime with the potential to reach a very high repetition rate combined with a high average output power. HML can be obtained in either active or passive mode-locking. Active techniques greatly reduce the temporal fluctuations induced by the amplified spontaneous emission noise and by the complex interaction processes between pulses. For instance, an intracavity electro-optic modulator can modulate the loss at a multiple of the fundamental cavity frequency [84]. In the following, we focus on passive HML resulting from repulsive soliton – soliton interaction. Passive HML has the potential to produce ultrahigh repetition rates that are not limited by the speed of electronic modulators, and its demonstration does not require the stabilization of the cavity length [81, 85 – 88]. Repetition rates largely exceeding the gigahertz are commonly obtained with a high supermode suppression.

Besides, another category of HML is based on a repetition of a basic pattern containing several solitons, such as soliton bunches and twin-pulse solitons [60, 89]. Even HML of complex structures can be obtained, such as that of NLPs [90], soliton crystals [61], and soliton rains [58, 91].

HML is a common operating regime for passively mode-locked fiber lasers, which occurs spontaneously for certain sets of cavity parameters, which imply the dominance of repulsive pulse-to-pulse interactions, such as those entailed by the gain depletion and recovery dynamics [50, 83]. In practice, it is found by varying manually some control parameters, such as the orientations of polarization controllers and the pumping power.

Surprisingly, in many HML fiber laser experiments, a CW component was noticed in the optical spectrum, suggesting that this component could play an important role in related HML mechanisms [61, 87, 88, 92]. However, it was theoretically shown that a small CW component allowed controlling the nature and the strength of the soliton interaction [93]. The conjunction of this theoretical result and the presence of a CW component in HML regimes suggest that an injected CW could modify the nature of soliton interactions, and possibly control the soliton distribution.

The latter has been addressed experimentally with a passively mode-locked DCF laser, very close to the configuration of Figure 10.1, except that it is all-fibered and that the amplifying medium is a 10 W DCF amplifier [53]. The external CW was provided by a tunable continuous-wave Er:Y-doped fiber laser injected into the main laser through a fiber coupler. Starting from different initial soliton distributions, it was shown that the presence of the injected CW component modified the

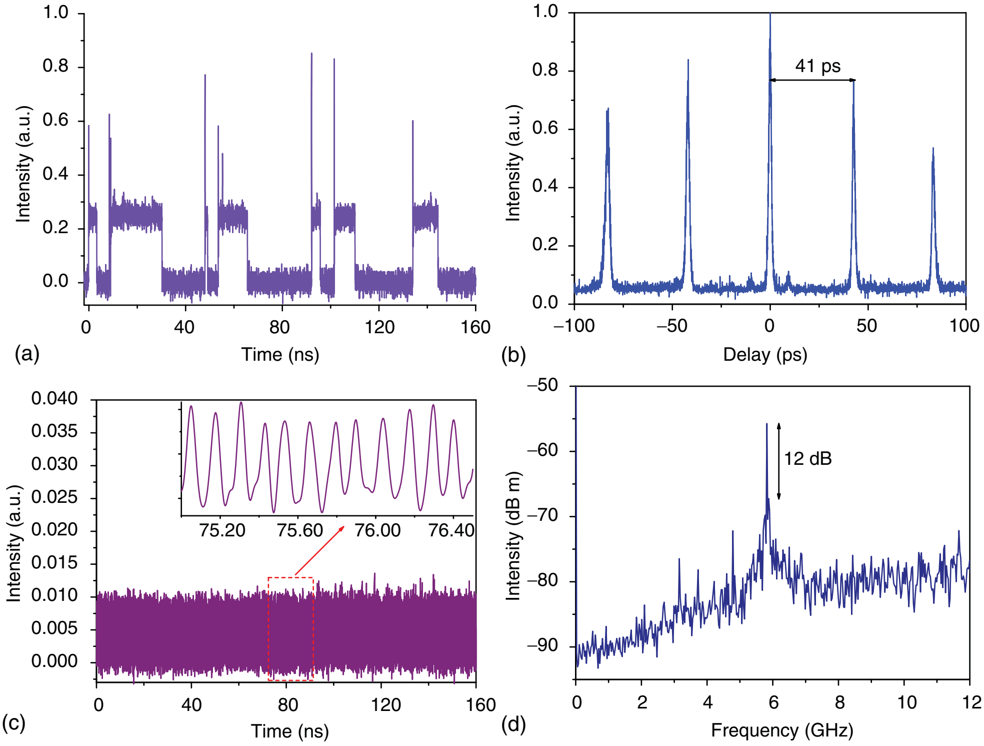

Figure 10.7 Initial soliton distribution (a) temporal oscilloscope recording, (b) optical autocorrelation trace. After applying the external injection, an HML regime is obtained: (c) temporal oscilloscope recording, and (d) RF spectrum (from [53]).

initial soliton pattern, depending on both the wavelength and the power of the injected signal. The most relevant results are summarized as follows.

The initial soliton pattern considered in Figure 10.7a is a stationary pattern comprising well-separated soliton packets. The autocorrelation trace of Figure 10.7b suggests that the soliton packets contain bound states or soliton crystals, with a typical separation of 41 ps between adjacent pulses. This is also corroborated by the optical spectrum, exhibiting a strong modulation with a period is 0.2 nm, whose structure is similar to that of Figure 10.3c.

When the injection laser is switched on and its wavelength tuned within the spectral width of the mode-locked laser, the soliton distribution becomes strongly affected. First, the spectral modulation disappears, indicating that the CW component breaks the coupling between solitons in tightly bound states. The final state, obtained for well-defined wavelength and power of the injection laser, is shown in Figure 10.7c. It consists of identical (if we extrapolate from the electronic noise) and equidistant solitons: the injected laser operates in an HML regime. The effect of the external CW component is, therefore, to induce a long-range repulsive interaction needed for HML. We can note that this phenomenon is reversible [53]. Indeed, if the power of the injection laser vanishes, the initial soliton pattern is restored, but when the injected power is set to its initial high level, the HML regime is retrieved. HML is also pointed out through the radio frequency (RF) spectrum given in Figure 10.7d. The harmonic repetition rate of the laser is 5.82 GHz, corresponding to the 945th harmonics, with a supermode suppression ratio of 12 dB.

These experimental results demonstrated that, in addition to the gain depletion and recovery [50], a CW component could induce a long-range repulsive interaction between solitons, which has to be taken into consideration in the modeling of HML. This stimulated additional theoretical investigations about the interaction between an external CW and dissipative solitons in a passively mode-locked fiber laser. Two theoretical approaches with different levels of complexity were developed. The first one used a scalar distributed model [54], based on a universal master equation [34]. It demonstrated that the injection of a CW component allowed the control of the soliton distribution, with the multisoliton pattern altered by tuning the CW frequency. Soliton crystal, gas, and liquid states were also retrieved numerically. The second theoretical model used a vectorial approach, taking precisely into account the mode-locking mechanism, with distributed gain and Kerr nonlinearity, as well as lumped polarization elements [55].

The mechanism of interaction is summarized as follows. The periodic propagation of a dissipative soliton through lumped intracavity elements generates dispersive waves, which resonantly interact with the soliton to form powerful extended temporal wings, corresponding to narrow high-amplitude spectral soliton sidebands [49]. This impacts the interaction between the injected CW and an individual soliton, as well as the interaction between solitons. First, the resonant interaction between the injected CW and the soliton occurs when the frequency of the CW falls within the spectral sideband of the soliton. Second, the resonant interaction between the injected CW and the dispersive soliton wing produces a resultant wave that modifies the motion of other solitons. Indeed, when the injected CW and the dispersive wing of a given soliton interfere destructively, this produces a monotonic change of the intensity of the resultant CW along the fiber cavity. This intensity gradient alters the velocity of neighbor solitons, leading to a repulsion between adjacent solitons. It is, therefore, possible to control the long-range interaction between solitons through the frequency tuning of the injected CW. Thus, it was possible to simulate numerically the transition from a bound soliton regime to passive HML, in good qualitative agreement with the experiments exposed previously. The simulated range of the repulsive interaction was about 100 times an individual soliton width [55], which is consistent with experimental data [53]. Note that the CW frequency tuning range allowing HML is narrow, about 1% of the spectral gain bandwidth. In addition, the model predicts a threshold value for the injected power above which HML locking occurs. Both results are consistent with the experimental results [53].

10.5
Complex Soliton Dynamics

10.5.1
Unfolding Complexity

Starting from the conventional single-pulse mode-locking, and having realized that mode-locked laser pulses follow dissipative soliton dynamics, there are two ways to unfold the complexity of the short-pulse cavity dynamics [4]. One way is to increase the number of pulses, as was developed in the previous two sections. The other way is to explore the bifurcations of the dynamics. For instance, period-doubling bifurcations, or period-N bifurcations in general, can take place when cavity parameters are varied. Hopf-type bifurcations will trigger pulsating states, with various pulsation types and timescales that are generally not commensurate with the cavity round-trip time. Transitions toward chaotic states can also take place, and their diversity goes well beyond the archetypal route to chaos linked to a cascade of period doubling bifurcations. Chaotic states that remain localized as short pulse packets traveling ceaselessly round the cavity are of great interest. They comprise solitons of exploding type and NLP regimes, which are actively investigated experimentally and numerically.

When the two ways to unfold complexity are combined, we find vibrating soliton molecules, and other pulsating soliton molecules, including periodic collisions and bounces between them. Dealing with large number of solitons, we can find interesting analogies with the states of the matter, as developed in Section 10.5.2. Multiple soliton interaction in the presence of a noisy background can lead to the peculiar "soliton rain" dynamics, detailed in Section 10.5.3. Chaotic pulse bunches feature among the most complex multisoliton dynamics found to date, and the notion can be extended to NLPs. Some of these dynamics have shown a clear relationship with the generation of optical rogue waves. These chaotic dynamics are presented in Section 10.5.4.

10.5.2
Analogy Between Soliton Patterns and the States of Matter

Considering the self-organization of numerous interacting individual constituents, we can make interesting analogies between soliton patterns and the states of matter. Mitschke introduced the notion of a transition between a soliton gas and a soliton crystal, in the case of a passive cavity [94]. In addition to soliton molecules, macromolecules, and crystals exposed in the previous sections, we now consider other distributions such as soliton gas and supersonic gas flow [59], soliton liquid [57, 59], and even more complex settings such as complex soliton polycrystals [59] and soliton rain [57].

The soliton supersonic gas flow is the analogous description of the HML regime presented in the previous section. Indeed, there is some amount of timing jitter among the pulse distribution that is less periodic than the distribution of solitons in a soliton crystal. This is reflected in the limitation of the supermode suppression ratio, as shown in Figure 10.7d. The statistical distribution of the timing jitter can compare with the distribution of relative velocities in a supersonic gas flow, yielding an effective temperature equivalent analogy [59].

Let us illustrate the soliton gas, liquid, and polycrystal states with the experiments performed using the experimental setup of Figure 10.1, in the anomalous dispersion regime ($\beta_2 L = -0.04\ \text{ps}^2$) that favors multiple pulsing with hundreds of solitons under high pumping power. When numerous solitons are in ceaseless random motions and occupy the whole cavity, the state can be dubbed a “soliton gas.” The soliton gas is a commonly observed regime in multipulse fiber lasers. Figure 10.8a provides a snapshot example of the time-distribution of 380 solitons along the cavity. The average separation between adjacent pulses is about 230 ps, with a large variance of 207 ps [59]. Note that the high-intensity peaks correspond to adjacent solitons that are not resolved within the 12-GHz bandwidth of the oscilloscope, whereas the majority of peaks share the same amplitude, as expected from dissipative solitons having the same energy for given cavity parameters.

Starting from this situation, by adjusting the mode-locking waveplates, the soliton gas undergoes a phase transition that is similar to condensation. The 15-ns-long condensate shown in Figure 10.8b fills around 15% of the cavity. Since solitons and groups of solitons still have important motions inside the condensate, between successive cavity round-trips, the condensate is analogous to a liquid of solitons.

Adjusting further the orientation of the polarization controllers, the condensed state freezes: the temporal distribution becomes constant between subsequent round-trips. We then have a solid state of clustered solitons. The two insets of Figure 10.9a show the lack of a long-range order. However, the optical spectrum of Figure 10.9b exhibits a regular modulation that reveals a degree of mutual

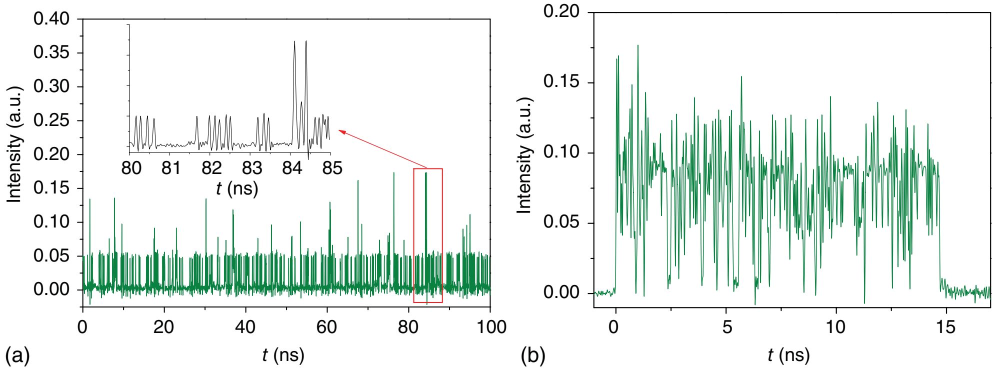

Figure 10.8 Snapshot of the temporal soliton distribution in (a) a soliton gas and (b) a soliton liquid (from [59]). These distributions change from one round-trip to the next.

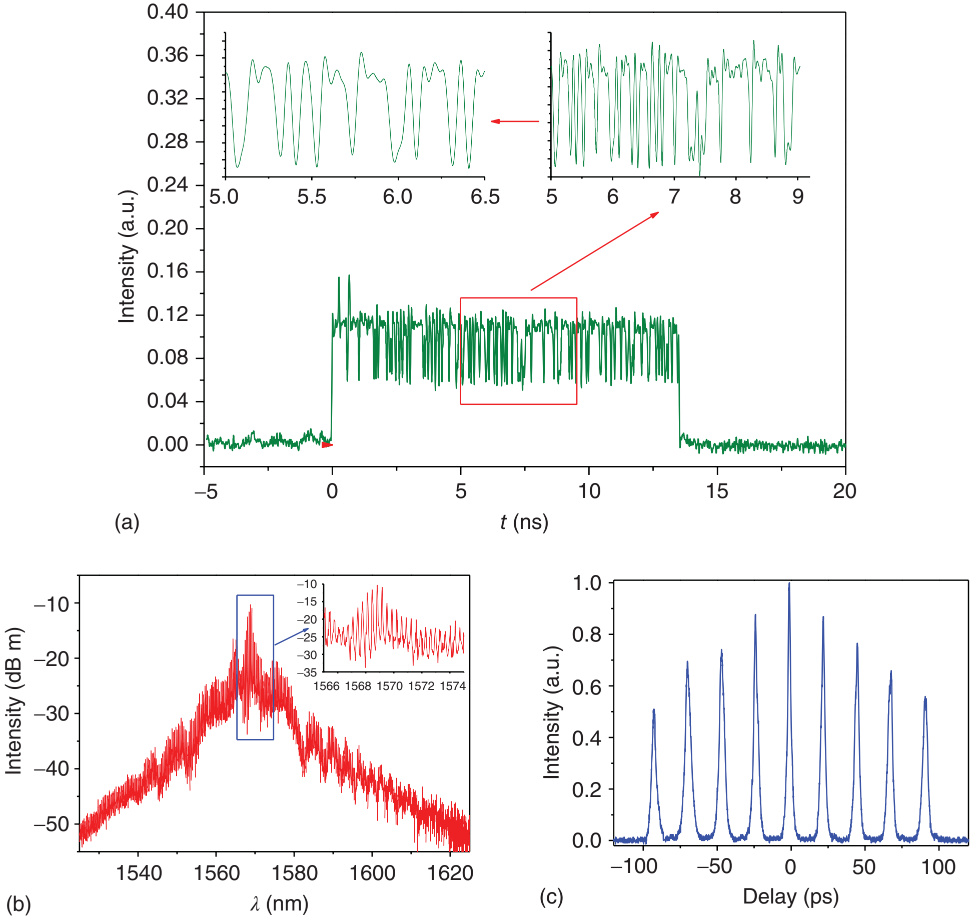

Figure 10.9 Soliton polycrystal. (a) Temporal distribution, (b) optical spectrum, and (c) optical autocorrelation trace (from [59]).

coherence between pulses, with a dominant separation of 23 ps, which is confirmed by the autocorrelation trace of Figure 10.9c. Despite the limited scanning range of the autocorrelator, the averaged number of regularly clustered pulses is estimated to be 8, whereas the total number of pulses in the solid condensed phase is around 520. Hence, the state is dubbed a “soliton polycrystal,” which exhibits precise order at the scale of few pulses but no periodic structure at the scale of the round-trip period. The soliton polycrystal can be viewed as an incoherent superposition of soliton microcrystals containing various numbers of self-phase-locked bounded pulses.

Soliton gas, liquid, polycrystal, and crystal states have also been observed in an F8L configuration, mode-locked with an NALM, strengthening the idea of universal collective dissipative soliton behaviors [56, 95].

10.5.3
Soliton Rain Dynamics

Soliton rain can take place when a soliton liquid phase coexists with a noisy CW background. Such coexistence is puzzling, since solitons are formed through the action of a saturable absorber, which is expected to filter out efficiently low-amplitude CWs. However, we have seen that solitons radiated dispersive waves through their permanent reshaping along the cavity links. In addition, NPE-based mode-locking offers a wide range of nonlinear transfer functions, by simply adjusting the polarizer controllers. Thus, it is possible to find cavity parameters entailing a weak effective saturable absorber, where the CWs are not efficiently filtered out, in the presence of intense soliton radiation. Such a weak mode-locker may also allow other CW components, which are reminiscent of nonmode-locked states, to survive and coexist with the soliton pulses. Consequently, the combination of all CW components will produce a highly multimode incoherent background, with large temporal fluctuations.

If we assume that at some time, the CW fluctuations will exceed the threshold at which a dissipative soliton can be formed, it entails that additional pulses will be effectively created in a random fashion inside the laser cavity. However, we know that a single soliton will generally have a different group velocity than that of soliton molecules and tight pulse bunches [71]. This can be interpreted in the spectral domain, by realizing that the centers of mass of their spectra are slightly different [96]. Then, the action of the nonzero averaged cavity dispersion will produce a relative drift motion—note that more complex interaction processes can also be involved. When the drift velocity is as low as a few meters per second, the whole dynamics can be monitored in real time on an oscilloscope, procuring a dramatic play of the interactions that take place in the laser cavity.

Soliton rain is a particularly vivid scenario, where new solitons formed at random times and various locations drift at a nearly constant relative velocity until they reach and become absorbed by the soliton liquid phase. Since the total number of solitons cannot grow indefinitely, but should fluctuate around an average value instead, the radiation of the liquid soliton phase is temporarily increased after the absorption of incoming solitons, producing a subsequent disappearance of a few solitons among the liquid soliton phase [97]. The whole process, which is quasi-stationary, was discovered with the Er-doped fiber laser setup sketched in Figure 10.10a [57]. The all-fiber laser was operated in the anomalous dispersion regime, with a relatively large pumping power in the range 400 – 800 mW, allowing the simultaneous circulation of around 40 dissipative soliton pulses in the cavity. The soliton rain dynamics was then selected among weakly mode-locked regimes, where both solitons and CW coexisted, by a precise adjustment of the fibered polarization controllers (PC) [57]. This coexistence is reflected in the optical spectrum of Figure 10.10b, which shows that the spectral power is shared about equally between CW and soliton components. Figure 10.10c provides a stroboscopic recording of the cavity output intensity at 50 Hz, highlighting the self-formation of solitons from the fluctuating background. In the moving frame of

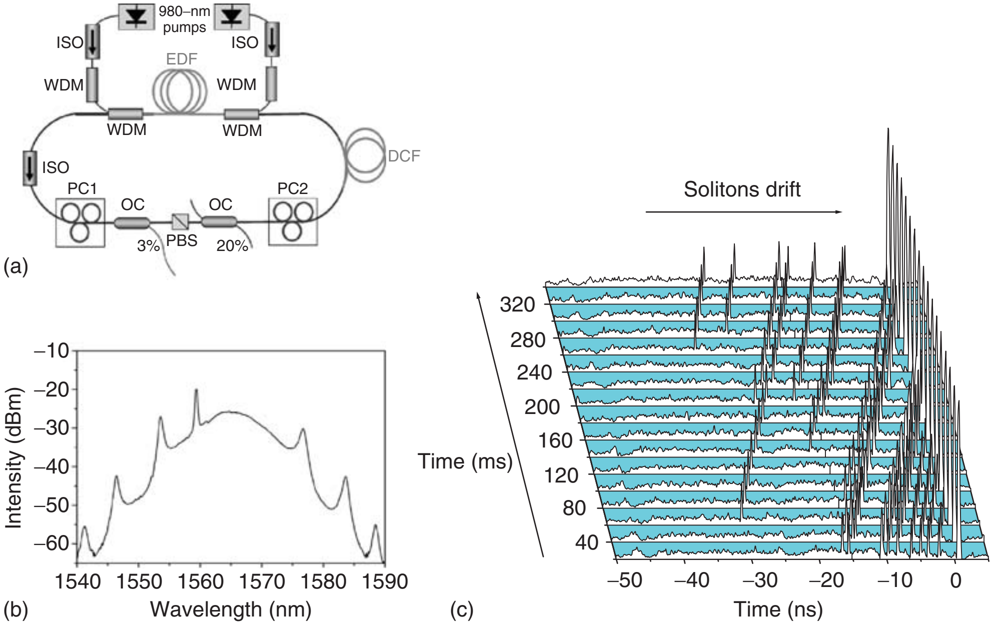

Figure 10.10 Soliton rain dynamics: (a) fiber laser setup. EDF, erbium-doped fiber; WDM, wavelength division multiplexer; ISO, polarization insensitive optical isolator; PBS, polarization beam splitter; PC, polarization controller; OC, output coupler; DCF, dispersion–compensation fiber. (b) Typical soliton rain optical spectrum. (c) Oscilloscope stroboscopic recording of the laser output intensity. The three "soliton rain" components, namely the noisy background, drifting solitons, and the large peak representing the liquid soliton phase, clearly appear (from [58]).

the liquid soliton phase, the individual solitons drift toward later times at a nearly constant velocity, here of the order of 2 meters per second, until they collide with the liquid phase. The structure of the latter is not resolved in this picture, resulting in a peak of high amplitude, which reflects the number of solitons it contains. The whole scenario can go on indefinitely, in a way that resembles the cycle of water in natural environment, the noisy background being as a vapor cloud from which raindrops coalesce and fall down. Radiation from the liquid soliton phase is analogous to evaporation, and the whole process is made possible owing to the continuous energy supply from the pump, analogous to the action of the sun.

Close-up views of the solitons impinging on the liquid soliton phase, and the subsequent soliton rearrangements and radiation, were obtained with a 45-GHz real-time oscilloscope and photodiode recording device. One example is provided in Figure 10.11. The analysis reveals that the liquid phase first absorbs the incoming solitons, processes major rearrangements, and then a comparable number of solitons vanish from the liquid in a timescale of the order of 100 ms.

There is a noise threshold, above which intensity fluctuations are amplified to form drifting solitons. When one lowers the pumping power to reduce

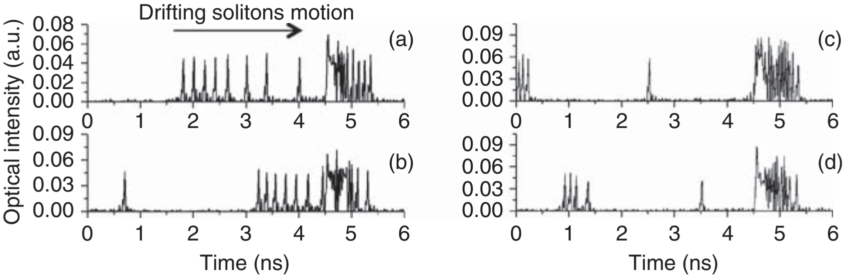

Figure 10.11 (a–d) Successive snapshots, separated by 40 ms, of the temporal close-up view of the drifting solitons impinging on the liquid soliton phase (from [97]).

the fluctuations below the threshold, the soliton rain ceases. Just below that threshold, the soliton rain can be triggered by the injection of an external CW laser, as was demonstrated in [57]. In the frame comoving with the liquid soliton frame, soliton rain possesses the characteristics of an excitable system (see the chapter from Parra-Rivas *et al.*): it has a given threshold, a well-defined response profile above threshold—the dissipative soliton pulse—and features a relaxation of the medium—due to the pulse drift. On the contrary, augmenting the pumping power so that the increased fluctuations frequently cross the threshold, “heavy soliton rain” can be experienced, with flow of drifting pulses dense to the extent that they start interacting among themselves during the drift time. In parallel, the liquid soliton phase increases with the pumping power, and at some point, may split into several liquid phases. In the latter condition, cavity harmonics of the soliton rain dynamics were observed [58].

Although operation in the anomalous dispersion regime provides the easiest access to the multiple pulsing that is required in soliton rain, similar dynamics could be observed with fiber ring lasers operated in the normal dispersion regime [98, 99]. Soliton rain was also reported in a figure-of-eight fiber laser [91]. These observations indicate that soliton rain, despite its peculiar complexity, represents a universal class of laser cavity dynamics.

10.5.4
Chaotic Pulse Bunches

As a pulsed laser cavity dynamics, chaotic pulse bunching appears paradoxical. Although its constituent pulses are so unstable that their shapes fluctuate continuously, the chaotic bunch of pulses maintains its overall integrity, as a well-localized entity that travels ceaselessly round the laser cavity.

Such a peculiar dynamics was unveiled from a fiber laser experiment reported in 1997 [100] and was then coined *noise-like pulse* dynamics. NLP dynamics were found to be quite generic in fiber laser cavities, even though a long cavity and a high pumping power were identified as particularly conducive factors [101–103]. For more than a decade, the lack of real-time characterization techniques adapted to the short timescales involved in the NLP dynamics increased the sense of mystery about this dynamics and its physical origins.

Involving time-averaged measurements, NLP is characterized by a wideband optical spectrum, which may exceed the bandwidth of the gain medium, highlighting the importance of nonlinear spectral broadening in the propagation dynamics. In a few experiments, the decisive interplay of the Raman effect could also be singled out [90, 104, 105]. The—averaged—optical autocorrelation trace displays an ultrashort coherence peak, which reflects the typical temporal granularity that is internal to the pulse bunch, sitting on a large pedestal, the latter reflecting the whole temporal extension of the noise burst.

Numerical simulations provide a clear insight into NLP or chaotic-pulse-bunch dynamics, as illustrated in Figure 10.12. In contrast to liquid soliton phases, it is not possible to follow individual pulses over long evolution times, as they collide, merge, or disappear rapidly. The displayed simulation was based on a rather simple fiber laser scalar model, which series pulse propagation through a normally dispersive fiber gain medium, an anomalous-dispersion passive fiber, a lumped saturable absorber and an output coupler [106]. A key result is that no birefringent or Raman effects are required to find chaotic pulse bunch regimes, in contrast to initial speculations.

The previous numerical simulations were also used to predict the occurrence of wave events of extreme amplitude, which belong to the class of dissipative optical rogue waves [106]. The "rogue wave" terminology originates from oceanography, where the tales of mariners' encounters with giant waves have been reconsidered positively through recent surveys, systematic recordings, and scientific modeling [107]. Waves whose amplitude is greater than twice the average of the one-third highest waves qualify as rogue waves (abnormality criterion), provided that they are formed and disappear unexpectedly, with the additional condition that their occurrence would be higher than the occurrence deduced from a

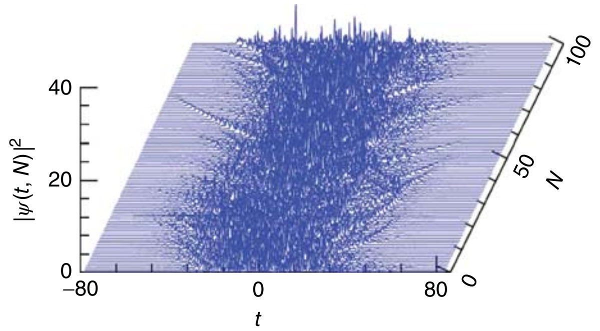

Figure 10.12 Numerical simulation of a noise-like pulse behavior in a fiber ring laser. The intracavity optical intensity is plotted, in dimensionless units, versus the cavity time t, for successive round-trip numbers N. The chaotic bunch of pulses, through nonlinear collisions, produces transient pulses of extreme intensity, akin to optical rogue waves (from [106]).

classical statistical distribution, such as a Gaussian one. The study of rogue waves has diffused into major areas in physics, including optics [108], where the fast dynamics have shown to be particularly advantageous to collect significant statistics in a reduced lapse of time. Note that in optics, since it is the field intensity that is directly recorded, and not the field amplitude, the quasi-totality of experimental papers apply the rogue wave abnormality criterion to the optical intensity measure, instead of applying it to the field amplitude.

Since the timescales of chaotic bunches may vary widely with the cavity parameters, it has been possible to find regimes where the internal pulse dynamics could be partially resolved in real time, using a high-speed detection scheme of 20-GHz electronic bandwidth [109]. The laser setup used was that sketched in Figure 10.10a. The capture of one extreme event is portrayed in a stroboscopic way by Figure 10.13a, using the recording of successive temporal intensity traces. The internal structure of the chaotic bunch is only partially resolved, with a temporal resolution of the order of 40 ps, whereas the temporal granularity indicated by the optical autocorrelation is of the order of 0.5 ps [109]. However, with a bunch duration of the order of a nanosecond, the temporal resolution allows to reveal rogue wave dynamics internal to the chaotic bunch. The probability distribution function (PDF) of the intensity maxima, for successive round-trips recorded over several hours, is displayed in Figure 10.13b: it features a heavy tail distribution, exceeding Gaussian statistics, with numerous events satisfying the three rogue wave criteria listed earlier. These extreme wave events are the consequences of nonlinear collisions that are internal to the pulse bunch. They do not result from a global cavity energy surge, as can be observed in *Q*-switched mode-locked regimes [110].

Most of the chaotic bunch of pulses produced by fiber lasers are not resolved in the time domain, the temporal resolution of the electronics detection being larger or equal than the bunch duration, with the latter in the range of tens of picoseconds, for instance. In such cases, to get beyond time-averaged measurements, a recent real-time characterization technique can be applied: the dispersive Fourier-transform technique (DFT) [111]. The DFT consists of sending the attenuated

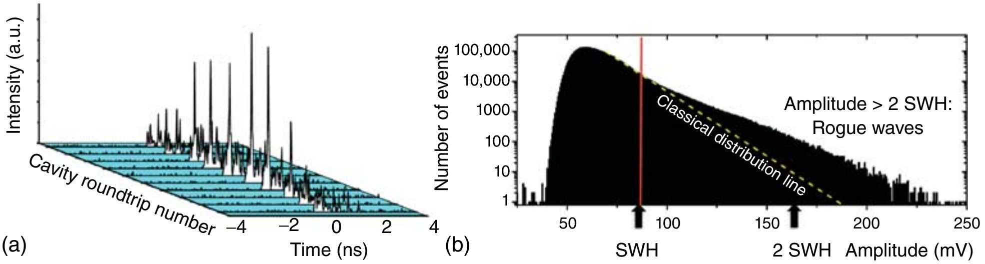

Figure 10.13 (a) Example of the stroboscopic recording of a rogue wave event at the laser output, with a 20-GHz electronic bandwidth. (b) Probability distribution function of the output optical intensity maxima, recorded as voltage amplitudes (in millivolt) by the 20-GHz oscilloscope (from [109]).

laser output pulses through a long dispersive line, in a linear propagation regime, so that the spectrum of each pulse is mapped into a temporal waveform, owing to the large accumulated dispersion. This way, shot-to-shot spectral fluctuations can be analyzed, with the guideline that observed spectral fluctuations are linked to the temporal dynamics internal to the NLP chaotic bunch [112].

The fiber laser of Figure 10.10a can produce NLP regimes featuring chaotic pulses that are a few tens of picoseconds long, and propagate in a quasi-stationary fashion round the cavity, in either anomalous or normal average chromatic dispersion regimes [113]. Obviously, the shorter the temporal scaling of the NLP emission, the larger is the generated spectral bandwidth. In particular, operation in the anomalous average dispersion regime has allowed the generation of 10-ps-long chaotic pulses, with an ultrashort temporal granularity of around 50 fs, which is illustrated by the optical autocorrelation trace of Figure 10.14a. The regime is associated with an average spectral width as large as 90 nm, well beyond the bandwidth of the Er-doped fiber gain medium. It is known that it is possible to exceed the gain bandwidth limitation by allowing the pulses to undergo a strongly modulated internal dynamics, where self-phase modulation (SPM) plays a key role, especially in the anomalous dispersion segment of the cavity [5]. This way, NLP in the anomalous dispersion regime can originate from the interplay between SPM, dispersion, and gain, when single plain pulses are unstable owing to the excess of SPM that entails pulse breaking over a short propagation distance.

The DFT technique is used to record successive single-shot spectra, revealing the high amount of spectral fluctuations that reflect the chaotic temporal dynamics, as illustrated in Figure 10.14b. Some isolated spectral events are also highly frequency shifted, which resembles a feature of soliton explosion dynamics [114], but unlike the latter, there is no recovery of quiet dynamics in between extreme spectral events. We can notice some similarity with the dynamics of supercontinuum generation, which produces highly fluctuating distorted spectra, in contrast to the relatively smooth averaged spectra that are generally presented in experimental articles. The reality of highly fluctuating spectra also reflects the low coherence level of these sources, with a total lack of coherence between successive cavity round-trips [112]. By recording the spectral maximum for each round-trip, and constructing a histogram of these maxima, it is possible to obtain a specific measure of spectral fluctuations. As highlighted by Figure 10.14c, the PDF features a heavy-tail distribution that satisfies the abnormality criterion of rogue waves. This way, spectral rogue waves have been found from the detailed characterization of NLP generation [113]. It has been conjectured that these spectral rogue waves are the observable counterpart of the temporal rogue waves that remain beyond direct measurement. Chaotic NLPs are also frequently observed in the normal dispersion regime, and in some situations, they can lead to rogue wave formations too [115, 116].

These studies have allowed to connect NLP emission to rogue wave dynamics, or more precisely, to show a significant overlap between the two domains of chaotic dynamics [113, 116].

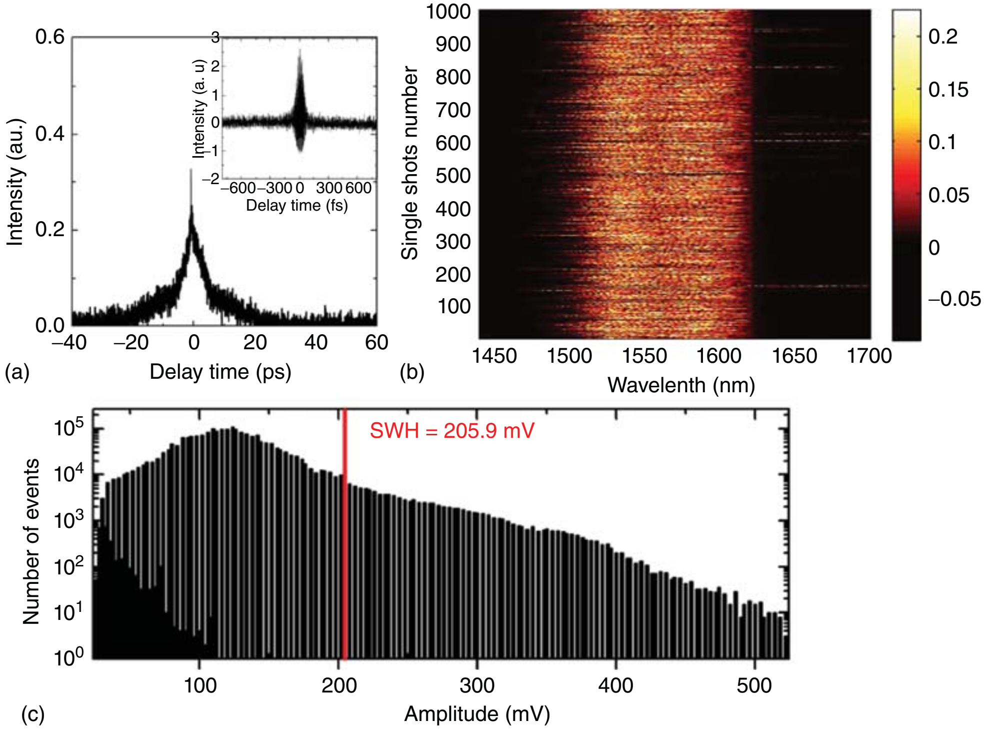

Figure 10.14 Characterization of a noise-like pulse regime obtained with the setup of Figure 10.10a, in the anomalous dispersion regime under 700-mW pumping. (a) Averaged (i.e., multishot) optical autocorrelation trace, and (b) series of successive single-shot optical spectra obtained with the dispersive Fourier-transform measurement technique, in color scale. The statistical distribution of the spectral maxima, recorded in millivolt by a 6-GHz oscilloscope, is displayed (c), revealing a heavy-tailed distribution that is a feature of rogue wave dynamics (from [113]).

10.6
Summary

Multiple pulse dynamics, even when it reaches a stationary state, offers countless self-organized patterns, from soliton molecules and macromolecules, which comprise numerous “isomers,” to the periodic arrangements of soliton crystals or harmonically mode-locked regimes. In all these states, multihysteresis is a central feature. It is quite tempting to develop the analogy between the rearrangements among soliton molecules and chemical reactions, as well as making parallels between major reorganizations among large soliton numbers and phase transitions in statistical physics. Yet it remains extremely difficult to formally develop these analogies, due in a great extent to the nonconservative nature of dissipative soliton interaction, as well as to the subtleties of phase-dependent interactions, and the complex interplay of multiple interaction processes and timescales. However, the recurrence of prototypical dynamics in a wide range of mode-locked laser architectures, for significant domains of parameters, fosters the idea of universal dynamical behaviors. In several cases, it has become clear that universal dynamics can be best portrayed by analogies with better known matter physics behavior, hence the vivid denominations of soliton molecule, crystal and rain dynamics, for instance. No doubt that the exploration of multipulse dynamics will continue to provide very telling analogies in future. As for possible technological implications, the development of pulse pattern control and the passive seeding of ultrastable harmonically mode-locked dynamics look promising prospects.

In nonlinear dissipative systems such as fiber lasers, there are many more dynamical possibilities than the ones referred to as mode-locked states. There is currently a surge of investigations concerning the dynamics of partially mode-locked lasers, which implies for instance revisiting peculiar dynamics such an NLP emission, with advanced real-time characterization techniques, and investigating statistical distribution of extreme pulse events. Recent findings have shown the significant overlap between areas of chaotic pulse or chaotic bunch of pulse dynamics that were initially investigated separately, such as NLP emission, dissipative rogue wave generation in multipulse lasers, and exploding solitons, the latter being developed in the following chapter of this book [114].

Acknowledgments

We thank all the contributors of the works developed in the present chapter, in particular our students and postdocs F. Amrani, S. Chouli, A. Haboucha, C. Lecaplain, A. Niang, and close collaborators J.M. Soto-Crespo and N. Akhmediev. A significant part of this research could take place owing to the ANR project SOLICRISTAL, and funding from the EEC and the Région Bourgogne.

References

1. Akhmediev, N. and Ankiewicz, A. (2005) *Dissipative Solitons*, Springer-Verlag, Berlin.
2. Picholle, E., Montes, C., Leycuras, C., Legrand, O., and Botineau, J. (1991) Observation of dissipative superluminous solitons in a Brillouin fiber ring laser. *Phys. Rev. Lett.*, **66**, 1454.
3. Vanin, E.V., Korytin, A.I., Sergeev, A.M., Anderson, D., Lisak, M., and Vázquez, L. (1994) Dissipative optical solitons. *Phys. Rev. A*, **49**, 2806.
4. Grelu, Ph. and Akhmediev, N. (2012) Dissipative solitons for mode-locked lasers. *Nat. Photonics*, **6**, 84.
5. Chouli, S., Soto-Crespo, J.M., and Grelu, Ph. (2011) Optical spectra beyond the amplifier bandwidth limitation in dispersion-managed mode-locked fiber lasers. *Opt. Express*, **19**, 2959.
6. Babin, S.A. et al. (2016) SRS-driven evolution of dissipative solitons in fiber lasers, in *Nonlinear Optical Cavity Dynamics* (ed. Ph. Grelu), John Wiley & Sons, Inc.
7. Okhotnikov, O., Grudinin, A., and Pessa, M. (2004) Ultra-fast fibre laser systems based on SESAM technology: new horizons and applications. *New J. Phys.*, **6**, 177.

8. Set, S.Y., Yaguchi, H., Tanaka, Y., and Jablonski, M. (2004) Ultrafast fiber pulsed lasers incorporating carbon nanotubes. *IEEE J. Sel. Top. Quantum Electron.*, **10**, 137.
9. Zhang, H., Bao, Q.L., Tang, D.Y., Zhao, L.M., and Loh, K. (2009) Large energy soliton erbium-doped fiber laser with a graphene–polymer composite mode locker. *Appl. Phys. Lett.*, **95**, 141 103.
10. Bonaccorso, F., Sun, Z., Hasan, T., and Ferrari, A.C. (2010) Graphene photonics and optoelectronics. *Nat. Photonics*, **4**, 611.
11. Bulushev, A.G., Dianov, E.M., and Okhotnikov, O.G. (1991) Self-starting mode-locked laser with nonlinear ring resonator. *Opt. Lett.*, **16**, 88.
12. Wu, S., Strait, J., and Fork, R.L. (1993) High-power passively mode-locked Er-doped fiber laser with a nonlinear optical loop mirror. *Opt. Lett.*, **18**, 1444.
13. Salhi, M., Haboucha, A., Leblond, H., and Sanchez, F. (2010) Theoretical study of figure-eight all fiber laser. *Phys. Rev. A*, **77**, 033 828.
14. Duling, I.N. III (1991) All-fiber ring soliton laser mode-locked with a nonlinear mirror. *Opt. Lett.*, **16**, 539.
15. Guy, M.J., Noske, D.U., and Taylor, J.R. (1993) Generation of femtosecond soliton pulses by passive mode locking of an ytterbium–erbium figure-of-eight fiber laser. *Opt. Lett.*, **18**, 1447.
16. Salhi, M., Amrani, F., Leblond, H., and Sanchez, F. (2010) Analytical investigation of figure-of-eight single-pulse all-fiber laser based on nonlinear amplifying loop mirror. *Phys. Rev. A*, **82**, 043 834.
17. Matsas, V.J., Newson, T.P., Richardson, D.J., and Payne, D.N. (1992) Selfstarting passively mode-locked fibre ring soliton laser exploiting nonlinear polarization rotation. *Electron. Lett.*, **28**, 1391.
18. Noske, D.U., Pandit, N., and Taylor, J.R. (1992) Subpicosecond soliton pulse formation from self-mode-locked erbium fibre laser using intensity dependent polarization rotation. *Electron. Lett.*, **28**, 2185.
19. Tamura, K., Haus, H.A., and Ippen, E.P. (1992) Self-starting additive pulse mode-locked erbium fiber ring laser. *Electron. Lett.*, **28**, 2226.
20. Komarov, A., Komarov, K., Meshcheriakov, D., Amrani, F., and Sanchez, F. (2010) Polarization dynamics in nonlinear anisotropic fibers. *Phys. Rev. A*, **82**, 013 813.
21. Aranson, I.S. and Kramer, L. (2002) The world of the complex Ginzburg–Landau equation. *Rev. Mod. Phys.*, **74**, 99.
22. Haus, H.A., Fujimoto, J.G., and Ippen, E.P. (1991) Structures for additive pulse mode locking. *J. Opt. Soc. Am. B*, **8**, 2068.
23. Leblond, H., Salhi, M., Hideur, A., Chartier, T., Brunel, M., and Sanchez, F. (2002) Experimental and theoretical study of the passively mode-locked Ytterbium-doped double-clad fiber laser. *Phys. Rev. A*, **65**, 063 811.
24. Akhmediev, N. and Ankiewicz, A. (1997) *Solitons: Nonlinear Pulses and Beams*, Chapman and Hall, London.
25. Soto-Crespo, J.M., Akhmediev, N.N., and Afanasjev, V.V. (1996) Stability of the pulselike solutions of the quintic complex Ginzburg–Landau equation. *J. Opt. Soc. Am. B*, **13**, 1439.
26. Komarov, A., Leblond, H., and Sanchez, F. (2005) Quintic complex Ginzburg–Landau model for ring fiber lasers. *Phys. Rev. E*, **72**, 025 604.
27. Ding, E. and Kutz, J.N. (2009) Operating regimes, split-step modeling, and the Haus master mode-locking model. *J. Opt. Soc. Am. B*, **26**, 2290.
28. Man, W.S., Tam, H.Y., Demokan, M.S., Wai, P.K.A., and Tang, D.Y. (2000) Mechanism of intrinsic wavelength tuning and sideband asymmetry in a passively mode-locked soliton fiber ring laser. *J. Opt. Soc. Am. B*, **17**, 28.
29. Grelu, Ph., Belhache, F., Gutty, F., and Soto-Crespo, J.M. (2003) Relative phase locking of pulses in a passively mode-locked fiber laser. *J. Opt. Soc. Am. B*, **20**, 863.
30. Martel, G., Chédot, C., Réglier, V., Hideur, A., Ortaç, B., and Grelu, Ph. (2007) On the possibility of observing bound soliton pairs in a “wave-breaking-free” mode-locked fiber laser. *Opt. Lett.*, **32** (4), 343.

31. Malomed, B.A. (2006) *Soliton Management in Periodic Systems*, Springer-Verlag.

32. Komarov, A., Leblond, H., and Sanchez, F. (2005) Multistability and hysteresis phenomena in passively mode-locked fiber lasers. *Phys. Rev. A*, **71**, 053 809.

33. Lega, J., Moloney, J.V., and Newell, A.C. (1994) Swift-Hohenberg equation for lasers. *Phys. Rev. Lett.*, **73**, 2978.

34. Komarov, K.P. (1986) Theory of stationary ultrashort pulses in solid-state lasers with passive mode-locking. *Opt. Spectrosc.*, **60**, 231.

35. Haboucha, A., Leblond, H., Salhi, M., Komarov, A., and Sanchez, F. (2008) Analysis of soliton pattern formation in passively mode-locked fiber laser. *Phys. Rev. A*, **78**, 043 806.

36. Zaviyalov, A., Iliew, R., Egorov, O., and Lederer, F. (2010) Lumped versus distributed description of mode-locked fiber lasers. *J. Opt. Soc. Am. B*, **27**, 2313.

37. Grudinin, A.D., Richardson, D.J., and Payne, D.N. (1992) Energy quantization in figure eight fibre laser. *Electron. Lett.*, **28**, 67.

38. Tang, D.Y., Zhao, L.M., Zhao, B., and Liu, A.Q. (2005) Mechanism of multisoliton formation and soliton energy quantization in passively mode-locked fiber lasers. *Phys. Rev. A*, **72**, 043 816.

39. Akhmediev, N.N., Ankiewicz, A., and Soto-Crespo, J.M. (1997) Multisoliton solutions of the complex Ginzburg–Landau equation. *Phys. Rev. Lett.*, **79**, 4047.

40. Gong, Y.D., Shum, P., Hiang, T., Cheng, Wen, Q., and Tang, D.Y. (2001) Bound soliton pulses in passively mode-locked fiber laser. *Opt. Commun.*, **200**, 389.

41. Grelu, Ph., Belhache, F., Gutty, F., and Soto-Crespo, J.M. (2002) Phase-locked soliton pairs in a stretched-pulsed fiber laser. *Opt. Lett.*, **27**, 966.

42. Haboucha, A., Leblond, H., Salhi, M., Komarov, A., and Sanchez, F. (2008) Coherent soliton pattern formation in a fiber laser. *Opt. Lett.*, **33**, 524.

43. Komarov, A., Haboucha, A., and Sanchez, F. (2008) Ultrahigh repetition rate bound-soliton harmonic passive mode-locked laser. *Opt. Lett.*, **33**, 2254.

44. Grudinin, A.B. and Gray, S. (1997) Passive harmonic mode locking in soliton fiber lasers. *J. Opt. Soc. Am. B.*, **14**, 144.

45. Gordon, J.P. (1983) Interaction forces among solitons in optical fibers. *Opt. Lett.*, **8**, 596.

46. Mitschke, F.M. and Mollenauer, L.F. (1987) Experimental observation of forces between solitons in optical fibers. *Opt. Lett.*, **12**, 355.

47. Malomed, B.A. (1991) Bound solitons in the nonlinear Schrödinger–Ginzburg–Landau equation. *Phys. Rev. A*, **44**, 6954.

48. Kelly, S. (1992) Characteristic sideband instability of periodically amplified average soliton. *Electron. Lett.*, **28**, 806.

49. Soto-Crespo, J.M., Akhmediev, N., Grelu, Ph., and Belhache, F. (2003) Quantized separation of phase-locked soliton pairs in fiber lasers. *Opt. Lett.*, **28**, 1757.

50. Kutz, J., Collings, B., Bergman, K., and Knox, W. (1998) Stabilized pulse spacing in soliton lasers due to gain depletion and recovery. *IEEE J. Quantum Electron.*, **34**, 1749.

51. Pilipetskii, A.N., Golovchenko, E.A., and Menuyk, C.R. (1995) Acoustic effect in passively mode-locked fiber ring lasers. *Opt. Lett.*, **20**, 907.

52. Gat, O., Weill, R., and Fischer, B. (2010) Noise induced pulse interaction: the Casimir effect in mode locked lasers. SIAM Conference on Nonlinear Waves and Coherent Structures, Philadelphia, USA.

53. Niang, A., Amrani, F., Salhi, M., Komarov, A., Leblond, H., and Sanchez, F. (2014) Harmonic mode-locking in a fiber laser through continuous external optical injection. *Opt. Commun.*, **312**, 1.

54. Leblond, H., Niang, A., Amrani, F., Salhi, M., and Sanchez, F. (2013) Motion of solitons of the complex Ginzburg–Landau equation: the effect of an external oscillating source. *Phys. Rev. A*, **88**, 033 809.

55. Komarov, A., Komarov, K., Niang, A., and Sanchez, F. (2014) Nature of soliton interaction in fiber lasers with continuous external optical injection. *Phys. Rev. A*, **89**, 013 833.

56. Amrani, F., Salhi, M., Leblond, H., Grelu, Ph., and Sanchez, F. (2011) Universal soliton pattern formation in passively mode-locked fiber lasers. *Opt. Lett.*, **36**, 1545.

57. Chouli, S. and Grelu, Ph. (2009) Rains of solitons in a fiber laser. *Opt. Express*, **17**, 11 776.

58. Chouli, S. and Grelu, Ph. (2010) Soliton rains in a fiber laser: an experimental study. *Phys. Rev. A*, **81**, 063 829.

59. Amrani, F., Haboucha, A., Salhi, M., Leblond, H., Komarov, A., and Sanchez, F. (2010) Dissipative solitons compounds in a fiber laser: analogy with the states of the matter. *Appl. Phys. B*, **99**, 107.

60. Zhao, L.M., Tang, D.Y., and Liu, D. (2010) Ultrahigh-repetition-rate bound-soliton fiber laser. *Appl. Phys. B*, **99**, 441.

61. Amrani, F., Niang, A., Salhi, M., Komarov, A., Leblond, H., and Sanchez, F. (2011) Passive harmonic mode-locking of soliton crystals. *Opt. Lett.*, **36**, 4239.

62. Richardson, D.J., Laming, R.I., Payne, D.N., Matsas, V.J., and Philips, M.W. (1991) Pulse repetition rates in passive, self-starting, femtosecond soliton fibre laser. *Electron. Lett.*, **27**, 1451.

63. Matsas, V.J., Richardson, D.J., Newson, T.P., and Payne, D.N. (1993) Characterization of a self-starting, passively mode-locked fiber ring laser that exploits nonlinear polarization rotation. *Opt. Lett.*, **18**, 358.

64. Tang, D.Y., Man, W.S., and Tam, H.Y. (1999) Stimulated soliton pulse formation and its mechanism in a passively mode-locked fiber soliton laser. *Opt. Commun.*, **165** (4-6), 189.

65. Gutty, F., Grelu, Ph., Huot, N., Vienne, G., and Millot, G. (2001) Stabilisation of modelocking in fibre ring laser through pulse bunching. *Electron. Lett.*, **37** (12), 745.

66. Liu, X. (2010) Hysteresis phenomena and multipulse formation of a dissipative system in a passively mode-locked fiber laser. *Phys. Rev. A*, **81**, 023 811.

67. Haboucha, A., Komarov, A., Leblond, H., Salhi, M., and Sanchez, F. (2008) Investigation of multiple pulsing and hysteresis phenomena in the erbium-doped double-clad fiber laser. *J. Opt. Adv. Mat.*, **10**, 164.

68. Haboucha, A., Komarov, A., Leblond, H., Sanchez, F., and Martel, G. (2008) Mechanism of multiple pulse formation in the normal dispersion regime of passively mode-locked fiber ring lasers. *Opt. Fiber Technol.*, **14**, 262.

69. Liu, X., Wang, L., Li, X., Sun, H., Lin, A., Lu, K., Wang, Y., and Zhao, W. (2009) Multistability evolution and hysteresis phenomena of dissipative solitons in a passively mode-locked fiber laser with large normal cavity dispersion. *Opt. Express*, **17**, 8506.

70. Komarov, A., Leblond, H., and Sanchez, F. (2005) Theoretical analysis of the operating regime of a passively mode-locked fiber laser through nonlinear polarization rotation. *Phys. Rev. A*, **72**, 063 811.

71. Grelu, Ph. and Soto-Crespo, J.M. (2004) Multisoliton states and pulse fragmentation in a passively mode-locked fibre laser. *J. Opt. B: Quantum Semiclassical Opt.*, **6**, S271.

72. Hsiang, W.W., Lin, C.Y., and Lai, Y. (2006) Stable new bound soliton pairs in a 10 GHz hybrid frequency modulation mode-locked Er-fiber laser. *Opt. Lett.*, **31**, 1627.

73. Nguyen, N.D. and Binh, L.N. (2008) Generation of bound solitons in actively phase modulation mode-locked fiber ring resonators. *Opt. Commun.*, **281**, 2012.

74. Grapinet, M. and Grelu, Ph. (2006) Vibrating soliton pairs in a mode-locked laser cavity. *Opt. Lett.*, **31**, 2115.

75. Grelu, Ph. and Akhmediev, N. (2004) Group interactions of dissipative solitons in a laser cavity: the case of 2+1. *Opt. Express*, **12**, 3184.

76. Leblond, H., Komarov, A., Salhi, M., Haboucha, A., and Sanchez, F. (2006) "Cis" bound states of three localized pulses of the cubic–quintic CGL equation. *J. Opt. A: Pure Appl. Opt.*, **8**, 319.

77. Zaviyalov, A., Grelu, Ph., and Lederer, F. (2012) Impact of slow gain dynamics on soliton molecules in mode-locked fiber lasers. *Opt. Lett.*, **37**, 175.

78. Malomed, B.A., Schwache, A., and Mitschke, F. (1998) Soliton lattice and gas in passive fiber-ring resonators. *Fiber Integr. Opt.*, **17**, 267.

79. Rutz, S. and Mitschke, F. (2000) Towards thermodynamics of solitons: cooling. *J. Opt. B: Quantum Semiclassical Opt.*, **2**, 364.

80. Leblond, H. (2008) The reductive perturbation method and some of its applications. *J. Phys. B: At. Mol. Opt. Phys.*, **41**, 043 001.

81. Lecaplain, C. and Grelu, Ph. (2013) Multi-gigahertz repetition-rate-selectable passive harmonic mode locking of a fiber laser. *Opt. Express*, **21**, 10 897.

82. Komarov, A., Komarov, K., and Sanchez, F. (2009) Quantization of binding energy of structural solitons in passive mode-locked fiber lasers. *Phys. Rev. A*, **79**, 033 807.

83. Kutz, J.N. (2006) Mode-locked soliton lasers. *SIAM Rev.*, **48**, 629.

84. Carruthers, T.F. and Duling, I.N. III (1996) 10-GHz, 1.3-ps erbium fiber laser employing soliton pulse shortening. *Opt. Lett.*, **21**, 1927.

85. Grudinin, A., Richardson, D., and Payne, D. (1993) Passive harmonic mode-locking of a fiber soliton ring laser. *Electron. Lett.*, **29**, 1860.

86. Ortaç, B., Hideur, A., Martel, G., and Brunel, M. (2005) 2-GHz passive harmonically mode-locked Yb-doped double-clad fiber laser. *Appl. Phys. B*, **81**, 507.

87. Amrani, F., Haboucha, A., Salhi, M., Leblond, H., Komarov, A., Grelu, Ph., and Sanchez, F. (2009) Passively mode-locked erbium-doped double-clad fiber laser operating in the 322nd harmonic. *Opt. Lett.*, **34**, 2120.

88. Sobon, G., Krzempek, K., Kaczmarek, P., Abramski, K.M., and Nikodem, M. (2011) 10 GHz passive harmonic mode-locking in Er–Yb double-clad fiber laser. *Opt. Commun.*, **284**, 4203.

89. Zhao, L.M., Tang, D.Y., Cheng, T.H., Lu, C., Tam, H.Y., Fu, X.Q., and Wen, S.C. (2008) Passive harmonic mode-locking of soliton bunches in a fiber ring laser. *Opt. Quantum Electron.*, **40**, 1053.

90. Boucon, A., Barviau, B., Fatome, J., Finot, C., Sylvestre, T., Lee, M.W., Grelu, Ph., and Millot, G. (2012) Noise-like pulses generated at high harmonics in a partially-mode-locked km-long Raman fiber laser. *Appl. Phys. B*, **106**, 283.

91. Niang, A., Amrani, F., Salhi, M., Grelu, Ph., and Sanchez, F. (2014) Rains of solitons in figure-of-eight passively mode-locked fiber laser. *Appl. Phys. B*, **116**, 771.

92. Zhang, Z.X., Zhan, L., Yang, X.X., Luo, S.Y., and Xia, Y.X. (2007) Passive harmonically mode-locked erbium-doped fiber laser with scalable repetition rate up to 1.2 GHz. *Laser Phys. Lett.*, **4**, 592.

93. Komarov, A., Komarov, K., Leblond, H., and Sanchez, F. (2007) Spectral-selective management of dissipative solitons in passive mode-locked fibre lasers. *J. Opt. A: Pure Appl. Opt.*, **9**, 1149.

94. Rutz, S., Körösi, T., and Mitschke, F. (2001) Manipulation of soliton ensembles by spectral filters. *Appl. Phys. B*, **72**, 101.

95. Amrani, F., Salhi, M., Leblond, H., Haboucha, A., and Sanchez, F. (2011) Intricate solitons state in passively mode-locked fiber lasers. *Opt. Express*, **19**, 13 134.

96. Grelu, Ph. and Soto-Crespo, J.M. (2008) Temporal soliton “molecules” in mode-locked fiber lasers: collisions, pulsations and vibrations, in *Dissipative Solitons: From Optics to Biology and Medicine*, Lecture Notes in Physics, vol. **751** (eds N. Akhmediev and A. Ankiewicz), Springer-Verlag, p. 137.

97. Sanchez, F., Grelu, Ph., Leblond, H., Komarov, A., Komarov, K., Salhi, M., Niang, A., Amrani, F., Lecaplain, C., and Chouli, S. (2014) Manipulating dissipative soliton ensembles in passively mode-locked fiber lasers. *Opt. Fiber Technol.*, **20**, 562.

98. Bao, C., Xiao, X., and Yang, C. (2013) Soliton rains in a normal dispersion fiber laser with dual-filter. *Opt. Lett.*, **38**, 1875.

99. Huang, S.S., Wang, Y.G., Yan, P.G., Zhang, G.L., Zhao, J.Q., Li, H.Q., and Lin, R.Y. (2014) Soliton rains in a graphene-oxide passively mode-locked ytterbium-doped fiber laser with all-normal dispersion. *Laser Phys. Lett.*, **11**, 025 102.
100. Horowitz, M., Barad, Y., and Silberberg, Y. (1997) Noiselike pulses with a broadband spectrum generated from an erbium-doped fiber laser. *Opt. Lett.*, **22**, 799.
101. Kang, J. and Posey, R. (1998) Demonstration of supercontinuum generation in a long-cavity fiber ring laser. *Opt. Lett.*, **23**, 1375.
102. Zhao, L.M., Dang, D.Y., Cheng, T.H., Tam, H.Y., and Lu, C. (2008) 120 nm Bandwidth noise-like pulse generation in an erbium-doped fiber laser. *Opt. Commun.*, **281**, 157.
103. Kobtsev, S., Kukarin, S., Smirnov, S., Turitsyn, S., and Latkin, A. (2009) Generation of double-scale femto/picosecond optical lumps in mode-locked fiber lasers. *Opt. Express*, **17**, 20710.
104. North, T. and Rochette, M. (2013) Raman-induced noiselike pulses in a highly nonlinear and dispersive all-fiber ring laser. *Opt. Lett.*, **38**, 890.
105. Aguergaray, C., Runge, A., Erkintalo, M., and Broderick, N. (2013) Raman-driven destabilization of mode-locked long cavity fiber lasers: fundamental limitations to energy scalability. *Opt. Lett.*, **38**, 2644.
106. Soto-Crespo, J.M., Grelu, Ph., and Akhmediev, N. (2011) Dissipative rogue waves: extreme pulses generated by passively mode-locked lasers. *Phys. Rev. E*, **84**, 016604.
107. Akhmediev, N. and Pelinovsky, E. (eds) (2010) Rogue waves—towards a unifying concept. Special Issue of *Eur. Phys. J. Spec. Top.*, **185**, 1–4.
108. Solli, D.R., Ropers, C., Koonath, P., and Jalali, B. (2007) Optical rogue waves. *Nature*, **450**, 1054.
109. Lecaplain, C., Grelu, Ph., Soto-Crespo, J.M., and Akhmediev, N. (2012) Dissipative rogue waves generated by chaotic pulse bunching in a mode-locked laser. *Phys. Rev. Lett.*, **108**, 233901.
110. Lecaplain, C., Grelu, Ph., Soto-Crespo, J.M., and Akhmediev, N. (2013) Dissipative rogue wave generation in multiple-pulsing mode-locked fiber laser. *J. Opt.*, **15**, 064005.
111. Goda, K. and Jalali, B. (2013) Dispersive Fourier transformation for fast continuous single-shot measurements. *Nat. Photonics*, **7**, 102.
112. Runge, A., Aguergaray, C., Broderick, N.G.R., and Erkintalo, M. (2013) Coherence and shot-to-shot spectral fluctuations in noise-like ultrafast fiber lasers. *Opt. Lett.*, **38**, 4327.
113. Lecaplain, C. and Grelu, Ph. (2014) Rogue waves among noise-like-pulse laser emission: an experimental investigation. *Phys. Rev. A*, **90**, 013805.
114. Chang, W. and Akhmediev, N. (2016) Exploding solitons and rogue waves in optical cavities, in *Nonlinear Optical Cavity Dynamics* (ed. Ph. Grelu), John Wiley & Sons, Inc.
115. Zavyalov, A., Egorov, O., Iliew, R., and Lederer, F. (2012) Rogue waves in mode-locked fiber lasers. *Phys. Rev. A*, **85**, 013828.
116. Runge, A., Aguergaray, C., Broderick, N.G.R., and Erkintalo, M. (2014) Raman rogue waves in a partially mode-locked fiber laser. *Opt. Lett.*, **39**, 319.

11

Exploding Solitons and Rogue Waves in Optical Cavities

Wonkeun Chang and Nail Akhmediev

11.1

Introduction

Exploding dissipative solitons were discovered in the numerical modeling of laser systems as early as 2000 [1], with more detailed study that followed later in 2001 [2]. Their existence was experimentally confirmed soon after in a Ti:sapphire laser [3]. Another very recent discovery of exploding solitons in a passively mode-locked fiber laser is presented in [4]. Exploding solitons are dissipative solitons with complex dynamics. They stay in a stationary regime of propagation with fixed profile for most of their evolution time. However, this state is unstable relative to radiation emission. The instability causes the growth of the amplitude of the radiation. The soliton then loses its shape and splits into pieces under the influence of waves that it emits. Once the radiation waves leave the area, the stationary state of the soliton is restored, although not exactly at the same position where it was initially. This completes a cycle, but the same instability forces the recovered soliton to enter the above-mentioned cycle again, and the process may continue indefinitely. The details of the stages involving radiation are not repeated exactly each time, and, therefore, the whole dynamics can be considered to be chaotic.

To some extent, the dynamics of exploding soliton resembles the phenomenon of intermittency in finite-dimensional dynamical systems [5]. However, we have to keep in mind that the system discussed here is infinite dimensional. As such, it may reveal significant differences from the dynamics of simple systems known so far. Analysis of such systems is also more complicated and based predominantly on numerical modeling.

Studying low-dimensional systems involves finding fixed points or limit cycles in the phase space and carrying out the linear stability analysis of these objects. In general, similar techniques can be applied for studying infinite-dimensional systems. In this case, a fixed point is a function rather than a single point. In case of dissipative solitons, we are dealing with localized functions. Solitons in dissipative systems can be either stationary or pulsating [2], and they can be classified as fixed points or limit cycles. Linear stability analysis for these objects produces infinite

Nonlinear Optical Cavity Dynamics: From Microresonators to Fiber Lasers, First Edition.
Edited by Philippe Grelu.
© 2016 Wiley-VCH Verlag GmbH & Co. KGaA. Published 2016 by Wiley-VCH Verlag GmbH & Co. KGaA.

number of eigenvalues [6, 7] in accordance with the fact that the system has infinite number of degrees of freedom. The dissipative soliton is stable provided that real parts of all eigenvalues are negative.

Exploding dissipative solitons are more complicated objects. Their unstable nature indicates that they may have eigenvalues with positive real parts. An example of stability analysis for an exploding soliton has been presented in [6]. This analysis shows indeed that a pair of complex conjugate eigenvalues has positive real parts that make the soliton unstable. However, an infinite number of other eigenvalues have negative real parts providing return of a localized solution to the stationary state.

The initial numerical studies of the exploding dissipative solitons in [1] and [2] have been performed for the cubic–quintic complex Ginzburg–Landau equation. This equation is one of the most popular models used for studying laser dynamics, and is considered as a master equation for a general type of passively mode-locked laser system. Of course, the model can be more explicit and take into account the lumped structure of the laser cavity [3]. Consequently, the variety of exploding solitons and dissipative solitons in general can be enormous.

Experimentally, exploding solitons in laser systems can be observed when the regime of the laser operation is extended beyond the stable stationary pulse generation. Each explosion usually lasts for several round-trips around the cavity. The pulse is chaotic during the explosion, where its shape changes every round-trip until the soliton returns back to stationary state. The details of each explosion are different from others and the intervals between the explosions are not exactly equal. Nevertheless, the pulse stays localized before, during and after each explosion and can be considered as a special form of a dissipative soliton.

One of the essential properties of exploding solitons is that they are very common, more so than the stable stationary solitons; namely, exploding solitons occupy larger areas in the space of the system parameters than stationary solitons [2]. Otherwise, it would be difficult to observe them experimentally. So far, there are two papers with experimental observations of the exploding solitons that are published [3, 4]. Another important property found in [2] is that their amplitude does not exceed a limit that is at a similar level to that of the soliton in its stationary stage. This is related to gain saturation imposed by the quintic dissipative term.

Exploding dissipative solitons is presently an emerging subject in physics studied by numerous groups around the world [8–17]. They have been found in reaction–diffusion systems [8–10, 18], which include chemical reactions [19], gas–discharge systems [20, 21], and a wide class of biological systems [22]. It should be noted that there is a principal difference between the two types of dissipative solitons. Dissipative solitons in optics are localized states of radiation, while in reaction–diffusion, gas-discharge, and biological systems they are localized states of matter. Equations describing them may seem similar but, physically, these are completely different objects. They can be generalized to combined systems where the matter and radiation are involved on equal basis [23]. However, in this chapter, only the optical dissipative solitons are considered.

The generation of chaotic pulses from laser cavities has been reported in numerous occasions, and several different types of chaotic pulses have been identified experimentally. These can take a form of *noise-like pulses* with a broadband spectrum [24, 25] or *broadband quasi-stationary pulses* [26]. There is also a number of other studies reporting the generation of laser pulses with chaotically changing shape [27–31]. Currently, there is no unified theory explaining the phenomena observed so far. One of the important features of these chaotic pulses is their wide spectral bandwidths relative to their single-soliton operation regime reaching 87 nm [32], 120 nm [25], or even 135 nm [33]. Consequently, these pulses may find applications as sources for supercontinuum generation [34], which could potentially lead to a new class of white light sources. This is a new way of generating supercontinuum outside the traditional techniques utilizing specialized fibers [35].

Another type of chaotic pulses is optical rogue waves. The term was introduced for the first time in 2007 [36] when analyzing the output radiation of supercontinuum generation in optical fibers [36]. The output consisted of pulses with chaotically varying amplitudes, and among those, the pulses with exceptionally high amplitudes were called *optical rogue waves*. It was also found that the probability of appearance of such pulses is higher than what is expected from the classical Gaussian distribution. This elevated probability of appearance is the common feature of optical and oceanic rogue waves.

The studies of optical rogue waves expanded in recent years covering various experimental situations. In addition to supercontinuum generation [37, 38], rogue waves have been found in transverse wave fields of wide cavities [39, 40], Raman fiber amplifiers [41, 42], in parametric processes [43], and in femtosecond filamentation [44]. The diversity of setups where these extreme events can be found is enormous [45–51]. It is not surprising that the optical rogue waves have much in common with their hydrodynamic counterparts [52, 53]. In turn, ideas from optics can be fruitfully applied to water waves [54]. Comprehensive review of optical rogue waves has been published recently by Dudley *et al.* [55].

From theoretical point of view, the number of systems that admit rogue wave solutions is also very large. They can be found as solutions of the nonlinear Schrödinger equation [56–58], Hirota equation [59–61], Sasa–Satsuma equation [62], Manakov equations [63, 64], Davey–Stewartson equations [65], and more complicated sets of nonlinear evolution equations [66–70].

When extreme waves are generated by mode-locked laser systems, these pulses can be called *dissipative rogue waves* (DRWs) [71]. Rogue waves in dissipative systems were first predicted theoretically and modeled numerically in two independent studies [71, 72]. The experimental observation of DRWs in a fiber ring laser followed shortly after these predictions [73]. It was found that the nonlinear interactions and collisions between multiple pulses traveling simultaneously and chaotically in the laser cavity may cause the formation of pulses with extreme amplitudes. One of the conditions for high-amplitude collisions is attraction between the pulses and consequently, their bunching in the cavity [71]. As the interaction between the pulses in a cavity is very sensitive to its parameters, the appearance of high-amplitude pulses is also strongly affected by these parameters. As a result, the probability of high-amplitude pulses can be higher or lower than the exponential tail of the probability distribution function [74]. This sensitivity provides a possibility for an efficient control of DRW generation [74]. Other notable reports of extreme events in laser systems include scarce and randomly emerging giant pulse generation observed in a Kerr-lens mode-locked Ti:sapphire laser [75], the rogue-wave-like probability distribution exhibited by a sporadic emission of Raman-induced noise-like pulses in a Yb-fiber laser [76], and the observation of both pulse-energy and spectral rogue waves in an Er-fiber laser [77].

Until now, no connection between the exploding dissipative solitons and DRW generation was investigated. At first sight, the two types of pulses have little in common since the peak amplitudes of previously known exploding solitons generally do not exceed a limit, which is comparable to that in their stationary regime. However, by definition, the amplitude of rogue waves takes extreme values. In this chapter, however, we show that on the contrary to previous belief, exploding solitons can be generated in the regime where their amplitudes grow well beyond the saturation limit. The process is chaotic and each of these giant pulses appear from *nowhere* and disappear *without a trace*, thus indicating that they belong to the class of rogue waves.

11.2
Passively Mode-Locked Laser Model

For numerical simulations, we used the mode-locked laser model shown schematically in Figure 11.1. Here, we use a lumped model for the laser cavity which provides a more accurate picture than the master equation approach used in [2]. The model consists of a gain medium where the energy is supplied, a delay line to control the cavity dispersion, a saturable absorber for mode-locking, and an output coupler to tap-out part of the energy circulating in the cavity. Equations describing the effects of each of the components on the optical field are chained in order to provide continuous circulation of pulses within the cavity.

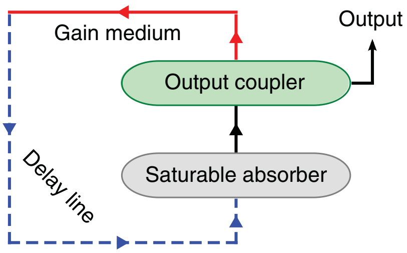

Figure 11.1 Model of the mode-locked laser used in the numerical simulations.

To be specific, the gain medium of length L_{GM} is modeled by a modified one-dimensional nonlinear Schrödinger equation:

$$\begin{aligned}\frac{\partial U}{\partial z} &= -i\frac{\beta_2}{2}\frac{\partial^2 U}{\partial t^2} + i\gamma|U|^2 U \\ &\quad + \frac{g_0/2}{1+\int_{\text{pulse}}|U|^2 dt/E_{\text{sat}}}\left(U + \sigma\frac{\partial^2 U}{\partial t^2}\right),\end{aligned} \tag{11.1}$$

where U is the complex envelope of the pulse in the time domain t, where the time frame moves with the pulse itself, and z is the longitudinal coordinate in the gain medium. The equation includes the effect of second-order dispersion with the coefficient β_2 and the Kerr nonlinearity with the coefficient γ. The last term describes the energy supply, where the power gain is given by g_0 with the gain saturation at E_{sat}. This expression assumes a parabolic gain profile in the frequency domain with the term containing σ.

In the delay line, shown by the blue dashed trajectory, only the second-order dispersion is taken into account. Hence, the field at the end of the delay line is given by

$$\tilde{U}_{\text{out}} = \exp\left(i\frac{D_{\text{DL}}}{2}\omega^2\right)\tilde{U}_{\text{in}}, \tag{11.2}$$

where $\tilde{U}$ denotes the Fourier transform of U, and hence $\tilde{U}_{\text{in}}$ and $\tilde{U}_{\text{out}}$ are the input and output fields in the frequency domain. D_{DL} is the total dispersion in the delay line.

The saturable absorber is the mode-locking device providing an intensity-dependent loss. The governing equation for it assuming an instantaneous response is given by

$$U_{\text{out}} = \sqrt{T_0 + \Delta T\frac{1}{1+P_{\text{sat}}/|U_{\text{in}}|^2}}\quad U_{\text{in}}, \tag{11.3}$$

where T_0 is the power transmission at a low power, ΔT is the modulation depth, and P_{sat} is the saturation power.

Finally, the loss introduced by the output coupler with a coupling loss k is given by

$$U_{\text{out}} = \sqrt{(1-k)}\quad U_{\text{in}}. \tag{11.4}$$

In the simulations, the observable optical field is recorded at the output coupler after each round-trip. By tuning the values of the parameters involved in this model, a rich variety of laser dynamics can be observed. Among others, we were able to observe various types of dissipative solitons. Exploding solitons in the normal dispersion regime in particular were found for the set of parameters given in Table 11.1. These are realistic parameters commonly used in fiber laser systems. Thus, we hope that the predicted effects can be observed experimentally.

Table 11.1 The set of parameters chosen in numerical simulations for generation of exploding solitons.

β_2	$0.024\ \text{ps}^2\text{m}^{-1}$
γ	$0.005\ \text{W}^{-1}\text{m}^{-1}$
g_0	$0.524\ \text{m}^{-1}$
σ	$0.01\ \text{ps}^2$
E_{sat}	1 μJ
L_{GM}	1 m
D_{DL}	$0.012\ \text{ps}^2$
T_0	0.65
ΔT	0.35
P_{sat}	4 W
k	0.3

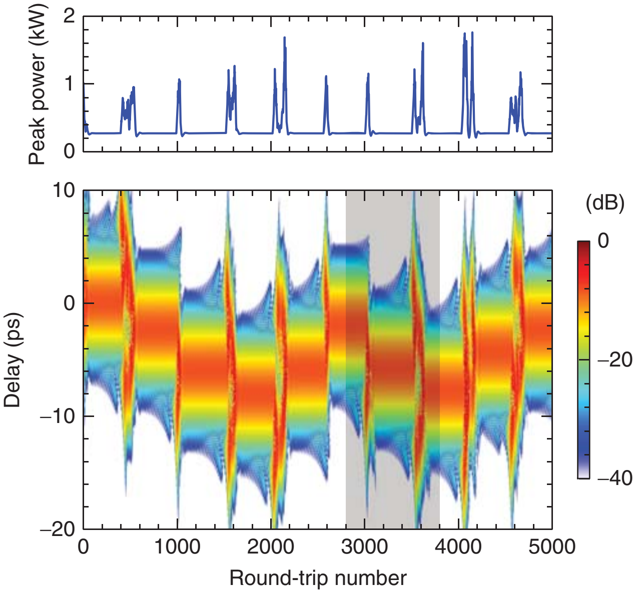

Figure 11.2 The recorded (top) peak power and (bottom, logarithmic scale) pulse profiles over 5000 round-trips showing nine consecutive explosions. The simulation parameters are given in Table 11.1. The gray-shaded area with two explosions is selected for detailed presentation in Figure 11.3.

11.3
The Results of Numerical Simulations

Figure 11.2 shows the evolution of pulse profiles and peak powers of the exploding soliton after each round-trip for 5000 cycles around the loop. It can be clearly seen that the exploding soliton stays in almost stationary state with a constant peak power (≈ 272 W) during long intervals. The soliton intermittently explodes bursting smooth profile into a set of subpulses, while the peak power sharply increases during the explosions. This instability is triggered by noise that is clearly visible around the soliton during the stationary interval. The noise is always present in the system, although the chaotic part of the structure grows relatively slowly and the process occupies many round-trips. Nevertheless, the likelihood of soliton explosion increases with every round-trip after an explosion, and hence the explosions occur at roughly regular intervals. The soliton explodes once the build-up of the instability causes the energy flow within the soliton to become turbulent. Remarkably, the original stationary state of the pulse is restored after each explosion. This restoration is the main mechanism behind the global robustness of exploding solitons. Basically, their dynamics is an infinite-dimensional analog of strange attractors [6].

Each explosion is chaotic, such that the exact details and the scale of the explosions are different and unpredictable. However, they have similar features keeping the soliton localized within certain ranges [6]. It can be seen from Figure 11.2 that the explosions occur either on both sides or predominantly on one side of the pulse. This is defined by the amount of radiation accumulated at each wing of the soliton before the explosion. In some cases, radiative waves appear on both sides leading to what is seemingly a “symmetric” explosion. In other cases, radiative waves appear only on one side causing the next explosion to be strongly “asymmetric” [78, 79]. Whether the next coming explosion will be “symmetric” or “asymmetric” depends on the noise profile left after the previous explosion, and is unpredictable [78]. The position of the peak may shift after each explosion. Figure 11.3 shows both the temporal and spectral details of the two explosions that occurred within the gray-shaded area in Figure 11.2.

During the stationary state, the soliton has a well-defined single maximum in the temporal domain, while the characteristic shape of its spectrum is almost rectangular. The radiation ripples on the edges of the soliton caused by the instability appear as an oscillation on top of the rectangular spectrum in the frequency domain. However, depending on whether the ripples form on the leading or the trailing edge, the spectral oscillation is either in the blue or the red side, respectively. For a “symmetric” explosion, the ripples form on both edges of the pulse, and hence oscillations on both sides of the spectrum. The spectral extent is not influenced much by the explosion; rather, its full width at half maximum is reduced due to the massive increase in the spectral peak.

It should be noted that the pulse energy for the case shown here is in the nanojoule range and, therefore, the gain saturation ($E_{\text{sat}} = 1$ μJ) does not play any role. On the contrary, the saturable absorber ($P_{\text{sat}} = 4$ W) is completely saturated in the central part of the pulse and serves to stabilize the background.

In previous studies of exploding solitons, the amplitude (or the peak intensity) of the soliton did not increase much during the explosions, but rather the bulk of energy appeared and disappeared on the sides of the soliton increasing briefly its width. In drastic contrast to previous studies, the explosions found in this work are located in the central part of the soliton causing the peak power to reach multiple

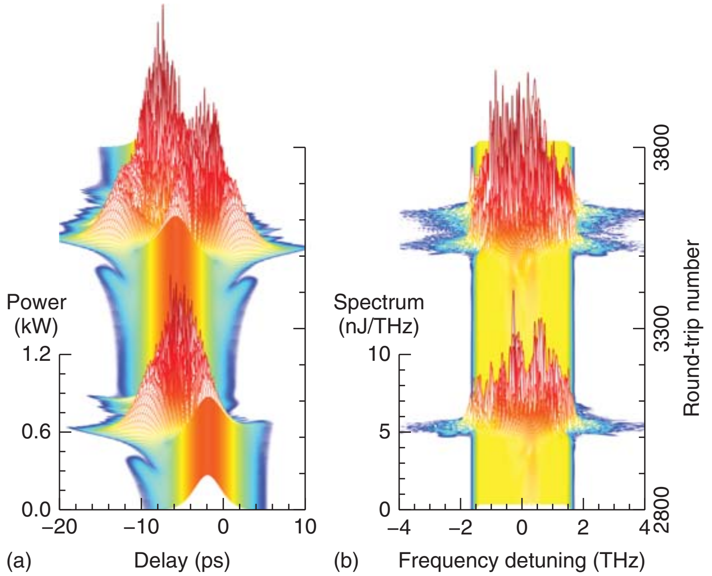

Figure 11.3 Two explosions selected from a large set of data. This selection is shown as gray area in Figure 11.2. The explosions are presented in (a) temporal and (b) spectral domains. We use the same logarithmic scale color map as in Figure 11.2. The first explosion occurs on one side of the soliton ("asymmetric"), whereas the second explosion occurs on two sides ("symmetric"). Consequently, the second explosion reaches higher peak power than the first one.

times that of the soliton in the stationary regime. Moreover, the solitons during the "symmetric" explosions tend to reach higher peak power than the "asymmetric" explosions. When exceptionally high peak power is reached, this particular explosion can be classified as a rogue wave. However, not all explosions grow up to the level of a rogue wave, and it is impossible to work out the strength of future explosions. Figuratively, extreme waves appear unexpectedly and disappear without leaving a trace.

11.4

In order to provide statistical data for explosions, we subdivided the peak power axis into small intervals and counted the number of events falling into each of these intervals. For each pulse recorded after a single round-trip, we identified the pulse peak power and counted it as one event. The collection of such data for ∼10 million round-trips is plotted in Figure 11.4. The scale on the left-hand side of this plot shows the number of events falling into a particular interval of peak powers with the width of 0.02 kW. Dividing the number of events by the width of this interval provides the corresponding probability density. The probability density is

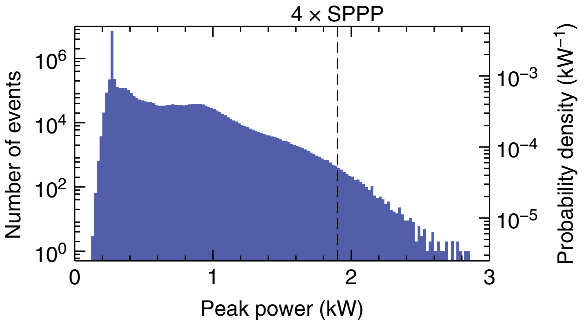

Figure 11.4 Historgram (log scale) of recorded pulse peak power after each round-trip for ∼10 million round-trips with uniform 0.02 kW intervals. The distribution shows a flattened tail at high peak powers. The scale on the right-hand side vertical axis shows the data in probability density given in the units of kW^{-1}. The dashed vertical line indicates four times the significant pulse peak power.

shown on the right-hand side vertical scale in the units of kW^{-1}. The choice of the power interval in constructing the histogram is dictated by the total number of events we were able to generate. The value of 0.02 kW provides a reasonably smooth curve for the probability density function (PDF).

The majority of the events occur at 272 W, which is the peak power at the stationary state. The curve is reasonably smooth with the exception of a small bump occurring at ∼900 W. This specific feature of the PDF reveals the increase of probability of certain peak power, which is laser parameter dependent and demonstrates a difference from the known classical distribution valid for linear waves. It also exhibits a longer flattened tail above 2.5 kW, which is only reached by the "symmetric" explosions. The highest peak power reached in this set of simulations is greater than 2.8 kW, which exceeds the peak power in its stationary regime of operation by more than 10 times.

We define significant pulse peak power (SPPP) as follows:

$$\mathrm{SPPP} = \left(\frac{3}{N} \sum_{m=1}^{N/3} \sqrt{P_m} \right)^2, \tag{11.5}$$

where P_m is a series of recorded peak powers sorted from high to low. This follows the significant wave height (mean value of the highest one-third of the recorded wave heights) convention used in water wave community, but adopted to optics where intensities or powers are more often measured rather than the amplitudes. For the same reason, we identify the peak powers that are greater than four times the SPPP to be classified as DRWs, which corresponds to the events that lie on the right-hand side of the vertical dashed line in Figure 11.4.

11.5
Conclusions

As a system with infinite number of degrees of freedom, a passively mode-locked laser can emit pulses with a large variety of profiles. We assume that stable stationary pulses are presently well studied. In addition, when pulses change their shape from one round-trip to another, the regimes are more complicated and, therefore, more interesting. The most intriguing objects are pulses that change their profile chaotically. The shape of these pulses is never repeated during the whole evolution time. Nevertheless, even chaotic pulses admit certain degree of classification. Such systematization can be useful not only from theoretical point of view but it can provide us with useful information about the spectra and other properties of pulses. This knowledge may allow us to create pulse-generating devices with the ability to switch from one regime to another.

In this chapter, we have found a connection between two types of chaotic pulses: exploding solitons and rogue waves. Each type of these objects has been separately studied in many previous publications but no connection has been established so far. The existence of such connection was unexpected and has been revealed in the course of massive numerical modeling. In this respect, it is important to point out that all previous studies of DRWs did involve the formation of multisoliton complexes in the cavity [71–73] with nonlinear interaction between the participating pulses. Simultaneous collision of several solitons was the major mechanism for the rogue wave formation. We should stress that in this study rogue waves are generated in the cavity with the normal dispersion operating in a single-pulse regime per round-trip. The main mechanism of their formation is transformation of an exploding soliton into a rogue wave. Thus, there is a fundamental difference between the DRW known before and DRW found in our present investigation. One of the practical aspects of this finding is that single-pulse generation per round-trip may require less pumping energy. At the same time, the spectral range of these pulses can be sufficiently wide for generation of white light.

To summarize, we have observed exploding solitons with extreme peak intensities in numerical modeling of dissipative solitons in a mode-locked laser cavity. We have found that their appearance is chaotic with elevated probability of events with higher peak exploding powers thus allowing us to conclude that we have observed DRW events in a single-pulse regime.

11.6
Acknowledgments

The authors acknowledge the support of the Australian Research Council (DE130101432 and DP140100265). Nail Akhmediev acknowledges the support of Volkswagen Stiftung.

References

1. Soto-Crepo, J.M., Akhmediev, N., and Ankiewicz, A. (2000) Pulsating, creeping, and erupting solitons in dissipative systems. *Phys. Rev. Lett.*, **85** (14), 2937–2940.
2. Akhmediev, N., Soto-Crespo, J.M., and Town, G. (2001) Pulsating solitons, chaotic solitons, period doubling, and pulse coexistence in mode-locked lasers: complex Ginzburg–Landau equation approach. *Phys. Rev. E*, **63** (5), 056602.
3. Cundiff, S.T., Soto-Crespo, J.M., and Akhmediev, N. (2002) Experimental evidence for soliton explosions. *Phys. Rev. Lett.*, **88** (7), 073903.
4. Runge, A.F.J., Broderick, N.G.R., and Erkintalo, M. (2015) Observation of soliton explosions in a passively mode-locked fiber laser. *Optica*, **2** (1), 36–39.
5. Pomeau, Y. and Manneville, P. (1980) Intermittent transition to turbulence in dissipative dynamical systems. *Commun. Math. Phys.*, **74** (2), 189–197.
6. Akhmediev, N. and Soto-Crespo, J.M. (2003) Exploding solitons and Shil'nikov's theorem. *Phys. Lett. A*, **317** (3–4), 287–292.
7. Soto-Crespo, J.M., Akhmediev, N., and Chiang, K. (2001) Simultaneous existence of a multiplicity of stable and unstable solitons in dissipative systems. *Phys. Lett. A*, **291** (2–3), 115–123.
8. Descalzi, O. and Brand, H.R. (2013) Quasi-one-dimensional solutions and their interaction with two-dimensional dissipative solitons. *Phys. Rev. E*, **87** (2), 022915.
9. Descalzi, O., Cartes, C., Cisternas, J., and Brand, H.R. (2011) Exploding dissipative solitons: the analog of the Ruelle-Takens route for spatially localized solutions. *Phys. Rev. E*, **83** (5), 056214.
10. Descalzi, O. and Brand, H.R. (2010) Transition from modulated to exploding dissipative solitons: hysteresis, dynamics, and analytic aspects. *Phys. Rev. E*, **82** (2), 026203.
11. Gonzalez, J.A., Bellorn, A., and Guerrero, L.E. (2005) Controlling soliton explosions. *Phys. Lett. A*, **338** (1), 60–65.
12. Carvalho, M.I. and Facao, M. (2012) Evolution of cubic–quintic complex Ginzburg–Landau erupting solitons under the effect of third-order dispersion and intrapulse Raman scattering. *Phys. Lett. A*, **376** (8–9), 950–956.
13. Latas, S.C.V. and Ferreira, M.F.S. (2010) Soliton explosion control by higher-order effects. *Opt. Lett.*, **35** (11), 1771–1773.
14. Hong, W.-P. (2006) Dynamics of pulsating, erupting, and creeping solitons in the cubic–quintic complex Ginzburg–Landau equation under the modulated field. *Z. Naturforsch., A: Phys. Sci.*, **61** (10–11), 525–533.
15. Song, L., Li, L., Li, Z., and Zhou, G.S. (2005) Effect of third-order dispersion on pulsating, erupting and creeping solitons. *Opt. Commun.*, **249** (1–3), 301–309.
16. Tian, H.P., Li, Z.H., Tian, J.P., Zhou, G.S., and Zi, J. (2004) Effect of nonlinear gradient terms on pulsating, erupting and creeping solitons. *Appl. Phys. B*, **78** (2), 199–204.
17. Crasovan, L.C., Malomed, B.A., and Mihalache, D. (2001) Erupting, flat-top, and composite spiral solitons in the two-dimensional Ginzburg–Landau equation. *Phys. Lett. A*, **289** (1–2), 59–65.
18. Descalzi, O., Akhmediev, N., and Brand, H.R. (2013) Exploding dissipative solitons in reaction–diffusion systems. *Phys. Rev. E*, **88** (4), 042911.
19. Tuckwell, H.C. (1979) Solitons in a reaction–diffusion system. *Science*, **205** (4405), 493–495.
20. Liehr, A.W. (2013) *Dissipative Solitons in Reaction Diffusion Systems: Mechanisms, Dynamics, Interaction*, Springer-Verlag, Berlin.
21. Purwins, H.-G., Bödeker, H.U., and Amiranashvili, Sh. (2010) Dissipative solitons. *Adv. Phys.*, **59** (5), 485–701.
22. Argentina, M., Coullet, P., and Krinsky, V. (2000) Head-on collisions of waves in an excitable FitzHugh–Nagumo system: a transition from wave annihilation to classical wave behavior. *J. Theor. Biol.*, **205** (1), 47–52.
23. Akhmediev, N., Soto-Crespo, J.M., and Brand, H.R. (2013) Dissipative solitons

with energy and matter flows: fundamental building blocks for the world of living organisms. *Phys. Lett. A*, **377** (13), 968–974.

24. Horowitz, M., Barad, Y., and Silberberg, Y. (1997) Noiselike pulses with a broadband spectrum generated from an erbium-doped fiber laser. *Opt. Lett.*, **22** (11), 799–801.

25. Zhao, L.M., Tang, D.Y., Cheng, T.H., Tam, H.Y., and Lu, C. (2008) 120 nm Bandwidth noise-like pulse generation in an erbium-doped fiber laser. *Opt. Commun.*, **281** (1), 157–161.

26. Kang, J.U. (2000) Broadband quasi-stationary pulses in mode-locked fiber ring laser. *Opt. Commun.*, **182** (4–6), 433–436.

27. Pottiez, O., Grajales-Coutino, R., Ibarra-Escamilla, B., Kuzin, E.A., and Hernandez-Garcia, J.C. (2011) Adjustable noiselike pulses from a figure-eight fiber laser. *Appl. Opt.*, **50** (25), E24–E31.

28. Horowitz, M. and Silberberg, Y. (1998) Control of noiselike pulse generation in erbium-doped fiber lasers. *IEEE Photonics Technol. Lett.*, **10** (10), 1389–1391.

29. Hernandez-Garcia, J.C., Pottiez, O., and Estudillo-Ayala, J.M. (2012) Supercontinuum generation in a standard fiber pumped by noise-like pulses from a figure-eight fiber laser. *Laser Phys.*, **22** (1), 221–226.

30. Lei, D., Yang, H., Dong, H., Wen, S., Xu, H., and Zhang, J. (2009) Effect of birefringence on the bandwidth of noise-like pulse in an erbium-doped fiber laser. *J. Mod. Opt.*, **56** (4), 572–576.

31. Tang, D.Y., Zhao, L.M., and Zhao, B. (2005) Soliton collapse and bunched noise-like pulse generation in a passively mode-locked fiber ring laser. *Opt. Express*, **13** (7), 2289–2294.

32. Takushima, Y., Yasunaka, K., Ozeki, Y., and Kikuchi, K. (2005) 87 nm Bandwidth noise-like pulse generation from erbium-doped fibre laser. *Electron. Lett.*, **41** (7), 399–400.

33. Vazquez-Zuniga, L.A. and Jeong, Y. (2012) Super-broadband noise-like pulse erbium-doped fiber ring laser with a highly nonlinear fiber for Raman gain enhancement. *IEEE Photonics Technol. Lett.*, **24** (17), 1549–1551.

34. Zaytsev, A., Lin, C.-H., You, Y.-J., Chung, C.-C., Wang, C.-L., and Pan, C.L. (2013) Supercontinuum generation by noise-like pulses transmitted through normally dispersive standard single-mode fibers. *Opt. Express*, **21** (13), 16056–16062.

35. Dudley, J.M., Genty, G., and Coen, S. (2006) Supercontinuum generation in photonic crystal fiber. *Rev. Mod. Phys.*, **78** (4), 1135–1184.

36. Solli, D.R., Ropers, C., Koonath, P., and Jalali, B. (2007) Optical rogue waves. *Nature*, **450** (7172), 1054–1057.

37. Dudley, J.M., Genty, G., and Eggleton, B.J. (2008) Harnessing and control of optical rogue waves in supercontinuum generation. *Opt. Express*, **16** (6), 3644–3651.

38. Solli, D.R., Ropers, C., and Jalali, B. (2008) Active control of rogue waves for stimulated supercontinuum generation. *Phys. Rev. Lett.*, **101** (23), 233902.

39. Montina, A., Bortolozzo, U., Residori, S., and Arecchi, F.T. (2009) Non-Gaussian statistics and extreme waves in a nonlinear optical cavity. *Phys. Rev. Lett.*, **103** (17), 173901.

40. Residori, S., Bortolozzo, U., Montina, A., Lenzini, F., and Arecchi, F.T. (2012) Rogue waves in spatially extended optical systems. *Fluctuation Noise Lett.*, **11** (1), 1240014.

41. Finot, C., Hammani, K., Fatome, J., Dudley, J.M., and Millot, G. (2010) Selection of extreme events generated in Raman fiber amplifiers through spectral offset filtering. *IEEE J. Quantum Electron.*, **46** (2), 205–213.

42. Hammani, K. and Finot, C. (2012) Experimental signatures of extreme optical fluctuations in lumped Raman fiber amplifiers. *Opt. Fiber Technol.*, **18** (2), 93–100.

43. Hammani, K., Fino, C., and Millot, G. (2009) Emergence of extreme events in fiber-based parametric processes driven by a partially incoherent pump wave. *Opt. Lett.*, **34** (8), 1138–1140.

44. Majus, D., Jukna, V., Valiulis, G., Faccio, D., and Dubietis, A. (2011) Spatiotemporal rogue events in femtosecond filamentation. *Phys. Rev. A*, **83** (2), 025802.

45. Zamora-Munt, J., Garbin, B., Barland, S., Giudici, M., Rios Leite, J.R., Masoller, C., and Tredicce, J.R. (2013) Rogue waves in optically injected lasers: origin, predictability, and suppression. *Phys. Rev. A*, **87** (3), 035802.

46. Buccoliero, D., Steffensen, H., Ebendorff-Heidepriem, H., Monro, T.M., and Bang, O. (2011) Midinfrared optical rogue waves in soft glass photonic crystal fiber. *Opt. Express*, **19** (19), 17973–17978.

47. He, J., Xu, S., and Porsezian, K. (2012) New types of rogue wave in an erbium-doped fibre system. *J. Phys. Soc. Jpn.*, **81** (3), 033002.

48. Antikainen, A., Erkintalo, M., Dudley, J.M., and Genty, G. (2012) On the phase-dependent manifestation of optical rogue waves. *Nonlinearity*, **25** (7), R73–R83.

49. Pisarchik, A.N., Jaimes-Reatigui, R., Sevilla-Escoboza, R., Huerta-Cuellar, G., and Taki, M. (2011) Rogue waves in a multistable system. *Phys. Rev. Lett.*, **107** (27), 274101.

50. Demircan, A., Amiranashvili, Sh., Brée, C., Mahnke, Ch., Mitschke, F., and Steinmeyer, G. (2013) Rogue events in the group velocity horizon. *Sci. Rep.*, **2**, 850.

51. Bludov, Yu.V., Driben, R., Konotop, V.V., and Malomed, B.A. (2013) Instabilities, solitons and rogue waves in PT-coupled nonlinear waveguides. *J. Opt.*, **15** (6), 064010.

52. Wabnitz, S., Finot, Ch., Fatome, J., and Millot, G. (2013) Shallow water rogue wave trains in nonlinear optical fibers. *Phys. Lett. A*, **377** (12), 932–939.

53. Wabnitz, S. (2013) Optical tsunamis: shoaling of shallow water rogue waves in nonlinear fibers with normal dispersion. *J. Opt.*, **15** (6), 064002.

54. Chabchoub, A., Hoffmann, N., Onorato, M., Genty, G., Dudley, J.M., and Akhmediev, N. (2013) Hydrodynamic supercontinuum. *Phys. Rev. Lett.*, **111** (5), 054104.

55. Dudley, J.M., Dias, F., Erkintalo, M., and Genty, G. (2014) Instabilities, breathers and rogue waves in optics. *Nat. Photonics*, **8**, 755–764.

56. Dubard, P. and Matveev, V.B. (2011) Multi-rogue waves solutions to the focusing NLS equation and the KP-I equation. *Nat. Hazards Earth Syst. Sci.*, **11** (3), 667–672.

57. Gaillard, P. (2011) Families of quasi-rational solutions of the NLS equation and multi-rogue waves. *J. Phys. A*, **44** (43), 435204.

58. Ohta, Y. and Yang, J. (2012) General high-order rogue waves and their dynamics in the nonlinear Schrödinger equation. *Proc. R. Soc. London, Ser. A*, **468**, 1716–1740.

59. Ankiewicz, A., Soto-Crespo, J.M., and Akhmediev, N. (2010) Rogue waves and rational solutions of the Hirota equation. *Phys. Rev. E*, **81** (4), 046602.

60. Chen, S. and Song, L.-Y. (2013) Rogue waves in coupled Hirota systems. *Phys. Rev. E*, **87** (3), 032910.

61. Tao, Y. and He, J. (2012) Multisolitons, breathers, and rogue waves for the Hirota equation generated by the Darboux transformation. *Phys. Rev. E*, **85** (2), 026601.

62. Bandelow, U. and Akhmediev, N. (2012) Persistence of rogue waves in extended nonlinear Schrödinger equations: integrable Sasa–Satsuma case. *Phys. Lett. A*, **376**, 1558–1561.

63. Baronio, F., Degasperis, A., Conforti, M., and Wabnitz, S. (2012) Solutions of the vector nonlinear Schrödinger equations: evidence for deterministic rogue wave. *Phys. Rev. Lett.*, **109** (4), 044102.

64. Vishnu Priya, N., Senthilvelan, M., and Lakshmanan, M. (2013) Akhmediev breathers, Ma solitons, and general breathers from rogue waves: a case study in the Manakov system. *Phys. Rev. E*, **88** (2), 022918.

65. Ohta, Y. and Yang, J. (2012) Rogue waves in the Davey-Stewartson I equation. *Phys. Rev. E*, **86** (3), 036604.

66. Zhao, L.-C. and Liu, J. (2013) Rogue-wave solutions of a three-component coupled nonlinear Schrödinger equation. *Phys. Rev. E*, **87** (1), 013201.

67. Xu, S., He, J., and Wang, L. (2012) Two kinds of rogue waves of the general nonlinear Schrödinger equation with derivative. *Europhys. Lett.*, **97** (3), 30007.

68. Bona, J.L. and Saut, J.-C. (2010) Dispersive blow-up II. Schrödinger-type equations, optical and oceanic rogue waves. *Chin. Ann. Math. Ser. B*, **31** (6), 793–818.
69. Zhaqilao (2013) On N th-order rogue wave solution to the generalized nonlinear Schrödinger equation. *Phys. Lett. A*, **377** (12), 855–859.
70. Gu, M. and Qin, Z. (2012) Rogue waves for the coupled Schrödinger–Boussinesq equation and the coupled Higgs equation. *J. Phys. Soc. Jpn.*, **81** (8), 084001.
71. Soto-Crespo, J.M., Grelu, Ph., and Akhmediev, N. (2011) Dissipative rogue waves: extreme pulses generated by passively mode-locked lasers. *Phys. Rev. E*, **84** (1), 016604.
72. Zaviyalov, A., Egorov, O., Iliew, R., and Lederer, F. (2012) Rogue waves in mode-locked fiber lasers. *Phys. Rev. A*, **85** (1), 013828.
73. Lecaplain, C., Grelu, Ph., Soto-Crespo, J.M., and Akhmediev, N. (2012) Dissipative rogue waves generated by chaotic pulse bunching in a mode-locked laser. *Phys. Rev. Lett.*, **108** (23), 233901.
74. Lecaplain, C., Grelu, Ph., Soto-Crespo, J.M., and Akhmediev, N. (2013) Dissipative rogue wave generation in multiple-pulsing mode-locked fiber laser. *J. Opt.*, **15** (6), 064005.
75. Kovalsky, M.G., Hnilo, A.A., and Tredicce, J.R. (2011) Extreme events in the Ti:sapphire laser. *Opt. Lett.*, **36** (22), 4449–4451.
76. Runge, A.F.J., Aguergaray, C., Broderick, N.G.R., and Erkintalo, M. (2014) Raman rogue waves in a partially mode-locked fiber laser. *Opt. Lett.*, **39** (2), 319–322.
77. Lecaplain, C. and Grelu, Ph. (2014) Rogue waves among noiselike-pulse laser emission: an experimental investigation. *Phys. Rev. A*, **90** (1), 013805.
78. Akhmediev, N. and Soto-Crespo, J.M. (2004) Strongly asymmetric soliton explosions. *Phys. Rev. E*, **70** (3), 036613.
79. Soto-Crespo, J.M. and Akhmediev, N. (2005) Exploding soliton and front solutions of the complex cubic–quintic Ginzburg–Landau equation. *Math. Comput. Simul.*, **69** (5–6), 526–536.

12
SRS-Driven Evolution of Dissipative Solitons in Fiber Lasers

Sergey A. Babin, Evgeniy V. Podivilov, Denis S. Kharenko, Anastasia E. Bednyakova, Mikhail P. Fedoruk, Olga V. Shtyrina, Vladimir L. Kalashnikov, and Alexander A. Apolonski

12.1
Introduction

It is known that in optical media with anomalous dispersion, in particular in a fiber laser cavity [1–3], it is possible to generate spectrally limited stable pulses that are called optical solitons. It was also found [4–6] that the regime of normal dispersion is more suitable for generating high-energy femtosecond pulses. In this regime, the femtosecond laser oscillator generates chirped pulses, that is, pulses with frequency modulation across its spectrum. The energy of these pulses may be ten or even hundred times more than that obtained for conventional solitons generated in the laser cavity with anomalous dispersion.

A cavity with net normal dispersion can be designed in different ways, and the regimes of generated chirped pulses are classified accordingly. Haus in his paper [7] proposed to use a scheme with alternating cavity parts of negative and positive dispersion thus providing dispersion management (DM). If total dispersion of such a DM cavity is close to zero, the oscillator generates so-called stretched pulses characterized by strong variations of the pulse duration at its round-trip. If the net cavity dispersion is positive and large enough, the pulse varies slowly in the normal-dispersion (amplifying) part of the cavity taking the shape close to parabolic. Such pulses are called self-similar [8] or similaritons [9]. Strong spectral filtering in the cavity is necessary in this case [10] to obtain stable pulses. As shown in [11], the similariton and soliton regimes can be realized sequentially inside one cavity in the parts with different dispersion signs.

The concept of dissipative solitons provides a unique frame of understanding for the existence and properties (including nearly constant parameters) of chirped pulses that can form and propagate stably in all-normal dispersion laser cavities [12–14]. High energy of the dissipative soliton is reached by means of high pulse chirping and the corresponding increase in its duration at fixed peak power.

Introduced in the 1990s [15, 16] as an extension of the term *soliton*, the term dissipative soliton (DS) describes localized structures of an electromagnetic field in nonconservative systems, where energy exchange with environment becomes

Nonlinear Optical Cavity Dynamics: From Microresonators to Fiber Lasers, First Edition.
Edited by Philippe Grelu.
© 2016 Wiley-VCH Verlag GmbH & Co. KGaA. Published 2016 by Wiley-VCH Verlag GmbH & Co. KGaA.

important in addition to a balance between nonlinearity and dispersion (or diffraction). Therefore, a balance between gain and loss is also needed to form a stable structure (see [17, 18] for a review of the DS basic principles and their emergence in optics, hydrodynamics, biology, etc.). Since the gain-to-loss balance is a typical requirement for laser generation, the concept of DSs has been successfully applied for description of pulse dynamics in a laser cavity (see [19, 20] for a review), especially for a broad class of passively mode-locked lasers [21]. The DS concept is also useful for practical purposes implying for the new cavity designs, in particular, those providing generation of high-energy femtosecond pulses. Being intrinsically one-dimensional, stable, and hands-free, all-fiber design of femtosecond oscillators is one of the most attractive for these purposes.

Implementation of the DS concept in fiber lasers led to the generation of $\sim$10 nJ pulses in a scheme with dispersion compensation [22] and 20 nJ pulses in an all-normal-dispersion (ANDi) fiber laser consisting of normal-dispersion elements only [23]. The pulses are externally compressed to $<$200 fs. It appeared that energy scaling is possible by the fiber cross-section enlargement. As a result, the pulse energy in fiber oscillators has been increased to $\sim$100 nJ at $\sim$100 fs duration [24].

In theory, stable chirped pulses in normal-dispersion cavity are usually described in the frame of cubic–quintic Ginzburg–Landau equation (CQGLE) applicable for small variations of the pulse parameters along the cavity; see, for example, [17, 19]. There exists an analytical solution of the equation [25] relevant to optical fibers in the case of relatively small chirp parameter f defined as

$$f = \frac{T\Delta}{4}, \tag{12.1}$$

where T is a pulse duration and Δ is its spectral width. Though the solution obtained in [25] is exact, it is applicable to the pulses close to spectrally limited ones, $f \simeq 1$. In contrast, in the discussed experiments dealing with energy scaling in fiber lasers, net normal dispersion value is high and pulses with chirp parameter $f \simeq 10-30$ are generated. So, new approaches are needed for solving a problem of limitations arising at the DS energy scaling by means of cavity lengthening.

In this chapter, we give an overview of our results on the theoretical description of highly chirped DS (HCDS) based on the approximate analytical solution of Ginzburg–Landau equation in high-chirp limit and its stability analysis [26, 27]. Following the developed analytical model describing stable HCDS solutions, we study experimentally the regime of highly chirped pulses in an Yb-doped fiber laser with passive mode-locking via nonlinear polarization evolution (NPE) and test the model predictions. The generated pulses are shown to have equal phase shifts induced by nonlinearity and dispersion, thus acquiring a linear chirp in accordance with the HCDS concept. The pulse chirp parameter grows almost linearly with the cavity length leading to nearly linear increase of the pulse energy. The linear scaling, in turn, is valid only up to some extent, beyond which the stability of the regime degrades significantly. The reason of the stability break is shown (both theoretically and experimentally) to be an excessive rotation of the polarization ellipse in the cavity. Therefore, polarization-maintaining fibers for increasing the scaling range of the HCDS regime can be a good choice. As a result of this study, an all-fiber configuration free of NPE overdriving based on long PM and short SM parts was proposed [28]. In this configuration, it appears possible to increase the cavity length up to 120 m, thus generating stable DSs with energies > 20 nJ and chirp parameters $f > 200$ being compressible down to $\sim$200 fs [29]. At this stage, a new limiting factor comes into play, namely stimulated Raman scattering (SRS).

The detailed analysis of the SRS-driven evolution of DS in such long cavities has been performed in the frame of nonlinear Schrödinger equation (NSE) in which SRS term is added, and the model has been compared with the experiments [30]. It appears possible to realize stable DS in the presence of strong SRS effect. Moreover, with a new laser scheme based on the critical elements described earlier and an additional Raman feedback loop, stable linearly chirped DSs at Stokes-shifted wavelength, so-called Raman dissipative solitons (RDS) were recently demonstrated [31]. Together with the main DS, the Raman DS (RDS) of different orders form a multicolor complex of coherent pulses with higher total energy that can be, under certain conditions, compressed to sub-100 fs duration. Potential applications of the RDSs and the DS–RDS complexes are discussed at the end of this chapter.

12.2
Generation of Highly Chirped Dissipative Solitons in Fiber Laser Cavity

12.2.1
Modeling

Newell showed in 1974 [32] that, in approximation of slowly varying amplitude, the equation for an envelope of the electromagnetic wave has a universal form and may be reduced to the cubic Ginzburg–Landau equation (CGLE). This equation and its generalizations, for example, including different higher-order nonlinear and dissipative effects, are used as a basis for description of wave dynamics in various physical phenomena, from hydrodynamics and plasma to femtosecond light pulses [7]. It is also important that this class of equations has soliton solutions in the broad range of physical parameters. It is clear that the solitons are observable in the experiment if they are stable. Therefore, many papers are devoted to the numerical studies of CGLE solutions stability, see, for example, [17] and citations therein.

As mentioned in Section 12.1, a physically important class of the soliton solutions of Ginzburg–Landau equation is the highly chirped dissipative solitons (HCDS). Strongly inhomogeneous phase distribution characterizes physically their capacity to redistribute energy without loss of stability. As will be demonstrated later, this property can provide energy scalability of HCDS. In the case of slow saturable absorber, whose relaxation time is comparable to or greater than the pulse duration, the CGLE can be solved exactly [33]. The solutions obtained in that paper have a spectral profile with sharp edges, typical for DSs. In the case of fast nonlinearity, where the response time of the medium is much shorter than the pulse duration, attempts of the DS description in the frame of CGLE approach revealed that the solutions are unstable against amplitude blow up [34]. A reason of such behavior is physically obvious for positive self-amplitude modulation (SAM): an intensity growth enhances a nonlinear gain that induces a further increase of intensity. As a result of such positive feedback, the peak power increases unlimitedly. Physical senselessness of such a solution is obvious: a nonlinear gain cannot grow unlimitedly. Hence, one may conclude that the CGLE should be modified by an inclusion of SAM saturation.

From this point of view, a simplest master equation for the envelope $E(z,t) = 1/\sqrt{2}(A_{z,t}e^{i(\omega t-kz)} + A^*_{z,t}e^{-i(\omega t-kz)})$ may be rewritten as [17]

$$\frac{\partial A}{\partial z} = iL\left(\frac{\beta_2}{2}\frac{\partial^2}{\partial t^2} - \gamma|A|^2\right)A + \left(-\sigma + \alpha\frac{\partial^2}{\partial t^2} + \kappa|A|^2\left(1-\zeta|A|^2\right)\right)A, \quad (12.2)$$

which is usually named as the CQGLE. Here, z coordinate is normalized by cavity length L. The first two terms describe group-delay dispersion (GDD) and self-phase modulation (SPM) distributed along the cavity; therefore, they grow with L. In long cavities (in the HCDS regime), these terms are much higher than the remaining four-point action terms describing a difference between loss and gain (σ), spectral filtering (α), SAM (κ), and SAM saturation (ζ) at a cavity round-trip. All the parameters are positive for the chosen designation. Spectral filtering is naturally present due to a finite width of the gain spectrum and may be enhanced by insertion of the additional filters into the cavity. SAM is implemented in experiments in various ways, namely by Kerr lensing [6], nonlinear optical loop mirror (NOLM) [4, 35], saturable absorber [36], or via nonlinear polarization evolution (NPE) [5, 7], thus providing mode-locking.

Equation (12.2) is applicable if variations of the pulse parameters are small at the cavity round-trip. As was shown in [37], Eq. (12.2) is applicable for the description of high-energy HCDSs formation in a Ti : Sa laser. The CQGLE also proved its effectiveness in the modeling of fiber lasers [14, 38–40]. A typical block scheme of ring fiber laser, which can be considered in the framework of CQGLE, is shown in Figure 12.1a.

The complex pulse envelope $A(t)$ averaged along a cavity can be found as a solution of Eq. (12.2) under the stationarity condition $\frac{\partial A}{\partial z} = iqA$, where q is the wave vector shift. An exact weakly chirped dissipative soliton solution of the CQGLE, which exists in a region of normal GDDs has been first demonstrated in [41]. Such a soliton can be expressed in the form $A = a(t)^{1+if'}$ (f' corresponds to dimensionless chirp parameter introduced earlier in the limit $f' \sim f \gg 1$) and its existence is provided by some fixed algebraic relations between the parameters of Eq. (12.2) [25]. Stability analysis and study of existence domain for this chirped soliton solution were performed in [25, 42, 43]. The high chirp limit $f \to \infty$ requires that changes of a field phase prevail over the field amplitude that corresponds to the following conditions imposed on the system parameters: spectral filtering is much weaker than the round-trip GDD ($\alpha \ll \beta_2 L$), and SAM

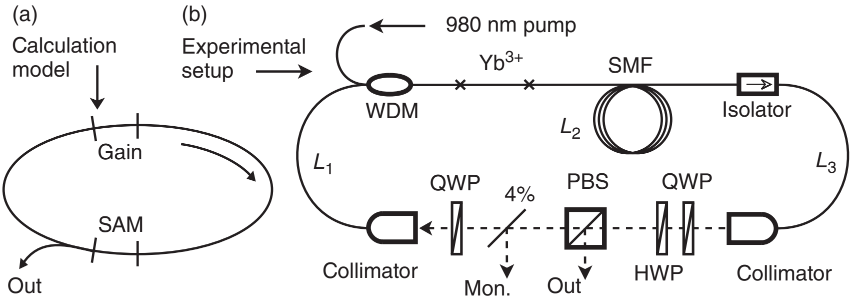

Figure 12.1 (a) Block scheme of a fiber laser with ring cavity configuration, (b) typical scheme of the real experimental setup.

is much weaker than the net SPM ($\kappa \ll \gamma L$). These conditions have to be fulfilled simultaneously to enhance the phase effects causing pulse chirping. In this limit, the chirp parameter is expressed simply via coefficients describing equation parameters (see [25], for instance):

$$f \simeq 3L/(2\alpha/\beta_2 + \kappa/\gamma). \tag{12.3}$$

The exact solution [25, 41] becomes singular for $f > \sqrt{3}$; that is why powerful technique to analysis of HCDSs with $f \gg 1$ based on the WKB ideology was invented in [26, 44]. Such an approach has been expanded in various generalizations of the nonlinear Ginzburg–Landau equation [45, 46]. In the next section, we present a sketch of the theory for energy scalable HCDSs.

12.2.1.1 Analytical Solution of CQGLE in the High Chirp Limit

In a nutshell, an HCDS solution of Eq. (12.2) in the limits of $f \gg 1$; $\alpha \approx \beta_2 L/2f \ll \beta_2 L$ and $\kappa \simeq \gamma L/f \ll \gamma L$ can be expressed in the following way [26, 27]. A scaling in the time domain $t = \tau f$ allows expressing a wave envelope in the form

$$A(z,t) = a(\tau, z)e^{if\Psi(\tau,z)-iqz}, \tag{12.4}$$

where $\phi(t) = f\Psi(t/f, z)$ is a phase. The physical sense of such a scaling is that a chirped pulse is stretched by f times in the time domain compared with a transform-limited pulse. In this case, the time (τ) derivatives of a and Ψ become finite in the limit of $f \to \infty$, and we can define explicitly the vanishing terms of Eq. (12.2). Substituting Eq. (12.4) in Eq. (12.2) and separating its real and imaginary parts results in two equations for $\frac{\partial\Psi}{\partial z}$ and $\frac{\partial a}{\partial z}$ (see [27]).

The first principal step consists of the assumption that for an HCDS ($f \gg 1$) one may neglect the terms of the order of $O(1/f^2)$. In a steady-state regime with $\left(\frac{\partial\Psi}{\partial z} = 0\right)$, it allows obtaining the strict relationship between an instantaneous power $P(t) = P(\tau f) = a^2(\tau)$ and an instantaneous frequency $\Omega(t) = \frac{\partial\phi}{\partial t} = \frac{\partial\Psi(\tau)}{\partial\tau}$:

$$P(\tau f) = P_m - \frac{\beta_2}{2\gamma}\Omega^2(\tau f), \tag{12.5}$$

where $P_m = q/\gamma$ is a peak power at a pulse center where $\Omega \equiv 0$. Thus, the shape of a pulse is defined explicitly by its instantaneous frequency. The requirement $P(\tau f) > 0$ in Eq. (12.5) leads to the conclusion that the spectrum has to be truncated at some maximum frequency deviation Δ:

$$\Delta^2 = \frac{2\gamma P_m}{\beta_2}. \tag{12.6}$$

It is important that the theory allows explicit expressing an instantaneous frequency in the form of first-order ordinary differential equation (for details see [27]).

The second principal step concerns excluding of the physically meaningless solutions corresponding to $\frac{d\Omega}{dt} = \infty$, that can be realized by the regularization technique [26, 47] removing the divergences. It leads to the two-valued expressions for the HCDS peak power P_m:

$$P_m^{\pm} = \frac{3}{8\zeta}\left(2 - C \pm \sqrt{(2-C)^2 - 16\frac{\sigma\zeta}{\kappa}}\right), \tag{12.7}$$

where parameter $C \equiv 2\alpha\gamma/\kappa\beta_2$ is introduced. Thus, there exist only two nonsingular HCDSs of CQGLE; its instantaneous frequency can be expressed in the following form:

$$\frac{d\Omega}{dt} = \frac{\kappa\zeta}{3\gamma L}\left[\Omega^2(t) + \frac{2\gamma}{\beta_2\zeta}(1+C) - \frac{10\gamma}{3\beta_2}P_m\right]\left(P_m - \frac{\beta_2}{2\gamma}\Omega^2(t)\right). \tag{12.8}$$

The solution to this equation may be written in an implicit form [26] for both positive ($P_m = P_m^+$) and negative ($P_m = P_m^-$) branches of Eq. (12.7):

$$\operatorname{arctanh}\left(\frac{\Omega(t)}{\Delta}\right) + \frac{1}{R}\arctan\left(\frac{\Omega(t)}{R\Delta}\right) = \frac{t}{T}. \tag{12.9}$$

Here, $\Delta = \sqrt{\frac{2\gamma}{\beta_2}P_m}$ defines the width of a truncated HCDS spectrum, $T = \frac{6\gamma^2 L}{\beta_2\zeta\kappa\Delta^3(1+R^2)}$ is a characteristic time that defines a pulse duration, and R is a parameter defining the pulse shape. The last can be expressed as

$$R = \sqrt{\frac{1+C}{\zeta P_m} - \frac{5}{3}} \tag{12.10}$$

The third principal step of the theory is its representation in the Fourier domain. With a scaled time variable $t = f\tau$, one may come to

$$A(\omega) = f\int d\tau\ a(\tau)e^{if(\Psi(\tau)-\omega\tau)}. \tag{12.11}$$

In the high-chirp limit of $f \to \infty$, the integral can be calculated by the method of stationary phase that results in the following asymptotical expression [48]:

$$A(\omega) = f a(\tau^*)e^{if(\Psi(\tau^*)-\omega\tau^*)} \cdot \sqrt{\frac{2\pi}{-if\left.\frac{d^2\Psi}{d\tau^2}\right|_{\tau=\tau^*}}}(1 + O(1/f)), \tag{12.12}$$

where $\tau^*(\omega)$ is the point of stationary phase defined by condition $\left.\frac{d\Psi}{d\tau}\right|_{\tau=\tau^*} = \omega$ for any frequency ω. Taking into account of $a^2(\tau) = P(t) = P_m - \frac{\beta_2}{2\gamma}\Omega^2(t)$ and $\frac{d^2\Psi}{d\tau^2} = f\frac{d\Omega}{d\tau}$ that is defined by Eq. (12.8) result in [27]

$$I(\omega) \equiv |A(\omega)|^2 \simeq \frac{6\pi\gamma L}{\zeta\kappa}\frac{1}{\omega^2 + R^2\Delta^2}(1 + O(1/f))\ at|\omega| < \Delta. \tag{12.13}$$

At $|\omega| > \Delta$, there is no point of stationary phase and, thus, the integral (Eq. (12.11)) tends to zero ($I(\omega) = 0$) asymptotically for $f \to \infty$.

As a result, the theory allows expressing the HCDS energy:

$$E \equiv \int \frac{d\omega}{2\pi} I(\omega) = \frac{12\pi\gamma L}{\zeta\kappa\Delta}\frac{\text{arcctg}(R)}{R}. \tag{12.14}$$

The most impressive phenomenon, which is revealed by the theory presented, is an energy scalability of HCDSs. As one can see, the HCDS shape $P(t)/P^{\pm} = B(t/T)$, spectral profile $I(\omega)/I(0) = A(\omega/\Delta)$, and pulse energy E depend on the only parameter R. If all six parameters of the initial equation are changed at an R value kept fixed, then the HCDS shape in time domain and its spectrum will change in a self-similar way, that is, its amplitude, duration, and chirp as well as the spectral amplitude and width will scale with the conservation of soliton shape. In the limiting case of $\zeta P_m \ll 1$ ($R \to \infty$), the solution $P(t)$ tends to $\text{sech}^2(t/T)$, that is, to the transform-limited CGLE solution. However, an opposite limit ($R \to 0$) corresponds to an HCDSs with rectangular profile.

Pulse energy, see Eq. (12.14), in these limiting cases tends to $\lim\limits_{R\to\infty} E = 0$ and $\lim\limits_{R\to 0} E = \infty$. The last limit for rectangular pulse reveals the phenomenon of perfect energy scalability of HCDSs, which is analogous to the dissipative soliton resonance reported in [49–51], and can be explicated in the form of so-called "master diagram" [44]. An iso-gain curve $\sigma = 0$ on the master diagram corresponds to condition of the HCDS marginal stability and the dissipative resonance condition for it is $\lim\limits_{C\to 2/3} E\kappa^{3/2}\zeta^{1/2}/\gamma\alpha^{1/2} = \infty$. If the parameters of spectral filtering, SAM, and net-gain σ are kept on some constant level, the energy scaling can be provided by simple scaling of fiber length L.

It is important to note, that HCDS solutions exist in the limited regions of the whole domain of CQGLE parameters [27]. Since the pulse power must take only positive real values, it follows from Eq. (12.7) that the HCDS solutions are absent in the region $C \equiv 2\alpha\gamma/\beta_2\kappa < 2 - 4\sqrt{\frac{\sigma\zeta}{\kappa}}$. The definitional domain for analytical solutions is shown in Figure 12.2 on the $\left(C, \frac{\sigma\zeta}{\kappa}\right)$ plane. Numbers (I) and (II) denote the regions where HCDSs do not exist [27]. The condition of the pulse spectrum limitation $R^2 > 0$ defines the HCDS existence regions for the positive ($P_m = P_m^+$) (IV) and the negative ($P_m = P_m^-$) (III, IV) branches. In this diagram, the dissipative resonance condition ($R = 0$) corresponds to the dividing border between the regions III and IV.

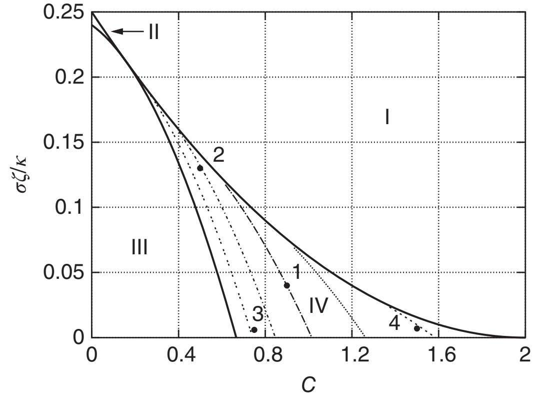

Figure 12.2 Solution existence areas in the plane $(C, \sigma\zeta/\kappa)$: positive $(P_m = P_m^+)$ branch of the analytic solution exists in the area IV, negative $(P_m = P_m^-)$ branch—in the areas III and IV. Coordinates of the example numerical solutions are marked by points. Dotted lines illustrate the paths with self-similar pulse shape corresponding to $R = \text{const}$ [27].

12.2.1.2 **Comparison of Analytics with Numerics**

It is important to analyze the stability of both branches of HCDS existing in the regions III and IV. Such an analysis was based on the numerical solution of Eq. (12.2). The technical details of the calculations can be found in [27].

In region IV of Figure 12.2, the points with coordinates $(C, \sigma\zeta/\kappa)$ equal to $(0.9, 0.04)$, $(0.5, 0.13)$, $(0.75, 0.006)$, $(1.5, 0.007)$ are marked by the numbers 1, 2, 3, and 4, respectively. For each point, we performed several simulations with various initial conditions including a Gaussian shape pulse, an analytical solution, and white noise [27]. It was found that for any parameter set inside region IV, there exists a stable analytical solution (positive branch). Numerical simulation with any initial perturbation converges to this solution. On the contrary, in region III, it was not possible to obtain any stable solution, even if the analytical solutions for negative branch were taken as the initial approximation. All the initial approximations either decay after 300–500 round-trips or broaden unlimitedly in time domain at the constant amplitude. Note that a similar behavior has been observed in [42] for the negative branch of the solution for weakly chirped soliton [41].

The obtained results lead to the conclusion that the negative branch solution is unstable in its all-definitional domain (regions III and IV), whereas the positive branch solution is stable in its region of existence (IV).

In region II, both solution are absent since $R^2 < 0$. We performed simulations for several points in regions I and III with different parameters of the initial equation. It was found that in region I there exist stable solutions corresponding to weak chirp $f \simeq 1$, whereas highly chirped solutions $f \gg 1$ are absent in this region. At the same time, we have not succeeded in realizing any stable either weakly or highly chirped solution in region III. Therefore, it is possible to

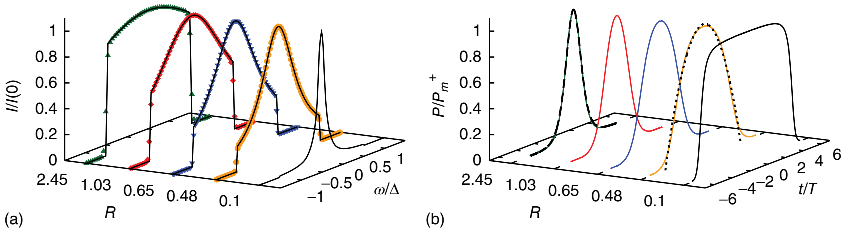

Figure 12.3 (a) Comparison between numerics (color) and positive branch of the analytical solution (solid black) for the spectral shape. (b) Time-domain shape of the positive branch (solid) and fitting (dashed) by parabola and sech^2. Additional black curve shows analytics in the limit $R \to 0$ ($R = 0.1$).

conclude that region IV is the only domain of existence and stability for all the highly chirped solutions of Eq. (12.2).

We also compared numerical simulation and analytical solution in points 1–4 of region IV in Figure 12.2. For all these points, the result of numerical simulation coincides with the analytical solution for positive branch in all its definitional domain (Figure 12.3). This means that the shape of the HCDS solution of the Eq. (12.2) at high chirp condition actually depends only on the value of parameter R being independent of other parameters of the equation. The values of parameter R for curves intersecting the points 1, 2, 3, and 4 shown in Figure 12.2 are equal to $R \simeq 1.03, 0.65, 0.48, 2.45$, correspondingly. The performed numerical analysis has shown that along these curves the solutions are self-similar, that is, the shape of the pulse and the shape of its spectrum do not change.

In Figure 12.3, the spectral and temporal shapes of HCDS are shown at various values of parameter R, corresponding to dashed lines in Figure 12.2. Analytical solutions are obtained from Eqs. (12.5) and (12.9). According to discussion in the analytical section, at $R = 2.45$ the pulse shape is approximated well by the expression sech^2, that is, is close to the shape of standard NLSE soliton. With decreasing R the shape is changed and tends to parabolic one in point 3 (near the left border of region IV). In the limiting case of $R \to 0$ (exactly at the left border of region IV), the pulse takes the shape close to rectangular one: $P = P_m^+(1 - R^2\tan^2(R\,t/T))$ at $t < \frac{T}{R}\frac{\pi}{2}$.

Since exact solutions of CQGLE [25, 41–43] are singular at high chirp, our demonstration of stable HCDSs of CQGLE has high theoretical and practical significance [27, 44]. Only one of two solutions appears to be stable (+ branch in notation of paper [26]) in the absence of gain saturation. This is similar to the case of weakly chirped solitons [25, 41–43]. This fact is rather common and follows from more general mathematical theory of bifurcations. In addition, direct comparison of the analytical solutions for the pulse spectra with the numerical ones demonstrates the 10^{-2}–10^{-4} accuracy for chirp parameters $f > 10$. The existence domain for the stable HCDS solutions with possibility of its self-start has been found in the CQGLE parameters set. Meanwhile it has been shown that the stable solutions correspond to the HCDS family with only one parameter

R described by the expression (12.10). Inside this family the pulse shape is changed from the conventional soliton shape of sech^2 at $R \to \infty$, to rectangular one at $R \to 0$, with a shape close to parabolic one in between: at $R \sim 0.5$. This parameter may be calculated for any experimental configuration and one can perform a quantitative comparison with experiment that makes a significant step in development of analytical theory.

The obtained theoretical results make it possible to classify experimentally observed HCDS pulses and to optimize experimental schemes aiming at the generation of pulses with various shapes.

12.2.2
Experiment and its Comparison with Simulation

Since the approximate analytical solution is applicable in the high-chirp limit, $f \gg 1$, it corresponds to conditions of most experiments with fiber lasers of ANDi type generating highly chirped pulses (HCP) [23, 29, 52, 53]. This model also shows that spectral shaping may be achieved even without strong spectral filtering produced by an additional filter element. Stability analysis of the solution [26] performed in papers [27, 54] has shown that only one of two solution branches appears to be stable. At that, stable solutions may be represented as one-parameter family with composite parameter R defining the pulse shape, as shown in Section 12.2.1.

In this section, we explore the developed analytical model [26, 27] for verification of the HCDS regime in the experiment, for optimization of the experimental scheme and for testing of energy scaling possibilities by means of cavity lengthening.

A scheme of the experimental setup that we use to study the regimes with HCP in a Yb-doped fiber laser [28] is presented in Figure 12.1b. The scheme is similar to those in [13, 23], but with one significant difference—we do not use any additional spectral filters for achieving the HCP regime. The laser consists of fiber and bulk optics parts. The fiber part includes (clockwise starting from the left top side): WDM coupler with 45 cm and 30 cm fiber tails, 15 cm active single-mode fiber (SMF) with high Yb^{3+} concentration, 80 cm passive XP1060 SMF of variable length and isolator with 30 and 85 cm tails. In the bulk optics part, we have quarter-wave (QWP) and half-wave plates (HWP), polarization beam splitter (PBS), 4% plate to monitor intracavity parameters of the laser and second QWP to produce slightly elliptic polarization at the input of the fiber part, necessary for NPE effect.

As the active fiber is highly doped its absorption amounts to 900 dB m^{-1} at 976 nm. A polarization insensitive fiber isolator has 2 dB losses at 1030 nm. The pumping is produced by a single-mode laser diode (LD) of up to 400 mW optical power at 976 nm. A monitoring port formed by 4% plate is used for measurements of the intracavity power and spectra. An output pulse train is observed on the output port of PBS used for output pulse width and power measurements. The pulse width is measured by scanning interferometric autocorrelator operating in the range from 10 fs to 6 ps. The pulse spectrum is measured by Yokogawa optical spectrum analyzer with wavelength range from 600 to 1700 nm and wavelength resolution of 0.02 nm. The pulse train is also monitored by a fast oscilloscope in combination with a 1-GHz photodiode.

In the experiment, we have realized the HCP regime at four different values of cavity length: 4.5, 3.6, 3.2, and 2.6 m with the corresponding repetition rate 44, 55, 63, and 78 MHz. In all configurations, the studied HCP regime is found to be stable. Its self-starting is achieved by means of HWP tuning, without any external amplitude modulator. The threshold pump power for stable mode-locking is varied from 250 to 350 mW. At lower powers, the laser generates CW radiation or stochastic pulses. At higher power, the mode-locking is unstable and tends to CW regime. Note that the power range of stable operation is significantly reduced in case of the longest cavity.

Several measurements of spectrum, autocorrelation trace and laser power have been taken for each cavity length. Both the intracavity and extracavity spectra have steep edges with more than 30 dB contrast that is typical for HCDS regime. Full width of the intracavity spectrum at −10 dB level is in the range of 12–14 nm. The measured output pulse width varies from 1.3 ps for the shortest cavity to 3 ps for the longest cavity. The pulses were compressed externally by diffraction grating pair to about 250 fs [28].

The energy of output pulses, measured at the output port of PBS is presented in Figure 12.4a. Dotted line is a linear fit for the first three groups of points. Different points in one group correspond to mode-locking regimes with different level of pump power and slightly different adjustments of the phase plates, correspondingly. The energy value for the fourth group of points deviates significantly from the linear dependence and, therefore, this group was excluded from the fitting. We consider this point and reasons of its deviation in later sections. Note that the intracavity power is ~2 times higher than the output one and amounts to 1 nJ.

We can also calculate chirp parameter (Eq. (12.1)) using measured values of the full spectral width Δ and duration of the chirped pulse T. The dependence of

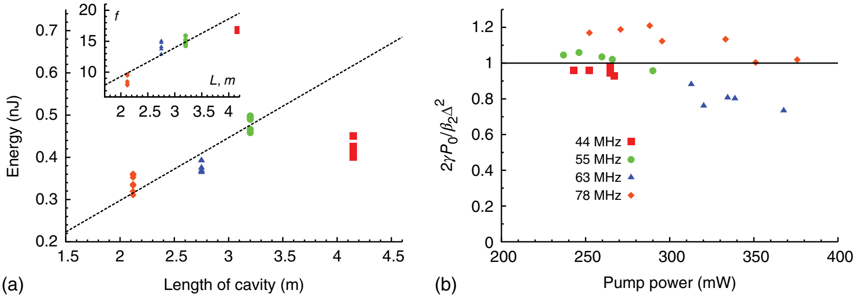

Figure 12.4 (a) Energy of the output pulses depends on cavity length; inset –dimensionless chirp parameter defined by Eq. (12.1); (b) nonlinearity and dispersion phase shift ratio over one round-trip in the cavity [28].

the dimensionless chirp parameter versus cavity length is presented in the inset in Figure 12.4a. Note that the chirp parameter value at the longest length is also out of the linear trend, similar to the pulse energy. Let us compare the obtained experimental results with theoretical relations [26, 27].

Since our experimental results are in the area of applicability of the analytical solution, we should observe the same behavior in the theory and experiment. One of the important consequences of the theory is possibility of scaling provided by the linear dependence of chirp parameter on the cavity length (see Eq. (12.3)). As can be seen from the experiment (inset in Figure 12.4a), it is true for three experimental points with cavity lengths shorter than 4 m, but at the fourth point the chirp parameter deviates significantly from the linear dependence, similar to the pulse energy (Figure 12.4a). Reasons of this deviation will be also discussed later.

Another important theoretical issue characterizing HCDS is a balance between nonlinearity and dispersion phase shifts (Eq. (12.6)), so in theory their ratio should be equal to unity (as presented in Figure 12.4b by thick line). The figure also presents experimental points for this ratio calculated from the measured data and the specified fiber parameters. Average peak power P_0 defining nonlinear phase shift is calculated as $P_0 = \sum_{i=1}^{3} P_i L_i / \sum_{i=1}^{3} L_i$, where P_i and L_i is the peak power and length in the ith section of cavity correspondingly (see Figure 12.1b). We have divided the cavity into three sections having different power levels. First one is between the fiber input and active fiber (minimum peak power). Second one is between active fiber and isolator (maximum peak power). Third one is between isolator and PBS.

The derived experimental points are marked by different colors/signs corresponding to different lengths (as in Figure 12.4a). The points locate around theoretical value in the region between 0.8 and 1.2 for all pump power and length values. We can, therefore, conclude that highly chirped pulses obtained in the experiment can be attributed to dissipative solitons. It is an important result meaning that a femtosecond oscillator can be described analytically by the developed theory in its applicability domain, $f > 10$. In order to explain significant deviation of the last point in length dependence (corresponding to the longest cavity length) both for energy and chirp parameters, we have applied numerical simulation described in the next section.

12.2.3

NPE Overdriving and its Influence on Dissipative Solitons

As follows from the experimental data (Figure 12.4) simultaneous linear growth of the chirp parameter and pulse energy with the cavity length breaks at some critical point (corresponding to cavity length of 4–4.5 m) that contradicts the analytical model predicting unlimited linear growth. To identify reasons leading to such critical behavior, we should go beyond the scalar model of CQGLE and perform numerical simulation in vectorial NPE model.

To describe directly polarization vector evolution, we should treat vectorial equation for electromagnetic field amplitude $E(z,t)$ (see, e.g., [55]):

$$\frac{\partial E_\pm}{\partial z} = \left[i\frac{\beta_2}{2}\frac{\partial^2}{\partial t^2} - i\gamma I \pm \frac{i\gamma}{3}(|E_+|^2 - |E_-|^2) \right] E_\pm + \frac{g_0}{1+\frac{W}{W_s}} \frac{1}{[1+\frac{1}{\Delta_1^2}\frac{\partial^2}{\partial t^2}]} E_\pm, \tag{12.15}$$

$$I = |E_+|^2 + |E_-|^2, \quad W = \int I(t)dt = \int \tilde{I}(\Omega)\frac{d\Omega}{2\pi}, \tag{12.16}$$

where $W_s = P_s T_R$ is the saturation energy, $T_R = Ln_0/c$ is the cavity round-trip time, Δ_1 is the half width of the gain spectrum, g_0 is the small-signal gain coefficient, and $E_\pm = (E_1 \pm iE_2)/\sqrt{2}$ are right-hand and left-hand circular polarizations of the electric field. In the simulation, we use experimental values of the dispersion, nonlinearity, and loss coefficients presented in Section 12.2.2. At each cavity length, an optimization of the output power is performed by means of the waveplates rotation thus changing polarization state. The calculated output pulse energy grows linearly with the cavity length. The growth is terminated at some critical length similar to that in experiments [28]. The higher the polarization ellipticity the lower the critical length and maximum pulse energy, accordingly. Herewith, the value of polarization rotation angle tends to $\pi/2$ at the critical length thus leading to ambiguity in SAM.

These results agree in general with previous results on normal-dispersion cavity fiber lasers [13, 23, 56] where NPE "overdriving" was mentioned, but here we clarify in detail the physical mechanism of limitations at cavity lengthening, explained on the base of the vectorial NPE model [55]. Note that the existence of critical length was mentioned in paper [56] where similar pulse energy level ($\approx$1 nJ) has been obtained in 18-m long (9.9 MHz) cavity of Er-doped fiber laser generating linearly chirped pulses compressed down to $\leq$ 200 fs. In paper [57], a possibility of energy scaling by cavity lengthening of Yb-doped fiber lasers is analyzed on the basis of numerical simulation demonstrating gradual degradation of stability at lengthening from $\sim$10 to $\sim$100 m.

The presence of critical length and its value in our experiments agree with the performed numerical simulation based on vectorial model for NPE effect [28]. The relatively low value of critical length in our case is defined by significant losses in bulk optics part of the cavity and light input–output of the fiber. At that, the reason for the HCDS regime break at critical length is found to be defined by the excessive ($> \pi/2$) rotation angle via NPE effect in the fiber leading to instabilities/stochasticity and multiple pulse regimes. For lower losses and lower ellipticity of the pulse polarization at the fiber input, the model predicts larger critical length, but its maximum value will be limited by random birefringence of the fiber and its sensitivity to environment.

Based on the earlier results, we can propose a possible way how to overcome this limit. To keep the rotation angle lower than $\pi/2$, one should increase the total length of the cavity by means of the polarization maintaining (PM) fiber in which rotation is absent, whereas the length of the conventional non-PM SMF fiber part should be fixed (or even shortened) to keep the NPE-induced rotation angle within $\pi/2$ limit. As a result, nonlinear phase shift (and corresponding dispersion shift) accumulated along the PM-fiber part will lead to the HCDS pulse formation, while nonlinear polarization rotation in SMF part will provide stable mode-locking. The experiments in this configuration confirm the absence of NPE overdriving effect, but revealed new limiting factor of cavity lengthening, namely SRS resulting in DS energy conversion into noisy Raman pulse (RP) generated at the Stokes-shifted wavelength. This effect will be considered in detail in the next section.

12.3
Scaling of Dissipative Solitons in All-Fiber Configuration

12.3.1
Different Ways to Increase Pulse Energy, Limiting Factors

Scaling of the pulse energy in the ANDi laser generating highly chirped DSs is possible by increasing its cavity length or mode-field diameter of the fiber. Outstanding results on energy scaling were obtained by implementing intracavity large-mode-area (LMA) photonic crystal fibers [24, 36]. Peak power of generated pulses achieves level of about 1 MW, which is close to the self-focusing threshold in the fiber of $\sim$2 MW [58]. At the same time, LMA fibers (with a core diameter $>$ 20 μ m) are not strictly single-mode, which adversely affects not only the quality of the beam, but also the stability of the single-pulse regime [59]. Moreover, such schemes utilize free-space polarization optics at the expense of environmental stability.

The most successful attempt of the YDFL cavity lengthening [23] resulted in the generation of $<$ 200 fs dechirped pulses with energy increased to $\sim$20 nJ at 12.5 MHz repetition rate (with 6 μ m core fiber and free-space optics). Using a narrow (5 nm) spectral filter inside a resonator, it was possible to obtain generation at a repetition frequency of 3 MHz [60]. In this case, the pulse energy at the output of the oscillator was 15 nJ, and the duration after compression was 670 fs. In addition, the work focuses on the prospects of amplification of such pulses, since the radiation of a chirped pulse generator can be sent directly to an amplifier, without using a stretcher, preamplifier, and modulator. Jiang *et al.* [61] reduced the pulse repetition frequency to 2.3 MHz using an Er-doped fiber as the active medium, which also acts as an efficient spectral filter. They succeeded to reach acceptable environmental stability in 90-m long SMF with NPE mode-locking in spite of its extreme sensitivity. High long-term stability of repetition frequency and laser operation was observed for more than two weeks, although the NPE effect in a long SMF is very sensitive to external influences. The maximum pulse energy at the laser output was 9.4 nJ.

Interesting results have also been obtained in attempts to increase the resonator length without spectral filters. The creation of a high-energy femtosecond pulse system with a repetition frequency of 4 MHz (resonator length 50 m) is reported in [62]. Here, the resonator of the master generator is made of SMF-28 telecommunication fiber with a core diameter of 8.5 μ m. Mode-locking is provided by the NPE effect, and the active medium is Yb-doped GTWave double-clad fiber. The master generator has two outputs with a total energy of ∼10 nJ per pulse. Kobtsev *et al.* [63] also increased the Yb laser length to a record value of 3.8 km, thereby reducing the repetition frequency to 77 kHz and increasing the pulse energy to 3.9 μ J. However, this regime was no longer the regime of highly chirped pulses: the spectral width was only 0.35 nm and the duration of the generated pulse was 3 ns. The autocorrelation function (ACF) of such pulses has a two-scale structure with a narrow peak and a broad valley, which correspond to stochastic mode-locking for which pulse compression is problematic. As the authors showed later by numerical simulation [57], a transition from coherent (chirped) pulses to stochastic ones in the SMF based schemes with NPE mode-locking occurs at the fiber length of about 100 m that is agreed with experiments [61]. In most other experiments, this length is shorter (∼10 m) because of higher losses and higher sensitivity to environment increasing random birefringence of the fiber, see discussion at the end of the previous section.

As reported in [64], the problem of stochastic regime in such ultralong SMF cavities can be principally solved by using another mode-locking technique, for example, point-action saturable absorber based on single-wall carbon nanotubes. The authors use a synchronously scanning streak camera and a monochromator to directly measure the pulse spectrogram. This measurement showed that the pulses have a relatively clean temporal profile, and its average chirp appears to be nearly linear in a broad range thus demonstrating a principal possibility of so-called giant-chirp oscillators. However, the authors note that it is not possible to compensate for the chirp over several nanoseconds pulse duration with any practical compression scheme. Moreover, the chirp characteristic has a significant spread in each point of about 0.1 part of the whole frequency range; therefore, it seems hardly possible to compress the pulses by more than 10 times.

Other ways to improve stochastic regime in ultralong cavities include more complicated cavity design [65] and implementation of active mode-locking technique [66] in Er-doped fiber laser. In [65] pulse energy of nearly 1.7 μ J is obtained at repetition rate is 35.1 kHz in a fiber laser with a linear-ring cavity. In [66], erbium fiber laser generates chirped pulses with energy 34 nJ at 163.8 kHz repetition rate.

Endeavors to improve environmental stability involved also a use of PM fibers in combination with saturable absorber mirror (SAM)[67] demonstrating generation of 1 nJ pulses at 17 MHz rate. In similar linear scheme with PM fibers and semiconductor SAM [60], pulse energy exceeded 2 nJ, but in both schemes dechirped pulses are longer (≥300 fs) than in NPE-based lasers because of long SAM relaxation time. In addition, all the discussed schemes utilize free-space optics that degrades both the system stability and limits possibilities of its practical use.

For practical applications of a laser system an all-fiber design is the most desirable, that is also true for femtosecond lasers. All-fiber NPE-based Yb oscillator delivering 1.8 nJ, 179 fs dechirped pulses at 33 MHz repetition rate was demonstrated by Schultz *et al.* [68]. The same group later developed an all-fiber Yb laser with higher (3.6 nJ) pulse energy [69]. Recently, good results were demonstrated with the use of NOLM [70] and NALM [71] (nonlinear optical or amplifying loop mirror, correspondingly) mode-locking techniques in an all-PM fiber cavity providing exceptional environmental stability. In [71], the authors develop an all-PM all-fiber giant chirp oscillator and present an evident possibility of energy upscaling by cavity lengthening. At the maximum cavity length $L = 100$ m, laser generates stable chirped pulses with energies of 16 nJ that can be compressed to 370 fs duration. At further cavity lengthening, the authors observed a strong Stokes signal induced by SRS and significant stability reduction of a laser generation. They interpreted this fact that SRS is the main reason of the stability break treating this mechanism as a fundamental limitation of energy scalability [72].

Note that in the hybrid SM–PM fiber oscillator free of NPE-overdriving discussed at the end of Section 12.2.3, proposed and realized in earlier papers [28, 29], the SRS effect is observed at comparable pulse energies achieved in shorter cavity, but it does not break the pulse stability even at higher pulse energies. This effect limits the DS energy above the SRS threshold converting all the excess energy into noisy pulse generated at the Stokes-shifted wavelength, but without stability break. The experimental realization of such an all-fiber oscillator together with results on its output parameters and further scaling limitations are presented in the next section.

12.3.2
SRS Threshold for Dissipative Solitons at Cavity Lengthening

The basic design of the DS all-fiber laser is depicted in Figure 12.5. This YDFL scheme is similar to conventional ring schemes of NPE mode-locked DS fiber lasers [13, 19, 20, 23, 24, 73]. A key difference is that the cavity is divided into two parts: very long passive PM fiber part (blue on the scheme) and very short

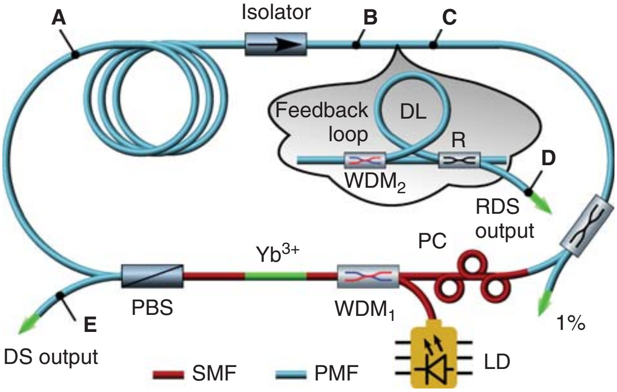

Figure 12.5 Experimental setup of an all-fiber highly chirped DS fiber oscillator.

SMF part (red on the scheme) between polarization controller (PC) and PBS. Such configuration was proposed for elimination of NPE overdriving (see Section 12.2.3) thanks to the possibility to control a rotation angle of the polarization ellipse by varying the length of SMF part of the cavity. The first realization of scheme [29] has confirmed the validity of this concept demonstrating stable mode-locking in a 30-m fiber cavity. In addition to mode-locking, the SMF part is also responsible for the pulse amplification, balancing the losses on the PBS output and spectral filtering naturally defined by the Yb^{3+} gain bandwidth and the spectral function of WDM_1 (see [29, 30] for details). Moreover, since the SMF part is much shorter than the PM part, the effects of mode-locking, gain, and filtering may be treated as point-action, while DS evolution defined by nonlinearity, dispersion, and the studied SRS effect is distributed along the PM fiber. It is an important assumption that is used for further simulations in Section 12.4.1. Mention that a cloud-inset on the scheme corresponds to the modification that allows us to convert a noisy Raman pulses to a new type of the solitons – RDSs. This opportunity is discussed in detail in Section 12.4.3.

The SMF part of the cavity with optimal length $L_{\mathrm{SMF}} \sim 1.5$ m consists of non-PM SMFs: passive fiber (Nufern 1060-XP) and a 15 cm piece of active Yb^{3+}-doped fiber (CorActive Yb-17-05) pumped by 976 nm single-mode LD via 976/1030 nm wavelength division multiplexer (WDM_1). Small-signal Yb^{3+} gain is ~25 dB at spectral maximum (~1025 nm). A PC and a PBS set before and after the SMF part provide NPE-driven self-amplitude modulation. The DS part consists of only PM fiber components: long section ($L_{\mathrm{PM}} = 25-115$ m) of passive PM fiber (Nufern PM980-XP), a PM isolator, and a 1% PM splitter, that is used for a monitoring the intracavity parameters of the generated pulses. The core diameter of the PM fiber used is $d \simeq 5.5$ μ m. The dispersion coefficient measured by the fiber white light interferometer has the value of $\beta_2 = 0.023$ ps^2 m^{-1}. At the outputs, we have some additional fiber splitters that are not present in Figure 12.5 being used for simultaneous measurements of power, radio frequency (RF) and optical spectra. All outputs of the laser were protected by angled physical contact (APC) connectors.

For a pulse compression, we use a standard double-pass compressor consisting of a grating pair (not shown in Figure 12.5 for simplicity). The pulse width is measured by scanning interferometric autocorrelator (Avesta AA-20DD) with input pulse duration ranges from 10 fs to 6 ps and by FROG (produced by Mesaphotonics) with the extended range up to 100 ps (hand made by means of an additional motorized translation stages). The pulse spectrum is characterized by conventional optical spectrum analyzer (Yokogawa 6370). Pulse train and radio frequency beating spectrum were monitored at the same time by 1-GHz photodiode on the oscilloscope and on Agilent N9010A spectrum analyzer, correspondingly.

A linearly polarized pulse is equally affected in PM fiber by dispersion and self-phase modulation providing large linear chirp [28]. So, the fiber laser exhibits generation of stable pulses in all the studied range of the cavity lengths with their duration 30–70 ps nearly proportional to cavity length. The key advantage is that the lengthening of PM-part does not lead to the stability loss: the total cavity

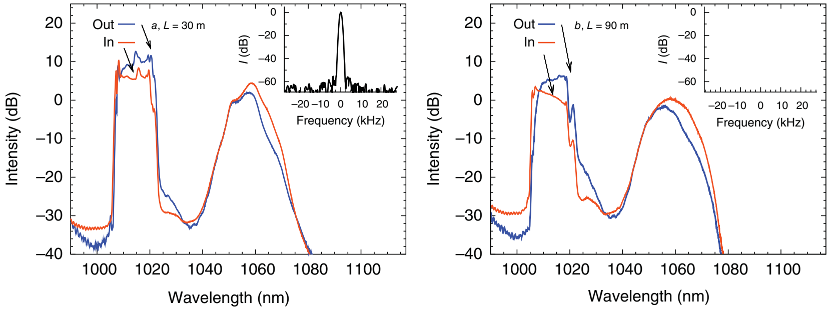

Figure 12.6 The measured optical pulse spectrum (in −inside the cavity at 1% port, out −out of the PM splitter): spectrum for a maximum DS output energy for 30 m and 90 m cavity length is present on (a) and (b) correspondingly.

length can be easily increased from $L \sim 30$ m to $L \sim 120$ m (repetition rate goes down from ~7 to ~1.7 MHz). However, already at the $L = 30$ m (that is about two times more than in Chong *et al.* [23]) another limiting factor comes into play, namely SRS. In addition to the main DS peak (centered at 1015 nm), a Raman peak (centered at 1060 nm) appears in the generated spectrum (see Figure 12.6). It becomes stronger for longer cavities, where a noisy RP develops with an energy comparable with that for a DS. This effect limits DS maximum energy without deteriorating its stability: RF spectra measured at ~750 MHz remain narrow (~1 kHz) and are of high contrast (~60 dB, see insets in Figure 12.6) in all studied range. For a 30 m cavity length, the maximum pulse energy achieved is 23 nJ (> 150 mW output power at 390 mW pumping), 17 nJ of which corresponds to the DS. To the moment of publication [29], this result was about one order of magnitude higher than the pulse energy in previous all-fiber YDFL configurations [68, 69], and comparable with the best results for SMF-based ANDi laser with bulk optics [23]. Notably, we used fibers of smaller diameters together with lower pump powers.

To our surprise, we have succeeded in the generation of stable DS pulses at lengths up to $L = 120$ m (corresponding to the repetition rate $F \sim 1.7$ MHz). At $L = 60$ m and $L = 90$ m, the pulse energy reaches the maximum value of 27 nJ (23 nJ of which corresponds to the DS). At the same time, the energy of intracavity DS pulse remains constant at different pump powers. In longer cavity (120 m), the output DS energy slightly decreases. Nevertheless, at all cavity lengths the optical spectrum has a shape characteristic for a highly chirped DS (with steep edges, see Figure 12.6b). More detailed discussion on intracavity and extracavity pulse energies can be found in [74].

For all cavity lengths, the ACF for both chirped and dechirped DS pulses has been measured. The intensity autocorrelation trace has triangle shape, see Figure 12.7a, that corresponds to the rectangular pulse shape of the same duration, in accordance with theoretical predictions [26, 27]. In terms of analytic solution for highly chirped DS [26, 27], this domain is characterized by a single composite parameter R tending to zero. However, the DS spectrum has

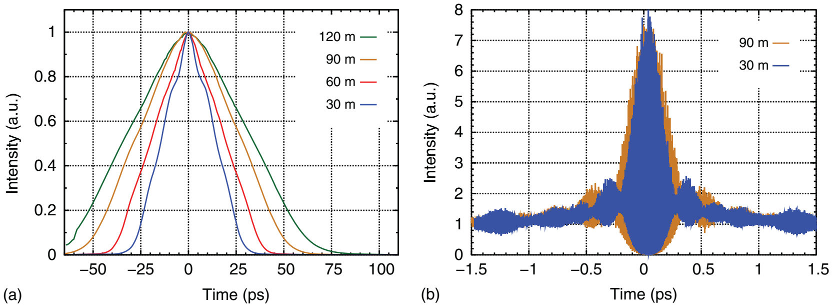

Figure 12.7 Autocorrelation functions: (a) by intensity for chirped pulse at different length of cavity and (b) interferometric for compressed pulse at 30 m and 90 m cavity length.

fluctuations that make difficult its comparison with the DS resonance shape (e.g., see [19]), but it definitely has steep edges with the corresponding ripples in the autocorrelation trace (Figure 12.7) after the compressor. The output pulses were externally compressed from 30 – 70 ps down to 200 – 300 fs (at a transform-limited pulse duration of 160 fs for 30 m cavity length); see Figure 12.7b. So, the resulting compression factor is as high as ∼150 at $L = 30$ m and is more than 200 for $L = 90$ m.

The auto- and cross-correlation traces of the DS and the Raman pulse indicate different chirp, although they copropagate in the laser cavity and have similar durations, with a ≥ 50 ps shift between their centers, that increase linearly with cavity length. Note that the importance of the Raman effect at the pulse chirping was first predicted in theoretical study by Schadt and Jaskorzynska [75]. Appearance of the Raman component in a high-energy fiber laser was mentioned without details and discussion by Kobtsev *et al.* [62].

Let us estimate a threshold energy for the Raman conversion of DS pulses. In the Raman process, an amplification of the wavelength-shifted Stokes wave from the noise level is induced by the DS pulse field. Therefore, the Stokes wave starts propagating together with the DS pulse and its power grows exponentially with the coefficient $g_R P_m$, where P_m is the DS peak power and g_R is the Raman gain coefficient normalized on the mode field area. Because the DS and Stokes pulses have different group velocities (v_0 and v_R, correspondingly) due to dispersion, the Stokes pulse “overpasses” the pump pulse (DS soliton) of duration $T \simeq 30$ ps after propagation of critical distance $L_C = T/\delta v^{-1} \sim 20$ m, where $\delta v^{-1} = v_0^{-1} - v_R^{-1} \simeq 1.5$ ps m^{-1}. Outside the interaction region, DS power tends to zero and the Stokes radiation starts to attenuate. So, the maximum Stokes power is shifted relative to the main DS pulse. We can estimate the maximum peak power of the Stokes pulse as

$$P_R = P_{\text{noise}} \exp\ (g_R P_m T/\delta v^{-1}). \tag{12.17}$$

Evaluation of the noise power that takes into account about a four-orders-of-magnitude difference between the pulse duration and the round-trip time, resulting in $P_{\text{noise}} \sim 10^{-8} P_m$, leads to the ratio for the peak powers and thereby to the following ratio of the Raman and DS pulse energies:

$$\frac{E_R}{E} \propto \frac{P_R}{P_m} \approx \exp\left(\frac{g_R P_m T}{\delta v^{-1}} - 18\right). \tag{12.18}$$

The Raman-component energy, $E_R \sim P_R T$, becomes comparable with the energy of the DS pulse, $E = P_m T$, at critical intracavity energy estimated as $E_{\text{cr}} \simeq 18\delta v^{-1}/g_R$. This estimate corresponds to ~10 nJ for our 5.5 μ m fiber with the Raman gain coefficient $g_R \simeq 2.5\ \text{W}^{-1}\,\text{km}^{-1}$. Note that critical output energy in the experiment is about two times higher than the intracavity one [29].

The smaller the core diameter, the lower the critical intracavity energy at which Raman scattering becomes significant. Therefore, to push further the scaling of the all-fiber dissipative-soliton laser, one should combine our approach with LMA fibers [24]. The Raman effect in this case will be suppressed because of the lower coefficient g_R. In such a combined SMF-PM all-fiber configuration with a 25 μ m core LMA, the estimation above gives $E_{\text{cr}} \sim 0.5$ μ J. As additional steps in the direction of the energy upscaling, one can increase the dispersion parameter δv^{-1}.

Expression (12.17) can be also rewritten through chirp parameter f. Substituting Eqs. (12.1) and (12.6) and taking that $\delta v^{-1} \approx \Delta_{\text{SRS}}\beta_2$, we obtain

$$P_R = P_{\text{noise}}\exp\left(\frac{g_R\Delta^2\beta_2/2\gamma \cdot 4f/\Delta}{\Delta_{\text{SRS}}\beta_2}\right) = P_{\text{noise}}\exp\left(\frac{2fg_R\Delta}{\gamma\Delta_{\text{SRS}}}\right), \tag{12.19}$$

where Δ_{SRS} is the Stokes shift in the fiber. Thus, the Raman gain induced by the DS depends mainly on its chirp parameter f since $\Delta < \Delta_{\text{SRS}}$ and $g_R < \gamma$ in fibers. It means that the SRS effect becomes much more important for highly chirped DSs.

Influence of noise and SRS on the DS energy scalability can also be considered in terms of *DS master diagram* [49]; its representation in a two-dimensional parametric space [76] is shown in Figure 12.8. Without noise and SRS a dissipative soliton is perfectly energy-scalable. The zero-level iso-gain defining the threshold of DS stability against a vacuum excitation is shown by solid black curve in Figure 12.8 and demonstrates the DS resonance existence for a chirped DS: $\lim_{C\to 2/3}E = \infty$. A soliton is unstable to right of this curve. However, such a perfect scalability, for example, in the form of dissipative soliton resonance, can be broken by a noise amplification and an SRS. When a noise and SRS contribute the DS stability border changes drastically (compare black, pink, and blue lines in Figure 12.8) so that an asymptotically unlimited accumulation of energy becomes impossible and the so-called "dissipative soliton resonance" disappears.

Although the Raman scattering is a parasitic effect in the problem of femtosecond fiber lasers energy scaling, it will be especially interesting to study in detail the features of the generated Stokes radiation and its interaction with the DS, which will help to answer the question why such a strong Raman scattering does not deteriorate the soliton in such a long cavity. Theoretical and experimental study of the detailed evolution for the DS in long fiber cavities in the presence of strong SRS effect is presented in the next section.

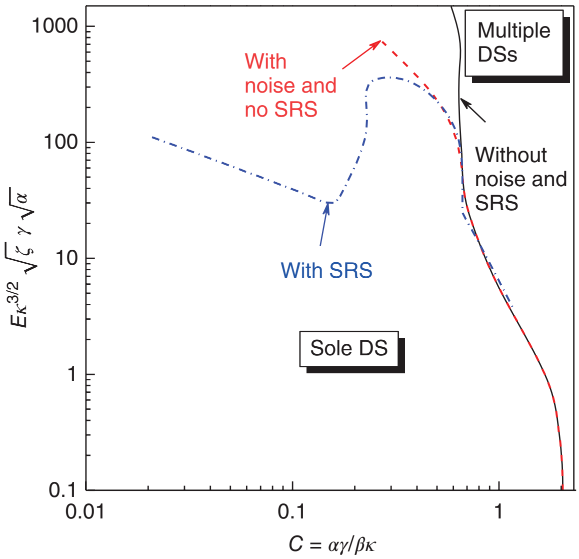

Figure 12.8 Stability thresholds ($\sigma = 0$) of HCDS solutions of CQGLE without noise and SRS (solid black curve), with noise and no SRS (red dashed curve), as well as with noise and SRS (blue dashed-dotted curve). A sole HCDS exists below and left of the corresponding curves. The parameters of CQGLE are $\kappa = 0.1\gamma L$ and $\zeta = 0.05\gamma L$. The spectral filtering parameter $\alpha = 366\ \text{fs}^2$ corresponds to an approximately 40 nm bandwidth. Other details can be found in [76].

12.4
SRS-Driven Evolution of Dissipative Solitons in Fiber Laser Cavity

12.4.1
NSE-Based Model in Presence of SRS

In this section, we report on the comprehensive theoretical and experimental study of the new physical effects defining DS formation and evolution in the presence of strong SRS. We demonstrate that SRS acts not only as an additional channel of energy dissipation destroying DS, but can also support it enabling thus the generation of a stable “DS—Raman pulse” bound complex in all-fiber ring laser cavities with order-of-magnitude larger lengths (>100 m) than in conventional NPE-mode-locked DS fiber lasers [19, 20, 23, 24, 73]. We also discuss the influence of SRS conversion and noise influence on the DS energy scalability. As a result, we have identified the maximal reachable energy of DS with a cavity lengthening.

We study an YDFL experimental scheme that is described in Section 12.3 and depicted in Figure 12.5. As already discussed, the main feature of the scheme is that it provides stable (overdriving-free) mode-locking via NPE in a short SMF part, whereas the cavity length is increased independently by means of PM fiber. Consider first the case without the cloud-inset.

12.4.1.1 **Model Details**

For numerical modeling of a fiber laser, we take into account the discreetness of its intracavity elements. Thus, the effects of mode-locking, gain, and filtering in the short SMF are treated as point-action, while DS evolution inside the long PM fiber in the presence of strong SRS is studied with generalized NLSE; see [19, 20, 77] and citation therein. To include the new effect of the DS spectrum conversion via Raman effect (in the PM fiber the DS and Raman pulses are equally polarized that was directly checked), we add SRS term in the equation, similar to the case of super-continuum generation (see, e.g., [78, 79]):

$$\frac{\partial A}{\partial z} = -i\frac{\beta_2}{2}\frac{\partial^2 A}{\partial t^2} + \frac{\beta_3}{6}\frac{\partial^3 A}{\partial t^3} + i\gamma\left(A(z,t)\int_0^\infty R(t')|A(z,t-t')|^2 dt'\right), \quad (12.20)$$

where $A(z,t)$ is the electric field envelope, β_2 and β_3 are the second- and third-order dispersion coefficients at the central frequency ω_0, γ is the Kerr nonlinearity coefficient, and $R(t)$ is the Raman response function, which includes both instantaneous electronic and delayed Raman contribution. In our simulations, we use the multiple-vibrational-mode model for the Raman response described in [80]. The calculated peak Raman gain (with the Stokes shift $\Delta\lambda = 45$ nm) is nearly equal to the experimental value of $g_R = 2.5 \quad \text{W}^{-1}\ \text{km}^{-1}$ [29]. The specific fiber parameters that are used in simulations throughout the paper are as follows: $\beta_2 = 22\text{ps}^2\ \text{km}^{-1}$ and $\beta_3 = 0.037\text{ps}^3\ \text{km}^{-1}$, $\gamma = 6\text{W}^{-1}\ \text{km}^{-1}$.

The equation was solved by using the symmetrized split-step Fourier-transform method. The simulations are run until the pulse field reaches the steady state after a certain number of cavity round-trips, taking into consideration the contribution of the point-action WDM having a stepwise transmission spectrum, amplification in Yb^{3+}-fiber and the NPE-induced intensity modulation described later.

Amplification in an Yb-doped active fiber l with a Lorentzian line of a 40 nm bandwidth, a central wavelength of $\lambda_0 = 1025$ nm, and a small-signal gain coefficient of $g_0(\lambda_0) \approx 170\ \text{dB m}^{-1}$ was simulated in the spectral domain. The gain saturation is modeled according to

$$g(E) = \frac{g_0}{1 + E/E_{\text{sat}}}, \quad (12.21)$$

where the total gain $g_0 l$ equals to 25 dB, $E = \int_{-T_R/2}^{T_R/2} |A(z,t)|^2 dt$ is the signal energy, $E_{\text{sat}} = P_{\text{sat}} T_R$ is the saturation energy, and T_R is the cavity round-trip time. The amplifier noise is simulated by an additive complex “white” noise with 10^{-7} W average power, which results in spectral noise level −40 dB relative to DS power (Figure 12.11b).

Since the SMF part in our scheme is short compared with PMF, the angle of the NPE-induced polarization rotation in SMF is small. So, we can describe the action of the NPE-based modulator in a scalar form by the cubic–quintic nonlinear term for the pulse amplitude $A(t)$ [39] and rewrite the nonlinear modulator transmission ρ, depending on the incident power $P = |A|^2$ in the following form:

$$\rho = \rho_{\max} - \left(\frac{P}{P_{\text{cr}}} - 1\right)^2 (\rho_{\max} - \rho_{\min}), \quad (12.22)$$

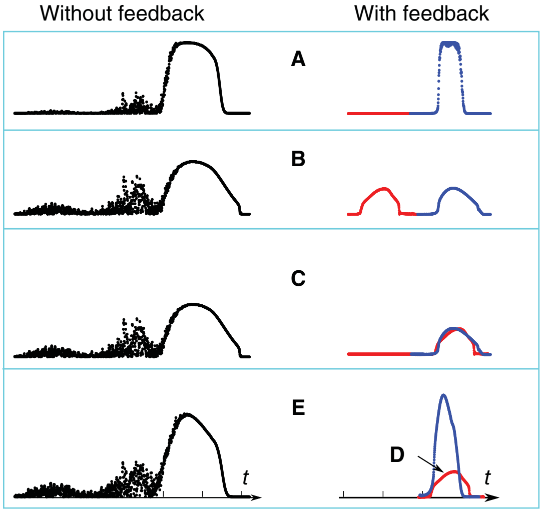

Figure 12.9 The calculated shapes of the generated pulses in corresponding points (A,B,C,D,E) of the scheme without and with the feedback loop shown in cloud-inset of Figure 12.5. The RP in box C (right) present before it attenuated by factor *R*.

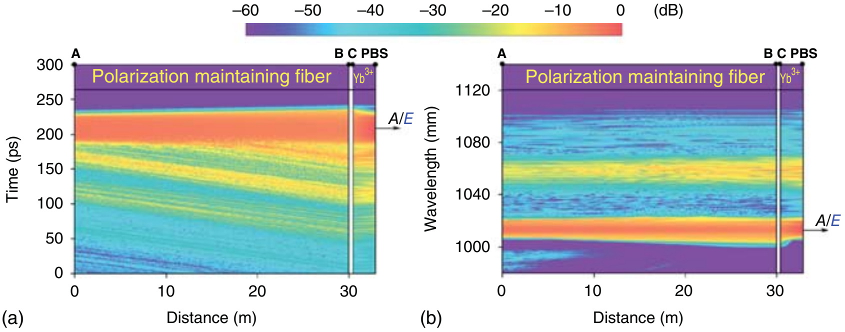

Figure 12.10 Evolution of the pulse shape (a) and spectrum (b) along PMF of $L = 30$ m in the scheme of Figure 12.5 without feedback loop.

where $\rho_{\min} = 0.05$ characterizes the minimal transmission at low powers and $\rho_{\max} = 0.5$ is the maximum transmission at the critical power $P_{\text{cr}} = 850$ W, which corresponds to the experimental data for the PBS splitting ratio in the DS regime.

12.4.1.2 Simulation, Comparison with Experiment

The numerical results have been compared with the experimental data obtained. First, such a comparison was made for $L = 30$ m.

Calculated pulse shapes are shown in Figure 12.9 (left column) in different points of the cavity. Stationary pulse evolution along the cavity is shown in Figure 12.10. A high-power (> 500 W) DS with a duration of 30 ps at point A ($z = 0$) propagates without significant changes of the shape, but its intensity is

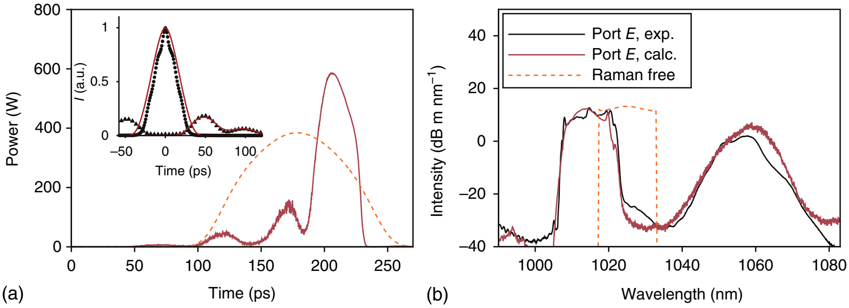

Figure 12.11 Calculated and measured pulse shapes (a) and spectra (b) and at the output port E in scheme of Figure 12.5 without feedback loop. Calculated and measured ACF and CCF traces are present in inset.

decreased down to 350 W ($z = 30$ m) due to generation of a noisy RP (represented by the lower stripe of "<"-shaped trace in Figure 12.10a). The DS and RP become fully separated due to dispersion at point B ($z = 30$ m), with spacing between the centers up to 50 ps. Pulse shapes at points A and B corresponding to the entrance and exit points of the PM fiber are also shown in Figure 12.9. Then, in a short SMF the pulses are filtered and amplified in an Yb^{3+} fiber. The power of the DS pulse reaches ~1 kW while amplification of the Stokes pulse is much smaller as its spectrum is far off the Yb^{3+} gain maximum. The amplified pulse is then equally divided by (a) PBS dumping the counter-polarized part (Figure 12.9, panel E in left column) out of the cavity and (b) sending the co-polarized part back into the PM fiber. The DS evolution then starts again at point A ($z = 0$) of the PMF. Note that the residual part of the RP generated on the previous round-trip enters the PMF together with the DS (the weak lower stripe in Figure 12.10a and the relevant forerunner (left) pulse in Figures 12.9 and 12.11a).

The corresponding spectra of the DS (centered at 1015 nm) and the RP (centered at 1060 nm) (Figure 12.10b) do not vary substantially and demonstrate significant noise of the RP. The calculated output spectra (port E in Figure 12.10) for the PMF length 30 m are compared in Figure 12.11b with the experimental ones demonstrating their good agreement. The corresponding pulse shapes in the time domain are also given here. One can see that the spectral structure realized in the experiment and numerical simulation does not correspond to that of a plain DS in the absence of SRS (dashed curves in Figure 12.11b, $f_R = 0$). Thus, the blue shift of the DS spectrum can be attributed to the SRS, which "eats" a red spectral part of DS. The spectral shift is limited by the WDM_1 loss increase at < 1005 nm.

The corresponding temporal pulse profiles calculated with and without the SRS term are shown in Figure 12.11a. The SRS-driven DS has 1.5-times higher power and 3-times shorter duration than the Raman-free DS. This means that the SRS effect leads to strong temporal–spectral filtering of the DS, resulting in its specific shape.

In the experiment, ACF and cross-correlation function (CCF) were extracted from experimentally measured FROG trace [81]. The experimental results shown

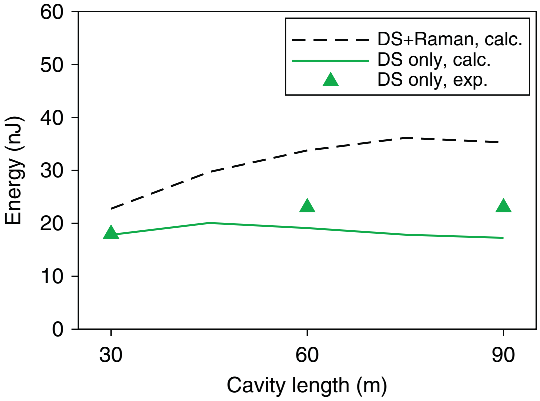

Figure 12.12 Energy of the DS in the experiment (green triangles) and simulation (green solid line). Calculated total energy for the DS and RP (dashed line). The experimental point obtained for $L =$ 120 m ($E \approx 20$ nJ) is not added because the pump power was reduced due to lower stability at this length.

in the inset of Figure 12.11 agree with the calculated ones: the triangular ACF confirms the rectangular DS shape, and the CCF shows the 50-ps delay of RP relatively to DS. The second peak of CCF (and third peak in time domain correspondingly) is an RP from previous round-trip. The FROG trace reveals partial coherence between DS and RP pulses that was also confirmed by a possibility to compress RP by 3–4 times [30].

The numerical results also confirm the experimental results of [29] so that the upper limit for the maximum DS energy was revealed for a 60-m-long fiber oscillator (Figure 12.12). The limit is defined by the SRS converting an excess energy of the DS to the RP. The energy of the RP becomes comparable to the DS level, but, surprisingly, such efficient conversion does not destroy a stable DS. For cavities up to 90 m, the DS energy limit defined by the excess energy conversion into the RP is lower than the limit defined by destabilization of the DS by increasing noise. The maximum RP energy is also limited because of its sufficient attenuation and generation of higher-order Stokes pulses. So total energy of the DS–RP complex in the experiment is also saturated at ~30 nJ level that is confirmed by the calculations (see Figure 12.12).

Therefore, we demonstrate that the stable DS pulses can be generated in a fiber oscillator in spite of strong SRS, in contrast to the conclusions of [72]. The generated noisy RP does not destroy the DS and can even form with it a stable bound complex. In this complex, the DS provides amplification for the RP, whereas the RP stabilizes the DS energy acting as a temporal and spectral filter for DS. Intuitively, the Raman process is incoherent and acts in our case as an additional energy loss channel. The DS stability cannot be affected by the RP, at least if we compensate the loss by proportional pumping. The pulse energy realized in our experiment is higher than that obtained in other all-fiber schemes in the absence of SRS, though

SRS-induced energy conversion defines an upper limit for the DS energy and substantially changes the DS energy scalability.

In the next section, we show that the RP noise seen in Figure 12.11, can be successfully suppressed by the feedback loop, shown as a cloud-like inset in Figure 12.5.

12.4.2
Generation of Stokes-Shifted Raman Dissipative Solitons

In the previous section, we demonstrated that SRS in the fiber laser converts the excess energy out of the coherent DS to a noisy Stokes-shifted RP thus limiting the maximum DS energy [29, 30]. The RP noise is ascribed to the fact that it starts from spontaneous emission reaching high energy after only one round-trip of the DS, which acts as a pump for the RP. Because of the difference in group velocities, the RP afterwards runs away from the DS.

In this section, we study a possibility to initiate the Raman pulse not from noise, but from a seed pre-pulse provided by a feedback for the RP at proper timing defined by the group velocity dispersion (see cloud-inset on Figure 12.5). As a result, we have discovered that a feedback provided by re-injection of an RP into the laser cavity leads to its transformation into a coherent RDS. Together, DS and RDS form a stable complex of higher total energy and broader spectrum than those of the DS alone.

If the pre-pulse is re-injected into a laser cavity with the proper amplitude, it will then be synchronously amplified by the DS circulating in the cavity, similar to synchronous pumping mode-locking technique [79, 82]. The difference in the group velocities of DS and RP is compensated by the bypass fiber of the feedback loop providing a necessary delay for the RP.

To test the effect of the RP feedback on the pulse structure, we first did numerical simulations with the generalized NLSE 12.20 . The pulse shapes calculated with feedback are shown in the diagrams of Figure 12.9. Evolution of the pulse temporal and spectral shapes along the cavity is shown in Figure 12.13. A stable noise-free RP was found for the feedback coefficients $R = P_f/P = 10^{-2}-10^{-6}$, where P is the circulating light power with its small re-injected part P_f.

The RP and DS co-propagate together as one stable two-color complex. For oscillator cavities longer than 80 m, the complex becomes unstable. In the range of cavity lengths supporting the stable complex, increase of the pump power leads to a multipulse regime similar to conventional solitons [83–87]. Within each complex, the energy is nearly equally divided between the DS and the noise-free RP (see Figure 12.9, panel B in right column). The pulse evolution along the cavity (Figure 12.13) demonstrates how a stable noise-free RP is formed at the beginning of PMF due to conversion of the "red" part of the DS into the Stokes-shifted wavelengths around 1060 nm. Then, the DS and RP separate due to dispersion. The delay line (DL) in the feedback loop compensates the dispersion shift and after partial outcoupling through ports D and E and amplifying in Yb^{3+} fiber, evolution starts again at point A. As can be seen (Figure 12.9), the feedback makes pulse

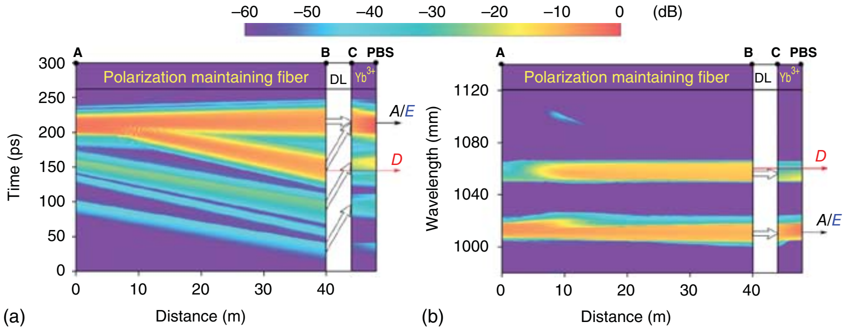

Figure 12.13 Evolution of the pulse shapes and spectra along the PMF and SMF (with the active Yb^{3+}-doped part) sections in a scheme of Figure 12.5 with the Raman feedback loop comprising the delay line (DL) shown as the white box, with parameters similar to that in the experiment. Points A, B, C, D, E, and PBS (polarization beam splitter) of the scheme of Figure 12.5 are marked at the corresponding distances [31].

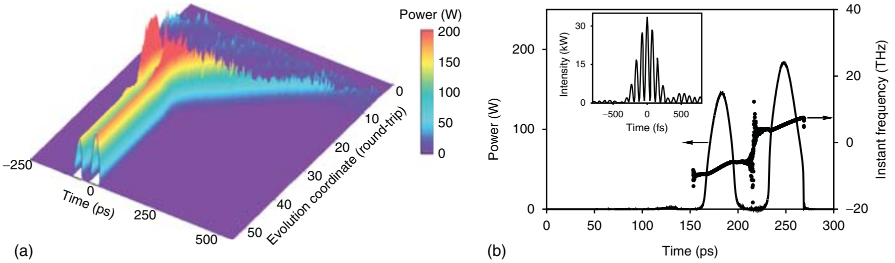

Figure 12.14 Pulse shapes: (a) the simulated feedback-defined evolution of the intracavity pulses in the scheme of Figure 12.5 (point B) versus the round-trip number. The zero time offset is bound to the position of the main dissipative soliton. (b) The calculated DS and RDS pulse shapes inside the cavity (point B in Figure 12.5) and their instant frequencies. Inset: the dechirped DS–RDS complex with 70-ps delay compensation in the Raman feedback loop [31].

evolution basically different (compare also Figure 12.10 with Figure 12.13). The noise is eliminated and the energy becomes concentrated in well-defined temporal and spectral ranges.

Figure 12.14a shows the transition from noise (the pre-pulse) to the steady-state pulse. In the initial state of the laser, amplification of noise starts at both fundamental and Raman wavelengths. Then, two chirped pulses are formed almost simultaneously. The resulting complex of two bound dissipative solitons (the main and Raman ones) circulates in the cavity in an extremely stable manner. The temporal shapes of stationary DS and RP are depicted in Figure 12.14b. Analysis of the RP spectral and temporal shape together with its spectral phase shown in Figure 12.14b led us to the conclusion that the noise-free RP realized numerically in the scheme shown in Figure 12.5 can be called a RDS.

Based on the detailed comparison, we can conclude that the RDS realized in [31] has the same equilibrium characteristics and demonstrates similar evolution dynamics as the chirped pulses generated in the ANDi laser configuration agreed to be dissipative solitons [14, 19, 88]. In addition to similar characteristics of the RDS and DS: temporal and spectral shapes, chirp and extracavity compression factors as well as their sensitivity to spectral filtering, the dissipative soliton nature of the coherent linearly chirped Raman pulse was also confirmed by a possibility of its description in the frame of CQGLE (see [31] for details).

We presented above all the basic arguments including the solutions of the two main equations in order to formulate unambiguously that the new stable Raman-shifted pulses are dissipative solitons. A fair comparison of NLSE and CGLE is a very demanding task, and we made only the first steps in this direction. The approximation of the uniformly distributed cavity relevant for CGLE is rather rough for any laser generating dissipative solitons, since typical amplitude variation at point-action dissipative sections (gain, filtering, outcoupling, etc.) of the laser cavity amount to about 1 order of magnitude, while temporal and spectral widths may exhibit much smaller changes; see [19, 20] and citations therein. The same is true for the new dissipative soliton generated via Raman process, where the amplitude variations are even stronger because of much higher Raman gain and lower feedback coefficient. The pulse widths are also slowly varying here, similar to that for conventional DS. We call a new soliton centered at 1060 nm a Raman DS in order to emphasize its origin leading to quantitative difference of the pulse dynamics from the main DS at similar qualitative behavior. The average characteristics of the DS and RDS are nearly the same and close to the dissipative soliton solutions of CGLE.

12.4.2.1 Proof-of-Principle Experiment

To verify such promising theoretical predictions, we realized experimentally the scheme shown in Figure 12.5 with feedback loop. The data presented in Figures 12.15 and 12.16 show that the pulses realized in the experiment are basically different from those observed without feedback, but in good agreement

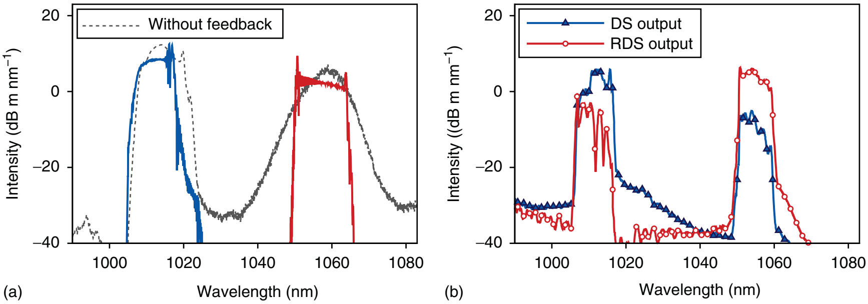

Figure 12.15 Output spectra: calculated (a) and measured (b) at the DS (blue) and RDS output (red) ports for the 40-m long cavity with the feedback coefficient $R = 10^{-4}$ and without feedback (gray). Note that the (i) the spectral division between output ports in the experiment (~10 dB) is not as high as in the simulations (> 40 dB), and (ii) the RDS port has significant spectral ripples around 1010 nm [31].

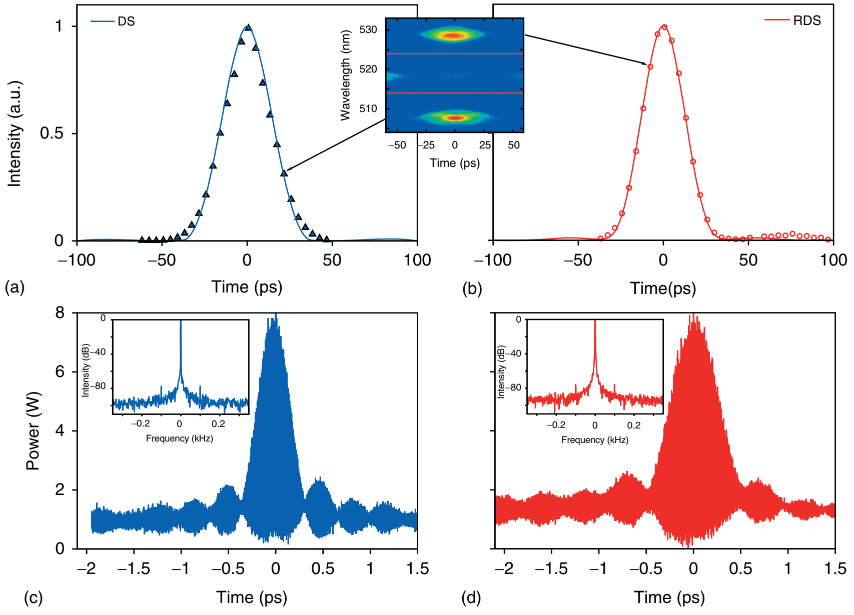

Figure 12.16 Autocorrelation traces and radio frequency beating spectra of the realized pulses. The measured (points) autocorrelation traces of the DS (a) and RDS (b), and the calculated (lines) for the 40-m cavity oscillator with the feedback coefficient $R = 10^{-4}$. Inset: the corresponding FROG traces; Interferometric ACF traces shown for DS (c) abd RDS (d) after a double-pass compressor consisting of a grating pair. The compressor introduces one-pass group delay dispersion of $D \approx -0.7\ \text{ps}^2$. Insets: Radio frequency spectra measured at a repetition rate of 5 MHz with 1 Hz bandwidth [31].

with the RDS predicted by simulation. The RDS's spectrum has a typical shape with steep edges, similar to the DS. The FROG trace (Figure 12.16) shows that the phases, pulse durations, and shapes of the DS and RDS are similar. The duration of the dechirped DS and RDS is measured to be 250–300 fs and 300–400 fs, correspondingly; see Figure 12.16c and d. The compression factor for the RDS is better than 100, that is, ~30 times higher than that for the noisy RP in [29, 30], and only slightly lower than that for the DS. The measured interferometric ACF for the RDS has a contrast close to 8:1 (Figure 12.16c and d), only slightly deviating from that for the dechirped DS. A radio frequency beat signal measured at the fundamental repetition rate and its 150th harmonic are also similar for the DS and RDS exhibiting a high contrast in the range of 60–100 dB (see insets in Figures 12.16c and d). These values are comparable with those for the ~10 nJ SRS-free DS generated in all-fiber configurations of Yb-doped fiber oscillators (see, e.g., [70]) and only slightly worse than the best results for the ~3 nJ Er-doped fiber oscillators [11]. In our case, the total pulse energy at the DS and RDS outputs is 25 nJ, with nearly equal division inside the cavity and a fourfold difference at the outputs because of selective DS amplification.

The first-order RDS described earlier substantially differs from a classical Raman soliton, which is a version of fundamental conservative soliton and appears as a result of the Raman frequency shift in the anomalous dispersion range [79, 82], for example, in transmission lines [89]. As the RDS is bound with the DS via a nonlinear Raman process, they are also different from one-color (i.e., of the same spectrum) bound solitons, or multisoliton complexes based on Kerr nonlinearity [18, 83–87]. In our case (see Figure 12.14b), the DS and RDS form a stable two-wavelength chirped DS complex that could be de-chirped into a single pulse under certain conditions. The fringe pattern in Figure 12.14b (inset) results from merging of the compressed coherent DS and RDS pulses behind the compressor. The fringe separation (∼40 fs) is defined by the whole spectral range of the solitonic DS + RDS complex, whose compressibility can be similar to the cases of nonlinear spectral broadening in fiber [79] or a Raman-active mode-locked laser [90]. It is worth noting that the fringe visibility, which shows the coherence quality, depends on the feedback, with the highest coherence reached for the values $10^{-4} < R < 10^{-2}$. The results of simulation also show that the coherence of the RDS and DS is immune to noise variations in a broad range.

We also found that the shape of RDS is very sensitive to parameters of linear spectral filters, similar to that for conventional dissipative solitons. More detailed analysis of RDS characteristics depending on cavity parameters is presented in the next section.

12.4.3
Characteristics of Raman dissipative Solitons

In this section we analyze how the optical spectra of DS and RDS are sensitive to variations of cavity parameters: linear and nonlinear (SRS-induced) filtering and the Raman feedback loop.

12.4.3.1 Variation of the Soliton Spectra with Filter Parameters

Linear filtering is provided by two WDM couplers, whose spectra are sensitive to temperature and can vary in the range of several nanometers. The first filter (marked as WDM_1 in Figure 12.5) is a self-made PM-fiber coupler based on the internal Lyot filter consisting of a properly oriented short PM-fiber piece and a PBS. Such a WDM coupler/splitter has a typical sinusoidal spectral function (Figure 12.17a) providing the wavelength division 1015/1060 nm for two output coupler arms. The second coupler (WDM_2 in Figure 12.5 of the paper) is a commercial one having a stepwise transmission spectrum function with the cutoff at 1005 nm. The influence of the filtering effect of WDM_1 on the DS is small, but nonlinear filtering becomes important due to strong Raman conversion, similar to that in the case of a noisy Raman pulse observed without WDM_1 and delay loop in [30]. As follows from our simulations, the SRS effect “eats” the long-wavelength wing of the DS spectrum thus pushing the soliton spectrum out of the gain maximum (1025–1030 nm) toward the WDM_2-induced cutoff at 1005 nm. This effect defines the short-wavelength edge of the generated spectrum.

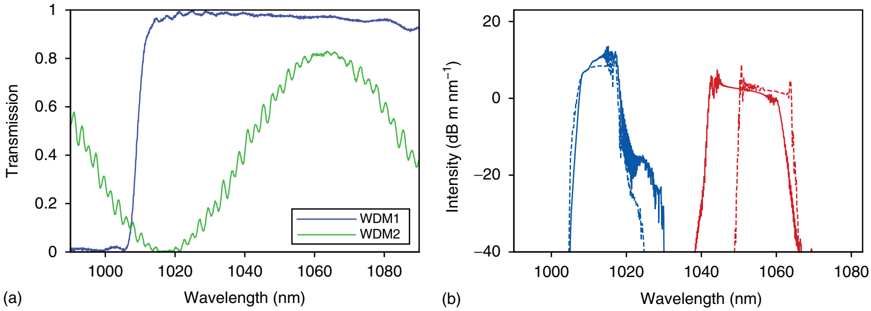

Figure 12.17 (a) Transmission spectra of the WDM_1 and WDM_2 couplers of the experimental scheme (Figure 12.5 of the paper). (b) Simulation results for the DS (blue) and RDS (red) spectra at different WDM_1 coupler parameters: 1010/1055 nm (solid) and 1015/1060 nm (dashed) at the fixed WDM_2 parameters (the cutoff wavelength at 1005 nm), for 70 ps Raman delay and 1025 (1030) nm gain maximum.

By numerically varying the exact position of the spectral maximum of the WDM_1 filter (Figure 12.17a), we found that the RDS spectral width is very sensitive to these variations. As one can see in Figure 12.17b that a shift of only 5 nm (the minimum value we can control in the experiment) leads to a significant change of both the RDS position and width. Because the RDS spectrum obtained with the 1015/1060 nm filter fits better to the transmission function of the WDM_1 coupler measured under the experimental conditions (Figure 12.17a), we used these data for comparing the calculated and experimental spectra (Figure 12.15).

12.4.3.2 Variation of the Soliton Spectra with the Raman Feedback Parameters

The maximum intracavity energy of the dissipative soliton depends on the feedback value $R = P_f/P$ logarithmically according to the equation for the SRS threshold energy, $E_{\mathrm{th}} \approx \ln(1/R)\delta v^{-1}/g_R$, where $\delta v^{-1} = v_{DS}^{-1} - v_R^{-1}$ is the inverse group velocity difference of the DS and RDS, and g_R is the Raman gain coefficient. The threshold energy for the experimental parameters is estimated as $E_{\mathrm{th}} \sim 10$ nJ. Variation of the soliton spectral shape with the feedback coefficient in experiment and simulation is presented in Figure 12.18. At the value $R < 10^{-6}$, the re-injected power P_f approaches the energy of the spontaneous emission at the Stokes-shifted wavelength ($P_{\mathrm{sp}}/P \sim 10^{-7}$), and the feedback becomes insufficient to overcome noise. At $R > 10^{-2}$, the single DS + RDS complex splits into two similar pulse complexes separated in time. Stable pulses in 40-m cavity are realized for $R = 10^{-2}–10^{-6}$ and delays in the range 50–80 ps (with optimum at ~70 ps).

12.4.4
Generation of Multicolor Soliton Complexes and Their Characteristics

The scheme shown in Figure 12.5, with additional feedback loops can be used for generating next-order Stokes pulses of similar spectral and temporal shapes.

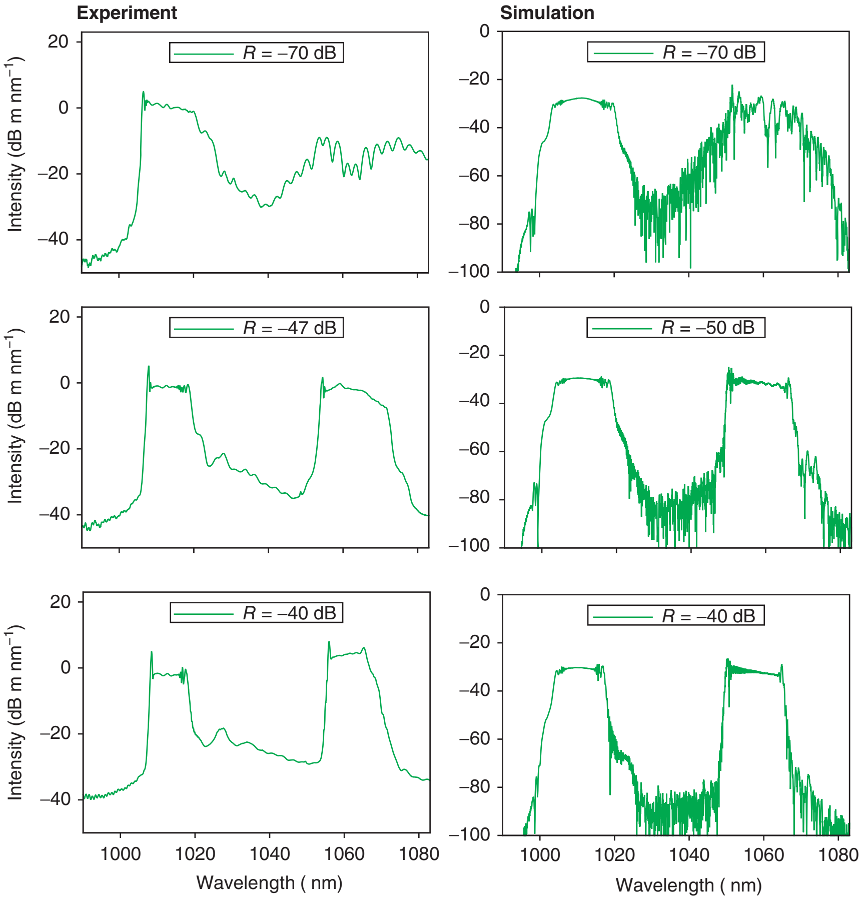

Figure 12.18 Intracavity spectra in experiment and simulation corresponding to different feedback coefficients. The spectra are measured at point B of the scheme of Figure 12.5.

We numerically realized a scheme with two feedback loops, with the corresponding results shown in Figures 12.19 and 12.20. Figure 12.19 illustrates the evolution of the chirped pulse in the stable three-color regime. To realize it, we made the following modifications of the scheme: (i) long ($L \approx 80$ m) PM fiber, (ii) two feedback loops, each of which comprises $\mathrm{WDM}_1^{(i)}$ splitter and $1 : R^{(i)}$ coupler (similar to the feedback loop in Figure 12.5) optimized for the first and second Stokes pulses ($i = 1, 2$): $R^{(1)} = 10^{-4}$, $R^{(2)} = 10^{-2}$. The regime becomes stable when we use, instead of sinusoidal WDM_1 (see Figure 12.17a), two special $\mathrm{WDM}_1^{(1)}$ and $\mathrm{WDM}_1^{(2)}$ splitters of a stepwise spectral function at cutoff wavelengths at 1035 nm and 1085 nm, correspondingly. An implementation of such “hard” filters eliminates the remaining small-amplitude parts of the Raman pulse, which cannot be fully suppressed in the case of a “soft” (sinusoidal) WDM_1 splitter (see Figure 12.13). Since each feedback loop operates independently, the scheme

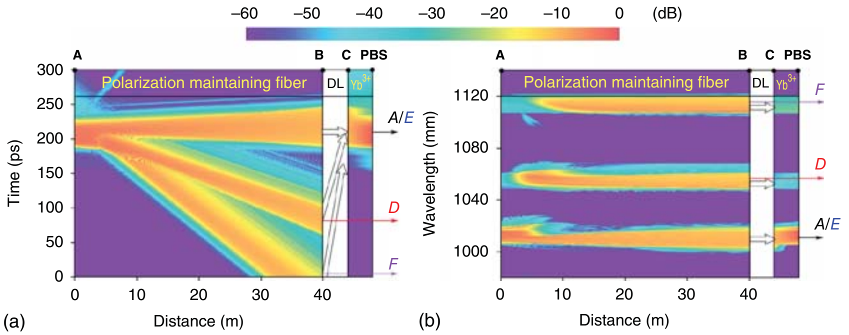

Figure 12.19 Evolution of the pulse shapes and spectra along the PMF and SMF sections in a scheme of Figure 12.5 in the case of two feedback loops providing delay and filtering for the first and second Stokes waves with the additional output port *F*.

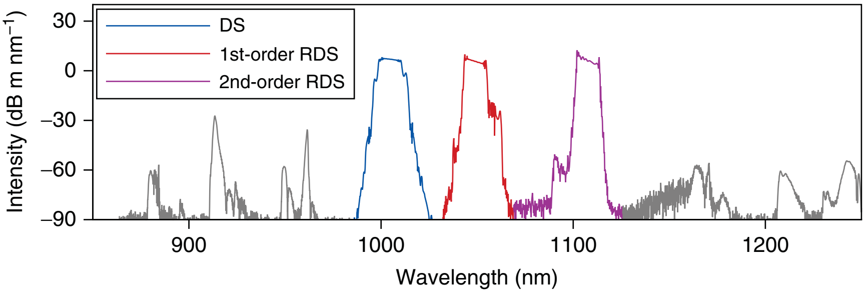

Figure 12.20 Three-color bound solitons. Results of simulation for the generated spectra in an 80-m-long PM-fiber cavity oscillator with the Raman feedbacks for the first-order Stokes ($R_1 = 10^{-4}$) and the second-order Stokes ($R_2 = 10^{-2}$) waves, in the presence of a band-stop filter at 1025 nm (10 nm width) and the following parameters of the *i*th feedback loop: delay time 140 ps ($i = 1$) and 280 ps ($i = 2$), step-wise $\text{WDM}_1^{(i)}$ couplers with cutoff wavelengths at 1035 nm ($i = 1$) and 1085 nm ($i = 2$).

offers a way to generate next Stokes orders by adding corresponding feedback loops in a routine manner.

A number of optimization steps remain to be made in order to realize this regime experimentally, including filter optimization. The open question is whether one can realize experimentally first- and second-order RDSs with the equidistant spectra shown in Figure 12.20. In this figure, one can see also higher-order noisy pulses at > 1150 nm as well as anti-Stokes components at < 1000 nm generated in frequency mixing processes.

It is significant that not only SRS, but also other nonlinear processes may be explored for generating broadband multicolor dissipative soliton complexes. As demonstrated for the femtosecond solid-state lasers [90, 91], the combined action of SRS and four-wave mixing allow intracavity spectral broadening similar to the phenomenon of supercontinuum generation in fibers [92]. Successful pulse synthesis based on the total phase and spectrum control was recently demonstrated for several synchronized few-cycle lasers operating in different spectral ranges [93] and for the light field synthesizer dealing with a coherent supercontinuum from a single few-cycle laser [94]. Based on our approach, intracavity pulse synthesis looks feasible, with an important advantage: it will be intrinsically stable.

12.5
Conclusions and Future Developments

An important class of the soliton solutions of Ginzburg–Landau equation, so-called HCDSs, is extensively analyzed in this chapter. Strongly inhomogeneous phase across such solitons characterizes their capacity to redistribute energy without loss of stability. This property provides energy scalability of HCDS, feasible in femtosecond laser oscillators either with the cavity length or active medium volume. The physical limitations of these steps are shown in the example of all-fiber femtosecond fiber laser oscillators based on nonlinear polarization evolution mode-locking mechanism. The reason of the stability break is an excessive rotation of polarization ellipse along the cavity [28]. The use of polarization-maintaining fibers allowed pushing further the cavity length limit. A laser configuration based on long PM and short SM parts resulted in a total cavity length of up to 120 m, with the following DS parameters: pulse energy > 20 nJ, the chirp parameter > 200 and a compressed pulse duration of 200–300 fs [29].

So-called master diagrams allow analysis of a complex laser operating in the positive dispersion regime by decreasing the number of efficient system parameters of the Ginzburg–Landau equation. Based on master diagrams, it is shown that laser noise is another factor influencing the pulse energy of the laser [76]. Being in its infancy, noise limitations of the maximal pulse energy are to be included in forthcoming descriptions of high-energy femtosecond lasers. Technically, the problem consists of determining the type and amplitude of noise.

For long laser cavities, a new limiting factor comes into play, namely SRS. The detailed analysis of the SRS-driven evolution of DS has been performed in frames of NSE in which the SRS term is added and the model has been compared with the experiment [30]. It appears possible to realize a stable DS in the presence of strong SRS. In general, the intrinsic Raman effect occurring in femtosecond fiber laser broaden our vision of the processes responsible for the pulse formation. One of its consequences is the appearance of a noisy Raman pulse linked to the main DS. On one hand, because of high Raman gain, the noisy RP can lead to the energy limitations of the main dissipative soliton. In principle, one or more RPs can reach energy comparable to that of the main DS. On the other, being properly treated, RPs nevertheless allow to scale the cavity length and pulse energy up to high extend.

The pulse structure becomes quite different in case of feedback that delays a noisy RP at its every cavity round-trip [31]. Being properly built, such feedback leads to formation of a RDS instead of a noise Raman pulse in the feedback-free case. The optimal feedback is very weak ($R \approx 10^{-4}$) but it is enough to convert noise into the coherent pulse due to high Raman gain. In this sense, it is similar to the weak random distributed feedback based on Rayleigh backscattering converting Raman amplified noise in fibers into the CW laser radiation [95, 96].

The results of numerical simulations of both DS and DS–RDS lasers based on Schrödinger and Ginzburg–Landau equations are consistent with each other and with the experiment. At high laser pump, the RDS energy can reach the energy of the main DS. The RDS occupies another spectral range thus reducing the "energy competition" with the DS. At higher pump and in the presence of second feedback, second-order RDS can be generated. RDSs are coherent clones of the DS, with the residual noise comparable to the DS. As a result, they can be compressed externally from tens of picoseconds to hundreds of femtoseconds pulses, similar to the DS. Though a laser with more than 100 m cavity is realized, the upper limit in terms of the pulse stability is still not reached.

Technically, the RDS approach reviewed in this book chapter allows for its straightforward extension to multi-RDS realization based on new fibers and fiber components. In principle, the approach offers a possibility of increasing the intracavity complex energy by generating RDSs of different polarizations in other cavity loops having a common part with the main cavity. By the use of different fiber materials, one can vary spectral positions and spectral widths of RDSs. By having a multi-RDS soliton complex with spectrally equidistant soliton components and using a combination of SRS and four-wave mixing, a smooth ultrabroadband spectrum looks feasible for its further compression in order to generate single pulses of tens of femtoseconds and shorter.

Unique features of the soliton complexes demonstrated in the all-fiber scheme such as high pulse energy, broad spectral range occupied by the complex, coherence of the solitons in the complex, offer new challenging applications. In medicine, coherence optical tomography and nonlinear or multiphoton fluorescence microscopy [97, 98] can benefit from broad high-power coherent spectrum. In both cases, high stability of the solitons will allow for collecting intrinsically weak signals from scattered light. Near-future high-bit rate periodic transmission lines with Raman pump can use more broadband and quiet laser sources based on soliton complexes demonstrated in this article. High power and low noise [89] will allow for longer passive fiber pieces between the amplifiers. Kerr nonlinearity could be considered as the mechanism that stabilizes the dissipative solitons in the complex. Alternatively, specialty fibers with properly designed dispersion for the main and frequency-shifted dissipative solitons can be used.

Multicolor dissipative soliton complexes offer further extensions for frequency comb spectroscopy [92, 99] and optical parametric amplification schemes (broadband seed) [100]; schemes for generating new spectral components in several synchronized enhancement cavities [101] containing a common nonlinear element, when each cavity is seeded by a certain RDS. Intrinsic stability and coherence of the complex will lead to a stable operation of the bundled enhancement cavities.

References

1. Duling, I.N. III (1991) Subpicosecond all-fibre erbium laser. *Electron. Lett.*, **27** (6), 544–545.
2. Fermann, M.E., Andrejco, M.J., Stock, M.L., Silberberg, Y., and Weiner, A.M. (1993) Passive mode locking in erbium fiber lasers with negative group delay. *Appl. Phys. Lett.*, **62** (9), 910–912.
3. Nakazawa, M., Yoshida, E., and Kimura, Y. (1993) Generation of 98 fs optical pulses directly from an erbium-doped fibre ring laser at 1.57 µm. *Electron. Lett.*, **29** (1), 63–65.
4. Ilday, F.O., Wise, F.W., and Sosnowski, T.S. (2002) High-energy femtosecond stretched-pulse fiber laser with a nonlinear optical loop mirror. *Opt. Lett.*, **27** (17), 1531–1533.
5. Lim, H., Ilday, F.O., and Wise, F.W. (2003) Generation of 2-nJ pulses from a femtosecond ytterbium fiber laser. *Opt. Lett.*, **28** (8), 660–662.
6. Fernandez, A., Fuji, T., Poppe, A., Fürbach, A., Krausz, F., and Apolonski, A. (2004) Chirped-pulse oscillators: a route to high-power femtosecond pulses without external amplification. *Opt. Lett.*, **29** (12), 1366–1368.
7. Haus, H.A., Tamura, K., Nelson, L.E., and Ippen, E.P. (1995) Stretched-pulse additive pulse mode-locking in fiber ring lasers: theory and experiment. *IEEE J. Quantum Electron.*, **31** (3), 591–598.
8. Ilday, F.O., Buckley, J.R., Clark, W., and Wise, F.W. (2004) Self-similar evolution of parabolic pulses in a laser. *Phys. Rev. Lett.*, **92** (21), 213 902/1–4.
9. Dudley, J.M., Finot, C., Richardson, D.J., and Millot, G. (2007) Self-similarity in ultrafast nonlinear optics. *Nat. Phys.*, **3** (9), 597–603.
10. Bale, B.G. and Wabnitz, S. (2010) Strong spectral filtering for a mode-locked similariton fiber laser. *Opt. Lett.*, **35** (14), 2466–2468.
11. Oktem, B., Ulgudur., C., and Ilday, F.O. (2010) Soliton-similariton fibre laser. *Nat. Photonics*, **4** (5), 307–311.
12. Kalashnikov, V.L., Podivilov, E., Chernykh, A., Naumov, S., Fernandez, A., Graf, R., and Apolonski, A. (2005) Approaching the microjoule frontier with femtosecond laser oscillators: theory and comparison with experiment. *New J. Phys.*, **7**, 217.
13. Chong, A., Buckley, J.R., Renninger, W.H., and Wise, F.W. (2006) All-normal-dispersion femtosecond fiber laser. *Opt. Express*, **14** (21), 10–095–10–100.
14. Renninger, W.H., Chong, A., and Wise, F.W. (2008) Dissipative solitons in normal-dispersion fiber lasers. *Phys. Rev. A*, **77** (2), 023 814/1–4.
15. Vanin, E., Korytin, A., Sergeev, A., Anderson, D., Lisak, M., and Vázquez, L. (1994) Dissipative optical solitons. *Phys. Rev. A*, **49** (4), 2806–2811.
16. Kerner, B.S. and Osipov, V.V. (1994) *Autosolitons: A New Approach to Problems of Self-Organization and Turbulence*, Kluwer Academic Publishers.
17. Akhmediev, N. and Ankiewicz, A. (2005) *Dissipative Solitons*, Lecture Notes in Physics, vol. **661**, Springer-Verlag, Berlin.
18. Akhmediev, N. and Ankiewicz, A. (2008) *Dissipative Solitons: From Optics to Biology and Medicine*, Springer-Verlag.
19. Grelu, P. and Akhmediev, N.N. (2012) Dissipative solitons for mode-locked lasers. *Nat. Photonics*, **6** (2), 84–92.
20. Renninger, W.H. and Wise, F.W. (2012) Dissipative soliton fiber laser, in *Fiber Lasers* (ed. O.G. Okhotnikov), John Wiley & Sons, Inc., pp. 97–134.
21. Haus, H.A. and Fellow, L. (2000) Mode-Locking of Lasers. *IEEE J. Sel. Top. Quantum Electron.*, **6** (6), 1173–1185.
22. Buckley, J.R., Wise, F.W., Ilday, F.O., and Sosnowski, T.S. (2005) Femtosecond fiber lasers with pulse energies above 10 nJ. *Opt. Lett.*, **30** (14), 1888–1890.
23. Chong, A., Renninger, W.H., and Wise, F.W. (2007) All-normal-dispersion femtosecond fiber laser with pulse energy above 20 nJ. *Opt. Lett.*, **32** (16), 2408–2410.

24. Lefrançois, S., Kieu, K., Deng, Y., Kafka, J.D., and Wise, F.W. (2010) Scaling of dissipative soliton fiber lasers to megawatt peak powers by use of large-area photonic crystal fiber. *Opt. Lett.*, **35** (10), 1569–1571.

25. Soto-Crespo, J.M., Akhmediev, N.N., Afanasjev, V.V., and Wabnitz, S. (1997) Pulse solutions of the cubic–quintic complex Ginzburg–Landau equation in the case of normal dispersion. *Phys. Rev. E*, **55** (4), 4783–4796.

26. Podivilov, E.V. and Kalashnikov, V.L. (2005) Heavily-chirped solitary pulses in the normal dispersion region: new solutions of the cubic–quintic complex Ginzburg–Landau equation. *JETP Lett.*, **82** (8), 467–471.

27. Kharenko, D.S., Shtyrina, O.V., Yarutkina, I.A., Podivilov, E.V., Fedoruk, M.P., and Babin, S.A. (2011) Highly chirped dissipative solitons as a one-parameter family of stable solutions of the cubic–quintic Ginzburg–Landau equation. *J. Opt. Soc. Am. B*, **28** (10), 2314–2319.

28. Kharenko, D.S., Shtyrina, O.V., Yarutkina, I.A., Podivilov, E.V., Fedoruk, M.P., and Babin, S.A. (2012) Generation and scaling of highly-chirped dissipative solitons in an Yb-doped fiber laser. *Laser Phys. Lett.*, **9** (9), 662–668.

29. Kharenko, D.S., Podivilov, E.V., Apolonski, A.A., and Babin, S.A. (2012) 20 nJ 200 fs all-fiber highly-chirped dissipative soliton oscillator. *Opt. Lett.*, **37** (19), 4104–4106.

30. Bednyakova, A.E., Babin, S.A., Kharenko, D.S., Podivilov, E.V., Fedoruk, M.P., Kalashnikov, V.L., and Apolonski, A. (2013) Evolution of dissipative solitons in a fiber laser oscillator in the presence of strong Raman scattering. *Opt. Express*, **21** (18), 20 556.

31. Babin, S.A., Podivilov, E.V., Kharenko, D.S., Bednyakova, A.E., Fedoruk, M.P., Kalashnikov, V.L., and Apolonski, A. (2014) Multicolour nonlinearly bound chirped dissipative solitons. *Nat. Commun.*, **5**, 4653.

32. Newell, A.C. (1974) *Nonlinear Wave Motion*, Lectures in Applied Mathematics, vol. **15**, American Mathematical Society, Providence, RI.

33. Komarov, K.P. (1986) Theory of stationary ultrashort pulses in solid-state lasers with passive mode locking. *Opt. Spektrosk.*, **60** (2), 379–384.

34. Chernykh, A.I. and Turitsyn, S.K. (1995) Soliton and collapse regimes of pulse generation in passively mode-locking laser systems. *Opt. Lett.*, **20** (4), 398–400.

35. Salhi, M., Haboucha, A., Leblond, H., and Sanchez, F. (2008) Theoretical study of figure-eight all-fiber laser. *Phys. Rev. A*, **77** (3), 033 828/1–9.

36. Ortaç, B., Baumgartl, M., Limpert, J., and Tünnermann, A. (2009) Approaching microjoule-level pulse energy with mode-locked femtosecond fiber lasers. *Opt. Lett.*, **34** (10), 1585–1587.

37. Naumov, S., Fernandez, A., Graf, R., Dombi, P., Krausz, F., and Apolonski, A. (2005) Approaching the microjoule frontier with femtosecond laser oscillators. *New J. Phys.*, **7**, 216–216.

38. Leblond, H., Salhi, M., Hideur, A., Chartier, T., Brunel, M., and Sanchez, F. (2002) Experimental and theoretical study of the passively mode-locked ytterbium-doped double-clad fiber laser. *Phys. Rev. A*, **65** (6), 063 811/1–9.

39. Komarov, A., Leblond, H., and Sanchez, F. (2005) Quintic complex Ginzburg–Landau model for ring fiber lasers. *Phys. Rev. E*, **72** (2), 025 604/1–4.

40. Bale, B.G., Kutz, J.N., Chong, A., Renninger, W.H., and Wise, F.W. (2008) Spectral filtering for high-energy mode-locking in normal dispersion fiber lasers. *J. Opt. Soc. Am. B*, **25** (10), 1763.

41. Akhmediev, N.N., Eleonskii, V.M., and Kulagin, N.E. (1987) Exact first-order solutions of the nonlinear Schrodinger equation. *Theor. Math. Phys.*, **72** (2), 809–818.

42. Soto-Crespo, J.M., Akhmediev, N.N., and Afanasjev, V.V. (1996) Stability of the pulselike solutions of the quintic complex Ginzburg–Landau equation. *J. Opt. Soc. Am. B*, **13** (7), 1439–1449.

43. Soto-Crespo, J.M., Akhmediev, N.N., and Town, G. (2002) Continuous-wave versus pulse regime in a passively mode-locked laser with a fast saturable absorber. *J. Opt. Soc. Am. B*, **19** (2), 234–242.

44. Kalashnikov, V., Podivilov, E., Chernykh, A., and Apolonski, A. (2006) Chirped-pulse oscillators: theory and experiment. *Appl. Phys. B*, **83** (4), 503–510.

45. Kalashnikov, V.L. and Apolonski, A. (2009) Chirped-pulse oscillators: a unified standpoint. *Phys. Rev. A*, **79** (4), 043 829/1–10.

46. Kalashnikov, V.L. (2009) Chirped dissipative solitons of the complex cubic–quintic nonlinear Ginzburg–Landau equation. *Phys. Rev. E*, **80** (4), 046 606/1–8.

47. Ablowitz, M. and Horikis, T. (2009) Solitons in normally dispersive mode-locked lasers. *Phys. Rev. A*, **79** (6), 063 845.

48. Mathews, J. and Walker, R.L. (1964) *Mathematical Methods of Physics*, Benjamin.

49. Chang, W., Ankiewicz, A., Soto-Crespo, J., and Akhmediev, N. (2008) Dissipative soliton resonances. *Phys. Rev. A*, **78** (2), 023 830/1–9.

50. Akhmediev, N., Soto-Crespo, J., and Grelu, P., (2008) Roadmap to ultrashort record high-energy pulses out of laser oscillators, *Phys. Lett. A*, **372** (17), 3124–3128.

51. Ding, E., Grelu, P., and Kutz, J.N., (2011) Dissipative soliton resonance in a passively mode-locked fiber laser, *Opts. Lett.*, **36** (7), 1146–1148.

52. Renninger, W.H., Chong, A., and Wise, F.W. (2008) Giant-chirp oscillators for short-pulse fiber amplifiers. *Opt. Lett.*, **33** (24), 3025–3027.

53. Wise, F.W., Chong, A., and Renninger, W.H. (2008) High-energy femtosecond fiber lasers based on pulse propagation at normal dispersion. *Laser Photonics Rev.*, **2** (1–2), 58–73.

54. Kalashnikov, V.L. and Chernykh, A.I. (2007) Spectral anomalies and stability of chirped-pulse oscillators. *Phys. Rev. A*, **75** (3), 033 820/1–5.

55. Tang, D.Y., Zhao, L.M., Zhao, B., and Liu, A.Q. (2005) Mechanism of multisoliton formation and soliton energy quantization in passively mode-locked fiber lasers. *Phys. Rev. A*, **72** (4), 043 816/1–9.

56. Chong, A., Liu, H., Renninger, W.H., and Wise, F.W. (2008) Femtosecond erbium-doped fiber lasers with large normal cavity dispersion. 2008 Conference on Lasers and Electro-Optics, IEEE, pp. 1–2.

57. Kobtsev, S.M. and Smirnov, S.V. (2011) Fiber lasers mode-locked due to nonlinear polarization evolution: Golden mean of cavity length. *Laser Phys.*, **21** (2), 272–276.

58. Boyd, R.W. (2003) *Nonlinear Optics*, 2nd edn, Academic Press, San Diego, CA.

59. Ding, E., Lefrançois, S., Kutz, J.N., and Wise, F.W. (2011) Scaling fiber lasers to large mode area: an investigation of passive mode-locking using a multimode fiber. *IEEE J. Quantum Electron.*, **47** (5), 597–606.

60. Chong, A., Renninger, W.H., and Wise, F.W. (2008) Environmentally stable all-normal-dispersion femtosecond fiber laser. *Opt. Lett.*, **33** (10), 1071–1073.

61. Jiang, K., Ouyang, C., Shum, P.P., Wu, K., and Wong, J.H. (2012) High-energy dissipative soliton with MHz repetition rate from an all-fiber passively mode-locked laser. *Opt. Commun.*, **285** (9), 2422–2425.

62. Kobtsev, S.M., Kukarin, S.V., Fedotov, Y.S., and Ivanenko, A.V. (2011) High-energy femtosecond 1086/543-nm fiber system for nano- and micromachining in transparent materials and on solid surfaces. *Laser Phys.*, **21** (2), 308–311.

63. Kobtsev, S.M., Kukarin, S., and Fedotov, Y.S. (2008) Ultra-low repetition rate mode-locked fiber laser with high-energy pulses. *Opt. Express*, **16** (26), 21–936–21–941.

64. Kelleher, E.J.R., Travers, J.C., Ippen, E.P., Sun, Z., Ferrari, A.C., Popov, S.V., and Taylor, J.R. (2009) Generation and direct measurement of giant chirp in a passively mode-locked laser. *Opt. Lett.*, **34** (22), 3526–3528.

65. Nyushkov, B., Denisov, V., Kobtsev, S., Pivtsov, V., Kolyada, N., Ivanenko, A., and Turitsyn, S. (2010) Generation of 1.7-μJ pulses at 1.55 μm by a self-mode-locked all-fiber laser with a kilometers-long linear-ringcavity. *Laser Phys. Lett.*, **7** (9), 661–665.
66. Koliada, N.A., Nyushkov, B.N., Ivanenko, A.V., Kobtsev, S.M., Harper, P., Turitsyn, S.K., Denisov, V.I., and Pivtsov, V.S. (2013) Generation of dissipative solitons in an actively mode-locked ultralong fibre laser. *Quantum Electron.*, **43** (2), 95–98.
67. Nielsen, C.K., Ortaç, B., Schreiber, T., Limpert, J., Hohmuth, R., Richter, W., and Tünnermann, A. (2005) Self-starting self-similar all-polarization maintaining Yb-doped fiber laser. *Opt. Express*, **13** (23), 9346–9351.
68. Schultz, M., Karow, H., Prochnow, O., Wandt, D., Morgner, U., and Kracht, D. (2008) All-fiber ytterbium femtosecond laser without dispersion compensation. *Opt. Express*, **16** (24), 19–562–19–567.
69. Mortag, D., Wandt, D., Morgner, U., Kracht, D., and Neumann, J. (2011) Sub-80-fs pulses from an all-fiber-integrated dissipative-soliton laser at 1 μm. *Opt. Express*, **19** (2), 546–551.
70. Zhao, L.M., Bartnik, A.C., Tai, Q.Q., and Wise, F.W. (2013) Generation of 8 nJ pulses from a dissipative-soliton fiber laser with a nonlinear optical loop mirror. *Opt. Lett.*, **38** (11), 1942–1944.
71. Erkintalo, M., Aguergaray, C., Runge, A., and Broderick, N.G.R. (2012) Environmentally stable all-PM all-fiber giant chirp oscillator. *Opt. Express*, **20** (20), 22–669–22–674.
72. Aguergaray, C., Runge, A., Erkintalo, M., and Broderick, N.G.R. (2013) Raman-driven destabilization of mode-locked long cavity fiber lasers: fundamental limitations to energy scalability. *Opt. Lett.*, **38** (15), 2644–2646.
73. Kieu, K., Renninger, W.H., Chong, A., and Wise, F.W. (2009) Sub-100 fs pulses at watt-level powers from a dissipative-soliton fiber laser. *Opt. Lett.*, **34** (5), 593–595.
74. Kharenko, D.S., Podivilov, E.V., Apolonski, A.A., and Babin, S.A. (2013) All-fiber highly-chirped dissipative soliton oscillator and its scaling. *SPIE Proc.*, **8601**, 86 012H–86 012H–6.
75. Schadt, D. and Jaskorzynska, B. (1987) Frequency chirp and spectra due to self-phase modulation and stimulated Raman scattering influenced by pulse walk-off in optical fibers. *J. Opt. Soc. Am. B*, **4** (5), 856–862.
76. Kalashnikov, V.L. (2014) Dissipative solitons in presence of quantum noise. *Chaotic Model. Simul.*, **1**, 29–37.
77. Turitsyn, S.K., Bale, B.G., and Fedoruk, M.P. (2012) Dispersion-managed solitons in fibre systems and lasers. *Phys. Rep.*, **521** (4), 135–203.
78. Blow, K. and Wood, D. (1989) Theoretical description of transient stimulated Raman scattering in optical fibers. *IEEE J. Quantum Electron.*, **25** (12), 2665–2673.
79. Agrawal, G.P. (2007) *Nonlinear Fiber Optics*, Academic Press.
80. Hollenbeck, D. and Cantrell, C.D. (2002) Multiple-vibrational-mode model for fiber-optic Raman gain spectrum and response function. *J. Opt. Soc. Am. B*, **19** (12), 2886–2892.
81. Trebino, R. (2002) *Frequency-Resolved Optical Gating: The Measurement of Ultrashort Laser Pulses*, Springer-Verlag.
82. Akhmanov, S.A., Vysloukh, V.A., and Chirkin, A.S. (1992) *Optics of Femtosecond Laser Pulses*, AIP, New York.
83. Grelu, P. and Akhmediev, N. (2004) Group interactions of dissipative solitons in a laser cavity: the case of 2+1. *Opt. Express*, **12** (14), 3184–3189.
84. Stratmann, M., Pagel, T., and Mitschke, F. (2005) Experimental observation of temporal soliton molecules. *Phys. Rev. Lett.*, **95** (14), 143 902.
85. Komarov, A., Leblond, H., and Sanchez, F. (2005) Multistability and hysteresis phenomena in passively mode-locked fiber lasers. *Phys. Rev. A*, **71** (5), 053 809.
86. Tang, D., Zhao, L., and Zhao, B. (2004) Multipulse bound solitons with fixed pulse separations formed by direct soliton interaction. *Appl. Phys. B*, **80** (2), 239–242.
87. Jang, J.K., Erkintalo, M., Murdoch, S.G., and Coen, S. (2013) Ultraweak

long-range interactions of solitons observed over astronomical distances. *Nat. Photonics*, **7** (8), 657–663.

88. Chong, A., Renninger, W.H., and Wise, F.W. (2008) Properties of normal-dispersion femtosecond fiber lasers. *J. Opt. Soc. Am. B*, **25** (2), 140–148.

89. Kumar, S. and Hasegawa, A. (1995) Suppression of the Gordon–Haus noise by a modulated Raman pump. *Opt. Lett.*, **20** (18), 1856–1858.

90. Sorokin, E., Kalashnikov, V., Naumov, S., Teipel, J., Warken, F., Giessen, H., and Sorokina, I. (2003) Intra- and extra-cavity spectral broadening and continuum generation at 1.5 μm using compact low-energy femtosecond Cr:YAG laser. *Appl. Phys. B*, **77** (2–3), 197–204.

91. Sander, M.Y., Ippen, E.P., and Kärtner, F.X. (2010) Carrier-envelope phase dynamics of octave-spanning dispersion-managed Ti: sapphire lasers. *Opt. Express*, **18** (5), 4948–4960.

92. Dudley, J.M. and Coen, S. (2006) Supercontinuum generation in photonic crystal fiber. *Rev. Mod. Phys.*, **78** (4), 1135–1184.

93. Cox, J.A., Putnam, W.P., Sell, A., Leitenstorfer, A., and Kärtner, F.X. (2012) Pulse synthesis in the single-cycle regime from independent mode-locked lasers using attosecond-precision feedback. *Opt. Lett.*, **37** (17), 3579–3581.

94. Wirth, A., Hassan, M.T., Grguras, I., Gagnon, J., Moulet, A., Luu, T.T., Pabst, S., Santra, R., Alahmed, Z.A., Azzeer, A.M., Yakovlev, V.S., Pervak, V., Krausz, F., and Goulielmakis, E. (2011) Synthesized light transients. *Science (New York)*, **334** (6053), 195–200.

95. Turitsyn, S.K., Babin, S.A., El-Taher, A.E., Harper, P., Churkin, D.V., Kablukov, S.I., Ania-Castañón, J.D., Karalekas, V., and Podivilov, E.V. (2010) Random distributed feedback fibre laser. *Nat. Photonics*, **4** (4), 231–235.

96. Turitsyn, S.K., Babin, S.A., Churkin, D.V., Vatnik, I.D., Nikulin, M., and Podivilov, E.V. (2014) Random distributed feedback fibre lasers. *Phys. Rep.*, **542** (2), 133–193.

97. Ishikawa-Ankerhold, H.C., Ankerhold, R., and Drummen, G.P.C. (2012) Advanced fluorescence microscopy techniques—FRAP, FLIP, FLAP, FRET and FLIM. *Molecules*, **17** (4), 4047–132.

98. Xu, C. and Wise, F.W. (2013) Recent advances in fiber lasers for nonlinear microscopy. *Nat. Photonics*, **7**, 875.

99. Schibli, T.R., Hartl, I., Yost, D.C., Martin, M.J., Marcinkevičius, A., Fermann, M.E., and Ye, J. (2008) Optical frequency comb with submillihertz linewidth and more than 10 W average power. *Nat. Photonics*, **2** (6), 355–359.

100. Cerullo, G. and De Silvestri, S. (2003) Ultrafast optical parametric amplifiers. *Rev. Sci. Instrum.*, **74** (1), 1.

101. Pupeza, I., Holzberger, S., Eidam, T., Carstens, H., Esser, D., Weitenberg, J., Rußbüldt, P., Rauschenberger, J., Limpert, J., Udem, T., Tünnermann, A., Hänsch, T.W., Apolonski, A., Krausz, F., and Fill, E. (2013) Compact high-repetition-rate source of coherent 100 eV radiation. *Nat. Photonics*, **7** (8), 608–612.

13
Synchronization in Vectorial Solid-State Lasers

Marc Brunel, Marco Romanelli, and Marc Vallet

13.1
Introduction

Diode-pumped solid-state lasers are widespread in research and in industry. They offer high efficiency and output power for applications and, in the context of nonlinear dynamics, they provide a wealth of operating regimes, from ultrastable single-frequency continuous-wave sources to the shortest femtosecond pulse emitters. Optically pumped insulator-based lasers are well known to exhibit a rich variety of generic phenomena such as relaxation oscillations, antiphase dynamics, Q-switching, mode-coupling and mode-locking, injection locking, soliton generation, and extreme events.

Solid-state lasers are well-described theoretically by rate-equations, which yield the dynamical evolution of the photon number and of the population inversion in a laser cavity. First derived by Statz and de Mars [1], this scalar formulation arises from a semiclassical description of the atom – field system, where the atomic polarization is adiabatically eliminated. It predicts the transient – spiking, relaxation oscillations – and steady-state outputs of monomode solid-state lasers, as well as of multimode lasers when spatial-hole burning effects are taken into account [2]. Typical features of solid-state lasers are a high-quality factor cavity, as compared with semiconductor lasers, for example, and a long population inversion lifetime, due to the screening effect of $4f$ electrons in rare-earth ions for instance. The lifetimes of population inversion and of the photon number rule the nonlinear dynamics commonly observed, which appear to be generic behaviors observed also in different contexts such as biology, chemistry, and electronics [3].

Most of solid-state lasers either in bulk or fiber forms provide single-polarization output waves, usually a linearly polarized state, that is enforced by a strong loss anisotropy. Loss anisotropies can be linear such as Brewster interfaces, or nonlinear such as Kerr loop mirrors. However, in optical cavities that are free of any strong loss anisotropy, *dual-polarization* operation is possible and has already been observed in a number of solid-state lasers. It is the aim of this chapter to examine such vectorial, or dual-polarized, lasers (DPL) where an intracavity phase anisotropy lifts the frequency degeneracy between the two polarization

Nonlinear Optical Cavity Dynamics: From Microresonators to Fiber Lasers, First Edition.
Edited by Philippe Grelu.
© 2016 Wiley-VCH Verlag GmbH & Co. KGaA. Published 2016 by Wiley-VCH Verlag GmbH & Co. KGaA.

eigenstates. We focus on cavities with localized gain and anisotropies, such as Nd : YAG or Er:Yb:Glass lasers, rather than fiber lasers, which are the subject of other chapters of this book. Our aim is to describe synchronization effects between the polarization states, under various forms: mode-locking and injection locking, with emphasis on the nonlinear dynamics leading to frequency locking.

This chapter starts with a description of *intracavity* self-locking effects in Section 13.2. We focus on peculiar synchronization dynamics of DPLs that are rooted in the vectorial nature of the system: self-pulsing in lasers with weak crossed phase and loss anisotropies, polarization self-modulation due to phase-locking in lasers containing a single quarter-wave plate (QWP), and dual-polarization frequency combs in mode-locked pulsed lasers, leading to original pulsed polarization sequences. Then, in Section 13.3, we give a detailed analysis of two-frequency continuous-wave or Q-switched lasers submitted to a resonant frequency-shifted *feedback*, and emphasize in particular the “bounded phase regime” regime, both numerically and experimentally.

13.2
Self-Locking in Dual-Polarization Lasers

13.2.1
Vectorial Description of the Cavity

Following the lines of laser polarization pioneers [4–8], the two eigenstates of the cavity electric field $\vec{E}$ are obtained from the eigenequation

$$\mathbf{M}\vec{E} = \lambda\vec{E}, \tag{13.1}$$

where $\mathbf{M}$ is a 2×2 Jones matrix given by the product of matrices representing each element inside the cavity, taken along a complete round-trip starting from a given reference plane, and λ a complex number. Based on the Jones representation of light polarization [9], this model assumes that the electric field $\vec{E}$ circulating inside the cavity is perfectly polarized, and that all elements have a linear response. The solutions $\vec{E}_i$ of this equation are the laser eigenvectors, associated with the eigenvalues λ_i. Each solution contains not only the light polarization states in the reference plane, but also the associated frequencies and relative losses. This linear model is the basis of all subsequent analyzes in this chapter, considering the oscillation of the two eigenstates in different anisotropic cavity configurations.

Before getting into synchronization mechanisms, let us first consider a simple Fabry–Perot cavity of length L along its $\hat{z}$ axis, closed by isotropic mirrors M_A and M_B whose reflectivities are r_A and r_B, as depicted in Figure 13.1a. G is the isotropic small-signal gain parameter. We insert a phase plate with birefringence ϕ whose Jones matrix is $\begin{pmatrix} e^{i\phi/2} & 0 \\ 0 & e^{-i\phi/2} \end{pmatrix}$ in the basis given by the neutral axes directions (labeled $\hat{x}$ and $\hat{y}$). The round-trip matrix of such a cavity is then

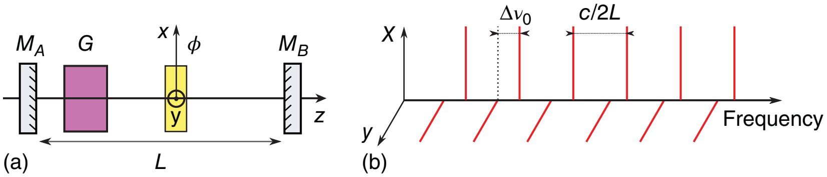

Figure 13.1 (a) Anisotropic laser cavity principle. G is the active medium gain and ϕ the birefringence. (b) Schematic of the two sets of eigenfrequencies.

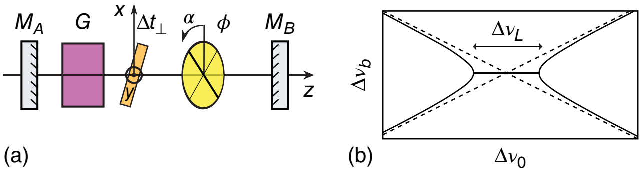

Figure 13.2 (a) Cavity with crossed phase and loss anisotropies. (b) Beat frequency versus birefringence. Dashed lines indicate the lossless case of Eq. (13.2 (adapted from [11]).

$\mathbf{M} = r_A r_B G^2 e^{2i\omega L/c} \begin{pmatrix} e^{i\phi} & 0 \\ 0 & e^{-i\phi} \end{pmatrix}$, whose eigenvalues $\lambda_{x,y} = r_A r_B G^2 e^{2i\omega L/c \pm j\phi}$ are associated with the eigenvectors $\vec{E}_x = \begin{pmatrix} 1 \\ 0 \end{pmatrix}$ and $\vec{E}_y = \begin{pmatrix} 0 \\ 1 \end{pmatrix}$. Hence, the eigenstates are linearly polarized along the phase plate neutral axes and this obviously applies everywhere along $\hat{z}$. When one writes a self-consistency condition $\lambda = 1$ to find the eigenfrequencies, the condition $\arg(\lambda_{x,y}) = 2i\omega L/c \pm \phi = 0 \bmod(2\pi)$ yields two sets of axial frequencies, each associated with one eigenpolarization. The *frequency difference* between two axial frequencies of the same order is given by

$$\Delta\nu_0 = \nu_y - \nu_x = \frac{c}{2L}\frac{\phi}{\pi}. \tag{13.2}$$

As a special case, here, one can notice that if the phase plate is a QWP, the birefringence is $\phi = \pi/2$, the eigenpolarization are still linear along the neutral axes, everywhere inside the cavity, and that the eigenfrequencies are separated by half the free spectral range of the cavity, that is $\frac{c}{4L}$.

13.2.2
Self-Pulsing in Lasers with Crossed Loss and Phase Anisotropies

Here, we focus on the situation where the birefringence is weak. Then, frequency locking between the two cavity eigenstates can be induced by a transverse, linear, loss anisotropy. Let us assume a linear phase retardance ϕ, together with a small linear loss anisotropy $\Delta t_\perp$. The linear phase retardance neutral axes are oriented at an angle α with respect to $\hat{x} - \hat{y}$ (see Figure 13.2a). For simplicity, we choose $\alpha = 45°$. When $\Delta t_\perp \ll 1$, resolution of Eq. (13.1) shows that the eigenvectors become slightly elliptical and a frequency degeneracy region $\Delta\nu_L = \frac{c}{2L}\frac{\Delta t_\perp}{\pi}$

appears [10]. One can then distinguish between two operating regimes, as can be seen in Figure 13.2b. On the one hand, when $|\Delta\nu_0| < \Delta\nu_L$, the two eigenstates have the same frequency but experience different losses. On the other hand, for $|\Delta\nu_0| > \Delta\nu_L$, the two eigenstates are also elliptical, experience the same losses, but their frequencies are no longer degenerate, leading to a beat frequency given by $\Delta\nu_b \approx \Delta\nu_0\sqrt{1 - \Delta{\nu_L}^2/\Delta{\nu_0}^2}$.

It has been shown in Refs [11, 12] that peculiar dynamics occur in solid-state lasers in the presence of such crossed phase and loss anisotropies, because of the nonlinear interaction between the two eigenstates in the active medium of class-B lasers. When the degeneracy region is of the order of the relaxation oscillation frequency f_R of the laser, a usual beat note is observed between the cold-cavity eigenstates (except for particular values $\Delta\nu_b = f_R$ and $\Delta\nu_b = 2f_R$ where complex behaviors appear). When the degeneracy region is slightly larger than f_R, a CW circularly polarized regime is observed as soon as $|\Delta\nu_0| < \Delta\nu_L$, that is, in the locking region. Strikingly, when $f_R < \Delta\nu_L$, self-pulsed regimes are observed. Multiple or single pulses are emitted at a repetition rate slightly smaller than f_R and peak powers about 10 times the corresponding CW power. One can find experimental results with Nd : YAG lasers using different, long and short, cavities in [11–13] and also with an Er : Yb:glass laser [14].

Besides, a theoretical model taking the cold-cavity locking region into account was developed in [11], reproducing experimental results very well. Starting form the density matrix formalism, one finds coupled differential equations governing the amplitudes and phases of the two laser eigenstates, as well as the population inversion in the active medium. The vectorial nature of the atom–field interaction appears through an angular Fourier expansion of the population inversion [15, 16] and phase-sensitive interactions are taken into account [17, 18]. For example, Figure 13.3 reproduces theoretical and experimental intensity versus time of a self-pulsed Nd:YAG laser under crossed loss and phase anisotropy conditions. It is interesting to note that, while the two eigenvectors are synchronized, that is, they are *frequency-locked*, their phase difference still evolves in time but remains *bounded* (see the simulation in Figure 13.3a). This phenomenon is fully characterized in Section 13.3 using lasers submitted to a frequency-shifted feedback.

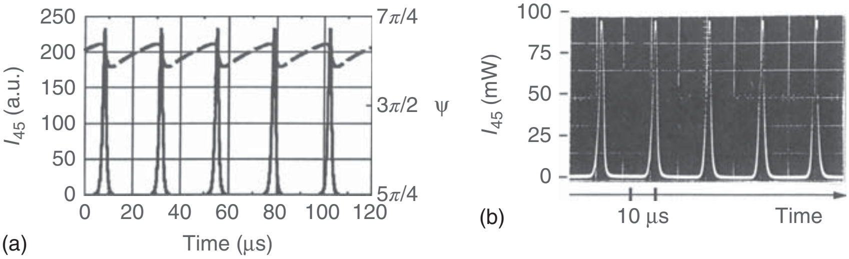

Figure 13.3 Self-pulsed regime in a vectorial laser (adapted from [11].) (a) Simulation. I_{45} is the intensity of the field after a polarizer at 45° of the eigenstate directions, Ψ is the phase difference between the two components of the field. (b) Corresponding experimental result.

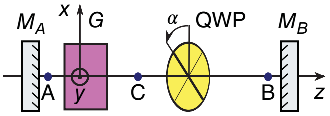

Figure 13.4 Laser cavity containing a quarter-wave plate crossed with an anisotropic gain.

13.2.3
Polarization Self-Modulated Lasers

A second example of synchronization in vectorial lasers appears in multimode lasers containing a single QWP and has been known as *polarization self-modulation*. This peculiar laser operation was observed in semiconductor lasers, either edge-emitting [19–21] or vertical-cavity surface-emitting [22–25]. Time and frequency approaches have been developed [26]. We discuss here the modal analysis, which is based on the resonance condition.

Considering the cavity of Figure 13.4 that contains a QWP, we look for the eigenstates when the gain itself is anisotropic, including birefringence and dichroism. We define the Jones matrix of the gain medium as $\mathbf{G} = \begin{pmatrix} g_x e^{i\phi/2} & 0 \\ 0 & g_y e^{-i\phi/2} \end{pmatrix} = \begin{pmatrix} \gamma_x & 0 \\ 0 & \gamma_y \end{pmatrix}$, assuming that the gain birefringence ϕ and the gain anisotropy axes are aligned, and $\hat{x}$ is the fast axis. We consider a QWP whose fast axis is oriented at an angle α with respect to $\hat{x}$, and whose matrix is noted $\mathbf{Q}_1$. Starting from mirror M_A the round-trip Jones matrix then writes $\mathbf{M} = r_A r_B e^{2i\omega L/c} \begin{pmatrix} \gamma_x^2 \cos 2\alpha & -\gamma_x\gamma_y \sin 2\alpha \\ -\gamma_x\gamma_y \sin 2\alpha & -\gamma_y^2 \cos 2\alpha \end{pmatrix}$. Solving Eq. (13.1), one finds the eigenvectors on M_A to be

$$\vec{E}_{A\pm} = \begin{pmatrix} (\gamma^2+1)\cos 2\alpha \pm \sqrt{(\gamma^2-1)^2\cos^2 2\alpha + 4\gamma^2} \\ 2\gamma \sin 2\alpha \end{pmatrix}, \tag{13.3}$$

where $\gamma = \gamma_y/\gamma_x$. From these solutions, the eigenvectors can be calculated now at any place inside the cavity: $\vec{E}_{C\pm} = \mathbf{G}\vec{E}_{A\pm}$ between the active medium and the QWP, and $\vec{E}_{B\pm} = \mathbf{Q_1}\vec{E}_{C\pm}$ on mirror M_B. Using these expressions, let us focus on the case $\alpha = 45°$ that was detailed in [20]. It is interesting to note that the eigenstates on M_A are linear at ±45° of the gain neutral axes $\hat{x}$ and $\hat{y}$, that is, $\vec{E}_{A\pm} = \begin{pmatrix} \pm 1 \\ 1 \end{pmatrix}$, for all values of γ. Moreover, in this peculiar situation, the resonance condition shows that the frequency difference is fixed at $\Delta\nu_0 = \frac{c}{4L}$, again for all values of the anisotropy γ. Of course, the eigenstates at points B and C depend on γ. In the general case, these are elliptically polarized and nonorthogonal. This is illustrated in Figure 13.5 for different values of the dichroism $|\gamma|$ and of the birefringence ϕ in the active medium. One can note that, without dichroism (left column, $|\gamma| = 1$), the eigenstates are always linear and orthogonal on the mirrors, hence at the laser outputs [27]. When the dichroism is increased, the eigenstates tend to align along the high-gain axis (at point C), resulting in elliptical and nonorthogonal polarizations at the output B. The limiting case is a degenerate situation where two identical circular

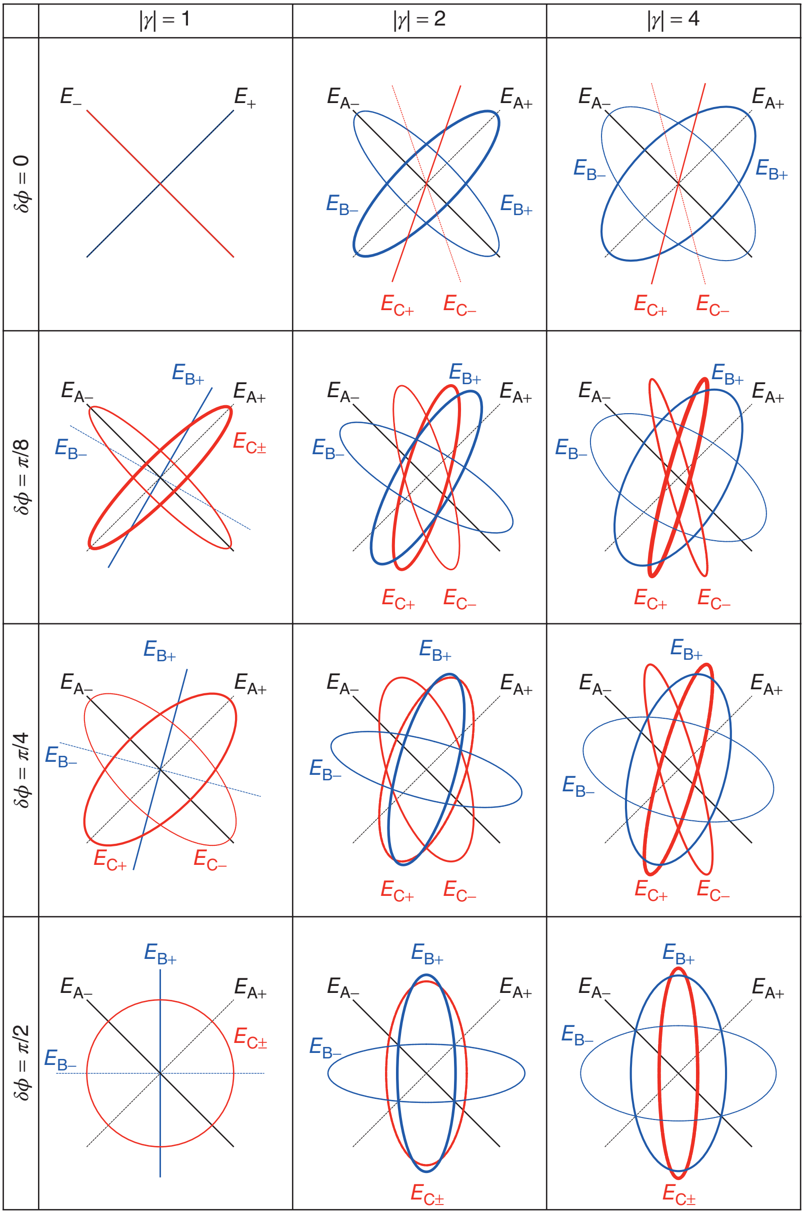
|γ| = 1
|γ| = 2
|γ| = 4
δφ = 0
δφ = π/8
δφ = π/4
δφ = π/2
E−
E+
EA−
EA+
EB−
EB+
EC+
EC−
EC±

Figure 13.5 Laser eigenstates at different locations inside the cavity of Figure 13.4.

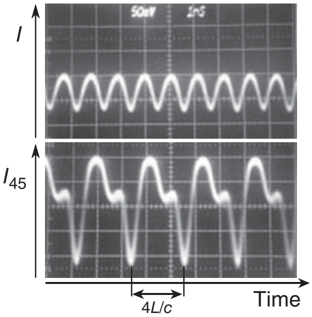

Figure 13.6 Polarization self-modulation in a few-mode Nd : YAG laser containing a QWP. (a) Single-eigenstate intensity. (b) Interference between the two oscillating eigenstates.

polarization are obtained in B (with nondegenerate frequencies), while keeping always the two linear orthogonal directions at output A.

The important point here is that, when the neutral axes of the QWP are at 45° of the gain (or loss) anisotropy, the two sets of eigenfrequencies are always equally spaced by half a free-spectral-range ($c/4L$). Hence, assuming multimode operation, beat-frequency locking due to nonlinear interaction inside the active medium [28] can lead to locking the phases of all the oscillating modes from both eigenstates [29]. The resulting output is recognized by a $c/2L$-periodic intensity pattern when only one eigenvector is selected, and by a typical $c/4L$-periodic pattern when the sum of the two eigenvectors is viewed through a crossed polarizer. This happens to be quite independent of the laser type (gas, semiconductor) and also of the birefringence type, linear or circular [21]. More recently, the interest for such polarization self-modulation was raised again in the context of delayed-feedback dynamics [30, 31].

As for solid-state lasers, it is worthwhile to note that the first report of polarization-modulated emission was made with an $LiNdP_4O_{12}$ laser [32]. In solid-state lasers the characteristic times are very different from those in semiconductor lasers; however, spatial hole-burning couples nonlinearly the intensities and phases in multimode operation [33–36]. Figure 13.6 shows an experimental result obtained with a simple, two-mirror 17-cm long cavity, Nd : YAG laser, containing a QWP. The active medium is slightly tilted, yielding a linear loss-type anisotropy, and the QWP axes are set at 45° of it. Three axial modes oscillate in each polarization, leading to a total of six optical frequencies. When only one eigenstate is selected by an analyzer, a $c/2L = 880\,\text{MHz}$ beat frequency is observed as evidenced by the upper trace in Figure 13.6. Conversely, interference between the two oscillating eigenstates is observed when the analyzer is rotated at 45°, yielding a typical $c/4L = 440\,\text{MHz}$ beat note, as shown by the lower trace in Figure 13.6.

13.2.4
Mode-Locked Dual-Polarization Lasers

As a third example of synchronization in solid-state lasers, we consider a dual-polarization laser, based on a diode-pumped active medium and two QWPs,

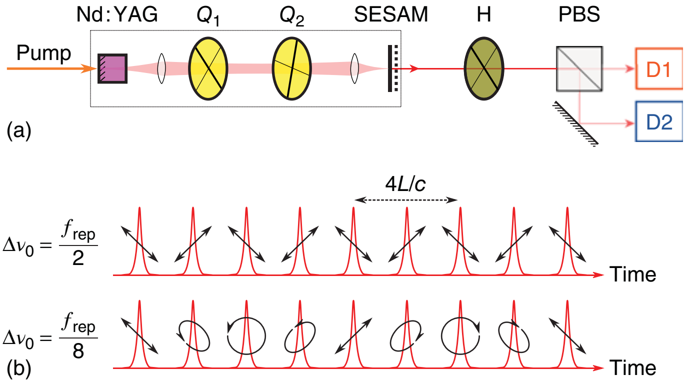
Nd:YAG
Q_1
Q_2
SESAM
H
PBS
Pump
D1
D2
(a)
4L/c
$\Delta\nu_0 = \frac{f_{\text{rep}}}{2}$
Time
$\Delta\nu_0 = \frac{f_{\text{rep}}}{8}$
(b)
Time

Figure 13.7 (a) Experimental laser and detection setup. H, half-wave plate; PBS, polarization beamsplitter; D1,D2, photodiodes. (b) Schematic polarization sequences emitted when $\Delta\nu_0 = f_{\text{rep}}/2$ and $\Delta\nu_0 = f_{\text{rep}}/8$.

containing also a fast saturable absorber inside the cavity. Here, the aim is to study the evolution of the laser polarization in the short-pulse regime, and we find connections with the preceding self-modulated case. The laser under consideration corresponds to the case of Figure 13.7a, with the important addition of a semiconductor saturable absorber mirror [37] in place of the output coupler. Two lenses are also added in order to manage the mode sizes inside the active medium and the saturable absorber. Details about this experiment can be found in [38, 39].

Let us consider two QWPs inside the cavity, a situation that was originally proposed by Evtuhov and Siegman [40], and independently by Kastler [41]. Starting from the preceding situation of a single QWP $\mathbf{Q}_1$ oriented at 45° of $\hat{x}$ and $\hat{y}$, we add another QWP, labeled $\mathbf{Q}_2$, whose fast axis is oriented at an angle α with respect to the fast axis of $\mathbf{Q}_1$. The matrix product of these two elements yields $\mathbf{Q}_1\mathbf{Q}_2 = \mathbf{R}(\alpha/2)\begin{pmatrix} 1 & 0 \\ 0 & e^{2i\alpha} \end{pmatrix}\mathbf{R}(-\alpha/2)$, showing that two QWPs are equivalent to a single phase retardance that can be adjusted by rotating one plate with respect to the other. Hence, the resonance condition with $\mathbf{M} = r_A r_B G^2 e^{2i\omega L/c}\mathbf{Q}_1\mathbf{Q}_2^2\mathbf{Q}_1$ yields eigenvectors that are linear and orthogonal at the cavity output mirrors, at ±45° of the adjacent QWP neutral axes, but circular with opposite handedness between the QWPs [42]. Note that this configuration corresponds to the one depicted in the lower left panel of Figure 13.5 ($\phi = \pi/2$ and $|\gamma| = 1$). An interesting property of these eigenvectors is that, for each eigenstate, the sum of the counter-propagating waves between the QWPs is a stationary helicoidal structure (also baptized “twisted-mode” [40]). The other interesting property comes from the calculation of the eigenfrequency difference, which happens to be simply proportional to the relative angle α:

$$\Delta\nu_0 = \nu_y - \nu_x = \frac{2\alpha}{\pi}\frac{c}{2L}. \tag{13.4}$$

Hence, a cavity containing two QWPs provides a simple means to build dual-frequency oscillators with a mechanically adjustable frequency difference. Such laser is studied here in the pulsed mode-locked case, and is also the basis of the dual-frequency laser in Section 13.3.

Based on this eigenstate calculation, and assuming that the laser emits the two eigenpolarizations, we consider two frequency combs shifted by $\Delta\nu_0 = \frac{2\alpha}{\pi}\frac{c}{2L} = \frac{2\alpha}{\pi}f_{\text{rep}}$ with respect to one another, as schematized in Figure 13.1b. The two eigenvectors are linear and orthogonal at the laser output, and we label their directions $\hat{x}$ and $\hat{y}$ in this part. As a simple textbook calculation, we sum n modes with a constant phase at the origin and equal amplitudes, and we find that the electric field then writes

$$\begin{bmatrix} E_x(t) \\ E_y(t) \end{bmatrix} = e^{i2\pi\nu_x t} \begin{bmatrix} 1 \\ e^{i(2\pi\Delta\nu_0 t+\psi)} \end{bmatrix} \sum_p A(t - p/f_{\text{rep}}). \tag{13.5}$$

Here, ν_x is the optical frequency of the $\hat{x}$-comb. ψ is the relative overall phase offset. $A(t)$ is the pulse envelope and $f_{\text{rep}} = c/2L$ is the repetition rate. From Eq. (13.5), the Jones vector $\vec{J}_p$ of the pth pulse of the train, at $t = p/f_{\text{rep}}$, is given by

$$\vec{J}_p = \frac{1}{\sqrt{2}} \begin{bmatrix} 1 \\ \exp\left(i\left(2\pi p \frac{\Delta\nu_0}{f_{\text{rep}}} + \psi\right)\right) \end{bmatrix}. \tag{13.6}$$

Equation 13.6 indicates that the polarization state varies from one pulse to another, forming polarization sequences depending on $\Delta\nu_0$ and ψ. We assume first that $\psi = 0$. Two examples are depicted in Figure 13.7b. For the case $\Delta\nu_0 = f_{\text{rep}}/2$, which is discussed in detail later, one gets at the laser output alternate linearly polarized pulses oriented successively at ±45° with respect to $\hat{x}$ and $\hat{y}$. For $\Delta\nu_0 = f_{\text{rep}}/8$, the pulse train consists of elliptically polarized pulses whose ellipticity varies gradually from one pulse to another, illustrating how the pulse train samples the polarization evolution. Obviously, the period of the polarization evolution is given by the beat-note period $1/\Delta\nu_0$.

In the time series depicted in Figure 13.8, we reproduce the experimental beats $|E_x + E_y|^2$ (upper trace), and $|E_x - E_y|^2$ (lower trace) for four increasing values of $\Delta\nu_0$, corresponding to $\alpha = \pi/10, \pi/8, \pi/6$, and $\pi/4$. The pulse repetition rate is $f_{\text{rep}} = 271$ MHz ($f_{\text{rep}}^{-1} = 3.7$ ns). In Figure 13.8b, where $\alpha = \pi/8$, that is $\Delta\nu_0 = f_{\text{rep}}/4$, note that the pulse train is a sequence of linear and circular polarizations (linear at +45°, left circular, linear at −45°, right circular). In Figure 13.8d, where $\alpha = \pi/4$, that is $\Delta\nu_0 = f_{\text{rep}}/2$, one gets alternate ±45° linearly polarized pulses. All the chronograms are in perfect agreement with Eqs. (13.5)–(13.6). We observe that the two eigenstates are emitted synchronously regardless of the value of $\Delta\nu_0$, despite the difference in their optical lengths. This effect can be attributed to nonlinear delays in the active medium and in the SESAM, where the two eigenstates are coupled.

13.2.4.1 **Phase Locking at $c/4L$**

We now investigate the peculiar case $\Delta\nu_0 \approx f_{\text{rep}}/2$. A stable phase-locking effect is observed for values of $\Delta\nu_0$ within $f_{\text{rep}}/2 \pm 30$ kHz. To evidence this behavior, we

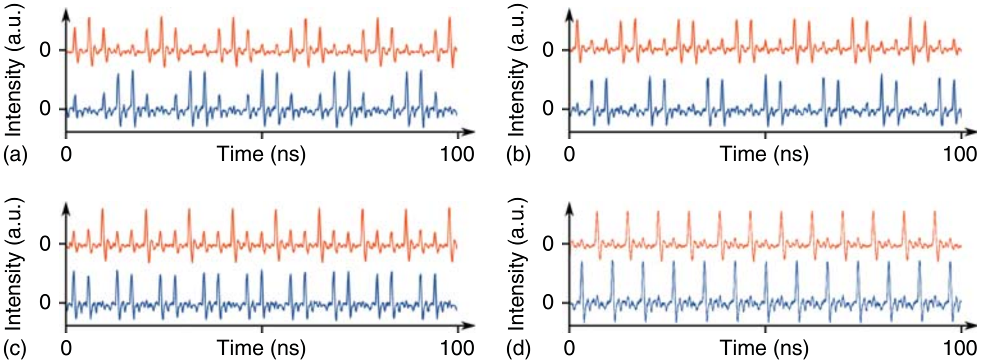

Figure 13.8 Experimental eigenstates beats $|E_x + E_y|^2$ (red), and $|E_x - E_y|^2$ (blue), for (a) $\Delta\nu_0 = f_{rep}/5$, (b) $\Delta\nu_0 = f_{rep}/4$, (c) $\Delta\nu_0 = f_{rep}/3$, and (d) $\Delta\nu_0 = f_{rep}/2$.

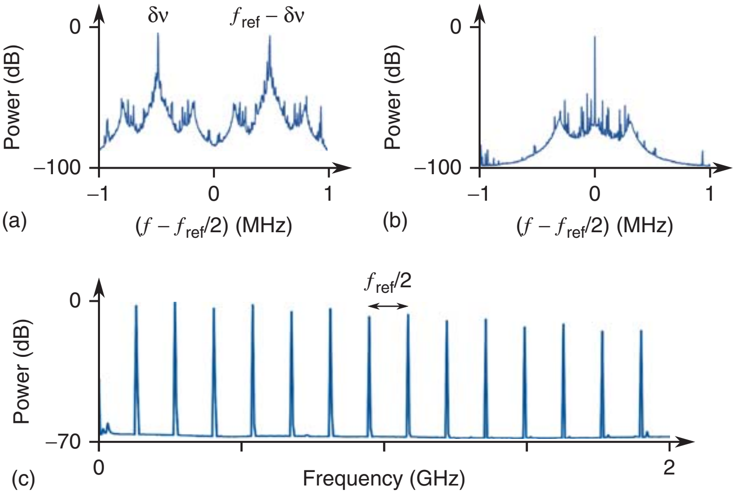

Figure 13.9 Experimental FFT spectrum of the laser output, when $\Delta\nu_0 \approx f_{rep}/2$. (a) $\Delta\nu_0$ outside the locking range. (b) $\Delta\nu_0$ inside the locking range, and (c) resulting $f_{rep}/2$-periodic spectrum.

monitor the electrical spectrum of the beat $\|E_x + E_y\|^2$ reported in Figure 13.9. There is a double peak around $f_{rep}/2$ when $\Delta\nu_0$ is outside the locking range (see Figure 13.9a with a 2 MHz span). When $\Delta\nu_0$ enters the locking range, these two peaks merge into one (Figure 13.9b). Then, a wider span (2 GHz) shows a comb with a perfect periodicity of $f_{rep}/2$ (Figure 13.9c). Peaks whose frequencies are equal to nf_{rep}, $n \in \mathbb{N}$, are the well-known beat-note frequencies between different modes of one eigenstate or the other. On the contrary, peaks whose frequencies are equal to $(n + 1/2)f_{rep}$ are beats between modes from the two eigenstates. The stability of the whole spectrum confirms the dual-comb locking. It is worthwhile to note that the linewidth of the peak at $f_{rep}/2$ is measured to be 10 Hz, as

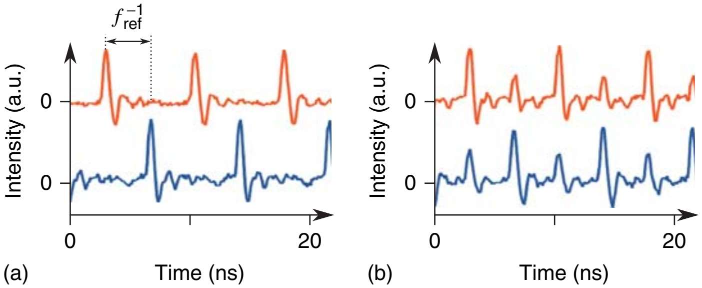

Figure 13.10 Experimental eigenstate beats $|E_x + E_y|^2$ (red), and $|E_x - E_y|^2$ (blue), when the comb frequency shift $\Delta\nu_0$ is locked at $f_{\text{rep}}/2$. (a) $\Psi = 0$ and (b) $\Psi = 0.39$ rad.

narrow as the peak at f_{rep}. We suspect the phase-locking at $\Delta\nu_0 = f_{\text{rep}}/2$ to be due to nonlinear coupling through four-wave mixing, similar to the polarization self-modulation discussed in Section 13.2.3. Note that similar phase-locking behavior is also observed at $\Delta\nu_0 = f_{\text{rep}}/3$ but with a smaller locking range (≤ 10 kHz).

We finally focus on an interesting feature of this locking range in relation with the relative phase ψ. When $\Delta\nu_0 = f_{\text{rep}}/2$, Eq. (13.6) becomes

$$\vec{J}_p = \frac{1}{\sqrt{2}} \begin{bmatrix} 1 \\ (-1)^p \exp(i\psi) \end{bmatrix}. \tag{13.7}$$

We find in this equation that ψ governs the polarization evolution of the pulse train. For example, when $\psi = 0$, one gets alternate ±45° linearly polarized pulses as in Figure 13.8d. If $\psi = \pi/2$, one gets left and right circularly polarized pulses. Experimentally, we find that ψ can be modified in a reproducible way by slightly translating the SESAM along the propagation axis (a few micrometers). Figure 13.10 shows eigenstate beat-note time series for $\Delta\nu_0$ locked at $f_{\text{rep}}/2$, for two values of ψ. Using Eq. (13.7), ψ can be measured experimentally from the modulation depth. Figure 13.10a and b corresponds, respectively, to $\psi = 0$ and $\psi = 0.39$ rad. For all the values of ψ, we check that the spectrum remains the same as depicted in Figure 13.9c. Furthermore, we verify that two successive pulses always hold orthogonal polarizations, that is, $\vec{E}_p \cdot \vec{E}^*_{p+1} = 0$ in agreement with Eq. (13.7).

13.3
Dynamics of Solid-State Lasers Submitted to a Frequency-Shifted

13.3.1
Description of the System

As discussed in Section 13.2, synchronization can be observed in a dual-polarization laser when the beat-note frequency is within a degeneracy range defined by the intracavity anisotropies, or when it operates in a multimode

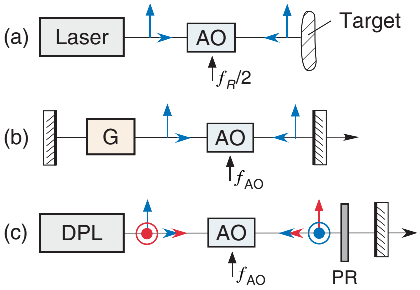

Figure 13.11 Frequency-shifted feedback schemes. AO, acousto-optic Bragg cell; PR, polarization rotator.

regime. Another way for controlling the laser dynamics is to use optical feedback. When the optical feedback loop includes a frequency shifter, typically an acousto-optic Bragg cell, various dynamics have been reported—especially in diode-pumped solid-state lasers. A first kind of frequency-shifted feedback (FSF), schematized in Figure 13.11a, benefits from the sensitivity of class-B lasers to FSF when the frequency shift is close to the laser relaxation oscillation frequency f_R [43]. For instance, Doppler velocimetry was demonstrated with microchip lasers [44], while Lacot and coworkers developed Laser Optical Feedback Imaging (LOFI) techniques based on the same effect [45]. In addition, when the laser operates in a two-frequency regime, the sensitivity of the laser to the FSF was shown to be even stronger [46, 47].

Another FSF scheme consists of using an *intracavity* Bragg cell (see Figure 13.11b) driven at a frequency f_{AO} that is far greater than f_R. The laser then exhibits a nonconventional frequency spectrum, once known as a *modeless* spectrum. First observed and theoretically studied in dye lasers [48, 49], intracavity FSF has been shown to yield pulsed regimes in solid-state lasers [50].

In the case of dual-polarization solid-state lasers, an external Bragg cell followed by a polarization-rotator can be used to couple the two modes, as depicted in Figure 13.11c [51, 52]. Here, the feedback frequency, that is $2f_{AO}$, is supposed to be close to the beat frequency. If one focuses on the dynamics of the beat pulsation, this scheme thus consists of an optically based radio frequency (RF) oscillator driven by an RF reference, here the synthesizer driving the Bragg cell. It is the aim of this section to describe the effect of a frequency-shifted feedback on the nonlinear dynamics of a dual-polarization solid-state laser, with emphasis on the synchronization mechanisms.

13.3.1.1 Experimental Setup

The setup under consideration is a dual-polarization, diode-pumped, solid-state laser similar to the Nd : YAG laser detailed in [53], followed by a feedback cavity (see Figure 13.12a). The laser cavity of length L is closed on one side by a mirror M_A, which is coated on the active medium (here Nd : YAG), and on the other side by a concave mirror M_B. An étalon ensures single longitudinal mode oscillation. Two eigenmodes E_x and E_y, polarized along $\hat{x}$ and $\hat{y}$, with eigenfrequencies ν_x and ν_y respectively, oscillate simultaneously. Two QWPs induce a frequency difference $\Delta\nu_0 = \nu_y - \nu_x$, finely tunable from 0 to $c/4L$, as discussed in Section 13.2. We

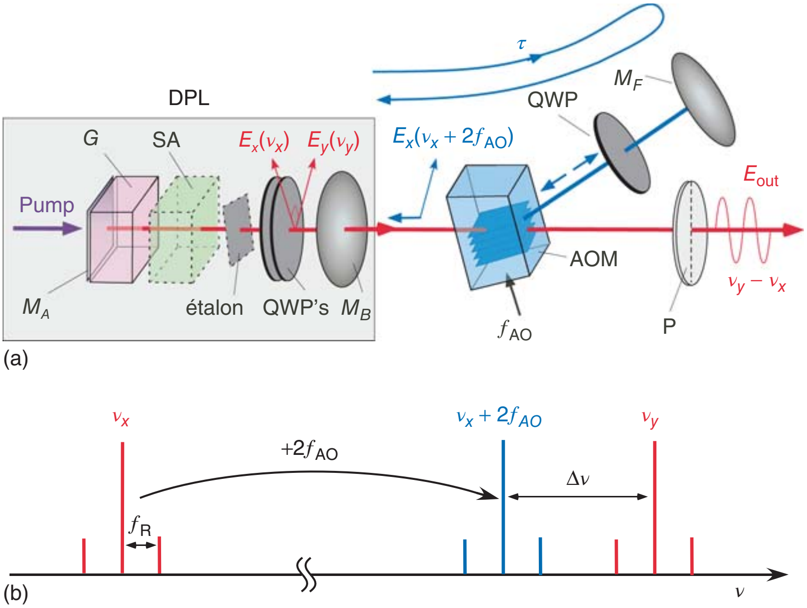

Figure 13.12 (a) Experimental setup. DPL, dual-polarization laser; SA, saturable absorber (pulsed regime only); P, polarizer; M_F, feedback mirror. (b) Diagram of the main frequencies involved in the dynamics of the system. ν_x corresponds to a wave polarized along x, while ν_y and $\nu_x + 2f_{AO}$ correspond to a y-polarization. f_R, relaxation oscillation frequency.

assume that $\Delta\nu_0$ is large enough to avoid coherent effects in the cross-saturation of the active medium. Each laser field interacts with its own population inversion reservoir [54].

A saturable absorber (SA) can be inserted in order to get passive Q-switching (PQS). SA is assumed to allow the simultaneous emission of x- and y-polarized pulses. In the case of Nd : YAG lasers, it was shown that a [001]-cut Cr : YAG crystal with the [001] crystallographic axis aligned along the laser optical axis, fulfills this condition when the intracavity phase anisotropy axes are oriented at 45° with respect to the Cr : YAG axes [11]. In this case, the saturable losses experienced by the two eigenstates are equal to the mean of the saturable loss coefficients associated with the [100] and [010] crystallographic axes.

The feedback cavity contains a Bragg cell, driven by a stable RF synthesizer, which provides an external phase reference. A QWP at 45° with respect to the $\hat{x}$ and $\hat{y}$ axes, followed by a mirror, flips the x and y polarizations after one round-trip. One can also use a Faraday rotator [47]. Finally, the laser beam is reinjected in the laser cavity after crossing again the Bragg cell. As a result, a x-polarized field oscillating at the frequency $\nu_y + 2f_{AO}$ and a y-polarized field oscillating at the frequency $\nu_x + 2f_{AO}$ are reinjected in the laser. We point out that the optical reinjection has no direct effect on E_x, because the frequency difference between ν_x and $\nu_y + 2f_{AO}$ is too large. For the same reason, multiple round-trips in the feedback cavity have no effect on the laser dynamics. For the dynamics analysis, there are thus three relevant optical frequencies, as drawn in Figure 13.12b. Note that each frequency carries two sidebands at $\pm f_R$ due to the relaxation oscillations.

Finally, the laser output is detected after a polarizer (P), leading to an electrical signal proportional to $I_{xy} = |E_x + E_y|^2$.

13.3.2
Lang–Kobayashi Rate Equations

The dynamics of the dual-polarization two-frequency laser is analyzed in the framework of two-mode rate-equations [54]. The system writes [53]

$$\dot{n}_{x,y} = \gamma_{\|} P - [\gamma_{\|} + \zeta(|E_{x,y}|^2 + \beta |E_{y,x}|^2)] n_{x,y}, \tag{13.8}$$

$$\dot{E}_x = [-\Gamma - a + \kappa(n_x + \beta n_y)] \frac{E_x}{2} + 2i\pi \nu_x E_x, \tag{13.9}$$

$$\dot{E}_y = [-\Gamma - a + \kappa(n_y + \beta n_x)] \frac{E_y}{2} + 2i\pi \nu_y E_y + e^{4i\pi f_{\mathrm{AO}} t + i\Psi} \gamma_e E_x(t - \tau). \tag{13.10}$$

$n_{x,y}$ are the two population inversions. $\gamma_{\|}$, Γ, and P are the population decay rate, cavity decay rate, and pumping rate, respectively. They are supposed to be identical for both x and y polarizations. κ and ζ are the atom/field coupling coefficients. β accounts for the cross saturation in the active medium. γ_e is the feedback strength [45], and accounts for the reflectivity of the mirror $\mathrm{M_F}$, the diffraction efficiency, the transmission of all the various optical components and the mode matching between the feedback beam and the laser intracavity field. τ and Ψ are, respectively, the delay and the phase associated with the feedback optical path. Furthermore, if a saturable absorber is inserted inside the cavity, an additional equation governing the evolution of the population inversion in the absorber has to be added to predict the pulsed operation [11]. As discussed in the previous section, in the case of Cr : YAG, the saturation term a can be identical for both eigenpolarizations. In this case, the time evolution of the absorption is governed by

$$\dot{a} = \gamma_a a_0 - \left[\gamma_a + \left(\sigma_a/\sigma_g\right)(1 + C_a)\left(|E_{x,y}|^2 + |E_{y,x}|^2\right)/2\right] a, \tag{13.11}$$

where a_0 is the unsaturated absorption coefficient. σ_a (σ_g) is the absorption (stimulated emission) cross section of the absorbing (laser) transition and C_a accounts for cross-saturation in the absorber.

The noise terms due to spontaneous emission have been disregarded in the rate equations. Numerical simulations indicate that they do not play a significant role in the dynamics. Besides, we do not introduce a phase/amplitude coupling terms, that is, the Henry factor, as is customary in solid-state lasers [3], although it has been shown that it may sometimes play a significant role in Nd lasers dynamics [55, 56]. Furthermore, in the case of CW lasers, under standard experimental conditions, the feedback is seen as instantaneous by CW diode-pumped solid-state lasers. Indeed, the laser dynamics evolve on time scales $\sim 1/f_R$ much bigger than τ, even for meter-long feedback cavities. This motivates neglecting τ in

Eq. (13.10) without altering the numerical solutions. This assumption has been checked numerically in a few typical cases. Finally, the set of rate equations has been written in the case of a four-level active medium [57]. Similar equations have been obtained in the case of a three-level active medium, such as Er : YAG, that lead to the same predictions [47].

13.3.2.1 **Phase Dynamics**

In order to study the synchronization properties of the system, we write the optical fields as

$$E_x = \sqrt{I_x} e^{i\phi_x} e^{2i\pi\nu_x t} e^{-i\psi}; \quad E_y = \sqrt{I_y} e^{i\phi_y} e^{2i\pi(\nu_x + 2f_{\mathrm{AO}})t}. \tag{13.12}$$

The relative phase $\Phi = \phi_y - \phi_x$ corresponds to the phase of the slowly varying amplitude of E_y relative to the phase $2\pi(\nu_x + 2f_{\mathrm{AO}})t$ of the reinjected field. Alternatively, Φ can be seen as the phase between the beat note oscillating at $\Delta\nu_0$ and the reference oscillating at $2f_{\mathrm{AO}}$. Deriving the evolution of Φ from Eqs. (13.8) – (13.10) leads to the following Adler-type equation

$$\dot{\Phi} = 2\pi\Delta\nu - \gamma_e \sqrt{\frac{I_x}{I_y}} \sin\Phi, \tag{13.13}$$

where $\Delta\nu = \nu_y - \nu_x - 2f_{\mathrm{AO}}$ is the detuning between E_y and the reinjected field (see Figure 13.12b). Equation (13.13) must be completed with equations for the intensities derived from Eqs. (13.9) – (13.10), that are appropriate for comparative studies between theory and experiments, since we have experimental access to the fields intensities and to the relative phase.

13.3.2.2 **Time-Scaled Rate Equations**

For the numerical simulations, it is more convenient to consider the complex fields with a scaled time s related to the physical time t by $t = 2\pi f_R s$. This normalization removes stiffness from the class-B laser equations [3]. This normalization is only relevant for the CW case. When the laser is passively Q-switched, the dynamics is not governed anymore by the relaxation oscillation frequency but by the cavity and absorber decay rates. We thus now focus on the CW case, that is, $a = 0$. The set of Eqs. (13.8) – (13.10) becomes

$$\frac{de_x}{ds} = \frac{(m_x + \beta m_y)}{1+\beta}\frac{e_x}{2}, \tag{13.14}$$

$$\frac{de_y}{ds} = \frac{(m_y + \beta m_x)}{1+\beta}\frac{e_y}{2} + i\Delta\, e_y + \gamma e_x, \tag{13.15}$$

$$\frac{dm_{x,y}}{ds} = 1 - \left(|e_{x,y}|^2 + \beta|e_{y,x}|^2\right) - \epsilon\, m_{x,y}\left[1 + (\eta - 1)(|e_{x,y}|^2 + \beta|e_{y,x}|^2)\right]. \tag{13.16}$$

Here, $e_{x,y}$ are the normalized amplitudes of the optical modes, $m_{x,y}$ describe the population inversions, η is the pump parameter, γ is the feedback strength, ϵ is the inversion lifetime, and $\Delta = (\Delta\nu_0 - 2f_{\mathrm{AO}})/f_R$ is the detuning. For more details on the correspondence between the normalized and the physical quantities, see [58].

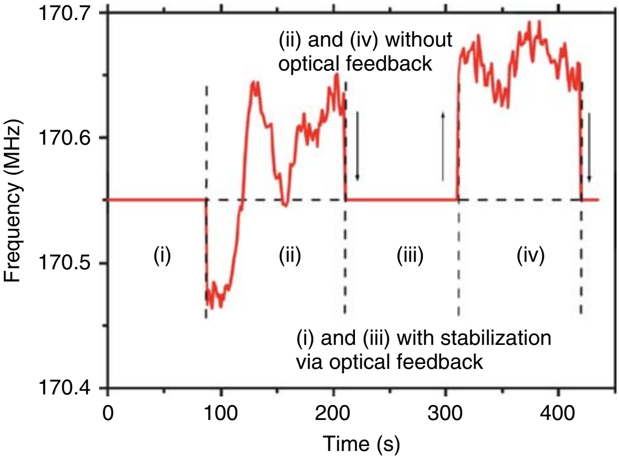

Figure 13.13 Time-domain analysis of the beating frequency with (i–iii) or without feedback (ii–iv) (from [51]).

From these equations, time series and spectra can be calculated using a standard fourth-order Runge–Kutta algorithm with an adaptative time-step. The spectra are obtained by convoluting the Fourier transform of the time series with a gate function that reproduces the spectral resolution of the electrical spectrum analyzer. All parameters can be found in [58] and references therein.

13.3.3
Phase Locking

13.3.3.1 Continuous-Wave Case

In free-running operation, that is without feedback, the beating frequency $\Delta\nu_0$ of DPLs fluctuates due to technical noises with a typical relative amplitude of a few percent. With feedback, the beat note locks to the reference if the detuning is in a phase-locking range. This can be seen in Figure 13.13, which reports, for a CW dual-polarization Er : Yb glass laser, the temporal fluctuations of the beat-note frequency successively in the free regime and in the FSF regime. The phase-locking range, which corresponds to the stationary solutions of Eq. (13.13), can be evaluated by stating that, for equal gain and intracavity losses, the feedback term leads to an intensity I_y slightly larger than I_x. The locking range then writes

$$-f_A \le \Delta\nu \le f_A, \tag{13.17}$$

where the so-called Adler frequency f_A is equal to $\gamma_e/2\pi$. By integrating the rate equations (13.14)–(13.16), we verified numerically that the locking range fits this analytical expression.

Equation (13.17) can be experimentally checked from the electrical spectrum of the beat note. As shown by Figure 13.14a, the electrical spectrum presents two peaks. They correspond to the beat note between the two eigenstates E_x and E_y and

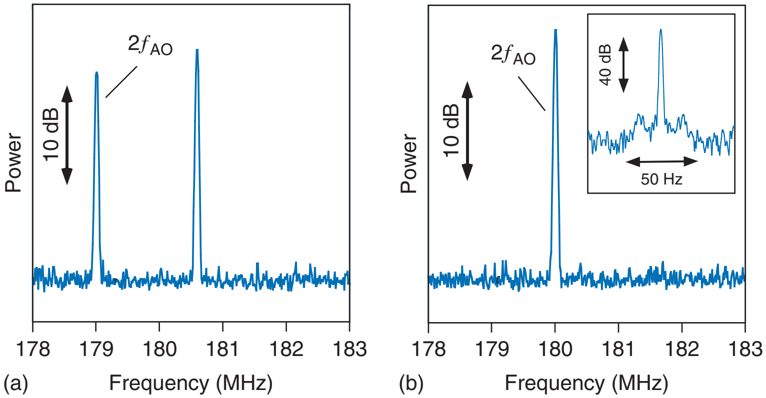

Figure 13.14 Typical experimental spectral analysis of the output pulse train power. (a) Unlocked beat note, that is, $|\Delta\nu| > f_A$. (b) Locked beat note, $|\Delta\nu| < f_A$ (from [53].)

to the beat note between E_x and the frequency-shifted field after one round-trip inside the feedback cavity, hence at frequency $2f_{AO}$. In this case, the detuning is obviously outside the locking range. When the RF is swept, there is a sudden jump of the beat note to the reference frequency $2f_{AO}$. Locking occurs, and the resulting spectrum contains a single beat line at a frequency $2f_{AO}$, as shown in Figure 13.14b. $2f_{AO}$ can then be tuned and the beat note stays locked as long as $|\Delta\nu| \leq f_A$. The experimental evolution of the locking range with respect to the feedback strength is linear, in agreement with theory. In the locking range, a close inspection of the peak reveals that the beat note replicates perfectly the RF synthesizer spectral purity, as reported in the inset of Figure 13.14b.

13.3.3.2 *Q*-Switching Case

We now address the question of phase-locking in the PQS regime. With seedless PQS dual-frequency lasers, the phase of the beat note is intrinsically lost between laser pulses. However, it was experimentally shown in [52] that the FSF scheme permits to induce a coherence of the beat note among many successive pulses in the pulse. The subhertz linewidth of the beat note indicates that the spectral purity of the reference is reported to the optically carried RF. This leads to potential applications in lidar–radar technique, for which pulse-to-pulse coherence has to be preserved [59, 60].

To evaluate the phase-locking range in the PQS regime, the delayed rate Eqs. (13.8)–(13.11) are integrated first with a detuning larger than f_A. The resulting output is reported in Figure 13.15a, where both the intensity $|E_{\mathrm{out}}|^2$ and the relative phase Φ are displayed. One can see here notably that the phase evolves monotonically with a rate of $2\pi\Delta\nu t$. There is hence no phase locking in this case. Conversely, when $|\Delta\nu| < f_A$, there is a dramatic change in the evolution of Φ during the pulse (see Figure 13.15b); namely, there is a clear forcing of the phase difference due to the feedback term. The analysis of many pulses in the train shows this behavior to be repetitive.

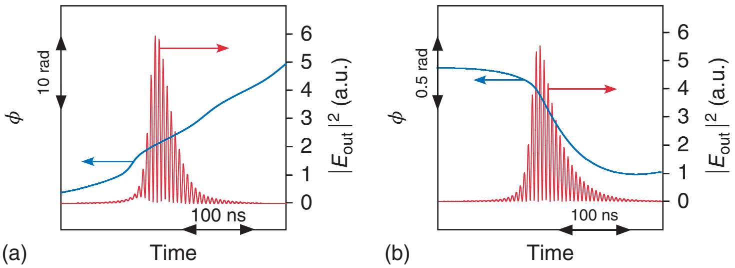

Figure 13.15 Computed intensity and relative phase time evolution of the output beam for (a) phase unlocking and (b) phase locking (adapted from [53]).

Finally, from these simulations, we can estimate a phase-locking range for the PQS case. Indeed, the slope sign change of the phase difference within each pulse gives a relevant indication of phase locking. A full locking range of about $1.5\,f_A$, instead of $2\,f_A$ in the CW regime, is numerically found. This reduction of the locking range in PQS operation was also observed experimentally. Note that the simulations predict a growing locking range as the feedback strength is increased, and also a quite weak effect of the delay τ, as long as τ is smaller than about a fourth of the pulse width T_P (here, $T_P = 40$ ns). Finally, as in the CW case, we have numerically checked that taking into account multiple delays for the feedback does not change the locking range at the first order.

13.3.4
Bounded Phase Dynamics

Up to now, the locking properties of the CW two-frequency laser under FSF was described by an Adler-type equation governing the relative phase Φ between the laser beat-note and the reference signal. If the frequency difference $\Delta\nu$ between the two oscillators is lower (higher) than a frequency detuning f_A, determined by the amount of feedback, the two oscillators are phase-locked (unlocked). However, driven oscillators can exhibit more subtle synchronization properties. Specifically, it has been found theoretical and experimental evidence of regimes of frequency locking *without phase locking*. These regimes, called phase entrainment [61, 62], phase trapping [63], or bounded phase [64, 65] appear when $\Delta\nu$ is bigger than f_A, thus extending the synchronization region beyond the standard Adler locking range.

To get a general overview of the dynamics, bifurcation diagrams are calculated by numerical integration of Eqs. (13.14)–(13.16), as a function of the control parameter $\Delta\nu$.

13.3.4.1 Intensity Bifurcation Diagram

The bifurcation diagram of Figure 13.16a is obtained by plotting the extrema of the output intensity I, calculated in the reference frame of the RF oscillator at $2f_{AO}$, in

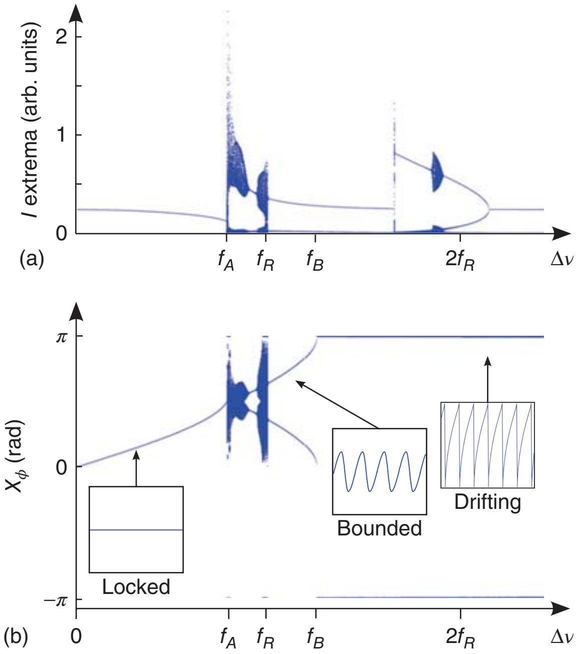

Figure 13.16 Computed bifurcation diagrams, as a function of $\Delta\nu$. (a) $I = |E_{\text{out}}|^2$ in the rotating frame at $2f_{\text{AO}}$. (b) The relative phase Φ. Three qualitatively different regimes appear: phase locking for $\Delta\nu < f_A$, bounded phase for $f_A < \Delta\nu < f_B$, and phase drifting when $\Delta\nu > f_B$.

order to remove the fast oscillations in the time series. First, the ratio f_A/f_R was set at 0.8. When $\Delta\nu$ is much larger than $2f_R$, I is slowly modulated by the feedback at a frequency $\Delta\nu$, as shown by the bifurcation diagram. This modulation results in two extrema lines. We stress that, even in the absence of feedback, the x-polarized mode is modulated due to the nonlinear coupling in the active medium (our system is thus substantially different from a master–slave configuration). When $\Delta\nu$ approaches $2f_R$, a period-doubling bifurcation appears. The amplitude of this subharmonic modulation rises as $\Delta\nu$ decreases, and suddenly jumps back to a simple harmonic modulation. When $\Delta\nu \simeq f_R$, the two modes are more sensitive to perturbations and the modulation develops gradually into a pulsed regime, as illustrated by the times series of Figure 13.17.

For $f_A < \Delta\nu < f_R$, the intensity dynamics becomes more complex (see Figure 13.18a and b). The associated power spectrum Figure 13.18c and d spans continuously a broad frequency range, much larger than the characteristic frequencies f_R, f_A, and $\Delta\nu$. The theoretical predictions are in good agreement with the corresponding experimental observations, which confirms the validity of the rate equation model. Finally, when $\Delta\nu < f_A$, the beating of the two eigenstates is phase-locked to the RF reference, and as a result, no modulation is observed.

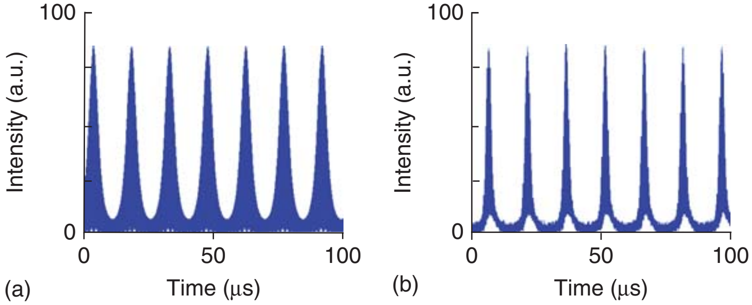

Figure 13.17 Simulated (a) and experimental (b) time series of $|E_{\text{out}}|^2$ for $\Delta\nu = 1.05 f_R$ (adapted from [58]).

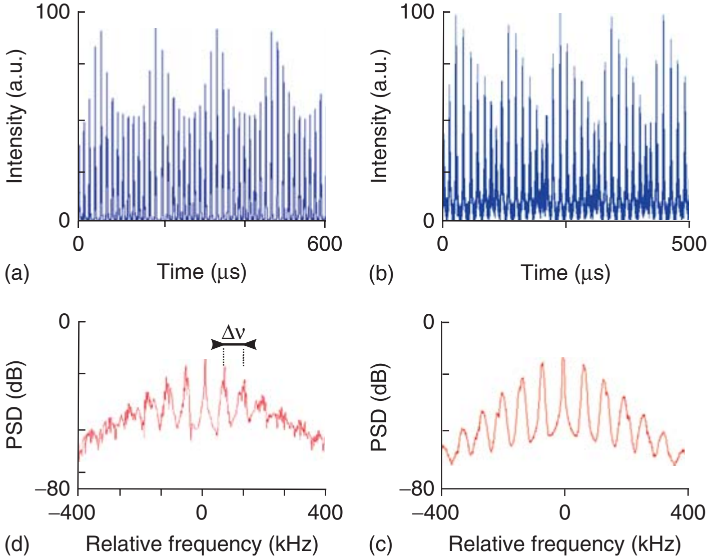

Figure 13.18 Simulated (a) and experimental (b) time series of $I = |E_{\text{out}}|^2$. Corresponding experimental (c) and simulated (d) power spectra. Here, $\Delta\nu = 0.88 f_R$ (adapted from [58]).

13.3.4.2 Phase Bifurcation Diagram

For the relative phase between the beating and the RF reference, the bifurcation diagram consists of plotting the local extrema X_Φ of Φ as a function of $\Delta\nu$ (see Figure 13.16b). When $\Delta\nu < f_A$, Φ is constant over time, that is, the two oscillators are phase-locked. Then, the relative phase remains bounded beyond f_A up to a certain value f_B of $\Delta\nu$, except for two narrow regions close to $\Delta\nu = f_R$ and $\Delta\nu = f_A$. This implies that the average frequency of the beat note coincides with the reference frequency; in other words, the interval $f_A < \Delta\nu < f_B$ defines a region of frequency locking without phase locking. Then, the oscillators unlock completely when $\Delta\nu > f_B$. Φ(t) being numerically restricted to the interval $[-\pi; \pi]$, it

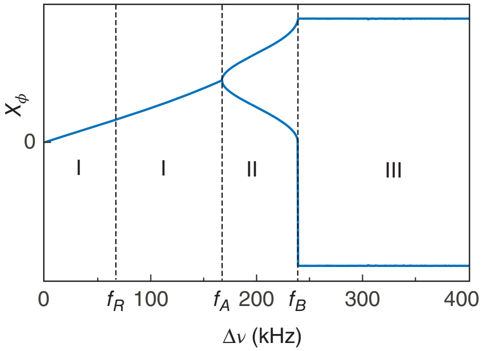

Figure 13.19 Computed phase bifurcation diagram for $f_R = 68$ kHz and $f_A = 170$ kHz. The reported value of $f_B = 240$ kHz corresponds to the experimental value.

results in a "sawtooth-like" time series, with abrupt vertical jumps as Φ(t) reaches the value of $\pm\pi$, which appear as extrema. We stress that, even if the intensity and phase dynamics are coupled, the sequence of bifurcations is not the same. Indeed, while f_A is a bifurcation point for both intensity and phase, at f_B where the phase becomes unbounded, no bifurcation occurs for the intensity. Furthermore, the period-doubling bifurcation on the intensity around $2f_R$ produces no special signature on the phase dynamics. Moreover, a bounded-phase regime cannot be recognized from the power spectrum. For instance, complex spectra such as the ones shown in Figure 13.18c and d corresponds to a bounded-phase regime. Finally, bounded-phase is not due to the resonance induced by the relaxation oscillation. For instance, if f_A becomes greater than f_R, by increasing the feedback strength, the period-doubling at $2f_R$ and complex behavior around f_A and f_R disappear and the bifurcation diagram becomes smooth, as shown in Figure 13.19, which corresponds to $f_A = 2.5f_R$. The three regimes can still be clearly observed but there is no more resonance at f_R. Note that, in the limit of strong coupling, that is, $f_A \gg f_R$, it has been shown that $f_B \approx \sqrt{2}f_A$ [63], in agreement with the experimental value of f_B reported in Figure 13.19.

13.3.4.3 Phasors

The transition from phase-locking (regime I) to phase (regime III) through bounded phase (regime II) can be experimentally observed on the phasor plots of $|E_{\text{out}}|^2$, in a reference frame rotating at the reference signal $2f_{\text{AO}}$. For small detuning, that is, $\Delta\nu < f_A$, phase-locking occurs, and the corresponding experimental phasor plot consists of just a fixed point (Figure 13.20a, regime I). If $\Delta\nu$ is increased above the Adler frequency f_A, the fixed-point solution loses stability through a supercritical Hopf bifurcation. The point representing I then rotates at the frequency $\Delta\nu$ on a limit cycle (regime II). The relative phase exhibits bounded, periodic temporal oscillations, whose amplitude increases with $\Delta\nu$. Finally, when $\Delta\nu$ is bigger than f_B, the origin of the plane lies inside the limit cycle and the phase variations are not bounded anymore (regime III).

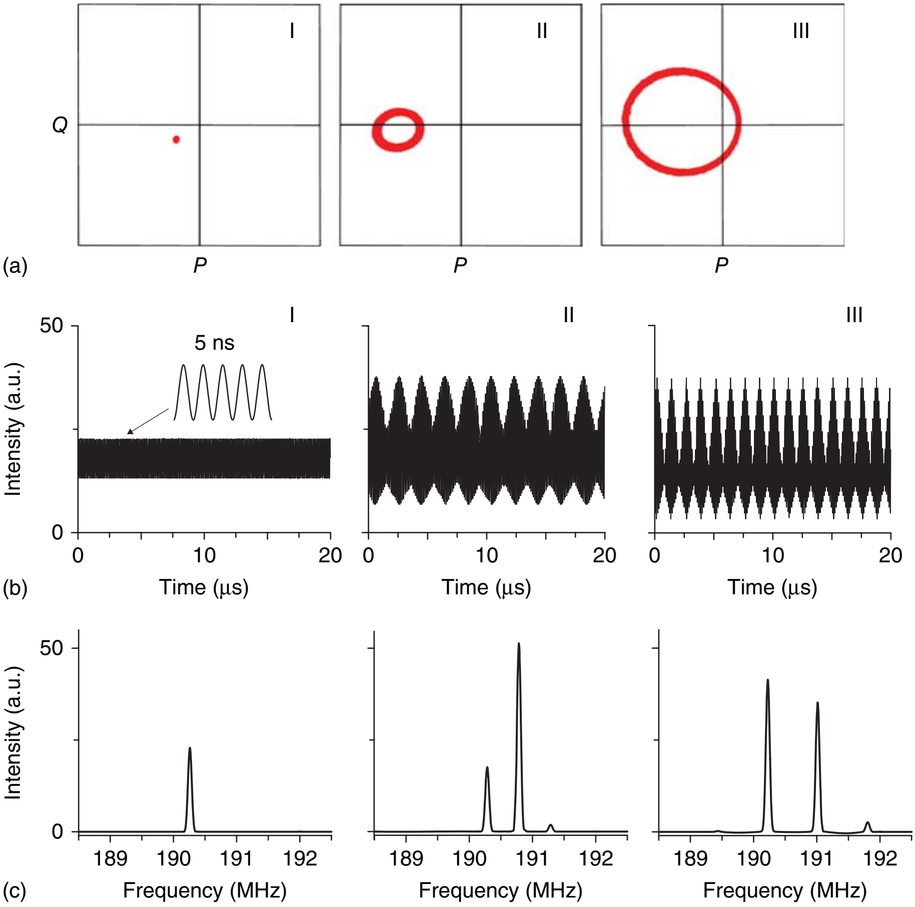

Figure 13.20 (a) Experimental phasor plots of the output signal $I = |E_{\text{out}}|^2$, in the reference frame rotating at $2f_{\text{AO}}$. Each plot contains 2000 points, recorded over 100 μs. (I) Phase-locking regime. (II) Bounded-phase regime. (III) Unbounded-phase regime. (b) Corresponding experimental time series. (c) Power spectra (taken from [66]).

In the time and frequency domains (Figure 13.20b and c), phase-locking (I) appears as pure sinusoidal oscillation, and the corresponding power spectrum consists of a single, sharp Fourier peak. On the contrary, in the bounded-phase (II) and in the unbounded-phase regime (III), the power spectrum shows two peaks at the natural frequencies $2f_{\text{AO}}$ and $\Delta\nu_0$ of the uncoupled optically carried oscillator and reference RF synthesizer, respectively, and the time series displays a beating, that is, a slow modulation of the amplitude of the oscillations.

13.3.4.4 Role of the Coupling in the Active Medium

When the eigenmodes E_x and E_y are not coupled via the active medium, that is, $\beta = 0$, the system is equivalent to a slave laser (optical field E_y) undergoing injection by a master laser (E_x whose frequency is shifted by $2f_{\mathrm{AO}}$). Although the case $\beta = 0$ was not experimentally reported in the literature for diode-pumped solid-state lasers, it was demonstrated from optical phasor plots in the case of optically injected semiconductor lasers [65, 67]. We have shown that, in the case of diode-pumped solid-state lasers, the numerically computed bifurcation diagram for $\beta = 0$ are similar to the one obtained in the case of strong coupling such as the one of Figure 13.19 [58]. It presents a supercritical Hopf bifurcation at the locking point f_A followed by a bounded phase solution up to f_B. Comparison with the phase bifurcation diagram of Figure 13.18 shows that β is responsible for higher-order bifurcations near f_A and for resonance at f_R and $2f_R$.

13.3.5
Measure of the Synchronization in the Bounded Phase Regime

From Figure 13.20, bounded and unbounded phase regimes appear very similar. First, the power spectra consist of two separate peaks at the natural frequencies of the oscillators. Second, in the Fresnel plane, both appear topologically equivalent and no bifurcation is seen through f_B [68]. To investigate quantitatively the status of phase synchronization in the bounded-phase regime, we use the single-sideband power spectral density (PSD) of the relative phase Φ, also called phase-. The PSD measures the strength of the phase fluctuations of an oscillator at all frequencies, and thus characterizes its quality [69]. In our setup, the PSD is computed from the relative phase $\Phi(t)$ extracted from the experimental time series. When the phase is unbounded (regime III), the average slope of the drifting phase is numerically subtracted in order to get a stationary process.

On the experimental spectra shown in Figure 13.21, one sees that, in the phase-locking regime, the phase fluctuations of the free-running laser are strongly suppressed, for example, by −30 dB at 1 kHz. For bounded-phase, the long-term

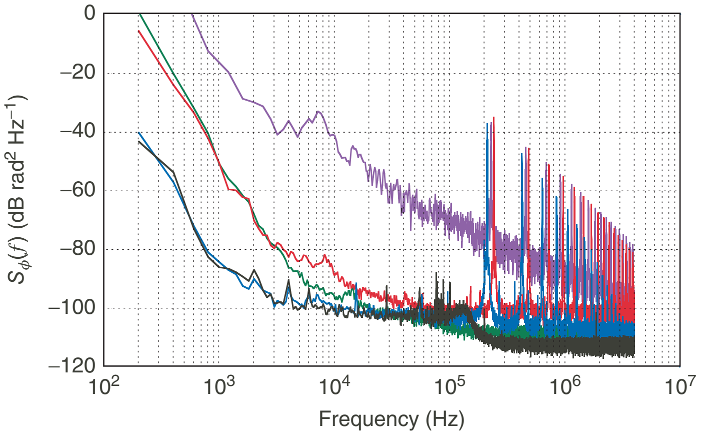

Figure 13.21 Measured phase spectra. Black: $\Delta\nu < f_A$. Blue: $f_A < \Delta\nu < f_B$. Violet: $\Delta\nu \simeq f_B$. Red: $\Delta\nu > f_B$. Green: free-running laser (from [66]).

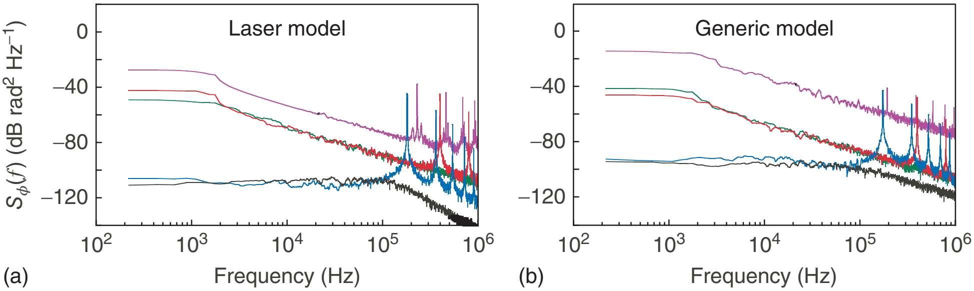

Figure 13.22 Computed phase spectra using the laser (a) or the generic (b) model. Black: $\Delta\nu < f_A$. Blue: $f_A < \Delta\nu < f_B$. Violet: $\Delta\nu \simeq f_B$. Red: $\Delta\nu > f_B$. Green: free-running oscillator. See [66] for details on the numerical parameters.

phase stability is shown to be the same as in the phase-locking regime. The low frequency part of the spectrum can hardly be distinguished in the two cases. Again, the low-frequency drifts and fluctuations are removed with respect to the free-running laser. The only differences consist of the narrow peaks at $\Delta\nu$, and its harmonics. These peaks correspond to the onset of the deterministic oscillation of the phase beyond the Hopf bifurcation point f_A. Conversely, for $\Delta\nu \simeq f_B$, there is a large increase of the phase noise. This can be understood by observing in Figure 13.20a that the limit cycle has a finite thickness, because of fluctuations of the parameters. Therefore, when $\Delta\nu \simeq f_B$, erratic phase slips occur because of noise. These stochastic, abrupt 2π phase jumps explain the huge amount of phase noise. Finally, the spectrum of the unbounded-phase regime corresponds essentially to the one of the free-running laser, apart from the high-frequency peaks. These results can be found theoretically, as shown in Figure 13.22 that reports the numerically calculated phase noise spectra using the laser model (Eqs. (13.14)–(13.16) of Section 13.3.2).

In order to check to which extent these findings are specific to our system, the following minimal model was numerically investigated:

$$\frac{dy}{ds} = (1 - i\Delta)y - (1 + i\alpha)|y|^2 y + e. \tag{13.18}$$

Here, y is the amplitude of a generic driven oscillator, Δ the detuning, and α a phase-amplitude coupling factor. Equation (13.18) contains just a linear term accounting for the growth of oscillations, a saturating nonlinearity, and an external forcing e, and has been shown to be a universal equation describing any periodically driven oscillator close to a supercritical Hopf bifurcation point [70]. The computed PSDs of y are plotted in Figure 13.22. The agreement with the laser model is striking, all the observed regimes being reproduced.

To resume, when looking at the long-term phase stability of the optically carried oscillator, the occurrence of a Hopf bifurcation at f_A is undetectable. Conversely, at f_B, a sharp transition occurs as a signature of the unlocking. The relevant boundary for the synchronization range is thus not the Adler frequency f_A, but the bounded-phase frequency f_B. From the viewpoint of dynamical systems, although phase-locking and bounded-phase are two qualitatively different regimes, separated by a bifurcation, this distinction turns out to be of little relevance with respect to synchronization. This appears to be generic for any driven oscillator undergoing a Hopf bifurcation.

13.4
Conclusion

In this chapter, we have reviewed frequency-locking effects among vectorial solid-state laser modes. To summarize, we discussed three types of synchronization: (i) self-locking of the two polarization eigenmodes that, in the case of class-B lasers, is found with a rich temporal dynamics when the frequency degeneracy range is of the order of the relaxation oscillation frequency, (ii) locking of the beat frequency at $c/4L$ in cavities containing a QWP, even in the pulsed mode-locked regime, and (iii) frequency locking of the beat frequency against an external reference using a frequency-shifted feedback scheme.

These effects are linked to the vectorial nature of light and could appear also in other types of lasers studied in different chapters of this book. We mention here just a few examples of possible connections. The self-locked mechanism in weakly birefringent cavities could operate in vertical-external-cavity surface-emitting lasers [71]. The polarization dynamics in the mode-locked case exhibit similarities with the polarization-locked solitons evidenced in fiber lasers [72, 73], where a Stokes description of light polarization is used (see Chapter 14). The FSF dynamics is also relevant to semiconductor lasers [74]. FSF is an efficient way to lock an optically carried microwave reference, leading to potential applications in the field of microwave photonics [75].

Finally, we note that most of the effects studied here are generic for nonlinearly coupled oscillators and can be transposed to other fields of research. For instance, the laser experiments on bounded-phase have stimulated recent studies on analogous phenomena in fluid dynamics [76] or in nanomechanical resonators [77].

Acknowledgments

The authors thank Jérémie Thévenin, Thomas Erneux, Sylvain Girard, Hervé Gilles, and all the fellows of the Optics and Photonics Department of the Institut de Physique de Rennes who contributed to the results reported here.

References

1. Statz, H. and de Mars, G. (1960) *Transients and Oscillation Pulses in Masers*, Quantum Electronics, Columbia University Press, New York, pp. 530–537.
2. Tang, C.L., Statz, H., and deMars, G. (1963) Spectral output and spiking behavior of solid-states lasers. *J. Appl. Phys.*, **34** (8), 2289–2295.

3. Erneux, T. and Glorieux, P. (2010) *Laser Dynamics*, Cambridge University Press.
4. de Lang, H. (1966) *Polarization Properties of Optical Resonators and Active*, Utrecht Rijksuniversitaet.
5. Garrett, C.G.B. (1967) Normal modes of a ferromagnetic laser with one brewster face. *IEEE J. Quantum Electron.*, **3** (4), 139–142.
6. Carlson, D. and Siegman, A.E. (1968) Intracavity electrooptic frequency tuning, polarization switching, and Q-switching of a Nd:YAG laser oscillator. *IEEE J. Quantum Electron.*, **4** (3), 93–98.
7. Greenstein, H. (1969) Some properties of a Zeeman laser with anisotropic mirrors. *Phys. Rev.*, **178**, 585–589.
8. Le Floch, A. and Le Naour, R. (1971) Polarization effects in Zeeman lasers with x–y-type loss anisotropies. *Phys. Rev. A*, **4**, 290–295.
9. Jones, R.C. (1941) A new calculus for the treatment of optical systems I. Description and discussion of the calculus. *J. Opt. Soc. Am.*, **31** (7), 488–493.
10. Emile, O., Brunel, M., Le Floch, A., and Bretenaker, F. (1998) Vectorial excess noise factor in common lasers. *Europhys. Lett.*, **43** (2), 153–157.
11. Brunel, M., Emile, O., Vallet, M., Bretenaker, F., Le Floch, A., Fulbert, L., Marty, J., Ferrand, B., and Molva, E. (1999) Experimental and theoretical study of monomode vectorial lasers passively Q switched by a Cr^{4+}:yttrium aluminum garnet absorber. *Phys. Rev. A*, **55** (2), 4052–4058.
12. Brunel, M., Emile, O., Alouini, M., Le Floch, A., and Bretenaker, F. (1999) Self-mode-locked pulsed monomode laser. *Opt. Lett.*, **24** (4), 229–231.
13. Dekker, P. and Dawes, J.M. (1998) Pulsed output from a dual-polarization CW diode-pumped Nd:YAG laser. *J. Opt. Soc. Am. B*, **15** (1), 247–251.
14. Alouini, M. (2001) Etude théorique et expérimentale des lasers solides Er^{3+} et Nd^{3+}*:* application des lasers bifréquences aux télécommunications optiques et hyperfréquences. PhD thesis. University of Rennes, France.
15. Zeghlache, H. and Boulnois, A. (1995) Polarization instability in lasers. I. Model and steady states of neodymium-doped fiber lasers. *Phys. Rev. A*, **52**, 4229–4242.
16. Khandokhin, P., Khanin, Y., Mamaev, Y., Milovsky, N., Shirokov, E., Bielawski, S., Derozier, D., and Glorieux, P. (1998) Polarization dynamics of a fibre Fabry–Perot laser with feedback. *J. Opt. B: Quantum Semiclassical Opt.*, **10** (1), 97.
17. Mandel, P., Etrich, C., and Otsuka, K. (1993) Laser with phase sensitive interactions. *IEEE J. Quantum Electron.*, **29** (3), 836–843.
18. Lugiato, L., Wang, K., and Sun, Y. (1994) Phase-dependent laser equations. *Opt. Commun.*, **105**, 397–410.
19. Loh, W.H., Ozeki, Y., and Tang, C.L. (1990) High-frequency polarization self-modulation and chaotic phenomena in external cavity semiconductor lasers. *Appl. Phys. Lett.*, **56** (26), 2613–2615.
20. Brunel, M., Vallet, M., Ropars, G., Le Floch, A., Bretenaker, F., Joulié, G., and Keromnes, J.C. (1997) Modal analysis of polarization self-modulated lasers. *Phys. Rev. A*, **55** (2), 1391–1397.
21. Vallet, M., Brunel, M., Bretenaker, F., Alouini, M., Le Floch, A., and Agrawal, G.P. (1999) Polarization self-modulated lasers with circular eigenstates. *Appl. Phys. Lett.*, **74** (22), 3266–3268.
22. Jiang, S., Pan, Z., Dagenais, M., Morgan, R.A., and Kojima, K. (1993) High-frequency polarization self-modulation in vertical-cavity surface-emitting lasers. *Appl. Phys. Lett.*, **63** (26), 3545–3547.
23. Badr, N., White, I., Tan, M., Houng, Y., and Wang, S. (1994) Enhanced polarisation self-switching in a vertical-cavity surface-emitting laser by gain saturation of transverse modes. *Electron. Lett.*, **30**, 1227–1229.
24. Robert, F., Besnard, P., Chares, M.L., and Stephan, G. (1997) Polarization modulation dynamics of vertical-cavity surface-emitting lasers with an extended cavity. *IEEE J. Quantum Electron.*, **33** (12), 2231–2239.
25. Ropars, G., Langot, P., Brunel, M., Vallet, M., Bretenaker, F., Le Floch, A., and Choquette, K.D. (1997) Experimental evidence of single round-trip oscillation

in polarization self-modulated vertical-cavity surface emitting lasers. *Appl. Phys. Lett.*, **70** (20), 2661–2663.

26. Tang, C.L. (1998) Laser polarization self-modulation effects. *J. Opt. B: Quantum Semiclassical Opt.*, **10** (1), R51.
27. Lai, N.D., Brunel, M., Bretenaker, F. (2003) Green two-frequency pulsed laser: intracavity doubling of helicoidal eigenstates. *J. Opt. Soc. Am. B*, **20** (4), 662–669.
28. Sargent, M., Scully, M., and Lamb, W. (1974) *Laser Physics*, Addison-Wesley.
29. Vallet, M., Brunel, M., Ropars, G., Le Floch, A., and Bretenaker, F. (1997) Theoretical and experimental study of eigenstate locking in polarization self-modulated lasers. *Phys. Rev. A*, **56**, 5121–5130.
30. Javaloyes, J., Mulet, J., and Balle, S. (2006) Passive mode locking of lasers by crossed-polarization gain modulation. *Phys. Rev. Lett.*, **97**, 163 902.
31. Gavrielides, A., Erneux, T., Sukow, D.W., Burner, G., McLachlan, T., Miller, J., and Amonette, J. (2006) Square-wave self-modulation in diode lasers with polarization-rotated optical feedback. *Opt. Lett.*, **31** (13), 2006–2008.
32. Otsuka, K. and Iwasaki, H. (1976) Stabilization of oscillating modes in a $\mathrm{LiNdP_4O_{12}}$ laser. *IEEE J. Quantum Electron.*, **12** (4), 214–217.
33. Kimura, T., Otsuka, K., and Saruwatari, M. (1971) Spatial hole-burning effects in a Nd:YAG laser. *IEEE J. Sel. Top. Quantum Electron.*, **7** (6), 225–230.
34. Otsuka, K., Georgiou, M., and Mandel, P. (1992) Intensity fluctuations in multimode lasers with spatial hole burning. *Jpn. J. Appl. Phys.*, **31** (9), 1250–1252.
35. Kärtner, F.X., Braun, B., and Keller, U. (1995) Continuous-wave mode-locked solid-state lasers with enhanced spatial hole burning. *Appl. Phys. B*, **61** (6), 569–579.
36. Flood, C.J., Walker, D.R., and van Driel, H.M. (1995) Effect of spatial hole burning in a mode-locked diode end-pumped Nd:YAG laser. *Opt. Lett.*, **20** (1), 58–60.
37. Keller, U., Weingarten, K.J., Kärtner, F.X., Kopf, D., Braun, B., Jung, I.D., Fluck, R., Hönninger, C., Matuschek, N., and Aus der Au, J. (1996) Semiconductor saturable absorber mirrors (SESAM's) for femtosecond to nanosecond pulse generation in solid-state lasers. *IEEE J. Sel. Top. Quantum Electron.*, **2** (3), 435–452.
38. Thévenin, J., Vallet, M., and Brunel, M. (2012) Dual-polarization mode-locked Nd:YAG laser. *Opt. Lett.*, **37** (14), 2859–2861.
39. Thévenin, J. (2012) Accrochages de fréquences dans les lasers vectoriels à état solide : étude du verrouillage de modes passif et de la réinjection décalée en fréquence. PhD thesis. University of Rennes, France.
40. Evtuhov, V. and Siegman, A.E. (1965) A "twisted-mode" technique for obtaining axially uniform energy density in a laser cavity. *Appl. Opt.*, **4** (1), 142–143.
41. Kastler, A. (1970) Champ lumineux stationnaire à structure hélicoïdale dans une cavité laser. *C.R. Acad. Sci. Paris B*, **271** (7), 999.
42. Le Floch, A. and Stephan, G. (1973) La condition de résonance dans les lasers anisotropes contenant des lames biréfringentes. *C.R. Acad. Sci. Paris B*, **277**, 265.
43. Otsuka, K. and Kawaguchi, H. (1984) Period-doubling bifurcation in detuned lasers with injected signals. *Phys. Rev. A*, **29**, 2953–2956.
44. Otsuka, K. (1994) Ultrahigh sensitivity laser doppler velocimetry with a microchip solid-state laser. *Appl. Opt.*, **33** (4), 1111–1114.
45. Lacot, E., Day, R., and Stoeckel, F. (2001) Coherent laser detection by frequency-shifted optical feedback. *Phys. Rev. A*, **64** (4), 043 815.
46. Nerin, P., Puget, P., Besesty, P., and Chartier, G. (1997) Self-mixing using a dual-polarisation Nd:YAG microchip laser. *Electron. Lett.*, **33**, 491–492.
47. Kervevan, L., Gilles, H., Girard, S., Laroche, M., and Leprince, P. (2007) Self-mixing laser doppler velocimetry with a dual polarization Yb:Er glass laser. *Appl. Phys. B*, **86**, 169–176.
48. Kowalski, F.V., Hale, P.D., and Shattil, S.J. (1988) Broadband continuous-wave laser. *Opt. Lett.*, **13**, 622–624.
49. Guillet de Chatellus, H. and Pique, J.P. (2010) Statistical properties of frequency

shifted feedback lasers. *Opt. Commun.*, **283**, 71–77.

50. Saber, H. and Brinkmeyer, E. (1994) Pulse generation in fiber lasers with frequency shifted feedback. *J. Lightwave Technol.*, **12**, 1360–1368.
51. Kervevan, L., Gilles, H., Girard, S., and Laroche, M. (2007) jitter suppression in a dual-frequency laser using optical feedback. *Opt. Lett.*, **32**, 1099–1101.
52. Brunel, M. and Vallet, M. (2008) Pulse-to-pulse coherent beat note generated by a passively Q-switched two-frequency laser. *Opt. Lett.*, **33** (21), 2524.
53. Thévenin, J., Vallet, M., Brunel, M., Gilles, H., and Girard, S. (2011) Beat-note locking in dual-polarization lasers submitted to frequency-shifted optical feedback. *J. Opt. Soc. Am. B*, **28** (5), 1104–1110.
54. Otsuka, K., Mandel, P., Bielawski, S., Derozier, D., and Glorieux, P. (1992) Alternate time scale in multimode lasers. *Phys. Rev. A*, **46**, 1692–1695.
55. Szwaj, C., Lacot, E., and Hugon, O. (2004) Large linewidth-enhancement factor in a microchip laser. *Phys. Rev. A*, **70**, 033 809–.
56. Fordell, T., Valling, S., and Lindberg, A.A.M. (2005) Modulation and the linewidth enhancement factor of a Nd:YVO$_4$ diode-pumped laser. *Opt. Lett.*, **30** (22), 3036–3038.
57. Siegman, A.E. (1986) *Lasers*, University Science Books.
58. Thévenin, J., Romanelli, M., Vallet, M., Brunel, M., and Erneux, T. (2012) Phase and intensity dynamics of a two-frequency laser submitted to resonant frequency-shifted feedback. *Phys. Rev. A*, **86** (3), 033 815.
59. Morvan, L., Lai, L.D., Dolfi, D., Huignard, J.P., Brunel, M., Bretenaker, F., and Le Floch, A. (2002) Building blocks for a two frequency laser lidar-radar: a preliminary study. *Appl. Opt.*, **41** (27), 5702–5712.
60. Pillet, G., Morvan, L., Dolfi, D., and Huignard, J.P. (2008) Wideband dual-frequency lidar–radar for high resolution ranging, profilometry and doppler measurement. *Proc. SPIE*, **7114**, 71140E.
61. Chakraborty, T. and Rand, R.H. (1988) The transition from phase locking to drift in a system of two weakly coupled van der pol oscillators. *Int. J. Nonlinear Mech.*, **5**/**6**, 369–376.
62. Braza, P.A. and Erneux, T. (1990) Constant phase, phase drift, and phase entrainment in lasers with an injected signal. *Phys. Rev. A*, **41** (11), 6470–6479.
63. Stephen Yeung, M.K. and Strogatz, S.H. (1998) Nonlinear dynamics of a solid-state laser with injection. *Phys. Rev. E*, **58**, 4421–4435.
64. Thévenin, J., Romanelli, M., Vallet, M., Brunel, M., and Erneux, T. (2011) Resonance assisted synchronization of coupled oscillators: frequency locking without phase locking. *Phys. Rev. Lett.*, **107** (10), 104101.
65. Kelleher, B., Goulding, D., Baselga Pascual, B., Hegarty, S.P., and Huyet, G. (2012) Bounded phase phenomena in the optically injected laser. *Phys. Rev. E*, **85**, 046 212.
66. Romanelli, M., Wang, L., Brunel, M., and Vallet, M. (2014) Measuring the universal synchronization properties of driven oscillators across a Hopf instability. *Opt. Express*, **22** (7), 7364–7373.
67. Kelleher, B., Goulding, D., Baselga Pascual, B., Hegarty, S.P., and Huyet, G. (2010) Phasor plots in optical injection experiments. *Eur. Phys. J. D*, **58** (2), 175–179.
68. Wieczorek, S., Krauskopf, B., Simpson, T., and Lenstra, D. (2005) The dynamical complexity of optically injected semiconductor lasers. *Phys. Rep.*, **416**, 1–128.
69. Rubiola, E. (2008) *Phase Noise and Frequency Stability in Oscillators*, Cambridge University Press.
70. Pikovsky, A., Rosenblum, M., and Kurths, J. (2003) *Synchronization: A Universal Concept in Nonlinear Sciences*, Cambridge University Press.
71. De, S., Potapchuk, V., and Bretenaker, F. (2014) Influence of spin-dependent carrier dynamics on the properties of a dual-frequency vertical-external-cavity surface-emitting laser. *Phys. Rev. A*, **90**, 013 841.
72. Cundiff, S.T., Collings, B., and Knox, W.H. (1997) Polarization locking in an

isotropic, modelocked soliton Er/Yb fiber laser. *Opt. Express*, **1**, 12.

73. Collings, B., Cundiff, S.T., Akhmediev, N.N., Soto-Crespo, J.M., Bergman, K., and Knox, W.H. (2000) Polarization-locked temporal vector solitons in a fiber laser: experiment. *J. Opt. Soc. Am. B*, **17**, 354.
74. Wang, L., Romanelli, M., Van Dijk, F., and Vallet, M. (2014) Photonic microwave oscillator based on monolithic DFB lasers with frequency-shifted feedback. *Electron. Lett.*, **50** (6), 451.
75. Lee, C.H. (2013) *Microwave Photonics*, CRC—Taylor & Francis.
76. Li, L. and Jupiner, M. (2013) Phase trapping and slipping in a forced hydrodynamically self-excited jet. *J. Fluid Mech.*, **735**, R5.
77. Barois, T., Perisanu, S., Vincent, P., Purcell, S., and Ayari, A. (2014) Frequency modulated self-oscillation and phase inertia in a synchronized nanowire mechanical resonator. *New J. Phys.*, **16**, 083 009.

14
Vector Patterns and Dynamics in Fiber Laser Cavities

Stefan Wabnitz, Caroline Lecaplain, and Philippe Grelu

14.1
Introduction

14.1.1
Pulsed Vector Dynamics with a Saturable Absorber

Fiber lasers not only represent an important class of sources of ultrashort optical pulses and coherent frequency combs for a host of applications, but also provide an ideal platform for exploring complex nonlinear temporal dynamics. Short-pulse generation is typically activated by the presence of a fast saturable absorber element inside the fiber cavity. Stable stationary pulse emission then results from a composite balance involving dissipative and dispersive effects, which is well described by the concept of a dissipative soliton [1, 2]. When the saturable absorber effect results from the use of the nonlinear polarization evolution (NPE) mechanism—see, for instance, the chapter by Sanchez *et al.* [3]—the presence of an intracavity polarizer makes the overall cavity dynamics akin to scalar dynamics. As a matter of fact, scalar propagation mode ls are widely used to model the dynamics of pulsed lasers, mode locked through NPE. However, most saturable absorbers do not require the use of an intracavity polarizer. When the whole cavity is free from significant loss anisotropy, the pulsed dynamics recovers the polarization degree of freedom. Hence, various polarization synchronization schemes can take place, such as dual-polarization mode-locking and phase-locking, as introduced in the chapter of Brunel *et al.* [4]. In fiber laser cavities, polarization-locked vector solitons have attracted significant attention, as convincing illustrations of a robust fundamental locking mechanism that takes place when using quasi-isotropic fibers, which are nevertheless affected by some unavoidable random birefringence [5, 6]. In the parameter space, polarization-locked vector solitons are surrounded by polarization-rotating vector solitons. The latter family comprises flipping and fast rotating vector solitons [5, 7, 8]. It also includes slowly rotating vector solitons, whose origin appears to involve a complex interplay between linear and nonlinear birefringence, and the polarization hole burning effect in the gain medium [6].

Nonlinear Optical Cavity Dynamics: From Microresonators to Fiber Lasers, First Edition.
Edited by Philippe Grelu.
© 2016 Wiley-VCH Verlag GmbH & Co. KGaA. Published 2016 by Wiley-VCH Verlag GmbH & Co. KGaA.

Even tightly bound states of mode-locked ultrashort pulses, namely dissipative soliton molecules [3], may exhibit complex polarization dynamics [9].

14.1.2
Vector Dynamics Without a Saturable Absorber

In spite of the fact that most of the short-pulse fiber laser dynamics are studied in the context of mode-locking, that is, with an intracavity saturable absorber, it is also interesting to investigate pulsed dynamics that can be obtained when the saturable absorption mechanism is reduced or even suppressed. For instance, considering the nonlinear transfer function obtained via NPE when it is followed by the discrimination of an intracavity polarizer, this transfer function can be continuously adjusted by simply rotating the waveplates preceding the polarizer. By reducing the amount of saturable absorption, the coexistence of multiple dissipative solitons and a quasi-continuous wave (CW) background is, in fact, possible. Furthermore, this peculiar situation is conducive to the generation of complex multiple pulse phenomena, such as the soliton rain [10]. In more general terms, the transition between soliton and turbulent pulse emission is controlled by the features of the nonlinear transfer function induced by the presence of the intracavity polarization analyzer. Also relevant to the transition to turbulence, we remind the existence of incoherent or chaotic pulses frequently observed in the vicinity of conventional mode-locking, which are called noise-like pulses [11–13].

When the fast saturable absorber element is removed, and the overall cavity polarization-dependent losses reach a relatively low level, nonlinear vector dynamics can be observed above some pumping power threshold. Quite surprisingly, the fiber laser may still exhibit pulsations at the cavity round-trip frequency, although the resulting mode-locking mechanism is now much weaker, and surrounded by significant noise [14]. As discussed in the literature, a recurrent feature of pulsations in vector fiber lasers is their antiphase dynamics, leading to temporal polarization switching between the two polarization modes of the cavity [14–19]. Although several physical interpretations of antiphase dynamics have been proposed, understanding the diversity of the temporal dynamics of fiber laser emission is challenging models developed to date. Roy *et al.* [14] developed a vector model based on the dynamics of gain competition in the laser, including the cavity boundary conditions. Such a model is helpful to interpret the buildup of polarization switching at the cavity round-trip frequency. Nevertheless, resorting to complex numerical simulations with several uncertain parameters may hamper the general classification of the universal dynamics that are observed in a variety of experimental setups.

Driven by the need for a simple and yet universal description of the polarization switching mechanism, the analogy between the observed polarization patterns and the polarization-domain-wall (PDW) solitary waves was suggested [17–19]. Temporal PDWs are localized nonlinear structures separating adjacent domains of different polarization in a dispersive Kerr medium. Originally predicted in 1994 [20, 21], PDWs were later experimentally observed in short lengths of nearly isotropic nonlinear optical fibers operating in the normal group-velocity dispersion (GVD) regime [22].

In the following sections of this chapter, we present an extensive analysis of the temporal polarization patterns that are observed in a vector fiber laser. We demonstrate that the universal approach based on a Ginzburg–Landau equation (GLE) extended to the coupling among two orthogonal polarization modes of the laser is able to qualitatively capture the main features of the experiments [23, 24]. In particular, we discuss the following remarkable fundamental feature: by means of nonlinear polarization coupling, it is possible to stabilize the otherwise irregular or even turbulent temporal emission of the laser that is observed when it operates in the scalar mode (i.e., with an intracavity polarizer). Thus, the fiber laser is an example of an extended physical system exhibiting the synchronization of chaotic nonlinear oscillators via their mutual coupling.

Chaos synchronization is a topic that has been extensively investigated for more than 20 years in several domains of physical sciences and engineering [25, 26]. By coupling independent chaotic oscillators, it is possible to control and stabilize their dynamics, which provides a powerful extension of the well-known synchronization of regular oscillators [27]. Chaos synchronization has numerous potential applications; consider, for example, secure communications [28, 29]. However, its experimental demonstrations have been mostly restrained to discrete oscillators, which can be described in terms of ordinary differential equations (ODEs). Spatiotemporal polarization effects in fiber lasers thus provide a significantly new and experimentally easily accessible avenue for the study of pattern formation in extended physical systems. Based on the coupled GLE approach, one may invoke thermodynamic analogies that permit to classify different stable and unstable regions in the parameter space, separated by phase transition curves [30–35].

As a matter of fact, besides being relevant to describe transverse and temporal pattern effects in lasers [1, 36, 37], the vector Ginzburg–Laudau model approach also applies to the dynamics of dissipative structure morphogenesis in a variety of nonequilibrium systems near a Hopf bifurcation. We may cite, for example, phase transitions [38, 39], superconductivity, superfluidity, Bose–Einstein condensation, field theory, Bénard convection [40], Taylor–Couette flow between rotating cylinders [41], plane Poiseuille flow [42], drift waves in plasmas, chemical reactions and turbulence [43, 44], ionization waves [45], liquid crystals [46], and biophysical systems [47].

14.2
Fiber Laser Models

In this section, we justify the use of the scalar and the vector cubic complex GLE equations as universal models for describing the temporal dynamics of fiber lasers that do not include a fast saturable absorber element. Throughout the chapter, we restrict our attention to the situations where a nonlinear cubic loss term appears in the GLE, both in the scalar and in the vector propagation regime of fiber lasers. This is in contrast with the master equations for laser mode-locking, which assume a nonlinear cubic gain term in GLE models.

We begin with the scalar complex GLE, which yields a simple qualitative modeling of optical wave turbulence in fiber lasers [48]. As we shall see, the unfolding classification of dynamics turns out to be particularly useful for the analysis of polarization effects in vector fiber lasers. Then, using a vector cubic GLE model, and exploring its equation parameters, we present numerical simulations showing the formation of a diversity of laminar states with antiphase dynamics between orthogonal polarization components.

When describing antiphase polarization dynamics in the average normal dispersion regime of the laser, it turns out that the steady-state polarization structures may be interpreted as resulting from a simpler, purely conservative balance between dispersion and nonlinearity. In other words, the stationary temporal polarization switching patterns, or PDWs, may be described by using the conservative limit of the vector GLE, namely the coupled nonlinear Schrödinger (NLS) equations [18, 23]. Such conservative model for polarization evolution and its predicted PDW dynamics are depicted at the end of the section.

14.2.1
The Scalar Cubic Ginzburg–Landau Equation

The scalar cubic GLE has been used in the early modeling of ultrashort-pulse generation in mode-locked lasers [49, 50]. In this case, the GLE featured a cubic nonlinear gain term to describe the action of the fast saturable absorber. It later turned out that, to prevent an energy blowup of the pulsed solutions, it was necessary to include a quintic nonlinear gain saturation term into the GLE [1, 51, 52].

Using the NPE mode-locking technique, the nonlinear transfer function of the cavity is adjusted by a mere rotation of the polarization controllers, and it is possible to change the sign of the effective cubic gain term. Doing so, the system becomes endowed with nonlinear loss, and unstable or chaotic light emission may result. Then, the laser dynamics may be analyzed, in principle, through a minimal universal complex cubic GLE [53]. In such a case, one may directly relate the free GLE parameters to a phase transition diagram among different regimes of either stable or chaotic light emission.

The corresponding cubic GLE is obtained by averaging pulse propagation over each cavity round-trip [54]:

$$\begin{aligned} t_r \partial_{t'} E = {} & \frac{(g_0 L - T^2)}{2} E + L\left(\beta_0 + i\frac{\beta_2}{2}\right)\partial^2_{\tau'} E \\ & - L\left(\frac{\sigma_0}{2} - i\gamma_0\right)|E|^2 E, \end{aligned} \tag{14.1}$$

where t' is a continuous (slow) temporal variable that stands for the round-trip number, τ' is a retarded time in the reference frame of the moving pulse, E is the complex field envelope ($|E|^2$ directly measures the optical power), t_r is the round-trip time for a cavity of length L, $g_0 > 0$ is the average distributed power gain at frequency ω_0 (which is supposed to coincide with a longitudinal mode of the cavity), and T is the amplitude transmission coefficient of the output coupler. The bandwidth-limited gain is represented by the parabolic approximation $G(\omega) = g_0(1 - (4/B^2)(\omega - \omega_0)^2)$, so that the spectral filtering term is $\beta_0 = 2g_0/B^2$. Moreover, β_2 is the average GVD, and $\gamma_0 = \omega_0 n_2/cA_{\text{eff}}$ is the nonlinearity coefficient of the fiber, where n_2 is the fiber nonlinear refractive index, and A_{eff} is the effective mode area of the single-mode fiber.

Note that the gain bandwidth limitation may result from the amplifier as well as from passive intracavity filters, such as the frequency-dependent transmissivity of the analyzer in the presence of fiber birefringence. As discussed earlier, the value and the sign of the nonlinear saturable gain coefficient σ_0 may be controlled by a proper orientation of the intracavity analyzer: henceforth, we take $\sigma_0 > 0$, leading to nonlinear gain saturation. It proves convenient to recast Eq. (14.1) using dimensionless units:

$$\partial_t U = U + (1 + i\beta)\partial_\tau^2 U - (1 - i\gamma)|U|^2 U, \tag{14.2}$$

where $t = \hat{g}t'/2t_r$, $\hat{g} = g_0 L - T^2$, $\tau = \tau'\sqrt{\hat{g}/2\beta_0 L}$, $U = \sqrt{\sigma_0 L/\hat{g}}E$, $\beta = -\beta_2/2\beta_0$, and $\gamma = 2\gamma_0/\sigma_0$.

The CW solution of Eq. (14.2) is $U_{\text{CW}}(t,\tau) = \sqrt{1 - \Omega^2}\exp\{i(Kt - \Omega\tau)\}$, where $K(\Omega) = \gamma - (\gamma + \beta)\Omega^2$. Stability of this CW solution results only if $\Omega^2 < [1 - \gamma\beta]/[2\gamma^2 - \gamma\beta + 3]$. Otherwise, a modulational instability (MI)—or Benjamin–Feir (BF) instability—develops. In particular, MI occurs even for arbitrarily slow temporal modulations whenever $\gamma\beta > 1$. The so-called BF line $\gamma\beta = 1$ is indicated by a dashed black line in Figure 14.1: all points above such line correspond to unstable CW solutions. Since Eq. (14.2) has only two free parameters, namely β (dispersion) and γ (self-phase modulation), we may represent in Figure 14.1 the global set of its domains of solutions. Transitions between

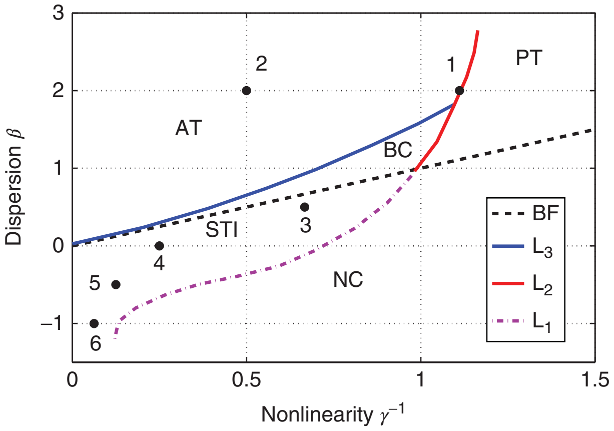

Figure 14.1 Phase diagram of stable or turbulent behavior of the scalar cubic GLE. See text for an explanation of the various acronyms.

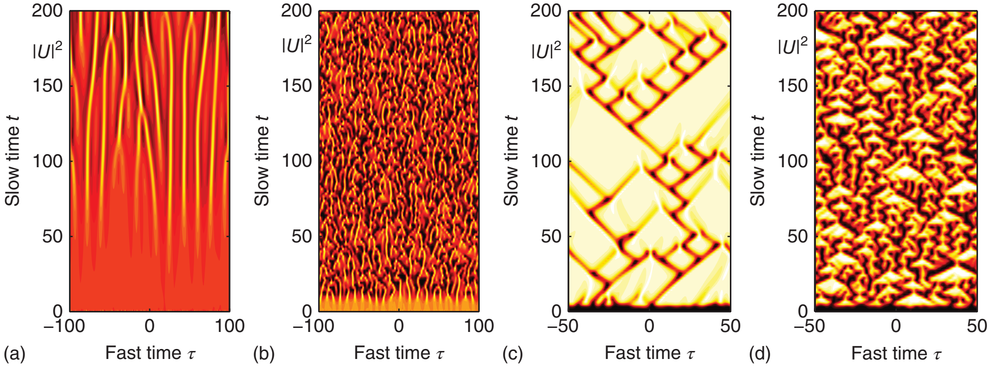

Figure 14.2 Evolution of the intensity $|U(t,\tau)|^2$: (a) $\beta = 2$, $\gamma = 0.9$ (PT regime, point 1 in Figure 14.1); (b) $\beta = 2$, $\gamma = 2$ (AT regime, point 2 in Figure 14.1); (c) STI regime with $\beta = 0.5$, $\gamma = 1.5$ (point 3 in Figure 14.1); (d) STI behavior at zero dispersion, $\beta = 0$, $\gamma = 4$ (point 4 in Figure 14.1).

domains of stable, intermittent, or chaotic emission states are represented by phase transition curves.

The dot-dashed magenta line L_1 in Figure 14.1 separates stable, nonchaotic (NC) CW emission from a domain of spatiotemporal intermittency (STI). Note that STI occurs in the modulationally stable regime. Points to the right of the solid red line L_2 and above the BF line correspond to the phase turbulence (PT) regime: here the irregular behavior is generated by chaotic phase slips, and the amplitude evolution is due to the phase dynamics. All points above the solid blue line L_3 in Figure 14.1 correspond to the amplitude turbulence (AT) regime. Finally, the narrow domain above the BF line and between the AT and PT lines is a regime of bi-chaos (BC) characterized by a mixing of the AT and PT properties.

Figure 14.2 illustrates the typical dynamics in the various domains of Figure 14.1. Figure 14.2a shows the evolution of the intensity $|U|^2$ in the PT regime for anomalous GVD: the field amplitude exhibits irregular oscillations about the unit value, but never drops down to zero. The strongly irregular behavior is in fact confined to the phase of the field. In sharp contrast, Figure 14.2b shows the chaotic amplitude evolutions that occur in the AT regime: we may observe random appearances of defects (dark points) separated by narrow bright stripes. Next, Figures 14.2c and d show two examples of intensity evolutions in the STI regime: symmetric diamond-shaped patches of CWs (bright laminar regions) are separated by propagating shocks and dark holes, which correspond to homoclinic trajectories generated at points of zero amplitude, where a phase slip occurs [55].

14.2.2
Vector Ginzburg–Landau Equations

Whenever the loss anisotropy of the whole laser cavity is low, it is necessary to consider a vector extension of the cubic GLE (14.2). For instance, starting from the NPE fiber laser configuration, this in principle would apply as soon as the intracavity polarizer is removed. But removing the polarizer erases the nonlinear transfer function that is associated with both NPE and polarization discrimination through the polarizer. However, we have to consider gain saturation and cross-gain saturation that take place in the rare-earth-doped fiber. Indeed, it is well known that cross-gain saturation favors the appearance of antiphase pulsations in fiber lasers [14, 56–61]. Cross-polarization gain modulation has even been predicted to enable passive mode-locking, in specific domains of parameters [62]. So, besides nonlinear gain saturation and bandpass filtering, a universal vector model should include cross-phase modulation as well as cross-gain saturation between the two orthogonally polarized laser modes. Our purpose here is to show that indeed such antiphase dynamics is observed when describing the dissipative dynamics of a vector fiber laser in terms of the coupled cubic Ginzburg–Landau, or vector Ginzburg–Landau equations (VGLE):

$$\begin{aligned}\partial_t U &= U + (1+i\beta)\partial_\tau^2 U - (1-i\gamma)|U|^2 U - (\eta - i\rho)|V|^2 U,\\ \partial_t V &= V + (1+i\beta)\partial_\tau^2 V - (1-i\gamma)|V|^2 V - (\eta - i\rho)|U|^2 V,\end{aligned} \tag{14.3}$$

where now $U(t,\tau)$ and $V(t,\tau)$ represent the two orthogonal polarization components of the field in the cavity. Here, η and ρ describe the action of nonlinear polarization cross-gain saturation and phase modulation, respectively. In this section, we consider the dynamics of solutions of the GLE (14.3) in the anomalous GVD regime (i.e., we set $\beta > 0$). In the next section, we study the laser polarization temporal dynamics in the normal dispersion regime. Note that we assume symmetric properties for the two polarizations, and do not include linear birefringence and temporal walk-off. Despite the apparent simplicity of this vector model, the presence of the two new cross parameters η and ρ considerably complexifies the numerical exploration of the dynamical domains, the latter being definitely more numerous than in the scalar case.

In the previous section concerning scalar wave propagation, the CW solution coexisted with a spatiotemporal chaotic attractor. In the vector case, STI is also observed in the numerical solution of the VGLE (14.3) for a relatively weak level of polarization cross-gain saturation (e.g., with $\eta = 0.1$, and $\rho = \eta\gamma$); see Figure 14.3a. Indeed, for $\eta \ll 1$, the CW solution of Eq. (14.3) of the form

$$U(t,\tau) = U_0 e^{iK_U t}; \quad V(t,\tau) = V_0 e^{iK_V t}, \tag{14.4}$$

where $K_U = \gamma U_0^2 + \rho V_0^2$, $K_V = \gamma V_0^2 + \rho U_0^2$, and $U_0^2 = V_0^2 = 1/(1+\eta)$ is stable whenever the BF condition $1 - \gamma\beta > 0$ is verified, *whereas the uncoupled solutions with* $U_0 = 0$ *or* $V_0 = 0$ *are unstable.* Figure 14.3a shows that, for low cross-gain saturation, the two polarization components obey fully independent STI dynamics.

On the other hand, the presence of sufficiently strong cross-gain saturation permits to substantially change the behavior of STI [31–34]. Indeed, Figure 14.3b shows that the polarization dynamics of the U and V components display an anticorrelation or antiphase behavior. The dark hole-like traveling structures in one polarization component are exactly superimposed with bright pulse-like

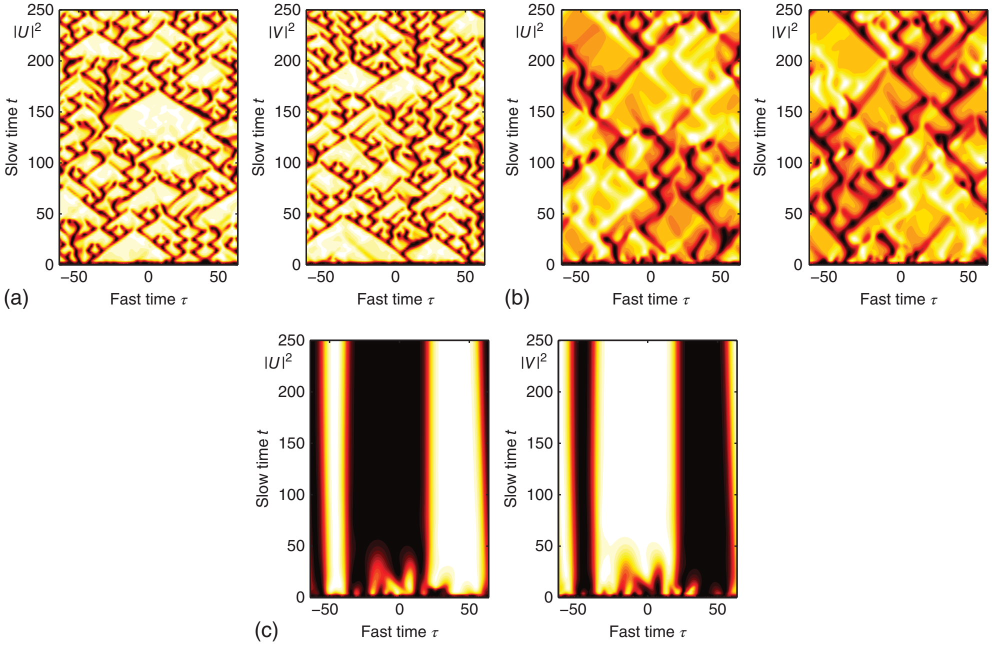

Figure 14.3 Evolution of the two polarization intensities for different values of the cross-gain saturation coefficient η: (a) $\eta = 0.1$; (b) $\eta = 0.6$; and (c) $\eta = 1.05$. Other parameters are $\gamma = 2$, $\beta = 0.2$, and $\rho = \gamma\eta$.

laminar structures in the orthogonal polarization. The antisymmetric-coupled STI regime eventually leads to the synchronization of spatiotemporal chaos. As the polarization cross-gain saturation coefficient η grows up to approach unity, the anticorrelated STI regime develops a metastable behavior leading to the decay into the stable CW solution with $U_0^2 = V_0^2 = 1/(1 + \eta)$.

Most strikingly, whenever $\eta > 1$ a single stable polarization component emerges, namely one has either $U_0 = 1, V_0 = 0$ or $U_0 = 0, V_0 = 1$ in Eq. (14.4). Indeed, numerical simulations of Eq. (14.3) show that, depending on the initial noise seed and after an initial transient, only one of the two orthogonal polarization states eventually survives. However, as soon as $\eta > 1.01$ (e.g., consider the case $\eta = 1.05$ shown in Figure 14.3c), light in the cavity switches in time among the two orthogonal polarizations. The resulting alternating temporal domains of orthogonal polarizations, separated by relatively fast domain-wall-like transitions, are also known in the theory of the VGLE as stable pairs of sources/sources that are separated by a shock [32, 35].

Let us move next into the BF unstable regime of Eq. (14.3). In this domain, as shown by Figure 14.4, it is possible to observe the generation of uniform and spatiotemporally stable lattices of anticorrelated (or antiphase) temporal solitons. The individual pulses in each polarization component are well matched by the exact

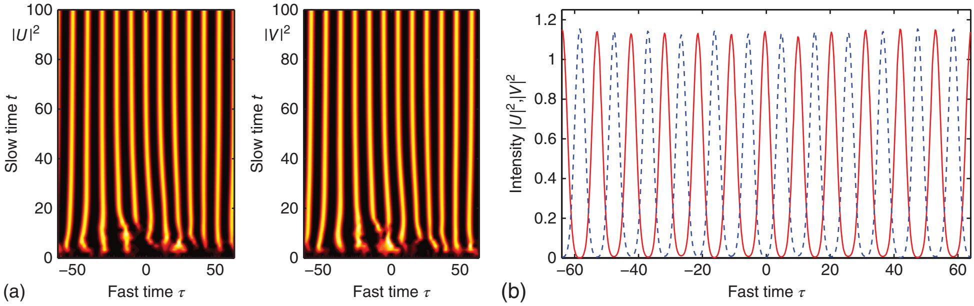

Figure 14.4 (a) Evolution of the two polarization intensities with $\gamma = 0.6$, $\beta = 3$, $\rho = -3$, and $\eta = 0.95$. (b) Intensity profiles of the two polarization components at $t = 100$.

soliton-like solution of the scalar complex cubic GLE [63]:

$$\begin{aligned} U(t,\tau) &= U_0 \mathrm{sech}(K\tau)\exp[i\theta(\tau) - i\Omega t], \\ \theta_t &= -Q\tanh(K\tau), \end{aligned} \tag{14.5}$$

which is also known as the Pereira–Stenflo solitary wave.

14.2.3
Vector Nonlinear Schrödinger Equation

In the previous section, we have seen that the dissipative nonlinear cross-gain saturation mechanism described by the VGLEs (14.3) leads to the regularization of the STI chaotic dynamics through the emergence of temporal domains of uniform polarization. The latter are connected by relatively sharp polarization switching events called *domain walls*.

Quite remarkably, polarization domains separated by domain walls can also be generated via the purely conservative interplay between self- and cross-polarization modulation, and chromatic dispersion. Although a fiber ring laser generally constitutes a strongly dissipative system, we may surmise that, in the quasi-CW regime of operation, the saturated linear gain and loss exactly balance each other at all times. In these conditions, we may wonder whether the slow temporal evolution (when compared with the cavity round-trip time) would not occur as determined by the sole balance of conservative effects. This is the objective of the present subsection, which demonstrates a fundamental process for the spontaneous emergence of polarization domains and domain walls through a relatively simple conservative nonlinear coupling model. It will be shown in the next section that this conservative process qualitatively captures the experimental observations when performed in the normal dispersion regime of the laser cavity, but fails to describe the diversity of reported polarization dynamics and instabilities, especially those observed within the anomalous dispersion regime.

If we assume intracavity pulse powers at the Watt level, then nonlinear effects will occur over a length scale L_{nl} that is in the range of $10^2 - 10^3$ meters, which is much longer than the typical fiber birefringence beat length L_b, the latter being in the range of 1–10 m. Hence, the nonlinear energy transfer between the two principal axes of the fiber can be neglected [64], as well as random polarization mode dispersion effects. As a result, conservative propagation is described by the incoherently coupled vector NLS equations (VNLSEs):

$$\begin{aligned} &i\partial_t U + \beta\partial_\tau^2 U + \gamma\left(|U|^2 + \frac{2}{3}|V|^2\right)U = 0,\\ &i\partial_t V + \beta\partial_\tau^2 V + \gamma\left(|V|^2 + \frac{2}{3}|U|^2\right)V = 0. \end{aligned} \tag{14.6}$$

where $\beta = -\beta_2/2$. The balance between nonlinearity and dispersion, which leads to polarization-domain-wall solitons, may be expressed in terms of the exact steady-state solutions of Eq. (14.6) [20, 21]. Writing the solutions of the VNLSEs (14.6) in the form of $(U, V)(t,\tau) = (u, v)(\tau)\sqrt{k_u/\gamma}\,\exp\,[ik_{u,v}t]$, one readily obtains the following coupled, second-order ODEs:

$$\begin{aligned} &\ddot{u} = -2u + 2u^3 + \frac{4}{3}uv^2,\\ &\ddot{v} = -2\sigma v + 2v^3 + \frac{4}{3}vu^2, \end{aligned} \tag{14.7}$$

with $T = \tau\sqrt{-k_u/2\beta}$, where we have assumed a normal GVD regime ($\beta < 0$), the overdots indicate T-derivatives, and $\sigma \equiv k_v/k_u$. Equation (14.7) describes the motion of a particle in the two-dimensional potential well $V(u, v) = u^2 + \sigma v^2 - u^4/2 - v^4/2 - 2u^2v^2/3$. Figure 14.5a shows that V has a local minimum at the origin $(u_m, v_m) = (0, 0)$. Moreover, whenever $\sigma > \sigma_{\text{bif}} = 2/3$, the two potential maxima located at $u = \pm 1$ and $v = 0$ bifurcate into four equal peaks in each quadrant, as shown in Figure 14.5b. Equation (14.7) has special separatrix solutions connecting different maxima of the potential V. Correspondingly, vector dark solitons are obtained for separatrices connecting maxima in opposite quadrants, whereas PDWs connect maxima situated in adjacent quadrants [20, 21]. The temporal polarization switching associated with the PDW is illustrated in Figure 14.5c: the field amplitudes $u(T)$ and $v(T)$ evolve according to the

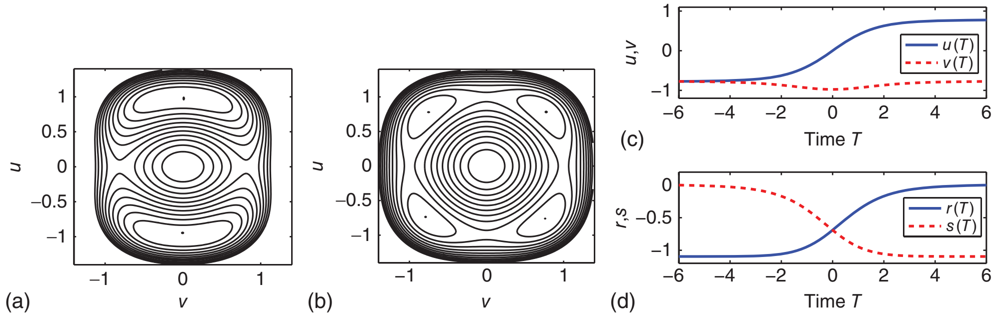

Figure 14.5 Left: contour plots of the potential function $V(u, v)$ in a linearly birefringent fiber: black dots indicate its maxima. Case with (a) $\sigma = 2/3$; and (b) $\sigma = 1$. Right: fast temporal evolution profile of the (c) (u, v) or (d) (r, s) components of a polarization domain wall.

separatrix emanating from, for example, the maximum of V in the bottom left (or third) quadrant of Figure 14.5b, and reaching the maximum of V in the upper left (or second) quadrant. The u component switches from negative to positive values, while the v component only exhibits a small hump in correspondence to the transition of the u envelope.

In Figure 14.5d, we also show the evolution of the polarization components of the field in a reference frame rotated by 45° with respect to the fiber principal axes, namely $r(T) = (u(T) + v(T))/\sqrt{2}$ and $s(T) = (u(T) - v(T))/\sqrt{2}$. In this frame, the PDW represents a full switching between orthogonal states of polarization, including between counter-rotating circular polarizations, since Eq. (14.7) is invariant upon an arbitrary constant phase shift among the u and v components.

14.2.4
Numerical Simulations

We qualitatively compared the spontaneous generation of PDWs predicted by the simple model of Eq. (14.6) with the results of detailed numerical simulations that used a comprehensive fiber laser model [23]. The interest of the latter is to reveal the build-up of polarization structures in the fiber laser, starting from the unpolarized amplified spontaneous emission (ASE) noise, after the field is recirculated through the various components (Er-doped fiber amplifier (EDFA), isolators, fibers, and couplers) constituting the actual experimental setup discussed in the following section.

Figure 14.6 compares the initial field features, after the first pass through the EDFA, with those after 1900 cavity round-trips. The initial spectrum follows the typical ASE distribution, and is associated with a random state of polarization (SOP). For the latter, the third Stokes parameter is plotted. It is defined as $S_3 = (I_R - I_L)/(I_R + I_L)$, so as to measure the relative intensity difference between right and left circular polarizations. After 1900 circulations in the cavity, a relatively narrow laser spectrum has shaped up, and the SOP illustrates the spontaneously generated PDWs. Indeed, the intracavity SOP spontaneously organizes in a train of randomly spaced PDWs, which represent a temporal switching of a few picoseconds duration between the two orthogonal circular polarizations. In this simulation example, the corresponding total intracavity intensity exhibits irregular temporal fluctuations with a typical time scale of a few picoseconds and the average value of $P = 5$ W. Thus, the full numerical solutions are in qualitative agreement with the PDW transitions predicted in the frame of the simple conservative VNLSE model.

14.3
Experiments of Vector Dynamics

In this section, we corroborate the theoretical analysis of Section 14.2 with the results of fiber laser experiments. The experimental observations reveal

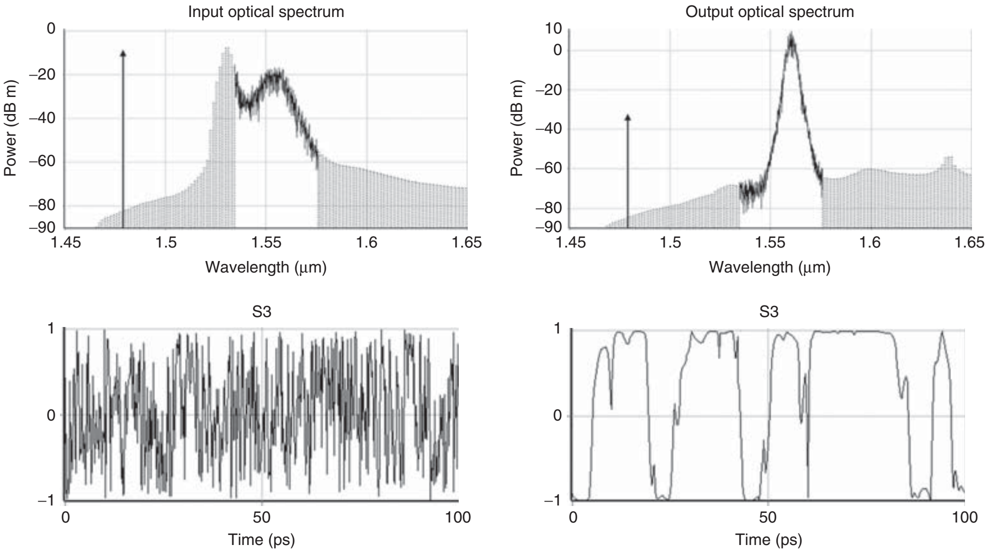

Figure 14.6 Numerically simulated optical spectrum and time evolution of the state of polarization (S_3 parameter) at the exit of the EDFA: (left column) at the first cavity round-trip; (right column) after $N = 1900$ circulations in the laser.

the emergence of either irregular or synchronized, antiphase polarization temporal structures in a vector fiber ring laser with no polarization-selective components. Let us emphasize the most striking features observed: the pulsations are fundamentally self-starting, and they are embedded into the cavity round-trip frequency. Clearly, the origin of the self-starting pulsations at the cavity repetition rate (or a multiple thereof) cannot be described by distributed models such as the VGLE (14.3) of the VNLSEs (14.6). We may thus conjecture that the development of periodic pulsations could be triggered by the Risken–Nummedal–Graham–Haken (RNGH) instability [65, 66]. At high pumping levels, which is always the case experimentally, Rabi splitting induces an additional gain for adjacent cavity modes, which start to oscillate and beat at the fundamental cavity frequency. The RNGH instability finds suitable conditions to develop in fiber lasers, due to the relatively long cavity lengths, which entail small intermode spacings and large gain and loss contributions per cavity round-trip.

A sketch of the fiber laser experimental setup is displayed in Figure 14.7. The laser is a ring cavity including a 3-m long EDFA, pumped by a 5-W Raman fiber laser source at 1.48 μm. Unidirectional laser emission is ensured by the presence of two polarization-insensitive optical isolators (ISO) enclosing the amplifier section. The cavity comprises an open-air section, where the polarization of the intracavity light field can be tuned by rotating quarter- and half-wave plates. Typical polarization-dependent losses are measured to be lower than 0.2 dB over a wavelength range of 10 nm, while the average birefringence is smaller than 4×10^{-6} [23].

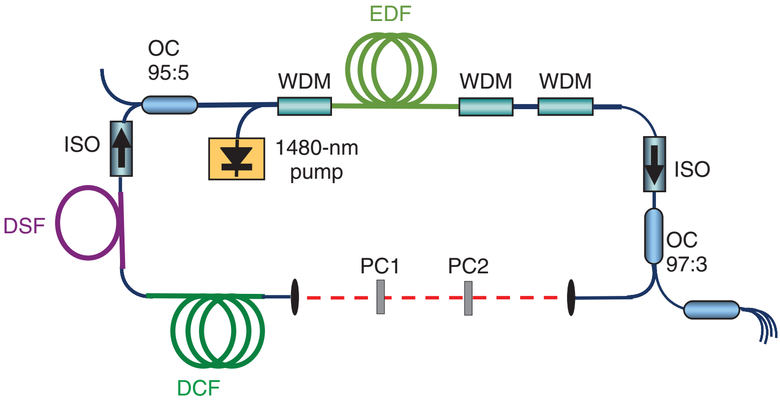

Figure 14.7 Fiber laser experimental setup. ISO, polarization-insensitive optical isolator; OC, output coupler; EDF, erbium-doped fiber; DSF, dispersion-shifted fiber; DCF, (optional) dispersion-compensating fiber; PC, quarter- and half-wave plates for polarization control; WDM, wavelength division multiplexer.

The net cavity dispersion results from the balance between the anomalous EDFA, SMF-28 pigtails, the 1.5 m-long dispersion-shifted fiber (DSF), and an additional length of a normally dispersive dispersion-compensating fiber (DCF). In the absence of the DCF, the average cavity GVD is $-0.013\,\mathrm{ps}^2$, and the fundamental cavity repetition rate is 23.9 MHz. Inserting a length of DCF, one may stepwise change the path-averaged dispersion and access the normal dispersion regime. The cavity output is examined by means of a polarization analyzer, sending simultaneously the two orthogonal polarization components to fast photodiodes, whose electrical signals are recorded without averaging by a 45-GHz, 120-GSa s^{-1} real-time oscilloscope. The two output polarizations are also monitored in the spectral domain by means of an optical spectrum analyzer with a resolution of 65 pm.

14.3.1
The Anomalous GVD: From Chaos to Antiphase Dissipative Dynamics

In the first place, the laser cavity of Figure 14.7 does not comprise the DCF length, so that it operates in the anomalous dispersion regime. The most accessible experimental degrees of freedom are the EDFA pump power, and the orientations of the two intracavity waveplates. By controlling these parameters, we observed phase transitions from polarization disorder to antiphase polarization domains, and vice versa. For instance, Figure 14.8 illustrates the successive transitions from polarization chaos to order, then back to chaos, which are observed upon a simple rotation of the intracavity half-wave plate, the pumping power being fixed at 2 W. More precisely, Figures 14.8a and d show initially independent chaotic temporal fluctuations in either polarization. For an orientation around $\theta = 284°$ of the

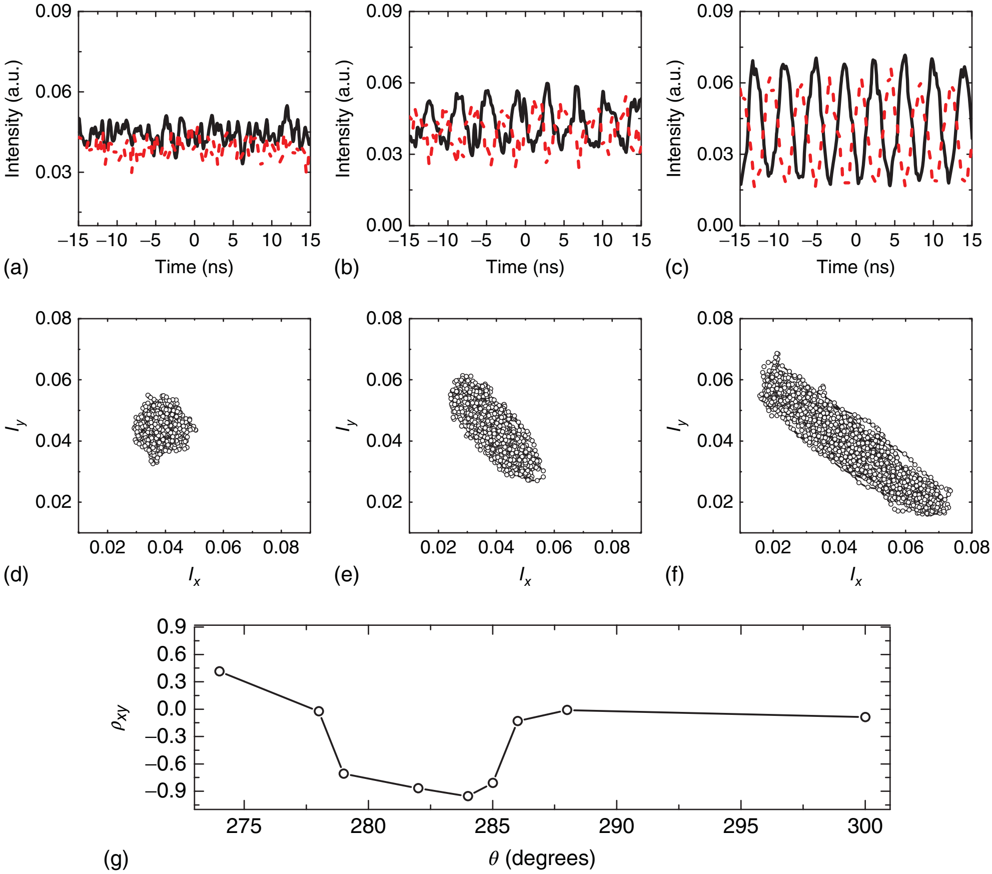

Figure 14.8 Transition from polarization disorder to antisynchronization, following the orientation θ of the intracavity half-wave plate. (a, b, c) temporal traces of the two orthogonal polarization states and (d, e, f) the corresponding scatter plots. (a, d) $\theta = 288°$, (b, e) $\theta = 285°$, (c, f) $\theta = 284°$, (g) Pearson correlation coefficient as function of θ.

half-wave plate, the temporal dynamics of the two laser polarizations becomes highly anticorrelated. Correspondingly, as displayed in Figures 14.8b and c, a train of antiphase pulses at the repetition rate of 260 MHz is observed. The degree of anticorrelation is measured by means of the Pearson correlation coefficient and plotted in Figure 14.8g. Analogous transitions are obtained by varying solely the pumping power in the EDFA, for specific orientations of the intracavity waveplates. This behavior is in good qualitative agreement with the predictions of the GLE model (14.3) (see Figure 14.4). These predictions indicate that, although the laser operates in the BF unstable regime, the nonlinear polarization coupling can impose the formation of highly stable trains of antiphase pulses. A long-term stability of the propagating structures, in the presence of a significant

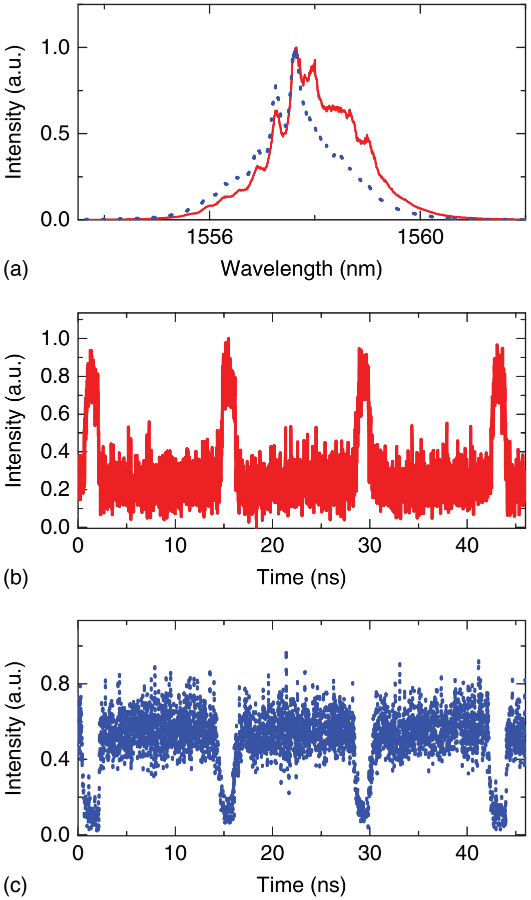

Figure 14.9 DW-like temporal dissipative structures within the anomalous-dispersion vector fiber laser: (a) optical spectra of the two orthogonal polarization states, and (b, c) their corresponding temporal traces. Dark PDW-like structures are indicated by blue-dotted temporal traces and spectra; bright PDW-like structures are indicated by red solid temporal traces and spectra.

amount of noise, is a typical signature of a strong attracting state in a dissipative system.

By exploring other dynamical domains through the tuning of the two-intracavity waveplates, which affect the nonlinear gain cross-saturation, we observe different transitions from polarization disorder to antiphase polarization domains and PDWs. As illustrated in Figure 14.9, polarization domains occur in the form of relatively long-lived polarization states separated by much narrower polarization switching walls, with a set of three polarization domains per round-trip in this example. The temporal duration of the narrow polarization-domain structures measured in Figures 14.9b and c is around 1.5 ns.

The optical spectra of both orthogonal polarization states, shown in Figure 14.9a, present a spectral asymmetry. This reveals a typical mechanism that sets in to compensate for a slight linear cavity birefringence affecting the two orthogonal polarization states. Indeed, the linear birefringence will induce a small group-velocity walk-off, which would break the locked vector temporal structures after a few cavity round-trips. However, there is a dynamical possibility to cancel this effect owing to the group-velocity chromatic dispersion. For that reason, the locked polarizations need to be centered at slightly different wavelengths. This mechanism is set forward and locked thanks to the nonlinear coupling of the two polarizations. It is beautiful to see that this mechanism solves, in this specific case, the problem of taking into account the linear cavity birefringence, which has not been included in our universal vector GLE model.

14.3.2
The Normal GVD: Polarization-Domain Walls

By inserting a suitable span of DCF in the vector fiber laser of Figure 14.7, we access the normal path-averaged chromatic dispersion, in order to compare the temporal polarization dynamics from both dispersion regimes. Once again, above a given pump power threshold (typically 1 W), coupled vector pulsations at the fundamental cavity repetition rate or at one of its harmonics are observed, with a shape essentially depending on the waveplate orientations. Whereas PDW-type structures are easily observed, periodic high-repetition rate trains of antiphase pulses akin to those of Figure 14.8 could not be retrieved. We believe that this results from the BF stability of the laser, with a hint from Figure 14.1, showing that the nonlinear dissipative term is able to secure the BF-stable domain of the normal dispersion regime, by expanding it into the lower part of the anomalous dispersion regime. However, the additional cross-polarization parameters at play in the vector dynamics are expected to affect this simple phase diagram picture.

As shown in Figure 14.10, the temporal duration of the polarization domains can be continuously adjusted by controlling the waveplate angle. The duration of the shortest PDW structure of Figures 14.10a and b is 8 ns. In the plots below, the PDW duration increases to 12 ns and 20 ns, while developing a squared overall shape, in Figures 14.10d, e and g, h, respectively. The corresponding optical spectra, for either polarization component, shown in Figures 14.10c, f, and i, exhibit only minor changes for the whole range of waveplate orientations (26–36°). The constant 0.5 nm shift between the major spectral peaks of the two polarization components results from the compensation of polarization mode dispersion, as was discussed in the previous section.

In the temporal domain, we note the presence of several spikes well above the average noise level, at the leading front of the bright pulses, independent of any artifact of the detection electronics. This feature suggests the presence of

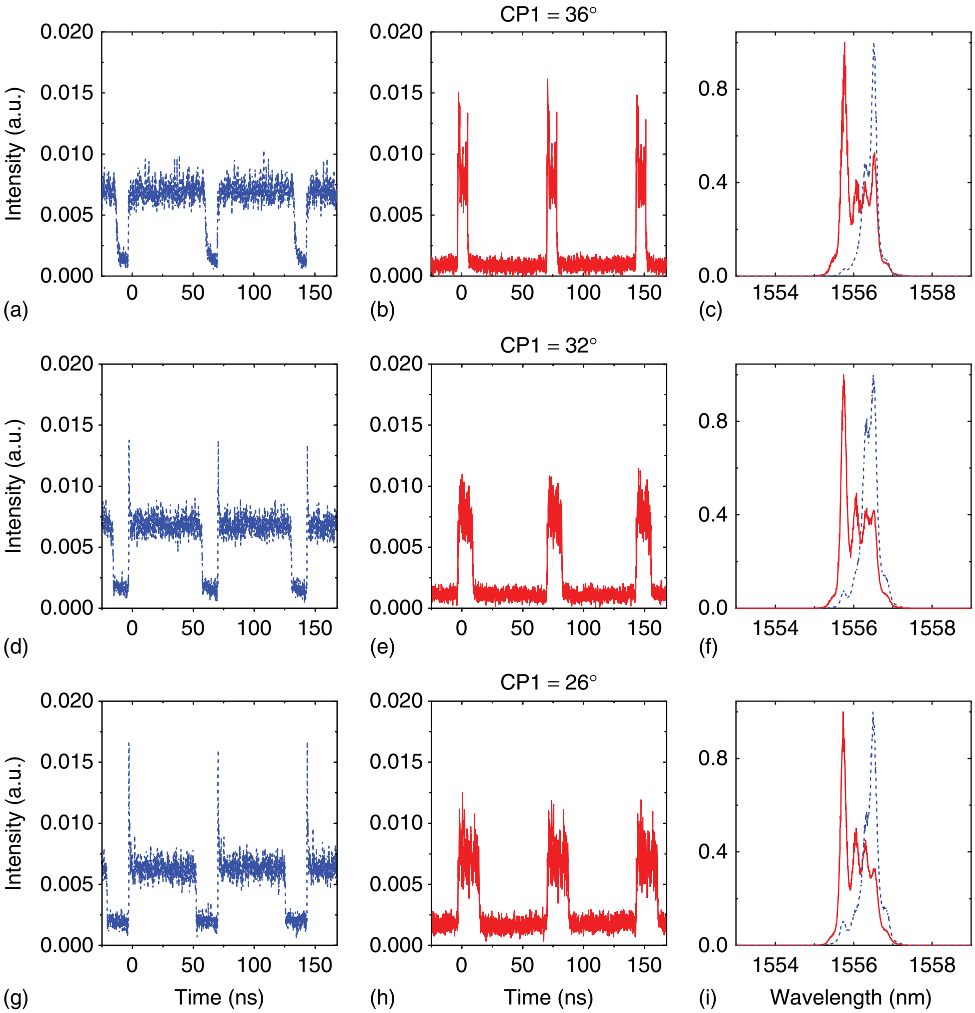

Figure 14.10 Influence of polarization control on the PDW-like structures: the temporal traces of the two orthogonal polarization states and their corresponding optical spectra are displayed for three different orientations (CP1 = 36°, 32°, and 26°) of the intracavity half-wave plate. Dark PDW-like structures are characterized by blue-dotted spectra, and bright PDW-like structures are characterized by red-line spectra.

a composite structure involving different time scales within each polarization domain, which is only partly resolved temporally. The noisy polarization switching that manifests at shorter times scales can be linked to the PDW transients discussed in Section 14.2.3, in the frame of the conservative VNLSE, triggered by the noise that superimposes to the upper and lower metastable CW states. On the other hand the long-term stability, over numerous cavity round-trip times, of the average PDW structures, involves the dissipative dynamics.

14.4
Summary

Despite the simplicity of the fiber laser setup, the vector dynamics that spontaneously shapes up, at sufficient pumping power, is quite involved, and definitely calls for additional investigations. Our present understanding can be summarized as follows. At first, an RNGH-type of instability converts the noisy, quasi-CW laser emission into nanosecond pulsations that repeat at the cavity fundamental frequency. These pulsations are subject to modulation or BF instabilities originating from the interplay of fiber nonlinearity, chromatic dispersion, and cross-gain saturation in the active fiber. The dominant resulting dynamics is characterized by the generation of antiphase polarization structures, separated by picosecond temporal polarization switching or domain walls.

The experimentally observed polarization dynamics may be qualitatively reproduced in terms of solutions of the complex cubic vector GLEs. Nonlinear polarization coupling can lead to the synchronization of spatiotemporal turbulence into ordered states of temporally alternating orthogonal polarization domains. Control of the intracavity polarization coupling may also favor the generation of stable antiphase soliton-like trains with high duty cycle, as well as coupled dark and bright soliton structures, which are obtained as the limit case of polarization domains with highly asymmetric durations.

We may conclude that vector fiber lasers do provide an easily accessible test bed for studying the complex dynamics of optical turbulence as well as its synchronization and control. Further developments may involve the analysis of interactions between solitons and a CW [67], the treatment of turbulence and instabilities in fiber Raman lasers [68], and conservative [69] or dissipative vector rogue wave generation [70]. From the application perspective, we envisage that the temporal polarization dynamics of vector fiber lasers may be exploited for chaos-based communication systems, where the decrypting of information is based on the synchronization of chaotic laser sources.

Acknowledgments

This research was funded by iXCore Foundation, the Italian Ministry of University and Research (MIUR, grant 2012BFNWZ2), and by the Agence Nationale de la Recherche (SOLICRISTAL project ANR-2010-BLANC-0417-01, and Labex ACTION program ANR-11-LABX-01-01).

References

1. Grelu, Ph. and Akhmediev, N. (2012) Dissipative solitons for mode-locked lasers. *Nat. Photonics*, **6**, 84.
2. Akhmediev, N. and Ankiewicz, A. (eds) (2005) *Dissipative Solitons*, Springer-Verlag.

3. Sanchez, F., Komarov, A., Grelu, Ph., Salhi, M., Komarov, K., and Leblond, H. (2015) Collective dissipative soliton dynamics in passively mode-locked fiber lasers, in *Nonlinear Optical Cavity Dynamics* (ed. Ph. Grelu), Wiley-VCH Verlag GmbH.
4. Brunel, M., Romanelli, M., and Vallet, M. (2015) Synchronization in vectorial solid-state lasers, in *Nonlinear Optical Cavity Dynamics* (ed. Ph. Grelu), Wiley-VCH Verlag GmbH.
5. Cundiff, S.T., Collings, B.C., Akhmediev, N.N., Soto-Crespo, J.M., Bergman, K., and Knox, W.H. (1999) Observation of polarization-locked vector solitons in an optical fiber. *Phys. Rev. Lett.*, **82**, 3988.
6. Sergeyev, S.V., Mou, C., Rozhin, A., and Turitsyn, S.K. (2012) Vector solitons with locked and precessing states of polarization. *Opt. Express*, **20**, 27434.
7. Zhao, L.M., Tang, D.Y., Wu, X., Zhang, H., and Tam, H.Y. (2009) Coexistence of polarization-locked and polarization-rotating vector solitons in a fiber laser with SESAM. *Opt. Lett.*, **34**, 3059.
8. Thévenin, J., Vallet, M., and Brunel, M. (2012) Dual-polarization mode-locked Nd:YAG laser. *Opt. Lett.*, **37**, 2859.
9. Tsatourian, V. et al. (2013) Polarization dynamics of vector soliton molecules in mode-locked fibre laser. *Sci. Rep.*, **3**, 3154.
10. Chouli, S. and Grelu, Ph. (2010) Soliton rains in a fiber laser: an experimental study. *Phys. Rev. A*, **81**, 063829.
11. Horowitz, M., Barad, Y., and Silberberg, Y. (1997) Noiselike pulses with a broadband spectrum generated from an erbium-doped fiber laser. *Opt. Lett.*, **22**, 799–801.
12. Runge, A.F., Aguergaray, C., Broderick, N.G.R., and Erkintalo, M. (2013) Coherence and shot-to-shot spectral fluctuations in noise-like ultrafast fiber lasers. *Opt. Lett.*, **38**, 4327–4330.
13. Lecaplain, C. and Grelu, Ph. (2014) Rogue waves among noise-like-pulse laser emission: an experimental investigation. *Phys. Rev. A*, **90**, 013805.
14. Williams, Q.L., Garcia-Ojalvo, J., and Roy, R. (1997) Fast intracavity polarization dynamics of an erbium-doped fiber ring laser: inclusion of stochastic effects. *Phys. Rev. A*, **55**, 2376.
15. Van Wiggeren, G.D. and Roy, R. (1999) High-speed fiber-optic polarization analyzer: measurements of the polarization dynamics of an erbium-doped fiber ring laser. *Opt. Commun.*, **164**, 107.
16. Abarbanel, H.D.I., Kennel, M.B., Buhl, M., and Lewis, C.T. (1999) Chaotic dynamics in erbium-doped fiber ring lasers. *Phys. Rev. A*, **60**, 2360.
17. Zhang, H., Tang, D.Y., Zhao, L.M., and Wu, X. (2009) Observation of polarization domain wall solitons in weakly birefringent cavity fiber lasers. *Phys. Rev. B*, **80**, 052302.
18. Zhang, H., Tang, D.Y., Zhao, L.M., and Knize, R.J. (2010) Vector dark domain wall solitons in a fiber ring laser. *Opt. Express*, **18**, 4428.
19. Wang, H.Y., Xu, W.C., Cao, W.J., Wang, L.Y., and Dong, J.L. (2012) Experimental observation of bright-dark pulse emitting in an all-fiber ring cavity laser. *Laser Phys.*, **22**, 282.
20. Haelterman, M. and Sheppard, A.P. (1994) Polarization domain walls in diffractive or dispersive Kerr media. *Opt. Lett.*, **19**, 96.
21. Haelterman, M. and Sheppard, A.P. (1994) Bifurcations of the dark soliton and polarization domain walls in nonlinear dispersive media. *Phys. Rev. E*, **49**, 4512.
22. Gutty, F., Pitois, S., Grelu, P., Millot, G., Thomson, M.D., and Dudley, J.M. (1999) Generation and characterization of 0.6-THz polarization domain-wall trains in an ultralow-birefringence spun fiber. *Opt. Lett.*, **20**, 1389.
23. Lecaplain, C., Grelu, Ph., and Wabnitz, S. (2013) Polarization-domain-wall complexes in fiber lasers. *J. Opt. Soc. Am. B*, **30**, 211.
24. Lecaplain, C., Grelu, Ph., and Wabnitz, S. (2014) Dynamics of the transition from polarization disorder to antiphase polarization domains in vector fiber lasers. *Phys. Rev. A*, **89**, 063812.
25. Pecora, L.M. and Carroll, T.L. (1990) Synchronization in chaotic systems. *Phys. Rev. Lett.*, **64**, 821–824.
26. Boccaletti, S., Kurths, J., Osipov, G., Valladares, D.L., and Zhou, C.S. (2002)

The synchronization of chaotic systems. *Phys. Rep.*, **366**, 1–101.

27. Wiesenfeld, K., Colet, P., and Strogatz, S.H. (1996) Synchronization transitions in a disordered Josephson series array. *Phys. Rev. Lett.*, **76**, 404–407.
28. Colet, P. and Roy, R. (1994) Digital communication with synchronized chaotic lasers. *Opt. Lett.*, **19**, 2056.
29. Garcia-Ojalvo, J. and Roy, R. (2001) Spatiotemporal communications with synchronized chaos. *Phys. Rev. Lett.*, **86**, 5204–5207.
30. Chaté, H. (1994) Spatiotemporal intermittency regimes of the one-dimensional complex Ginzburg–Landau equation. *Nonlinearity*, **7**, 185–204.
31. Sagaguchi, H. (1996) Traveling wave-standing wave transition in the coupled complex Ginzburg–Landau equation. *Phys. Scr.*, **T67**, 148.
32. Amengual, A., Hernández-Garcia, E., Montagne, R., and San Miguel, M. (1997) Synchronization of spatiotemporal chaos: the regime of coupled spatiotemporal intermittency. *Phys. Rev. Lett.*, **78**, 4379.
33. Montagne, R. and Hernández-Garcia, E. (2000) Localized structures in coupled Ginzburg–Landau equations. *Phys. Lett. A*, **273**, 239.
34. Hernández-Garcia, E., Hoyuelos, M., Colet, P., San Miguel, M., and Montagne, R. (1999) Spatiotemporal chaos, localized structures and synchronization in the vector complex Ginzburg–Landau equation. *Int. J. Bifurcation Chaos*, **09**, 2257.
35. van Hecke, M., Storm, C., and van Saarloos, W. (1999) Sources, sinks and wavenumber selection in coupled CGL equations and experimental implications for counter-propagating wave systems. *Physica D*, **134**, 1–47.
36. San Miguel, M. (1995) Phase instabilities in the laser vector complex Ginzburg–Landau equation. *Phys. Rev. Lett.*, **75**, 425–428.
37. Soto-Crespo, J.M., Akhmediev, N.N., Collings, B.C., Cundiff, S.T., Bergman, K., and Knox, W.H. (2000) Polarization-locked temporal solitons in a fiber laser: theory. *J. Opt. Soc. Am. B*, **17**, 366–372.
38. Haken, H. (1978) *Synergetics: An Introduction*, Springer-Verlag, Berlin.
39. Manneville, P. (1990) *Dissipative Structures and Weak Turbulence*, Academic Press, San Diego, CA.
40. Cross, M.O. and Hohenberg, P.C. (1993) Pattern formation outside of equilibrium. *Rev. Mod. Phys.*, **65**, 874.
41. Kogelman, S. and DiPrima, R.C. (1970) Stability of spatially periodic supercritical flows in hydrodynamics. *Phys. Fluids*, **13**, 1.
42. Stewartson, K. and Stuart, J.T. (1971) A nonlinear instability theory for a wave system in plane Poiseuille flow. *J. Fluid Mech.*, **48**, 529.
43. Kuramoto, Y. and Yamada, T. (1976) Turbulent state in chemical reactions. *Prog. Theor. Phys.*, **56**, 679.
44. Kuramoto, Y. and Tsuzuki, T. (1976) Persistent propagation of concentration waves in dissipative media far from thermal equilibrium. *Prog. Theor. Phys. Suppl.*, **55**, 356–369.
45. Bekki, N. (1981) Nonlinear modulation of ionization waves. *J. Phys. Soc. Jpn.*, **50**, 659.
46. Buka, A. and Kramer, L. (eds) (1996) *Pattern Formation in Liquid Crystals*, Springer-Verlag, New York.
47. Flyvbjerg, H., Hertz, J., Jensen, M.H., Mouritsen, O.G., and Sneppen, K. (eds) (1997) *Physics of Biological Systems*, Springer-Verlag, Heidelberg.
48. Wabnitz, S. (2014) Optical turbulence in fiber lasers. *Opt. Lett.*, **39**, 1362.
49. Martinez, E., Fork, R.L., and Gordon, J.P. (1985) Theory of passively mode-locked lasers for the case of a nonlinear complexpropagation coefficient. *J. Opt. Soc. Am. B*, **2**, 753.
50. Haus, H.A., Fujimoto, J.G., and Ippen, E.P. (1991) Structures for additive-pulse mode locking. *J. Opt. Soc. Am. B*, **8**, 2068.
51. Kodama, Y., Romagnoli, M., and Wabnitz, S. (1992) Soliton stability and interactions in fiber lasers. *Electron. Lett.*, **28**, 1981–1982.
52. Chernykh, A.I. and Turitsyn, S.K. (1995) Soliton and collapse regimes of pulse generation in passively mode-locking laser systems. *Opt. Lett.*, **20**, 398–400.

53. Shraiman, B.I., Pumir, A., van Saarloos, W., Hoenberg, P.C., Chaté, H., and Holen, M. (1992) Spatiotemporal chaos in the one-dimensional complex Ginzburg–Landau equation. *Physica D*, **57**, 241–248.
54. Haelterman, M., Trillo, S., and Wabnitz, S. (1992) Dissipative modulational instability in a nonlinear dispersive ring cavity. *Opt. Commun.*, **91**, 401–407.
55. van Hecke, M. (1998) Building block of spatiotemporal intermittency. *Phys. Rev. Lett.*, **80**, 1896.
56. Otsuka, K., Mandel, P., Bielawski, S., Derozier, D., and Glorieux, P. (1992) Alternate time scale in multimode lasers. *Phys. Rev. A*, **46**, 1692–1696.
57. Le Boudec, P., Jaouen, C., François, P.L., Bayon, J.-F., Sanchez, F., Besnard, P., and Stéphan, G. (1993) Antiphase dynamics and chaos in self-pulsing erbium-doped fiber lasers. *Opt. Lett.*, **18**, 1890–1892.
58. Poustie, A.J. (1995) Polarization cross saturation in an Er3+-doped fiber ring laser. *Opt. Lett.*, **20**, 1868–1870.
59. Sanchez, F. and Stephan, G. (1996) General analysis of instabilities in erbium-doped fiber lasers. *Phys. Rev. E*, **53**, 2110–2122.
60. Louvergneaux, E., Rogister, F., and Glorieux, P. (2007) Spatiotemporal antiphase dynamics in coupled extended optical media. *Phys. Rev. Lett.*, **99**, 263901.
61. Prati, F., Pessina, E.M., de Valcárcel, G.J., and Roldán, E. (2004) Spatiotemporal antiphase dynamics in coupled extended optical media. *Opt. Commun.*, **237**, 189–199.
62. Javaloyes, J., Mulet, J., and Balle, S. (2006) Passive mode locking of lasers by crossed-polarization gain modulation. *Phys. Rev. Lett.*, **97**, 163902.
63. Pereira, N.R. and Stenflo, L. (1977) Nonlinear Schrödinger equation including growth and damping. *Phys. Fluids*, **20**, 1733.
64. Crosignani, B., Piazzolla, S., Spano, P., and Di Porto, P. (1985) Direct measurement of the nonlinear phase shift between the orthogonally polarized states of a single-mode fiber. *Opt. Lett.*, **10**, 89.
65. Pessina, E.M., Bonfrate, G., Fontana, F., and Lugiato, L.A. (1997) Experimental observation of the Risken–Nummedal–Graham–Haken multimode laser instability. *Phys. Rev. A*, **56**, 4086–4093.
66. Voigt, T., Lenz, M.O., Mitschke, F., Roldán, E., and de Valcárcel, G.J. (2004) Experimental investigation of Risken–Nummedal–Graham–Haken laser instability in fiber ring lasers. *Appl. Phys. B*, **79**, 175–183.
67. Leblond, H., Niang, A., Amrani, F., Salhi, M., and Sanchez, F. (2013) Motion of solitons of the complex Ginzburg–Landau equation: the effect of an external frequency-shifted source. *Phys. Rev. A*, **88**, 033809.
68. Turitsyna, E.G., Smirnov, S.V., Sugavanam, S., Tarasov, N., Shu, X., Babin, S.A., Podivilov, E.V., Churkin, D.V., Falkovich, G., and Turitsyn, S.K. (2013) The laminar–turbulent transition in a fibre laser. *Nat. Photonics*, **7**, 783.
69. Baronio, F., Degasperis, A., Conforti, M., and Wabnitz, S. (2012) Solutions of the vector nonlinear Schrödinger equations: evidence for deterministic rogue waves. *Phys. Rev. Lett.*, **109**, 044102.
70. Lecaplain, C., Grelu, Ph., Soto-Crespo, J.M., and Akhmediev, N. (2012) Dissipative rogue waves generated by chaotic pulse bunching in a mode-locked laser. *Phys. Rev. Lett.*, **108**, 233901.

15
Cavity Polariton Solitons

Oleg A. Egorov and Falk Lederer

15.1
Introduction

The research on the physics of localized structures (solitons) in nonlinear systems covers many branches of physical sciences, including optics, fluid dynamics, particle physics, and biology [1–4]. Depending on the physical setting, localization can occur in one, two, or three dimensions. One of the qualitative principles, underpinning the formation of localized structures, is that the dispersion-induced broadening is compensated by the nonlinearity of an appropriate sign. In addition, if loss is present as in non-Hamiltonian systems, it has to be compensated by an external energy source [4]. Most generally, if dispersive spreading happens, as for quantum mechanical particles, with positive/negative effective mass, then an attractive/repulsive nonlinearity is required to compensate for the dispersion [3].

Currently, there is a growing body of research on collective nonlinear dynamics of half-light/half-matter quasi-particles (polaritons) being formed as a result of strong light–matter interaction. In the strong coupling regime, the photons are replaced by polaritons [5]. One prominent example of such polaritons are exciton-polaritons in semiconductor microresonators operating in the strong coupling regime [6–11]. In the past several years, extensive studies of polaritons in this environment have been largely motivated by the investigation of polaritonic Bose–Einstein condensation [12–14] and the transition to superfluidity [15, 16]. Depending on the semiconductor material used exciton-polaritons have been observed for temperatures reaching from a few kelvins [6] to room temperature [7, 17]. The latter can boost their potential for practical applications as, for instance, new sources of coherent light [18].

The existence of exciton-polaritons results in extraordinary optical properties of these microcavities [9–11]. On the one hand, Coulomb interactions among excitons evoke a strong and fast nonlinear response to an applied optical field [19, 20], which is by far stronger than the relevant photonic nonlinearity. For instance, optical bistability was observed for an input power two orders of magnitude less [21–23] than required in the weak-coupling regime [24–28]. On the other hand, the lower branch of the polariton dispersion relation, that is, the dependence of

Nonlinear Optical Cavity Dynamics: From Microresonators to Fiber Lasers, First Edition.
Edited by Philippe Grelu.
© 2016 Wiley-VCH Verlag GmbH & Co. KGaA. Published 2016 by Wiley-VCH Verlag GmbH & Co. KGaA.

the polariton frequency on the in-plane wave vector, has a peculiar nonparabolic shape with inflection points where the effective polariton mass changes its sign. In particular, low-threshold parametric four-wave mixing [29–37] can be achieved provided that the pump momentum exceeds a critical value and is incident at an angle beyond the “magic angle,” that is, beyond the inflection point.

Self-localization effects, that is, the formation of solitons, with exciton-polaritons attract growing attention within the past decade. Spontaneous formation of quantized vortices [38, 39] and the nucleation of dark solitons [40–44] have been observed as a natural ingredient and a by-product of the turbulent dynamics of the exciton-polariton condensate.

A direct research on the physics of formation and an effective control of polariton solitons has been undeveloped and remains an open issue. In an experimental paper [45], the authors claimed for the first time to our knowledge the observation of localized structures in a strongly coupled semiconductor microcavity driven by an external optical field. Further experimental investigations of coherently driven semiconductor microcavities [46–48] provided evidences of a suppressed dispersive spreading of polariton wave-packages moving on top of the homogeneous background. However, a rigorous theoretical proof of the existence of self-localized structures in polaritonic microresonators has been missing.

Our recent theoretical studies have shown that the interplay between polaritonic dispersion and strong excitonic nonlinearity indeed allows for the formation of a manifold of spatially localized, self-confined solutions, termed *cavity polariton solitons* (CPSs) [49–57]. Because of the permanent energy supply by an external pump and the intrinsic losses they belong to the general class of dissipative solitons and are, therefore, strong attractors [4].

From a fundamental point of view, the semiconductor microresonators provide a unique platform for a multidisciplinary study of self-localization effects, known from different branches of physics. For instance, an intuitive physical picture behind the formation of resting CPSs [49, 53] can be traced back to the pioneering work on *cavity solitons* in the weak coupling regime with parabolic dispersion [24–28]. Other localized solutions, as for instance moving one-dimensional CPSs [50, 51], resemble temporal solitons propagating in optical fibers [2, 58] and in fiber loops with a coherent pump [59]. Indeed, the formation of these polariton solutions can be explained by the balance between the negative effective mass of the polaritons and the repulsive polariton–polariton interaction.

However, frequently there are only minor analogies to conventional dissipative solitons as, for instance, the formation of two-dimensional moving CPSs [52] near the inflection point of the dispersion relation. In sharp contrast to many other solitonic systems, these bright two-dimensional polariton solitons exist for a negative effective mass along the direction of the pump momentum and a positive mass along the orthogonal direction. Apparently, parametric interaction between different spectral components of the CPS [54] can explain its stability and robust motion even for opposite signs of the polaritonic dispersion along the two orthogonal directions. Recently, this theoretical prediction of two-dimensional moving CPSs [52] has been confirmed experimentally [60, 61].

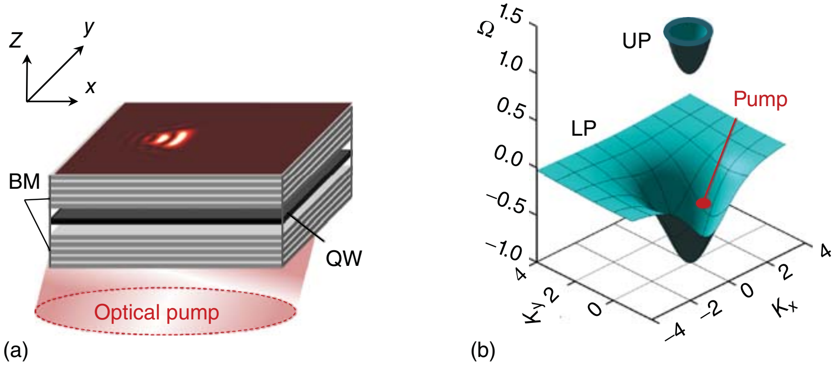

Figure 15.1 (a) Sketch of a microcavity driven by a coherent optical pump. The semiconductor quantum well (QW) is sandwiched between two Bragg mirrors (BM). (b) Respective polariton dispersion curves in the strong coupling regime. LP and UP depict lower and upper polariton branches, respectively, for a single QW configuration ($l = 1$).

In this chapter, we review the physics behind the formation of CPSs in semiconductor microresonators driven by an external coherent optical pump (Figure 15.1a). In Section 15.2, we put forward the mathematical model and discuss both the polaritonic dispersion and the properties of homogeneous nonlinear solutions. In particular, the lower polariton branch exhibits an inflection point where the second-order dispersion changes sign (see Figure 15.1b). Then, in Section 15.3, the formation of one-dimensional moving CPSs is considered for pump beams tilted beyond the “magic angle.” Here, the negative effective mass of the polaritons (or negative second-order dispersion) can be compensated by the repulsive exciton–exciton interaction. In Section 15.4, we perform an analytical analysis of the degenerate four-wave mixing effects, which can support the formation of polariton solitons localized in the direction orthogonal to the pump momentum. This parametric localization is a crucial mechanism with regard to the stabilization of two-dimensional CPSs [52] (see Section 15.5).

15.2
Mathematical Model

We are dealing with semiconductor microcavities (see Figure 15.1a), where polaritons may form due to the coupling of quantum well (QW) excitons and microcavity photons. We start by introducing the standard model [9–11, 15, 62] for the case of l identical QWs:

$$\partial_t E - i\nabla^2 E + (\gamma - i\Omega_p)E = i f(|\Psi|^2)\Psi + E_p e^{ik_p x}, \tag{15.1}$$

$$\partial_t \Psi - i d\nabla^2 \Psi + (\gamma - i\Omega_p)\Psi + i l^{-1}|\Psi|^2\Psi = i f(|\Psi|^2)E. \tag{15.2}$$

Here, E and Ψ are the averages of the photon and exciton creation or annihilation operators, and polarization effects are disregarded. The normalization is such that $(\Omega_R/g)|E|^2$ and $(\Omega_R/g)|\Psi|^2$ are the photon and exciton numbers per unit area. Ω_R is the Rabi frequency (for a single QW) and g is the exciton–exciton interaction coefficient. $\Omega_p = (\omega_p - \omega_{c,0})/\Omega_R$ is the detuning of the pump frequency ω_p from the identical cavity and exciton resonances ($\omega_c = \omega_0$). The cavity is driven by a plane pump wave with the amplitude E_p, k_p is the transverse momentum of the pump wave determined by the angle of incidence. The time t is measured in units of $1/\Omega_R$. The cavity and the exciton damping constants are assumed to be equal (γ) and normalized to Ω_R. The transverse coordinates x, y are normalized to the value $x_0 = \sqrt{c/2k_0 n\Omega_R}$ where c is the vacuum light velocity, n is the effective refractive index of the cavity, and $k_0 = n\omega_p/c$ is the length of the wave vector. The normalized amplitude of the external pump E_p is related to the incident intensity I_{inc} as $|E_p|^2 = g\gamma I_{\text{inc}}/\hbar\omega_p\Omega_R^2$ [36]. For the sake of generality we are taking into account the parabolic dispersion (effective mass approach) of the excitons where the exciton dispersion coefficient is normalized to the photon diffraction coefficient as $d = \hbar\omega_c n^2/m_{\text{exc}}c^2$, where m_{exc} is the effective exciton mass. Realistically, it holds $d \sim 10^{-4}$–10^{-5} and will be frequently set to zero.

The term $f(|\Psi|^2) \equiv [l/(1 + |\Psi|^2/n_s l)]^{1/2}$ is a measure of the exciton–photon coupling strength and accounts for its saturation with increasing exciton density [62]. Here, $n_s = N_s g/\Omega_R$ is the normalized excitons saturation density. Starting with an effective Hamiltonian for the interacting electrons and holes one arrives at Eqs. (15.1) and (15.2) with saturation effects included [10, 20, 31]. This model is valid for moderate saturations and fits well the experimental measurements of the Rabi splitting [62]. The saturation density can be approximated as $N_s \approx 0.117/\pi a_{\text{exc}}^2$ where a_{exc} is the exciton radius [19]. For InGaAs/GaAs quantum wells, the dimensionless quantity amounts to $n_s \simeq 0.5$–1.0.

As a guideline for realistic estimates, one can use parameters of a microcavity with a single InGaAs/GaAs quantum well: $\hbar\Omega_R \simeq 2.5$ meV, $\hbar g \simeq 10^{-4}$ eV μm^2; see [15, 22]. Therefore, a unit of t corresponds to 0.25 ps and a unit of x to $x_0 \sim 1$ μm. Assuming the relaxation times of excitons and the cavity life time to be 2.5 ps gives $\gamma \simeq 0.1$. In accordance with this set of parameters, the normalized driving amplitude $|E_p|^2 = 1$ corresponds to an external pump intensity of about 6 kW cm^{-2}.

The linear polariton dispersion relation: First, we briefly describe the linear polariton dispersion, which is defined as the dependency of the frequency Ω (or energy) from the transverse momentum components k_x and k_y. Assuming that $E, \Psi \sim e^{-\gamma t} e^{-i\Omega t + ik_x x + ik_y y}$ and dropping the pump term and nonlinear effects, we find from Eqs. (15.1) and (15.2) the eigenvalue problem

$$i\Omega_{\pm}(k)\vec{p}_k = \begin{pmatrix} ik^2 & -i\sqrt{l} \\ -i\sqrt{l} & idk^2 \end{pmatrix} \vec{p}_k, \tag{15.3}$$

where $\vec{p}_k = \{e_k, \psi_k\}$ is the polariton basis vector and $\Omega_{\pm}(k)$ are the eigenfrequencies. e_k and ψ_k describe the content of the photonic and excitonic components of polaritons (Hopfield coefficients) [5]. The solution to the eigenvalue problem (15.3) yields the linear polariton relation

$$\Omega_{\pm}(k) = \frac{(1+d)k^2}{2} \pm \sqrt{l + \frac{1}{4}(1-d)^2k^4}, \tag{15.4}$$

where $k^2 = k_x^2 + k_y^2$ and $\Omega_{\pm}$ are the relative frequencies of the upper polariton (UP) and lower polariton (LP) branches, respectively; see Figure 15.1b. For $k = 0$, we get the Rabi splitting, $\Delta\Omega = \Omega_+(0) - \Omega_-(0) = 2\sqrt{l}$ (or $\Delta\omega = 2\sqrt{l}\Omega_R$). It represents the separation of the two branches of the dispersion curve in the center ($k = 0$) and for identical excitonic and photonic resonances ($\omega_0 = \omega_c$). In the strong-coupling regime, the Rabi splitting exceeds the line-width ($\Delta\Omega > \gamma$).

Bistability: The nonlinearity of polaritons is accounted for by the terms proportional to the exciton density. The bistable response of the microresonator is one of the consequences of this nonlinearity and an important prerequisite for the existence of localized solutions. Neglecting saturation effects ($n_s \to \infty$) but accounting for the exciton–exciton repulsion, one finds that $E(E_p)$ is multivalued provided that

$$\left(\Omega_p - dk_p^2 - \sqrt{3}\gamma\right) - \frac{\left(\Omega_p - k_p^2 + \sqrt{3}\gamma\right) l}{\left(\gamma^2 + \left(\Omega_p - k_p^2\right)^2\right)} > 0. \tag{15.5}$$

This cumbersome condition determines two intervals of Ω_p, where polariton bistability can be observed [49]. It simplifies for $\gamma = 0$ giving two bistability intervals $\Omega_-(k_p) < \Omega_p < k_p^2$ and $\Omega_p > \Omega_+(k_p)$. The first interval belongs to the LP branch, and, thus, may be termed LP bistability [15, 22, 29]. The second one is located within the UP band.

The energy gap between the upper and lower polariton branches shrinks for larger polariton densities due to the saturation of the photon–exciton coupling ($n_s \neq \infty$). As a result, the bistability can appear in a new frequency interval Ω_p just below the UP branch [53].

15.3
One-Dimensional Bright Cavity Polariton Solitons

In this section, we study the formation of one-dimensional CPSs propagating along the plane of a semiconductor microresonator coherently driven by an external optical pump. The choice of the operating frequency and the angle of incidence guarantee that the optical pump excites the polaritons with nonzero transverse momenta in the vicinity of the lower polariton branch. For sufficiently large pump momenta, the effective mass becomes negative, so that the repulsive polartion–polariton interaction promotes the stability of these bright CPSs. In Section 15.3.1, we derive the effective nonlinear model in the vicinity of the lower polariton branch. In order to embrace the inflection point and to account for the varying dispersion, we include higher-order dispersion terms. Then, in Section

15.3.2, the formation of moving bright polariton solitons is considered for the pump beams tilted beyond the “magic angle.” High-order multi-hump CPSs and their relation to parametric effects are discussed in Section 15.3.3.

15.3.1
Amplitude Equation in the Polaritonic Basis

To understand the physics behind the polariton soliton formation and to identify the domains of their existence, we proceed by expanding the linear polariton dispersion around the pump momentum, and derive a single equation for the amplitude of the lower (and upper) branch polaritons containing an effective nonlinearity and multiple dispersion terms. In this derivation, we simplify the nonlinear saturation of the coupling considering only the first density-dependent term in the Taylor expansion $f(|\Psi|^2) \approx l^{1/2} - |\Psi|^2/2n_s l^{1/2}$. We also assume that $\{E, \Psi\} \simeq \int a(t,k)\vec{p}_k e^{ikx}dk$, where $a(t,k)$ is the Fourier amplitude of the kth component. We assume that the spectrum of the polariton wave packet is centered around k_p and expand $\Omega_\pm(k)$ up to the fourth order in $|k - k_p|$. The resulting equation for the amplitude of the polariton wave packet

$$A(t,x) = \int_{-\infty}^{\infty} a(t,k)e^{i(k-k_p)x}d(k-k_p)$$

is

$$\begin{aligned} &i\partial_t A + iD_1\partial_x A + D_2\partial_x^2 A - iD_3\partial_x^3 A - D_4\partial_x^4 A \\ &\quad + i\gamma A + \Delta_p A - \xi|A|^2 A = i\eta E_p, \end{aligned} \tag{15.6}$$

where $\Delta_p = \Omega_p - \Omega_\pm(k_p)$ is the effective frequency detuning, γ the loss, $D_1 = \partial_k \Omega_\pm|_{k_p}$ the transverse group velocity, and $D_2 = (1/2)\partial_k^2\Omega_\pm|_{k_p}$, $D_3 = (1/6)\partial_k^3\Omega_\pm|_{k_p}$, $D_4 = (1/24)\partial_k^4\Omega_\pm|_{k_p}$ are the dispersion coefficients. The essential difference between weak and strong coupling regimes, relevant to our study, is not the mere existence of the LP branch, but the fact that it exhibits an inflection point, $\partial_k^2\Omega_- = 0$ at $k = k_{\text{mag}}$, where the second-order dispersion changes sign (cf. Figure 15.2a and b).

Note that, in general, the effective transverse mass of polaritons is a 2×2 tensor. The mass component corresponding to the direction of the pump momentum changes its sign from positive to negative for $k > k_{\text{mag}}$, while the mass in the orthogonal direction stays positive. Normalizing the excitonic component of the linear polariton eigenmode such that $|\psi_{k_p}|^2 \equiv 1$ results in an equivalence of the polariton and exciton densities ($|A|^2$).

The effective nonlinearity coefficient for the lower (−) and upper (+) polariton branches is expressed as

$$\xi^\pm(k_p) = \frac{\left(k_p^2 \mp \sqrt{4l + k_p^4}\right)\left(\left(k_p^2 \mp \sqrt{4l + k_p^4}\right) + 2l/n_s\right)}{l\left(\left(k_p^2 \mp \sqrt{4l + k_p^4}\right)^2 + 4l\right)}, \tag{15.7}$$

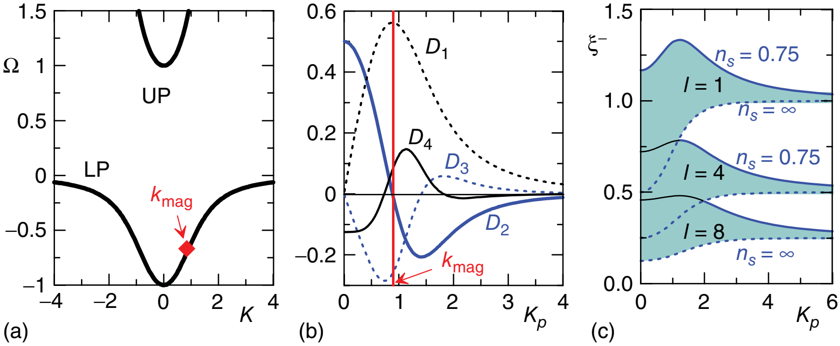

Figure 15.2 (a) Polariton dispersion: lower (LP) and upper (UP) polariton branches in the strong coupling regime. (b) Dispersion coefficients of the lower polaritons (LP) versus pump momentum. (c) The effective nonlinear coefficient ξ^- of the LP versus pump momentum for different numbers of quantum wells ($l = 1, 4, 8$) and saturation densities n_s. The solid (dashed) lines depict $n_s = 0.75$ ($n_s = \infty$).

whereas the efficiency of the optical pump reads as

$$\eta^{\pm}(k_p) = \frac{2\sqrt{l}\left(k_p^2 \mp \sqrt{4l + k_p^4}\right)}{\left(\left(k_p^2 \mp \sqrt{4l + k_p^4}\right)^2 + 4l\right)}. \tag{15.8}$$

Due to the hybrid nature of the exciton-polaritons, both coefficients Eqs. (15.7) and (15.8) strongly depend on the pump momentum k_p. The effective nonlinearity is defocusing ($\xi^{\pm} > 0$) for the lower as well as the upper polariton branch for a weakly saturating nonlinearity $n_s \to \infty$. Note that the nonlinearity coefficient (ξ^+) of the upper polariton branch can change its sign for strong saturation effects [53, 55]. Strong saturation effects contribute additionally to the effective nonlinearity of the lower polariton branch increasing the nonlinear coefficient ξ^- (compare the lines with $n_s \neq \infty$ and $n_s = \infty$ in Figure 15.2c). Therefore, we assume that the saturation of the photon–exciton coupling does not change qualitatively the nonlinear solutions but only reduces the intensity thresholds required for their excitations. Perhaps unexpectedly the effective nonlinearity becomes weaker for a configuration with a larger number of the quantum wells l (cf. Figure 15.2c). This can be explained by the fact that the excitons redistribute between several QWs reducing the polariton–polariton scattering probability.

The model (15.6) is generic for a wide class of dissipative nonlinear systems with spatial or temporal dispersion. For normal pump incidence, $k_p = 0$, the model is identical to a previously studied one in the context of light-only cavity solitons in a passive microresonators with Kerr nonlinearity; see, for example, [26–28, 63] and references therein. Beyond the parabolic approximation, this model has been used for the investigation of passive microresonators with an embedded periodic photonic structures [64–67]. It also describes the temporal solitons propagating in a passive ring cavity made of standard optical fibers with an instantaneous Kerr nonlinearity [59].

From these studies, it is known that the points where the *homogeneous solutions* (HS) destabilize are the potential bifurcation points for solitons to emerge [27]. The HSs response may be either monostable or bistable. In accordance with the model (15.6), the operating frequency has to be slightly above the corresponding resonance $\Omega_p > \gamma\sqrt{3}$ for a defocusing nonlinearity ($\xi > 0$); see [63]. As a result, one can find two intervals of polaritonic bistability associated with the lower and upper polaritonic branches in agreement with the conditions for bistability (Eq. (15.5)).

15.3.2
CPSs Beyond the "Magic Angle" and Their Stability

The effective polariton mass and the second-order dispersion coefficient D_2 change their sign from positive to negative at $k_p > k_{\mathrm{mag}}$. For k_p equal and close to k_{mag}, the third-order dispersion designated by the coefficient D_3, see Eq. (15.6) and Figure 15.2b, becomes the leading linear effect essentially affecting the polariton dynamics. As we increase k_p further, the value of D_3 drops and the polariton dispersion is determined by the competition of the D_2 and D_4 terms. Both $D_2 < 0$ and $D_4 > 0$ promote the existence of bright solitons for a repulsive nonlinearity. In this regime, $D_1 \neq 0$ and hence any soliton found there is expected to move.

To prove that drifting structures are indeed solitons, we consider Eqs. (15.1) and (15.2) with $\partial_y = 0$ and seek moving solitons in the form: $E(t,x) = \tilde{E}(\tilde{x})e^{ik_p x}$, $\Psi(t,x) = \tilde{\Psi}(\tilde{x})e^{ik_p x}$, where $\tilde{x} = x - vt$ and v is the velocity (yet to be determined). For the single QW configuration ($l = 1$), $\tilde{E}$ and $\tilde{\Psi}$ obey

$$(2k_p - v)\partial_{\tilde{x}}\tilde{E} - i\partial^2_{\tilde{x}}\tilde{E} + (\gamma - i\Omega_p + ik_p^2)\tilde{E} = i\tilde{\Psi} + E_p, \tag{15.9}$$

$$(2dk_p - v)\partial_{\tilde{x}}\tilde{\Psi} - id\partial^2_{\tilde{x}}\tilde{\Psi} + (\gamma - i\Omega_p + idk_p^2)\tilde{\Psi} + i|\tilde{\Psi}|^2\tilde{\Psi} = i\tilde{E}. \tag{15.10}$$

Note that the saturation of the exciton–photon coupling does not have any qualitative impact on the results discussed in this chapter and, therefore, can be disregarded, $n_s \to \infty$. The soliton solutions of the above-mentioned system were found using a modification of the Newton method allowing to treat v as an unknown variable.

Moving bright CPSs have been found by numerically solving Eqs. (15.9) and (15.10). Plots illustrating the dependence of the maximal soliton amplitude on the pump field and the associated bistability curves for HSs ($\partial_{x,y} = 0$) are shown in Figure 15.3a and c. The branch of moving bright CPSs bifurcates subcritically from the right bend of the bistability loop. Figures 15.3b and d show typical transverse profiles of these bright CPSs. The solitons themselves have oscillating tails at their rear, also known from other moving cavity solitons [64, 66, 67]. They emerge for k_p slightly below k_{mag}, and the intervals of their stability expand with increasing k_p. Note that Eq. (15.6) with the third-order dispersion term D_3 supports both bright and dark localized solutions irrespective of the sign of nonlinearity [64]. Similarly, bright and dark polariton solitons may coexist provided that k_p is close to k_{mag} [55].

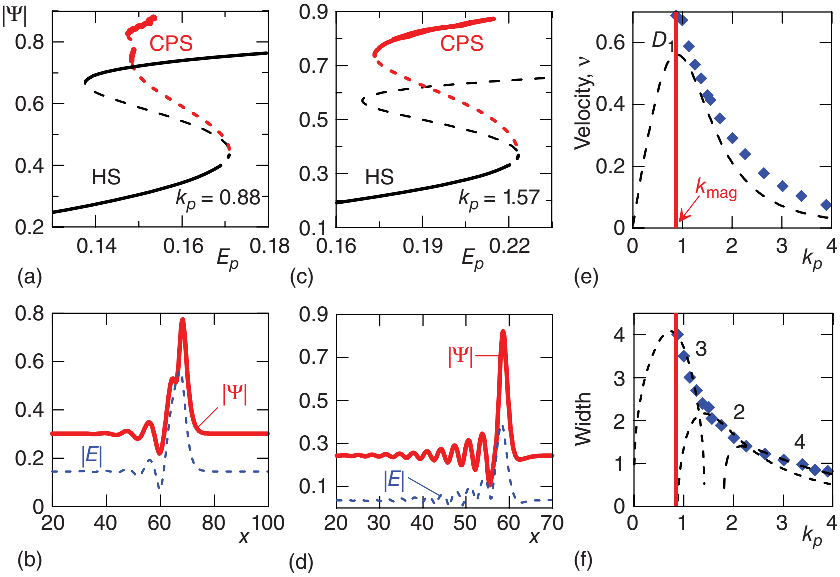

Figure 15.3 Moving bright cavity polariton solitons (CPS) beyond the "magic angle" bifurcating from the homogeneous solution (HS). (a, c) Maxima of the excitonic components versus the pump amplitude E_p for two different pump momenta k_p. The full/dashed lines correspond to stable/unstable solutions, respectively. (b, d) The respective soliton profiles for $E_p = 0.149$ (b) and $E_p = 0.19$ (d). The pump frequencies are $\Omega_p = -0.38$ (a, b) and $\Omega_p = -0.05$ (c, d). (e) Drift velocity of CPS versus pump momentum k_p. Numerical results—diamonds; analytical results: $D_1(k_p)$—dashed line. (f) CPS width versus pump momentum k_p. Numerical results—diamonds; analytical results: appropriately scaled $\sqrt[m]{D_m}$ with $m = 2, 3, 4$—dashed lines.

The velocity of the CPS is treated as an unknown parameter self-consistently determined by our numerical method with the soliton profile in Eqs. (15.9) and (15.10). It turns out that v is close, but not equal, to D_1; see Figure 15.2b. The maximum of the soliton velocity v occurs at $k = k_{\mathrm{mag}}$, and decreases rapidly with increasing k_p; see Figure 15.3e. This is in remarkable contrast to what happens if dispersion is parabolic, where the soliton velocity continuously increases with k_p. For our choice of parameters, v must be multiplied by $\simeq 4 \times 10^6\ \mathrm{m\,s^{-1}}$ to give the physical velocity. It implies that a soliton with $v = 0.25$ will traverse across a typical distance of ~100 μm in ~100 ps. This is 40 times larger than the polariton life time. Hence, the solitons have enough time to be excited, formed, and experimentally observed [60, 61].

We recall that an all-optical delay line based on the lateral drift of cavity solitons has been proposed and experimentally demonstrated in semiconductor microresonators operating in the weak coupling regime [28, 68]. In such devices, the carrier lifetime is considerably longer than the photon lifetime and, hence, the cavity soliton drift speed is limited by the maximum value approaching several micrometer per nanosecond. This is several orders of magnitude smaller than the drift velocities accessible for the moving polariton solitons (Figure 15.3e). This appreciable difference is directly related to the different nonlinear mechanisms in weak (photonic nonlinearity) and strong (excitonic nonlinearity) coupling regimes.

To characterize the influence of the different dispersion orders on the soliton shape, we display their width versus the momentum k_p; see Figure 15.3f. Changing k_p, we have kept constant the detuning of the polariton frequency from the pump frequency, $\Delta_p = 0.3$, by adjusting the detuning of the pump field from the cavity resonance, Ω_p, which explicitly enters into the full model. For large k_p, the excitonic part dominates over the photonic component (compare the profiles in Figure 15.3b and d). That is why the polariton solitons can be much narrower than the pure photonic cavity solitons in the weak coupling regime and may attain widths well below the ones allowed by the photonic dispersion. The soliton width is expected to scale with the dominant dispersion coefficients as $\sim \sqrt[m]{D_m}$ $(m = 2, 3, 4)$. Figure 15.3f compares the numerically found soliton width (diamonds) with the scaling given by the different dispersion orders (dashed lines). Third-order dispersion describes well the soliton width for relatively small k_p, where $D_2 \simeq 0$. A further inclination brings D_2 on the top, while the third-order dispersion vanishes. A further increase of k_p brings fourth-order dispersion into the play, which starts to compete with D_2.

15.3.3
Multi-Hump Cavity Polariton Solitons

In addition to the single-hump moving CPSs considered earlier, the original model (Eqs. (15.1) and (15.2)) also supports multi-hump solutions. Their existence is directly related to the (in)stability of the HSs. A typical bistability loop for cavity polaritons is shown in Figure 15.4a. The lower homogeneous state remains stable through most of the bistability range. This prevents a spontaneous

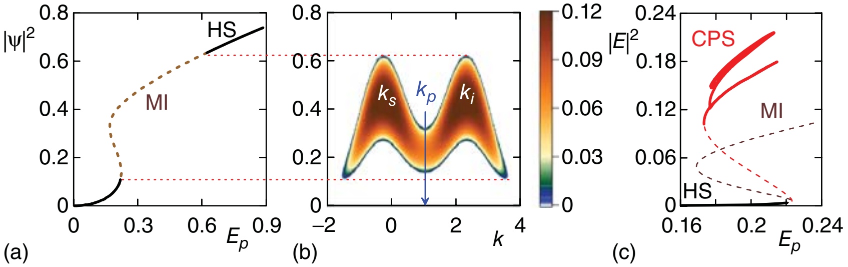

Figure 15.4 Origin of multi-hump solitons. (a) Excitonic component $|\Psi|^2$ of the homogeneous solution (HS) versus the pump amplitude E_p. Dashed lines represent unstable states and MI designates modulational instability. (b) Growth rate $(\Re\lambda)$ of the unstable perturbation as a function of momentum k and HS intensity $|\Psi|^2$. (c) Red line (CPS) shows the intensity maximum of the photonic component ($|E|^2$) of the soliton profile. The soliton branch exhibits a folded structure corresponding to the single- and multi-hump soliton families. Parameters are $\Omega_p = -0.05$, $k_p = 1.5708$.

appearance of instability and provides a stable background for solitons. In the present case, the upper branch of the bistability loop as well as a minor part of the lower branch just before the right turning point become modulationally unstable. This *modulational instability* (MI) is associated with the parametric generation of field components with nonzero momenta k. Figure 15.4b shows the linear growth rate $\Re\lambda(k)$ of the unstable perturbations of the form $\sim \exp[(ikx + \lambda(k)t)]$ as function of their momenta k and the HS intensity. The unstable momenta are concentrated around the two well-defined points associated with the signal (k_s) and the idler (k_i) components. The origin of this parametric gain is well understood [15, 29–37] and directly related to the nonparabolic shape of the lower branch of the polariton dispersion relation. It allows for the resonant scattering of two pump polaritons into the signal–idler pair conserving both the frequency and the kinetic momentum $2k_p = k_s + k_i$ simultaneously. Since the unstable momenta are concentrated around the two well-defined points, this degenerated parametric four-wave mixing process results in the transformation of an unstable homogeneous state into a traveling roll pattern with one of the roll's sideband peaking close at zero momentum.

Solitons we have reported here (see Section 15.3.2 and in [50]) are essentially isolated islands of this pattern. The CPS branch exhibits a folded structure corresponding to the single- and multi-hump soliton families (see Figure 15.4c). As the number of humps increases, the solitons develop toward a periodic pattern state. Figures 15.5a, c, and e show the single-, double-, and multi-hump CPS profiles. Each CPS moves with a velocity approximately determined by the slope of the linear polariton dispersion curve. The oscillatory tails are invariant upon propagation, so that there is no radiation loss and the moving solitons preserve their overall profiles. Apart from the large central peak, the soliton spectra have sidebands with different amplitudes (see Figure 15.5b,d,f). Note

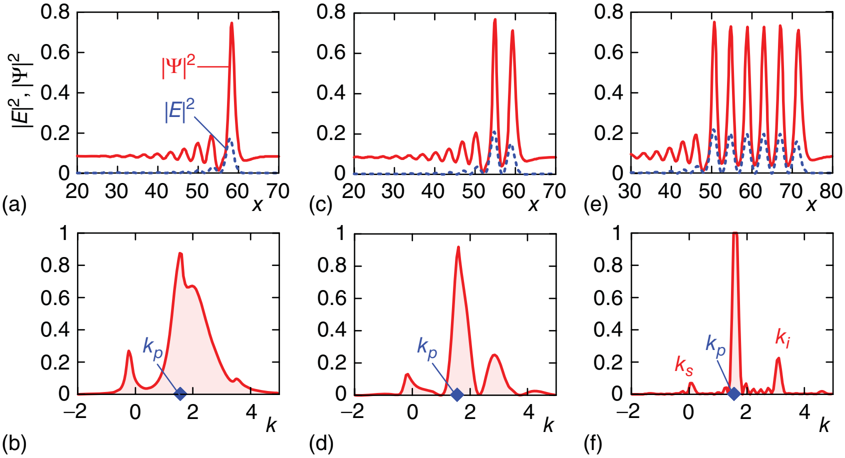

Figure 15.5 Intensity profiles of single-hump (a, b), double-hump (c, d), and multi-hump (e, f) CPS for $E_p = 0.21$. The spatial profiles (a, c, e) and the corresponding profiles (b, d, e) in momentum space are displayed. Other parameters are identical to those in Figure 15.4.

that while plotting the solitons in the momentum space we have subtracted the delta-function corresponding to the infinite energy carried by the soliton background. For single-hump solitons, the sidebands are very asymmetric. However, for double-hump and, especially, for multi-hump solitons, the most prominent sidebands are symmetric with respect to k_p. The location of the sidebands is approximately given by the momenta with the maximal instability growth rate of the upper branch of the polariton bistability loop (compare the unstable momenta in Figure 15.4b and sideband components in Figure 15.5f). This confirms that as the number of humps increases the solitons evolve toward a periodic sequence of moving beams. Hence, the solitons can be qualitatively considered as the spots of the spatially confined parametric conversion of the pump polaritons into the signal and idler ones.

We note that parametric solitons in cavities with frequency conversion have been reported in a number of studies; see, for example, [69–72] and references therein. The nonlinearity describing the parametric wave mixing is no longer simply focusing or defocusing and leads to solitons with novel properties. The presence of the parametric four-wave mixing plays a key role for the self-localization of exciton-polaritons in two-dimensional environments, which we describe in the following section.

15.4
Two-Dimensional Parametric Polariton Solitons

Previously, we have demonstrated that one-dimensional bright CPSs are forced to move with a fixed velocity determined by the pump momentum $k_p > k_{\text{mag}}$ in order to compensate the repulsive interparticle interactions by the dispersion of a negative mass particle; see Section 15.3 and [50]. However, the peculiar nonparabolic shape of the lower polariton branch allows for a low-threshold parametric four-wave mixing of pump, signal, and idler waves [15, 29–37]. In general, parametric wave mixing is associated with a particular nonlinear phase modulation, which permits to balance the effect of linear dispersion of either sign [69–72]. Therefore, it may be anticipated that four-wave mixing qualitatively alters the physics of polariton solitons.

In this section, we prove the existence and study the properties of two-dimensional *parametric polariton solitons* (PPS), which form trains of moving wave packets. This mechanism provides a reasonable intuitive explanation of the polariton localization in the direction orthogonal to the pump momentum, where the polariton exhibits a positive effective mass (the y-direction in Figure 15.6) [52, 54].

15.4.1
Amplitude Equations for the Participating Waves

To understand the physics behind the parametric polariton soliton formation and to identify domains of their existence, we proceed by assuming that the polariton wave packet has three components with momenta centered around the pump

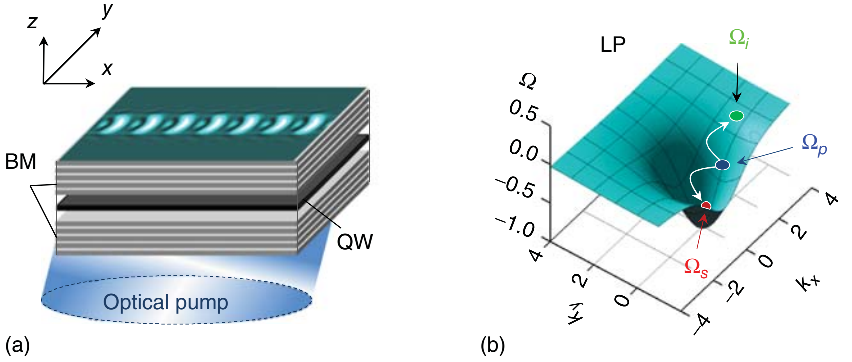

Figure 15.6 Formation of parametric polariton solitons. (a) Sketch of the microcavity driven by a coherent optical pump. The semiconductor quantum well (QW) is sandwiched between two Bragg mirrors (BM). (b) Lower branch (LP) of the polariton dispersion curve. The frequencies of the pump, signal, and idler polaritons are $\Omega_{p,s,i}$, respectively.

($k_x = k_p$, $k_y = 0$), signal ($k_x = k_s$, $k_y = 0$), and idler ($k_x = k_i$, $k_y = 0$) momenta, respectively. The corresponding frequencies are Ω_p, Ω_s, and Ω_i. Thus, we may express E and Ψ in Eqs. (15.1) and (15.2) as (see [32, 36])

$$\begin{aligned} E(x,y,t) &= A_p(y,t)(e_p/\psi_p)e^{ik_px} + A_s(y,t)(e_s/\psi_s)e^{ik_sx-i(\Omega_s-\Omega_p)t+i\delta t} \\ &\quad + A_i(y,t)(e_i/\psi_i)e^{ik_ix-i(\Omega_i-\Omega_p)t-i\delta t}, \\ \Psi(x,y,t) &= A_p(y,t)e^{ik_px} + A_s(y,t)e^{ik_sx-i(\Omega_s-\Omega_p)t+i\delta t} \\ &\quad + A_i(y,t)e^{ik_ix-i(\Omega_i-\Omega_p)t-i\delta t}. \end{aligned} \tag{15.11}$$

Here, $A_{p,s,i}(y,t)$ are the slowly varying complex amplitudes and $e_{\mathrm{p,s,i}}$ and $\psi_{\mathrm{p,s,i}}$ are the components of $\vec{p}_{k_x,k_y}$; see Eq. (15.3). δ is a free parameter, which has to be determined self-consistently with the soliton profiles, and designates an additional frequency shift between signal and idler polaritons. A similar frequency shift has been used in the theory of parametric solitons in cavities with a quadratic nonlinearity [70]. Inserting the ansatz (15.11) into Eqs. (15.1) and (15.2), the following set of differential equations can be derived:

$$\begin{aligned} & i\,\frac{\partial A_p}{\partial t} + D_p\frac{\partial^2 A_p}{\partial y^2} + (i\gamma + \Delta_p)A_p \\ &\qquad - \xi_p\left(|A_p|^2 + 2|A_s|^2 + 2|A_i|^2\right)A_p - 2\xi_p A_s A_i A_p^* = W, \end{aligned} \tag{15.12}$$

$$\begin{aligned} & i\,\frac{\partial A_s}{\partial t} + D_s\frac{\partial^2 A_s}{\partial y^2} + (i\gamma + \Delta_s - \delta)A_s \\ &\qquad - \xi_s\left(2|A_p|^2 + |A_s|^2 + 2|A_i|^2\right)A_s - \xi_s A_p^2 A_i^* = 0, \end{aligned} \tag{15.13}$$

$$\begin{aligned} & i\,\frac{\partial A_i}{\partial t} + D_i\frac{\partial^2 A_i}{\partial y^2} + (i\gamma + \Delta_i + \delta)A_i \\ &\qquad - \xi_i\left(2|A_p|^2 + 2|A_s|^2 + |A_i|^2\right)A_i - \xi_i A_p^2 A_s^* = 0, \end{aligned} \tag{15.14}$$

where $\Delta_{p,s,i} = \Omega_{p,s,i} - \Omega_{-}(k_{p,s,i}, k_y = 0)$ are the effective frequency detunings of the polaritons from the frequency of the noninteracting polaritons. The coefficients $D_{p,s,i} = (1/2)\partial^2_{k_y}\Omega_{-}(k_{p,s,i}, k_y)|_{k_y=0}$ are the y-components of the effective masses of the pump, signal, and idler polaritons; see Figure 15.6b. The coefficients $\xi_{p,s,i} \equiv \xi^{-}(k_{p,s,i})$ describe self- and cross-interactions of the participating polaritons, which can be calculated by using Eq. (15.7). The external pump amplitude is $W = \eta E_p$, where the pump efficiency coefficient $\eta = \eta^{-}(k_p)$ is given by Eq. (15.8).

Obviously, the transverse momentum has only a minor qualitative effect on the effective nonlinear coefficient, which increases monotonically from $\xi = 1/2$ (for $k_x = 0$ and $n_s = \infty$) to $\xi = 1$ (for $k_x = \infty$). Thus, for convenience, we may assume $\xi_{p,s,i} = \xi = 1$, which does not impose any constraints on the results discussed later.

15.4.2
Families of Parametric Polariton Solitons

Without signal and idler components ($A_{s,i} = 0$), only dark polariton solitons are stable for the repulsive (defocusing) nonlinearity and a positive polariton mass (dispersion) [49]. Even though a stationary version of the mathematical model (15.12) exhibits bright localized solutions within the bistability interval of the HS, these bright solitons (BS) are genuinely unstable. These unstable BSs bifurcate from the HS at the point where modulational instability sets in (see the dotted line in Figure 15.7a and the profile in Figure 15.7b). The BS branch terminates at the so-called Maxwell point, while touching the upper state of the HS bistability loop. At the Maxwell point, the lower and upper homogeneous states can be connected

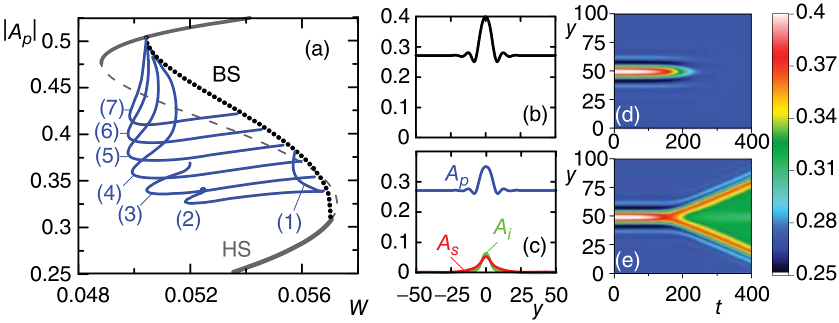

Figure 15.7 Formation of parametric polariton solitons (PPS). (a) Maxima of the pump component of PPSs for different detunings of the signal component: (1) $\Delta_s = 0.15$, (2) $\Delta_s = 0.25$, (3) $\Delta_s = 0.35$, (4) $\Delta_s = 0.45$, (5) $\Delta_s = 0.55$, (6) $\Delta_s = 0.65$, (7) $\Delta_s = 0.75$. The black dotted line marks the unstable pump-only bright soliton (BS), which bifurcates from the pump-only homogeneous solution (HS). (b) Amplitude profile of the unstable pump-only BS for $W = 0.055$. (c) Pump, signal, and idler components of an unstable PPS close to the bifurcation point for $W = 0.055$ and $\Delta_s = 0.35$ (PPS branch "3"). (d) Evolution dynamics of the unstable pump-only BS, shown in (b). (e) Destabilization dynamics of the unstable PPS, shown in (c). Other parameters: $\Delta_{p,i} = 0.25$, $D_p = 0.23$, $D_s = 0.5$, $D_i = 0.03$.

by a resting front (for details see [26, 27, 49, 55] and references therein). Various termination scenarios of dissipative localized structures have been a subject of recent intense research; see, for example, [73] and references therein. The unstable pump-only BSs tend either to transform into two moving fronts between the lower and upper branches of the HS, or to disappear. The latter scenario is shown in Figure 15.7d. This destabilization dynamics changes drastically if the signal and idler waves are involved ($A_{s,i} \neq 0$) (Figure 15.7e). Thus, it may be expected that four-wave mixing qualitatively alters the physics of polariton solitons.

Indeed, even in the simplest case of the HS, the trivial pump-only ($A_{s,i} = 0$) solution becomes unstable giving rise to the generation of signal and idler polaritons provided that the pump amplitude (A_p) exceeds a threshold value [36]. First, we discuss briefly the parametric threshold for the generation of small signal and idler polaritons in the undepleted pump limit ($|A_p| >> |A_{s,i}|$). Looking for solutions of Eqs. (15.13) and (15.14) in the form $A_{s,i}(t) = a_{s,i}e^{\lambda t}$ and $A^*_{s,i}(t) = b_{s,i}e^{\lambda t}$ for the constant pump component A_p and keeping only linear terms in the fluctuations $a_{s,i}$ and $b_{s,i}$, one gets an eigenvalue problem for λ with the solution

$$\Re\lambda = -\gamma \pm \sqrt{\xi^2|A_p|^4 - \frac{1}{4}\left(\left(\Delta_s + \Delta_i\right) - 4\xi|A_p|^2\right)^2}. \tag{15.15}$$

The pump-only solution becomes parametrically unstable provided that $\Re\lambda > 0$. Thus, the parametric threshold can be defined as $\Re\lambda(|A_p|) = 0$, where the parametric instability of the trivial signal and idler states just sets in. This threshold is then given by

$$|A_{\mathrm{PT}}|^2 = \frac{2(\Delta_s + \Delta_i) \pm \sqrt{(\Delta_s + \Delta_i)^2 - 12\gamma^2}}{6\xi}. \tag{15.16}$$

The physics does not change qualitatively for a nonuniform pump profile. For instance, if the pump component $A_p(y)$ coincides with the pump-only BS solution (see Figure 15.7b), the inhomogeneous signal and idler components are generated (see Figure 15.7c) provided that the maximum of the BS amplitude exceeds the parametric threshold A_{PT} approximately given by Eq. (15.16).

To rigorously calculate the profile of the PPSs beyond the undepleted pump approximation, we used the stationary version ($\partial A_{p,s,i}/\partial t = 0$) of Eqs. (15.12 –15.14). Note that the unknown frequency shift δ between signal and idler waves has to be calculated self-consistently with the PPS profile that includes all three components. Figure 15.7a shows the PPS branches for several values of the signal polariton detuning Δ_s. Both the existence domain and the shape of the PPS depend strongly on this detuning. The PPS branches approach the pump-only BS solution close to the parametric threshold points ($|A_{\mathrm{PT}}|$). In accordance with Eq. (15.16), these bifurcation points shift upwards along the pump-only solution branch with increasing frequency detunings of the signal and idler polaritons. More precisely, the parametric threshold is located slightly below the bifurcation point of PPS (see PPS branch and PT point in Figure 15.8a). A phase shift due to diffraction of the nonuniform pump component explains this small discrepancy.

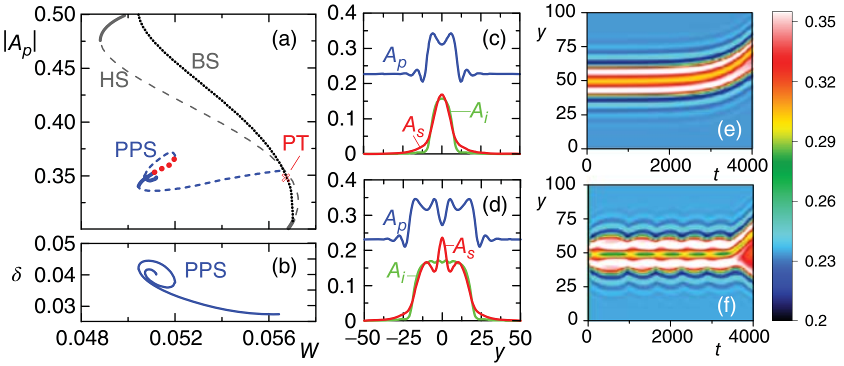

Figure 15.8 Stable and unstable 1D parametric polariton solitons. (a) Branches of homogeneous solutions (HS), unstable bright solitons (BS) and parametric polariton solitons (PPS). The dashed lines designate unstable solutions. The thick dotted red line shows the slightly unstable PPS (see text). PT depicts the parametric threshold point given by Eq. (15.16). (b) Frequency shift (δ) between signal and idler components of the PPS versus the external pump amplitude W. (c) Amplitude profiles of stable fundamental PPS for $W = 0.0505$ and (d) stable second-order PPS for $W = 0.051$. (e, f) Evolution dynamics of unstable PPS: destabilization due to an asymmetric eigenmode with $\lambda = 0.0018$ for the pump amplitude $W = 0.0511$ (e). Destabilization due to a symmetric eigenmode with $\lambda = 0.00014 \pm i0.015$ for the pump $W = 0.0517$ (f). Other parameters: $\Delta_{p,i} = 0.25$, $\Delta_s = 0.35$.

The signal and idler components of the PPS increase off the bifurcation point (cf. Figure 15.8a). The selection rule for the frequency detuning δ between the signal and idler components of the PPS is closely related to the relative energy balance. Indeed, similar to the case of nondegenerated optical parametric oscillators (OPO) [70], any steady-state solution, such as soliton solutions of the model (15.12)–(15.14), has to satisfy the condition

$$\gamma_s \int |A_s(y)|^2 dy = \gamma_i \int |A_i(y)|^2 dy, \qquad (15.17)$$

where $\gamma_{s,i}$ are the losses of the signal and idler polaritons (in our case $\gamma_{s,i} = \gamma$). This additional condition for the energy balance fixes the free parameter δ, which can be calculated self-consistently with the soliton profile (see Figure 15.8b). After the turning point, the PPS consists of three components comparable in their amplitudes (cf. Figure 15.8c and d).

It is well known that the turning points of the soliton branches are associated with saddle-node bifurcations and, therefore, with a change of the soliton stability (see, for instance [69, 71, 72]). To study the stability of PPSs, the response of the system to a weak perturbation has to be calculated using the linear stability analysis [15]. To this aim, we are looking for the solution of Eqs. (15.12 –15.14) around the stationary state $S_{p,s,i}(y)$ (with the corresponding value of the frequency shift δ) in the form $A_{p,s,i}(y,t) = S_{p,s,i}(y) + a_{p,s,i}(y)e^{\lambda t}$ and $A^*_{p,s,i}(y) = S^*_{p,s,i}(y) + b_{p,s,i}(y)e^{\lambda t}$, and keeping only linear terms in the fluctuations $a_{p,s,i}(y)$ and $b_{p,s,i}(y)$, one gets the eigenvalue problem for λ. A stationary solution $S_{p,s,i}(y)$ is stable, provided that all eigenvalues of the linear perturbation spectra have negative real parts.

Figure 15.8c and d shows examples of stable fundamental and second-order PPSs. Apparently, sufficiently strong signal and idler components may stabilize the initially unstable pump-only BS. Direct numerical simulations confirm that these stable localized solutions are attractors. Therefore, they can be excited from a fairly wide range of initial conditions. It is typical for a dissipative system [4] that the system's parameters determine completely the shape and the free frequency detuning δ of the PPS of the model (Eqs. (15.12)–(15.14)).

The fundamental PPS can undergo destabilization (see thick dotted red line in Figure 15.8a). One may anticipate two typical scenarios of their destabilization. In the first case close to the destabilization point, the linear spectrum of the perturbations has an antisymmetric (with respect to the soliton center y_0) eigenmode $[a_{p,s,i}(y - y_0) = -a_{p,s,i}(y_0 - y), b_{p,s,i}(y - y_0) = -b_{p,s,i}(y_0 - y)]$ with a purely real negative eigenvalue λ. The evolution of this eigenmode leads to spontaneous symmetry breaking of the parametric soliton profile resulting in a transverse (y-direction) motion and an eventual decay (Figure 15.8e). We note that temperature-induced changes in the cavity detuning [74] or an additional delayed feedback [75] can evoke similar spontaneous symmetry breaking and motion of cavity solitons in a coherently driven optical resonator.

For an increasing pump amplitude, the PPS undergoes another Hopf-type bifurcation caused by a spatially symmetric eigenmode with a complex eigenvalue λ. This PPS undergoes oscillations and decays eventually (cf. Figure 15.8f).

15.4.3
Excitation and Dynamics of PPSs

To excite PPSs in a setting close to an experimental setting, one can use a seed pulse such that an additional pump term $E_{\text{seed}}(y,t)e^{ik_{\text{seed}}x-i\Omega_{\text{seed}}t}$ is required in the original model (Eqs. (15.1) and (15.2)). This seed pulse has a temporal duration of several photon lifetimes is extended along the x-direction and localized in y-direction. After a sufficiently long time interval (several photon-lifetimes), the intracavity field evolves into a train of moving wave packets; see Figure 15.9a and b. Expanding these periodic solutions into Fourier series in x, we find three distinct components corresponding to the signal, the idler, and the pump. The y dependencies of these components coincide with the soliton profiles discussed in the previous section; see Figure 15.8c. The train is periodic in x with period $P_x \approx 2\pi/|k_p - k_{\text{seed}}|$. It moves along the x-direction with phase velocity $v \approx 2\pi|\Omega_p - \Omega_{\text{seed}}|/|k_p - k_{\text{seed}}|$.

Figure 15.9c gives a summary of the families of PPSs for different pump amplitudes and k_{seed} (for a fixed seed power and the frequency $\Omega_{\text{seed}} = -0.5$). We note that only stable (dynamically) and slightly unstable solutions can be obtained solving the dynamical model (Eqs. (15.1) and (15.2)). The amplitude and period of the pattern depends on the transverse momentum of the seed pulse k_{seed}. The seed pulse excites a signal polariton with the transverse momentum k_{seed} and frequency

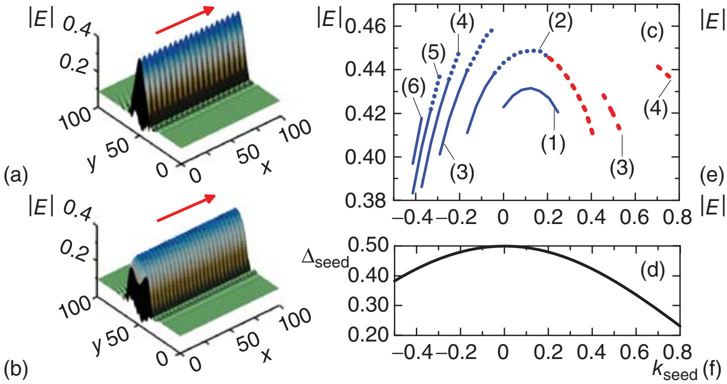

Figure 15.9 Family of 1D PPSs and their destabilization into 2D wave packets. (a, b) 2D profiles of stable PPS calculated in the original model (Eqs. (15.1) and (15.2)) for (a) $E_p = 0.136$ and $k_{seed} = 0$, (b) $E_p = 0.140$ and $k_{seed} = -0.4138$. The (red) arrow shows the direction of pattern motion. (c) Families of PPSs as a function of the seed pulse momentum (k_{seed}) calculated in the original model (Eqs. (15.1) and (15.2)) for different amplitudes of the pump beam: (1) for $E_p = 0.1355$, (2) $E_p = 0.136$, (3) $E_p = 0.137$, (4) $E_p = 0.138$, (5) $E_p = 0.139$, (6) $E_p = 0.140$. (d) Effective detuning of the signal polariton versus the seed pulse momentum ($\Omega_{seed} = -0.5$). (e, f) Modulationally unstable PPSs develop into (e) trains of well-separated 2D peaks for $E_p = 0.138$ and $k_{seed} = 0.7448$, (f) moving 2D cavity polariton solitons for $E_p = 0.1375$ and $k_{seed} = 0.4966$. For all calculations, $\Omega_p = -0.25$ and $k_p = 1.2$.

Ω_{seed}, which corresponds to the effective detuning $\Delta_{seed} = \Omega_{seed} - \Omega_{-}(k_{seed}, k_y = 0)$ of the model considered in the previous section (see Figure 15.9d). Therefore, varying the tilt of the seeding pulse and, thus, its transverse momentum k_{seed}, one can switch between different PPS branches within the soliton family presented in Figure 15.7a.

As it was shown in the previous section (cf. Figure 15.7a), the existence domain of stable PPS shifts into the direction of smaller optical pump amplitudes (E_p) for increasing signal detunings (Δ_s). In qualitative agreement, the seed pulse with a small momentum $k_{seed} \approx 0$, and thus with the maximum detuning, see Figure 15.9e, excites a PPS for a weaker optical pump E_p (and vice versa). The slight asymmetry with respect to $k_{seed} = 0$ can be explained by the fact that the effective masses of the signal and the idler polaritons are not constants as it was assumed in the model (Eqs. (15.12)–(15.14)). Our results unambiguously show the existence of a soliton family, which is continuously parameterized by the transverse momentum of the signal beam. Choosing an appropriate seed momentum, we can excite parametric solitons almost in the entire interval where the pump-only HS is bistable.

There is a qualitative difference of the stability properties of PPSs for negative and positive values of k_{seed}. Decreasing the momentum offset between signal and pump polaritons ($k_p - k_{seed}$) usually results in soliton destabilization on time scales much larger than the polariton life time (see dotted and dashed lines in Figure 15.9c). For negative momenta k_{seed}, the solitons found by direct numerical modeling of Eqs. (15.1) and (15.2) inherit both destabilization scenarios discussed in the previous section. Indeed, the PPSs undergo both symmetry breaking and motion instability (similar to Figure 15.8e) or they become oscillatory unstable (similar to Figure 15.8f), while increasing either the pump amplitude or the signal momentum (see dotted lines in the Figure 15.9c).

For positive k_{seed}, the PPS can become modulationally unstable against periodically modulated perturbations in x direction, that is, along the direction of the pump momentum (see dashed red lines in the Figure 15.9c). This modulational instability can trigger the fragmentation of the periodic pattern into a train of well-separated two-dimensional structures, see Figure 15.9e, which have a straightforward association with 2D CPSs reported in our recent work [52]. Other types of periodic trains of well-isolated multipeak structures have also been observed in our modeling; see an example of a triple peak one shown in Figure 15.9f.

Summarizing these results proves that four-wave mixing of microcavity polaritons promotes their localization in the direction associated with a positive effective mass. As a result, stable bright PPSs can be formed in the direction orthogonal to the pump momentum. Unlike nonparametric cavity solitons [28] they constitute a one-parameter soliton family. This soliton family can be continuously parameterized with the transverse momentum of the signal polariton, whereas the phase matching condition fixes the momentum of the idler component. The frequency-matching conditions together with the energy balance between signal and idler polaritons provide strict selection rules for the frequencies of the signal and idler components of the PPS. Any solution of this soliton family can be excited by means of the seed pulse with the appropriate momentum and frequency. Modulational instability can trigger the PPS into a train of well-separated two-dimensional localized solutions, which is discussed in the following section.

15.5
Two-Dimensional Moving Bright CPSs

These results indicate that two nonlinear mechanisms, having a different physical origin, permit self-localization of polariton packages along both transverse directions. The first one (see Section 15.3) is associated with the compensation of the negative mass of polaritons (or negative dispersion) by the repulsive (defocusing) nonlinearity. The second mechanism (see Section 15.4) is based on a four-wave mixing process of polaritons, which promotes the formation of bright parametric solitons in the direction associated with the positive effective mass, that is, in the direction orthogonal to the pump momentum.

The primary aim of this section is a rigorous theoretical proof of existence and stability of CPSs localized in both transverse dimensions [52]. We note that the generalization of the 1D solutions toward the 2D case is not straightforward because the effective mass of polaritons has different signs along x and along y directions, with the latter being perpendicular to the pump momentum (see Figure 15.6).

We have performed a set of simulations to match experiments. In order to achieve this, we have added the term $E_{\text{seed}}(x, y, t)e^{ik_{\text{seed}}x - i\Omega_{\text{seed}}t}$ representing a pulse, seeding a localized excitation to the equation for E. Using an elliptically shaped Gaussian beam elongated along the y axis and having a 5 ps duration, we have observed that the soliton profiles along x are easily generated, while their edges in the y direction are either converging, so that the beam is shrinking, or diverging, so that the beam is expanding [52, 55]. Remarkably, in a narrow window of the pump amplitudes the shrinking in y direction is suppressed, so that the emerging structures remain localized in both spatial coordinates over long propagation distances. Performing tedious numerical simulations of Eqs. (15.1) and (15.2) over the time spans exceeding 2.5 ns, we have found that 2D solitons with single and double humps represent stable attractors for a generic class of initial conditions within a finite interval of pump intensities (see Figure 15.10a and b). Figure 15.10c shows the branches of single- and double-hump stable 2D bright solitons. Both branches terminate at the respective Maxwell points, that is, a special value of the pump, such that the front between a respective 1D soliton stripe and an HS does not move (for details see [49, 52, 55] and references therein). The seed momenta applied in our simulation were $k_{\text{seed}} = 0$ (seed is orthogonal to the cavity plane) and $k_{\text{seed}} = k_p$ (seed is collinear with the pump). Both choices have led to the excitation of 2D CPSs, albeit for different powers. The $k_{\text{seed}} = k_p$ case appeared to be more efficient.

In order to elucidate the influence of the parametric four-wave mixing effects, we performed a Fourier transformation of both single- and double-hump CPS profiles and plot this spatial spectra in Figure 15.10d and e, respectively. Even though their spectra are broad, the signal and idler components are clearly distinguishable, especially for the double-hump solution (Figure 15.10e). Moreover, it turned

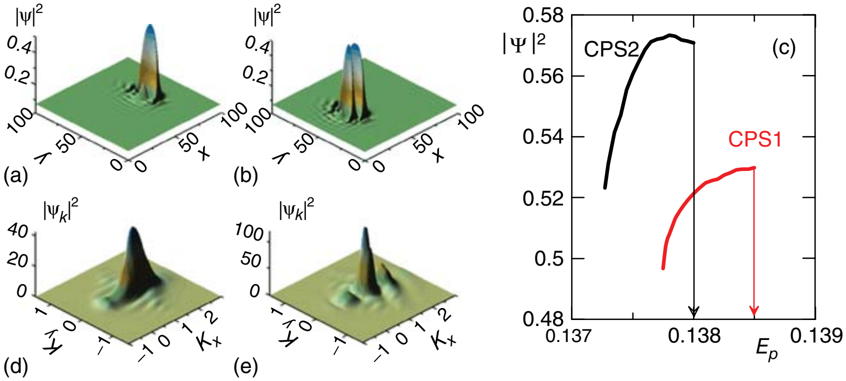

Figure 15.10 Two-dimensional stable bright polariton solitons. Profiles of the excitonic components $|\Psi|^2$ of the single-hump (a) and double-hump (b) 2D stable bright polariton solitons for $E_p = 0.1378$. (c) Maxima of $|\Psi|^2$ for different soliton solutions versus the pump amplitude E_p. CPS1 and CPS2 correspond to single- and double-hump solitons, respectively. Respective spatial spectra of the single- (d) and double-hump (e) 2D stable bright polariton solitons. Other parameters: $\Omega_p = -0.25$, $k_p = 1.2$.

out that the both 2D solitons are well approximated by a single wave packet of a periodic pattern, which represents PPS considered in the previous section (see Figure 15.9). These results imply that the parametric process indeed promotes localization of polaritons along the direction corresponding to the positive effective mass.

Thus, perhaps surprisingly, stable 2D polariton solitons may exist even if the polariton masses along orthogonal directions have opposite signs. From a fundamental point of view, to the best of our knowledge, this 2D CPS is a unique example of such localized solution. Unlike the X-waves existing in conservative systems [76] 2D CPSs are finite-energy localized states and possess exponentially decaying tails caused by the dissipations, which is natural for nonequilibrium systems.

15.6
Summary

We have reviewed the properties of bright polariton solitons having nonzero transverse momenta and existing in the spectral proximity of the lower polariton branch. We have gathered comprehensive numerical evidence unambiguously supporting the existence and practical stability of 2D solitary structures in polaritonic microcavities. These solitons are sustained due to the interplay of two distinct nonlinear mechanisms responsible for localization along orthogonal directions. Localization along the direction collinear with the pump momentum happens because the dispersion induced by the negative polariton mass is balanced by the repulsive polariton–polariton interaction. Localization along the orthogonal direction, where the effective mass is positive, occurs due to a parametric four-wave mixing process. Each of these processes taken separately supports two distinct families of 1D solitons, cf. Figures 15.3 and 15.9a.

Apart from the fundamental significance of our findings, they hold promise for practical applications. This promise arises from the fast (picoseconds) and strong nonlinear response of exciton-polaritons [9], prevailing in these aspects against the pure photonics nonlinearity appearing in semiconductor devices operating in the weak coupling regime. To date, potentially very attractive applications of 2D cavity solitons [28] have suffered from both the large excitation times and power requirements. Thus, the hybrid, half-light, half-matter polariton solitons have potentially significant advantages in all-optical signal-processing applications over the light-only cavity solitons.

Acknowledgments

Financial support by the Deutsche Forschungsgemeinschaft (DFG project EG344/2-1) and the Thuringian Ministry for Education, Science and Culture (TMESC project B514-11027) is acknowledged.

References

1. Scott, A. (1999) *Nonlinear Science*, Oxford University Press, Oxford.
2. Agrawal, G. (2001) *Nonlinear Fiber Optics*, Academic Press.
3. Kivshar, Y. and Agrawal, G. (2003) *Optical Solitons: From Waveguides to Photonic Crystals*, Academic Press, San Diego, CA.
4. Akhmediev, N. and Ankiewicz, A. (2005) *Dissipative Solitons*, Springer-Verlag, Berlin.
5. Hopfield, J.J. (1958) Theory of the contribution of excitons to the complex dielectric constant of crystals. *Phys. Rev.*, **112**, 1555.
6. Weisbuch, C., Nishioka, M., Ishikawa, A., and Arakawa, Y. (1992) Observation of the coupled exciton–photon mode splitting in a semiconductor quantum microcavity. *Phys. Rev. Lett.*, **69**, 3314.
7. Houdre, R., Stanley, R., Oesterle, U., Ilegems, M., and Weisbuch, C. (1994) Room-temperature cavity polaritons in a semiconductor microcavity. *Phys. Rev. Lett.*, **49**, 16 761.
8. Haug, H. and Koch, S.W. (1993) *Quantum Theory of the Optical and Electronic Properties of Semiconductors*, 2nd edn, World Scientific Publishing Co. Pte. Ltd., Hong Kong.
9. Kavokin, A., Baumberg, J., Malpuech, G., and Laussy, F. (2007) *Microcavities*, Oxford University Press.
10. Deveaud, B. (2007) *The Physics of Semiconductor Microcavities*, Wiley-VCH Verlag GmbH, Weinheim.
11. Sanvitto, D. and Timofeev, V. (2012) *Exciton Polaritons in Microcavities*, Springer-Verlag, Berlin.
12. Kasprzak, J., Richard, M., Kundermann, S., Baas, A., Jeambrun, P., Keeling, J.M., Marchetti, F.M., Szymanska, M.H., Andre, R., Staehli, J.L., Savona, V., Littlewood, P.B., Deveaud, B., and Dang, L.S. (2006) Bose–Einstein condensation of exciton polaritons. *Nature (London)*, **443**, 409.
13. Balili, R., Hartwell, V., Snoke, D., Pfeiffer, L., and West, K. (2007) Bose–Einstein condensation of microcavity polaritons in a trap. *Science*, **316**, 1007.
14. Deveaud-Plédran, B. (2012) On the condensation of polaritons. *J. Opt. Soc. Am. B*, **29**, 138.
15. Carusotto, I. and Ciuti, C. (2004) Probing microcavity polariton superfluidity through resonant Rayleigh scattering. *Phys. Rev. Lett.*, **93**, 166 401.
16. Amo, A., Lefrere, J., Pigeon, S., Adrados, C., Ciuti, C., Carusotto, I., Houdre, R., Giacobino, E., and Bramati, A. (2009) Superfluidity of polaritons in semiconductor microcavities. *Nat. Phys.*, **5**, 805.
17. Christopoulos, S., Baldassari, G., Grundy, A.J., Lagoudakis, P.G., Kavokin, A.V., Baumberg, J.J., Christmann, G., Butte, R., Feltin, E., Carlin, J.F., and Grandjean, N. (2007) Room-temperature polariton lasing in semiconductor microcavities. *Phys. Rev. Lett.*, **98**, 126 405.
18. Schneider, C., Rahimi-Iman, A., Kim, N.Y., Fischer, J., Savenko, I.G., Amthor, M., Lermer, M., Wolf, A., Worschech, L., Kulakovskii, V.D., Shelykh, I.A., Kamp, M., Reitzenstein, S., Yamamoto, A.F.Y., and Höfling, S. (2013) An electrically pumped polariton laser. *Nat. Lett.*, **497**, 348.
19. Schmitt-Rink, S., Chemla, D.S., and Miller, D.A. (1985) Theory of transient excitonic optical nonlinearities in semiconductor quantum-well structures. *Phys. Rev. B*, **32**, 6601.
20. Rochat, G., Ciuti, C., Savona, V., Piermarocchi, C., Quattropani, A., and Schwendimann, P. (2000) Excitonic Bloch equations for a two-dimensional system of interacting excitons. *Phys. Rev. B*, **61**, 13 856.
21. Tredicucci, A., Chen, Y., Pellegrini, V., Boerger, M., and Bassani, F. (1996) Optical bistability of semiconductor microcavities in the strong-coupling regime. *Phys. Rev. A*, **54**, 3493.
22. Baas, A., Karr, J.P., Eleuch, H., and Giacobino, E. (2004) Optical bistability in semiconductor microcavities. *Phys. Rev. A*, **69**, 023 809.
23. Bajoni, D., Semenova, E., Lemaitre, A., Bouchoule, S., Wertz, E., Senellart, P., Barbay, S., Kuszelewicz, R., and Bloch, J. (2008) Optical bistability in a gaas-based

polariton diode. *Phys. Rev. Lett.*, **101**, 266 402.

24. Michaelis, D., Peschel, U., and Lederer, F. (1997) Multistable localized structures and superlattices in semiconductor optical resonators. *Phys. Rev. A*, **56**, R3366.
25. Brambilla, M., Lugiato, L., Prati, F., Spinelli, L., and Firth, W. (1997) Spatial soliton pixels in semiconductor devices. *Phys. Rev. Lett.*, **79**, 2042.
26. Rosanov, N. (2002) *Spatial Hysteresis and Optical Patterns*, Springer-Verlag, Berlin.
27. Peschel, U., Michaelis, D., and Weiss, C.O. (2003) Spatial solitons in optical cavities. *IEEE J. Quantum Electron.*, **39**, 51.
28. Ackemann, T., Firth, W.J., and Oppo, G. (2009) Fundamentals and applications of spatial dissipative solitons in photonic devices. *Adv. At. Mol. Opt. Phy.*, **57**, 324.
29. Baas, A., Karr, J.P., Romanelli, M., Bramati, A., and Giacobino, E. (2004) Optical bistability in semiconductor microcavities in the nondegenerate parametric oscillation regime: analogy with the optical parametric oscillator. *Phys. Rev. B*, **70**, 161 307(R).
30. Ciuti, C., Schwendimann, P., Deveaud, B., and Quattropani, A. (2000) Theory of the angle-resonant polariton amplifier. *Phys. Rev. B*, **62**, 4825(R).
31. Ciuti, C., Schwendimann, P., and Quattropani, A. (2003) Theory of polariton parametric interactions in semiconductor microcavities. *Semicond. Sci. Technol.*, **18**, 279.
32. Whittaker, D.M. (2001) Classical treatment of parametric processes in a strong-coupling planar microcavity. *Phys. Rev. B*, **63**, 193 305.
33. Savvidis, P.G., Baumberg, J.J., Stevenson, R.M., Skolnick, M.S., Whittaker, D.M., and Roberts, J.S. (2000) Angle-resonant stimulated polariton amplifier. *Phys. Rev. Lett.*, **84**, 1547.
34. Gippius, N., Tikhodeev, S., Kulakovskii, V., Krizhanovskii, D., and Tartakovskii, A. (2004) Nonlinear dynamics of polariton scattering in semiconductor microcavity: bistability vs. stimulated scattering. *Europhys. Lett.*, **67**, 997.
35. Whittaker, D.M. (2005) Effects of polariton-energy renormalization in the microcavity optical parametric oscillator. *Phys. Rev. B*, **71**, 115 301.
36. Wouters, M. and Carusotto, I. (2007) Parametric oscillation threshold of semiconductor microcavities in the strong coupling regime. *Phys. Rev. B*, **75**, 075 332.
37. Krizhanovskii, D.N., Gavrilov, S.S., Love, A.P.D., Sanvitto, D., Gippius, N.A., Tikhodeev, S.G., Kulakovskii, V.D., Whittaker, D.M., Skolnick, M.S., and Roberts, J.S. (2008) Self-organization of multiple polariton–polariton scattering in semiconductor microcavities. *Phys. Rev. B*, **77**, 115 336.
38. Lagoudakis, K., Wouters, M., Richard, M., Baas, A., Carusotto, I., Andre, R., Dang, L., and Deveaud-Pledran, B. (2008) Quantized vortices in an exciton-polariton condensate. *Nat. Phys.*, **4**, 706.
39. Lagoudakis, K.G., Ostatnický, T., Kavokin, A.V., Rubo, Y.G., André, R., and Deveaud-Plédran, B. (2009) Observation of half-quantum vortices in an exciton-polariton condensate. *Science*, **326**, 974.
40. Amo, A., Pigeon, S., Sanvitto, D., Sala, V.G., Hivet, R., Carusotto, I., Pisanello, F., Leménager, G., Houdré, R., Giacobino, E., Ciuti, C., and Bramati, A. (2011) Polariton superfluids reveal quantum hydrodynamic solitons. *Science*, **332**, 1167.
41. Flayac, H., Solnyshkov, D.D., and Malpuech, G. (2011) Oblique half-solitons and their generation in exciton-polariton condensates. *Phys. Rev. B*, **83**, 193 305.
42. Hivet, R., Flayac, H., Solnyshkov, D.D., Tanese, D., Boulier, T., Andreoli, D., Giacobino, E., Bloch, J., Bramati, A., Malpuech, G., and Amo, A. (2012) Half-solitons in a polariton quantum fluid behave like magnetic monopoles. *Nat. Phys.*, **8**, 724.
43. Solnyshkov, D., Flayac, H., and Malpuech, G. (2012) Stable magnetic monopoles in spinor polariton condensates. *Phys. Rev. B*, **85**, 073 105.
44. Flayac, H., Solnyshkov, D.D., Shelykh, I., and Malpuech, G. (2013) Transmutation

of skyrmions to half-solitons driven by the nonlinear optical spin hall effect. *Phys. Rev. Lett.*, **110**, 016 404.

45. Larionova, Y., Stolz, W., and Weiss, C. (2008) Optical bistability and spatial resonator solitons based on exciton-polariton nonlinearity. *Opt. Lett.*, **33**, 321.
46. Amo, A., Sanvitto, D., Laussy, F.P., Ballarini, D., del Valle, E., Martin, M.D., Lemaître, A., Bloch, J., Krizhanovskii, D.N., Skolnick, M.S., Tejedor, C., and Vina, L. (2009) Collective fluid dynamics of a polariton condensate in a semiconductor microcavity. *Nature (London)*, **457**, 291.
47. Sanvitto, D., Amo, A., Laussy, F.P., Lemaitre, A., Bloch, J., Tejedor, C., and Vina, L. (2010) Polariton condensates put in motion. *Nanotechnology*, **21**, 134 025.
48. Amo, A., Sanvitto, D., and Vina, L. (2010) Collective dynamics of excitons and polaritons in semiconductor nanostructures. *Semicond. Sci. Technol.*, **25**, 43 001.
49. Yulin, A.V., Egorov, O.A., Lederer, F., and Skryabin, D.V. (2008) Dark polariton solitons in semiconductor microcavities. *Phys. Rev. A*, **78**, 061 801(R).
50. Egorov, O.A., Skryabin, D.V., Yulin, A.V., and Lederer, F. (2009) Bright cavity polariton solitons. *Phys. Rev. Lett.*, **102**, 153 904.
51. Skryabin, D., Egorov, O., Gorbach, A., and Lederer, F. (2010) One-dimensional polariton solitons and soliton waveguiding in microcavities. *Superlattices Microstruct.*, **47**, 5.
52. Egorov, O.A., Gorbach, A.V., Lederer, F., and Skryabin, D.V. (2010) Two-dimensional localization of exciton polaritons in microcavities. *Phys. Rev. Lett.*, **105**, 073 903.
53. Egorov, O.A., Skryabin, D.V., and Lederer, F. (2010) Polariton solitons due to saturation of the exciton–photon coupling. *Phys. Rev. B*, **82**, 165 326.
54. Egorov, O.A., Skryabin, D.V., and Lederer, F. (2011) Parametric polariton solitons in coherently pumped semiconductor microcavities. *Phys. Rev. B*, **84**, 165 305.
55. Egorov, O.A., Skryabin, D.V., and Lederer, F. (2012) Theory of polariton solitons in semiconductor microcavities, in *Nonlinear Photonics and Novel Optical Phenomena*, Springer Series in Optical Sciences, vol. **170**, Springer-Verlag, pp. 171–193.
56. Egorov, O.A. and Lederer, F. (2013) Formation of hybrid parametric cavity polariton solitons. *Phys. Rev. B*, **87**, 115 315.
57. Egorov, O.A. and Lederer, F. (2014) Pseudospin-induced motion of cavity polariton soliton molecules. *Opt. Lett.*, **39**, 4029.
58. Bakonyi, Z., Michaelis, D., Peschel, U., Onishchukov, G., and Lederer, F. (2002) Dissipative solitons and their critical slowing down near a supercritical bifurcation. *J. Opt. Soc. Am. B*, **19** (3), 487.
59. Leo, F., Coen, S., Kockaert, P., Gorza, S., Emplit, P., and Haelterman, M. (2010) Temporal cavity solitons in one-dimensional Kerr media as bits in an all-optical buffer. *Nat. Photonics*, **4**, 471.
60. Sich, M., Krizhanovskii, D., Skolnick, M.S., Gorbach, A.V., Hartley, R., Skryabin, D., Cerda-Mendez, E., Biermann, K., Hey, R., and Santos, P. (2012) Observation of bright polariton solitons in a semiconductor microcavity. *Nat. Photonics*, **6**, 50.
61. Sich, M., Fras, F., Chana, J.K., Skolnick, M.S., Krizhanovskii, D.N., Gorbach, A.V., Hartley, R., Skryabin, D.V., Gavrilov, S.S., Cerda-Méndez, E.A., Biermann, K., Hey, R., and Santos, P.V. (2014) Effects of spin-dependent interactions on polarization of bright polariton solitons. *Phys. Rev. Lett.*, **112**, 046 403.
62. Houdre, R., Gibernon, J., Pellandini, P., Stanley, R., Oesterle, U., Weisbuch, C., Gorman, J., Roycroft, B., and Ilegems, M. (1995) Saturation of the strong-coupling regime in a semiconductor microcavity: free-carrier bleaching of cavity polaritons. *Phys. Rev. B*, **52**, 7810.
63. Lugiato, L.A. and Lefever, R. (1987) Spatial dissipative structures in passive optical systems. *Phys. Rev. Lett.*, **58**, 2209.

64. Egorov, O., Lederer, F., and Staliunas, K. (2007) Subdiffractive discrete cavity solitons. *Opt. Lett.*, **32**, 2106.
65. Egorov, O., Lederer, F., and Kivshar, Y. (2007) How does an inclined holding beam affect discrete modulational instability and solitons in nonlinear cavities? *Opt. Express*, **15**, 4149.
66. Egorov, O., Lederer, F., and Staliunas, K. (2010) Theory of Bloch cavity solitons. *Phys. Rev. A*, **82**, 43 830.
67. Etrich, C., Iliew, R., Staliunas, K., Lederer, F., and Egorov, O. (2011) Ab initio dissipative solitons in an all-photonic crystal resonator. *Phys. Rev. A*, **84**, 21 808.
68. Pedaci, F., Barland, S., Caboche, E., Genevet, P., Giudici, M., Tredicce, J., Ackemann, T., Scroggie, A., Firth, W., Oppo, G., Tissoni, G., and Jäger, R. (2008) All-optical delay line using semiconductor cavity solitons. *IEEE J. Quantum Electron.*, **92**, 011 101.
69. Skryabin, D. (1999) Instabilities of cavity solitons in optical parametric oscillators. *Phys. Rev. E*, **60**, 3508.
70. Skryabin, D.V., Champneys, A.R., and Firth, W.J. (2000) Frequency selection by soliton excitation in nondegenerate intracavity down-conversion. *Phys. Rev. Lett.*, **84**, 463.
71. Etrich, C., Michaelis, D., and Lederer, F. (2002) Bifurcations, stability, and multistability of cavity solitons in parametric downconversion. *J. Opt. Soc. Am. B*, **19**, 792.
72. Michaelis, D., Peschel, U., Etrich, C., and Lederer, F. (2003) Quadratic cavity solitons - the up-conversion case. *J. Opt. Soc. Am. B*, **29**, 255.
73. Avitabile, D., Lloyd, D.J., Burke, J., Knobloch, E., and Sandstede, B. (2010) To snake or not to snake in the planar Swift-Hohenberg equation. *SIAM J. Appl. Dyn. Syst.*, **9**, 704.
74. Scroggie, A., McSloy, J., and Firth, W. (2002) Self-propelled cavity solitons in semiconductor microcavities. *Phys. Rev. E*, **66**, 036 607.
75. Tlidi, M., Vladimirov, A., Pieroux, D., and Turaev, D. (2009) Spontaneous motion of cavity solitons induced by a delayed feedback. *Phys. Rev. Lett.*, **103**, 103 904.
76. Trapani, P.D., Valiulis, G., Piskarskas, A., Jedrkiewicz, O., Trull, J., Conti, C., and Trillo, S. (2003) Spontaneously generated X-shaped light bullets. *Phys. Rev. Lett.*, **91**, 93 904.

16

Data Methods and Computational Tools for Characterizing Complex Cavity Dynamics

J. Nathan Kutz, Steven L. Brunton, and Xing Fu

16.1

Introduction

Data-driven methods [1] are transforming the engineering, physical, and biological sciences. Indeed, innovative uses of machine learning [2–4], dimensionality reduction [1–4], equation-free methods [5–7], sparse sensing [8–11], and/or network characterization techniques are allowing for significant advances in engineering designs for the prediction and control of highly complex, often networked, systems. Integrating together one or more of the aforementioned methodologies often provides transformative analytical tools and algorithms for characterizing the underlying, typically low-dimensional, dynamics of the complex system. Despite their myriad successes, many of these innovative mathematical strategies have yet to be applied to a wide range of engineering systems. Of particular interest in this manuscript is the use of modern data methods for building self-tuning optical systems such as mode-locked lasers [12–16]. Thus, we demonstrate how machine learning strategies coupled with sparse sensing can provide a transformative paradigm for enacting adaptive and robust control laws for self-tuning complex systems.

To demonstrate how data-driven modeling strategies can be applied generally in complex systems, a case study of mode-locked fiber lasers is conducted. Although more than two decades in development, such fiber lasers have yet to realize an adaptive, robust, and self-tuning control schemes capable of revolutionizing both commercial and academic sectors of ultrafast science. Critical to moving this technology forward are the recently demonstrated servo-control of optical components [17, 18]. With the ability to algorithmically modulate and control the waveplates and polarizer in a nonlinear polarization rotation (NPR)-based laser, all the critical components exist to enact a data-driven control strategy [12–16] using adaptive, equation-free control architectures [19]. We demonstrate that robust and self-tuning mode-locked operation can be achieved by integrating data methods so that fiber laser performance is optimized. To our knowledge, this is the first demonstration in the optical sciences of the

Nonlinear Optical Cavity Dynamics: From Microresonators to Fiber Lasers, First Edition.
Edited by Philippe Grelu.
© 2016 Wiley-VCH Verlag GmbH & Co. KGaA. Published 2016 by Wiley-VCH Verlag GmbH & Co. KGaA.

integration of machine learning techniques with adaptive control, thus allowing for potentially transformative performance gains in fiber lasers.

The NPR-based mode-locked laser is chosen for illustration since it is one of the most commercially successful lasers to date due to its reliance on simple off-the-shelf telecom components, rendering it a highly cost-effective mode-locking source. In addition, it is anticipated that within the next decade, mode-locked fiber lasers will close the order-of-magnitude performance gap in comparison with their solid-state counterparts [20], a performance gap largely imposed by the multipulsing instability (MPI) [21–23] that may be circumvented and/or suppressed with the control architectures advocated here. Specifically, one of the most intriguing possibilities for designing around the deleterious MPI is the NPR laser where cavity saturable absorption is achieved using a combination of waveplates and polarizer [24–27]. Tremendous performance advances have been recently made in power delivery by using all-normal dispersion fiber cavities [28–30] and/or self-similar pulse evolutions [31–33]. Indeed, a distinct and critical advantage of such lasers is that the transmission function generated by the NPR dynamics is periodic, thus allowing for engineering strategies whereby the MPI can be circumvented and significant, order-or-magnitude performance gains can be achieved [15, 23, 34]. However, such commercial lasers must enforce strict environmental control to maintain performance, that is, the fiber is pinned into place and shielded from temperature fluctuations. Such system sensitivity has prevented performance advances, limiting power and pulse widths. Our adaptive control strategy overcomes this cavity sensitivity while optimizing, resulting in significant performance enhancements.

The demonstrated success of the data methods applied to the laser system is only a single realization of the transformative power of the advocated techniques. In this chapter, we first outline the key data methods that are broadly applicable across disciplines. This is followed by a discussion of the adaptive, equation-free control architecture that is capable of self-tuning a complex system. With these two subjects discussed, the mode-locked fiber laser is demonstrated in full detail, showing the power and success that can be achieved in combining the methods. A number of other example problems are illustrated before our concluding remarks and technological outlook are espoused.

16.2
Data Methods

Before proceeding to apply the mathematical techniques of data analysis (see [1] for extensive details), we first highlight some of the important methods that have led to transformative ways to characterize complex systems. This includes methods of machine learning aimed at reducing the dimensionality of a given problem, methods that make use of a small number of measurements (sparse sampling) to reconstruct full state estimates, and sophisticated search algorithms for building libraries of known low-dimensional dynamics.

16.2.1
Dimensionality-Reduction: Principal Components Analysis

The goal of machine learning strategies is to reveal critical insight into underlying, and often dimensionally reduced, correlated patterns and/or clusters of activity in a given system [2–4]. Such underlying patterns are central in creating an expert-in-the-loop framework that can replace human expertise in decision making and control strategies. In the framework of a complex system, the goal is to use such mathematical strategies to allow an algorithm to learn the underlying characteristics and behavior, both good and bad, of the system itself. With such an algorithm, one can envision replacing a highly experienced researcher with a fully automated and extremely rapid self-tuning system. Given the successful and highly transformative impact that machine learning is having across all disciplines, it is natural to also implement such strategies in fiber laser systems.

To be more precise about the nature of the dimensionality reduction, consider the dynamics of a complex system given by the governing equations

$$\mathbf{u}_t = N(\mathbf{u}, \mathbf{u}_x, \mathbf{u}_{xx}, \dots, x, t), \tag{16.1}$$

where $\mathbf{u}(x, t)$ is a vector field that is a function of both space (x) and time (t), and $N(\cdot)$ determines the nonlinear evolution of the system that depends upon space, time, $\mathbf{u}$, and its spatial derivatives. Such nonlinear equations do not generally have close-form solutions, thus inducing one to attempt numerical solutions that can take the form

$$\mathbf{u}(x, t) = \sum_{n=0}^{N} a_n(t)\psi_n(x) = \mathbf{a}\boldsymbol{\Psi}, \tag{16.2}$$

where $\psi_n(x)$ are spatial basis modes and $a_n(t)$ are their temporal evolution determined by Galerkin projection [1]. Note that the matrix $\boldsymbol{\Psi}$ is the collection of all spatial modes (arranged in columns), while the corresponding time-evolution can be represented by the vector $\mathbf{a}$. Typically, the N-modes are chosen for either computational convenience, such as Fourier modes, or for their known application to the specific problem at hand, such as one of the many special functions of mathematical physics. For many complex systems, such as Galerkin projection requires $N \gg 1$ in order for the solution to converge to the correct solution, thus requiring a high-dimensional computation and many compute cycles.

Dimensionality reduction can be used to circumvent the problem of solving such high-dimensional systems. In particular, we use methods based upon the singular value decomposition (SVD), or alternatively a variant of *principal component analysis* (PCA), *proper mode decomposition* (POD), *Hotelling transform*, *empirical orthogonal function*s (EOF), *reduced order modeling* (ROM), *dimensionality reduction*, and/or *Karhunen–Loève decomposition*, as it also known in the literature (see [1] and references therein). The goal is to discover the *optimal* basis to be used in Eq. (16.2). First, we collect K snapshots of our dynamics in a matrix $\mathbf{A}$:

$$\mathbf{A} = [\mathbf{u}(x, t_j)\ \mathbf{u}(x, t_{j+1})\ \cdots\ \mathbf{u}(x, t_{j+K-1})]. \tag{16.3}$$

The SVD guarantees the decomposition of the matrix into three matrices

$$\mathbf{A} = \mathbf{\Psi}\mathbf{\Sigma}\mathbf{V}^*, \tag{16.4}$$

where $\mathbf{\Psi}$ contains the guaranteed optimal modes, in an L^2 sense, representing the snapshots in $\mathbf{A}$ while $\mathbf{V}$ gives the time-dynamics of these modes. The diagonal matrix $\mathbf{\Sigma}$ contains the non-negative singular values ordered in terms of their importance (dominance) and provides the necessary criteria for determining the number of modes necessary to perform a low-rank approximation to the dynamics. In particular, low-dimensional projection is accomplished by recognizing that in most systems one can truncate with r modes in Eq. (16.2) with $r \ll N$. Thus, dimensionality reduction is accomplished by identifying and using an optimal mode basis.

16.2.2
Search Algorithms and Library Building

Optimization of cavity performance is of primary importance in our advocated self-tuning architecture. However, for high-dimensional parameter spaces, the objective function landscape often has numerous local minima and maxima, thus rendering many convex optimization strategies useless for finding global minima/maxima. For such problems, use of the so-called genetic algorithms, which are a subset of evolutionary algorithms, becomes instrumental [1]. The principle is quite simple and mirrors what is perceived to occur in evolution and/or genetic mutations. In particular, given a set of feasible trial solutions (either constrained or unconstrained), the objective function is evaluated. In the language of genetic algorithms, the objective function is now called the *fitness function*. The idea is to keep those solutions that give the maximal value of the objective function and mutate them in order to try and do even better. Thus beneficial mutations, in the sense of giving a better maximization, are kept while those that perform poorly are thrown away, that is, survival of the fittest. This process is repeated through a prescribed number of iterations, or generations, with the idea that better and better fitness function values are generated via the mutation process. The advantage of such a strategy is that the maximization process does not get stuck in local maxima, allowing the algorithm to find the global maximizer. The genetic algorithm and machine learning strategy partner naturally to give an optimal way of informing an expert-in-the-loop strategy.

To be more precise about the algorithm, consider the parameter optimization problem for a given complex system. In particular, we are typically given an objective function, $O(\mathbf{u}, \mathbf{p})$, that we wish to maximize. Here, $\mathbf{u}$ is the state of the system as governed by Eq. (16.1), while the vector $\mathbf{p}$ contains all the tuning (input) parameters into the system. Assume that m initial guesses are given for vector $\mathbf{p}$ and denote the ith initial guess as $\mathbf{p}_i$, where $i = 1, 2, \cdots, m$. In the next step (generation), m solutions of the complex system (Eq. (16.1)) and the corresponding objective functions are computed. The complex dynamics is simulated over a sufficiently long time so that attractive states, if it is in a favorable parameter regime, occur. The objective function of the solutions is compared with each other after each generation and ordered so that the first $p < m$ gives the most favorable values of the objective function. Then,

$$\mathbf{p}_i \quad i = 1, 2, \cdots, p$$

are kept, while

$$\mathbf{p}_i \quad i = p + 1, p + 2, \cdots, m$$

are discarded. As a supplement to the $m - p$ discarded parameter sets, $m - p$ new trial parameter sets $(\mathbf{x}_k)$ where $k = m - p, \cdots, m$ are randomly mutated from the p best objective function values. This process is repeated for a finite number of generations. One can also build a control loop on the algorithm, which enables the algorithm to continue running until the objective function value potentially converges. Genetic algorithms are now common place for optimizing high-dimensional parameter spaces.

If the parameter space $\mathbf{p}$ is reasonably small, then alternatives to the genetic algorithm can be implemented. In particular, we have advocated a toroidal search algorithm to both to identify favorable states that may be used in conjunction with the adaptive controller, and also to identify and estimate the underlying parameters, which was advocated in [12, 13]. In the case of an NPR mode-locked laser, all of the control inputs are periodic, so the input space forms a high-dimensional torus. It is possible to efficiently sample this toroid by increasing each of the control angles at incommensurate angular rates. This means that the ratio of each of the angular rates is an irrational number, and it is simple to show that after large enough time, the sampling scheme will approach arbitrarily close to every point in the input space. It turns out that for two rotating angles, the optimal incommensurate rates will be related by the golden ratio. If the input parameters are not naturally periodic, they can be easily made to be so by periodic extension. Thus, a nonperiodic input parameter $\beta \in [0, 1]$ can be made periodic by first scanning from zero to unity and then from unity back to zero, thus allowing for a toroidal search.

Exploring the input parameter space is a central part of the overall control strategy. Both the genetic algorithm and the toroidal search provide a necessary mechanism for identifying a set of candidate solutions for use with the adaptive control algorithm. In addition to a set of candidate solutions, the search algorithms also provide well-stereotyped patterns that change with parameters that may be otherwise difficult to measure directly. Therefore, we use the library-building phase to construct a library of toroidal search patterns as we slowly vary the input parameters. Once the library is built, when the complex system is turned on, or when it suffers from a large disturbance and the optimal solution is degraded, we repeat a short toroidal search protocol and compare against our library to estimate the underlying parameter values. Once the parameters are identified, it is possible to go directly to the predetermined optimal inputs. At this point, the adaptive controller is applied to compensate for any uncertainty or error in the parameter estimation, and also to track slowly varying changes to parameters.

16.2.3
Sparse Measurements and Compressive Sensing

Sparsity is playing an increasingly important role in many practical engineering systems [8–11]. The term refers to the limited number, or sparse, measurements and/or small number of modes required to represent a given state of a system. In engineering systems, sparsity arises naturally as a consequence of the limited number of sensors that monitor a high-dimensional system. Thus, the full state can rarely be measured, but some small subset is used to infer the full state. Consider the dynamical system Eq. (16.1) that we assumed to be of dimension $N \gg 1$. To monitor the system in practice, a limited number of measurements q are taken of the full state

$$\hat{\mathbf{u}} = \mathbf{\Phi}\mathbf{u}, \tag{16.5}$$

where $\hat{\mathbf{u}}$ is a q-dimensional measurement of the full N-dimensional space $\mathbf{u}$ (note that $q \ll N$). The matrix Φ is the measurement matrix that projects the full state onto the sparse number of measurements. In most complex systems, the measurements taken are at given spatial locations so that the Φ matrix takes the following form:

$$\Phi = \begin{bmatrix} 0 & \cdots & 0\ 1 & 0 & \cdots & & & & & & 0 \\ 0 & \cdots & & & \cdots & 0 & 1 & 0 & \cdots & & 0 \\ 0 & \cdots & & & & & \cdots & 0 & 1\ 0 & \cdots & 0 \end{bmatrix}, \tag{16.6}$$

where the nonzero entries are the spatial locations of the complex system where measurements take place.

Recall from Eq. (16.2) that an expression is given for the modal expansion of the complex field $\mathbf{u}$. Combining with Eq. (16.5) gives the following:

$$\hat{\mathbf{u}} = \mathbf{\Phi\Psi a}. \tag{16.7}$$

This equation, where the measurements $\hat{\mathbf{u}}$, modes $\mathbf{\Psi}$, and measurement locations $\mathbf{\Phi}$ are all known, is the crux of compressive sensing [8–11]. Specifically, this linear algebra system is a highly underdetermined system for $\mathbf{a}$ given that the number of measurements q are much smaller than the dimension of the system N. Thus, there exists an infinite number of solutions to this problem. A standard way to produce a solution is by computing the pseudoinverse of the matrix composition $\mathbf{\Phi\Psi}$. This gives a nonsparse solution $\mathbf{a}$ that has the smallest L^2-norm (or Cartesian length). However, since we know the dynamics are low rank in the optimal basis $\mathbf{\Psi}$, we can instead solve this underdetermined system by finding the solution $\mathbf{a}$ that satisfies

$$\mathbf{a} = \arg \min_{\mathbf{a}} \| \mathbf{a}\|_1 \text{such that } \mathbf{\Phi\Psi a} = \hat{\mathbf{u}}, \tag{16.8}$$

where the subscript on the norm denotes the L^1 norm. This optimization problem is known to yield sparsity-promoting solutions, where most of the components of the vector $\mathbf{a}$ are zero. In so doing, the nonzero entries of $\mathbf{a}$ are found to be the most significant in representing the solution with only a small number of modes needed [1]. Thus, the sparse representation of the solution allows one to easily *classify* and *reconstruct* the solution with a limited number of measurements [1, 13, 14].

16.2.4
Sparse Representation and Classification

In addition to compressive sensing, we can also use the associated concept of sparse representation. For our purposes, we use a sparse number of features of our data (a spectrogram to be precise) to represent the dynamics. In practice then, what is required is a method for *classifying* the current state or the system with a representative (sparse) library. The algorithm implemented here creates a large number of objective function spectrograms by using the toroidal search. These are then correlated with each other via an SVD. Only the dominant SVD modes (capturing 99.9% of the correlation energy) are retained and used to characterize a particular parameter space.

More precisely, assume that we have computed the spectrogram (or some other feature selection) $\mathbf{S}_k$ for a large number of possible parameter values k ranging from 1 to M. For each k, we apply the SVD to the spectrogram [1]:

$$\mathbf{S}_k = \mathbf{U}_k \mathbf{\Sigma}_k \mathbf{V}_k^*, \tag{16.9}$$

where $\mathbf{U}_k = [\mathbf{u}_{k_1} \mathbf{u}_{k_2} \cdots \mathbf{u}_{k_n}]$. For each parameter value k, we keep the first m ($m < n$) modes of $\mathbf{U}_k$ containing the most energy, resulting in a low-rank approximation to $\mathbf{S}_\mathrm{k}$. These modes are stored in the modal library $\mathbf{U}_L$ such that

$$\mathbf{U}_L = [\tilde{\mathbf{U}}_1\ \tilde{\mathbf{U}}_2\ \cdots\ \tilde{\mathbf{U}}_M], \tag{16.10}$$

where the kth sublibrary $\tilde{\mathbf{U}}_k$ contains the first m modes of $\mathbf{U}_k = [\mathbf{u}_{k_1} \mathbf{u}_{k_2} \cdots \mathbf{u}_{k_m}]$. Since we have kept only a small number of the modes, this is the basis for the sparse representation. Once we have constructed our dimensionally reduced modes library, we can take a measurement of the complex system (the objective function) and compute the spectrogram. Note that the sampling time does not have to be of the same length as the time series collected when the library was built. We perform an SVD reduction on the measured spectrogram and keep the first m modes as before. With the most important (dominant) modes from the measurement in hand, we can do an L_1-norm library search, thus promoting sparsity in our solution [1]. In the L^1-norm search, our objective is to find a vector

$$\mathbf{a} = \arg \min_{\mathbf{a}} \|\mathbf{a}\|_1 \text{ subject to } \mathbf{U}_L \cdot \mathbf{a} = \mathbf{u}_{m_1}. \tag{16.11}$$

Here, we require the number of library modes to be greater than the dimensionality of the frequency domain. Given this condition, this becomes an underdetermined linear system of equations. The L^1-norm minimization produces a sparse vector $\mathbf{a}$. The nonzero elements of vector a act as a classifier (indicator function) for identifying which sublibrary the birefringence falls into. Thus, if the largest element falls into the ith sublibrary, the recognized birefringence value is equal to K_i.

This sparsity-promoting optimization, when used in conjunction with the unique spectrograms, gives a rapid and accurate classification scheme. More sophisticated sparse classification/recognition strategies can be applied if desired [35], potentially yielding even better recognition results.

16.3
Adaptive, Equation-Free Control Architecture

In partnership with the data methods highlighted in the previous section, it is important to implement a system controller that is capable of making use of the data and which does not rely on standard *linear* input–output relationships, especially as the systems under consideration are driven strongly by nonlinearity. Thus, an *equation-free* control architecture, meaning we may not know the underlying governing equations, is highly desirable. Extremum-seeking control is an adaptive control law that finds and tracks local maxima of an objective function by sinusoidally varying a set of input parameters and measuring the consequent variation of the objective function [19]. The resulting controller does not rely on a model of the dynamics that relate the input parameters to the objective function, making it especially useful for complex, nonlinear systems with disturbances that are difficult to model. Instead, the measured variation in the objective function is compared with the varying input signal to dynamically improve an estimate of the optimal input parameter. If designed correctly, extremum seeking is guaranteed to stably converge to a neighborhood of the control input p^* that yields a local maximum of the objective function.

Figure 16.1 shows an extremum-seeking controller for a complex system with a single-input and a single-output (SISO). The algorithm works by adding a perturbation signal $a \sin(\omega t)$ to the *best guess* of the input $\hat{p}$ that maximizes the quantity of interest, namely, the objective function. The perturbation passes through the system and results in a perturbation in the output. The high-pass filter of this output is a signal that oscillates about zero mean. Multiplying the high-pass filtered

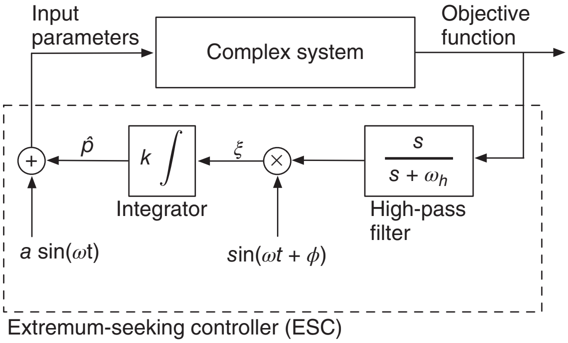

Figure 16.1 Schematic for single-input, single-output (SISO) extremum-seeking controller.

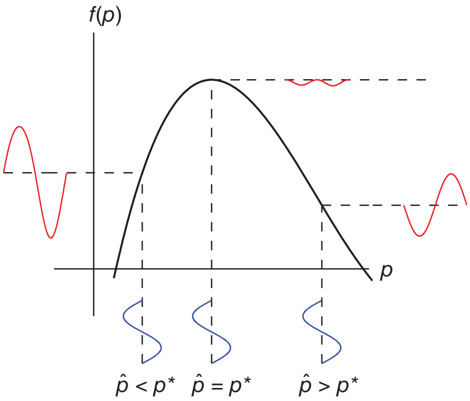

Figure 16.2 Illustration of sinusoidal perturbation to the input $\hat{p}$ near an optimal value p^*. If $\hat{p} < p^*$, then the demodulated signal ξ (see Figure 16.1) is purely positive, and $\hat{p}$ moves to the right towards p^*. Similarly, if $\hat{p} > p^*$ then ξ is purely negative and $\hat{p}$ moves left. When $\hat{p} = p^*$, then the integral of ξ is zero, and $\hat{p}$ does not move. Notice that the signal ξ is larger when the slope of the function is larger .

output by the input perturbation yields a *demodulated* signal ξ that is positive when $\hat{p} < p^*$ and negative when $\hat{p} > p^*$. Finally, integrating the demodulated signal into our estimate $\hat{p}$ brings the estimate $\hat{p}$ closer to the optimal value p^* corresponding to a local maximum. The input and output sinusoids are plotted in Figure 16.2.

There are a number of important considerations when designing an extremum-seeking controller. First, there are three distinct time-scales of interest in the problem: (i) slow—external disturbances to be rejected, (ii) medium—perturbation frequency ω, and (iii) fast—internal system dynamics. The perturbation frequency ω must be chosen to be faster than the external disturbances (such as slow changes in birefringence) and slower than the internal system dynamics. For the laser system, or optical systems in general, the internal dynamics are extremely fast compared with the time it takes to change the polarizer angles, making extremum-seeking control an optimal tool for control purposes.

16.4
Prototypical Example: Self-Tuning Mode-Locked Fiber Lasers

To demonstrate how the data methods presented can be integrated together in a coherent fashion, we consider the NPR mode-locked fiber laser where saturable absorption is achieved using a combination of waveplates and polarizer [24–33]. The transmission function generated by the NPR laser is periodic, thus allowing for engineering strategies whereby the MPI can be circumvented and significant order-of-magnitude performance gains can be achieved [15, 23, 34].

It is envisioned that such performance gains can be achieved with a self-tuning architecture.

16.4.1
Governing Equations

The propagation of the slowly varying envelop of the electric field in the fiber is well-described by the coupled nonlinear Schrödinger equation (CNLS) [36, 37]:

$$\begin{aligned} i\frac{\partial u}{\partial z} + \frac{D}{2}\frac{\partial^2 u}{\partial t^2} - Ku + (|u|^2 + A|v|^2)\, u + Bv^2u^* &= iRu, \\ i\frac{\partial v}{\partial z} + \frac{\partial D}{2}\frac{\partial^2 v}{\partial t^2} + Kv + (A|u|^2 + |v|^2)\, v + Bu^2v^* &= iRv. \end{aligned} \tag{16.12}$$

In these equations, $u(z,t)$ and $v(z,t)$ are the two orthogonally polarized electric field envelopes in the optical fiber. The variable t is time in the frame of reference of the propagating pulse nondimensionalized by the full-width at half-maximum of the pulse, and z is the propagation distance normalized by the cavity length. The functions u and v are often referred to as the fast and slow components, respectively. The parameter K is the average birefringence, while D is the average group velocity dispersion of the cavity. The nonlinear coupling parameters A and B correspond to the cross-phase modulation and the four-wave mixing, respectively. They are determined by physical properties of the fiber, and $A + B = 1$. For this case (a silica fiber), $A = 2/3$ and $B = 1/3$. The dissipative terms Ru and Rv account for the saturable, bandwidth-limited gain (e.g., from the Yb-doped fiber amplification) and attenuation. They satisfy the following equation:

$$R = \frac{2g_0(1+\tau\partial_t^2)}{1 + (1/e_0)\int_{-\infty}^{\infty}(|u|^2 + |v|^2)dt} - \Gamma,$$

where g_0 is the nondimensional-pumping strength, and e_0 is the nondimensional saturating energy of the gain medium. The pump bandwidth is τ, and Γ quantifies losses due to output coupling and fiber attenuation.

16.4.2
Jones Matrices for Waveplates and Polarizers

The application of the waveplates and passive polarizer after each round-trip through the cavity may be modeled by the discrete application of Jones matrices [38].

$$W_{\lambda/4} = \begin{bmatrix} e^{-i\pi/4} & 0 \\ 0 & e^{i\pi/4} \end{bmatrix}, W_{\lambda/2} = \begin{bmatrix} -i & 0 \\ 0 & i \end{bmatrix}, W_p = \begin{bmatrix} 1 & 0 \\ 0 & 0 \end{bmatrix}.$$

Here, $W_{\lambda/4}$ is the quarter-wave plate (α_1 and α_2), $W_{\lambda/2}$ is the half-wave plate (α_3), and W_p is the polarizer (α_p). If the principle axes of these objects are not aligned with the fast field of the cavity, it is necessary to include the addition of a rotation matrix:

$$J_j = R(\alpha_j)W_jR(-\alpha_j),\;\; R(\alpha_j) = \begin{bmatrix} \cos(\alpha_j) & -\sin(\alpha_j) \\ \sin(\alpha_j) & \cos(\alpha_j) \end{bmatrix},$$

where α_j is a waveplate or polarizer angle ($j = 1, 2, 3, p$). These rotation angles will be the control variables, allowing us to find mode-locked solutions. Recent experiments show that these variables can be easily manipulated through electronic control [17].

16.4.3
Performance Monitoring and Objective Function

Given the governing equations, extensive numerical simulations can be performed in order to identify parameter regimes where mode-locking occurs. Each of these regimes can in turn be evaluated for their ability to produce high-energy, high-peak-power mode-locked states. In addition to being a costly exercise, such studies also rarely match the real cavity dynamics since, for instance, parameters such as the fiber birefringence K are unknown. This motivates our use of machine learning, optimization, and adaptive control strategies for characterizing the laser cavity. Interestingly, the integration of all three methods can be achieved without a detailed theoretical knowledge of the cavity equations, that is, they are *equation-free* methods in the sense that learning the laser characteristics and applying adaptive control only relies on experimental measurements of the underlying system.

For any such data-driven strategy to be effective, we require an objective function, with local maxima that correspond to high-energy mode-locked solutions. Although we seek high-energy solutions, there are many chaotic waveforms that have significantly higher energy than mode-locked solutions. Therefore, energy alone is not a good objective function. Instead, we divide the energy function E by the fourth-moment (kurtosis) M_4 of the Fourier spectrum of the waveform

$$O = \frac{E}{M_4},$$

which is large for undesirable chaotic solutions. This objective function, which has been shown to be successful for applying adaptive control, is large when we have a large amount of energy in a tightly confined temporal wave packet [12].

16.4.4
Sparse Representation for Birefringence Classification

The most challenging technological issue around the NPR-based mode-locked fiber laser is its sensitivity to birefringence changes. Indeed, temperature changes and/or small physical modifications of the fiber itself can easily compromise what was an ideal mode-locked state. This is why commercial versions of this laser must enforce strict environmental control to maintain performance, that is, the fiber is pinned into place and shielded from temperature fluctuations. Such system sensitivity has prevented performance advances, limiting power and pulse widths.

State-of-the-art theoretical models for characterizing birefringence have treated the birefringence as a stochastically varying parameter along the length of fiber. But even this is unsatisfactory since a user of a fiber laser needs to know precisely, and at all times, the birefringence in order for models to accurately predict the cavity dynamics. This is virtually an impossible task given the fact that temperature fluctuations and/or physical placement of the fiber can significantly alter the birefringence distribution. The machine learning algorithms advocated [14] simply learn a relationship between the average birefringence and the objective function, thus recognizing the average cavity birefringence and adjusting the cavity parameters accordingly in order to optimize performance. Such a recognition task is significantly faster than re-executing the toroidal or genetic algorithm search as it allows one to move immediately to near the optimal solution where adaptive control can then maintain peak performance.

To classify the birefringence, we use sparse representation [14] based upon producing a spectrogram of the objective function from the time-series output of the toroidal search. For different average birefringence values, unique spectrograms are produced, thus providing an underlying pattern that can be used for recognition and evaluation of the K value. This sparsity-promoting optimization, when used in conjunction with the unique spectrograms, gives a rapid and accurate classification scheme for the fiber birefringence, achieving accuracy rates up to 98%. And even if misclassified, the algorithm produces a birefringence that is only slightly off, thus still allowing for a rapid tuning of the laser cavity to the optimal waveplate and polarizer settings. Thus, birefringence recognition can be easily accomplished.

16.4.5
Self-Tuning Laser

The sparse search algorithm is tested using the precomputed spectrograms with Gaussian random noise added. In our test, the birefringence K is varied following a Gaussian random walk. For each trial, the spectrogram corresponding to the current birefringence is computed and the L_1-norm sparse search is executed. The recognition algorithm is tested in two scenarios: (i) well-aligned data given the assumption that the servo motors that control the waveplates and polarizers work without error and (ii) the misaligned data that consider the error in the initial angle of the servo motors. In both of these scenarios, the sparse search works very well. In the well-aligned case, a birefringence recognition (classification) rate of 98% is achieved, while in the misaligned case, we get an 88% recognition rate. It should also be noted that even when our recognition algorithm fails to find the correct birefringence value, the error between the true birefringence and the recognized value is very small. Thus, even if we use the misclassified birefringence, it is likely that the predicted optimal parameters will be near the true optimal parameters, and the adaptive controller [19] will bring the laser system back to peak performance.

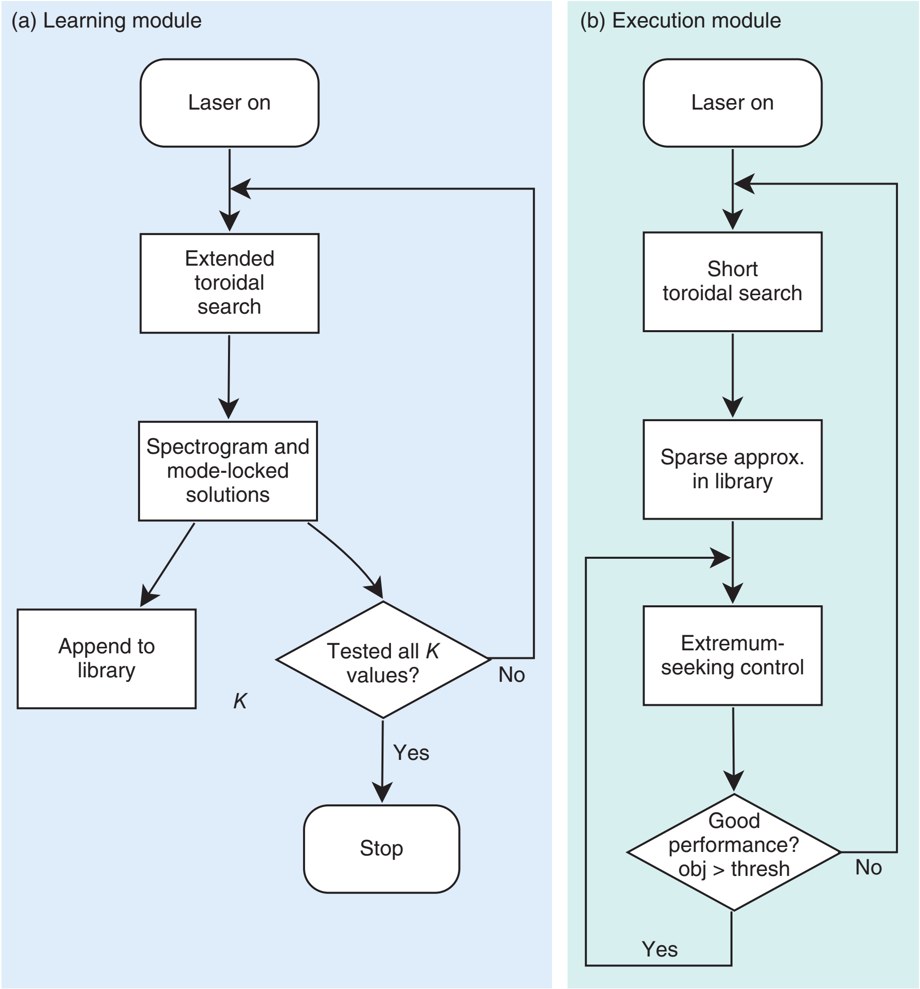
(a) Learning module
Laser on
Extended toroidal search
Spectrogram and mode-locked solutions
Append to library
Tested all K values?
No
K
Yes
Stop
(b) Execution module
Laser on
Short toroidal search
Sparse approx. in library
Extremum-seeking control
Good performance? obj > thresh
No
Yes

Figure 16.3 Flowchart of self-tuning that includes both a training and execution module.

Once the birefringence is classified, the optimal waveplate and polarizer settings are then already known from the toroidal search algorithm. This ultimately leads to an efficient, self-tuning laser since the waveplates and polarizers can be adjusted directly to their nearly optimal positions using servo-control motors [17, 18]. At that point, the extremum-seeking control can be used to keep the system in an optimal mode-locked state. Specifics of the physical implementation are illustrated in Figure 16.3 with the training and execution algorithms highlighted. The flow charts and algorithm architecture illustrate the practical implementation of the method.

In Figure 16.4, we vary the birefringence K according to a large-amplitude sawtooth pattern (left) and according to a pseudorandom walk (right). In each of these

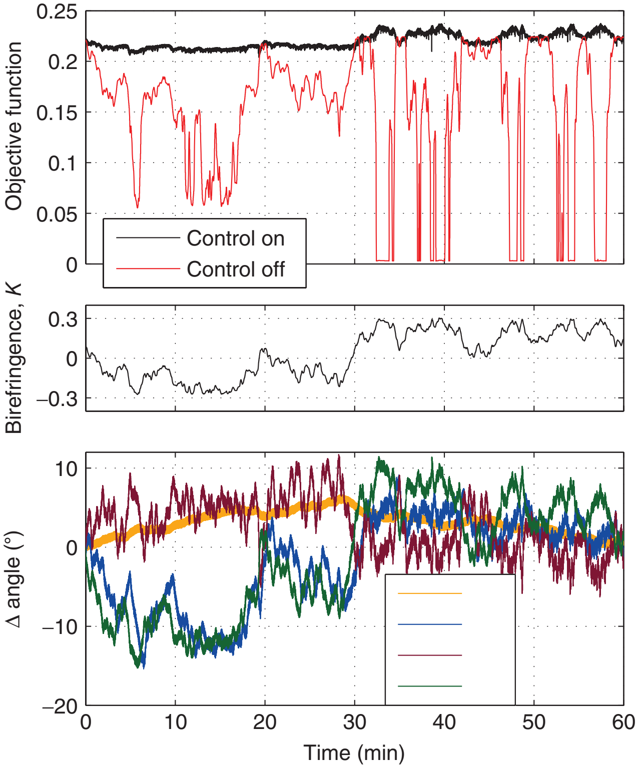

Figure 16.4 Performance of extremum-seeking controller despite significant variance (random walk) in birefringence over time. Without control, the objective function crashes repeatedly with birefringence fluctuations, resulting in failure to mode-lock over large ranges of parameter space. With control, the system remains at a high-performance mode-locked state for the entire trial.

cases, the extremum-seeking controller is compared with the case when no control is applied and the polarizer angles are fixed at the optimal values for $K = 0.1$. For both aggressive K disturbances, the extremum-seeking controller maintains a high-energy mode-locked state, although the uncontrolled system frequently loses mode-locking. It is interesting to note that the fourth input parameter, α_p tracks the K disturbance nearly linearly. The objective function fluctuates slightly in the case with controller, since the local maximum value varies with the birefringence K. This result is central in illustrating the power of the advocated methods. Indeed, the controller simultaneously varies the four angles corresponding to waveplates and polarizer in a single-NPR laser to maintain a high-energy mode-locked state despite large, rapid changes in the birefringence K. The amplitude and frequency of the disturbance are chosen to be more aggressive than expected values, demonstrating that the controller successfully rejects disturbances in a worst-case scenario.

16.5
Broader Applications of Self-Tuning Complex Systems

The previous example of a mode-locked laser provides a proof-of-concept of the power of the algorithmic innovations associated with equation-free control in combination with machine learning and sparse approximation. However, the methodology extends far beyond just mode-locked lasers. The following three subsections detail three different applications where the mathematical strategies apply.

16.5.1
Phased Array Antennas

Phased array antennas [39], shown in Figure 16.5, are of growing importance due to their ability to actively produce directed electromagnetic energy patterns. Phased array antennas can be manipulated in order to control the relative phases of the respective signals feeding the antennas that make up the array. In so doing, the effective radiation pattern of the array is reinforced in a desired direction and suppressed in undesired directions. Thus, an antenna array is a group of multiple active antennas coupled to a common source or load to produce a directive radiation pattern. Usually, the spatial relationship of the individual antennas also contributes to the directivity of the antenna array. Use of the term “active antennas” is intended to describe elements whose energy output is modified due to the presence of a source of energy in the element (other than the mere signal energy, which passes through the circuit) or an element in which the energy output from a source of energy is controlled by the signal input. The term *active antennas* also suggests that control principles can be used to manipulate the arrays to produce a desired radiation pattern. One common application is with a standard multiband television antenna, which has multiple elements coupled together. The steering of phased array antennas is analogous to the pulse shaping technique using an array of liquid crystal cells [40]. In both cases, principled methods for controlling the output field are keys to successful technologies.

In military applications, phased array radar systems are highly desirable due to the rapidity with which the beam can be steered. Thus, phased array radars allow a warship, for instance, to use one radar system for surface detection and tracking (finding ships), air detection and tracking (finding aircraft and missiles), and missile uplink capabilities. Before using these systems, each surface-to-air missile in flight required a dedicated fire-control radar, which meant that ships could only engage a small number of simultaneous targets. Phased array systems can be used to control missiles during the midcourse phase of the missile’s flight. During the terminal portion of the flight, continuous-wave fire control directors provide the final guidance to the target. Because the radar beam is electronically steered, phased array systems can direct radar beams fast enough to maintain a fire control quality track on many targets simultaneously while also controlling several in-flight missiles. In such dynamic phased arrays, each array element incorporates

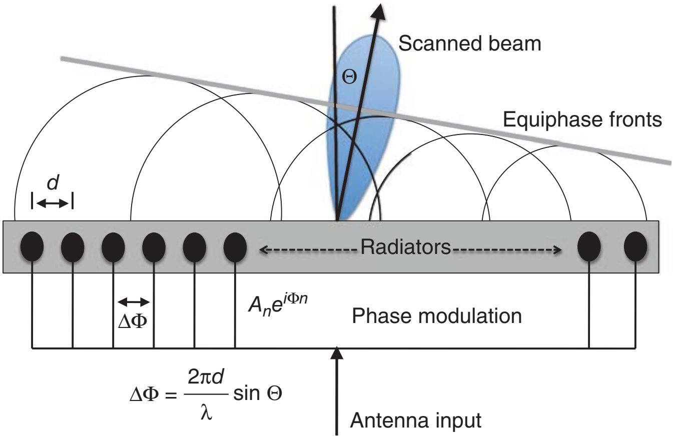

Figure 16.5 Configuration of a phased array antenna. The ability to electronically produce phase shifting in a principled way provides rapid control and adjustment of the scanning electromagnetic beam. The self-tuning algorithm proposed here provides an "intelligent" algorithm capable of robustly producing the desired beam alignment.

an adjustable phase shifter that is collectively used to move the beam with respect to the array face. Dynamic phased array requires no physical movement to aim the beam. The beam is moved electronically. This can produce antenna motion fast enough to use a small pencil-beam to simultaneously track multiple targets while searching for new targets using only one radar set (track while search). As an example, an antenna with a 2-degree beam with a pulse rate of 1 kHz will require approximately 16 s to cover an entire hemisphere consisting of 16,000 pointing positions. This configuration provides six opportunities to detect a Mach 3 vehicle over a range of 100 km (62 μm), which is suitable for military applications. The position of mechanically steered antennas can be predicted, which can be used to create electronic countermeasures that interfere with radar operation. The flexibility resulting from phase array operation allows beams to be aimed at random locations, which eliminates this vulnerability. This is also desirable for military applications.

Much like the mode-locked laser, a learning module can be executed on the phased array antenna in order to learn the regions (via a toroidal search) that produce the optimal system behavior based upon one or more objective functions. The library of learned behavior can then be utilized with a sparse number of measurements on the emitted electromagnetic field in order to rapidly identify the state of the system. Thus, the controller can rapidly push the system to almost optimal behavior before the extremum-seeking control can be applied to keep the radar array stabilized even in the presence of disturbances. Such an algorithm would be transformative not only to standard phased array antennas, but also to the newly emerging technologies of holographic, meta-material arrays [41].

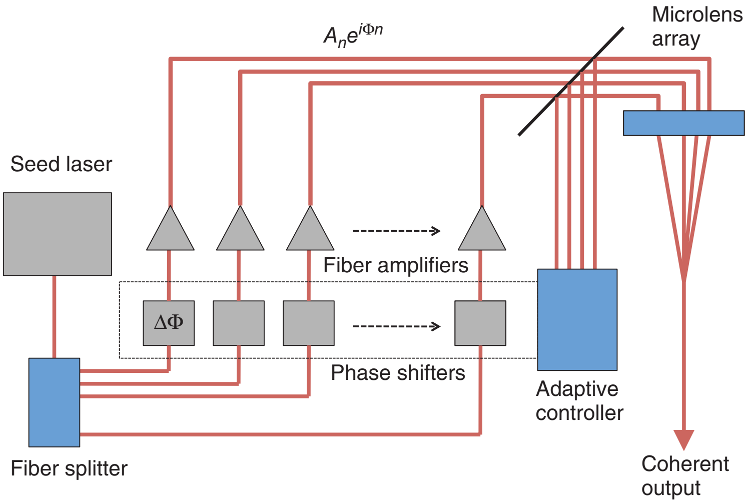

Figure 16.6 Configuration of a coherent beam-combining experiment where modulation of the input beam phase into individual fiber amplifiers allows for a principled way for rapid control and adjustment of the output coherent laser beam.

16.5.2
Coherent Laser Beam Combining

An application that combines both self-tuning lasers and control of phase across multiple agents is coherent laser beam combining [42] (Figure 16.6). Coherent beam combining resembles phased array radar—an array of emitters transmitting in phase to generate a coherent output. In principle, operating the emitters in phase and combining their beams properly can generate a steerable beam, but so far most effort has gone to combining the outputs. Diode coherent beam combination was demonstrated with up to 900 laser stripes in the 1990s, but the need for single-mode output and tight phase-locking requirements limited output to 5.5 W. New techniques and the use of master-oscillator sources to drive many parallel amplifiers have overcome those limitations. Recently, Fan *et al.*[43, 44] and colleagues at MIT Lincoln Laboratories (Lexington, MA) produced 38.5 W continuous wave from an array of 218 individually addressable slab-coupled-optical-waveguide (semiconductor) amplifiers (SCOWAs). First, a diffractive optical element split the seed laser beam into 21 outputs, and delivered them to parallel amplifiers with large circular mode profiles on a 200 μm pitch. A double-pass through the amplifier array produced 21 parallel beams, which were monitored to generate phase-locking signals. Then, a second diffractive optical element, aligned orthogonally to the first, divided each of those 21 parallel outputs into 11 parts, one for double-pass amplification of each of 11 parallel SCOWA arrays. This produced phase-locked output from 218 of the 231 stripes in the second-stage SCOWA arrays; the remaining 13 stripes did not work. Phase control over that large number of elements was crucial for success. The novel architecture proposed here for self-tuning lasers and phased array antennas can revolutionize beam combining since it provides a self-tuning phase-locking technology that is critical for beam combining.

16.5.3
Neuronal Stimulation

Another application of the algorithm outlined here, and which is highlighted to illustrate how broad the method can be, is to the emerging field of deep brain stimulation (DBS). In particular, the algorithm represents a critical advancement in providing a principled approach to understanding how to stimulate the hippocampus in order to suppress or enhance key features of neural activity associated with symptoms of certain movement and psychiatric disorders. DBS therapy is an adjustable and reversible treatment that uses a surgically implanted device, similar to a heart pacemaker, to deliver mild electrical pulses to precisely targeted areas of the brain. The stimulation can be programmed and adjusted by a trained clinician to maximize symptom control and minimize side effects. Currently, the stimulation protocols are governed by experts in the loop doctors. However, the above-mentioned algorithm proposes to replace these assessments, or work with such critical insight, to develop an automatic and principled approach to achieving best performance. The construction of such models are imperative not only for a fundamental understanding of memory encoding/decoding tasks, but also for constructing controls laws appropriate for aiding in such tasks. On a basic level, *sparsity* will play a critical role in any modeling efforts due to the fact that only a limited number of sensors can be placed in the hippocampus, thus sparsity is imposed by necessity, not choice, for both state read-out and stimulus-based control strategies (Figure 16.7).

The self-tuning architectures work since advances in neuroscience over the past decade have revealed two critical, and seemingly ubiquitous, phenomena: (i) meaningful input/output of signals in high-dimensional networks of neurons are encoded in low-dimensional patterns of dynamic activity [45–48], and (ii) sparsity plays a key role in encoding and decoding strategies, especially in neural computation [49, 50]. This typifies the state-of-the-art in neuroscience, which manifests the most sophisticated functionality in information processing and computation known in any system. Such observations lead us to conjecture that neuronal ECoG recordings, and other modalities of invasive and noninvasive data, will allow us to probe the latent, low-dimensional structure of neural activity relating to a variety of neurological disorders, including memory deficits. A direct implication of such a data-driven modeling strategy is that we can gain traction on prediction, state-estimation, and control of multiple neurological disorders, including PTSD, depression, borderline personality disorder, general anxiety disorder, traumatic brain injury, substance abuse/addiction, fibromyalgia/chronic pain, and epilepsy.

To understand how such a seemingly complex biological systems such as the hippocampus can robustly, efficiently, and accurately process neural information, one must fundamentally understand the intersection and integration of (i) sparse

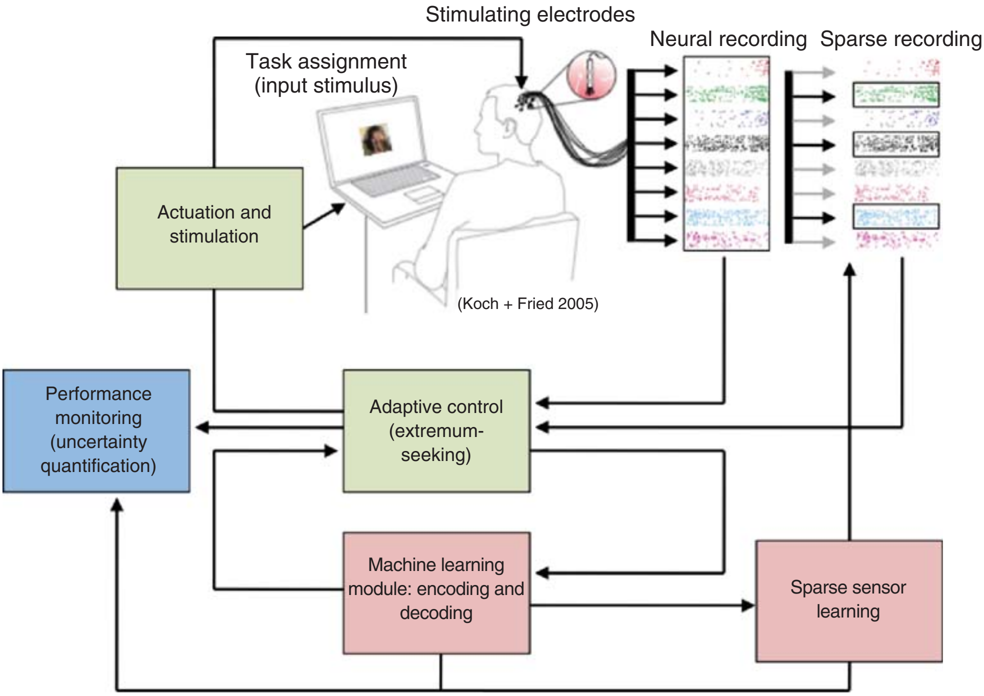
Stimulating electrodes
Neural recording
Sparse recording
Task assignment
(input stimulus)
Actuation and stimulation
(Koch + Fried 2005)
Performance monitoring (uncertainty quantification)
Adaptive control (extremum-seeking)
Machine learning module: encoding and decoding
Sparse sensor learning

Figure 16.7 Self-tuning architecture for neurostimulation. As with other complex systems, the algorithm relies on library building strategies, adaptive control, and sparse sensing/representation to provide an efficient algorithm for control.

networks of neurons [49, 50], (ii) adaptive control theory, and (iii) compressive sensing, each of which has individually evoked a paradigm shift in their respective fields. The successful integration of these methods, which also falls broadly under machine learning strategies, has the potential to revolutionize our understanding of how memory encoding/decoding strategies are biophysically constructed in the hippocampus, thereby revealing the fundamental nature of the algorithms enacted for processing stimulus and enacting control. More broadly, these studies highlight a potential central paradigm of memory: sparsity is leveraged to its full advantage in making classification decisions [51] and informing control strategies in memory encoding/decoding. Thus, sparsity is not only a theoretical conception, but it may also have a direct technological impact on hippocampus stimulation strategies.

16.6
Conclusions and Technological Outlook

We have demonstrated the practical implementation of an adaptive, robust, and self-tuning algorithm that can be used in conjunction with a variety of complex systems arising in the engineering, physical, and biological sciences. Such a scheme has enormous technological advantages for the efficient and optimal operation of such systems. Specifically, state-of-the-art machine learning and state classification methods, along with adaptive control schemes that are mode l independent, form the critical methodology necessary to revolutionize control strategies, impacting both the commercial and research sectors associated with many application areas. Although we demonstrate the methodology within the context of NPR-based fiber lasers, due to newly developed servo-control of optical components, the data-driven strategies are generic and capable of self-tuning almost any optical system, for instance. Here, by combining such machine learning strategies with adaptive control, we demonstrate that robust and self-tuning mode-locked operation can be achieved and fiber laser performance can be efficiently optimized. This is a clear demonstration in the optical laser context of the integration of machine learning techniques with adaptive control, thus allowing for potentially transformative performance gains in fiber lasers.

The success of such self-tuning strategies hinges on two critical components: (i) identifying input (control) parameters and (ii) constructing an appropriate objective function that is feasible and serves well as a proxy for system performance. The algorithms for both learning the system behaviors and applying adaptive control are both *equation-free* methods [1]. Thus, they do not rely on one's ability to construct accurate model equations. Rather, all characterization is done directly from experimental data and no reliance is made on a faithful model. Such strategies are highly advantageous since modeling often fails to provide accurate quantitative prediction of laser cavity dynamics. Even in the two-decade-old problem of NPR-based mode-locking, models have proved to be of value for qualitative modeling, but have had limited quantitative use since phenomenon such as the randomly varying birefringence simply are beyond our capabilities to model due to their extreme sensitivity and stochastic nature. The methods advocated here do not suffer from such sensitivity, they simply adapt to the changes and optimize for global performance.

Naturally, the methods presented have limitations and their own performance barriers. But we believe that many of these can be overcome with additional work in this area. Specifically, extremum seeking does not scale well with arbitrarily many input variables. The controller convergence takes significantly longer time with multiple parameters, and the design is more complicated. In addition, the radius of perturbation grows with the number of parameters, and for the mode-locked laser, this perturbation may kick the system into an unstable or chaotic regime. This is compounded by the need for a sufficiently large perturbation signal to achieve a reasonable signal to noise ratio. The use of reduction techniques such as principal components analysis (PCA) may allow us to determine low-dimensional control inputs that reduce the dimension of the input space. Similar to the machine learning methods demonstrated, the key is to identify low-dimensional spaces that provide an accurate representation of the complex dynamics.

Acknowledgments

J.N. Kutz acknowledges support from the U.S. Air Force Office of Scientific Research (AFOSR) (FA9550-09-0174).

References

1. Kutz, J.N. (2013) *Data-Driven Modeling and Scientific Computation*, Oxford University Press, Oxford.
2. Bishop, C.M. (2006) *Pattern Recognition and Machine Learning*, Springer-Verlag.
3. Duda, R., Hart, P., and Storck, D. (2001) *Pattern Classification*, John Wiley & Sons, Inc.
4. Murphy, K. (2012) *Machine Learning: A Probabilistic Perspective*, MIT Press.
5. Schmid, P. (2010) Dynamic mode decomposition of numerical and experimental data. *J. Fluid Mech.*, **656**, 5–28.
6. Rowley, C., Mezić, I., Bagheri, S., Schlatter, P., and Henningson, D. (2009) Spectral analysis of nonlinear flows. *J. Fluid Mech.*, **641**, 115–127.
7. Kevrekidis, I.G. and Samaey, G. (2009) Equation-free multiscale computation: algorithms and applications. *Annu. Rev. Phys. Chem.*, **60**, 321–344.
8. Baraniuk, R.G. (2007) Compressive sensing. *IEEE Signal Process Mag.*, **24**, 118–120.
9. Candès, E.J., Romberg, J., and Tao, T. (2006) Stable signal recovery from incomplete and inaccurate measurements. *Commun. Pure Appl. Math.*, **8**, 1207–1223.
10. Candès, E.J. and Tao, T. (2006) Near optimal signal recovery from random projections: universal encoding strategies? *IEEE Trans. Inf. Theory*, **52**, 5406–5425.
11. Donoho, D. (2006) Compressive sensing. *IEEE Trans. Inf. Theory*, **52**, 1289–1306.
12. Brunton, S.L., Fu, X., and Kutz, J.N. (2013) Extremum-seeking control of a mode-locked laser. *IEEE J. Quantum Electron.*, **49**, 852–861.
13. Brunton, S.L., Fu, X., and Kutz, J.N. (2014) Self-tuning fiber lasers. *IEEE J. Sel. Top. Quantum Electron.*, **20**, 1101408.
14. Fu, X., Brunton, S.L., and Kutz, J.N. (2014) Classification of birefringence in mode-locked fiber lasers using machine learning and sparse representation. *Opt. Express*, **22**, 8585–8597.
15. Fu, X. and Kutz, J.N. (2013) High-energy mode-locked fiber lasers using multiple transmission filters and a genetic algorithm. *Opt. Express*, **21**, 6526.
16. Andral, U., Si Fodil, R., Amrani, F., Billard, F., Hertz, E., and Grelu, P. (2015) Fiber laser mode locked through an evolutionary algorithm. *Optica*, **4**, 275–278.
17. Shen, X., Li, W., Yan, M., and Zeng, H. (2012) Electronic control of nonlinear-polarization–rotation mode locking in Yb-doped fiber lasers. *Opt. Lett.*, **37**, 3426–3428.
18. Radnatarov, D., Khripunov, S., Kobtsev, S., Ivanenko, A., and Kukarin, S. (2013) Automatic electronic-controlled mode locking self-start in fibre lasers with non-linear polarisation evolution. *Opt. Express*, **21**, 20626–20631.
19. Krstić, M. and Wang, H.H. (2000) Stability of extremum seeking feedback for general nonlinear dynamic systems. *Automatica*, **36** (4), 595–601.
20. Richardson, D.J., Nilsson, J., and Clarkson, W.A. (2010) High power fiber lasers: current status and future perspectives. *J. Opt. Soc. Am. B*, **27**, B63–B92.
21. Namiki, S., Ippen, E.P., Haus, H.A., and Yu, C.X. (1997) Energy rate equations for mode-locked lasers. *J. Opt. Soc. Am. B*, **14**, 2099–2111.
22. Bale, B.G., Kieu, K., Kutz, J.N., and Wise, F. (2009) Transition dynamics for multi-pulsing in mode-locked lasers. *Opt. Express*, **17**, 23137–23146.
23. Li, F., Wai, P.K.A., and Kutz, J.N. (2010) Geometrical description of the onset of multi-pulsing in mode-locked laser cavities. *J. Opt. Soc. Am. B*, **27**, 2068–2077.

24. Haus, H.A. (2000) Mode-locking of lasers. *IEEE J. Sel. Top. Quantum Electron.*, **6**, 1173–1185.

25. Tamura, K., Ippen, E.P., Haus, H.A., and Nelson, L.E. (1993) 77-fs Pulse generation from a stretched-pulse mode-locked all-fiber ring laser. *Opt. Lett.*, **18**, 1080–1082.

26. Tamura, K. and Nakazawa, M. (1995) Optimizing power extraction in stretched pulse fiber ring lasers. *App. Phys. Lett.*, **67**, 3691–3693.

27. Lenz, G., Tamura, K., Haus, H.A., and Ippen, E.P. (1995) All-solid-state femtosecond source at 1.55 μm. *Opt. Lett.*, **20**, 1289–1291.

28. Chong, A., Renninger, W.H., and Wise, F.W. (2008) Properties of normal-dispersion femtosecond fiber lasers. *J. Opt. Soc. Am. B*, **25**, 140–148.

29. Chong, A., Buckley, J., Renninger, W., and Wise, F. (2006) All-normal-dispersion femtosecond fiber laser. *Opt. Express*, **14**, 10095.

30. Renninger, W., Chong, A., and Wise, F.W. (2008) Dissipative solitons in normal-dispersion fiber lasers. *Phys. Rev. A*, **77**, 023814.

31. Bale, B. and Wabnitz, S. (2010) Strong spectral filtering for a mode-locked similariton fiber laser. *Opt. Lett.*, **35**, 2466–2468.

32. Ilday, F.O., Buckley, J., and Wise, F.W. (2004) Self-similar evolution of parabolic pulses in a laser cavity. *Phys. Rev. Lett.*, **92**, 213902.

33. Renninger, W.H., Chong, A., and Wise, F.W. (2010) Self-similar pulse evolution in an all-normal-dispersion laser. *Phys. Rev. A*, **82**, 021805.

34. Li, F., Ding, E., Kutz, J.N., and Wai, P.K.A. (2011) Dual transmission filters for enhanced energy in mode-locked fiber lasers. *Opt. Express*, **19**, 23408–23419.

35. Wright, J., Yang, A., Ganesh, A., Sastry, S., and Ma, Y. (2009) Robust face recognition via sparse representation. *IEEE Trans. Pattern Anal. Mach. Intell.*, **31**, 210–227.

36. Menyuk, C.R. (1989) Pulse propagation in an elliptically birefringent Kerr media. *IEEE J. Quantum Electron.*, **25**, 2674–2682.

37. Menyuk, C.R. (1987) Nonlinear pulse propagation in birefringent optical fibers. *IEEE J. Quantum Electron.*, **23**, 174–176.

38. Jones, R.C. (1941) A new calculus for the treatment of optical systems. I. Description and discussion of the calculus. *J. Opt. Soc. Am.*, **31**, 488–493.

39. Hansen, R.C. (2009) *Phased Array Antennas*, John Wiley & Sons, Inc.

40. Weiner, A.M. (2011) Ultrafast optical pulse shaping: a tutorial review. *Opt. Commun.*, **284**, 3669–3692.

41. Enoch, S., Tayeb, G., Sabouroux, P., Guerin, N., and Vincent, P. (2002) A metamaterial for directive emission. *Phys. Rev. Lett.*, **89**, 213902.

42. Hecht, J. (2008) Photonic Frontiers: beam combining—combining beams can boost total power. *Laser Focus World*, **44**, 7.

43. Fan, T.Y. (2005) Laser beam combining for high-power, high-radiance sources. *IEEE J. Sel. Top. Quantum Electron.*, **11**, 567.

44. Montoya, J., Augst, S.J., Creedon, K., Kansky, J., Fan, T.Y., and Sanchez, A. (2012) External cavity beam combining of 21 semiconductor lasers using SPGD. *Appl. Opt.*, **51**, 1724–1728.

45. Rabinovich, M., Volkovskii, A., Lecanda, P., Huerta, R., Abarbanel, H.D.I., and Laurent, G. (2001) Dynamical encoding by networks of competing neuron groups: winnerless competition. *Phys. Rev. Lett.*, **87**, 068102.

46. Rabinovich, M., Huerta, R., Varona, P., and Afraimovich, V.S. (2008) Transient cognitive dynamics, metastability, and decision making. *PLoS Comput. Biol.*, **4**, e1000072.

47. Laurent, G., Stopfer, M., Friedrich, R.W., Rabinovich, M.I., Volkovskii, A., and Abarbanel, H.D.I. (2001) Odor encoding as an active, dynamical process: experiments, computation and theory. *Annu. Rev. Neurosci.*, **24**, 263–297.

48. Gold, J.I. and Shadlen, M.N. (1999) Representation of a perceptual decision in developing oculomotor commands. *Nature*, **404**, 390–394.

49. Ganguli, S. and Sompolinsky, H. (2012) Compressed sensing, sparsity, and dimensionality in neuronal information processing and data analysis. *Annu. Rev. Neurosci.*, **35**, 485–508.

50. Olshausen, B. and Field, D. (2004) Sparse coding of sensory inputs. *Curr. Opin. Neurobiol.*, **14**, 481–487.

51. Brunton, B.W., Brunton, S.L., Proctor, J.L., and Kutz, J.N. (2013) Optimal Sensor Placement and Enhanced Sparsity for Classification. arXiv.

17

Conclusion and Outlook

Philippe Grelu

The past decade has witnessed major conceptual advances in nonlinear optical cavity dynamics, particularly as it concerns ultrafast dynamics. As a logical prospect, we now anticipate the soaring of novel applications, in terms of innovative, compact, and reliable pulsed optical sources and signal-processing units. This transfer from fundamental science to the photonic industry still requires considerable maturing efforts. To start with, in lab proof-of-concept experiments, tiny microresonators or microlasers will usually be connected to bulky optical equipment to make them operate stably and efficiently. One prerequisite to industrialization is the use of power-efficient integrated optics all along the line. Then, the question of selecting adequate technological platforms and possibly matching them becomes crucial. Whenever the density of integrated components should be large, the use of planar technology seems to be an unavoidable transition for many envisaged applications, in analogy with the past developments in electronics. Although the expansion of silicon photonics is certainly a key enabling technology [1], it may not be the panacea for a range of demanding applications at conventional telecom wavelengths, due to waveguide losses, two-photon absorption and coupling issues to and from silica waveguides. Concerning the latter, we note the important progress made with adiabatic tapers, and recently, with apodized waveguide grating couplers [2, 3].

As customary in photonics, the achievement of a critical overall performance enabling the deployment of a given technology depends on material scientists surpassing themselves. Silicon nitride nowadays constitutes an advantageous CMOS – compatible platform for nonlinear optics [4]. Chalcogenide glasses, and other highly nonlinear soft glasses, have long been considered as promising nonlinear materials that can be processed in either fibers or thin films [5]. However, optical cavity design is demanding in terms of minimal losses and high damage threshold, so that figures of merit of materials with the highest nonlinearities generally remain deceptive. Among these considerations, the optical wavelength constitutes a key parameter. There is a surge of experimental development in the spectral region around 2 μm and beyond. Concerning optical sources, the access to the fingerprint spectral region for environmental monitoring, as well as medical applications, constitutes legitimate motivations. It is anticipated that the

Nonlinear Optical Cavity Dynamics: From Microresonators to Fiber Lasers, First Edition.
Edited by Philippe Grelu.
© 2016 Wiley-VCH Verlag GmbH & Co. KGaA. Published 2016 by Wiley-VCH Verlag GmbH & Co. KGaA.

use of small footprint, highly sensitive, spectroscopic analyzers will be generalized. After the remarkable success of quantum cascade lasers in the mid-infrared [6], fiber lasers are gradually filling the 2 – 3 μm gap, with, in particular, highly efficient thulium-based ultrashort-pulsed sources between 2 and 2.5 μm [7].

As for the performance of nonlinear materials, upshifting the wavelength above 2 μm can be particularly advantageous: for instance, the two-photon absorption in silicon is removed, whereas losses in most chalcogenide compounds are reduced. Consequently, there will be a marked need for efficient and compact wavelength converters, in particular, between the conventional 1.5-μm and the novel 2-μm region of interest for optical data communication and processing. These converters could be developed from specifically designed nonlinear optical cavities, such as optomechanical microdisk resonators [8].

Most likely, optimal ultrafast photonic devices will require hybrid material design including, typically, highly nonlinear material for the optical cavity, and low-loss transparent material for signal transport. Hybrid optical cavities and lasers can also take advantage from the advances made with materials such as semiconductor nanowires or graphene, and interact with plasmonic structures. These prospects leave room for intense research efforts in the coming decade.

Now, let us move back to the realm of the fundamental investigations in nonlinear optical cavity dynamics. Far from being exhaustive, this research part is continuously thriving, fueled from novel experimental possibilities and stimulating conceptual bridges among topics. In other words, the tree of nonlinear optical systems will continue burgeoning [9].

We can highlight the revived interest for chaotic wave field dynamics, boosted by the focus of the scientific community on extreme wave event – rogue wave – investigation, where optics seems to host the most versatile set of demonstrations. Owing to light recirculation, active (lasers) and passive (driven) optical cavities allow to thoroughly investigate these phenomena over a large range of time scales. These investigations will certainly continue, probably with a more acute focus on coherence properties. In the midst of dissipative and chaotic wave fields, notions of coherence, localization, and turbulence need to be further explored [10 – 12]. The concept of mode-locking will benefit from a more quantitative statistical description applicable to a wide range of optical cavity systems, particularly in the context of frequency-comb generation [13, 14]. The notion of cavity entropy represents a valuable tool in that respect [15], whereas interacting multiple pulses in an optical cavity make a paradigmatic system for developing further analogies with the physics of matter [16, 17].

Within the semiconductor platform, the progress in the fundamental investigations of spatiotemporal cavity dynamics remains strongly dependent on technological advances. The quest for laser light bullets goes on. In this respect, multimode fiber lasers could have their word too.

The study of a discrete set of coupled microcavities represents a fascinating way to expand the dynamical scope, with a prospect of monitoring dimensional transitions in spatiotemporal dynamics. Considering the excitable behavior of a semiconductor laser cavity [18], a chain of coupled micropillar semiconductor lasers would make a one-dimensional neural network. After the generalization of high-quality nanocavity arrays, the door will be open to almost limitless neuromimetic photonic architectures. But to start with, few-cavity laser systems already present fascinating features, such as spontaneous symmetry breaking for coupled photonic-crystal nanolasers [19]. Finally, the exploration of nonlinear optical systems subjected to various types of delayed optical feedback reveals a vast range of dynamics and is also propitious to applications and remarkable analogies with other nonlinear systems [20–24].

References

1. Leuthold, J., Koos, C., and Freude, W. (2010) Nonlinear silicon photonics. *Nat. Photonics*, **4**, 535–544.
2. Shoji, T., Tsuchizawa, T., Watanabe, T., Yamada, K., and Morita, H. (2002) Low loss mode size converter from 0.3-micron square Si-wire waveguides to single mode fibres. *Electron. Lett*, **38**, 1669–1670.
3. Li, C., Zhang, H., Yu, M., and Lo, G.Q. (2013) CMOS-compatible high efficiency double-etched apodized waveguide grating coupler. *Opt. Express*, **21**, 7868–7874.
4. Moss, D.J., Morandotti, R., Gaeta, A.L., and Lipson, M. (2013) New CMOS-compatible platforms based on silicon nitride and Hydex for nonlinear optics. *Nat. Photonics*, **7**, 597–607.
5. Eggleton, B.J., Luther-Davies, B., and Richardson, K. (2011) Chalcogenide photonics. *Nat. Photonics*, **5**, 141–148.
6. Faist, J. (2013) *Quantum Cascade Lasers*, Oxford University Press.
7. Sorokina, I.T., Dvoyrin, V.V., Toltsik, N., and Sorokin, E. (2014) Mid-IR ultrashort pulsed fiber-based lasers. *IEEE J. Sel. Top. Quantum Electron.*, **20**, 0903412.
8. Liu, Y., Davanço, M., Aksyuk, V., and Srinivasan, K. (2014) Electromagnetically induced transparency and wideband wavelength conversion in silicon nitride microdisk optomechanical resonators. *Phys. Rev. Lett.*, **110**, 223603.
9. Lugiato, L., Prati, F., and Brambilla, M. (2015) *Nonlinear Optical Systems*, Cambridge University Press.
10. Turitsyna, E.G. *et al.* (2013) The laminar-turbulent transition in a fibre laser. *Nat. Photonics*, **7**, 783–786.
11. Churkin, D.V. *et al.* (2015) Stochasticity, periodicity and localized light structures in partially mode-locked fibre lasers. *Nat. Commun.*, **6**, 7004.
12. Conforti, M. *et al.* (2015) Turbulent dynamics of an incoherently pumped passive optical fiber cavity: quasisolitons, dispersive waves, and extreme events. *Phys. Rev. A*, **91**, 023823.
13. Herr, T. *et al.* (2014) Temporal solitons in optical microresonators. *Nat. Photonics*, **8**, 145–152.
14. Johnson, A.R., Okawashi, Y., Lamont, M.R., Levy, J.S., Lipson, M., and Gaeta, A.L. (2014) Microresonator-based comb generation without an external laser source. *Opt. Express*, **22**, 1394–1401.
15. Fischer, B. and Bekker, A. (2013) Many-body photonics. *Opt. Photon. News*, **24**, 40–47.
16. Sanchez, F. *et al.* (2014) Manipulating dissipative soliton ensembles in passively mode-locked fiber lasers. *Opt. Fiber Technol.*, **20**, 562–574.
17. Oren, G., Bekker, A., and Fischer, B. (2014) Classical condensation of light pulses in a loss trap in a laser cavity. *Optica*, **1**, 145–148.
18. Selmi, F., Braive, R., Beaudoin, G., Sagnes, I., Kuszelewicz, R., and Barbay, S. (2014) Relative refractory period in an excitable semiconductor laser. *Phys. Rev. Lett.*, **112**, 183902.
19. Hamel, P. *et al.* (2015) Spontaneous mirror-symmetry breaking in coupled photonic-crystal nanolasers. *Nat. Photonics*, **9**, 311–314.
20. Paquot, Y. *et al.* (2012) Optoelectronic reservoir computing. *Sci. Rep.*, **2**, 287.

21. Verschueren, N., Bortolozzo, U., Clerc, M.G., and Residori, S. (2013) Spatiotemporal chaotic localized state in liquid crystal light valve experiments with optical feedback. *Phys. Rev. Lett.*, **110**, 104101.

22. Yanchuk, S. and Giacomelli, G. (2014) Pattern formation in systems with multiple delayed feedbacks. *Phys. Rev. Lett.*, **112**, 174103.

23. Sciamanna, M. and Shore, K.A. (2015) Physics and applications of laser diode chaos. *Nat. Photonics*, **9**, 151–162.

24. Marconi, M., Javaloyes, J., Barland, S., Balle, S., and Giudici, M. (2015) Vectorial dissipative solitons in vertical-cavity surface-emitting lasers with delays. *Nat. Photonics*, **9**, 450–453.

Index

a
absorption effects 108, 117
auto-correlation function (ACF) 291, 294, 300, 301, 305
acousto-optic 328–329
acousto-optic modulator (AOM) 23, 24
addressing pulse 23
Adler
– equation 331, 334
– frequency 332, 337, 340
– locking range 334
all-optical buffer 12
amplitude equations in polaritonic basis, 374, 381 *see also* exciton-polaritons
all-normal-dispersion (ANDi) 278, 286, 290, 294, 304
anisotropy 317–327
– birefringence 318
– gain 321
– loss 319
– phase 317–320, 329
anomalous dispersion 166, 171, 176
anomalous group velocity dispersion 141, 142, 151
aspect ratio 77
astronomical units 27
attractor, quasi 20

b
bandwidth
– gain 215–217, 220, 221
– laser-optical 217, 218, 224
– laser-radio frequency 217–219, 225, 226, 231
– microcavity resonance 214, 216, 222, 224
beat note 319, 320, 323, 325–328, 331–336, 338, 341
bifurcation 170, 179
– cross-saturation 324, 330
– diagram 334–337
– Er:Yb:glass 318, 332
– Hopf 20, 337, 339–341
– subcritical 17
birefringence
– cavity 362
– effects 108
bistability 77–83, 88–91, 98, 99, 169, 172
– dispersive optical 15, 17, 18
– optical 1
– of polaritons, 373, 376, 382 *see also* exciton-polaritons
bistable
– behavior 196
– device 190
bound state 233, 234, 238, 243, 245
boundary conditions
– absorbing 109, 111
– effect on soliton dynamics 113, 121–123
– for a ring cavity 117–118, 125
breather 177, 178, 182
Brillouin scattering 22
buffer, memory
– all-optical 86, 94

c
canard explosion 111, 114, 122
cavity polariton solitons, 373–389 *see also* dissipative soliton(s)
– families of solitons 385–387
– moving bright 373, 376–379, 387–389
– multi-hump 378–380
– 1D bright 373, 376–378
– parametric polariton solitons (PPS) 380–387
– 2D bright 387–389

Nonlinear Optical Cavity Dynamics: From Microresonators to Fiber Lasers, First Edition.
Edited by Philippe Grelu.
© 2016 Wiley-VCH Verlag GmbH & Co. KGaA. Published 2016 by Wiley-VCH Verlag GmbH & Co. KGaA.

cavity soliton (CS), 12 *see also* soliton, cavity
- interaction 25
- Kerr 25
- laser 12
- plasticity 21
- temporal 13, 21, 23

C-band 220
centro-symmetric structure 208
CGL *see* complex Ginzburg–Landau (CGL)
chalcogenide, glasses 419
chaos 82, 97, 179, 180
- bi- 352
- synchronization 349

chaotic 234, 247, 252–255, 257
- wave fields 420

chirp parameter 278, 280, 287, 288, 296
chromatic dispersion 165, 166, 168
CMOS 2, 220, 228, 419
complex Ginzburg–Landau (CGL) 232, 238, 241
complex Ginzburg–Landau equation 264
compressive sensing 400, 401, 413
continuous wave (CW)
- component 243–245, 250
- driven resonator 13

conversion efficiency 202, 205
Cubic-quintic Ginzburg-Landau equation (CQGLE) 280, 282, 285, 288, 297, 303
- asymptotical solution 283
- exact solution 281
- experiment 286
- fiber lasers 280
- numerical solution 284

critical coupling 195, 205, 206, 209
cross-gain saturation 353, 355, 361
cross-phase modulation 353
crystalline resonator 129–132, 136, 142, 145–147, 151, 153–156
CW *see* continuous wave (CW)

d

dark soliton 177
delay 77, 79, 80, 84, 85, 87–91, 93–97, 218, 220, 222, 225
detuning 15
diagram 180
dimensionality reduction 395, 397, 414
dispersion 16, 213, 215, 216, 220
- anomalous 16, 27, 277, 306
- effects 108, 117, 120, 125
- managed system 32
- normal 277–279
- relation, 371–373 *see also* polariton dispersion

dispersive Fourier-transform (DFT) technique 254, 255
dispersive waves (DW) 31, 233, 235, 239, 246, 250
dissipation 77, 79, 80, 83, 88, 91, 97, 99, 228
dissipative rogue wave 265, 266, 271, 272
dissipative soliton(s), 231–234, 236, 238–240, 242, 244, 246–250, 252, 254, 256, 263–267, 272, 369–389 *see also* soliton, dissipative
- cavity polariton soliton (CPS) 373–389
- cavity soliton (CS) 370
- energy scalability 279, 283, 292, 296, 302
- families of solitons 385–387
- highly-chirped 278, 279, 281
- multicolor complex 279, 309
- Raman 279, 302
- resonance 283, 284, 295, 296
- weakly-chirped 280, 284

dissipative structures, localized (LDS) 11
domain walls 355
drift 107–108, 125
- in ring cavities 120–121
- in the Swift–Hohenberg equation 109–110, 113

drifting cavity solitons *see* soliton, cavity (CS); soliton, drifting
driving strength 15
dynamics, antiphase 348, 350, 353

e

eigen
- equation 318
- frequency 319, 323, 324, 328
- mode 328, 338, 341
- polarization 319, 325, 330
- state 318–327, 329, 332, 335, 342, 343
- value 318, 319
- vector 318–321, 323–325

electrostriction 27
equation-free 395, 396, 402, 409, 414
erbium (Er)-doped fiber amplifier 357, 359, 360
Er-doped 235, 250, 255
excitability 80, 82, 88, 90–93, 97, 99, 113
- of cavity solitons *see* soliton, cavity (CS); soliton, excitable
- of dissipative solitons *see* soliton, dissipative; soliton, excitable
- quasi-threshold 114, 115
- threshold 113
- types of 113–114

exciton-polaritons 369–389
- amplitude equations 371, 374, 381
- bistability of polaritons 373, 376, 382

- cavity polariton solitons (CPS) 373–389
- dispersion of polaritons 371–373
- Hopfield coefficients 372–373
- modulational instability (MI) 378–379, 387
- nonlinearity of polaritons 372, 375
- parametric interaction of polaritons 379–381, 383, 385–387
- polaritonic basis 372–373
- saturation of Rabi splitting 372

exploding soliton 263, 264, 266–269, 272
external injection 233, 245
extremum-seeking control 402, 403, 407, 410

f

feedback 79, 80, 89–91, 93–99
- delayed 323, 330, 333–334
- frequency-shifted 318, 320, 327–341
- loop 279, 302, 304, 306, 307
- optical 79, 80, 91, 93–99
- optoelectronic 89, 90, 98

femtosecond pulse 277, 278, 290
Fermi-Pasta-Ulam, recurrence 16
2f–3f method 154, 155
fiber
- dispersion
  - – compensating 359
  - – shifted 359
- erbium doped fiber amplifier (EDFA) 220–224
- laser cavity 213–215, 220, 222
- lasers 5, 347, 357, 420
  - – vector 350, 353, 362
- resonator 83
- twist 199
- ytterbium doped fiber amplifier (EYDFA) 221, 222, 224

figure of eight laser (F8L) 232, 240, 249
F8L *see* figure of eight laser (F8L)
four wave mixing 213, 214
- dissipative four wave mixing (DFWM) 213, 214, 228
- filter drive four wave mixing 214, 215, 224, 228

fragmentation 238
free spectral range (FSR) 165, 166
- fiber cavity loop 213, 214, 216–222, 224, 226–228
- filter 213
- microcavity 217, 218, 221, 223, 224, 228

frequency comb 4, 318, 325, 326
- Jones 318
- matrix 318, 321
- vector 325

frequency-resolved optical gating (FROG) 293, 300, 301, 305
front 77, 80, 88, 89
- pinning 88–92, 99

g

gain 173, 176, 215–217, 220, 221
- bandwidth 215–217, 220, 221
- bandwidth-limited 351
- dynamics 239, 241–244
- saturable gain 215
- saturation 353

Gaussian distribution 203
Ginzburg–Landau equation 107, 349
gradients 21
group velocity dispersion (GVD) 31

h

harmonic generation
- second (SHG) 190, 200
- third (THG) 190, 200

harmonic mode-locking (HML) 233, 234, 242, 244–247
heteroclinic, connection 90
high-chirp limit 283, 285
higher-order dispersion, 374–375 *see also* polariton dispersion
HML *see* harmonic mode-locking (HML)
homoclinic
- connection 88
- orbit 97
- snaking 80, 88, 90, 99
- trajectory 352

homogeneous response 19
Hopf
- bifurcation 20, 349
- threshold 29, 30

hybrid (HE,EH) modes 191
hyperbolic-secant pulse 21
hysteresis 196, 197, 233–238, 256

i

inflection point, 370–371, 374 *see also* polariton dispersion
inhomogeneity *see also* polariton dispersion
- applying a perturbation to 114
- in periodically pumped ring cavities 119–123
- in the Swift–Hohenberg equation 109–111

injected CW *see* external injection
instability 235, 243
- Benjamin–Feir 351
- modulation (MI) 15, 17, 18, 213

instability (*contd.*)
- modulational 351
- radio frequency 214, 221, 224, 225, 227, 228
- Risken–Nummedal–Graham–Haken 358
- supermode instability 214, 219, 221, 224

interaction (soliton) 232, 233, 235, 238, 239, 244–247, 250, 256
interaction strength 25

k

Kelly sidebands 32
Kerr
- comb generation 32
- combs 116, 129, 130, 133, 134, 141, 144, 148, 163–167, 173, 175, 182
- effect 117, 232, 237, 246
- frequency combs 116, 125
- nonlinearity *see* Kerr, effect

l

laser
- cavity 278, 279, 295, 297, 302, 304
- dissipative four wave mixing 213, 214, 228
- fiber 277–281, 286, 289, 291–293, 295–298, 302, 310
- filter drive four wave mixing 214, 215, 224, 228
- forced-, driven-, injected 78, 86, 92–98
- mode-locked 213
- modulation instability 213
- multimode 79, 91, 97, 98
- ring 97, 98, 280, 292, 297
- semiconductor 77–84, 86, 88, 93, 94, 98
- solid-state 317, 320, 323, 327, 328, 330, 339
- soliton 78, 79
- supermode instability 214, 219, 221, 224
- vertical cavity surface emitting 77, 78, 80, 81, 86, 89, 91, 95, 98

lidar–radar 333
light
- bullets 3
- emission, chaotic 350

limit cycle 31
localized structures, 4, 77–91, 94, 95, 97–99, 369–389 *see also* dissipative soliton(s)
- chaotic 82
- lasing 78, 98
- spatial 79
- temporal 78, 79, 83, 87, 98

locking
- frequency 318, 320, 323, 341
- frequency-without phase 334, 336
- injection 317, 318
- Laser Optical Feedback Imaging (LOFI) 328
- mode 317, 318
- phase 318, 325, 327, 332–334, 337–341
- range 326, 327, 332–334
- self 318–327, 341

lower-polariton branch, 373, 375, 381 *see also* polariton dispersion
Lugiato–Lefever equation (LLE), 3, 15, 21, 31, 34, 118 *see* spatio-temporal, model
- derivation for a ring cavity 116–118
- homogeneous solutions 118
- with inhomogeneities and drift 120–121
- patterns *see* pattern(s), in the Lugiato–Lefever equation
- solitons *see* cavity soliton (CS)

m

machine learning 395–398, 405, 406, 409, 413, 414
“magic angle,” 370–371, 374 *see also* polariton dispersion
master diagram 283, 296
memory, buffer
- all-optical 86, 94

microcavity, 214–223, 227, 228, 369, 371, 420 *see also* microresonator
- free spectral range (FSR) 217, 218, 221, 223, 224, 228
- modes 216–220, 224, 225
- quality factor (high-Q) 214, 219, 220, 228
- resonance bandwidth 214, 216, 222, 224

microcoil resonator 189, 190
- broken 197
- uniform 193

microfiber, optical 189
microresonator, 4, 369, 371 *see also* microcavity
- microresonator with quantum well (QW) 369, 371
- planar microresonator 369, 371
- semiconductor microresonator 369, 371

mirror
- imperfections 108
- misalignment effects 108

modal expansion model 166, 167, 174
mode(s)
- cavity modes 213, 214, 216–221, 223–225, 227
- dispersion curve 191
- locking 278, 280, 287, 290–293, 296, 298, 302, 310

– microcavity modes 216–220, 224, 225
– mode-locking 213, 214, 217, 218, 227, 228
– phase of a mode 213, 219–222, 225, 227, 228
– supermodes 213, 214, 219, 221, 224
mode-locked lasers 395, 396, 403, 409 411, 414
mode-locking 350
– passive- 353
– polarization- 347
mode-locking (passive) 78, 82–85, 87, 98, 213, 214, 217, 218, 227, 228
– fundamental 82–85
– harmonic 83–85, 87
modulational instability of polaritons 378–379, 387
modulation(al) instability, 6 *see also* primary comb
multiple pulsing 233–236, 248, 252, 257
multipulse *see* multiple pulsing
multiscale approach 241
multistability 85, 86, 233–235, 237

n
nonlinear amplifying loop mirror (NALM) 292
nanofiber, optical 189
nanophotonics 189
Nd:YAG 320, 324, 328, 342, 343
neural network 421
Newton cradle 123
NLP *see* noise-like pulse (NLP)
NLSE *see* nonlinear Schrödinger equation (NLSE)
noise
– amplified spontaneous emission 357
– laser amplitude noise, 214, 221, 224, 225, 227, 228 *see also* radio frequency instability
– laser phase noise 214, 226, 228
noise-like pulse (NLP) 234, 244, 247, 252, 253, 255, 257, 265, 266
nonlinear optical loop mirror (NOLM) 280, 292
nonlinear
– polarization evolution 347
– saturable gain 351
– Schrödinger equation 350
nonlinear polarization evolution (NPE) 232, 235, 236, 238, 250
– overdriving 289, 293
– overdriving-free 279, 290
– scalar form 299
– vectorial model 288
nonlinear Schrödinger equation (NLSE) 14, 117, 118, 168, 279, 285, 298, 302, 303
– externally-driven 14
nonlinear transfer function 198
nonlinearity 278, 280, 287–289, 293, 298, 306, 311
– effective 192
– multipole 208
– surface dipole 208
– thermal 199
normal dispersion 166, 175, 177
NPE *see* nonlinear polarization evolution (NPE)
numerical methods
– Fourier-transform 298
– symmetrized split-step 298

o
optical microcoil resonator (OMR) 189
optical micro-nanofiber (OMN) 189
– loop resonator 205
– uniformity 209
optical micro-resonators 189, 193–197
optical rogue wave 265
optomechanical, resonator 420
overlap integrals 202

p
parametric interaction of polaritons 379–381, 383, 385–387
– amplitude equations 381
– signal, idler and pump polaritons 381
passive Q-switching 317, 318, 329, 331, 333–334, 342, 344
– bounded 318, 334–341, 344
– drifting 335, 337, 338, 344
– entrainment 334, 344
– noise 340, 344
– noise spectrum 339, 340
– phase 333
– phase-amplitude coupling (Henry factor) 330, 340
– phasor plot 337–339, 344
– trapping 334, 345
pattern(s) 107–108
– in the Lugiato–Lefever equation 118–119
– periodic 17
– in the Swift–Hohenberg equation 108–109
– turing 16
pattern (soliton) 233, 234, 238, 240, 241, 244–247, 256, 257
Pearson correlation coefficient 360

Pereira–Stenflo solitary wave 355
phase
– kink, soliton 80, 91
– locked loop 228
– matching 200, 201, 203
– of mode 213, 219–222, 225, 227, 228
– noise 214, 226, 228
– optical 78, 91–99
– space 87, 90, 92, 93, 95
– space topology 80, 91, 99
– symmetry 78, 80, 82, 98
– transition 248, 256
phase-locking 173
phase-transition
– curve 349
– diagram 350, 362
piezoelectric fiber stretcher 22
platform, technological 419
polariton dispersion 371–373
– higher-order dispersion 374–375
– inflection point 370–371, 374
– lower-polariton branch 373, 375, 381
– "magic angle," 370–371, 374
– upper-polariton branch 373
polaritons, 369–389 *see also* exciton-polaritons
polarization
– chaos 359
– Cr:YAG 329, 330
– dependent loss 358
– domain 355
– – wall 348, 356, 357, 361, 362
– – wall soliton 356
– dual 317–330, 332, 342–344
– dynamics 7
– helicoidal 324, 343
– hole burning 347
– insensitive optical isolator 358
– Lang–Kobayashi 330
– mode dispersion 356, 362
– rate equations 317, 332, 333, 335, 342
– relaxation oscillations 317, 320, 328–331, 337, 341
– Runge–Kutta 332
– saturable absorber 324, 329, 330, 343
– self-modulation 318, 321, 323, 327, 342, 343
– self-pulsing 318–320
– state of 357
– stiffness 331
– time-scaled 331
primary comb 171, 174, 179
principal component analysis 397
probability density function 270, 271
pulsations
– antiphase 353
– self-starting 358
pulses
– antiphase- 360
– noise-like 348

q
quality factor 165

r
Rabi splitting, 358, 372–373 *see also* exciton-polaritons
radio frequency instability 214, 221, 224, 225, 227, 228
Raman gain 295, 296, 298, 304, 307
Raman pulse 290, 293–295, 297, 298, 302, 303, 306
resonances 166
resonator 165
– knot 189
– loop 189
– microcoil 189
rogue wave 6, 181, 234, 247, 253–257, 420

s
self amplitude modulation (SAM) 280, 281, 283, 289, 291
Semiconductor saturable absorber mirror (SESAM) 324, 325, 327, 343
saturable absorber 78, 80, 82–84, 86, 98, 279, 280, 291
– fast 347, 348, 350
– shock 352, 354
saturable gain 215
scalar equation 237, 238
self-phase modulation 202, 206
self-referencing 130, 154, 155, 163
shock 352, 354
significant pulse peak power 271
silicon
– nitride 419
– – resonator 31
– photonics 419
slow light 195
slowly varying envelope 166
soliton 11, 176, 180
– advected 111, 115
– cavity (CS) 2, 12, 78, 80, 107, 116
– crystal 6, 233, 234, 238–248, 256
– dissipative 2, 11, 20, 77, 80, 83, 97, 99, 107–108, 125, 347
– drifting 121, 123–124
– effect of boundary conditions 123

– evolution after a perturbation 123–124
– excitable 114–116, 123
– gas 247–249
– Kerr 12
– liquid 247, 248, 250
– molecule 177, 233, 238, 239, 243, 247, 256, 257
– optical 2
– oscillatory 114
– periodic emission 111
– phase 80, 91
– pinned 110, 111, 120, 121, 123
– polycrystal 247, 249
– rain 234, 244, 247, 250–252
– stationary 119
– in the Swift–Hohenberg equation 109
– temporal 354
– topological 99
– train of 111–112, 114, 122–123, 125
– vector 347
– vector dark 356
soliton–solitary pulses 213, 222, 225, 228
sparsity 400–402, 406, 412, 413
spatial
– inhomogeneity *see* inhomogeneity
– structure *see* pattern(s), dissipative soliton(s), cavity soliton (CS)
spatio-temporal
– chaos 354
– chaotic attractor 353
– dynamics 420
– intermittency 352, 353
– model 167
spectra
– optical 286, 293, 294, 306
– radio frequency 293, 305
self phase modulation (SPM) 280, 281
stimulated Raman scattering (SRS) 279, 296
– model 298
– multiple-vibrational-mode 298
– threshold 292, 296
stability analysis 168
steady-state equilibrium 168, 176
step-index fiber 191
Stokes parameter 357
strong light-matter coupling, 369–389 *see also* exciton-polaritons
subcritical 171, 180
supercritical 171, 179
supermode suppression 244, 246, 248
surface roughness 203
Swift–Hohenberg equation 108
– dispersion relation 109
– with inhomogeneities and drift 109
– Lyapunov functional 108
– patterns *see* pattern, in the Swift–Hohenberg equation
– solitons *see* soliton, dissipative; soliton, in the Swift–Hohenberg equation
symmetry, translation 13, 21

t
tapering, optical fiber 189
temporal cavity solitons 13, 21, 23
– breathing 29
thulium, fiber laser source 209
train
– of pulses 119, 120, 125
– of solitons *see* soliton, cavity (CS); soliton, dissipative; soliton, train of
transverse electric (TE) modes 191
transverse magnetic (TM) modes 191
turbulence
– amplitude 352
– phase 352
turing pattern *see* primary comb

u
upper-polariton branch 373 *see* polariton dispersion

v
vertical-cavity surface-emitting laser (VCSEL)

w
wavelength converters 420
– acoustic response 28
wavelength-division multiplexing (WDM) 281, 286, 292, 293, 298, 300, 306–309
whispering gallery mode

z
zero-dispersion wavelength (ZDW) 3 1